A performance-based design framework for base-isolated buildings against ground-borne vibration

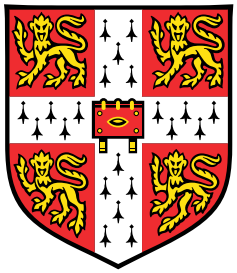

Giuseppe Sanitate

Supervisor: Dr. James P. Talbot

Department of Engineering

University of Cambridge

This dissertation is submitted for the degree of

Doctor of Philosophy

Homerton College

September 2019

Declaration

This thesis is the result of my own work and includes nothing which is the outcome of work done in collaboration except as declared in the Acknowledgements and specified in the text. It is not substantially the same as any that I have submitted, or, is being concurrently submitted for a degree or diploma or other qualification at the University of Cambridge or any other University or similar institution except as declared in the Acknowledgements and specified in the text. I further state that no substantial part of my thesis has already been submitted, or, is being concurrently submitted for any such degree, diploma or other qualification at the University of Cambridge or any other University or similar institution except as declared in the Acknowledgements and specified in the text. It does not exceed the prescribed word limit for the relevant Degree Committee

Giuseppe Sanitate

September 2019

Abstract

Title: A performance-based design framework for base-isolated buildings against ground-borne vibration

Author: Giuseppe Sanitate

Ground-borne vibration in buildings is a recurrent design concern for new developments in the vicinity of surface or underground railways, a common question being whether or not a building necessitates some form of vibration mitigation. This question is commonly tackled by comprehensive numerical modelling of the source of vibration (train excitation), the propagation path (the ground) and the receiver (the building), allowing interaction between the different parts of the complex system with the main focus on the vibration and re-radiated noise levels in the building. Although numerical modelling may be necessary for absolute predictions, it is computationally expensive and not suitable for design purposes. In such a context, different configurations of the foundation and the building may be investigated in order to minimise vibration levels.

A widespread measure of mitigation is base-isolation: the building is mounted on an isolation system composed of either rubber bearings or steel springs. The goal is to de-couple the building from the soil-foundation system in order to reduce the levels of vibration and re-radiated noise in its interior. Despite innovations in the bearings themselves, it is not yet clear how best to evaluate the isolation performance, which relates to the level of attenuation provided. In this dissertation, the Power Flow Insertion Gain ($PFIG$) is adopted as the main metric for the isolation performance. In the context of design, it is desirable to consider simplified methods and models that are able to capture the underlying physics of the problem and to provide an estimation of the isolation performance in terms of the $PFIG$.

A new design analysis framework is presented that can be adopted for this purpose with reference to a staged approach, which relates inherently to the topic of dynamic soil-structure-interaction (SSI).

The design analysis framework considers the free-field vibration represented by incident plane wave-fields, in the form of P-, SV- or Rayleigh waves. A series of simplified methods and/or models are then adopted to account for the *added-foundation effect* (AFE) and the *added-building effect* (ABE) associated with the construction of the foundation and the building respectively. The design analysis framework introduced here is conceptually general, but it is contextualised to the case of portal-frame buildings and surface foundations.

The different assumptions related to the design approach are systematically tested against a rigorous approach that involves the modelling of the building and the soil-foundation system by means of the Dynamic Stiffness Method (DSM) and the Boundary Element Method (BEM) respectively. The frequency-dependent value of the $PFIG$ obtained by the design and the rigorous frameworks, for different incident wave-fields, is in good agreement. The design framework can be then used to inform the design of a base-isolated building, based on the attainable isolation performance, at a limited computational cost. For the specific case of a purely vertical input motion at the base of the building (i.e. normally incident P-wave), the design framework leads to an approximate closed-form expression for the $PFIG$. The latter has conceptual significance and, together with the design framework presented in this dissertation, may form the basis for future guidelines on the design of base-isolated buildings against ground-borne vibration.

Acknowledgements

The work described in this dissertation was carried out at the Engineering Department of the University of Cambridge between October 2015 and September 2019. The project was suggested by Dr. James P. Talbot, who acted as my research supervisor, and the industrial parter WSP Ltd. It has been both an honour and a pleasure to work with Dr. James P. Talbot during these years. I would like to express my gratitude for his continued and enthusiastic support, motivation, insightful comments and for his support during the measurement campaign: really a two-man job!

I am very grateful to WSP Ltd for providing funding for the research. I thank both Dr. Mark O'Connor and Dr. Waleed Hamad for their continued interest and for their positive feedback on the research project. I also would like to thank the contractor Canary Wharf Ltd for granting access to the construction site of the South Bank Place development, without which the experimental campaign would have not been possible. A special thanks goes to Prof. Geert Degrande and colleagues in Katholieke Universiteit Leuven for providing the ElastoDynamics Toolbox (EDT) and the Boundary Element Method Toolbox (BEMFUN), which are used in this work.

I would like to thank also colleagues and friends Dr. Arnau Clot Razquin, Dr. Carlos Pascual, and Dr. Alessandra Bonfanti for the interesting and useful engineering discussions and for the support during the writing of the thesis. I am also grateful to Dr. Fiorenzo Fazzolari for the helpful discussions on plate theory and for the time spent together here at the Department.

A heartfelt thanks goes to my parents Antonio and Rosa, my sisters Sandra and Vittoriana, and all relatives that have supported me during my studies abroad. Thanks also to Elena for sharing this experience with me and for her support during the writing up. Last but not least, I would like to thank all my friends in Italy and abroad for their continued support and presence.

I would like to dedicate this thesis to my parents,
my sisters and to the little one, Adele

Table of contents

List of figures

List of tables

Chapter 1

Introduction

1.1 Motivation for the research

Ground-borne noise and vibration in buildings has become an important matter of concern in crowded cities, due to the pressure to build ever closer to urban railways. Road and railway lines are located either at the surface or underground and, although not being an exclusive source, the induced vibration is referred to as ground-borne vibration. This leads to important serviceability considerations in the built environment, which may involve both vibration and re-radiated noise within existing buildings and/or future developments still being designed. Moreover, evidence suggests that the urban population is expected to grow in the next decades [5] with a simultaneous expansion of the railway infrastructure. An example of this is the city of London: a population growth of about 8.8 % is expected to follow in 10 years time [6]. To accommodate this increase, railway expansion projects are taking place to connect peripheral areas of the city as well as increasing railway links in the city centre. Examples of this are the Crossrail project [7], which is intended to deliver the new Elizabeth line running across London from east to west, and the more recent Crossrail 2 project [8] connecting the far north-east part of the city to the south-west.

Existing buildings are subject to these new railway routes, which make urban areas, once deemed quiet, potentially vulnerable to vibration and re-radiated noise. The Elizabeth line [9] is now close to completion and expected to open on March 2021 [7]. The line includes both surface and underground railways. Apart from having implications on the built environment during its construction (e.g. ground movements and possible building damage from tunneling operations [10, 11]), the opening of a new railway route changes the vibration levels in the surrounding. This is the result of a rather

complex interaction involving the source (including a possible dynamic interaction between railway tunnels [12]), the built environment and all of what lies in between in the ground. There is evidence to suggest that this last part may involve complex subterrenean structures, since a mapping of seven boroughs in London has counted over 4500 new residential basements [13], comprising gyms, pools, cinemas and wine cellars [14] of different sizes, which have been granted planning consent since 2008. The presence of such man-made underground structures, paired with the inherently complex nature of the ground, makes the task of vibration and noise predictions an arduous job for the practising engineer.

A different scenario may be encountered in practice for the development of new buildings. In major cities, the limited availability of quiet sites often leaves no alternative but to develop in the vicinity of an existing surface and/or underground railway. An example is the redevelopment of the Shell Centre at South Bank in London [15]. The 9-storey wings of the iconic Shell Centre have been demolished to make room for 7 new and tall residential and office buildings. A genuine question then arises on whether or not ground-borne noise and vibration will affect negatively the life standards of the occupants of the new buildings, the latter being generally different from the pre-existing ones. This is part of ground-borne noise and vibration assessments that may involve scoping, empirical methods [16] and/or predictions based on numerical modelling [17]. The goal is to ascertain whether or not vibration and re-radiated noise levels within the building are below accepted thresholds provided by existing standards [3, 18] and/or studies on human well-being [19, 20]. Occasionally, the concern is the disturbance of sensitive equipment in specialist manufacturing or research facilities [21].

A recent study of a collection of 56 commercial vibration assessments [22] from 9 different countries, reports that ground-borne noise and vibration predictions are above the allowable limits in the 31 % and 44 % of the investigated cases respectively. The limits dictated by existing standards, paired with the increasing public awareness [23] and the future growth of the urban population, make the use of vibration abatement measures inevitable for controlling vibration and re-radiated noise in buildings that are prone to unacceptable levels. Different mitigating measures are available for reducing vibration and re-radiated noise levels and they will be discussed in Chapter 2.

A common mitigating measure is base-isolation: the building is mounted on an isolation system composed of either rubber bearings or steel springs. Base isolation of buildings has been used since the 1960s [24] and still represents a valid mitigation technique. It relies on the decoupling of the building from its foundation [25] for reducing the levels of transmitted vibration and re-radiated

noise within the building. Different types of building have been mounted on springs in the past, including offices and apartments [17, 26, 27], and specialist buildings such as concert halls [28, 29], cinemas [30], broadcasting studios [31] and hospitals [32]. Despite being a commonly adopted strategy, there is still a lack of guidelines covering the design of base-isolated buildings.

The practising engineer is required to evaluate the benefit of inserting isolation, once the latter is deemed necessary. At the moment, this is often addressed by consideration of a mass-on-a-spring model, in which the building is represented by a rigid mass on the spring representing the isolation. There is enough evidence to suggest that this overestimates the isolation performance [33, 34]. Moreover, no account is given to the soil-structure interaction, hence completely disregarding the presence of the ground underneath the building.

The current research presented in this dissertation has the aim of developing practical guidelines for the evaluation of the isolation performance in ground-borne vibration. This is undertaken by a first-principles approach and by breaking down the complex soil-foundation-building interaction by assuming incident wave-fields as representative of ground-borne vibration, thus without modelling the source explicitly and neglecting any source-receiver interaction. The aim is to provide a rigorous but efficient methodology for the practising engineer, based on a staged approach that considers the dynamic soil-foundation-building interaction. This research project has been proposed by Dr. J.P. Talbot and the industrial partner WSP Ltd with the intent of forming such guidelines for the design of base-isolated buildings against ground-borne vibration. It has been inspired by the aforementioned Shell redevelopment project to be constructed just above the Northern and Bakerloo lines at South Bank in London.

1.2 Objectives of the research

The primary aim of this research is to provide the basis for a design analysis framework of base-isolated buildings against ground-borne vibration. This is to be achieved by developing simplified methods and models for addressing the dynamic soil-foundation-building interaction in the context of ground-borne vibration. For this purpose, a staged-approach is considered in order to have control on each part of the dynamic soil-foundation-building interaction. Different objectives for the research can be identified as follows:

- to summarise the basics of the underlying physics and to break down the dynamic soil-foundation-building interaction into two parts that define a staged approach: the soil-foundation interaction and the soil-foundation-building interaction;
- to introduce a reference problem that may be approached by both a rigorous and a design analysis framework; the two analysis frameworks are related by means of simplifying assumptions that are tested by comparison;
- to introduce and to test a simplified method and model for considering the soil-foundation interaction of a concrete slab foundation;
- to introduce a simplified foundation-building model for addressing the soil-foundation-building interaction;
- to compare the results of the isolation performance obtained by the design and the rigorous analysis frameworks in order to validate the former;
- to seek experimental evidence of the soil-foundation and the soil-foundation-building interaction by means of a measurement campaign undertaken during the construction of the Shell redevelopment project.

Both the design and the rigorous analysis frameworks refer to numerical modelling undertaken with programs written specifically for this dissertation using the technical computing software Matlab [35]. Moreover, rigorous models of the soil-foundation system have been implemented by means of the Matlab toolboxes EDT [36, 37] and BEMFUN [38], kindly provided by Prof. Degrande and colleagues in Katholieke Universiteit Leuven.

1.3 Outline of the dissertation

This dissertation is divided into five different parts, which are tightly connected.

An overview of the previous work related to ground-borne vibration and relevant to this dissertation is presented in Chapter 2. The general problem is introduced with a discussion on the source of vibration, and on the response and modelling of the ground, the foundation and the building. A summary of the commonly adopted measures at the source, at the receiver and in between the two is presented with the main focus on base-isolation. A review on the available metrics for the evaluation

of the effectiveness of mitigating measures is presented. The chapter concludes with a summary of the current practice as to decide whether to base-isolate a building.

Chapter 3 presents a single-point coupling model aimed at investigating the salient aspects of base-isolation. A simplified foundation-building model is then presented with reference to surface foundations and portal-frame buildings. This model is used to evaluate the isolation performance in a simplified manner starting from an input motion. The chapter concludes with design considerations relevant to base-isolated buildings.

Chapter 4 focuses on the investigation of the soil-foundation interaction of a concrete slab foundation with consideration of incident wave-fields. The consideration of rigid regions at the free-surface of the slab is then discussed in Chapter 5 with the review of Iguchi's method as a simplified method to obtain the response of such regions, which is the input motion for the subsequent soil-foundation-building interaction.

Chapter 6 presents the suggested design analysis framework, assembling together the simplified methods and models investigated in Chapter 3, 4 and 5. A rigorous analysis framework is then adopted for comparison and validation of the design framework.

Finally, Chapter 7 reports salient experimental results regarding the measurement campaign undertaken at the Shell redevelopment project at South Bank in London.

The dissertation concludes with a summary of the main outcomes of the research and of possible future research efforts to be undertaken for both a better understanding of the performance of base-isolated buildings and for exploring potential application of the design analysis framework.

Chapter 2

Literature review

Many researchers have investigated parts of the problem related to ground-borne vibration generated by railways and road traffic. Here, at the University of Cambridge, several doctoral theses have been produced on the topic of ground-borne vibration. Research has been carried out on vibration from surface vehicles by Hunt [39] and Ng [40], and from underground railways by Forrest [41]. The latter has been extended by Hussein [42] with the development of the easy-to-use PiP software [43], with the purpose of helping practising engineers to predict vibration levels from an underground tunnel. Transmission of vibrations in piled foundations has been studied by Lo [44] and, more recently, by Kuo [45] with additional reference to twin-tunnel systems. A study on commonly adopted simplifying assumptions for the contact at the soil-tunnel interface, and for soil layering and inhomogeneity has been carried out by Jones [46]. As far as the transmission into buildings is concerned, Cryer [47] approached the problem of modelling the complex building-foundation-soil system by making use of simplifications from periodic structure theory [48]. Talbot [33] extended the latter model, based on the Dynamic Stiffness Method [49], and developed a model of the pile foundation based on the Boundary Element Method (BEM), for studying pile-soil-pile interaction. Moreover, he introduced the concept of Power Flow Insertion Gain ($PFIG$) as a scalar metric for studying the performance of base-isolated buildings against ground-borne vibration. This thesis has the main objective of extending the work of Talbot [33], not to increase the complexity of the foundation-building modelling, but rather to search for simplified methods and models that may provide guidelines for the design of base-isolated buildings. The part that follows in this chapter is a summary of past research efforts in the topic of ground-borne vibration of buildings.

2.1 The problem of ground-borne vibration of buildings

Figure 2.1 illustrates the general problem of ground-borne vibration in buildings. The level of re-radiated noise and perceptible vibration in the building is the final output of an intricate physical problem which involves the mutual interaction of the building with the surrounding ground and the vibration source. Excessive levels of vibration and/or re-radiated noise may cause disturbance to building occupants [50] and/or disruption in specialistic buildings such as, for instance, hospitals [32] and/or concert halls [28]. A number of strategies are available for addressing this problem, the goal of these being to act either at the source [51, 52], through the transmission path (e.g. wave barriers [53]), or at the receiver (building). A particular example of the latter is base isolation, whereby the entire building is supported by springs [54]. As it will be seen in Section 2.6.3, many examples exist of base-isolated buildings located close to different sources of vibration such as underground and surface railway lines. Base isolation of buildings has been used since the 1960s [55] and essentially relies on the decoupling of the building from its foundation [56]. Although it represents a popular technique,

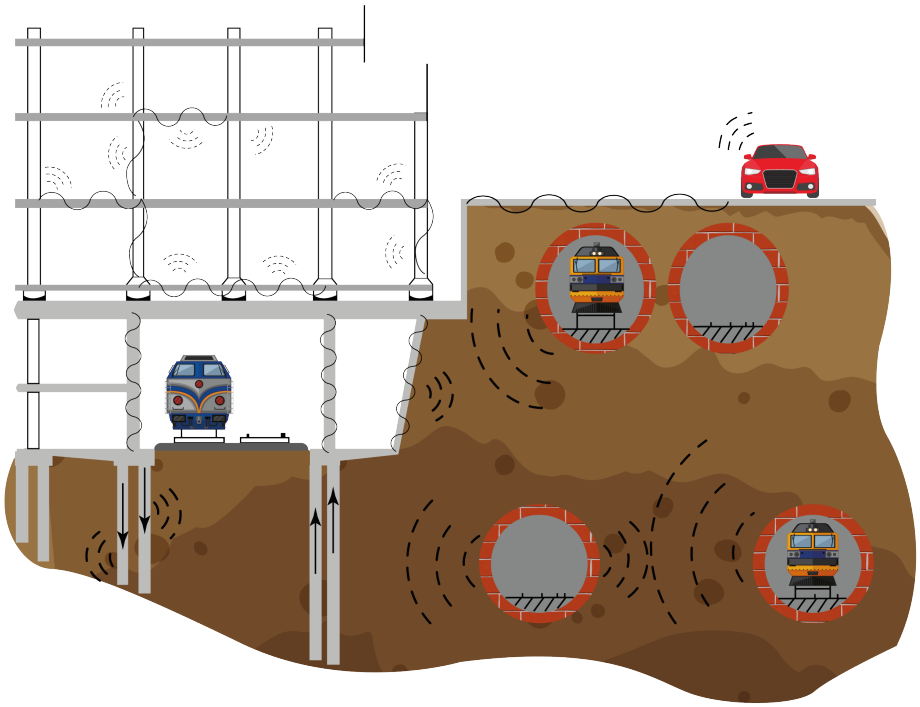

Fig. 2.1 A general problem of ground-borne vibration of a building in the vicinity of train lines and roads. To reduce the transmitted vibration into the building, the latter is mounted on rubber bearings above the basement level. The figure is a re-make of that of Talbot [33], and it is inspired by a diagram of the Wellington Hospital, London, by Grootenhuis [32].

there is a lack of knowledge about the key parameters that influence the dynamic behaviour of the building and the efficiency of the isolation. This dissertation aims at filling this gap by providing an understanding of base-isolation via simplified methods and models. In the following, a summary of the different parts of the problem, as illustrated in Figure 2.1, is presented by starting with the description of the sources of vibration.

2.2 Sources of vibration in the built-environment

Sources of vibration in the vicinity or within buildings can be either natural or man-made. The first type is represented by earthquakes, tremors and wind. The second type can be direct, such as machines or occupant activity (walking, jumping, etc.) within the structure, or indirect, due to construction activities and the passage of vehicles and trains on roads and railway lines. The vibration generated by the latter is commonly referred to as ground-borne vibration.

2.2.1 Seismic vibration

Seismic activity originates at a geological fault where different tectonic plates meet [57]. Because of continental drift, a shear stress build-up manifests along the fault until the frictional resistance is overcome and the plates slip over each other releasing strain energy. The latter travels in the form of waves through the earth's crust reaching the surface and inducing a relatively strong motion. The latter is characterised by a peak-ground-acceleration (pga), often registered at the bedrock, and by a frequency spectrum, which hardly shows relevant components higher than 10 Hz. Hence, a low-frequency, predominantly horizontal, ground motion is considered as an input in more or less advanced analyses of the soil-foundation-building system [58]. Although, earthquake engineering has theoretical concepts in common with ground-borne vibration problems, especially regarding soil dynamics, the different frequency range and the presence of possible non-linearities lead to a somewhat different engineering perspective. It may be worth noticing that the non-linear behaviour of soils influences greatly their properties and may become significant when the shear strains are in the range $10^{-2} - 10^{-3}$ [59], which is often the case during large-magnitude earthquakes [60]. Conversely, in ground-borne vibration, experimental evidence, provided by Connolly et al. [61], suggests shear strain levels of the order of 10^{-4} in the far-field of a surface railway. This indicates

the use of linear-elasticity for the modelling of soils in ground-borne vibration for locations that are sufficiently far away from the source.

2.2.2 Construction activities

Construction activities that lead to vibration in the surrounding built-environment include piling, tunnelling, compaction of ground, excavation and blasting. These are temporary vibration sources that rarely affect the cosmetic and structural performance of nearby buildings, and generally concern the nuisance of their occupants. Hiller & Hope [62] give an overview of the levels of peak-particle-velocity (ppv) that can be expected for different activities and compare them with acceptable thresholds of the British Standards for both human perception [63] and for possible damage levels in buildings [64]. As of today, construction works are often located in urban areas, the piling activity covers particular interest, with several techniques (drop-hammer, vibro-hammer and press-in piling) having a different effect in terms of induced ground-borne vibration [65, 66]. Levels of vibration due to construction activities typically lie between 6 and 160 mm/s [62] and the frequency content, which depends on the specific activity, is generally lower than 100 Hz.

2.2.3 Road traffic

Experimental work on traffic-induced ground-borne vibration has been carried out by Hunt [39], who has highlighted the influence of the type of road surface on the frequency-content of the resulting spectra, which can be confined below 40 Hz (e.g. trunk road) and/or have content up to 100 Hz and more (e.g. concrete motorway). He also reported a main feature of the resulting spectra having two peaks below 20 Hz, which correspond to the body-bounce and wheel-hop frequencies of vehicles. This has been also demonstrated by the experimental work of Hao [67], who reports a magnitude of the associated velocity response spectrum between 0.1 and 1 mm/s. An additional consideration for traffic-induced vibration is the presence of speed control cushions and humps. This has been explored experimentally by Watts [68], who concluded that such measures may lead to perceptible levels of vibration in residential areas.

2.2.4 Underground and surface railways

The mechanisms through which moving trains induce ground-borne vibrations in the surrounding ground have been reviewed in a recent paper by Lombaert et al. [69], while a discussion of the main

vehicle and track parameters affecting the induced vibration levels is offered by Thompson et al. [70]. Three mechanisms are important for the production of vibration: quasi-static loading, parametric loading and the loading induced by the wheel/rail roughness.

The quasi-static loading results in a low-frequency vibration from 0 to 20 Hz and it is associated with the deflection of the rail-system under each bogie of the train. As the the train moves, these local deflection 'bowls' move with it, thus inducing an harmonic excitation at a fixed location in the surrounding soil.

Parametric excitation results from periodic features of the rail-system, including the associated supporting structure. The periodic change can be stiffness related and usually involves the presence of regularly spaced sleepers on which the rails rest. As the wheels of trains pass from the suspended rail to the supported rail, a sudden change of stiffness is experienced, which results in parametric excitation at the *sleeper-passing* frequency. This depends on the velocity and the sleeper spacing and, for common railways, can have values between 40 and 140 Hz for ordinary or high speed trains respectively [69]. Experimental measurements by Heckl et al. [71] demonstrate the importance of such a phenomenon, with a clear identification of the sleeper-passing frequency for trains with different velocity on the same railway. Although this is the most noticeable cause of parametric excitation, any other spatial variation of the track and/or the subsoil can induced such a mechanism; this may involve, for instance, variation of the ballast conditions, variation of ground properties and any other defect of the infrastructure (e.g. badly aligned rail joints).

In general, the wheel and/or the rail roughness is considered the predominant cause of ground-borne vibration for conventional railways [72]. The rolling noise is caused by undulations of the wheel and the rail surfaces, which may result from rail corrugation. This has been categorised by Grassie & Kalousek [73] in six different categories, which occur because of different damage mechanisms and result in different wavelengths of the rail roughness. The latter, together with wheel circumference and the train velocity, are the main parameters for the definition of the induced harmonic forces at the wheel-rail interface. Without any detailed description in this summary, relevant studies on this topic have been carried out by Remington [74, 75] and Thompson et al. [76]. How the induced vibration propagates through the soil and reaches a building via its foundation is reviewed in the next section by discussing the ground and foundation dynamic response.

2.3 Ground and foundation response

This section gives an overview of soil dynamics, associated with both incident wave-fields and forced excitation, as well as summarises the existing modelling methods for the dynamic response of foundations.

2.3.1 Wave propagation in soils

The simplest idealisation of the ground is a homogeneous, isotropic, linear-elastic half-space. This representation is traditionally adopted in soil dynamics because offers a useful interpretation of wave propagation in a solid [77, 78, 57]. The latter can support two different *body waves*: *P-waves* or *compressional waves* that are characterised by a particle motion along the direction of propagation and *S-waves* or *shear waves* with a particle motion that is perpendicular to the direction of propagation. Shear waves may be further divided into *SV-waves* that are polarized in the vertical plane and *SH-waves* with a particle motion constrained in the horizontal plane. Body waves are non-dispersive and correspond to wave equations obtained from the dynamic equilibrium of a continuum as reviewed in Appendix C. The propagating speeds V_P and V_S, related to P- and S-waves respectively, depend only on the Lamé constants λ_s, μ_s and the density ρ_s of the soil.

While propagating body waves travel undisturbed in a homogeneous full-space free of obstacles and/or boundaries, they undergo *mode conversion* next to boundary conditions, for instance, in the form of a stress-free horizontal plane, which materialises the half-space condition. In the latter, a third type of non-dispersive wave exists known as Rayleigh wave, after the pioneering work of Lord Rayleigh [79], which propagates at a speed V_R along the free surface as discussed in more detail in Appendix C.

In general, all three types of wave propagate from a localised source at the free-surface [80]. The partition of the average radiated power among the three wave types was first investigated by Miller & Pursey [81, 82] with reference to a flexible circular vertical source (i.e. constant stress distribution). Based on this assumption, the calculation of the radiated power, performed at a great distance from the source (i.e. in the *far-field*), is based on the superposition of point loads composing the flexible source. No phase difference between waves originating from different portions of the source is assumed, which is true only for the limiting *static case* [83]. For a vertical circular source on the free-surface of an elastic half-space with Poisson's ratio $\nu_s = 1/4$, Miller & Pursey found that

about $2/3$ of the total radiated power is carried by Rayleigh waves. This classical work is commonly referred to as a benchmark in soil and foundation dynamics [84]. For instance, Woods referred to a schematic representation of the results of Miller & Pursey as an introductory understanding of the vibration field generated by a localised source at a free-surface. This was part of a larger experimental study on the effectiveness of trench barriers as mitigating measures from vibration sources [85]. After about 25 years, Meek and Wolf [83] revisited the approach of Miller & Pursey [82] for the calculation of the radiated power by considering the actual dimension of the circular source. This was achieved by means of an integration method adopted by Gazetas [86] whose specifics are beyond the scope of this review. The main outcome is that the radiated power quota associated with different wave types is not frequency independent, as for the point-load solution, but strongly dependent on both the dimension of the source and its frequency. In particular, Rayleigh waves carry an amount of radiated power that decreases with increasing frequency and dimension of the source [83]. This is an important outcome for the adoption of a *strength-of-material* approach when evaluating the radiation impedance of localised sources by means of *cone models* [87, 83, 84]. The latter are adopted throughout this dissertation with further details discussed in Chapter 3 and the formulation reviewed in Appendix A.

Elastic waves are attenuated by two mechanisms: *radiation damping* and *material damping*. The former is associated with the increasing area of the wave-front of the propagating wave. Based on the classical result of Miller & Pursey [81] for the vertical point load solution, the area of the hemispherical wave-front for *body waves* increases proportionally to the squared distance r^2 from the source. The total radiated power, which is proportional to the squared amplitude of the displacement [82, 84], has to remain unchanged so that the displacement amplitude must decrease proportionally to $1/r$. The latter is indicative of the general radiation condition for body waves, although a more accentuated attenuation is expected near the free surface typically proportional to $1/r^2$. Surface waves are confined close to the free-surface, typically within one wavelength, so that the wave-front is cylindrical with an area that increases proportionally to the distance r. It follows that the displacement amplitude associated to Rayleigh waves is attenuated proportionally to $1/\sqrt{r}$.

Additional attenuation of waves is also related to the dissipation of energy by friction during the cyclic compression or shear deformation in the soil. This mechanism is usually referred to as material damping and will be discussed further in Chapter 3. In the following an overview of the modelling strategies for foundation systems is presented.

2.3.2 Modelling of foundations

Significant literature exists on the response of foundations. This is a topic of interest in many disciplines such as structural and earthquake engineering, and vibration engineering. This conceptual sub-division is related to the different cases in which the compliance of a foundation system, beneath a super-structure (e.g. building, nuclear power plant, off-shore structure, etc.), has to be considered for the determination of static loads and/or differential settlements at the foundation level, for the definition of an input motion to be considered for the structural response to earthquakes at relatively low frequencies, for the definition of an input motion due to ground-borne vibration at relatively high frequencies and/or for considering the dispersion of energy in the soil starting from a vibration source in the interior of the super-structure (e.g. vibrating machine). It is seldom required to consider a foundation model for the sake of obtaining its response, but rather as part of a theoretical and/or numerical strategy to account for a dynamic soil-structure interaction (SSI) analysis adopted, for instance, for the response of a soil-foundation-building system. Such strategies refer, as reviewed by Wolf [84] and Kramer [57], to two different approaches: a *direct method*, in which the soil-foundation-building system is solved at once, usually referring to the same theoretical or numerical approach; and a *substructure method*, in which the soil-foundation and the building domains are considered separately, typically by referring to different theoretical and/or numerical approaches, and then coupled together by ensuring compatibility and equilibrium conditions at the foundation-building interface. An extensive use of the second method is made in this dissertation. The dynamic soil-structure interaction encompasses many different aspects, as stated by Kausel [88], which can be connected, yet having important differences. Those of interest in this dissertation are related to the response of both a soil-foundation and a soil-foundation-building systems to incident wave-fields, with the aim of studying their influence on the variation of vibration levels as the construction of a building progresses.

The foundation system of reference that is discussed in the following is a surface foundation, as assumed in the rest of the dissertation. As it will be seen in Chapter 3, it is then required to consider both the soil-foundation interaction of a foundation system to incident wave-fields and to refer to a forced-excitation of the foundation for the coupling with a building. Besides this conceptual distinction, the surface foundation may be modelled by different approaches depending on whether the rigid or the flexible conditions apply. The first assumption may be deemed valid in earthquake-related problems, which involve low frequencies and long wavelengths, and therefore allow the

foundation to respond rigidly. In contrast, the frequency range associated with ground-borne vibration from railways, which is the subject of this thesis, lies between approximately 25 Hz and 250 Hz. The resulting wavelengths of the incident wave-field are therefore relatively short and comparable with the dimensions of a typical foundation. In this case, the flexibility of a foundation must be considered.

There are different approaches that have been used to study the response of both rigid and flexible, surface foundations. What follows is not intended to be an exhaustive summary of research contributions to the topic, but rather a discussion on the available theoretical models and on the existing, approximate, foundation models. The study of the dynamic response of foundations dates back to the pioneering work of Reissner [89], who explored the behaviour of a circular disk on an elastic half-space subjected to a vertical, time-harmonic load. Since then, many researchers have contributed to the topic by considering different shapes for the foundation, different contact conditions at the soil-foundation interface, and different theoretical and/or numerical approaches for obtaining the foundation response. An exhaustive review of the main contributions is given by Kausel [88], who introduces the work of Veletsos & Wei [90] and Luco & Westmann [91] as the beginning of the modern era in SSI. These refer to the response of rigid foundations. The first study has considered the lateral and rocking response of a rigid, circular foundation with relaxed boundary conditions at the soil-foundation interface such that the horizontal translational motion is evaluated independently of the rocking motion (and viceversa). A result of this study is the definition of stiffness and damping coefficients of an equivalent spring-damper representation of the soil-foundation system. This introduced idealisation is of paramount importance in earthquake engineering, with several following studies using both theoretical and numerical methods to obtain the frequency-dependent sping and damper coefficients associated with a rigid foundation. Luco & Westmann [91] have approached rigorously the problem of the dynamic response of a rigid, strip foundation with a welded contact at the interface with the elastic half-space and subject to time-harmonic vertical, shear and moment forces. The solution refers to a plane-strain problem and is obtained in the form of Fredholm integrals for the vertical, horizontal and rocking response of the foundation. In another study by Wong & Luco [92], the response of surface, rigid foundations of arbitrary shape is obtained by a numerical procedure by making use of three-dimensional Green's functions for the elastic half-space. A constant stress distribution is assumed on each element defined by a discretization of the foundation domain. A similar approach is used by Karabalis & Beskos [93], but with the definition of a time-domain boundary element formulation. Alternatively, a strength-of-material

approach is used by Meek & Veletsos [94] and by Meek & Wolf [95] for obtaining approximate, frequency-dependent expressions for the spring and damper coefficients of a rigid foundation of arbitrary shape. The theory behind these models is reviewed in the book of Wolf [84], and discussed in this dissertation, in Chapter 3 and Appendix A, for the development of simplified foundation models that can be adopted in ground-borne vibration problems.

Additional attention in the literature has been devoted to the response of rigid foundations to incident wave-fields in the form of P-, SV- and/or SH-waves. Among others, Wong & Luco [96] and Qian & Beskos [97] have studied this problem by looking at either a single or two adjacent rigid foundation respectively. Of particular interest, as used in this dissertation, is the work of Iguchi [98, 99], who introduced a method (Iguchi's method) for obtaining the approximate response to a single and/or adjacent rigid foundations to incident wave-fields. This, together with a boundary-element formulation for surface, rigid foundations, is discussed further in Chapter 5. Moreover, the context in which both the simplified models for the force-response relationship of rigid foundations and Iguchi's method become relevant in ground-borne vibration and in this study are discussed in Chapter 3.

There are few studies, in the context of earthquake engineering, which remove the assumption of rigid response of the foundation. Iguchi & Luco [100] presented an approximate method, based on the subdivision method mentioned earlier [92], for studying the out-of-plane response of a flexible foundation. A comparison is then made on the stiffness (spring) and radiation (damper) coefficients between the flexible foundation and an equivalent rigid foundation of the same area. A complementary problem which considers two adjacent, flexible foundation subjected to incident SH-waves has been studied by Tham et al. [101] by a combined boundary-finite element approach. In the context of dynamic SSI in ground-borne vibration, Auersch & Schmid [102] have considered a combined boundary-finite element formulation for studying the response of a two-dimensional (i.e. structural wall) and a one-dimensional (i.e. flexible foundation as a beam) concrete structure to an horizontally incident wave in the soil. Although the two-dimensional feature of a concrete slab foundation is neglected, they concluded that the response of the flexible, one-dimensional foundation follows the same wave pattern of the excited free-field of the soil, but with reduced amplitudes with increasing frequency. This is a general result that is confirmed by the investigation of the soil-foundation interaction as approached in Chapter 4. A more recent study on this topic has been presented by Auersch [1], who considered an infinitely-long, flexible, strip foundation subject to an incident

Rayleigh wave. The outcome of this study form the basis for the investigation undertaken in Chapter 4, where they will be discussed in detail. The next section gives an overview of the numerical methods available for modelling ground-foundation systems.

2.3.3 Numerical methods for soil-foundation models

From the previous overview of the research efforts in foundation modelling, it can be concluded that it is rarely possible to obtain analytical solutions associated with the response of a foundation. Moreover, different configurations of the soil-foundation system, such as soil layering and/or irregular geometry, make the use of numerical modelling necessary. The main numerical methods used in ground-borne vibration are briefly reviewed in the following.

Finite Difference Method

One of the earliest developments intended to overcome the difficulty of finding closed-form solutions for complex problems, in structural vibration, is the finite-difference method (FDM). Depending on the problem, one-dimensional, two-dimensional or three-dimensional, and depending on the formulation (e.g. elasticity, visco-elasticity, etc.), the equations of motion are derived for the continuous domain and then evaluated at a grid of nodes, representing the domain, by replacing the associated derivatives by finite-difference approximations. The governing equations for the domain can be then reported to a set of algebraic equations that can be solved by matrix algebra. More details on the procedure can be found, for instance, in a report of Blanch [103] or in the relevant textbooks. Although this method has been adopted in the past, nowadays its use has been overtaken by more efficient numerical methods (e.g. the Finite Element Method). However, this method remains popular in the ground-borne vibration industry, for instance the FINDWAVE [104] package is adopted to model ground-borne vibration from train lines [105].

Finite Element Method

Another numerical method that finds a widespread use in structural vibration is the Finite Element Method (FEM). The method refers to the adoption of finite-sized elements for which the governing equations are known and relatively simple (e.g. beam elements). The domain is then meshed with a number of finite elements, which may refer to different formulations (e.g. beam, shell, continuum elements) and then assembled together to yield a system of algebraic equations that

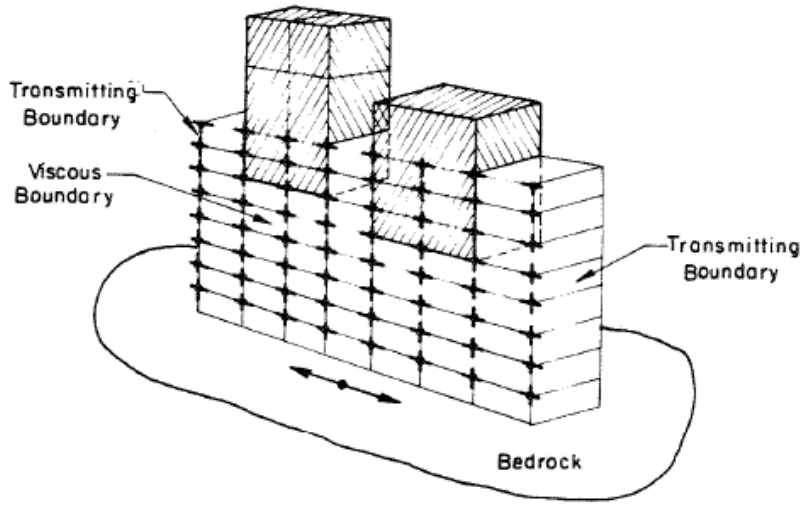

Fig. 2.2 An illustration from Lysmer et al. [107] of a FEM modelling for structure-soil-structure interaction analysis

can be solved by matrix algebra. The details of the method are beyond the scope of this review and can be found in many textbooks available in literature, for instance the book of Zienkiewicz [106]. An example of application of the FEM to dynamic SSI is reported by Lysmer et al. [107], with the development of FLUSH, one of the first examples of a soil-structure interaction software in earthquake engineering (see Figure 2.2). There are two main aspects worth discussing for the adoption of the FEM for wave propagation problems in soil-foundation-structure systems. One relates to the assumed dimension for the finite-element mesh. The use of a relatively coarse mesh may result in the filtering of high-frequency components for which the associated short wavelengths cannot be modelled by widely spaced nodes. Kuhlemeyer and Lysmer [108] provide a rule of thumb for the maximum element dimension that should be limited between one-eight and one-fifth of the shortest wavelength involved in the wave propagation problem in hand. In reality, as it will be seen in Chapter 5 for the response of a finite slab foundation, this depends on the formulation of the adopted finite-element and on the type of wave propagation problem (e.g. relevance of possible diffracted wave-fields). It should be noted that the computational cost of the method increases with an increasing number of elements. This has an important influence when modelling the semi-infinite extent of the ground by means of the FEM. According to the finite-element formulation, the element mesh should extend towards infinity to address this issue. At the early stages of the use of FEM for SSI analyses, the domain would be curtained at a 'long-enough' distance from the structure without properly ensuring the radiation condition at the boundaries. This has the two-fold effect of

increasing the computational cost of the model and to suffer from potential, spurious reflections of waves from the boundaries that could impair the accuracy of the structural response. Much effort has been dedicated to the development of absorbing boundaries, which, defined at the boundary of the ground domain, may decrease the number of elements required and increase the accuracy of the model. A first attempt was made by Lysmer & Kuhlemeyer [109]; they introduced the viscous boundaries, as used in FLUSH, consisting of damper elements based on the properties of the soil. The effectiveness of such absorbing boundary is optimal for normally incident waves, but can result in important reflections for generally incident waves. Other available absorbing boundaries, used at the early stages of the topic, are reviewed by Kausel [110]. Another strategy is presented by Bettess [111] and Bettess & Zienkiewicz [112] with the definition of *infinite elements*; they suggest the use of shape functions analogous to Lagrange polynomials, but including an exponential decay term. A similar strategy is proposed by Basu & Chopra [113] with the use of perfectly matched layers that are able to absorb, almost perfectly, outgoing waves with non-tangential angles-of-incidence. This is a commonly adopted strategy in commercial FEM software, for instance Abaqus [114].

Boundary Element Method

In contrast with the FEM, the boundary element method (BEM) [115] is well suited to problems with unbounded domains. Thanks to the use of the Betti-Rayleigh reciprocity theorem and the use of elastodynamics fundamental solutions (Green's functions), the problem can be formulated on the boundary of the domain, thus only the boundary needs discretizing rather than the full domain. This effectively reduces the dimension of the problem by one, when compared to a FEM model of a given domain, with a resulting benefit in computational cost. Moreover, the radiation condition to infinity is automatically satisfied by the use of the fundamental solutions. It follows that the BEM is an ideal numerical method for modelling a soil-foundation system; in particular, it is adopted in this dissertation by means of the BEMFUN [38] toolbox using the fundamental solutions from the EDT [37, 116, 36] toolbox, both developed in Matlab [35]. Whatever is the numerical method adopted, deterministic values of the properties of the soil and the foundation should be provided. The following section comments on this and other aspects to highlight, in general terms, the uncertainties associated with a soil-foundation system.

2.3.4 Uncertainties associated with a ground-foundation system

A comment worth making relates to the actual conditions of the ground of a site that involves the presence of a building and a source of vibration (e.g. underground railway). The propagation of the vibration, potentially in the vicinity of vibration-prone structures, is influenced not only by the properties and the wave-propagation within the soil, but also by the scattering of waves due to the presence of any obstacles. These may manifest, in urban areas, in the form of services (e.g. water pipelines and sewers) and/or any other subterranean structure. A site in such a developed urban area is commonly referred to as a *brown-field* site. It may be then the case that the idealised homogeneous elastic half-space condition scarcely materialises in practice. Indeed, even if the site of interest falls onto an undeveloped land (i.e. *green-field* site) in the vicinity of a railway, this usually involves heterogeneous ground conditions, which, in fortunate occasions, may involve only soil layering. The complexity of the ground, in both the green-field and the brown-field sites, leads to scattering of body and surface waves that may make ground-borne vibration challenging to predict.

With reference to an underground railway source and to the green-field condition, Jones [46] considered different simplifying assumptions that are commonly adopted in practice to make ground-borne vibration predictions. Two assumptions have been tested: the welded contact at the tunnel-soil interface [117] and the homogeneous assumption for the soil [118]. Jones et al. [119] have explored the effect of additional assumptions for a total of six commonly disregarded aspects of the underground railway environment, namely, the presence of a twin tunnel, piled foundations, track with discontinuous slabs, soil inhomogeneity, inclined soil layers, and irregular contact at the tunnel-soil interface. The resulting variations due to the simplifying assumptions of not considering such conditions ranged from ± 5 dB to ± 20 dB. In the ground-borne vibration community, a common level of accuracy is in the order of ± 5 dB; these results indicate clearly that the accuracy, obtained by considering simplifying assumptions, may be poor and not acceptable in practice. In general, for any prediction of the vibration level in the building prior its construction, it is advisable to compare measurements at the surface of the green-field or brown-field site with the predicted vibration levels obtained by modelling the source and the ground, in order to check for significant sources of uncertainty. Recently, Kuo et al. [120] have suggested a hybrid procedure, consisting of a combination of field measurements and numerical methods, that is based on the separation of the source and the propagation terms, based on the conceptual definitions provided by the Federal Transit Administration [16]. They argue that such a hybrid approach may address the issues related to either a strictly numerical approach, with

consideration of deterministic properties of the involved parameters, or to empirical methods, which are commonly used in practice and based on a collection of experimental data. This general discussion indicates the difficulty of any absolute prediction of vibration levels because of the uncertainties associated with a source-soil-foundation system. Next, an overview is given on the dynamic response of a building.

2.4 Building response

The advancement of building technology and the use of open-space architecture have led to structures whose elements are lighter, wider and less damped than those used in the traditional construction industry [25]. Primary structural resonances occur at relatively low frequency, in the same frequency range of train-induced ground-borne vibration. Consequently, the passing trains may cause ground-borne vibration that in turn are amplified at floor level depending on the mass, stiffness and damping distribution within the building. For lightly damped buildings, a typical train spends enough time passing by a building in order to trigger a resonance state [32]. Differently from other types of low-frequency excitations (e.g. earthquake), the short wavelengths and the generally-oriented wave-field associated with ground-borne vibration lead to an input motion with different phase and amplitudes next to each column at the base of the building. At column-floor connections, the axial and bending vibration of a column are partially converted in bending and axial vibration of beams, and viceversa. Generally, the levels of vibration are attenuated up to the building (i.e. at higher floors) because of the energy dissipated during the vibration, assuming there are no other sources of vibration within the building. Vibration levels depend on the specific location, the direction examined and the frequency content of the input motion.

The magnitude of ground-borne vibration rarely reaches levels that might concern the cosmetic and structural performance of the building [25]. The main issue is related to the annoyance of the occupants. Structural vibration of building components such as floors, walls and partitions radiates sound, known as re-radiated noise, that can be significant within the audible frequency range, above approximately 20 Hz. A common mitigating measure for such a serviceability issue, as discussed in Section 2.6.3, is base-isolation of buildings. In the following a review of available modelling strategies for base-isolated buildings, and buildings in general, is presented.

2.4.1 Modelling base-isolated buildings

The principle of base-isolation may be illustrated by the transmissibility of a single-degree-of-freedom (SDoF) system composed by a rigid mass, representing the building, and a spring, representing the isolation. For a unit vertical input w at the base of the spring, the response of the rigid mass w_b is reported against the dimensionless frequency f/f_S in Figure 2.3 for an isolation with viscous and/or hysteretic damping (a discussion on structural damping is presented in Chapter 3). This is a classical example in mechanical vibration that is qualitatively discussed here, more details can be found in literature [121]. The response of the mass results in an amplification at low frequencies with a maximum, for a lightly damped isolation, at about the natural frequency of the undamped system defined as $f_S = \frac{1}{2\pi}\sqrt{\frac{k_S}{M}}$, with k_S the stiffness of the spring and M the mass of the building. The building response is attenuated for frequencies greater than $\sqrt{2}\,f_S$. In ground-borne vibration, it is required to reduce vibration in buildings at frequencies higher than 20 Hz. According to the rather simplistic SDoF model in Figure 2.3, lowering the amplitude of the building's response w_b by a factor of 10, compared to the input w, at 20 Hz requires a spring stiffness k_S that provides a natural frequency f_S of about 6 Hz for a building with mass M. The frequency f_S is referred to as the *isolation frequency* and is a commonly accepted parameter for the design of an isolation system serving a building of

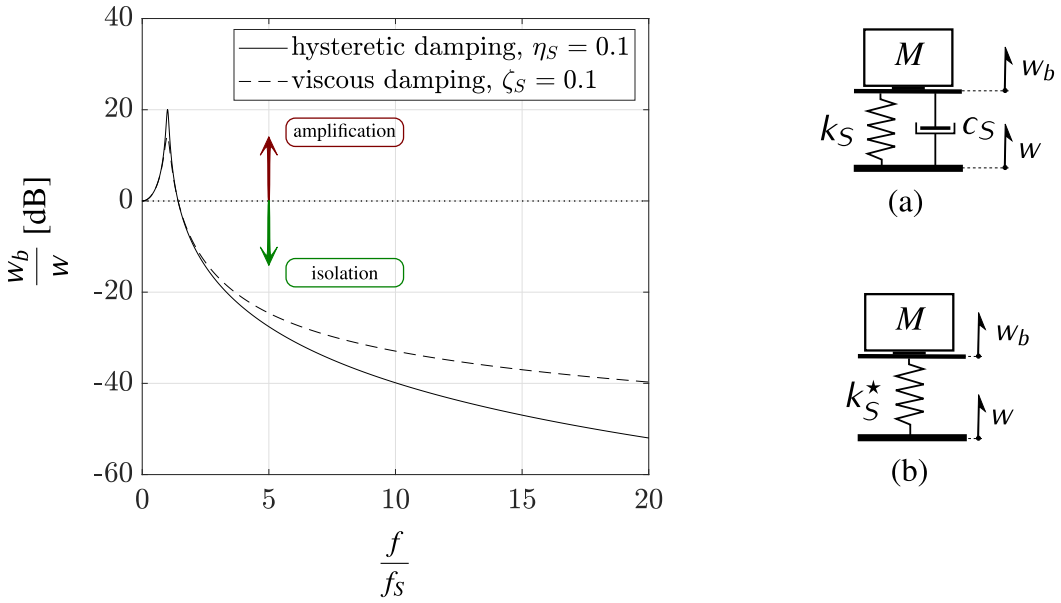

Fig. 2.3 Transmissibility for a SDoF model of a base-isolated building, where the building is represented by a rigid mass and the isolation bearing by a linear spring of constant k_S. Damping in the isolation bearing may be accounted for by (a) viscous dashpot or (b) a complex (hysteretic) spring stiffness.

a given mass M. It follows that an extensive use of the SDoF system is done in practice, not only for defining the specification of an isolation system, but also for evaluating the associated isolation performance by means of the transmissibility in Figure 2.3. In reality, as it will be discussed in this thesis, the physics of the problem is much more complicated and the results in Figure 2.3 tend to overestimate the isolation performance. The latter should be evaluated by means of more appropriate models that account for the soil-foundation-building interaction [122], the multi-directional input representing the vibration environment and a more realistic building model. This is explored in this dissertation starting from the simplified foundation-building models investigated in Chapter 3. Other theoretical models for a base-isolated building, and for buildings in general, are commented in the following as found in literature.

2.4.2 Theoretical models of buildings

Theoretical models of buildings are based either on analytical solutions, usually referring to an idealised building model (e.g. a bar model), or on numerical methods (e.g FEM, see Section 2.3.3) when more involved building models (e.g. complex geometry) need to be investigated.

An improvement to the SDoF discussed earlier can be made by considering the flexibility of the building by means of a bar model. Newland & Hunt [123] and Grootenhuis [32] have explored this possibility showing that the modal behaviour of the building as a bar, with several natural frequencies below 200 Hz, is relevant in the frequency-range of interest with a potential reduction of isolation performance; especially so when a simple foundation model, underneath the building, is adopted to account for radiation of energy into the ground [123]. Similar building models are proposed by Swallow [124] and Sharif [27], but considering also lumped masses and additional springs concentrated at the floors level to represent their contribution to the dynamic response; it is shown that some of the low-frequency behaviour of real building columns is captured.

While these simplified models are able to highlight some of the flaws of the SDoF, they are still limited for their one-dimensional nature. They do not account for the multi-directional input, inducing also bending vibration in the column, and the fact that actually a building is composed of a series of columns inter-connected by floors. A step towards these aspects is made by Cryer [47], who considered a two-dimensional portal-frame building model, via the application of the Dynamic Stiffness Method [49], of infinite extent by making use of the periodic structure theory [125, 48]. An approximate pile foundation model (Novak's pile, see Appendix A), is considered beneath each

column to account for the soil-foundation-building interaction and the three-dimensional radiation condition. Cryer's model demonstrates the importance of the latter with a significant amount of vibrational energy into the ground when the soil-foundation-building system is subject to a point excitation at one of the pile-heads. While some of the features of the SSI are captured, the model still consider only vertical vibration for each pile without accounting for pile-soil-pile interaction. This task is taken on by Talbot [33, 34], who developed a generic model for evaluating the performance of base-isolated building. The model includes the same two portal-frame building of Cryer, but this time considering a BEM model of a pile foundation beneath each column. Based on the results obtained with this generic model, Talbot proposes a better metric , the Power Flow Insertion Gain ($PFIG$), for evaluating the isolation performance; this is discussed further in Section 2.6.4.

Attempts in literature exist to model ground-borne vibration by the finite element method (FEM); for a discussion on some aspects of the method related to SSI see Section 2.3.3. Chua et al. [126] used a FEM model to predict vibration levels in a four-storey office block above twin double-box underground railway tunnels. The model uses a plain-strain assumption to reduce the computational cost and implements non-reflecting boundary to reduce wave reflections. A comparison of results with measured value of peak particle velocity (ppv), at the floor level, is provided with a difference of about 4 dB, but the comparison between the associated third-octave band RMS values is less favourable. A more comprehensive model is developed by Fiala et al. [127, 128] of a three-story office building in the vicinity of a surface railway line. The incident wave-field from a high-speed train is considered by means of lumped-parameter model of the a moving vehicle on a longitudinally invariant track. A three-dimensional FEM model of the building and a BEM model of the ground is considered, while the acoustic response in the rooms is computed via a spectral finite element formulation. The study is numerical and it does not offer comparison with measured quantities, but provides some results for the evaluation of mitigating measures; this will be discussed in Section 2.6.3. A numerical model of a 3-story building has been adopted by Clot et al. [129] for investigating the possibility of modelling the three-dimensional building but only with reference to the vertical degree-of-freedom. The comparison with a complete FEM model gives some indication of the response agreement, but no comments are made on the associated inaccuracy for absolute prediction of vibration levels. Recently, an investigation on the influence of uncertain subsoil conditions has been carried out by Papadopoulos et al. [130] by means of a finite element model with perfectly matched layers (see Section 2.3.3) absorbing boundaries and by assigning a probabilistic value to the shear modulus in the

soil. The models discussed here can be computationally expensive to a different extent depending on the adopted formulation. However, they all are rarely adopted by practising engineers for predictions of vibration levels, especially at the design stage.

Another method with high computational cost is the finite-difference method (FDM) (see Section 2.3.3). This finds application in ground-borne vibration of buildings. An example is the commercial software FINDWAVE [104], which can be used to model a tunnel-soil-foundation-building system in the time-domain [105].

Statistical Energy Analysis [131] is another numerical technique for structural vibration. Craik [132] has explored the use of this method for the prediction of sound transmission of a three-storey building by modelling 98 subsystems; comparison between measured and calculated coupling loss factors between different subsystems has shown a favourable agreement at relatively high frequencies, but differences up to 15 dB in the frequency-range of interest of ground-borne vibration. Trochides [133] adopts a SEA approach to model building vibration from an underground tunnel; comparison between the results of the approach and measured values of the mean square velocity, in frequency-bands, at the building's floor of a scaled model is made. While the frequency-dependent trend is captured, significant differences are shown at relatively low frequencies with more than 10 dB differences in the 250 Hz band. As these examples demonstrate, in order for SEA to be applied in structural vibration of buildings, the structure must have a sufficient modal density so that individual modes are unimportant, and the vibrational response may be described in terms of the average vibrational energy. This is something that rarely occurs in ground-borne vibration of buildings, for which the frequency range of interest goes down to 20 Hz where the modal behaviour of the building can be important. For this reason SEA is considered inappropriate in the field of ground-borne vibration of buildings. In the next section methods commonly adopted by practising engineers for modelling buildings are explored.

2.4.3 Empirical models of buildings

A number of empirical models for investigating the vibration response of buildings to train lines are found in literature. They all refer to a subdivision of the general problem in three main terms referring to the source, the propagation path and the receiver. These are all considered as independent and they are evaluated on the basis of a statistical set of measurement data referring to octave or third-octave bands.

Two empirical procedures are presented by Hood et al. [134] for both the prediction of vibration and re-radiated noise within buildings in the vicinity of underground railways. Both the calculation procedures start with track-side measurement data and combine them with a series of factors or transfer functions obtained by a statistical analysis of available measurements collected in a database. A similar approach is followed by Kuppelwieser [135], with the difference that some of the transfer functions along the step-by-step procedure may be obtained either by theoretical models or by database analysis. Additional examples of similar, semi-empirical procedures are proposed by Melke [136] and Madshus et al. [137].

While these empirical methods may be useful as scoping methods for predicting the vibration and re-radiated noise levels within the building, they should be accompanied by a more rigorous theoretical method that accounts for the physics of the problem. The limitations of empirical methods are as follows: the difficulty for a compiled database of measurements to be statistically significant for a plurality of sources, propagation paths and building typologies; and the fact that actually the adopted factors and/or transfer functions are assumed to be independent for each part of the problem (source, propagation and receiver), while in fact they are interconnected.

2.5 Human response to ground-borne noise and vibration

Human response to vibration and re-radiated noise is not easily identifiable since it relies on the individual, both in terms of physical and emotional sensitivity. Moreover, measuring acceptable vibration levels does not guarantee acceptable noise levels, and vice versa. The noise caused by vibrating structural components may be annoying even though the vibration cannot be felt. Alternatively, a low-frequency vibration, between 10 and 60 Hz [135], could be annoying while the related noise is acceptable.

The degree of discomfort due to vibration depends on the duration, the number of occurrences and whether the event occurs during the day or the night. The standard BS 6472-1:2008 [3] introduces the concept of the vibration dose value expressed as:

$$\mathrm{VDV} = \left(\int_{t=0}^{T} a_w^4(t)\,dt \right)^{\frac{1}{4}} \tag{2.1}$$

where $a_w^4(t)$ is the frequency-weighted acceleration and T is the duration of the vibration event. Continuous, intermittent and shock exposure can be considered with the calculation of an equivalent

Place and time	Low probability	Possible	Probable
Residential buildings 16 h day	0.2 to 0.4	0.4 to 0.8	0.8 to 1.6
Residential buildings 8 h night	0.1 to 0.2	0.2 to 0.4	0.4 to 0.8

Table 2.1 Vibration dose values $[m/s^{1.75}]$ ranges which might result in various probabilities of adverse comment within residential buildings (from BS 6472-1:2008 [3]).

VDV value. This metric of human exposure to vibration is advantageous when compared with the RMS values because it accounts also for the duration of the vibration event and not only for its magnitude. Table 2.1 provides ranges of VDV with an associated (qualitative) probability of occupants' adverse comment. Values for both VDV during the day and the night are given, being the latter more restrictive. Other standards refer to different descriptors of vibration levels, such as KB values of the DIN 4150-2:1999 [138] or the VdB values of the Transit Noise and Vibration Impact Assessment document [16].

There is still a lack of guidance for what concerns the acceptable limits of re-radiated noise. Some documents of transportation agencies (FTA [16] and TfL [139]) suggest that a sound pressure value $L_{AS,max}$ of 35 dBA represents, generally, the dividing line between barely perceptible and distinctively perceptible noise. The threshold of noise levels depends also on the category of the building under examination. The threshold values for residences and buildings where people normally sleep are lower than those attaining buildings with primarily daytime use [16]. Another document of the Transit Cooperative Research Program by Zapfe et al. [140] defines the "probability of high annoyance" based on a survey of 1306 residents in the vicinity of railway lines in five different cities. This study confirms that the probability of high annoyance for a 35 dBA sound level is in the range of 6% to 11%, close to the value of 12% suggested by FICON [141] for which significant average community reaction is expected. These indications are confirmed by a recent study of the effects of ground-borne noise from railway tunnels on sleep [20].

The human exposure and annoyance depend upon both perceivable vibration and re-radiated noise. Howarth and Griffin [142] first suggested that a combined value of both noise and vibration levels can better indicate the human response. Thus, while the current standards and technical reports refer to either vibration or noise levels as indicators of the human exposure, the scientific community is oriented towards overall railway impact descriptors that are able to consider both the vibration and re-radiated noise levels. Peris et al. [143, 19] argue that future guidelines should pay special attention to night disturbances when designing railway impact descriptors, since night activities on

railways, for example maintenance operations, can induce higher level of annoyance than daytime train pass-bys.

2.6 Measures for reducing ground-borne vibration

A number of strategies are available for mitigating ground-borne vibration in buildings, by addressing the source, the propagation path or the building itself. A general review of the different measures is presented in the following.

2.6.1 Measures taken at the source

Measures taken directly on the train infrastructure have the obvious result of benefiting any nearby structure by reducing the induced incident wave-field. Track maintenance is the first consideration, with particular attention to track settlements and damage or deterioration of rail crossings. Talbot [52] has investigated the influence of rail crossings of a tram railway on the sound pressure levels within the auditorium of the Royal Concert Hall in Nottingham. It has been shown that increased values of up to 10 dB(A) may be obtained with respect to sound pressure levels induced by the tram on a plain line of the railway. As a measure of reducing re-radiated noise, a new lift-over crossing design was suggested effectively reducing the sound pressure levels by up to 6 dB(A). Moreover, the comparison of the noise levels before and after a grinding operation on the line suggests that rail grinding, as part of a mantainance operation, may reduce re-radiated noise by up to 3 dB(A), although this consideration is site-specific. An additional measure available for surface railways is the inclusion of ballast mats in the design of the track infrastructure. This is explored numerically by Costa et al.[51], who conclude that this method of mitigation acts both on the train-track system and on the induced wave-field but shows amplifications of vibration levels at relatively low frequencies, up to 40 Hz for the examined case.

Different measures may involve the modification of the bogie design. Wilson et al. [144] suggest that by reducing the suspension stiffness and the unsprung mass it is possible to reduce the induced vibration associated with the bounce and wheel-hop modes. There is a number of rubber products that are aimed at reducing noise and vibration transmission and are posed beneath the rails, the base-plates, and/or the sleepers [33].

An important measure taken at the source is the installation of a floating slab track (FST), often used with underground railways. This involves mounting the whole track system on a concrete foundation slab that isolated by means of rubber bearings or steel springs. Although it may be an effective mitigating measure, Forrest [41] suggests that its performance can be impaired by interaction with the soil-tunnel system. It is not always possible to act at the source of the vibration problem, especially when the concern is about a new building to be erected in the vicinity of an existing railway. In these cases measures are to be taken along the propagation path or at the building.

2.6.2 Measures along the propagation path

The modification of the propagation path may be an alternative for reducing the vibration associated with an incident wave-field at given site. This often involves the construction of deep trenches or underground barriers, between the source and the receiver, that are able to shield a vulnerable site by diffraction of the incident wave-field. One of the first investigations on screening of surface waves is credited to Woods [85], who set up an experimental work based on dimensionless width, height and length of open trenches related to the Rayleigh wave at the site. A relation for the reduction factor with dimensionless distance is obtained with the general conclusion that larger trenches are required at greater distance from the source, in the form of a vibrating footing, to accomplish a given amplitude reduction. An additional insight is obtained by Hung et al. [145], who consider both open and in-fill trenches. They show that open trenches are most effective and that the effectiveness of such barriers depends on their dimensions compared to the wavelength involved in the problem. Coulier et al. [53], after a numerical and experimental investigation on the effectiveness of stiff barriers, arrive at the same conclusions showing reduction from 5 to 12 dB for their particular experimental set up.

An additional method is a subgrade stiffening, mostly used for surface railways on relatively soft soil. This consists of introducing a stiffer layer just below the railway, sometimes known as wave impedance block (WIB). A recent study by Thompson et al. [146] shows that a reduction of induced vibration of about 4 to 10 dB can be obtained in the relevant 16-50 Hz third-octave bands. While those discussed here are all viable measures in a green-field condition, the presence of infrastructure may make their use unsuited for urban areas. In this situation, there is no alternative left but to act at the receiver, the building.

2.6.3 Measures taken at the building

Different options may be adopted in the building to reduce structural vibration in its interior due to ground-borne vibration. A commonly used measure is base-isolation, but other options may be explored at the design stage of a foundation-building system.

Base-Isolation

Base-isolation of buildings is a well established technique that is adopted to reduce vibration transmission into the building by inserting isolation bearings at the base of the primary structure in order to de-couple the building from the soil-foundation system [25]. The first example of an isolated building in the UK is Albany Court, a seven-storey building erected over St. James' Park Underground Station, London in 1965 [55]. At that time both the improving technology of structural rubber and the awareness towards ground-borne vibration led the way to mounting a building on rubber bearings. An alternative is the adoption of helical steel springs that were deemed uneconomical and lacking of inherent damping until the 1980s [147]. Nowadays, steel springs are occasionally used in practice but they are generally more expensive of rubber bearings. Common examples of isolated buildings include offices and apartments [17, 26, 27], and specialist buildings such as concert halls [28, 29], cinemas [30], broadcasting studios [31] and hospitals [32]. Although base-isolation represents a valid mitigating measure, there remains a significant lack of design guidance for its implementation. In particular, there is a need for generic, design evaluation methods that account for the essential dynamic behaviour of a building whilst remaining versatile, robust and efficient at the design stage [25].

The isolation system is usually composed of steel springs or laminated rubber bearings installed above the foundation level and below the portal-frame primary structure of the building. It is common, especially for relatively tall buildings, to expect a structural core providing later stability against horizontal loads (e.g. wind). In this case, a layer of elastomeric material, in addition to the bearings beneath the columns, may be interposed between the foundation and the structural core. Although comparison between steel springs and rubber bearings may be found in literature [55, 148–150], the adoption of one technology over the other depends on different aspects of the building design and requirements.

Design of natural rubber components are discussed by Lindley [151], with additional resources that can be found in the books of Naeim [152] and Kelly [153], also with reference to base-isolation of buildings against seismic loading. The dynamic behaviour of laminated rubber bearings is complex

and depends strongly on the type of rubber (i.e. natural, synthetic, etc.). In general, a rubber-like material presents a non-linear behaviour with elastic properties that may vary both with the strain amplitude and the frequency. However, with the small-strain regime associated with ground-borne vibration (of the order of 0.01%), Talbot [33] argues that the effects of said non-linearity are negligible. Moreover, Lindley supports the idea of a negligible frequency-dependency of the elastic modulus of rubber that, for filled rubber above 5°, may vary in the order of 25%. However, a generally higher stiffness of the bearing should be expected in the dynamic regime when compared with the static counterpart, with a ratio that goes from 1.3 to 2 for natural and synthetic rubber respectively [55]. A property of rubber bearings is the inherent damping provided by the material, with values of 2%-3% of critical for low-damping natural and/or synthetic rubber. Higher level of damping may be achieved with the addition of fillers, although this is relevant for higher strain amplitudes experienced for seismic loading [152]. A particular aspect of rubber bearings is the dependency of the provided dynamic stiffness on the effective deflection suffered by the bearing, which in turn depends on the static loading. It becomes evident that the dynamic stiffness provided by the bearing during the life of a base-isolated building may differ from the value calculated at the design stage by means of the isolation frequency f_S and the total mass M (see Section 3.4.1).

On the other hand, steel springs provide a dynamic stiffness that is not influenced by the effective deflection and depends only on the geometry and properties of the helical spring [154]. The static and dynamic stiffness are equal and there is no frequency-dependency of this value. Moreover, the spring behaves linearly given the small-strain elastic behaviour of steel. Steel springs have inherently very low damping, and it is sometimes required to add damping by interposing a layer of dissimilar material (e.g. felt) [55].

Additional aspects may become relevant for the design of an isolation system: structural safety, fire resistance, temperature-dependency, material exposure, cost, etc. Although these are not discussed here, information may be found in the cited literature and in the British Standard [155] withdrawn in 2013. It is worth noticing that base-isolation has significant implications on both the structural design of the building and the total cost of the development, with a cost incidence that may vary from 0.75% and 4% of the total cost of the development according to the cases discussed in the literature [55, 33].

Foundation Design

Another example of mitigation at the receiver is the introduction of a thick slab foundation to help suppress the vibration, primarily by stiffening the base of the building. This approach is usually employed for specialist manufacturing facilities, such as silicon wafer fabs [156], where particularly stringent vibration criteria must be met. It has also been suggested as a straightforward approach for commercial and residential buildings, since it may simply involve constructing a thicker slab than pure structural considerations dictate. However, the extent to which a slab influences the ground vibration field is not clear, and there is little or no guidance for designers. Auersch [1] has explored the influence of an infinitely-long flexural concrete plate in reducing the vibration levels due to an incident Rayleigh wave. The numerical study is carried out by a frequency wave-number approach and considering a relaxed boundary condition at the soil-plate interface. He concludes that in fact the thickness of the foundation drives the attenuation at relatively high frequencies but that amplification occurs at low frequencies. Sanitate & Talbot [157] have considered the problem discussed by Auersch, but this time treating the foundation as concrete elastic layer of infinite extent. The topic is investigated in this thesis, thus more details are given in Chapter 4.

Building Design

In principle, it is possible to act directly at the design stage of a building to avoid resonant dynamic behaviour of the building in the frequency-range of the source (e.g. train line excitation). However, there are two main difficulties. First, a serviceability issue, such as vibration and re-radiated noise within the building, comes in an advanced stage of the design process. At this point, the main structural components have already been designed for bearing capacity. There is little space for a change in the conceptual design of the structure and, in any case, structural and architectural considerations commonly have precedence for the design concept. Moreover, because of the broad-band excitation from 20 to 200 Hz, typical of train-induced vibration, and because of the multi-modal response of a complex building, it is not possible to avoid relevant modal behaviour of the building. Measures may involve the adjustment of mass and stiffness of the floors to move their natural frequencies away from the frequency content of the source. However, this does not avoid a potential transmission of vibration from the columns, which are subject to the incident wave-field. Potential mitigation measure may be taken in the form of damping treatments for floors and partitions, especially when resonant behaviour cannot be avoided. When low levels of noise and vibration are required in part of the

building, for example a recording studio, a floating slab or a "room within a room" system can be adopted [158]. As will be discussed in Chapter 7, a consequence of adding a floating slab is that of introducing potential amplifications that may occur, for instance, when a different source (and frequency) of excitation appears to be relevant. In the next section a discussion is presented on the possible metrics for describing the performance of mitigating measures.

2.6.4 Metrics for the performance evaluation of a mitigating measure

A metric is required for the performance evaluation of any of the explored mitigating measures. Depending on the requirement, the interest can be towards either an absolute or a relative metric of performance. The need for using absolute metrics is related, for instance, to thresholds of vibration and re-radiated noise levels assigned to residential and office buildings. On the other hand, relative metrics provide an idea of the effectiveness of a measure by comparing two scenarios of the source-soil-foundation-building system: with and without the mitigating measure. This, in the context of base-isolated buildings, may provide the practising engineer with the benefit of inserting isolation underneath a building that is still being designed. It is clear that although absolute predictions may be verified experimentally, relative measures may be challenging to obtain experimentally. However, there are examples in literature that are moving towards this direction [159, 160].

Absolute prediction of performance

Absolute predictions of performance can refer to either measure levels of vibration and re-radiated noise within a building or to values obtained by high-fidelity numerical models. The standard BS 6472-1 [3] provides indications (Annex D) as to how to estimate building vibration. The discussion is kept rather general, with the possible description of the vibration source through the analysis of an elastic half space, two-dimensional or three-dimensional finite element method (FEM), finite-difference techniques and boundary element techniques. In particular, FEM is suggested for the numerical prediction of the building vibration. No indication is given about the role of soil-structure interaction and how this might change the displacement field to be applied at the base of the FEM model of the building (Talbot [122]). According to what the standard illustrates, the practising engineer should rely on sophisticated methods of analysis even when assessing the performance of base isolation during the design of a building in the vicinity of a vibration source. This approach is computationally expensive and requires a high level of expertise with numerical methods.

Insertion Gain

Thanks to the advancement of computational tools, the use of commercial finite-difference and/or finite element software is, in some cases, pursued by engineers for a detailed vibration isolation assessment [161]. However, the analysis of the results in terms of waveforms does not lead to clear outcomes in terms of isolation performance, because of the inherent complexity of the problem. The results are usually shown in terms of Insertion Gain (IG) given by the reduction of the response, expressed in decibel, at one location along one direction (e.g. vertical) in the interior of the building. This is reported in Equation 2.2 with $u^{(\text{iso})}$ and $u^{(\text{uniso})}$ the response in the isolated and unisolated configurations of the building.

$$IG = 20\log_{10}\left\{\left|\frac{u^{(\text{iso})}}{u^{(\text{uniso})}}\right|\right\} \tag{2.2}$$

The same metric can be used for other mitigating measures. Woods [85] has referred to a reduction factor of equivalent meaning. Many examples from the literature for ground-borne vibration make use of this metric [33, 146, 53]. It should be noted that, depending on the importance of modal behaviour in the frequency range of interest, this metric can be subject to large spatial variability. This will be discussed in more detail in Chapter 6. Moreover, the IG refers only to one direction of vibration, while in a portal-frame building both axial and bending behaviour are important. There is the need to refer to a metric that considers the multi-directionality of the vibration, yet maintaining a convenient scalar form.

Power Flow Insertion Gain

A scalar measure that is able to account for the multi-directional vibration in a general structure is the mean-vibrational power. Langley [162] presents a discussion on the theoretical analysis of power flow in beams and frameworks. Talbot [33] uses the mean-vibrational power to investigate the isolation performance of base-isolated buildings. This is done by introducing the metric of Power Flow Insertion Gain as reported in Equation 2.3.

$$PFIG = 10\log_{10}\left\{\left|\frac{\bar{P}^{(\text{iso})}}{\bar{P}^{(\text{uniso})}}\right|\right\} \tag{2.3}$$

It should be noted that the mean-vibrational power is the power dissipated in one cycle of vibration for a given domain of the structure. Thus, reference can be made to different parts of the structure, say different rooms of a base-isolated building, to ascertain differences in isolation performance in terms of $PFIG$. There are many examples of $PFIG$ used in the context of ground-borne vibration for the performance of different mitigating measures. Hussein & Hunt [163] refer to a power flow method to calculate the radiated power upwards, where a building foundation would be expected, from an underground tunnel. A study from Coulier et al. [164] investigates the source-receiver interaction by reporting differences in terms of $PFIG$ for two scenarios with and without considering the interaction. Villot & Jean [159] refer to a field prediction of the performance of mitigating measures in terms of $PFIG$. From these examples, it can be seen that the $PFIG$ is finding favour in the research community of ground-borne vibration.

2.7 The decision to base-isolate a building

The decision of whether to isolate a building often relies on measurements of vibration levels taken either at the free-surface (i.e. green or brown field) or in nearby buildings with similar features of the building to be designed [33]. This procedure is commonly used, sometimes paired with numerical predictions of the vibration levels within the building [17]. The latter may be highly affected by the uncertain parameters involved in the problem; the figure of the prediction accuracy discussed in Section 2.3.4 indicates that care should be taken when basing the decision to isolate a building solely on the results of absolute vibration levels obtained by a deterministic numerical analysis.

The decision then falls into a cost-benefit analysis between the reduction of vibration levels attainable by base-isolation and its cost. A thorough review of the implications of isolation for a building is given by Talbot [33]. Practical implications include the reduction of stiffness and structural stability, requirement for additional stiffening and consideration on settlements of the base-isolated building. Besides the practical implications, the practising engineer needs to know the benefit of the isolation to make an informed decision. For this purpose, especially for large projects, comprehensive numerical methods are used to evaluate the isolation performance. This leads inevitably to a large computational cost and a considerable amount of time for carrying out parametric studies. This design strategy is clearly not best suited for a cost-benefit analysis. The ideal strategy would involve the adoption of simplified methods and models, based on engineering

science, that could actually give insights into the performance of base isolation at a preliminary stage. The paramount aim of this dissertation is to investigate on such a first-principles approach.

What often happens is that, during the design of base-isolated buildings, reference is made to the simplistic model of the mass-on-a-spring (see Waller [55]) for obtaining the transmissibility, hence the performance of base-isolation. This model is too simplistic and does not account for [122]:

1. the influence of soil-structure interaction;
2. the actual distribution of mass and stiffness;
3. the damping within the superstructure.

As a result, the efficiency of isolation is, most probably, overestimated because refers to an infinitely stiff soil-foundation system (i.e. rigid base, see Chapter 3). Both the complexity of computational models and the simplicity of the mass-on-a-spring model highlight the need for the development of a design analysis framework that still relies on a simple representation of the foundation-building system, but that is able to capture the underlying physics for the performance of base-isolated buildings, for instance the dynamic soil-foundation-building interaction (SSI). The design analysis framework for the evaluation of the isolation performance, as presented in Chapter 6, is the main outcome of this research.

2.8 Conclusions

Different sources of ground-borne vibration have been reviewed, with roads and railways being the most relevant. As reported by Talbot [33], peak vibration levels occur in the range from 10 to 80 Hz and significant levels rarely exist above 200 Hz. An overview of the ground and foundation response has been presented to both review the principles of wave propagation in soils and to summarise the main research contributions in foundation dynamics that are of relevance for this dissertation. A brief overview is presented of the possible numerical methods for modelling the dynamic soil-foundation response. Research efforts are also discussed on the level of inaccuracy that may follow from common assumptions adopted in ground-borne vibration. Overall inaccuracies for absolute prediction of vibration levels may be expected in the order of ± 5 dB to ± 20 dB.

A general discussion on the building response is presented, together with a qualitative overview of the mass-on-a-spring model of a base-isolated building. It has been pointed out that this model neglects

the soil-foundation-building interaction, an aspect that is of much importance for the evaluation of the isolation performance of a base-isolated building. A brief overview of the human response to vibration and re-radiated noise summarises the thresholds of the vibration dose values and of the sound pressure levels, which are the drivers for possible mitigating measures.

Many of them are discussed with strategies that involve the modification of the source, the propagation path or the building. In this last case, base-isolation is considered of interest for this dissertation, and a discussion of rubber bearings and steel springs is presented. The isolation performance of such devices is often considered in terms of the Insertion Gain and/or the Power Flow Insertion Gain. These have been found to be widely used in the ground-borne community, and they will be adopted in the following of this dissertation. The decision process of whether to base-isolate a building is then commented, with the conclusion that the practising engineer requires simplified methods and models to inform his/her decision. Often, the mass-on-a-spring model is adopted for this purpose with the result of an overestimated isolation performance. Alternative simplified methods and models are to be developed in this dissertation with a resulting design analysis framework for base-isolated buildings. A key physical aspect to consider is to account for the dynamic soil-foundation-building interaction by means of a simplified model. This is investigated in the next chapter.

Chapter 3

A simplified SSI approach for ground-borne vibration of buildings

Predictions of isolation performance for a base-isolated building are desirable for addressing design-oriented specifications, yet they are difficult to obtain without an in-depth modelling of the source, the ground, the building and their interaction. Apart from being computationally expensive, the latter approach requires a detailed specification of many parameters that may be inherently difficult to determine. Moreover, at the design stage, many of the features of the building itself are yet to be established and the comparison of different configurations may be of interest. During the design of a base-isolated building, it is desired to refer to a rather simplified foundation-building model that is able to capture the essential physics of the problem. Because of the intrinsic assumptions of the simplified foundation-building model, which are presented in this chapter, the focus is limited to properly address the soil-structure interaction (SSI) in a simplified manner that may be adopted by practising engineers. This possibility is investigated in this chapter starting from a general design scenario, which makes reference to specific foundation and building typologies.

3.1 SSI in ground-borne vibration: a general design scenario

A general, three-dimensional vibration problem is introduced in the following with particular attention to soil-foundation and soil-foundation-building interaction. This serves as a general design scenario that, by introducing simplifying assumptions, is traced back to a reference problem that accounts for three-dimensional propagation in the soil-foundation system and a two-dimensional representation

of the building. The design scenario refers to a specific class of foundation and building typologies, namely, surface slab foundations and portal-frame buildings. In reality, pile foundations and complex building designs (e.g including a structural core, façade, etc.) are found in practice. Although these cannot be redirected to the design scenario examined in this dissertation, the latter provides a general strategy to approach the SSI in ground-borne vibration. Starting from the design scenario, additional assumptions are introduced for the identification of a single-point coupling model that is further explored in the remaining sections.

3.1.1 Modelling stages and construction process

Let us consider the general case of the construction of a building in the vicinity of a source of vibration represented by buried or surface train lines. Figure 3.1 shows the main construction stages that are

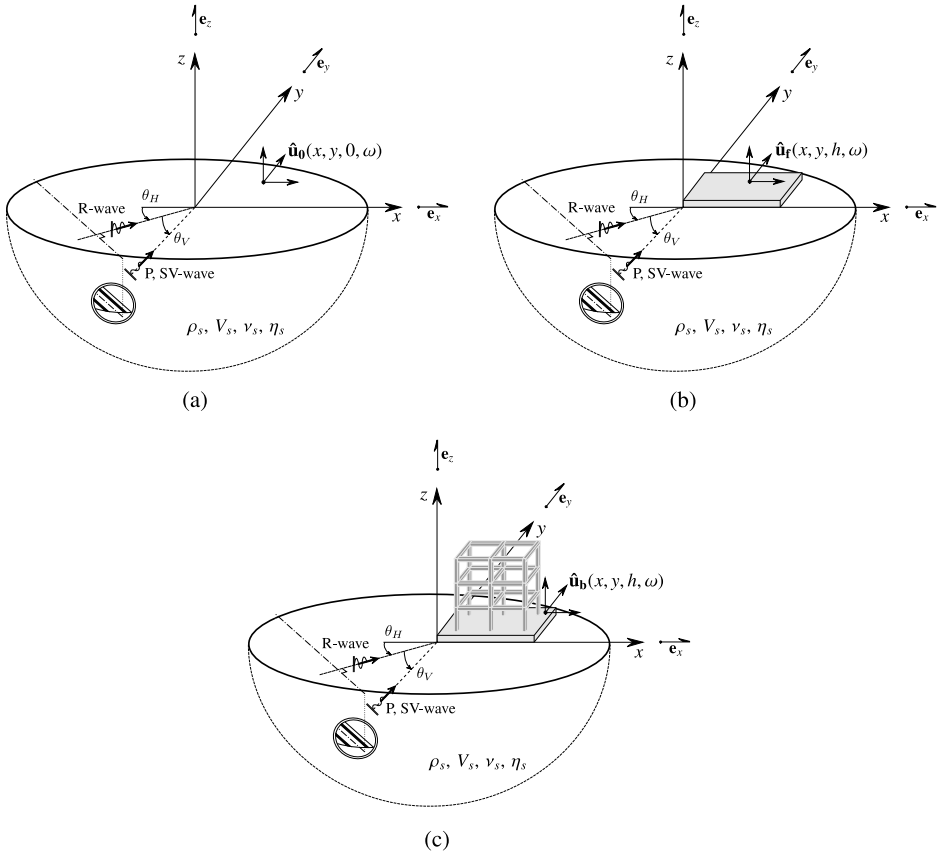

Fig. 3.1 Overview of the general vibration problem: (a) *free-field* displacement generated by underground and/or surface railways; (b) *free-surface* displacement field on the upper surface of the foundation accounting for soil-foundation interaction; (c) displacement field at the base of the building accounting for soil-foundation-building interaction.

also representative of the modelling steps for such a vibration problem. The vibration generated by the source can be expressed in terms of a *free-field* displacement $\mathbf{u_0}(\mathbf{x},t)$ that may represent either on-site vibration measurements that are taken prior any construction activities or the displacement field obtained by some source-propagation modelling of the railway and/or the ground. For the sake of simplicity, wave-fields in the form of incident P- and SV-wave at a vertical angle θ_V and a horizontal angle θ_H are considered here. Moreover, the case of a surface source is represented by a Rayleigh wave at an angle θ_H. Because of the plane-wave assumption, the wave-field can be assumed to be time-harmonic so that $\mathbf{u_0}(\mathbf{x},t) = \hat{\mathbf{u}}_\mathbf{0}(\mathbf{x},\omega)\, e^{i\omega t}$, where ω is the angular frequency and the exponential term in the time variable t is omitted in the following. The construction of a finite slab foundation of thickness h on the free-surface of the ground modifies the initial *free-field* displacement because of the soil-foundation interaction (*added-foundation effect*), with the resulting displacement field $\hat{\mathbf{u}}_\mathbf{f}(x,y,h,\omega)$ at the top of the foundation. The vibration levels are further changed with the construction of the building. The coupling between the building and the soil-foundation system leads to a displacement field $\hat{\mathbf{u}}_\mathbf{b}(\mathbf{x},\omega)$ in the ground and building domain, and a displacement field $\hat{\mathbf{u}}_\mathbf{b}(x,y,h,\omega)$ at the foundation-building interface (*added-building effect*).

3.1.2 A reference problem of ground-borne vibration

Additional assumptions are introduced for obtaining a reference problem that may be addressed by simplified methods and models. A plane-strain excitation in the $x-z$ plane is considered assuming $\theta_H = 0$. Moreover, the slab foundation is assumed to be infinite along the x and y direction so that it can be modelled as an infinite, homogeneous, linear-elastic layer, as shown in Figure 3.2b. The added-foundation effect can be then examined in terms of the frequency-wavenumber displacement amplitudes as discussed in Chapter 4.

A two-dimensional portal-frame building model is considered (see Figure 3.2d). The 2D assumption may result in a reduced *modal density* along the frequency-spectrum when compared with a three-dimensional building model. However, it is believed that the impedance at the base of the building, which is of interest for the SSI, may be reasonably captured with this simplification. This assumption is often found in literature with reference to periodic [47, 125, 33] and finite [165, 166] building models. The portal-frame model represents the primary structure of a concrete-framed building, and it accounts for the propagation of longitudinal and bending waves in the individual floors and columns, and their conversion at the column-floor connection (i.e. node). A symmetrical

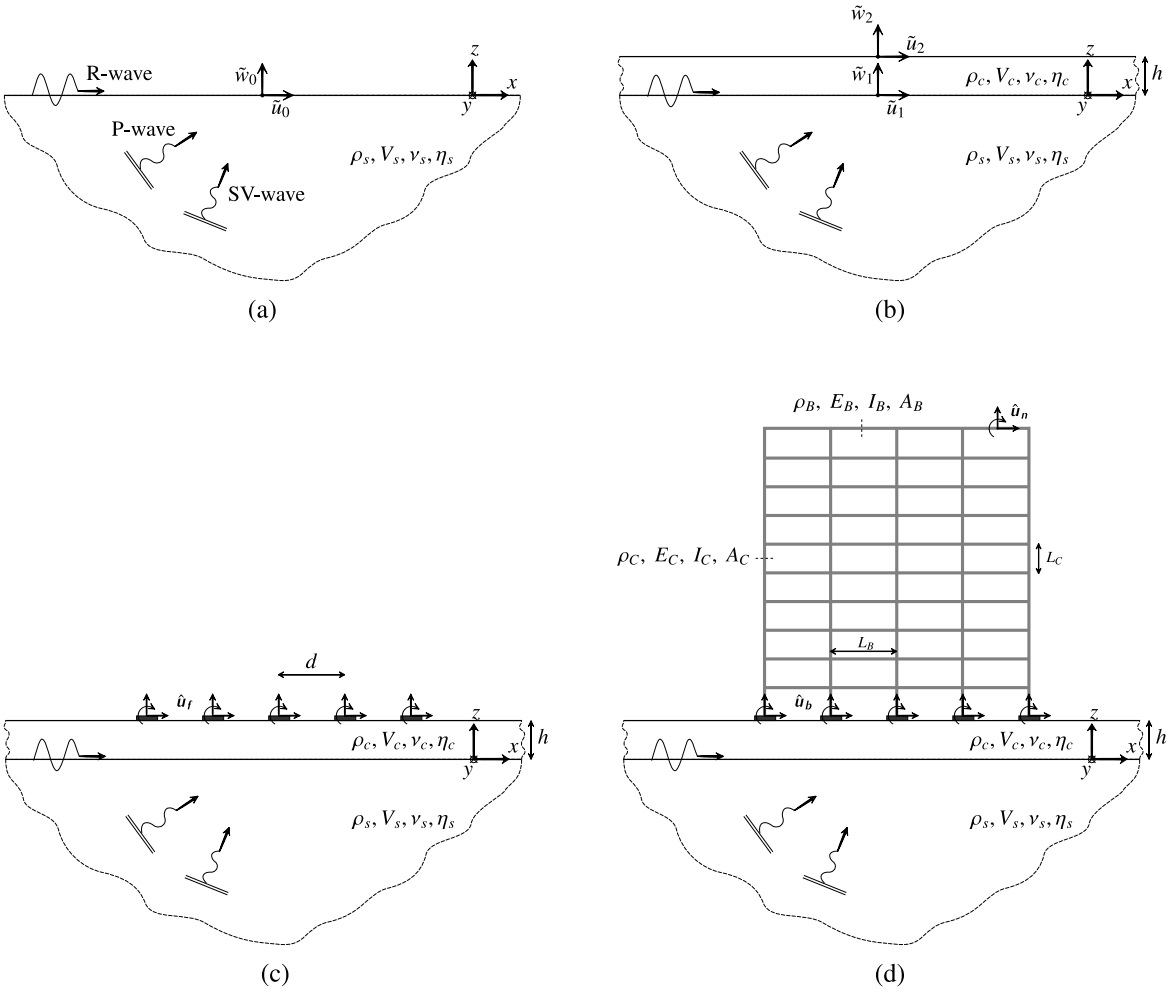

Fig. 3.2 Overview of the reference problem: (a) *free-field* displacement generated by plane-wave excitation; (b) *free-surface* displacement field on the slab foundation as an elastic layer accounting for soil-foundation interaction; (c) response of rigid footings resting on the slab foundation; (d) displacement field at the base and within the building accounting for soil-foundation-structure interaction.

building of 10 storeys and 4 bays is considered (see Figure 3.2d). Table 3.1 summarises the main geometrical and mechanical data of the elements comprising the building, which refer to commonly assumed values of typical concrete structures [167]. Details of the adopted beam-bar formulation for the 2D model are given in Section 6.2.2 and Appendix B, while simplified building models, referring to the same reference problem, are presented in Section 3.3.

The coupling points between the building and the soil-foundation system, as illustrated in Figure 3.2d, refer to the bases of the building's columns. The latter are modelled with an Euler beam-bar formulation with the assumption that *plane sections remain plane* after deformation. The coupling

of the building with the soil-foundation system must be then consistent with this assumption; this is achieved by considering rigid regions of similar geometry to the columns' cross-section as coupling regions at the free-surface of the soil-foundation system. Two soil-foundation systems may be considered for the coupling:

- a series of *rigid foundations* resting on an elastic half-space (i.e. ground), which is a direct coupling of the building with the soil (*benchmark #1*);
- a series of *rigid footings* resting on an elastic layer (i.e. slab foundation) overlying an elastic half-space, which is the coupling of the building with the soil-foundation as reported in Figure 3.2d (*benchmark #2*).

The use of rigid foundations and/or footings may limit the range of incident wave-fields that can be properly studied because of the relatively short wavelengths involved in ground-borne vibration. Whether or not the coupling of a portal-frame building with the soil-foundation system actually leads to a rigid-like contact, in the frequency range of interest for ground-borne vibration, is still an open question that may deserve investigation. A possible frequency-range of validity for the latter assumption may be found by referring to the same argument valid for the discretization in Finite Element Analysis (FEA). The discussion is then limited to incident wave-fields whose shortest apparent wavelengths are at least 5-8 times larger than the dimension of the column [108, 107]. Given typical ranges for the shear wave speed in the soil $V_S = 150 - 300$ m/s and the dimension of the column's cross-section $2b = 0.5$ m, the corresponding maximum frequency that can be considered

Column	Young's Modulus	$E_C = 30$ GPa	**Beam**	Young's Modulus	$E_B = 30$ GPa
	Density	$\rho_C = 2400$ kg/m^3		Density	$\rho_B = 2400$ kg/m^3
	Area	$A_C = 0.25$ m^2		Area	$A_B = 1.25$ m^2
	Length	$L_C = 3$ m		Length	$L_B = 5$ m
	Moment of Inertia	$I_C = 0.0052$ m^4		Moment of Inertia	$I_B = 0.0065$ m^4
	Damping loss factor	$\eta_C = 0.1$		Damping loss factor	$\eta_B = 0.1$
Soil	Shear wave velocity	$V_s = 200$ m/s	**Frame**	Number of bays	4
	Poisson ratio	$\nu_s = 1/3, \underline{0.49}$		Number of storeys	10
	Density	$\rho_s = 2000$ kg/m^3	**Footings**	Number of footings	5
	Damping ratio in shear	$\zeta_s = 0.05$		Area of footing	A_C
Slab	Young's Modulus	$E_c = 30$ GPa	**Nonstruct.**	Building cat.	A - residential
foundation	Poisson ratio	$\nu_c = 0.15$	**dead load**	Partition cat.	1 - weight ≤ 1 kN/m
	Mass density	$\rho_c = 2500$ kg/m^3		non-struct. floor	density 1600 kg/m^3
	thickness	$h = \underline{0.7}, 1.5$ m		non-struct. floor	thickness 0.1 m
	Damping loss factor	$\eta_c = 0.1$			

Table 3.1 Data for the reference problem illustrated in Figure 3.2.

may lie between 60 and 120 Hz. While the latter argument may set limitations on the use of a rigid foundation and/or footing model in ground-borne vibration, it is believed that it is a necessary assumption for approaching the soil-structure interaction in its simplest form.

A commonly adopted parameter in foundation vibration analysis is the dimensionless frequency $a_0 = \omega b/V_s$. Considering typical values of the shear wave speed V_s as above, the columns' dimension $2b = 0.3 - 2$ m, and a frequency range of interest between 20 and 250 Hz, the range of a_0 in ground-borne vibration goes approximately from 0.05 to 10. Unless otherwise specified, Table 3.1 lists the salient properties of the soil-foundation and building models used in this dissertation.

3.1.3 SSI of a single-point coupling model

The reference problem may be examined with respect to a single-point coupling at the base of each column of the building. This further simplification results from neglecting:

- the through-soil coupling between adjacent rigid footings; this is discussed further in Chapter 5 with reference to the distance d and the dimension $2b$ of the footings;
- the through-floor coupling of the columns in the building; this is discussed further in Chapter 6 by means of comparison between simplified and rigorous building models.

A single-point coupling model is presented in Figure 3.3 in the framework of a SSI analysis as introduced in previous sections. The notation is kept general so that it can be conceptually represen-

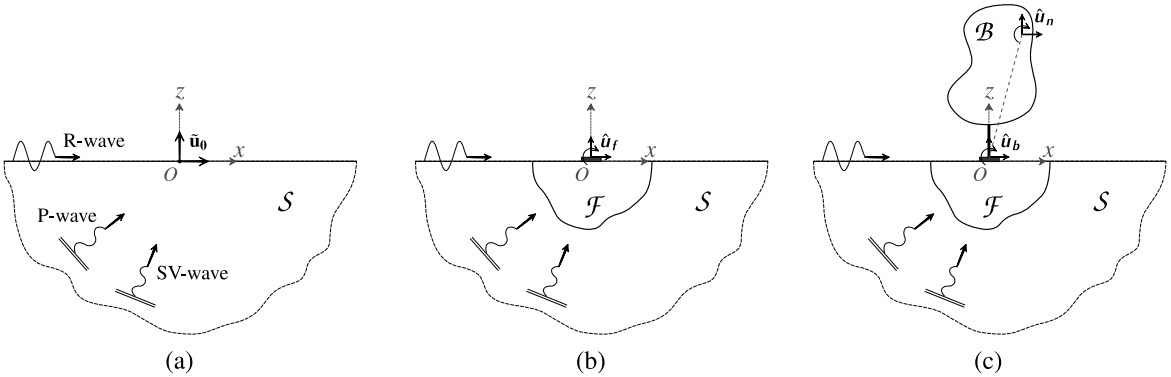

Fig. 3.3 Schematic illustration for the SSI associated with a single-point coupling model. (a) An incident plane wave in the 3D soil system $\mathcal{S}$ leads to the resulting free-surface amplitude $\tilde{\mathbf{u}}_\mathbf{0}$. (b) The presence of a 3D foundation $\mathcal{F}$ is then considered with the resulting response $\hat{\boldsymbol{u}}_\boldsymbol{f}$ at a point O at the free-surface. (c) A 2D building model $\mathcal{B}$ is coupled to the soil-foundation system $\mathcal{F}$-$\mathcal{S}$ with the resulting displacement $\hat{\boldsymbol{u}}_\boldsymbol{b}$ and $\hat{\boldsymbol{u}}_\boldsymbol{n}$ at the base and in the remainder of $\mathcal{B}$ respectively.

tative of both simplified and/or more rigorous models. The three-dimensional (3D) unbounded soil system is denoted by $\mathcal{S}$, the 3D foundation model by $\mathcal{F}$ and the two-dimensional building model by $\mathcal{B}$. As far as the building response is concerned, the added-foundation effect is represented by the response of the footing $\hat{\boldsymbol{u}}_f$. For the reference problem in Figure 3.2, this is divided into two parts: the coupling of a slab foundation (see Chapter 4) and the consideration of the rigid footings at the free-surface (see Chapter 5). In this chapter, the added-building effect is of interest with reference to the single-point coupling model in Figure 3.3b and c.

The displacement after the coupling of $\mathcal{B}$ on $\mathcal{S}$-$\mathcal{F}$ may be written in the form:

$$\hat{\boldsymbol{u}}_b(\mathbf{x_o},\omega) = \hat{\boldsymbol{u}}_f(\mathbf{x_o},\omega) + \widehat{\boldsymbol{H}}_f(\mathbf{x_o},\mathbf{x_o},\omega)\,\hat{\boldsymbol{f}}_f(\mathbf{x_o},\omega) \tag{3.1}$$

with $\widehat{\boldsymbol{H}}_f$ the *frequency-response function (FRF)* matrix of the soil-foundation model $\mathcal{F}$-$\mathcal{S}$ and $\hat{\boldsymbol{f}}_f$ the forces exerted by the building on the foundation at the coupling point O. The displacement and force vectors refer to the 3 DoFs in the $x-z$ plane and can be expanded as follows:

$$\boldsymbol{u} = \left[u,\, w,\, \varphi\right]^T$$

$$\boldsymbol{f} = \left[s,\, f,\, q\right]^T$$

For equilibrium $\hat{\boldsymbol{f}}_f = -\hat{\boldsymbol{f}}_b$, with $\hat{\boldsymbol{f}}_b$ the forces that the foundation exerts onto the building through the point O. The symbol '$\hat{}$' is used for a quantity in the space-frequency domain, with only the space dependence explicitly reported in the following. In general, for a building model $\mathcal{B}$, the response-force relationship can be written in the form:

$$\hat{\boldsymbol{u}}_{bg}(\mathbf{x_g}) = \begin{bmatrix}\hat{\boldsymbol{u}}_b(\mathbf{x_o})\\ \hat{\boldsymbol{u}}_n(\mathbf{x_n})\end{bmatrix} = \begin{bmatrix}\widehat{\boldsymbol{H}}_{bb}(\mathbf{x_o},\mathbf{x_o}) & \widehat{\boldsymbol{H}}_{bn}(\mathbf{x_o},\mathbf{x_n})\\ \widehat{\boldsymbol{H}}_{nb}(\mathbf{x_n},\mathbf{x_o}) & \widehat{\boldsymbol{H}}_{nn}(\mathbf{x_n},\mathbf{x_n})\end{bmatrix}\begin{bmatrix}\hat{\boldsymbol{f}}_b(\mathbf{x_o})\\ \hat{\boldsymbol{f}}_n(\mathbf{x_n})\end{bmatrix} = \widehat{\boldsymbol{H}}_{bg}(\mathbf{x_g},\mathbf{x_g})\,\hat{\boldsymbol{f}}_{bg}(\mathbf{x_g}) \tag{3.2}$$

with $\mathbf{x_g} = \mathbf{x_o} \cup \mathbf{x_n}$, $\mathbf{x_o}$ collecting the DoFs at point O and $\mathbf{x_n}$ collecting those in the remainder of $\mathcal{B}$. Under the assumption that there are no external forces at $\mathbf{x_n}$, the force-response relationship at O may be written:

$$\hat{\boldsymbol{f}}_b = \left[\widehat{\boldsymbol{H}}_{bb}\right]^{-1}\hat{\boldsymbol{u}}_b = \left[\widehat{\boldsymbol{H}}_b\right]^{-1}\hat{\boldsymbol{u}}_b = \widehat{\boldsymbol{K}}_b\,\hat{\boldsymbol{u}}_b \tag{3.3}$$

with $\widehat{K}_b$ the *condensed* dynamic stiffness matrix [168] of $\mathcal{B}$ at the coupling point O. By substitution of Equation 3.3, with consideration of equilibrium, into Equation 3.1:

$$\begin{aligned} & \hat{u}_b = \hat{u}_f - \widehat{H}_f \left[\widehat{H}_b\right]^{-1} \hat{u}_b \\ \therefore \quad & \left[\mathbf{I} + \widehat{H}_f \left[\widehat{H}_b\right]^{-1}\right] \hat{u}_b = \hat{u}_f \\ \therefore \quad & \hat{u}_b = \left[\mathbf{I} + \widehat{H}_f \left[\widehat{H}_b\right]^{-1}\right]^{-1} \hat{u}_f = \left[\mathbf{I} + \widehat{H}_f \widehat{K}_b\right]^{-1} \hat{u}_f = \mathbf{B}\, \hat{u}_f \\ & \hat{u}_b = \left[\mathbf{I} + \widehat{H}_f \widehat{K}_b\right]^{-1} \hat{u}_f = \mathbf{B}\, \hat{u}_f \end{aligned} \tag{3.4}$$

Equation 3.4 is a classical result [25] when analysing the SSI by means of the sub-structure method [166]. The matrix $\mathbf{B}$ is representative of the added-building effect related to the DoFs $\mathbf{x_o}$ of a single-point coupling model as in Figure 3.3. The response of the building at $\mathbf{x_n}$ can be retrieved from Equation 3.2 and 3.3 as:

$$\hat{u}_n = \widehat{H}_{nb} \left[\widehat{H}_b\right]^{-1} \hat{u}_b = \widehat{H}_{nb} \left[\widehat{H}_b\right]^{-1} \mathbf{B}\, \hat{u}_f = \widehat{H}_{nb}\, \widehat{K}_b\, \mathbf{B}\, \hat{u}_f \tag{3.5}$$

It is evident from Equation 3.4 that the added-building effect is characterised by the FRF matrix $\widehat{H}_f$ of the soil-foundation system and by the dynamic stiffness matrix $\widehat{K}_b$ of the building at the coupling point. The next sections review well-known simplified models for both the soil-foundation and the building as represented in Figure 3.3. These may be used to address the added-building effect and to establish a *design approach* for base-isolated buildings that fall into the reference problem as depicted in Figure 3.2.

3.2 Modelling the foundation

A simplified model for a rigid foundation on a homogeneous and elastic half-space may be obtained by a strength-of-material approach introduced by Elhers [169] almost 80 years ago. Many researchers have built on this idea with the purpose of obtaining a simplified dynamic stiffness formulation. Meek and Veletsos [94] presented a formulation for the lateral and rocking motion of a rigid foundation. This was revisited by Meek and Wolf [87] with a generalisation of the truncated *cone models* for such a foundation system to vertical, lateral, rocking and torsional motion. An overview of such models is

given by Wolf [84], with the focus on the time-domain and the frequency-domain formulations of the dynamic stiffness provided by a foundation (e.g. rigid foundation, footing, etc.). The development of simplified foundation models found extensive application for the SSI associated with earthquake ground motions. This represents a *low-frequency* problem for which the wavelength associated with the wave-excitation is larger than the dimensions of the foundation-building system. Ground-borne vibration involves a much higher frequency content that ranges from 20 to 250 Hz. It follows that the response of a building to ground-borne vibration may be defined as a *mid-frequency* problem. The novelty of the approach adopted in this dissertation is that of using the aforementioned simplified foundation models, well-known in the earthquake engineering community, for problems related to ground-borne vibration. This is supported by the fact that cone models are obtained by a doubly-asymptotic assumption for which the response of the foundation model converges to the rigorous solution both at low and high frequencies. In the following the simplified foundation models for a rigid foundation (i.e. benchmark #1) and a rigid footing (i.e. benchmark #2) are presented and validated against the rigorous Boundary-Element-Method models that will be presented in Chapter 5 and 6.

3.2.1 A simplified model of a rigid foundation

Figure 3.4 illustrates the notation of the formulation for the different degrees of freedom for cone models referring to a rigid foundation. Different aspects have been investigated by Meek and Wolf for the validity of the suggested cone model for a rigid foundation [84]. The necessity of considering Rayleigh waves propagating from a localised source, an inherent shortcoming of cone models, may be

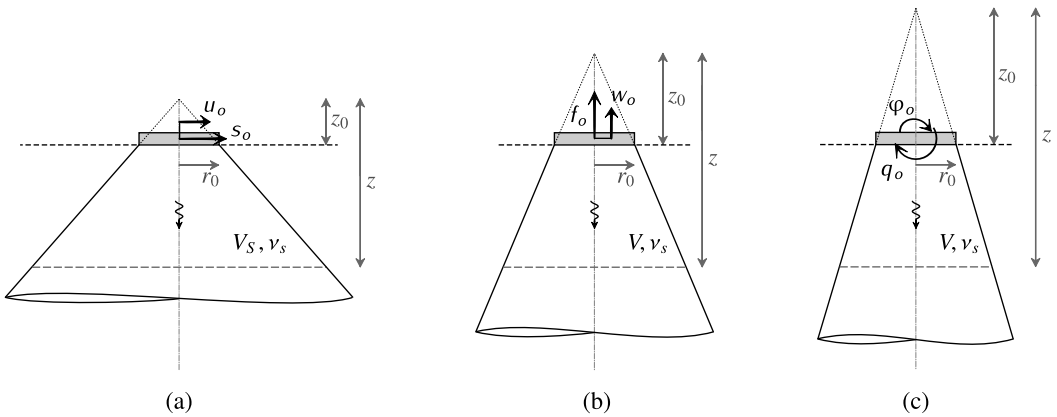

Fig. 3.4 Schematic representation of cone models for a rigid foundation on a homogeneous and elastic half-space representing the ground. Cone properties are shown for the (a) horizontal, (b) vertical and (c) rocking degree of freedom as defined in Table A.1.

evident from classical results of wave propagation in soils [81, 82, 85]. On closer examination, this concern is unfounded for a localised source with *finite dimension* (e.g. foundation), which radiates only a minority of the total power by Rayleigh waves for a dimensionless frequency a_0 greater than 3.5 [170, 83]. For a_0 smaller than this value, Meek and Wolf [170] argue that, as far as the impedance of the foundation is concerned, the cone is located well within the *far-field* boundary of 0.5 λ_R as found by Rücker [171] on the basis of the results of Miller and Pursey [81]. According to Rücker,

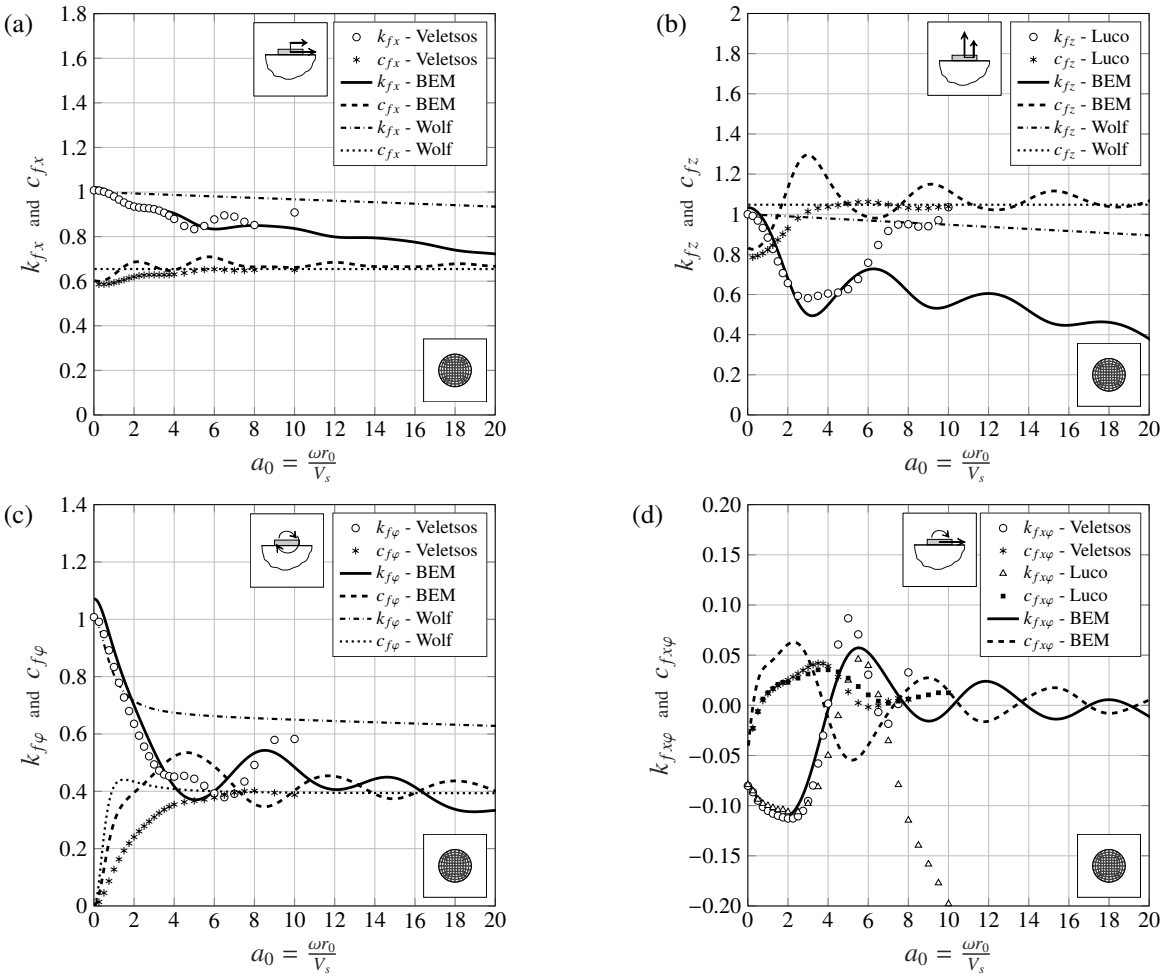

Fig. 3.5 Comparison of the *spring* and *damping* coefficients, as defined in Appendix A, of a circular rigid foundation on an elastic half-space ($\nu_s = 1/3$) obtained by a rigorous BEM approach discussed in Chapter 5 (*black line*), by the cone model formulation by Wolf [84] (*gray line*) and by different relaxed-boundary approaches by Veletsos [90] and Luco [172] (*markers*) for (a) horizontal, (b) vertical, (c) rocking motion and for (d) the horizontal-rocking coupling term.

the attenuation of the displacement amplitude in the *near-field* is inversely proportional to the distance r, well in agreement with the cone model (see Equation A.11).

Figure 3.5 shows the spring and damping coefficients, as defined in Appendix A, associated with a circular foundation resting on an elastic half-space with $\nu_s = 1/3$ and with low material damping $\eta_s = 0.01$. The doubly-asymptotic nature of the cone model is evident from the convergence to the rigorous BEM solution at low and high frequencies of the spring and damping coefficients respectively. The rigorous BEM solution refers to a discretization of the foundation, as in Figure 3.5, with quadratic elements. This is obtained by means of the EDT [116, 36] and BEMFUN [38] Toolboxes following the formulation presented in Chapter 5. Additional results are shown for comparison with reference to two studies by Veletsos and Wei [90] and by Luco and Mita [172], who considered a relaxed-boundary condition at the soil-foundation interface. Also in this case, the spring and damping coefficients appear to converge to the rigorous solution at low and high frequencies respectively. Figure 3.5(d) shows the spring and damping coefficients, related to the static horizontal stiffness $K_{fx}^{(st)}$, obtained by the rigorous approach and by the relaxed-boundary approaches aforementioned. It is evident that the horizontal-rocking dynamic stiffness is one order of magnitude smaller than the direct terms for the other DoFs. Moreover, both the spring and damping coefficient converge to zero at relatively high frequencies. Based on this observation, it appears reasonable to neglect this term when defining the dynamic stiffness matrix of a simplified foundation model as reported in Appendix A. The implications of the latter on the added-building effect are investigated in Section 3.5.1 with reference to the results obtained by a rigorous BEM model of the foundation.

An important comment regards the validity of the vertical and rocking cone models for soils with a high Poisson's ratio (i.e. high compressional wave speed). While, as demonstrated by Meek and Wolf [83], the damping coefficient for both $\nu_s = 1/3$ and $\nu_s = 1/2$ may be written in the form $c_{fz} = \rho_s 2V_s A_0$, between these two values of the Poisson's ratio the doubly asymptotic approximation of the cone model essentially breaks down. This represents a limitation on the use of cone models in ground-borne vibration and, for Poisson's ratio values in this range, the cone model holds a valid approximation only for low values of frequency. By a qualitative inspection of Figure 3.6, the comparison with the rigorous solution obtained by BEM suggests the use of cone models up to a value of approximately $a_0 = 2$, which corresponds to 250 Hz for the reference problem in Section 3.1.2. Meek and Wolf [83] propose the idealised division between *compressible* soils, with $\nu_s \leq 1/3$, and *nearly incompressible* soils with $\nu_s > 1/3$. The difference in behaviour is evident for the vertical and rocking motions: a parabolic decrement of the spring coefficient at relatively low frequencies is present. According to Meek and Wolf this is physically interpretable by a *trapped mass*

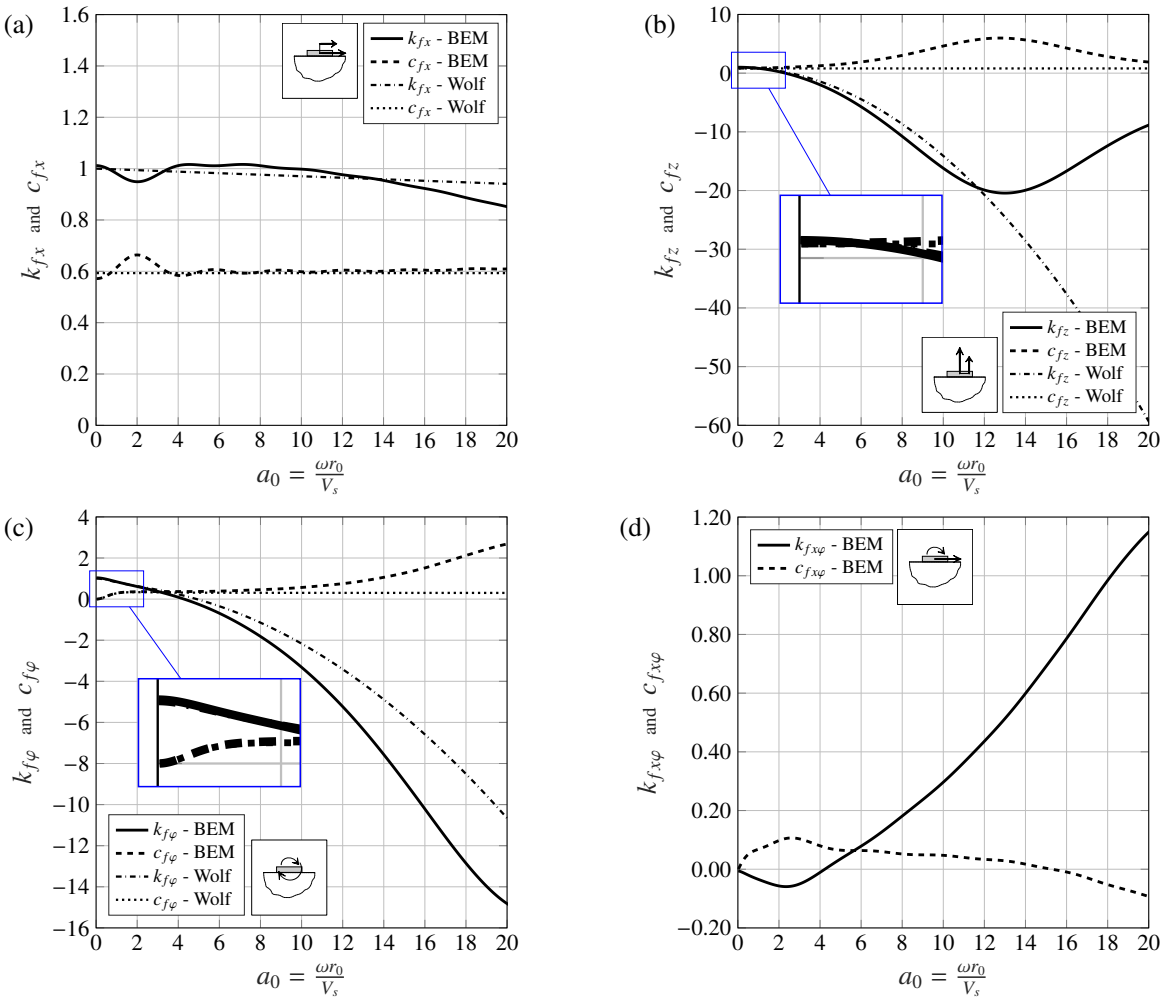

Fig. 3.6 Comparison of the *spring* and *damping* coefficients, as defined in Appendix A, of a circular rigid foundation on an elastic half-space ($\nu_s = 0.49$) obtained by a rigorous BEM approach discussed in Chapter 5 (*black line*), by the cone model formulation by Wolf [84] (*gray line*) for (a) horizontal, (b) vertical, (c) rocking motion and for (d) the horizontal-rocking coupling term.

effect of the soil beneath the foundation. Yet, they do not provide an explanation for the divergence of the damping coefficient that tends to the value suggested by the cone model only at relatively high frequencies (see Figure 3.6(b)). The case of a rigid foundation represents a reasonably simple case of foundation that is suitable for summarising the assumptions associated with the cone model. However, the use of such model in ground-borne vibration is pertinent to each coupling region at the base of each column of the building. In this context, the direct coupling of the building with the soil is unrealistic since a foundation is often interposed between the two (e.g. concrete slab foundation).

3.2.2 A simplified model of a rigid footing

Moving on to the case of rigid footings as introduced in Section 3.1.2, the case of a rigid footing resting on an elastic layer overlying a rigid bedrock has been treated by Meek and Wolf [95] who introduced an *unfolded cone model* (see Figure 3.7). Multiple reflections within the layer are considered compatibly with the cone model assumption (see Appendix A). The resulting dynamic stiffness formulation is in reasonable agreement with rigorous solutions for both the impulse response analysed in the time-domain and the harmonic response in the frequency-domain [95]. An extension of the rigid footing model is presented by Wolf [84], who considered the presence of an elastic half-space underneath the layer. This is done by consideration of a *refraction coefficient* that accounts for the dispersion of energy within the half-space at each reflection-refraction at the interface. The unfolded cone model formulation, reviewed in Appendix A, is adopted in this dissertation for obtaining a simplified foundation model that refers to the more realistic reference problem as depicted in Figure 3.2. Figure 3.8 and 3.9 show a comparison between the spring and damping coefficients of a square rigid footing obtained by the unfolded cone models and the rigorous approach. Two cases are examined referring to a 0.7 m and a 1.5 m thick concrete slab foundation (i.e. layer). The unfolded cone models provide a very good approximation for the damping coefficient, which, as expected,

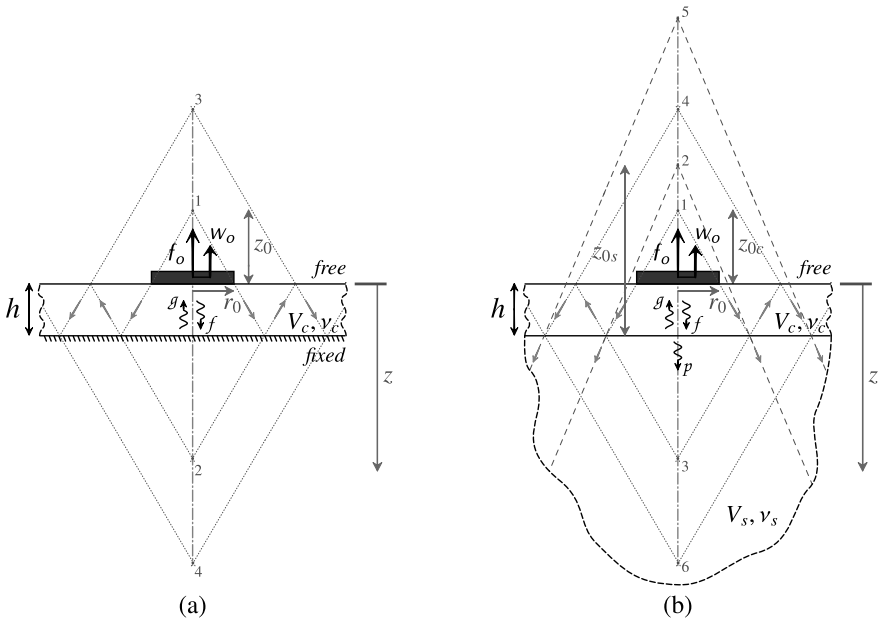

Fig. 3.7 Schematic representation of unfolded cone models for a rigid footing on an elastic layer overlying (a) a bedrock and (b) a homogeneous and elastic half-space.

converges to the rigorous counterpart at high frequencies. The approximate spring coefficient better approximates the rigorous counterpart for translational motions and for a thicker layer, obtaining only an agreement in terms of the order of magnitude for the rocking case. Although the horizontal-rocking spring coefficient $k_{fx\varphi}$ has the same order as the horizontal and rocking direct terms, the damping coefficient $c_{fx\varphi}$, which governs at relatively high frequencies, is close to zero. It seems then reasonable to neglect the horizontal-rocking coupling in a simplified formulation for a rigid footing. The simplified foundation model described and discussed in this section for either a rigid foundation or a rigid footing is labelled *model fW*. The label is just intended to ease the discussion with the association of the simplified model to the most prominent author (i.e. Wolf [84]). The dynamic

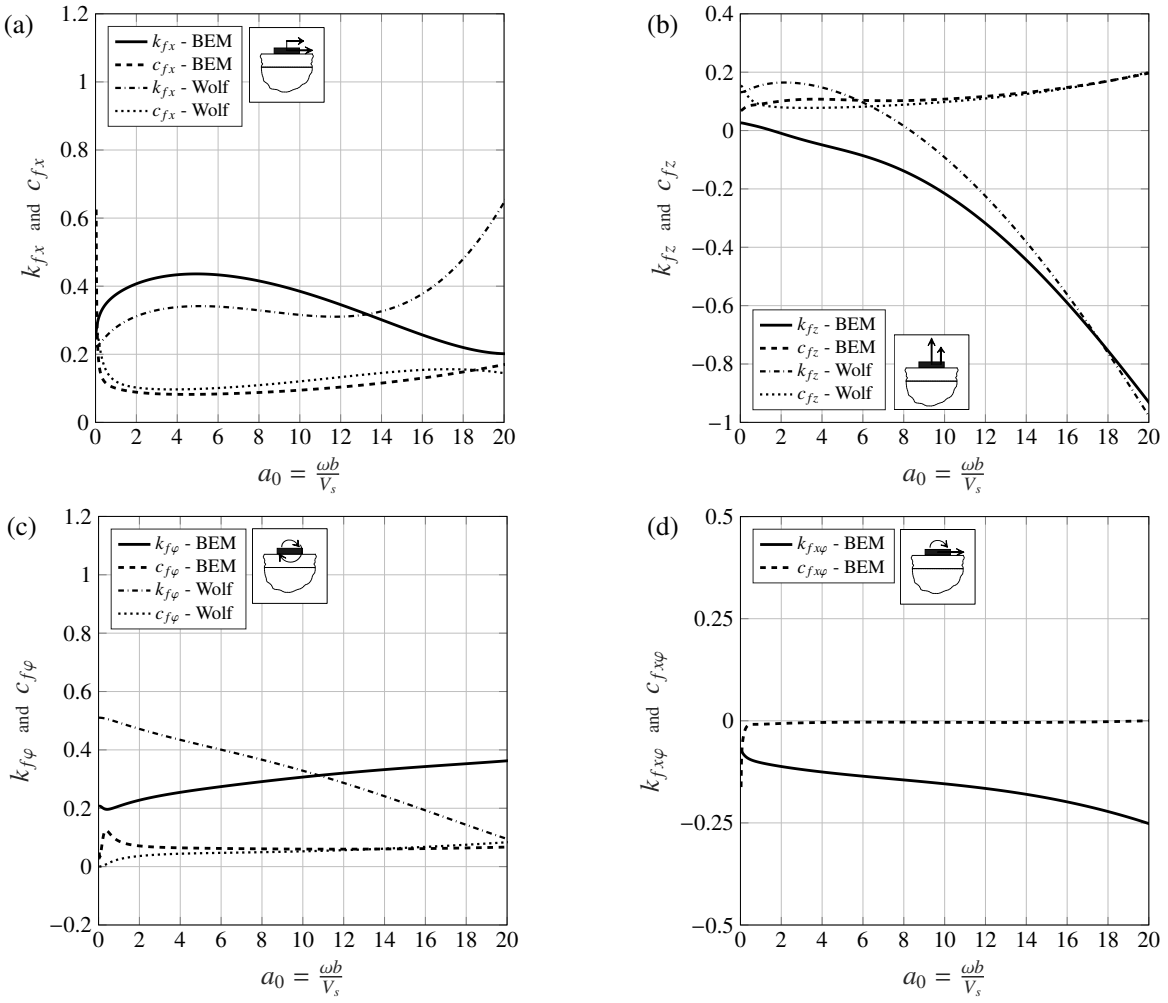

Fig. 3.8 Cone model and rigorous results for the *spring* and *damping* coefficients, as defined in Appendix A, of a square rigid footing of half-width b on an elastic layer ($h = 0.7$ m) overlying an half-space ($\nu_s = 0.49$).

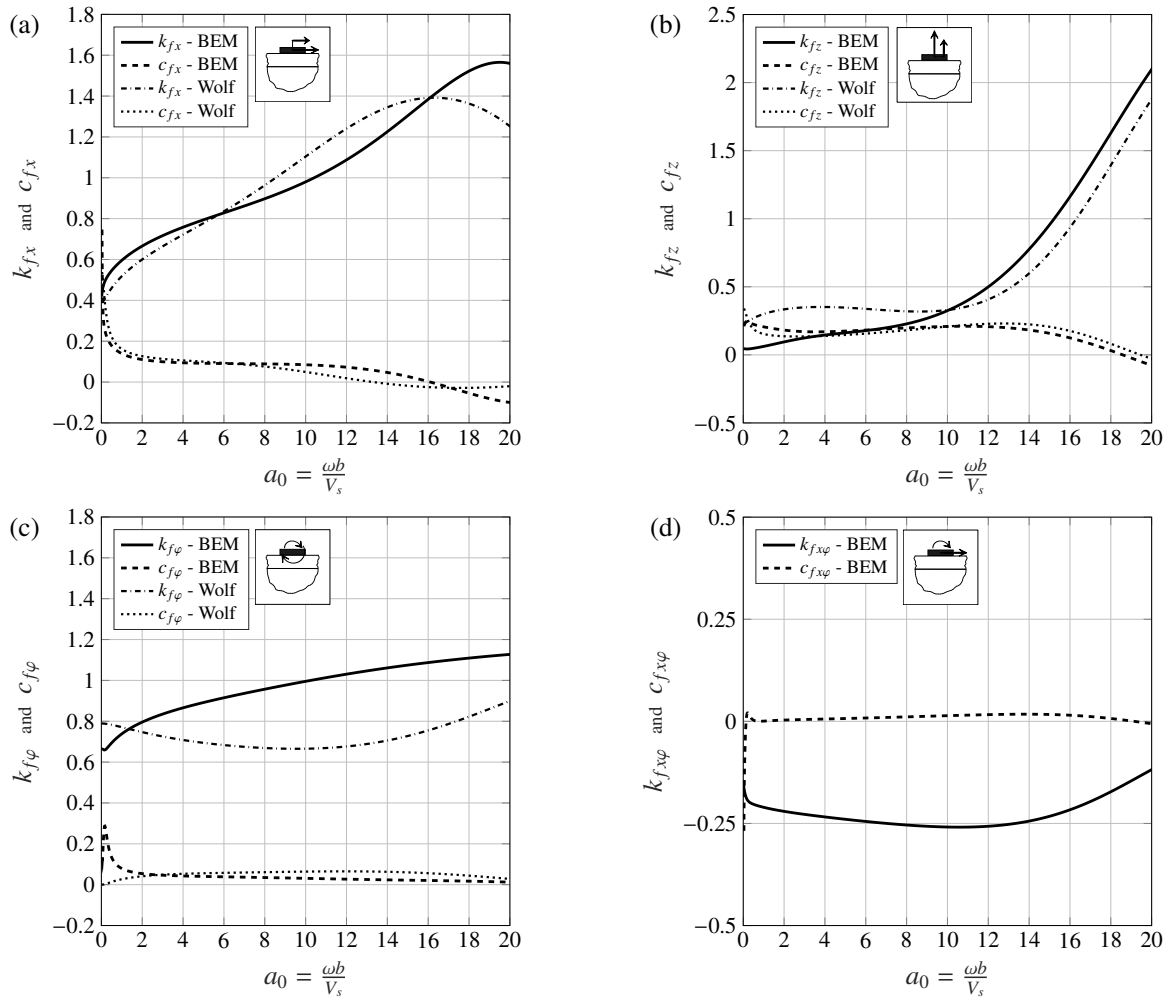

Fig. 3.9 Cone model and rigorous results for the *spring* and *damping* coefficients, as defined in Appendix A, of a squared rigid footing of half-width b on an elastic layer ($h = 1.5$ m) overlying an half-space ($\nu_s = 0.49$).

stiffness matrix of this model, with reference to the single-point coupling model, may be written in the form:

$$\widehat{\boldsymbol{K}}_{\boldsymbol{fW}} = \begin{bmatrix} \widehat{K}_{fWx} & 0 & 0 \\ 0 & \widehat{K}_{fWz} & 0 \\ 0 & 0 & \widehat{K}_{fW\varphi} \end{bmatrix} \tag{3.6}$$

The rigorous foundation model for either a rigid foundation or a rigid footing is labelled *model fB*, with the B standing for BEM model. Although the latter will be discussed in detail in Chapter 5 and 6, it is used in this chapter for validation of the model fW. The dynamic stiffness matrix of model fB,

with reference to the single-point coupling model, may be written in the form:

$$\widehat{\boldsymbol{K}}_{\boldsymbol{fB}} = \begin{bmatrix} \widehat{K}_{fBx} & 0 & \widehat{K}_{fBx\varphi} \\ 0 & \widehat{K}_{fBz} & 0 \\ \widehat{K}_{fB\varphi x} & 0 & \widehat{K}_{fB\varphi} \end{bmatrix} \tag{3.7}$$

Both the foundation models include the radiation damping, as discussed in Section 2.3, in their formulation. Material damping may be introduced via the correspondence principle as illustrated in the following.

3.2.3 Damping in soil-foundation models

Damping in the soil is assumed to be hysteretic, as described by a frequency-independent loss factor in shear η_s. This assumption has been confirmed by numerous experimental wave-field studies and laboratory tests [173, 174]. Although, in general, the damping properties in soils depend on a number of factors such as the strain amplitude, the effective mean principal stress, the void ratio, the number of loading cycles and the degree of saturation for clays [175], it is assumed that the hysteretic damping model is valid for many soils over the frequency-range and the moderate strain amplitude [61] observed in ground-borne vibration.

Material damping describes the energy losses within a loaded portion of soil caused by inter-particle slip and contact friction. In a homogeneous, linear-elastic representation of the soil, as adopted in this dissertation, the damping model has to depend upon the particle motion within the soil. The latter depends on the wave-type considered (see Appendix C) so that two damping loss factors can be associated with the shear and compressional waves. Damping is introduced in the soil by means of complex shear and compressional wave speeds, as defined in Equation 3.8, which relates to the use of complex moduli (i.e. correspondence principle).

$$V_S' = V_S \sqrt{1 + i\eta_S} \tag{3.8a}$$

$$V_P' = V_P \sqrt{1 + i\eta_P} \tag{3.8b}$$

It is indeed necessary to provide two values of damping loss factors to properly describe damping in soils, one for each elastic constants chosen to describe the soil. This dissertation makes use of the assumption adopted by Hunt [39], in which the material damping is assumed to occur entirely through

shear strain and, consequently, no damping is associated with the volumetric strain. Based on this assumption, it is then possible to find a relation between the two damping loss factors:

$$\eta_P = \frac{4}{3}\frac{\mu}{\lambda+2\mu}\eta_S = \frac{4}{3}\left(\frac{V_S}{V_P}\right)^2\eta_S \tag{3.9}$$

with λ, μ representing the Lamé constants (see Appendix C). On the basis of this assumption, the damping used in this dissertation relates to the definition of the value $\eta_s = \eta_S$.
Since the slab foundation is modelled as an equivalent elastic layer, the damping properties for the concrete slab are defined by a loss factor η_c in accordance with the previous discussion. As a general comment, it is worth stressing that having a valid soil-foundation model that correctly accounts for the radiation damping provided by the unbounded nature of the ground is of more concern then the precise modelling of the material damping [84, 33].

With reference to the simplified foundation models presented in this chapter, the dynamic stiffness, related to the damped soil-foundation system, may be obtained from Equations A.16 in the form:

$$\widehat{K}_{fj}(a_0') = K_{fj}^{(\mathrm{st})}(1+i\eta_j)\left[k_{fj}(a_0') + ia_0' c_{fj}(a_0')\right] \tag{3.10}$$

with $a_0' = (\omega r_0)/V_S'$, $i = \sqrt{-1}$, and η_j the damping loss factor relevant to the motion of the foundation, which is η_S for the horizontal motion and η_P for the vertical and rocking response.

3.3 Modelling the building

Simplified models for the building are considered next with reference to a single-point coupling model as presented in Section 3.1.3.

3.3.1 The column model

An initial attempt at modelling the building with a distributed mass and stiffness up its height may be addressed with a *column* model of length L, cross-sectional area A, second moment of area I, density ρ and Young's modulus E. This model completely disregards the presence of the floors between adjacent columns, thus neglecting the conversion of axial and bending motion from the column into bending and axial motion in the floor, and vice versa. As a result, each column acts independently from one another without the effect of the through-floor coupling.

In the case of identical columns, as for the reference problem in Section 3.1.2, the investigation can be traced back to the SSI of a single column that acts as a beam against horizontal u and rocking φ input, and as a bar against a vertical w input at its base. The SSI can be then approached as in Section 3.1.3 with a single-point coupling at the base of the column. The dynamic stiffness matrix $\widehat{\boldsymbol{K}}_{bC}$ of the column at point O and/or the FRF matrix $\widehat{\boldsymbol{H}}_{bC}$ can be retrieved from the global dynamic stiffness matrix $\widehat{\boldsymbol{K}}_{gC}$ of the column. The latter can be obtained via the Dynamic-Stiffness Method (DSM), as reviewed in Appendix B. By considering $\theta = \pi/2$, the column's properties as in Table 3.1 and the total height of the building (i.e. $L = 30$ m for the reference problem), a force-response relation at the ends of the column, analogous to Equation B.13, can be written in the form:

$$\hat{\boldsymbol{f}}_{gC} = \begin{bmatrix} \hat{\boldsymbol{f}}_{bC} \\ \hat{\boldsymbol{f}}_{nC} \end{bmatrix} = \begin{bmatrix} \widehat{\boldsymbol{K}}_{bbC} & \widehat{\boldsymbol{K}}_{bnC} \\ \widehat{\boldsymbol{K}}_{nbC} & \widehat{\boldsymbol{K}}_{nnC} \end{bmatrix} \begin{bmatrix} \hat{\boldsymbol{u}}_{bC} \\ \hat{\boldsymbol{u}}_{nC} \end{bmatrix} = \widehat{\boldsymbol{K}}_{gC}\, \hat{\boldsymbol{u}}_{gC} \tag{3.11}$$

with the subscripts $\boldsymbol{b}$ and $\boldsymbol{n}$ referring to the base and the free-end of the column respectively. Imposing the free condition $\hat{\boldsymbol{f}}_{nC}$ at the top of the column , the force-response relation at the base may be written:

$$\hat{\boldsymbol{f}}_{bC} = \widehat{\boldsymbol{K}}_{bC}\, \hat{\boldsymbol{u}}_{bC} = \left[\widehat{\boldsymbol{H}}_{bC}\right]^{-1} \hat{\boldsymbol{u}}_{bC} \quad \text{with} \quad \widehat{\boldsymbol{K}}_{bC} = \widehat{\boldsymbol{K}}_{bbC} - \widehat{\boldsymbol{K}}_{bnC}\left[\widehat{\boldsymbol{K}}_{nnC}\right]^{-1} \widehat{\boldsymbol{K}}_{nbC} \tag{3.12}$$

with $\widehat{\boldsymbol{K}}_{bC}$ the condensed dynamic stiffness matrix at the base of the column. Based on the assumptions for the elastic bar and Euler beam, the axial and bending motion are uncoupled for the single column model described here. The longitudinal V_A and bending V_B wave speeds can be retrieved from the axial k_A and bending k_B wavenumbers in Equation B.4:

$$V_A = \frac{\omega}{k_A} = \sqrt{\frac{E}{\rho}} \qquad V_B = \frac{\omega}{k_B} = \sqrt{\omega}\sqrt[4]{\frac{EI}{\rho A}} \tag{3.13}$$

The non-dispersive nature of the longitudinal waves is evident from the frequency independent wave speed V_A. On the other hand, bending waves are dispersive with a frequency dependent wave speed V_B.

The dynamic stiffness matrix of a column at its base in the global reference system can be then expressed as:

$$\widehat{\boldsymbol{K}}_{\boldsymbol{bC}} = \begin{bmatrix} \widehat{K}_{bCx} & 0 & \widehat{K}_{bCx\varphi} \\ 0 & \widehat{K}_{bCz} & 0 \\ \widehat{K}_{bC\varphi x} & 0 & \widehat{K}_{bC\varphi} \end{bmatrix} \tag{3.14}$$

It is illustrative to examine the axial response of the column.

3.3.2 Axial response and structural damping

The axial response of the column model can be examined separately since it is uncoupled from the bending response. The axial dynamic stiffness at the base of the column can be found as [121]:

$$\widehat{K}_{bCz} = -EA\,k_A \tan(k_A L) \tag{3.15}$$

For completeness the axial dynamic stiffness matrix for the column model is reported in the following:

$$\begin{bmatrix} \hat{f}_1 \\ \hat{f}_2 \end{bmatrix} = \frac{EA\,k_A}{\sin(k_A L)} \begin{bmatrix} \cos(k_A L) & -1 \\ -1 & \cos(k_A L) \end{bmatrix} \begin{bmatrix} \hat{w}_1 \\ \hat{w}_2 \end{bmatrix} = \widehat{\boldsymbol{K}}_{\boldsymbol{gC}}^{(A)} \begin{bmatrix} \hat{w}_1 \\ \hat{w}_2 \end{bmatrix} \tag{3.16}$$

with the subscripts 1 and 2 referring to the ends at the base and at the top of the column. The *fixed-free* condition for the column relates to the boundary conditions (BC) $\hat{w}_1 = \hat{f}_2 = 0$, which from Equation 3.16 can be written as:

$$\hat{f}_2 = EA\,k_A \cot(k_A L)\hat{w}_2 = 0$$

For a non-trivial solution, the latter yields $\cot(k_A L) = 0$ and the n fixed-free natural frequencies for the axial response of the column are given by:

$$k_A L = (2n-1)\frac{\pi}{2} \quad \text{or} \quad \omega_n = (2n-1)\frac{\pi V_A}{2L} \qquad \text{with} \quad n = 1,2,...,\infty \tag{3.17}$$

At these frequencies the column acts as a vibration absorber restraining the motion at its base [121]. For the column model of the building representing the reference problem with $L = 30$ m, these

frequencies are found as:

$$f_n = (2n-1)\frac{V_A}{4L} \approx (2n-1)\,29.5 \text{ Hz} = 29.5, 88.5, 147.5, 206.5... \text{ Hz} \tag{3.18}$$

The *free-free* condition relates to the BC $\hat{f}_1 = \hat{f}_2 = 0$ that are satisfied in the non-trivial case for:

$$\det\left\{\widehat{\boldsymbol{K}}_{gC}^{(A)}\right\} = -EA\,k_A \sin(k_A L) = 0$$

The latter yields the n free-free natural frequencies for the axial response of the column:

$$k_A L = (n-1)\pi \quad \text{or} \quad \omega_n = (n-1)\frac{\pi V_A}{L} \qquad \text{with} \quad n = 1,2,...,\infty \tag{3.19}$$

At these frequencies the column is dynamically de-coupled at its base leaving any input motion undisturbed. For the reference problem these frequencies are found as:

$$f_n = (n-1)\frac{V_A}{2L} \approx (2n-1)\,59 \text{ Hz} = 0, 59, 118, 177, 236... \text{ Hz} \tag{3.20}$$

which include the free-body motion in the static case.

Although what reviewed here is basic structural dynamics, it will be seen that it has an important role for interpreting the added-building effect of a building idealised as a column. The discussion above refers to an undamped column. In reality dissipative forces are present during the motion of the column, which have the effect of broadening the modal bandwidth and reduce the resonance associated with the modal response of the finite column.

In general, the dynamic response of a building is damped by two main mechanisms: *material damping* and *boundary damping*. The former is related to the energy dissipation that occurs in the bulk material while the latter is due to dissipation of energy through structural connections of different members (e.g. columns, floors, façade, etc.).

Material damping is often modelled as *viscous damping* [176]. The dissipative force introduced in the system is proportional to velocity and can be thought of as produced by a viscous damper. The damper coefficient can be proportional to mass, with a damper element connecting each elemental mass to the ground, or proportional to each elemental stiffness with a damper element in parallel. Either one of the two damping models may be adopted, leading to a constant modal bandwidth (mass-proportional) or to a a modal bandwidth proportional to frequency squared (stiffness-proportional), as reviewed by

Newland [121]. An alternative damping model in the frequency domain is the *hysteretic* damping introduced in the structural system by assigning complex values to the elastic constants defining the material [177]. For instance, for the beam-bar elements used in this dissertation, a complex Young's modulus $E(1+i\eta)$ can be assigned for considering the stress-strain phase difference as a result of material damping. In general, the *damping loss factor* η is frequency dependent, indeed it has to be to ensure causality [178].

It is illustrative to consider different models of material damping for the axial response of the column. This can be done by consideration of dissipative forces per unit area to be added in Equation B.1a, this time with reference to the vertical DoF w. In practice, a combination, also referred to as *Rayleigh damping*, of the mass-proportional and stiffness-proportional viscous damping models is commonly used (e.g. in FEM codes). For this purpose, the following dissipative forces per unit area may be considered:

$$f_d = -\alpha\rho\,\dot{w}(z,t) + E\beta\frac{\partial\dot{w}(z,t)}{\partial z} \tag{3.21}$$

with the terms α and β defining the half-power bandwidth for the j^{th} vibration mode with the damping coefficient ζ_j:

$$\Delta\omega_j = 2\zeta_j\omega_j = \alpha + \beta\omega_j^2 \tag{3.22}$$

For the case of a hysteretic damping model the consideration of a complex elastic constant is equivalent to considering an additional frequency-independent dissipative force in the form:

$$f_d = Ei\eta\frac{\partial w(z,t)}{\partial z} \tag{3.23}$$

with the damping loss factor η defining the half-power bandwidth for the j^{th} vibration mode as follows:

$$\Delta\omega_j = 2\zeta_j\omega_j = \eta\,\omega_j \tag{3.24}$$

Figure 3.10 shows the magnitude of the axial dynamic stiffness at the base of the column for a mass-proportional ($\beta = 0$) and a stiffness-proportional ($\alpha = 0$) viscous damping model. Comparison is made with the result obtained with the hysteretic damping model, as adopted in this dissertation. The values of α, β and η are chosen such that the half-power bandwidth for the first natural frequency is $\Delta\omega_1 = \eta\,\omega_1 = 0.1\omega_1$. It is evident that, for the case of mass-proportional viscous damping, the peaks and troughs of the dynamic stiffness in Figure 3.10 have constant $\Delta\omega_j$, having an equally

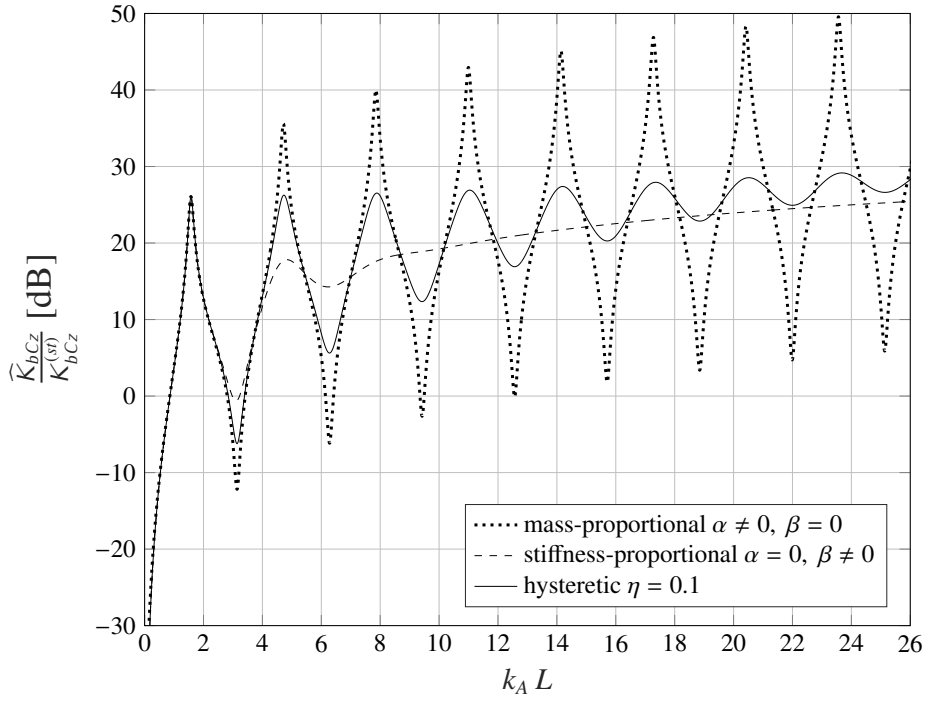

Fig. 3.10 Magnitude in dB of the axial dynamic stiffness $\widehat{K}_{bCz}$ at the base of the column with reference to the respective static vale $K^{(st)}_{bCz} = EA/L$. The properties of the column as in Table 3.1 are used with the total height of the building $L = 30$ m.

important influence along the frequency-spectrum for the response of the column. On the other hand, the hysteretic damping model, and more so the stiffness-proportional viscous damping, results in decreasing magnitudes of successive peaks and troughs in the frequency-spectrum. The latter is an important feature that may justify the use of a semi-infinite column model for relatively tall buildings and/or at relatively high frequencies, as discussed in the following section.

Regarding the material damping model adopted in this dissertation, there is experimental evidence [179] on reinforced concrete columns suggesting that the damping loss factors are not strongly dependent on frequency, and that different configurations of reinforcement lead to small damping variation for a single column. Newland and Hunt [179] find values in the order of $\eta = 0.01$ related to a single column and highlight the difficulty in modelling damping in a complete building, suggesting a tenfold value of η in such a case. This is in agreement with the damping value assigned to concrete buildings in earthquake engineering for the definition of design spectra based on a single degree-of-freedom representation of the building [58]. On the basis of this reasoning, and since no precise damping model exists for a building, the hysteretic damping model with $\eta = 0.1$ is adopted in

this dissertation for the members composing the building. This is in line with previous work on numerical modelling of concrete buildings in ground-borne vibration [47, 33], although lower [127, 166] and intermediate [180–182] values are occasionally adopted in the literature.

3.3.3 The damper model

Let us now consider a very tall building whose columns we can treat as semi-infinite. With reference to the axial behaviour seen earlier, the displacement $w(z,t)$ along a column can be described by a travelling wave propagating outwardly with speed V_A:

$$w(z,t) = w(z - V_A t) \tag{3.25}$$

No reflected waves travel in the opposite direction since the boundary is virtually at $z \to \infty$. By differentiation of Equation 3.25 with respect to the coordinate z and time t we can write:

$$\frac{\partial w}{\partial z} = \frac{\partial w(z - V_A t)}{\partial z} = \frac{\partial w(\xi)}{\partial \xi}\frac{\partial \xi}{\partial z} = \frac{\partial w(\xi)}{\partial \xi} \qquad \text{with } \xi = z - V_A t$$

$$\frac{\partial w}{\partial t} = \frac{\partial w(z - V_A t)}{\partial t} = \frac{\partial w(\xi)}{\partial \xi}\frac{\partial \xi}{\partial t} = -V_A \frac{\partial w(\xi)}{\partial \xi}$$

It follows that:

$$\frac{\partial w}{\partial z} = -\frac{1}{V_A}\frac{\partial w}{\partial t} \tag{3.26}$$

and the expression for the force at the base of the column can be calculated as:

$$f_b = -EA\frac{\partial w}{\partial z}\Big|_{z=0} = \frac{EA}{V_A}\frac{\partial w_b}{\partial t} = \rho A V_A \frac{\partial w_b}{\partial t} = c_{bDz}\frac{\partial w_b}{\partial t} \tag{3.27}$$

The axial force-response relationship at the base of a very tall column may be then idealised as that of a *damper* with a viscous force that is proportional to velocity by a *damper coefficient* $c_{bDz} = \rho A V_A$. The "very tall" condition is related to the assumption that the vibrational energy entering the building at its base is completely dissipated along its height. This implies that the bending and axial waves generated from the excitation at the base of the building travel up the structure and are damped out before reaching the boundaries. Hence the building, although being of finite dimensions, may be assumed infinitely tall from a purely wave-propagation standpoint, as viewed at the base.

A similar approach may be followed for obtaining damper coefficients related to the bending response of a semi-infinite column. Let us consider the general bending response in Equation B.5b for the element in the local coordinate system as in Figure B.1 in Appendix B. By considering only forward propagating waves the constants c_3 and c_4 in Equation B.5b are eliminated. By applying the two groups of BC at $x = -L/2$:

$$\begin{cases} w(0) = w_b \\ \varphi(0) = 0 \end{cases} \qquad \begin{cases} w(0) = 0 \\ \varphi(0) = \varphi_b \end{cases} \tag{3.28}$$

The unknown constants c_5 and c_6 may be determined from Equations B.5b and B.6 for the two BC groups as follows:

$$\begin{cases} c_5 = \dfrac{w_b}{2}(1-i) \\ c_6 = \dfrac{w_b}{2}(1+i) \end{cases} \qquad \begin{cases} c_5 = \dfrac{\varphi_b}{2}(1+i) \\ c_6 = -c_5 \end{cases} \tag{3.29}$$

The shear force s_b and the moment q_b at the left-hand ($x = -L/2$) of the element are determined from Equations B.5b and B.6 for each group of constants in Equation 3.29. After some algebra and a coordinate transformation in the global reference for the column (i.e. $\theta = \pi/2$, see Appendix B), the dynamic stiffness matrix for the *damper element* representing the semi-infinite column can be written as:

$$\widehat{\boldsymbol{K}}_{\boldsymbol{bD}} = \begin{bmatrix} \widehat{K}_{bDx} & 0 & \widehat{K}_{bDx\varphi} \\ 0 & \widehat{K}_{bDz} & 0 \\ \widehat{K}_{bD\varphi x} & 0 & \widehat{K}_{bD\varphi} \end{bmatrix} = \begin{bmatrix} EIk_B^3(i-1) & 0 & EIik_B^2 \\ 0 & EAik_A & 0 \\ EIik_B^2 & 0 & EIk_B(i+1) \end{bmatrix} \tag{3.30}$$

It should be noted that the impedance functions in Equation 3.30 may be interpreted by an alternative reasoning to the infinite bar-beam used here. Indeed, they represent *average impedance functions* related to a "random" finite bar-beam [183], with the assumption of the interval of resonance frequency uncertainty being much larger than the modal bandwidth. For a more detailed discussion the reader is re-directed to the book of Lyon [183], where an example for a finite and an infinite plate is presented.

Figure 3.11 shows the comparison between the dynamic stiffness of the column and damper models with reference to the direct terms for the horizontal, vertical and rocking DoFs, and to the horizontal-rocking cross-stiffness term. It is evident that the damper approximation is able to capture the order of magnitude of the dynamic stiffness terms, but it neglects the modal behaviour of the

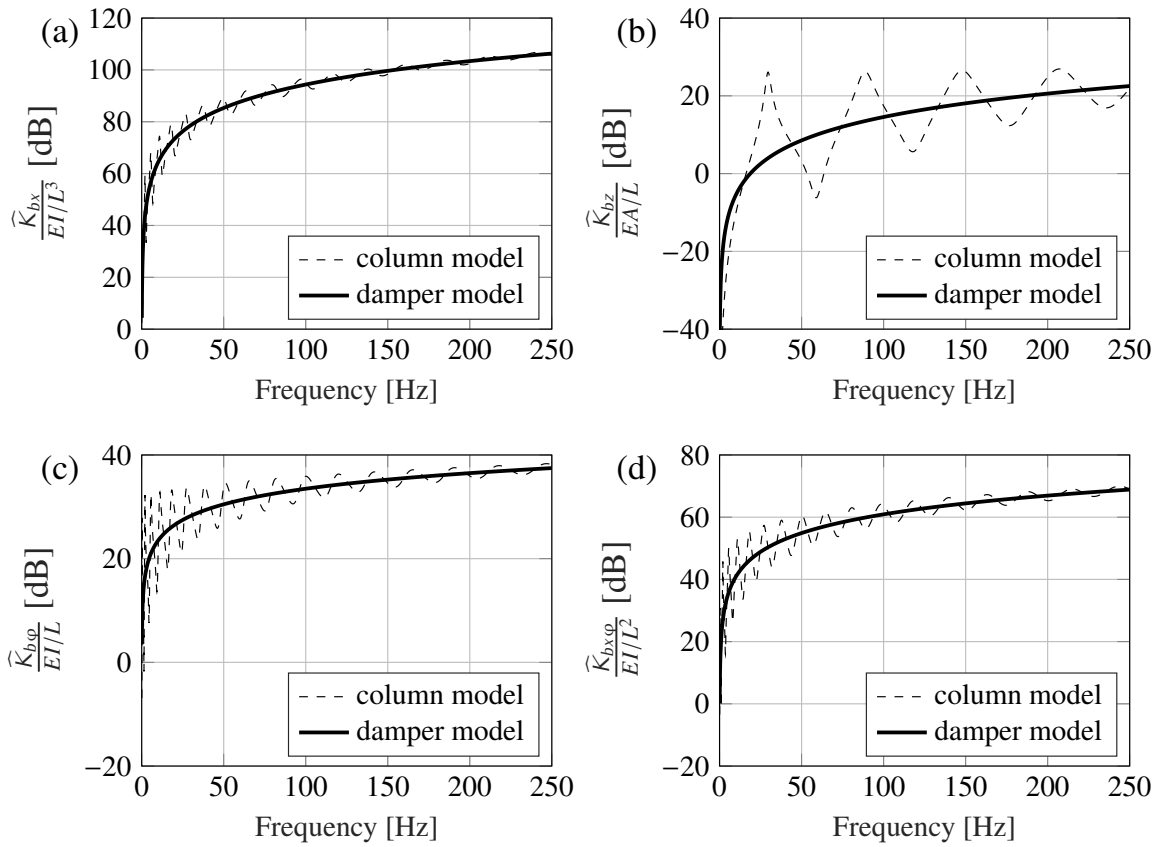

Fig. 3.11 Magnitude in dB of the terms of the dynamic stiffness matrix for the column model $\widehat{\boldsymbol{K}}_{\boldsymbol{bC}}$ (dashed line) and for the damper model $\widehat{\boldsymbol{K}}_{\boldsymbol{bD}}$ (solid line). The properties of the column as in Table 3.1 are used with the total height of the building $L = 30$ m with hysteretic damping ($\eta = 0.1$).

building modelled as a column. The extent to which the latter is important depends on the level of damping in the building, the actual height of the building and on the frequency range of interest.

The dynamic stiffness terms in Equation 3.30 may be rearranged to yield the viscous forces of the damper element related to the velocity of the relevant DoFs:

$$f_{bz} = EAik_A w_b = \rho A V_A \dot{w}_b$$

$$s_{bx} = EIk_B^3(i-1)u_b = \rho A V_B(i+1)\dot{u}_b\,; \qquad q_{bx} = EIik_B^2 u_b = \frac{\rho A}{\omega}V_B^2\dot{u}_b \tag{3.31}$$

$$q_{b\varphi} = EIk_B(i+1)\varphi_b = \frac{\rho A}{\omega^2}V_B^3(1-i)\dot{\varphi}_b\,; \qquad s_{b\varphi} = EIik_B^2\varphi_b = \frac{\rho A}{\omega}V_B^2\dot{\varphi}_b$$

The forces at the base of the semi-infinite column can be interpreted as viscous forces related to a velocity in the corresponding direction of motion and either a frequency-independent or frequency-

dependent damper coefficient. The infinitely tall building may be then idealised as a damper that dissipates the energy at a certain rate. The mean vibrational power related to the contribution of a single viscous force in Equation 3.31 can be written as:

$$\bar{P}_{bD} = -\frac{1}{2} Re\{ \dot{w}_{bD} f^{\star}_{bD} \} \tag{3.32}$$

with the symbol ' $\star$ ' indicating the complex conjugate. By using the force-velocity relation in Equation 3.31 in the form $f_{bD} = c_{bD}\, \dot{w}_{bD}$, Equation 3.32 can be re-written:

$$\bar{P}_{bD} = -\frac{1}{2} Re\{ \dot{w}_{bD}\, c^{\star}_{bD}\, \dot{w}^{\star}_{bD} \} = -\frac{1}{2} Re\{ c^{\star}_{bD} \} |\dot{w}^{2}_{bD}| = -\frac{1}{2} Re\{ c_{bD} \} |\dot{w}^{2}_{bD}| \tag{3.33}$$

Since the $Re\{ c_{bD} \}$ is positive in Equation 3.31 for all the DoFs considered, the mean vibrational power flow is negative, indicating that, on average, power is input (i.e. dissipated) [162] in the damper element representing the infinitely tall building. It is possible to find in the literature an opposite sign convention for the mean vibrational power [33], which does change the sign in Equation 3.32 but leaves the physical meaning unaltered.

3.4 Base-isolated buildings

Base-isolation is a common mitigation measure that allows to de-couple, to a certain extent, the building from the soil-foundation system in order to reduce levels of vibration and re-radiated noise within the building. The modelling strategy adopted in this dissertation is reviewed in the following. The response of a base-isolated single-point coupling model is also investigated and expressions are found for the Insertion Gain and the Power Flow Insertion Gain, as defined in Chapter 2.

3.4.1 Modelling the isolation

Each isolator is modelled as a linear, massless spring with reference to the horizontal, vertical and rocking DoFs, without any consideration of possible horizontal-rocking coupling effects. An isolator can be then described by three values of stiffness referring to the three DoFs considered and associated with the three modes of deformation, as shown for a rubber bearing in Figure 3.12.

In practice, it is common to refer to the *isolation frequency* f_S as the main design parameter for the base-isolation system. This stems from the assumption of the isolated building behaving as a

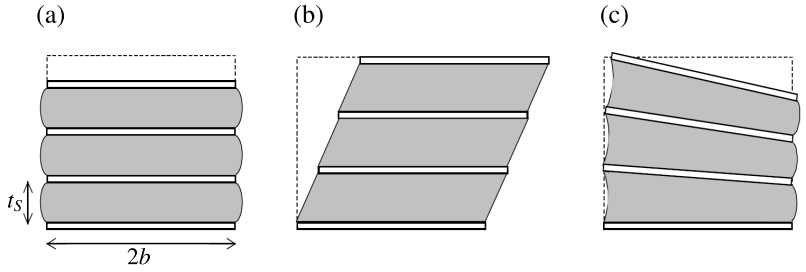

Fig. 3.12 Schematic illustration of the three modes of deformation, for a rubber isolation bearing, associated with the three stiffnesses for the three DoFs: vertical k_{Sz}, horizontal k_{Sx} and rocking $k_{S\varphi}$ (from Talbot [33]).

rigid mass on a spring excited vertically at its base. Although this assumption is fallacious because it neglects the complex dynamic behaviour of the building, its interaction with the soil-foundation system and the multi-directional input, it provides a general and convenient concept for characterising isolation systems. Each isolator is assumed to have a frequency-independent vertical stiffness as follows:

$$k_{Sz} = (2\pi f_S)^2 M_T \tag{3.34}$$

with M_T the total mass *per column*, which is comprehensive of structural and non-structural loads. The definition of the vertical stiffness in Equation 3.34 is commonly adopted in practice for the convenient concept of the isolation frequency. However, the isolation stiffness and damping are the relevant parameter that drive the performance.

In reality, as discussed in Section 2.6.3, the dynamic stiffness provided by rubber bearings depends on the deflection, which in turn depends on the static loading. The latter depends on the overall static response of the base-isolated building, isolation system included. This non-linear behaviour of the rubber bearings is neglected here and the isolation stiffness is obtained by assuming a redistribution of the static loading at the base of a base-isolated building, of which there is some evidence in practice [184] for sufficiently soft bearings. The mass associated with the axial static loading at the base of each column may be then obtained by means of the gravitational acceleration $g \approx 9.81$ m/s^2, and the isolation stiffness can be calculated according to Equation 3.34.

In this dissertation, the total mass of a building is taken as that defined in the building codes EN 1991-1-1 [185] and EN 1990 [186] for the actions on buildings and their combination with respect to the serviceability state. Let us assume that the additional mass of non-structural elements can be idealised as spread over the floor area with a thickness of 0.10 m and a density of 1600 kg/m^3.

Partitions are additional non-structural elements to be considered based on their contribution in terms of mass-per-floor [185]. The total mass of the building may be obtained from the *quasi-permanent* combination of structural (G_1), non-structural (G_2) masses (permanent actions), and any variable actions $q_{k(j)}$ [186]:

$$M_b = \sum_j G_{1(j)} + \sum_j G_{2(j)} + \sum_j \Psi_{2(j)} q_{k(j)} \tag{3.35}$$

where the factor $\Psi_{2(j)}$ accounts for the alternate presence of the specific variable action during a long period of time. The variable action considered here is the live load, which depends on the building category. For the reference problem discussed in Section 3.1.2 with the data as in Table 3.1, the total mass of the building M_b is divided by the number of columns in order to obtain the total mass per column M_T, which amounts roughly to 235 tonnes.

For the simplified foundation-building models used in this chapter, unless otherwise specified, the mass M_T in Equation 3.34 is calculated by assuming the building as column of mass $M_T = M_C = \rho_C A_C L$ with $L = 30$ m for the reference problem.

The horizontal and rocking stiffness of the isolator are assigned as $k_{Sx} = k_{S\varphi} = 0.5\, k_{Sz}$. In general, for laminated rubber bearings, the ratios k_{Sx}/k_{Sz} and $k_{S\varphi}/k_{Sz}$ depend on the shape factor and geometrical properties of the bearing [152]. However, this value is considered to be typical of base isolation bearings on the basis of a previous investigation by Talbot [33]. Moreover, it is understood that different values of k_{Sx} and $k_{S\varphi}$, or a different model for the isolation altogether, may be adopted in future work without affecting the general discussion provided here. Material damping is accounted for by means of the hysteretic model already discussed in Section 3.3.2. Damping loss factors of 0.01 and 0.1 are considered as representative of limiting values and indicative of undamped steel spring and a high-hysteresis rubber bearing respectively [33].

In practice, depending on the area to be isolated (e.g. single column, structural core, etc.), the isolation system may be installed in the form of a single or a cluster of isolators. In this dissertation, referring to the reference problem in Section 3.1.2, the former is used to de-couple the structure at the base of a column. A two-point connection $O' - O$ is then established in the form of a linear, massless spring with a resulting force-response relationship:

$$\begin{bmatrix} \boldsymbol{f}(\mathbf{x}_{\mathbf{0}'}) \\ \boldsymbol{f}(\mathbf{x}_{\mathbf{0}}) \end{bmatrix} = \begin{bmatrix} \boldsymbol{k}_S & -\boldsymbol{k}_S \\ -\boldsymbol{k}_S & \boldsymbol{k}_S \end{bmatrix} \begin{bmatrix} \boldsymbol{u}(\mathbf{x}_{\mathbf{0}'}) \\ \boldsymbol{u}(\mathbf{x}_{\mathbf{0}}) \end{bmatrix}$$

$$\text{with} \quad \boldsymbol{k}_S = \begin{bmatrix} k_{Sx} & 0 & 0 \\ 0 & k_{Sz} & 0 \\ 0 & 0 & k_{S\varphi} \end{bmatrix} \tag{3.36}$$

where O' and O are points at the bottom and top of the vertically oriented isolator respectively. In the following section, the presence of such an isolation system is contextualised to the SSI of a single-point coupling model, similar to that seen in Section 3.1.3.

3.4.2 A single-point coupling model for an isolated building

The SSI associated with a single-point coupling model for a base-isolated building is illustrated in Figure 3.13. Analogous to Figure 3.3, by assuming the building $\mathcal{B}$ is free of external forces at $\mathbf{x_n}$ the force-response relationship at O for the building alone can be written as:

$$\boldsymbol{f}_b(\mathbf{x_o}) = \widehat{\boldsymbol{K}}_b \boldsymbol{u}_b(\mathbf{x_o}) \tag{3.37}$$

The coupled response of the isolator-building system may be studied with the assembled dynamic stiffness matrix as follows:

$$\begin{bmatrix} \hat{\boldsymbol{f}}_u(\mathbf{x_{o'}}) \\ \hat{\boldsymbol{f}}_b(\mathbf{x_o}) \end{bmatrix} = \begin{bmatrix} \boldsymbol{k}_S & -\boldsymbol{k}_S \\ -\boldsymbol{k}_S & \boldsymbol{k}_S + \widehat{\boldsymbol{K}}_b \end{bmatrix} \begin{bmatrix} \hat{\boldsymbol{u}}_u(\mathbf{x_{o'}}) \\ \hat{\boldsymbol{u}}_b(\mathbf{x_o}) \end{bmatrix} \tag{3.38}$$

Given no external forces at O (i.e. $\hat{\boldsymbol{f}}_b(\mathbf{x_o}) = \mathbf{0}$), the force-response relationship of the base-isolated building at its base (i.e. at the bottom of the isolator) may be written in the form:

$$\hat{\boldsymbol{f}}_u(\mathbf{x_{o'}}) = \left[\boldsymbol{k}_S - \boldsymbol{k}_S \left[\boldsymbol{k}_S + \widehat{\boldsymbol{K}}_b \right]^{-1} \boldsymbol{k}_S \right] \hat{\boldsymbol{u}}_u(\mathbf{x_{o'}}) = \widehat{\boldsymbol{K}}_{Sb} \hat{\boldsymbol{u}}_u(\mathbf{x_{o'}}) \tag{3.39}$$

with $\widehat{\boldsymbol{K}}_{Sb}$ the condensed dynamic stiffness matrix of the base-isolated building at its base. Following the same reasoning as in Equation 3.4, the displacement at O' after the coupling of the base-isolated building with the soil-foundation system can be related to the pre-existing displacement $\hat{\boldsymbol{u}}_f$ as:

$$\hat{\boldsymbol{u}}_u(\mathbf{x_{o'}}) = \left[\mathbf{I} + \widehat{\boldsymbol{H}}_f \, \widehat{\boldsymbol{K}}_{Sb} \right]^{-1} \hat{\boldsymbol{u}}_f(\mathbf{x_o}) = \mathbf{B}^{(\mathrm{iso})} \, \hat{\boldsymbol{u}}_f(\mathbf{x_o}) \tag{3.40}$$

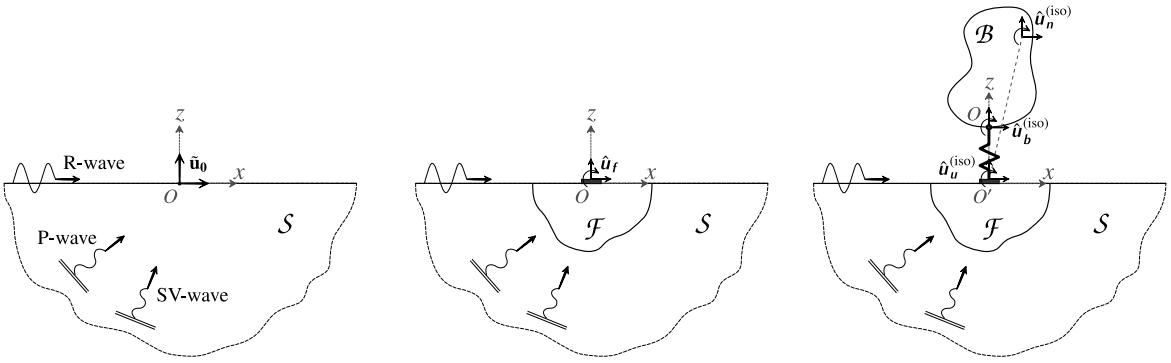

Fig. 3.13 Schematic illustration for the SSI associated with a single-point coupling model for a base-isolated building. (a) An incident plane wave in the 3D soil system $\mathcal{S}$ leads to the resulting free-surface amplitude $\tilde{\mathbf{u}}_\mathbf{0}$. (b) The presence of a 3D foundation $\mathcal{F}$ is then considered with the resulting response $\hat{\boldsymbol{u}}_f$ at a point O at the free-surface. (c) A base-isolated 2D building model $\mathcal{B}$ is coupled to the soil-foundation system $\mathcal{F}$-$\mathcal{S}$ with the resulting displacement $\hat{\boldsymbol{u}}_b^{(\mathrm{iso})}$ at the base of the building (i.e. top of isolation), $\hat{\boldsymbol{u}}_u^{(\mathrm{iso})}$ at the bottom of isolation and $\hat{\boldsymbol{u}}_n^{(\mathrm{iso})}$ in the remainder of $\mathcal{B}$.

By considering Equation 3.38 and imposing the condition $\hat{\boldsymbol{f}}_b(\mathbf{x_o}) = \mathbf{0}$, the response at the base of the building is given by:

$$\hat{\boldsymbol{u}}_b(\mathbf{x_o}) = \left[\boldsymbol{k}_\mathcal{S} + \widehat{\boldsymbol{K}}_b\right]^{-1} \boldsymbol{k}_\mathcal{S}\, \hat{\boldsymbol{u}}_u(\mathbf{x_{o'}}) = \left[\boldsymbol{k}_\mathcal{S} + \widehat{\boldsymbol{K}}_b\right]^{-1} \boldsymbol{k}_\mathcal{S}\, \mathbf{B}^{(\mathrm{iso})}\, \hat{\boldsymbol{u}}_f(\mathbf{x_o}) = \mathbf{C}^{(\mathrm{iso})}\, \hat{\boldsymbol{u}}_f(\mathbf{x_o}) \tag{3.41}$$

Similarly to the unisolated case (see Equation 3.5), the response within the building may be obtained as:

$$\hat{\boldsymbol{u}}_n(\mathbf{x_n}) = \widehat{\boldsymbol{H}}_{nb} \left[\widehat{\boldsymbol{H}}_b\right]^{-1} \hat{\boldsymbol{u}}_b(\mathbf{x_o}) = \widehat{\boldsymbol{H}}_{nb}\, \widehat{\boldsymbol{K}}_b\, \mathbf{C}^{(\mathrm{iso})}\, \hat{\boldsymbol{u}}_f(\mathbf{x_o}) \tag{3.42}$$

with reference to the global FRF matrix $\widehat{\boldsymbol{H}}_{bg}$ in Equation 3.2 of the building alone.

3.4.3 Measures of isolation performance

The main existing methods for the evaluation of a mitigating measure have been reviewed in Section 2.6.4. Among these, the *IG* and the *PFIG* have been discussed as two scalar metrics that are able to give insights into the efficacy of a mitigating measure. For base-isolation, these are given by a comparison of the isolated and unisolated configuration of the building.

In the following, the *IG* and the *PFIG* are calculated with reference to the formalism adopted for the single-point coupling model in Sections 3.1.3 and 3.4.2. The insertion gain refers to one degree of freedom at one location in the building. The response for the isolated and unisolated case can be

retrieved from Equations 3.42 and 3.5 respectively as:

$$\hat{w}_n^{(\mathrm{iso})} = \widehat{H}_{nb}\,\widehat{K}_b\,\mathbf{C}^{(\mathrm{iso})}\,\hat{\boldsymbol{u}}_f \tag{3.43a}$$

$$\hat{w}_n^{(\mathrm{uniso})} = \widehat{H}_{nb}\,\widehat{K}_b\,\mathbf{B}^{(\mathrm{uniso})}\,\hat{\boldsymbol{u}}_f \tag{3.43b}$$

with $\widehat{H}_{nb}$ being a $[1 \times 3]$ vector for the single-point coupling model under examination. For definition, it follows from Equation 2.2:

$$IG = 20\log_{10}\left\{\left|\frac{\hat{w}_n^{(\mathrm{iso})}}{\hat{w}_n^{(\mathrm{uniso})}}\right|\right\} = 20\log_{10}\left\{\left|\frac{\widehat{H}_{nb}\,\widehat{K}_b\,\mathbf{C}^{(\mathrm{iso})}\,\hat{\boldsymbol{u}}_f}{\widehat{H}_{nb}\,\widehat{K}_b\,\mathbf{B}^{(\mathrm{uniso})}\,\hat{\boldsymbol{u}}_f}\right|\right\} \tag{3.44}$$

Equation 3.44 illustrates the dependence of the IG on the input motion $\hat{\boldsymbol{u}}_f$ as the response of the foundation model to an existing vibration field $\hat{\mathbf{u}}_\mathbf{0}$, on the properties of the building alone (i.e. $\widehat{H}_{nb}$ and $\widehat{K}_b$), and on the added-building effect represented by the matrices $\mathbf{B}^{(\mathrm{uniso})}$ and $\mathbf{C}^{(\mathrm{iso})}$ for the unisolated and isolated building respectively. The argument of the logarithm in Equation 3.44 may be simplified further when considering simplified foundation-building models, as will be seen in the next section.

The power-flow insertion gain defined by Equation 2.3 may be also re-formulated in the formalism of the single-point coupling model. Let us consider the mean vibrational power entering the building $\mathcal{B}$ at O:

$$\begin{aligned}\bar{P} &= -\frac{1}{2}Re\left\{\hat{\boldsymbol{f}}_b^{\star}\cdot(i\omega)\hat{\boldsymbol{u}}_b\right\} = -\frac{1}{2}Re\left\{(i\omega)\left[\hat{\boldsymbol{f}}_b^{\star}\right]^T\hat{\boldsymbol{u}}_b\right\} = \\ &= -\frac{1}{2}Re\left\{(i\omega)\hat{\boldsymbol{f}}_b^{\dagger}\hat{\boldsymbol{u}}_b\right\} = -\frac{1}{2}Re\left\{(i\omega)\hat{\boldsymbol{u}}_b^{\dagger}\widehat{K}_b^{\dagger}\hat{\boldsymbol{u}}_b\right\}\end{aligned} \tag{3.45}$$

with the symbols ' * ',' ^{T} ' and ' † ' indicating the conjugate, the transpose and the Hermitian conjugate of a matrix respectively. By substitution of the displacement vector $\hat{\boldsymbol{u}}_b$ in Equations 3.41 and 3.4 for the isolated and unisolated case, we obtain:

$$\bar{P}_b^{(\mathrm{iso})} = -\frac{1}{2}Re\left\{(i\omega)\hat{\boldsymbol{u}}_f^{\dagger}\left[\mathbf{C}^{(\mathrm{iso})}\right]^{\dagger}\widehat{K}_b^{\dagger}\mathbf{C}^{(\mathrm{iso})}\hat{\boldsymbol{u}}_f\right\} \tag{3.46a}$$

$$\bar{P}_b^{(\mathrm{uniso})} = -\frac{1}{2}Re\left\{(i\omega)\hat{\boldsymbol{u}}_f^{\dagger}\left[\mathbf{B}^{(\mathrm{uniso})}\right]^{\dagger}\widehat{K}_b^{\dagger}\mathbf{B}^{(\mathrm{uniso})}\hat{\boldsymbol{u}}_f\right\} \tag{3.46b}$$

so that the $PFIG$ can be written in the form:

$$PFIG = 10\log_{10}\left\{\left|\frac{\bar{P}_b^{(\mathrm{iso})}}{\bar{P}_b^{(\mathrm{uniso})}}\right|\right\} = 10\log_{10}\left\{\left|\frac{Re\left\{(i\omega)\hat{\boldsymbol{u}}_f^{\dagger}\left[\mathbf{C}^{(\mathrm{iso})}\right]^{\dagger}\widehat{\boldsymbol{K}}_b^{\dagger}\mathbf{C}^{(\mathrm{iso})}\hat{\boldsymbol{u}}_f\right\}}{Re\left\{(i\omega)\hat{\boldsymbol{u}}_f^{\dagger}\left[\mathbf{B}^{(\mathrm{uniso})}\right]^{\dagger}\widehat{\boldsymbol{K}}_b^{\dagger}\mathbf{B}^{(\mathrm{uniso})}\hat{\boldsymbol{u}}_f\right\}}\right|\right\} \tag{3.47}$$

As seen for the IG in Equation 3.44, the numerator and denominator in the argument of the logarithm defining the $PFIG$ depend on chain matrix multiplications that can be simplified further only with respect to a simplified foundation-building model as presented in the next section.

3.5 A simplified multi-directional foundation-building model

The simplified foundation, building and isolation models presented in Sections 3.2, 3.3 and 3.4 may be adopted for the evaluation of the added-building effect and the isolation performance with reference to a single-point coupling model as presented in Sections 3.1.3, 3.4.2 and 3.4.3. This is illustrated in the following for both the case of rigid foundations (benchmark #1) and/or rigid footings (benchmark #2) for the soil-foundation system, and a column and/or damper representation of the building. Additionally, the commonly used assumption of the building as a rigid mass (model bM) is also explored. Figure 3.14 illustrates schematically the simplified foundation-building models

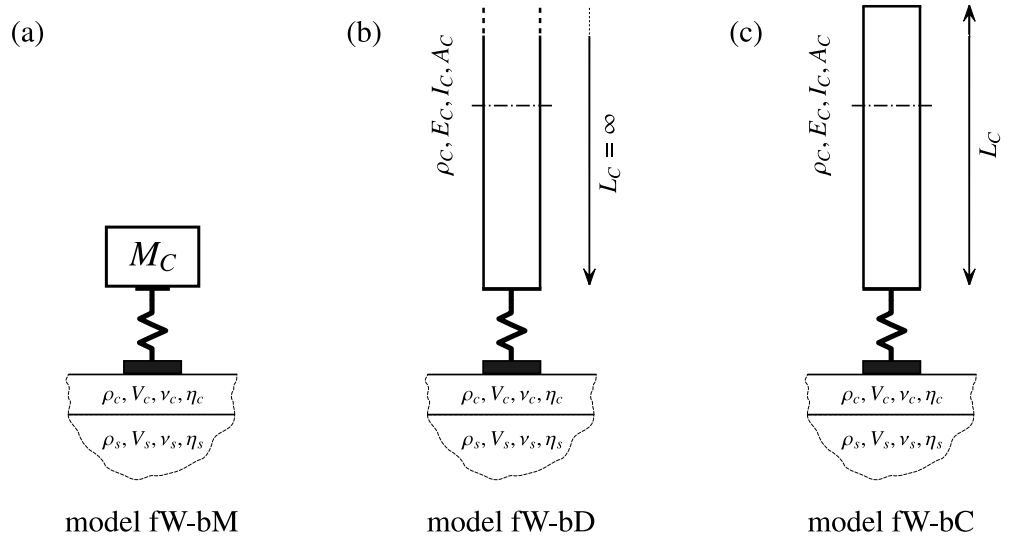

Fig. 3.14 Schematic representation of the simplified foundation-building models referring to a cone model of the rigid footing (i.e. benchmark #2) and the base-isolated building represented by (a) the column as a rigid mass, (b) an infinitely tall column (i.e. damper) and (c) a column of finite length on a spring representing base-isolation.

examined here. The purpose of this section is to introduce the *cone-damper model* (model fW-bD) as a simplified model for the design of base-isolated buildings with reference to the soil-foundation-building interaction. This will be validated against the rigorous approach discussed in Chapter 6.

3.5.1 The Added-Building Effect

The added-building effect, for both the unisolated and isolated case, may be studied by inspection of the matrix **B** as obtained in the Sections 3.1.3 and 3.4.2:

$$\mathbf{B}^{(\text{uniso})} = \left[\mathbf{I} + \widehat{H}_f\, \widehat{K}_b\right]^{-1} \tag{3.48a}$$

$$\mathbf{B}^{(\text{iso})} = \left[\mathbf{I} + \widehat{H}_f\, \widehat{K}_{Sb}\right]^{-1} \tag{3.48b}$$

By considering the model fB-bD, the matrix **B** for the unisolated building may be expressed as:

$$\mathbf{B}^{\,(\text{uniso})} = \left[\mathbf{I} + \widehat{H}_{fB}\, \widehat{K}_{bD}\right]^{-1} =$$

$$= \begin{bmatrix} 1 + \widehat{H}_{fBx}\, \widehat{K}_{bDx} + \widehat{H}_{fBx\varphi}\, \widehat{K}_{bD\varphi x} & 0 & \widehat{H}_{fBx}\, \widehat{K}_{bDx\varphi} + \widehat{H}_{fBx\varphi}\, \widehat{K}_{bD\varphi} \\ 0 & 1 + \widehat{H}_{fBz}\, \widehat{K}_{bDz} & 0 \\ \widehat{H}_{fB\varphi x}\, \widehat{K}_{bDx} + \widehat{H}_{fB\varphi}\, \widehat{K}_{bD\varphi x} & 0 & 1 + \widehat{H}_{fB\varphi x}\, \widehat{K}_{bDx\varphi} + \widehat{H}_{fB\varphi}\, \widehat{K}_{bD\varphi} \end{bmatrix}^{-1} \tag{3.49}$$

A similar expression may be obtained for the isolated case by consideration of $\widehat{K}_{SbD}$ for the base-isolated building model. It follows that, for the single-point coupling model, the 3×3 matrix **B** can be expressed in general terms as:

$$\mathbf{B} = \begin{bmatrix} B_{xx} & 0 & B_{x\varphi} \\ 0 & B_{zz} & 0 \\ B_{\varphi x} & 0 & B_{\varphi\varphi} \end{bmatrix} \tag{3.50}$$

While the added-building effect for the horizontal and rocking DoFs depends on both the horizontal and the rocking input motions, it is clear from Equation 3.49 that it is uncoupled from the vertical input motion. The horizontal-rocking coupling terms of $\widehat{H}_f$ (if any) and $\widehat{K}_b$ lead to rather involved expressions of the coupled horizontal and rocking added-building effect, which can be hardly investigated in detail. On the other hand, the adoption of simplified foundation-building models effectively allows

the de-coupling of the vertical and horizontal-rocking DoFs, with the added-building effect in the vertical direction serving as a conceptual reference that can be investigated further in the following.

The Added-Building Effect for vertical input

Let us consider the case of the unisolated building for the reference problem in Section 3.1.2. By considering a single-point coupling model, the building can be represented by a damper (model bD), a finite column of length $L = 30$ m (model bC) or by the finite column as a rigid mass (model bM). The term B_{zz} in Equation 3.50 for the unisolated case can be obtained, according to Equation 3.48a, as:

$$\mathrm{B}_{zz}^{(\mathrm{uniso})} = \frac{\hat{w}_b^{(\mathrm{uniso})}}{\hat{w}_f} = \frac{1}{1+\dfrac{\widehat{K}_{bz}}{\widehat{K}_{fz}}} \tag{3.51}$$

Figure 3.15 shows the added-building effect in the vertical direction by reporting the magnitude of B_{zz} obtained with a cone model of a rigid foundation (model fW, benchmark #1) and the simplified models of the building as discussed above. Two different values of Poisson's ratio for the soil are considered: $\nu_s = 1/3$ (Figure 3.15a and c), representative of compressible soils, and $\nu_s = 0.49$ (Figure 3.15b and d) for nearly incompressible soils. The high-frequency trend is investigated in Figure 3.15c and d in terms of the dimensionless frequency $k_A L = a_0 \dfrac{L}{b}\dfrac{V_s}{V_A}$. According to the range of a_0 as presented in Section 3.1.2, and considering a tall building of 60 m, the maximum value of $k_A L \approx 340$. A larger range is investigated in the following for the sole purpose of examining the limit value, at high frequencies, of the added-building effect. In the case of the building as a finite column, the motion at the foundation-building interface is restrained at the fixed-free natural frequencies of the column as defined in Equation 3.18. Local maxima are evident at approximately the free-free natural frequencies of the column as defined in Equation 3.20. The first amplification occurs at the natural frequency of the column as a rigid mass on the complex and frequency dependent springs, combined in series, provided by the soil-foundation system and the column itself. For the benchmark #1, the spring associated with the column is stiffer than the one provided by the rigid foundation. It follows that an upper bound for the frequency at which the first amplification occurs is the natural frequency of the column as a rigid mass on the soil-foundation system alone (i.e. dotted line in Figure 3.15).
Although the rigid mass model is able to capture the first amplification, it fails to describe properly the attenuation at higher frequencies, which is over-estimated with respect to the column model and

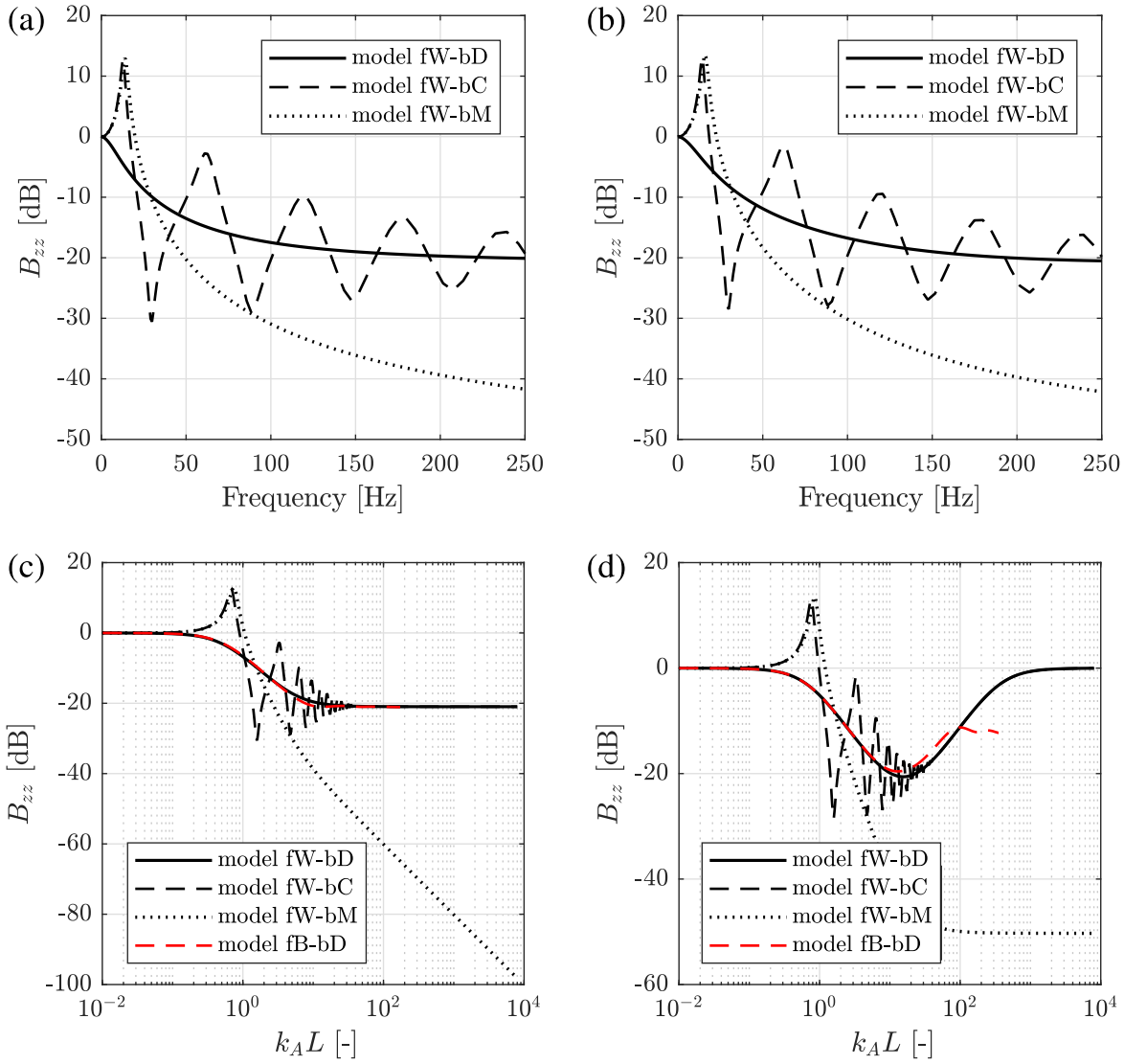

Fig. 3.15 Comparison of the magnitude of the term B_{zz} obtained by modelling the building as a damper (bD), a finite column (bC) or a rigid mass (bM). The cone model of a rigid foundation on an elastic half-space with Poisson's ratio $\nu_s = 1/3$ (a) and (c) or $\nu_s = 0.49$ (b) and (d) are considered for comparison of a compressible or incompressible soil respectively. The results for the model fB-bD, referring to a rigorous BEM model of the foundation, are also shown for comparison.

goes with 20 dB/decade for compressible soils while reaching a constant value for $\nu_s = 0.49$. On the other hand, the damper model is able to capture the same trend of attenuation obtained with the column model, but neglecting the restraining and/or the amplification effects due to the modal behaviour.

The results for compressible and nearly compressible soils hold no differences in the frequency range of interest (see Figure 3.15a and b), although they lead to a different trend of attenuation at high

frequencies (see Figure 3.15c and d). This can be investigated by means of closed-form expressions that may be obtained from Equation 3.51 by substitution of the vertical dynamic stiffness of a rigid foundation (see Appendix A) and of the simplified building model under investigation. For instance, the cone model of a rigid, square foundation and the damper model (see Equation 3.30) for the reference problem lead to the term B_{zz} in decibels:

$$B_{zz}^{(\text{uniso})} = -20\log_{10}\left\{\left|1+0.75\frac{\rho_C}{\rho_s}\frac{V_A}{V_S}(1-\nu_s)\frac{ia_0}{1+(ia_0)^2\delta+ia_0c_{fz}}\right|\right\} \tag{3.52}$$

$$\text{with} \qquad \delta = 0.75\frac{\delta_m}{\pi}(1-\nu_s); \quad \text{and} \quad c_{fz} = 0.75\frac{V}{V_s}(1-\nu_s)$$

with the damping coefficient c_{fz} and the dimensionless frequency $a_0 = \omega r_0/V_S$ as introduced in Appendix A, and δ related to the trapped mass effect discussed in Section 3.2 and Appendix A, which is present only for nearly incompressible soils (i.e. $\nu_s > 1/3$).

For compressible soils with $\nu_s = 1/3$, $\delta = 0$ and the limiting value of B_{zz} at high frequencies yields:

$$\begin{aligned}\lim\left(B_{zz}^{(\text{uniso})}\right)_{a_0\to\infty} &= -20\log_{10}\left\{\left|1+0.75\frac{\rho_C}{\rho_s}\frac{V_A}{V_S}\frac{(1-\nu_s)}{c_{fz}}\right|\right\} = \\ &= -20\log_{10}\left\{\left|1+\frac{\rho_C}{\rho_s}\frac{V_A}{V_P}\right|\right\}\end{aligned} \tag{3.53}$$

Equation 3.53 provides a limiting value of attenuation, based solely on the impedance mismatch at the foundation-building interface, for the added-building effect related to benchmark #1, which corresponds approximately to the value -21 dB (see Figure 3.15c). This is confirmed by the result obtained considering a BEM model of the rigid foundation (i.e. model fB) as illustrated in Figure 3.15c. For nearly incompressible soils, $\delta \neq 0$ and the limiting value of B_{zz} leads to no attenuation:

$$\lim\left(B_{zz}^{(\text{uniso})}\right)_{a_0\to\infty} = -20\log_{10}\left\{\left|1+0.75\frac{\rho_C}{\rho_s}\frac{V_A}{V_S}\frac{(1-\nu_s)}{ia_0\delta}\right|\right\} = 0 \tag{3.54}$$

However, the discussion in Section 3.2 has proven that the trapped mass effect, at high frequencies, is only relevant for the special case of $\nu_s = 1/2$. In reality, for values $1/3 < \nu_s < 1/2$, an intermediate trend between those shown in Figure 3.15c and d, with a constant limiting value, may be expected as confirmed by the result of model fB-bD in Figure 3.15d.

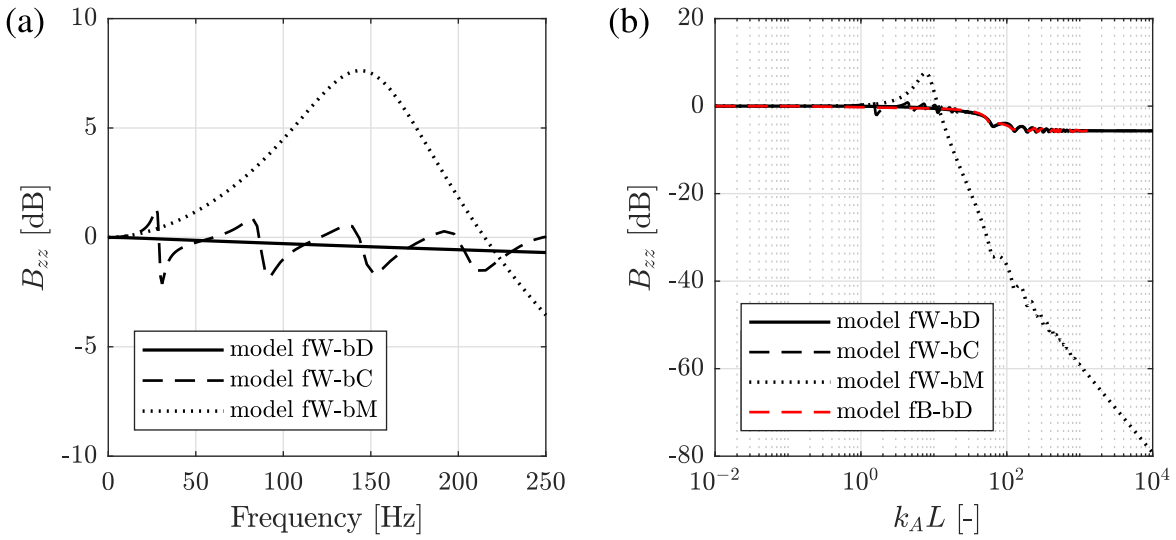

Fig. 3.16 Comparison of the magnitude of the term B_{zz} obtained by modelling the building as a damper (bD), a finite column (bC) or a rigid mass (bM). The soil-foundation system refers to a cone model of a rigid footing on a slab foundation (h = 1.5 m, see Table 3.1) overlying an elastic half-space with Poisson's ratio $\nu_s = 0.49$. No differences are found for the results (not reported here) obtained for Poisson's ratio $\nu_s = 1/3$. The results for the model fB-bD, referring to a rigorous BEM model of the foundation, are also shown for comparison.

This discussion and the investigation of Figure 3.15 highlight the role of the impedance mismatch at the foundation-building interface for the added-building effect. Moreover, it is demonstrated that, as long as the frequency-dependent parameters of the soil-foundation system and of the building are adequately captured, simplified foundation-building models may be adopted for the SSI analysis.

For sake of completeness, the case of a rigid footing on a slab foundation (i.e. benchmark #2) is considered next. Figure 3.16 shows the magnitude of B_{zz}. In this case, a lower value of attenuation is expected because of the stiffer soil-foundation system, which is 2 orders of magnitude greater than the one of benchmark #1. As before, by examining the results for the column model, the first amplification occurs at the natural frequency of the column as a rigid mass on the springs of stiffness $\widehat{K}_{bCz}$ and $\widehat{K}_{fz}$ combined in series. This time $\widehat{K}_{fz} >> \widehat{K}_{bCz}$ so that the equivalent spring stiffness is smaller then the value $\widehat{K}_{bCz}$ and the first amplification occurs at a frequency smaller than the fixed-free natural frequency of the finite column. This is completely misinterpreted by the rigid mass model (i.e. dotted line in Figure 3.16), which gives the first amplification at a much greater frequency. Restraining effects are visible at the fixed-free natural frequencies of the column. Moreover, because of the elastic layer (i.e. slab foundation), additional restraining effects are present at the free-free natural frequencies of the layer, which corresponds to the dimensionless frequencies

$k_A L \approx 63, 126, 189\ldots$ (see Figure 3.16b). Also in this occasion, the damper model of the building fits well the added-building effect obtained with the column model. It is worth noticing that the same results are obtained by adopting $\nu_s = 1/3$ or $\nu_s = 0.49$. At high frequencies, the magnitude of B_{zz} tends to a constant value, showing that no trapped mass effect is present in the case of a rigid footing on a slab foundation with $\nu_c = 0.15$ (see Table 3.1) overlying a soil with either $\nu_s = 1/3$ or $\nu_s = 0.49$.

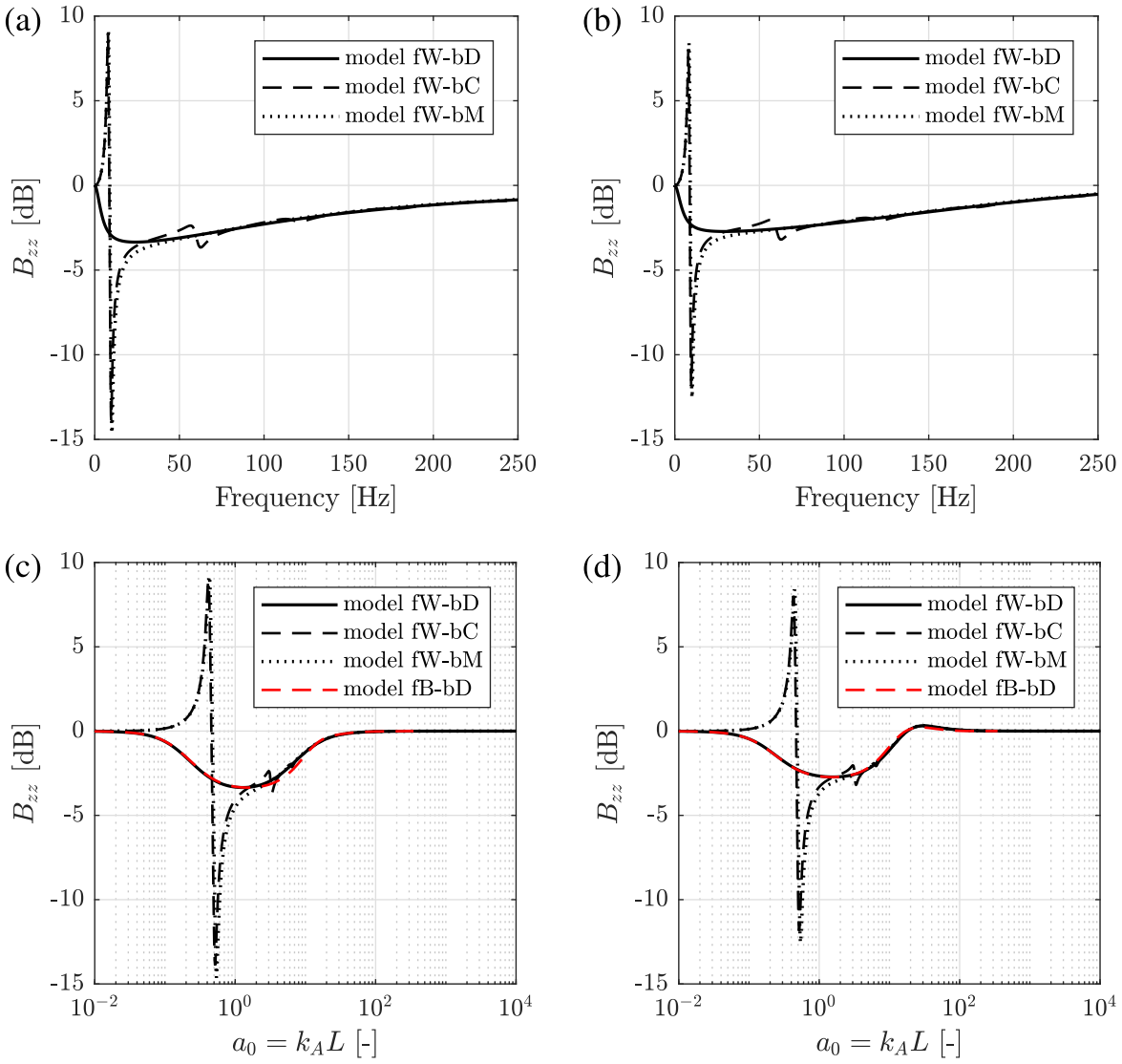

Fig. 3.17 Comparison of the magnitude of the term B_{zz} for a base-isolated building obtained by modelling the building as a damper (bD), a finite column (bC) or a rigid mass (bM). The cone model of a rigid foundation on an elastic half-space with Poisson's ratio $\nu_s = 1/3$ (a) and (c) or $\nu_s = 0.49$ (b) and (d) are considered for comparison of a compressible or incompressible soil respectively. The results for the model fB-bD, referring to a rigorous BEM model of the foundation, are also shown for comparison.

This may be explained by noticing that, as far as the foundation-building interface is concerned, at high frequencies the elastic layer may be seen as an elastic half-space and the limiting value of B_{zz} may be found, similarly to Equation 3.53, as:

$$\lim \left(B_{zz}^{(\text{uniso})}\right)_{a_0\to\infty} = -20\log_{10}\left\{\left|1+\frac{\rho_C}{\rho_c}\frac{V_A}{V_{Pc}}\right|\right\} \tag{3.55}$$

which provides an added-building attenuation of -5.8 dB that approximates well the result in Figure 3.16b.

Let us now consider the isolated case. Starting from the result in Equation 3.48b, the term B_{zz} can be expanded as:

$$\mathrm{B}_{zz}^{(\text{iso})} = \frac{\hat{w}_b^{(\text{iso})}}{\hat{w}_f} = \frac{1}{1+\dfrac{\widehat{K}_{Sbz}}{\widehat{K}_{fz}}} = \frac{1}{1+\dfrac{\widehat{K}_{bz}}{\widehat{K}_{fz}}\left(\dfrac{1}{1+\dfrac{\widehat{K}_{bz}}{k_{Sz}}}\right)} \tag{3.56}$$

By substitution of the vertical dynamic stiffness for the rigid foundation and the building as a damper (model fW-bD) the following closed-form expression in decibels is obtained:

$$B_{zz}^{(\text{iso})} = -20\log_{10}\left\{\left|1+0.75\frac{\rho_C}{\rho_s}\frac{V_A}{V_S}(1-\nu_s)\frac{ia_0}{1+(ia_0)^2\delta+ia_0c_{fz}}\left(\frac{1}{1+ia_0\dfrac{V_Ar_0}{a_{0S}^2V_SL}}\right)\right|\right\} \tag{3.57}$$

with a_0 and r_0 as previously defined (see Appendix A), and $a_{0S} = 2\pi f_S r_0/V_s$ related to the isolation frequency introduced in Section 3.4. Equation 3.57 clearly shows a reduced attenuation in comparison with the added-building effect for the unisolated case. Moreover, for both compressible and nearly incompressible soils no attenuation is expected at high frequencies. This is illustrated in Figure 3.17 for compressible (a) and (c) and nearly incompressible soils (b) and (d), referring to the data in Table 3.1, for an isolation frequency $f_S = 10\,\text{Hz}$. Similarly to the unisolated case, the first amplification occurs at the natural frequency of the column as a rigid mass on the springs, combined in series, provided by the soil-foundation, the column and the isolation. The latter has the smallest value of dynamic stiffness so that 10 Hz, in this case, is an upper bound for the frequency at which the first amplification appears. The restraining effect obtained for the column model is limited compared to the unisolated counterpart previously examined. Moreover, the frequencies at which the latter appears are shifted

compared to the unisolated counterpart. This can be qualitatively explained by looking at the the dynamic stiffness of the base-isolated column at its base:

$$\widehat{K}_{SbCz} = \frac{\widehat{K}_{SbCz} k_{Sz}}{\widehat{K}_{SbCz} + k_{Sz}} = -\frac{EAk_A \tan(k_A L) k_{Sz}}{k_{Sz} - EAk_A \tan(k_A L)} \tag{3.58}$$

From Equation 3.58, the fixed-free natural frequencies of the base-isolated column can be found as the roots of the following equation:

$$k_{Sz} = EAk_A \tan(k_A L) \tag{3.59}$$

which can be expressed in the dimensionless form as:

$$(k_{AS} L)^2 = k_A L \tan(k_A L) \tag{3.60}$$

with $k_{AS} = 2\pi f_S / V_A$. Figure 3.18 shows the dimensionless functions at the left and right side of Equation 3.60. Their intersections give the fixed-free natural frequencies of the base-isolated column, which shift towards the free-free natural frequencies of the column alone. It follows that peaks and troughs of the magnitude of B_{zz} are adjacent as illustrated in Figure 3.17. Figure 3.19

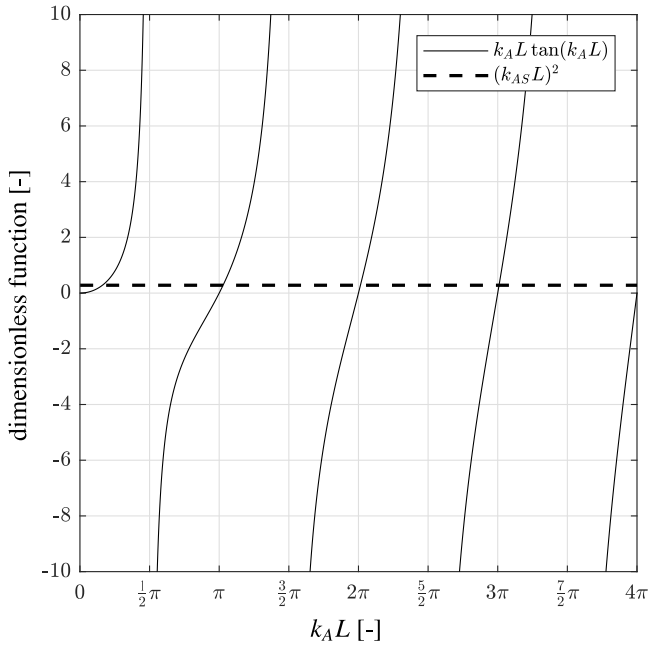

Fig. 3.18 Dimensionless functions reported for the graphical determination of the fixed-free natural frequencies of a base-isolated column with isolation frequency $f_S = 10$ Hz.

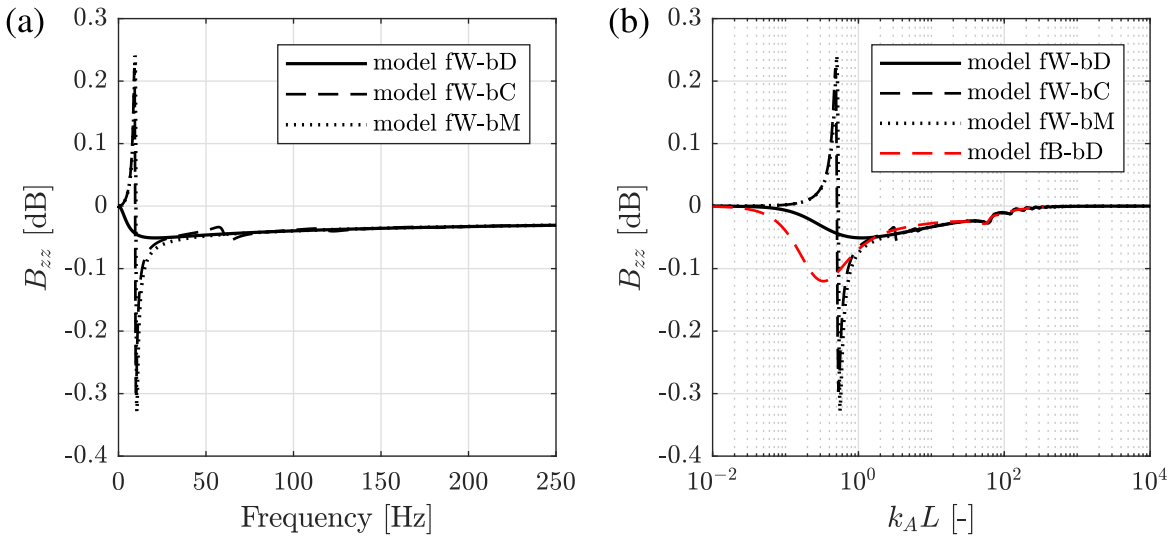

Fig. 3.19 Comparison of the magnitude of the term B_{zz} for a base-isolated building obtained by modelling the building as a damper (bD), a finite column (bC) or a rigid mass (bM). The soil-foundation system refers to a cone model of a rigid footing on a slab foundation (h = 1.5 m, see Table 3.1) overlying an elastic half-space with Poisson's ratio $\nu_s = 0.49$. No differences are found for the results (not reported here) obtained for Poisson's ratio $\nu_s = 1/3$. The results for the model fB-bD, referring to a rigorous BEM model of the foundation, are also shown for comparison.

shows the added-building effect for the simplified models of the base-isolated building, this time with reference to benchmark #2. The general trend is still valid and the previous general discussion applies.

The Added-Building Effect for horizontal-rocking input

The detailed description of the added-building effect in the vertical direction provides a general understanding of the effect of coupling a building to a soil-foundation system. This can, in principle, be extended to the horizontal and rocking DoFs. However, the horizontal-rocking coupling makes it difficult to obtain closed-form expressions for the relevant terms of the matrix **B**, as can be seen from Equation 3.49. Here, a qualitative discussion is made with the focus on the comparison between the results obtained with the simplified foundation model fW and the rigorous counterpart fB. The agreement between the two does not only depend on the cone-model assumption for the direct terms $\widehat{H}_{fWx}$ and $\widehat{H}_{fW\varphi}$, as introduced in Appendix A, but also on neglecting the horizontal-rocking coupling terms $\widehat{H}_{f\varphi x}$ in the simplified model fW.

Figure 3.20 shows the comparison for the B_{xx} term in the case of compressible (Figure 3.20a) and nearly incompressible soils (Figure 3.20b) obtained for benchmark #1. The agreement between

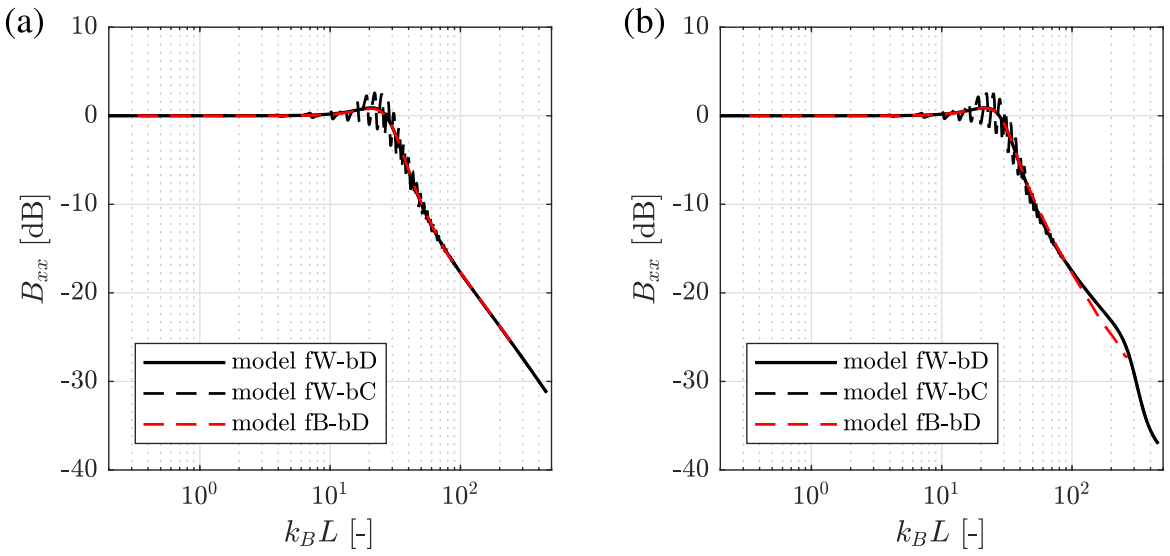

Fig. 3.20 Comparison of the magnitude of the term B_{xx} obtained by modelling the building as a damper (bD) or a finite column (bC). The cone model fW of a rigid foundation on an elastic half-space with Poisson's ratio $\nu_s = 1/3$ (a) or $\nu_s = 0.49$ (b) are considered for comparison of a compressible or incompressible soil respectively. The results for the model fB-bD, referring to a rigorous BEM model of the foundation, are also shown for comparison.

the results of model fW-bD and model fB-bD is favourable throughout the frequency range of interest for the case of $\nu_s = 1/3$. A similar agreement is obtained for $\nu_s = 0.49$ with differences at high frequencies in the order of 2 dB. There are no differences between Figure 3.20a and b up to a frequency $k_B L \approx 200$, indicating that the Poisson's ratio of the soil has a weak influence on the response of the unisolated building for most part of the frequency range of interest. It is worth noticing the amplification, for both compressible and nearly incompressible soils, in the order of 1 dB at $k_B L \approx 20$. The latter corresponds to $k_A L \approx 1.9$ for the benchmark problem, at which frequency an attenuation of about 10 dB is obtained for vertical vibration (see Figure 3.15). This highlights the importance of considering not only vertical but also horizontal vibration in ground-borne vibration problems, an aspect that is sometimes overlooked in practice.

For the term $B_{\varphi\varphi}$, as shown in Figure 3.21, the results for the model fW-bD show considerable attenuation up to 28 dB at $k_B L \approx 55$, after which a reduced attenuation is expected. Overall, a weak influence of the Poisson's ratio is found for part of the frequency range, with relevant differences up to 15 dB at high frequencies due to the trapped-mass effect, as discussed previously for vertical vibration (see Figure 3.15). By considering the modal behaviour of the building as a column (i.e. model fW-bC), amplifications and restraining effects are evident, for both B_{xx} and $B_{\varphi\varphi}$, at the

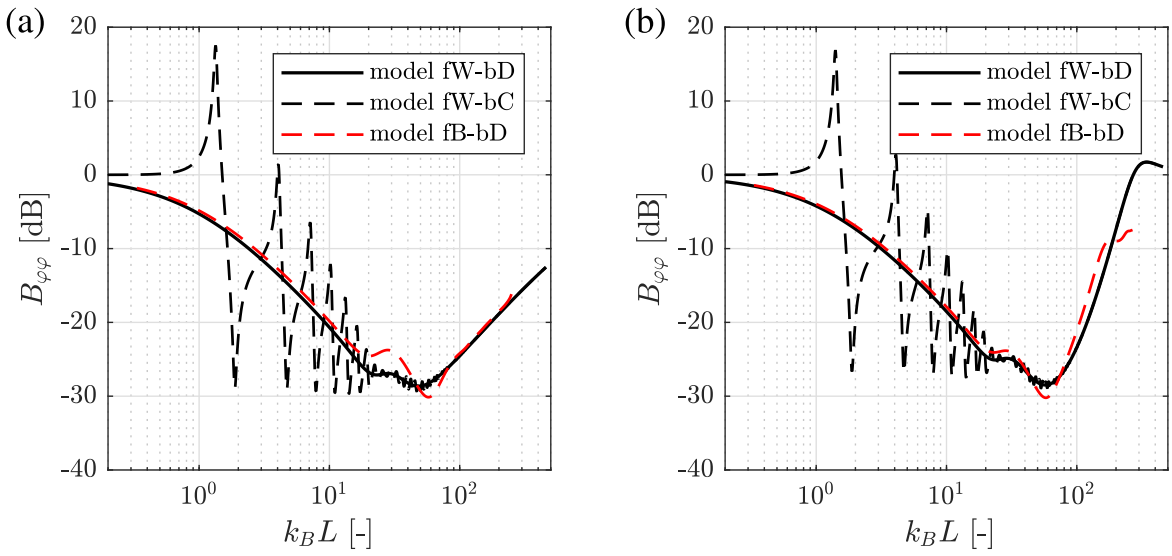

Fig. 3.21 Comparison of the magnitude of the term $B_{\varphi\varphi}$ obtained by modelling the building as a damper (bD) or a finite column (bC). The cone model fW of a rigid foundation on an elastic half-space with Poisson's ratio $\nu_s = 1/3$ (a) or $\nu_s = 0.49$ (b) are considered for comparison of a compressible or incompressible soil respectively. The results for the model fB-bD, referring to a rigorous BEM model of the foundation, are also shown for comparison.

clamped-free natural frequencies of the column [121]:

$$k_B L \approx 1.88, 4.69, 7.85, 11.00, \ldots \tag{3.61}$$

This effect is more pronounced for the term $B_{\varphi\varphi}$. In general, a good agreement is found between the results of $B_{\varphi\varphi}$ obtained for the model fW-bD and the model fB-bD.

Figure 3.22 shows the horizontal-rocking coupling terms $B_{x\varphi}$ and $B_{\varphi x}$ for benchmark #1 with $\nu_s = 0.49$. For the former, important differences up to 15 dB are found between the results of model fW-bD and model fB-bD at relatively low frequencies, with an improved agreement at relatively high frequencies. On the other hand, good agreement along the frequency range of interest is found for the term $B_{\varphi x}$ with difference up to 4 dB at high frequencies.

The more realistic case of benchmark #2 is examined next in Figure 3.23. It is worth noticing that the previous general comments are still valid in this case. The decreased attenuation, compared to the results for benchmark #1, observed for the direct terms B_{xx} and $B_{\varphi\varphi}$, is due to the stiffer soil-foundation system comprising the slab foundation. Moreover, the horizontal-rocking coupling terms $B_{x\varphi}$ and $B_{\varphi x}$ appear to provide, with respect to the counterparts of benchmark #1 in Figure 3.22, an increased attenuation at low frequencies and the same order of attenuation or an amplification

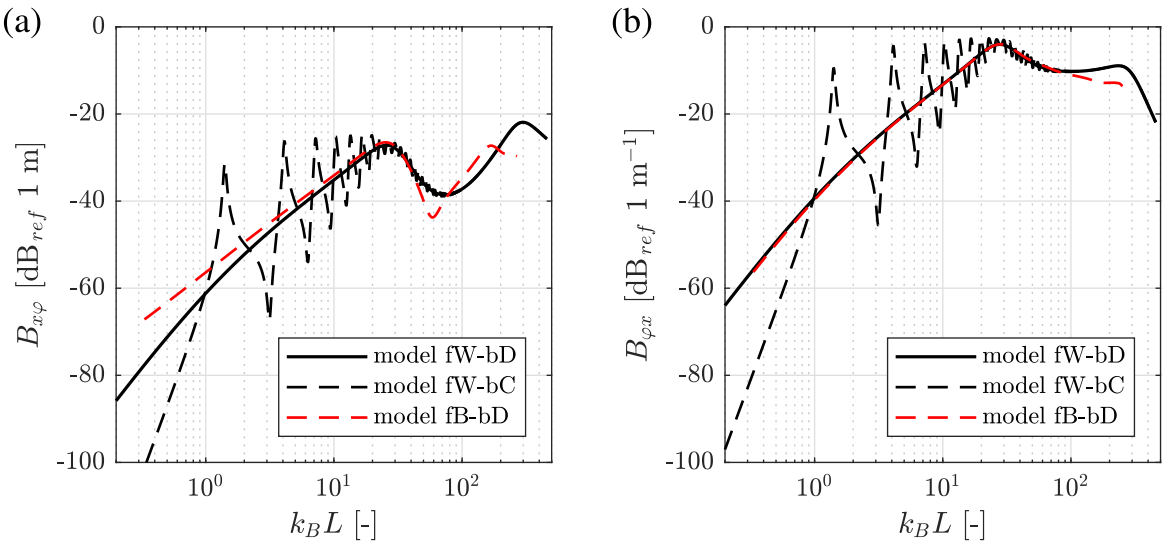

Fig. 3.22 Comparison of the magnitude of the term $B_{x\varphi}$ (a) and $B_{\varphi x}$ (b) obtained by modelling the building as a damper (bD) or a finite column (bC). The cone model fW of a rigid foundation on an elastic half-space with Poisson's ratio $\nu_s = 0.49$. is considered. The results for the model fB-bD, referring to a rigorous BEM model of the foundation, are also shown for comparison.

at high frequencies for $B_{x\varphi}$ and $B_{\varphi x}$ respectively. It must be noted that the terms $B_{x\varphi}$ and $B_{\varphi x}$ have dimensions of [m] and [m^{-1}] respectively. It follows that their contribution to the added-building effect must be evaluated directly on the transfer function $\hat{u}_{bi}/\hat{u}_{fi}$. The transfer functions for the lateral and rocking motion can be obtained as:

$$\frac{\hat{u}_b}{\hat{u}_f} = B_{xx} + B_{x\varphi}\frac{\hat{\varphi}_f}{\hat{u}_f} = B_{xx} + B_{x\varphi}\Theta_f \tag{3.62a}$$

$$\frac{\hat{\varphi}_b}{\hat{\varphi}_f} = B_{\varphi x}\frac{\hat{u}_f}{\hat{\varphi}_f} + B_{\varphi\varphi} = \frac{B_{\varphi x}}{\Theta_f} + B_{\varphi\varphi} \tag{3.62b}$$

The transfer function $\Theta_f = \hat{\varphi}_f/\hat{u}_f$ has dimensions [m^{-1}] and depends on the added-foundation effect of a rigid footing associated with an assumed incident wave-field. An approximate method for evaluating the added-foundation effect of rigid foundations and footings is presented in Chapter 5. An approximate expression of Θ_f is shown in Equation 5.45 and it is used here for evaluating the transfer functions $\hat{u}_b/\hat{u}_f$ and $\hat{\varphi}_b/\hat{\varphi}_f$, as shown in Figure 3.24, by considering an incident wave-field associated with a travelling Rayleigh wave in the elastic half-space. The parameter Θ_f depends on the ratio $\tilde{w}_2/\tilde{u}_2$ between the vertical and horizontal response amplitudes in the frequency-wavenumber domain associated with the added-foundation effect of the slab as an elastic layer (see Chapter 4). The transfer functions and the terms B_{xx} and $B_{\varphi\varphi}$ are reported in Figure 3.24. By comparison, it is

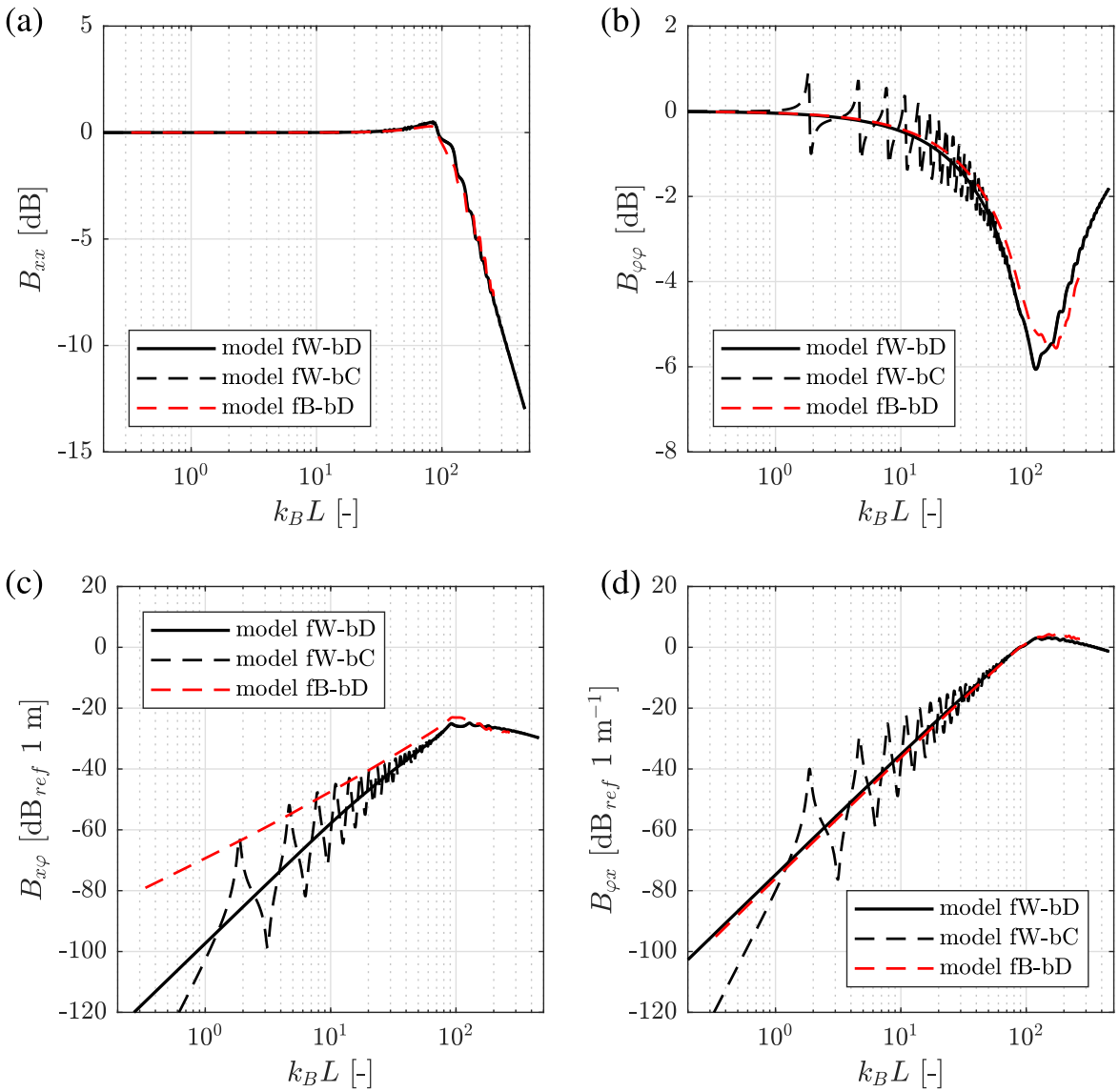

Fig. 3.23 Comparison of the magnitude of the term B_{xx} (a), $B_{\varphi\varphi}$ (b), $B_{x\varphi}$ (c) and $B_{\varphi x}$ (d) obtained by modelling the building as a damper (bD) or a finite column (bC). The soil-foundation system refers to a cone model fW of a rigid footing on a slab foundation (h = 1.5 m, see Table 3.1) overlying an elastic half-space with Poisson's ratio $\nu_s = 0.49$. The results for the model fB-bD, referring to a rigorous BEM model of the rigid footing, are also shown for comparison.

evident that the coupling terms $B_{x\varphi}$ and $B_{\varphi x}$, together with the parameter Θ_f have an important effect at relatively high frequencies. The amplification and the restraining effects are associated with the kinematic interaction of the rigid footing with the incident wave-field, a matter that is further discussed in Chapter 5. The transfer functions in Figure 3.24 show that, as far as the building's response in concerned and for the single-point coupling model examined here, the use of a simplified foundation

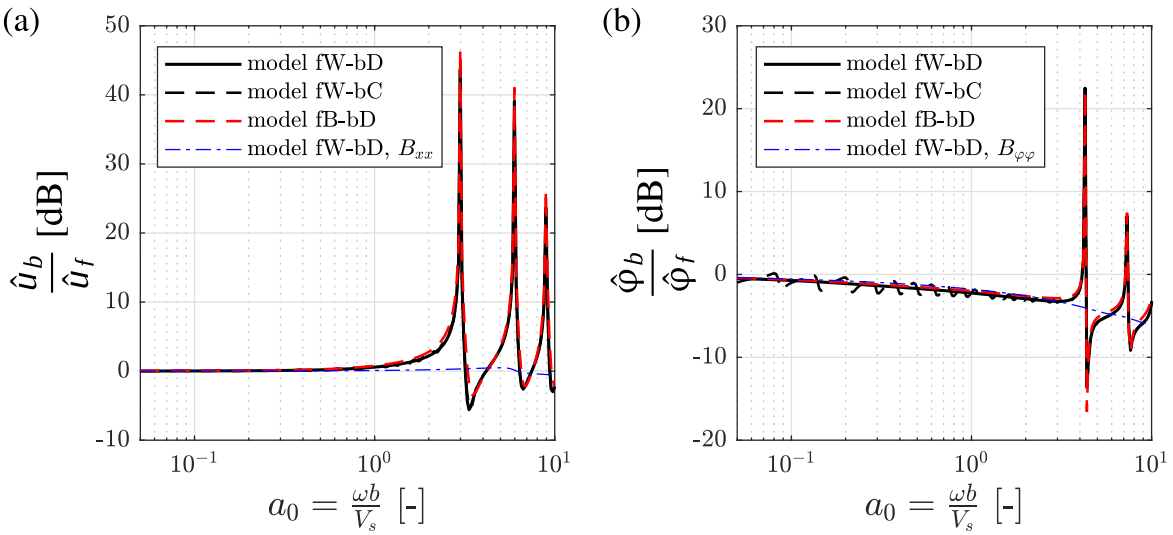

Fig. 3.24 The added-building effect for the horizontal-rocking response of the simplified foundation-building model fW-bD is shown in terms of the transfer functions (a) $\hat{u}_b/\hat{u}_f$ and (b) $\hat{\varphi}_b/\hat{\varphi}_f$ for a travelling Rayleigh wave and for benchmark #2 ($h = 1.5$ m, see Table 3.1) - unisolated case. Results for the model fB-bD, and the terms B_{xx} and $B_{\varphi\varphi}$ are also reported for comparison.

model is able to capture very well the SSI obtained with a more rigorous model. This suggests that the lateral-rocking cross-coupling terms of the rigid footing model have a minor influence on the SSI and that it is reasonable to use simplified foundation models for design purposes.

The added-building effect related to the base-isolated building is illustrated, in terms of the matrix components B_{xx}, $B_{\varphi\varphi}$, $B_{x\varphi}$ and $B_{\varphi x}$, in Figure 3.25 for the benchmark #2 and for $\nu_s = 0.49$. The agreement between the results of model fW-bD and model fB-bD is favourable for B_{xx} and $B_{\varphi\varphi}$, with a reduced level of attenuation with respect to the unisolated counterpart seen before. Conversely, a rather poor agreement is obtained for the term $B_{x\varphi}$ with differences as large as 35 dB. A better agreement is obtained for $B_{\varphi x}$ at relatively low frequencies, with differences up to 15 dB at high frequencies. Similarly to the unisolated case, the transfer functions $\hat{u}_u/\hat{u}_f$ and $\hat{\varphi}_u/\hat{\varphi}_f$ are shown in Figure 3.26. Differences between the results of model fW-bD and model fB-bD are small as is the added-building effect associated with an isolated building. The amplification and restraining effects associated with kinematic interaction are restricted to a very narrow frequency-band and they may differ in magnitude depending on the foundation model used.

The added-building effect as investigated in this section provides a first-principles approach to understand how the construction of a portal-frame building may affect the vibration field at the foundation-building interface. The simplified foundation-building model fW-bD may be adopted for

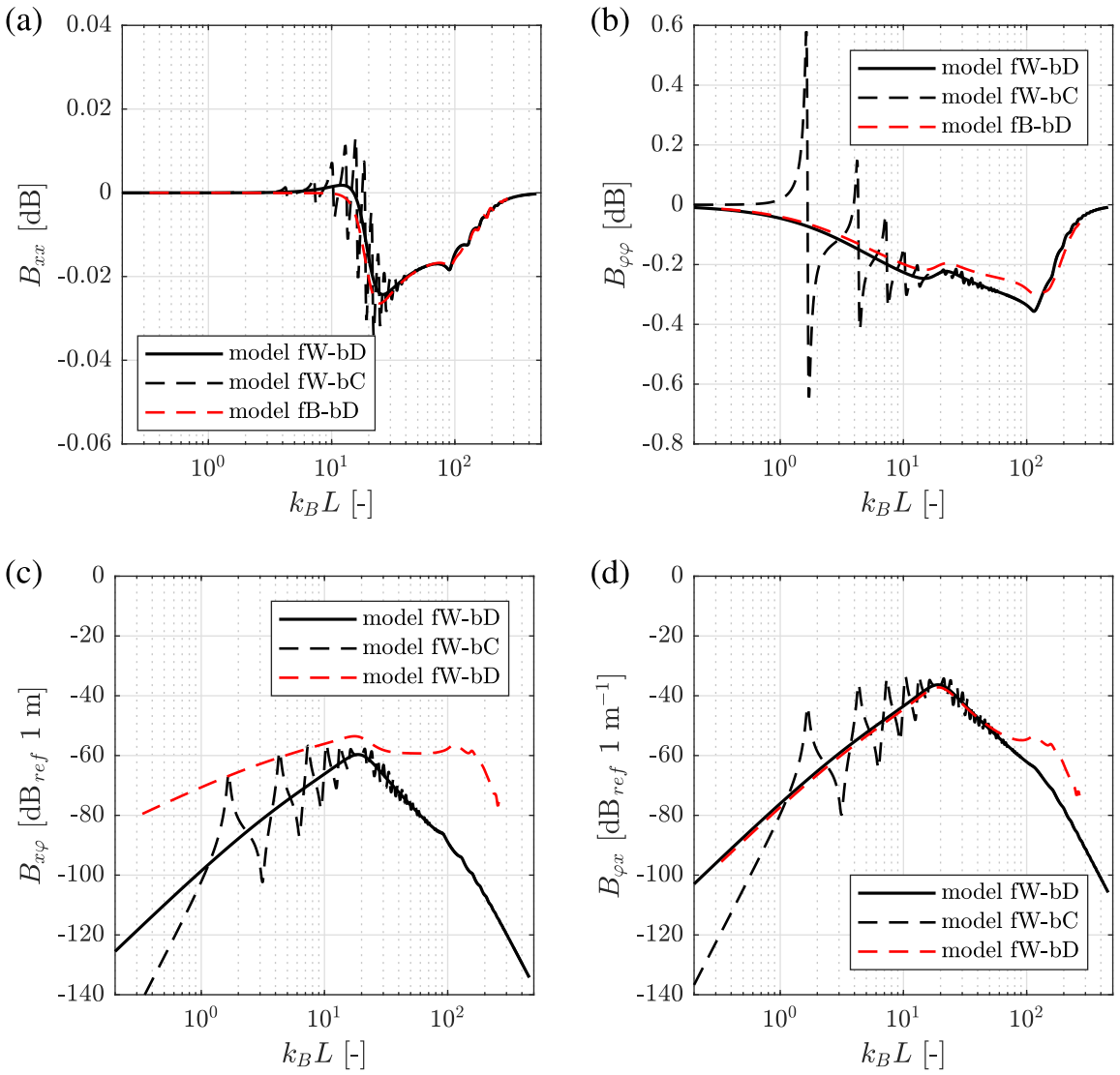

Fig. 3.25 Comparison of the magnitude of the term B_{xx} (a), $B_{\varphi\varphi}$ (b), $B_{x\varphi}$ (c) and $B_{\varphi x}$ (d) obtained by modelling the building as a damper (bD) or a finite column (bC). The soil-foundation system refers to a cone model of a rigid footing on a slab foundation (h = 1.5 m, see Table 3.1) overlying an elastic half-space with Poisson's ratio $\nu_s = 0.49$. The results for the model fB-bD, referring to a rigorous BEM model of the rigid footing, are also shown for comparison.

answering this question. Starting from a vibration field $\hat{\boldsymbol{u}}_{\boldsymbol{f}}$ at the coupling points, the vibration input $\hat{\boldsymbol{u}}_{\boldsymbol{b}}$ at the base of the unisolated building, and/or $\hat{\boldsymbol{u}}_{\boldsymbol{u}}$ for the isolated case, may be obtained by means of the transfer functions presented in this section for the vertical (Figures 3.16 and 3.19), and the lateral and rocking (Figures 3.24 and 3.26) vibration. The vibration field $\hat{\boldsymbol{u}}_{\boldsymbol{b}}$ or $\hat{\boldsymbol{u}}_{\boldsymbol{u}}$ may be then applied at the base of a more rigorous unisolated or isolated building model (e.g. Finite-Element-Method model) for obtaining vibration levels within the building. The extent to which this strategy holds valid depends

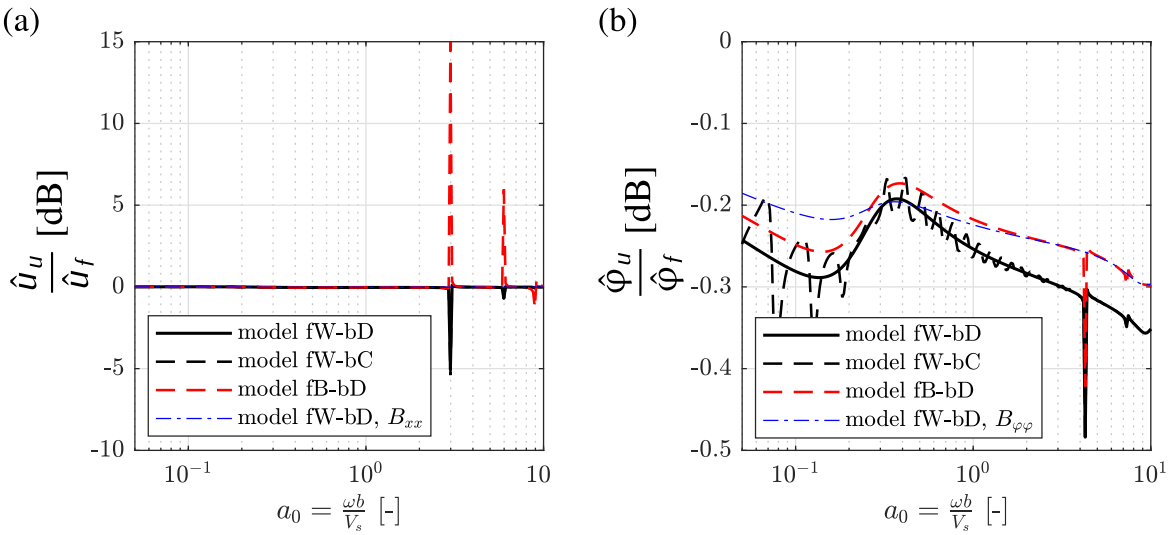

Fig. 3.26 The added-building effect for the horizontal-rocking response of the simplified foundation-building model fW-bD is shown in terms of the transfer functions (a) $\hat{u}_u/\hat{u}_f$ and $\hat{\varphi}_u/\hat{\varphi}_f$ for a travelling Rayleigh wave and for benchmark #2 (h = 1.5 m, see Table 3.1) - isolated case. Results for the model fB-bD, and the terms B_{xx} and $B_{\varphi\varphi}$ are also reported for comparison.

on the assumption of the building behaving as a damper and the soil-foundation system as a cone model at the contact points. The latter assumption is extensively checked against the results, in terms of the components of **B**, of the model fB-bD in Figures 3.15-3.26, holding good agreement for the direct terms but some deviations for the horizontal-rocking coupling terms, which have a negligible effect on the transfer functions of interest. The comparison in this section has regarded only the magnitude of the response and, of course, the phase information may have an important role on the adoption of the simplified models presented here for absolute predictions. Other relevant aspects are the through-soil coupling for the soil-foundation system and the through-floor coupling in the building with respect to the coupling points for a portal-frame building. These aspects are inherently neglected in the single-point coupling model and will be discussed further in Chapter 6. While the use of the model fW-bD for absolute vibration predictions may be an interesting alternative and/or backing option to the rigorous soil-foundation-building interaction, its investigation is left for further work to be address. In this dissertation, the adoption of the model fW-bD is confined to the evaluation of the isolation performance for base-isolated buildings.

3.5.2 Isolation performance

The isolation performance as introduced in Section 3.4.3 is here investigated with reference to the simplified foundation-building models. First, the equivalence of the *PFIG* and the *IG* for a single-point coupling model subjected to vertical input is proven in the following. Then, the isolation performance for vertical, horizontal and/or rocking input is investigated with reference to different values of isolation frequency f_S and different foundation typologies.

Equivalence of *IG* and *PFIG* for vertical input

The equivalence between the *IG* and the *PFIG* for a single-input-single-output model has been demonstrated by Talbot [33]. Here, the proof is contextualised to the single-point coupling model as used in this dissertation and presented in Section 3.1.3 and 3.4.2. For the sake of argument, let us treat the building model $\mathcal{B}$ as general as possible with fully-coupled vertical, horizontal and rocking DoFs. It may be required to evaluate the isolation performance of such a system in terms of the IG, as already defined in Equation 3.44, for a vibration field $\hat{\boldsymbol{u}}_{\boldsymbol{f}}$ at O or O' before the coupling of the unisolated or the base-isolated building respectively. From Equation 3.43a, the response at one location, in the vertical direction for the base-isolated building may be expressed as:

$$\hat{w}_n^{(\mathrm{iso})} = \begin{bmatrix} C_{xx}\left(\widehat{H}_{zx}^{(nb)}\widehat{K}_{bx} + \widehat{H}_{z\varphi}^{(nb)}\widehat{K}_{b\varphi x}\right) + C_{\varphi x}\left(\widehat{H}_{zx}^{(nb)}\widehat{K}_{bx\varphi} + \widehat{H}_{z\varphi}^{(nb)}\widehat{K}_{b\varphi}\right) \\ C_{zz}\widehat{H}_{zz}^{(nb)}\widehat{K}_{bz} \\ C_{x\varphi}\left(\widehat{H}_{zx}^{(nb)}\widehat{K}_{bx} + \widehat{H}_{z\varphi}^{(nb)}\widehat{K}_{b\varphi x}\right) + C_{\varphi\varphi}\left(\widehat{H}_{zx}^{(nb)}\widehat{K}_{bx\varphi} + \widehat{H}_{z\varphi}^{(nb)}\widehat{K}_{b\varphi}\right) \end{bmatrix}^T \begin{bmatrix} \hat{u}_f \\ \hat{w}_f \\ \hat{\varphi}_f \end{bmatrix} \tag{3.63}$$

Similarly, from Equation 3.43b, the response at the same location, in the vertical direction for the unisolated building may be expressed as:

$$\hat{w}_n^{(\mathrm{uniso})} = \begin{bmatrix} B_{xx}\left(\widehat{H}_{zx}^{(nb)}\widehat{K}_{bx} + \widehat{H}_{z\varphi}^{(nb)}\widehat{K}_{b\varphi x}\right) + B_{\varphi x}\left(\widehat{H}_{zx}^{(nb)}\widehat{K}_{bx\varphi} + \widehat{H}_{z\varphi}^{(nb)}\widehat{K}_{b\varphi}\right) \\ B_{zz}\widehat{H}_{zz}^{(nb)}\widehat{K}_{bz} \\ B_{x\varphi}\left(\widehat{H}_{zx}^{(nb)}\widehat{K}_{bx} + \widehat{H}_{z\varphi}^{(nb)}\widehat{K}_{b\varphi x}\right) + B_{\varphi\varphi}\left(\widehat{H}_{zx}^{(nb)}\widehat{K}_{bx\varphi} + \widehat{H}_{z\varphi}^{(nb)}\widehat{K}_{b\varphi}\right) \end{bmatrix}^T \begin{bmatrix} \hat{u}_f \\ \hat{w}_f \\ \hat{\varphi}_f \end{bmatrix} \tag{3.64}$$

Equations 3.63 and 3.64 illustrate the coupling of the three DoFs, with the vertical displacement $\hat{w}_n$ that depends on the horizontal, vertical and rocking motion of the foundation $\hat{\boldsymbol{u}}_{\boldsymbol{f}}$.

Let us consider the special case of the foundation being subjected only to a vertical motion $\hat{w}_f$. Because of the single-point coupling assumption, the resulting vertical motion $\hat{w}_n$ depends only on $\widehat{K}_{bz}, \widehat{H}_{fz}, \widehat{k}_{Sz}$ and on the FRF in the vertical direction $\widehat{H}_{zz}^{(nb)}$ between the base and the chosen location within the building. The Insertion Gain can be then evaluated from Equation 3.44 as:

$$IG_z = 20\log_{10}\left\{\left|\frac{C_{zz}}{B_{zz}}\right|\right\} \tag{3.65}$$

Equation 3.65 shows how, in this special case, the IG_z at any location within the building is equivalent to the IG_z evaluated at the base of the building.

By assuming the axial and the bending response of the building model to be uncoupled (e.g. model bC), the FRFs $\widehat{H}_{zx}^{(nb)}$ and $\widehat{H}_{z\varphi}^{(nb)}$ are null and Equation 3.65 is valid, in this case, also in the case of multi-directional input $\hat{\boldsymbol{u}}_{\boldsymbol{f}}$.

The isolation performance for the whole building, for a vertical input $\hat{w}_f$, may be found, in terms of the $PFIG$, by consideration of Equation 3.47:

$$\begin{aligned}
PFIG &= 10\log_{10}\left\{\left|\frac{Re\left\{(i\omega)\, w_f^{\star}\, C_{zz}^{\star}\, \widehat{K}_{bz}^{\star}\, C_{zz} w_f\right\}}{Re\left\{(i\omega)\, w_f^{\star}\, B_{zz}^{\star}\, \widehat{K}_{bz}^{\star}\, B_{zz}\, w_f\right\}}\right|\right\} = \\
&= 10\log_{10}\left\{\left|\frac{Re\left\{(i\omega)\, |C_{zz}|^2\, \widehat{K}_{bz}^{\star}\, |w_f|^2\right\}}{Re\left\{(i\omega)\, |B_{zz}|^2\, \widehat{K}_{bz}^{\star}\, |w_f|^2\right\}}\right|\right\} = \\
&= 10\log_{10}\left\{\left|\frac{\omega\, Im\left\{\widehat{K}_{bz}\right\} |C_{zz}|^2\, |w_f|^2}{\omega\, Im\left\{\widehat{K}_{bz}\right\} |B_{zz}|^2\, |w_f|^2}\right|\right\} = \\
&= 20\log_{10}\left\{\left|\frac{C_{zz}}{B_{zz}}\right|\right\}
\end{aligned} \tag{3.66}$$

Equations 3.66 and 3.65 show the equivalence of the $PFIG$ and the IG for the evaluation of the isolation performance of a single-point coupling model of a soil-foundation-building system with the soil-foundation system subjected to a vertical input $\hat{\boldsymbol{u}}_{\boldsymbol{f}} = [0 \quad \hat{w}_f \quad 0]^T$. Although this result refers to this specific case, it suggests the validity of the $PFIG$ as a scalar metric for the evaluation of isolation performance.

Isolation performance for vertical input

The simplified foundation-building models introduced in this chapter may be adopted for the evaluation of the isolation performance for a vertical input. Equation 3.65 may be expanded by substitution of B_{zz} from Equation 3.51 and C_{zz} from Equation 3.41 as:

$$\mathrm{PFIG} = \mathrm{IG}_z = \frac{C_{zz}}{B_{zz}} = \frac{1+\dfrac{\widehat{K}_{bz}}{\widehat{K}_{fz}}}{1+\dfrac{\widehat{K}_{bz}}{\widehat{K}_{fz}}+\dfrac{\widehat{K}_{bz}}{k_{Sz}}} = \frac{1}{1+\dfrac{\widehat{K}_{bz}}{k_{Sz}}\left(\dfrac{1}{1+\dfrac{\widehat{K}_{bz}}{\widehat{K}_{fz}}}\right)} \tag{3.67}$$

or in decibels:

$$PFIG = IG_z = -20\log_{10}\left\{\left|1+\frac{\widehat{K}_{bz}}{k_{Sz}}\left(\frac{1}{1+\dfrac{\widehat{K}_{bz}}{\widehat{K}_{fz}}}\right)\right|\right\} \tag{3.68}$$

Although this relatively simple expression for the IG_z is only achievable in the specific case discussed here, Equation 3.68 may provide a general insight for the design of base-isolated buildings. Equation 3.68 is also valid for the $PFIG$ by virtue of Equation 3.66. The isolation performance is related to the two stiffness ratios $\widehat{K}_{bz}/k_{Sz}$ and $\widehat{K}_{bz}/\widehat{K}_{fz}$.

By considering the foundation-building model fW-bD for benchmark #1, Equation 3.68 may be expressed as:

$$PFIG = IG_z = -20\log_{10}\left\{\left|1+\frac{ia_0}{a_{0S}^2}\frac{V_A r_0}{V_S L}\frac{1}{\left(1+0.75ia_0\dfrac{\rho_C V_A}{\rho_s V_S}\dfrac{(1-\nu_s)}{1-a_0^2\delta+ia_0 c_{fz}}\right)}\right|\right\} \tag{3.69}$$

Similarly to that seen for the added-building effect, limit expressions for $a_0 \to \infty$ may be obtained for the IG_z in the case of compressible and/or nearly incompressible soils:

$$\lim\left(IG_z\right)_{a_0\to\infty} = -20\log_{10}\left\{\left|1+\frac{ia_0}{a_{0S}^2}\frac{\rho_s V_P}{\rho_C V_S}\frac{r_0}{L}\right|\right\} \qquad \text{for} \quad \nu_s \le 1/3 \tag{3.70a}$$

$$\lim\left(IG_z\right)_{a_0\to\infty} = -20\log_{10}\left\{\left|1+\frac{ia_0}{a_{0S}^2}\frac{V_A}{V_S}\frac{r_0}{L}\right|\right\} \qquad \text{for} \quad \nu_s > 1/3 \tag{3.70b}$$

Figure 3.27 shows the comparison between the IG_z in the vertical direction at the base of the simplified building models investigated in this chapter. The results obtained by using a cone model fW for the

rigid foundation are shown in Figure 3.27 for $\nu_s = 1/3$ (a) and for $\nu_s = 0.49$ (b) in the frequency range of interest. The results of the column model fW-bC show the first amplification occurring at the natural frequency of the column as a rigid mass on the springs in series provided by the isolation, the column and the soil-foundation system. The first trough appears at the same frequency for which the first amplification is observed for B_{zz} as discussed for the added-building effect. Peaks and troughs are then present along the frequency range as the result of the axial modal behaviour of the column in both the isolated and unisolated configurations. The limit expressions in Equations 3.70a and 3.70b are reported in Figure 3.27(a) and (b) respectively. Although for compressible soils this represents an upper bound of the actual IG_z, Equation 3.70b fails to provide a useful estimation of IG_z for the case $\nu_s = 0.49$.

This may be explored further in Figure 3.27(c) and (d) where a large range of $a_0 = \omega r_0/V_s$ is considered for checking the agreement of the limit values with the IG_z of model fW-bD. It appears clear that Equations 3.70a and 3.70b may or may not be useful for base-isolation design depending on the range a_0 for the practical case of interest. For the reference problem, $a_0^{(\max)} \approx 2.2$ and while the limit expression gives a conservative estimate of the isolation performance for $\nu_s = 1/3$, the limit expression for $\nu_s = 0.49$ does not. In the latter case, the frequency-dependency of $\widehat{K}_{bz}$ and $\widehat{K}_{fz}$ leads to discrepancies of the limit expression with the IG_z of model fW-bD that are relevant in the frequency range $a_0 = 0.1 - 50$. Moreover, while an excellent agreement between the results of model fW-bD and model fB-bD is obtained for $\nu_s = 1/3$, the agreement for the case $\nu_s = 0.49$ is less satisfactory at high frequencies. This is because of the trapped-mass effect that is overestimated in the cone model for soils with $\nu_s < 1/2$, as already discussed in Section 3.2.

The presence of a slab foundation is examined next by considering the benchmark #2. Figure 3.28 shows the results of the IG_z in the same format as before, but only for $\nu_s = 1/3$ for the soil beneath the slab. The same results, not reported here, are obtained for $\nu_s = 0.49$, suggesting that the properties of the half-space beneath the layer may have a weak influence on the isolation performance. It may be then sufficient to consider the elastic layer as an elastic half-space, as already done for the added-building effect in Equation 3.55. The limit value in Equation 3.70a may be then contextualized to the material properties of the slab foundation and, since $\nu_c < 1/3$ from Table 3.1, it can expressed as:

$$\lim \left(IG_z\right)_{a_0 \to \infty} = -20 \log_{10} \left\{ \left| 1 + \frac{i a_{0c}}{a_{0Sc}^2} \frac{\rho_c V_{Pc}}{\rho_C V_{Sc}} \frac{r_0}{L} \right| \right\} \qquad \text{for} \quad \nu_c \leq 1/3 \tag{3.71}$$

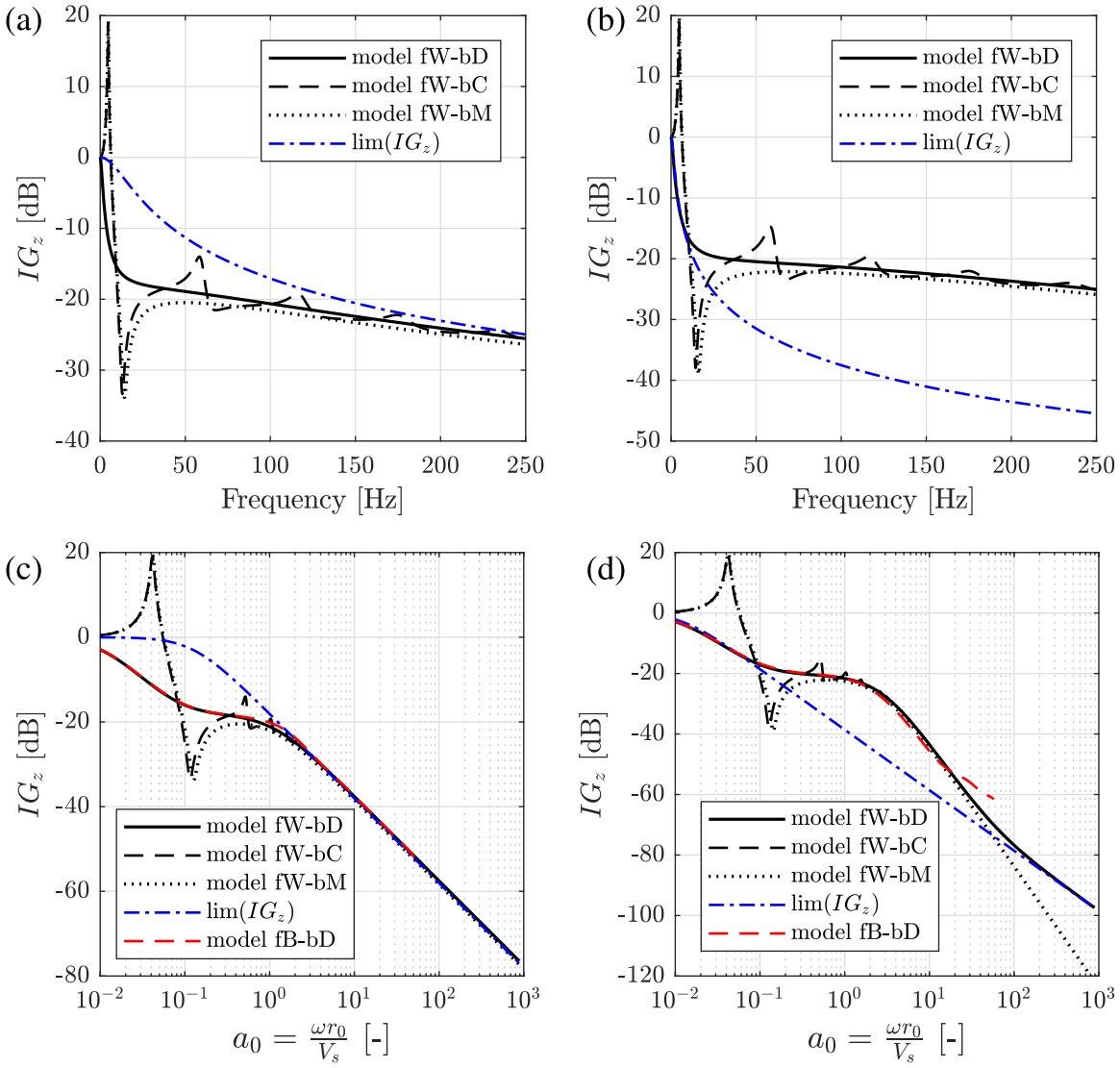

Fig. 3.27 Comparison of the Insertion Gain in the vertical direction (IG_z) at the base of the simplified building models and considering a vertical input w_f. Comparison is made between the results obtained by considering a cone model (solid black line) and a BEM model (dashed red line) for the rigid foundation. The benchmark #1 is considered with $\nu_s = 1/3$ (a) and (c), and $\nu_s = 0.49$ (b) and (d). Both the frequency range in Hz (a) and (b), and in terms of $a_0 = \omega r_0/V_s$ (c) and (d) are shown for reference. An isolation frequency of $f_S = 5$ Hz is considered with the rest of data as in Table 3.1.

with V_{Sc} and V_{Pc} the shear and compressional wave speeds in the concrete slab, $a_{0Sc} = \omega_S r_0/V_{Sc}$ the dimensionless isolation frequency and $a_{0c} = \omega r_0/V_{Sc}$. The limit value in Equation 3.71 is plotted against a_0 in Figure 3.28 (blue dash-dotted line) and compared with the results obtained by the model fW-bD and the model fB-bD, which refer to the simplified and the rigorous representation of the rigid footing. There is favourable agreement for the better part of the frequency range of

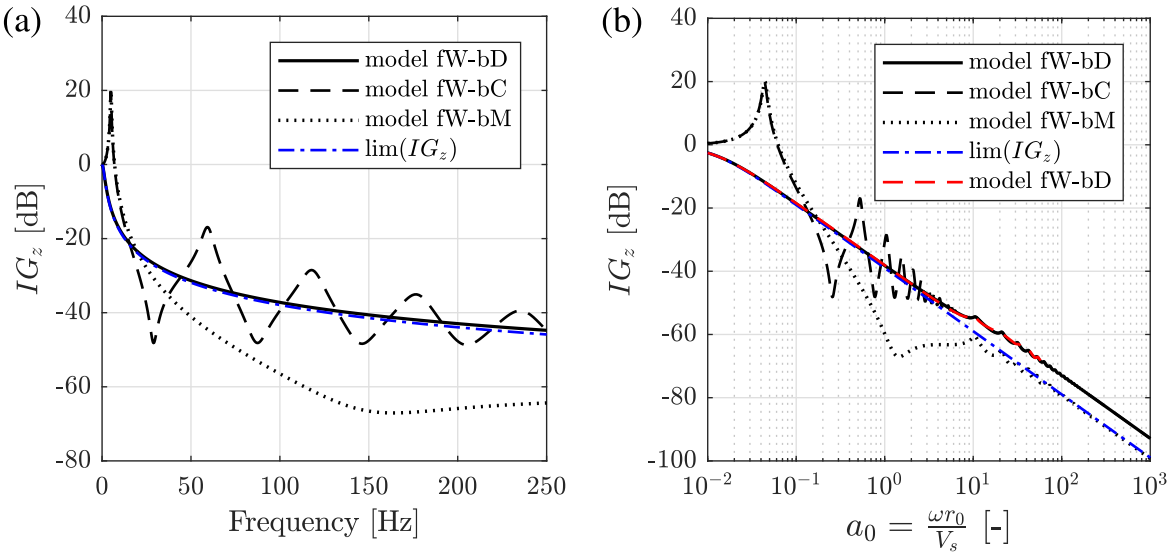

Fig. 3.28 Comparison of the Insertion Gain in the vertical direction (IG_z) at the base of the simplified building models and considering a vertical input w_f. Comparison is made between the results obtained by considering a cone model (solid black line) and a BEM model (dashed red line) for the rigid footing. The benchmark #2 is considered with $\nu_s = 1/3$. The case of $\nu_s = 0.49$ gives the same results and it is not reported here. Both the frequency range in Hz (a), and in terms of $a_0 = \omega r_0/V_s$ (b) are shown for reference. An isolation frequency of $f_S = 5$ Hz is considered with the rest of data as in Table 3.1.

interest (see Section 3.1.2). The limit expression then overestimates the isolation performance at high frequencies with differences of the order of 2 dB for $a_0 \approx 5$ and 5 dB for $a_0 \approx 10$. This divergence of results is counter-intuitive since at high frequencies the impedance of the rigid footing on the elastic layer is expected to converge to the impedance of the rigid foundation on an equivalent elastic half-space. Nonetheless, given the complexity of the model fW for the rigid footing (i.e. benchmark #2 - see Appendix A), it is challenging to look for the source of this inconsistency. It follows that the adoption of the limit value of the isolation performance in Equation 3.71 covers, with good approximation, the results of the IG as found by Equation 3.68 up to, say, $a_0 \approx 5$.

Isolation performance for horizontal-rocking input

The case of horizontal-rocking input is examined here. As it is evident from Equations 3.44 and 3.47, by considering an horizontal-rocking input $\hat{\boldsymbol{u}}_{\boldsymbol{f}} = [\hat{u}_f \quad 0 \quad \hat{\varphi}_f]^T$, it is not possible to obtain simplified expressions for the isolation performance. Even for the two extreme cases of purely horizontal $\hat{\boldsymbol{u}}_{\boldsymbol{f}} = [\hat{u}_f \quad 0 \quad 0]^T$ and/or purely rocking $\hat{\boldsymbol{u}}_{\boldsymbol{f}} = [0 \quad 0 \quad \hat{\varphi}_f]^T$ input, the isolation performance depends also on the horizontal-rocking coupling of the soil-foundation system and of the building model. In

the following, the IG and the $PFIG$ for the benchmark #1 and #2 are examined for the two cases. In the cases shown here, an isolation frequency of $f_S = 5$ Hz is considered. The influence of the latter on the isolation performance is investigated separately in the following section. Figure 3.29 shows the results for the IG and the $PFIG$ related the cone-damper model fW-bD by considering $\hat{\boldsymbol{u}}_{\boldsymbol{f}} = [\hat{u}_f \quad 0 \quad 0]^T$. The results are shown in terms of the IG_x referring to the horizontal DoF by

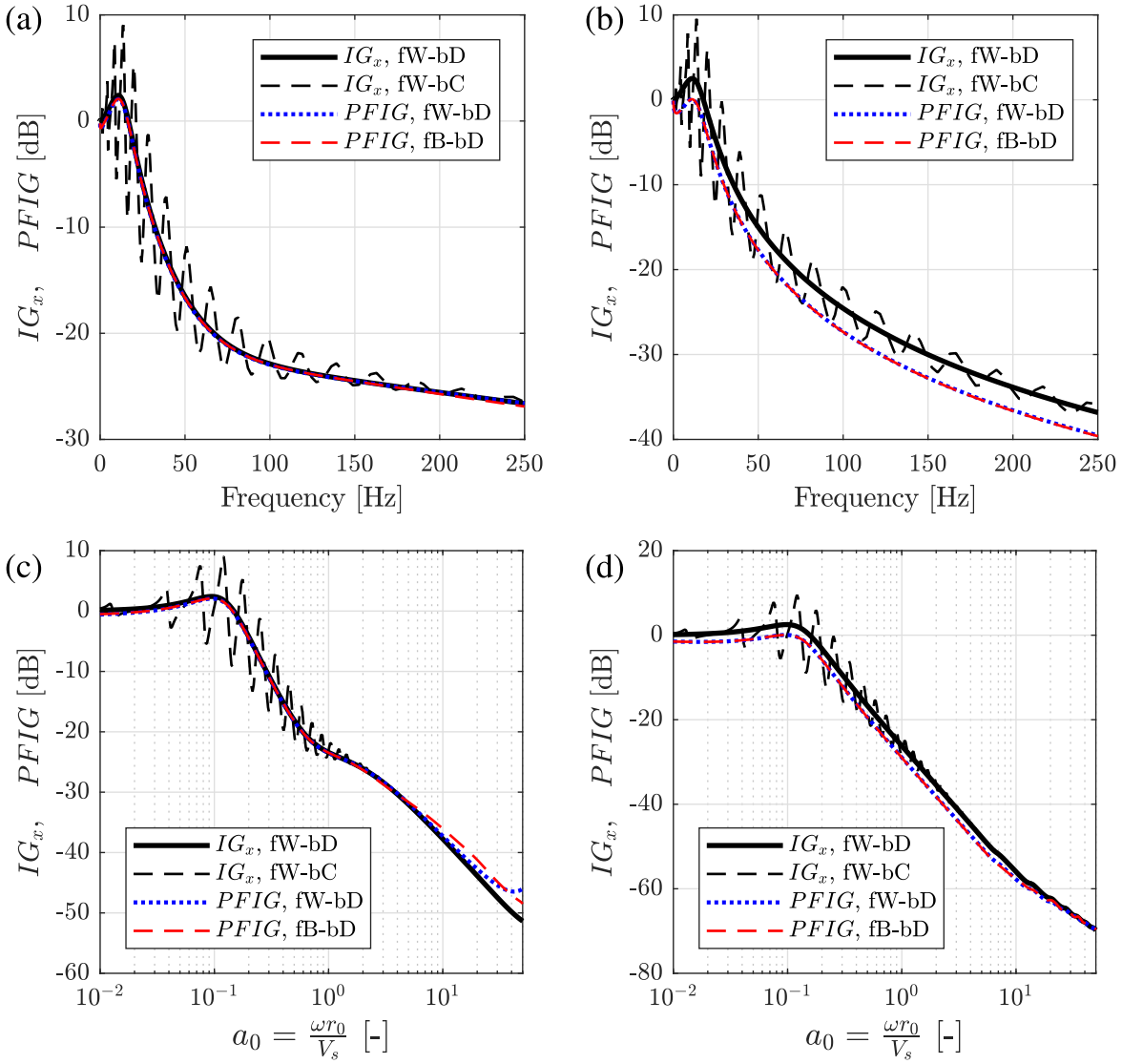

Fig. 3.29 Comparison of the Insertion Gain in the horizontal direction (IG_x) at the base of the simplified building models and considering a horizontal input u_f. Comparison is made between the results obtained in terms of IG_x and $PFIG$. The results in terms of the $PFIG$ for the model fB-bD (dashed red line) are also reported. Both the benchmark #1 (a) and (c), and the benchmark #2 (b) and (d) are considered with $\nu_s = 0.49$. Both the frequency range in Hz (a) and (b), and in terms of $a_0 = \omega r_0/V_s$ (c) and (d) are shown for reference. An isolation frequency of $f_S = 5$ Hz is considered with the rest of data as in Table 3.1.

means of the vector $\widehat{\boldsymbol{H}}_{\boldsymbol{nb}} = [\widehat{H}_{xx}^{(bb)} \quad \widehat{H}_{xz}^{(bb)} \quad \widehat{H}_{x\varphi}^{(bb)}]$ as used in Equation 3.44. Results are shown in the frequency range of interest (Figure 3.29(a) and (b)) and in terms of a_0 (Figure 3.29(c) and (d)) for both the benchmark #1 ((Figure 3.29(a) and (c)) and benchmark #2 ((Figure 3.29(b) and (d)). In both cases, positive values are obtained at relatively low frequencies when considered both the model fW-bD and the model fW-bC. This indicates an amplification of the vibration levels at low

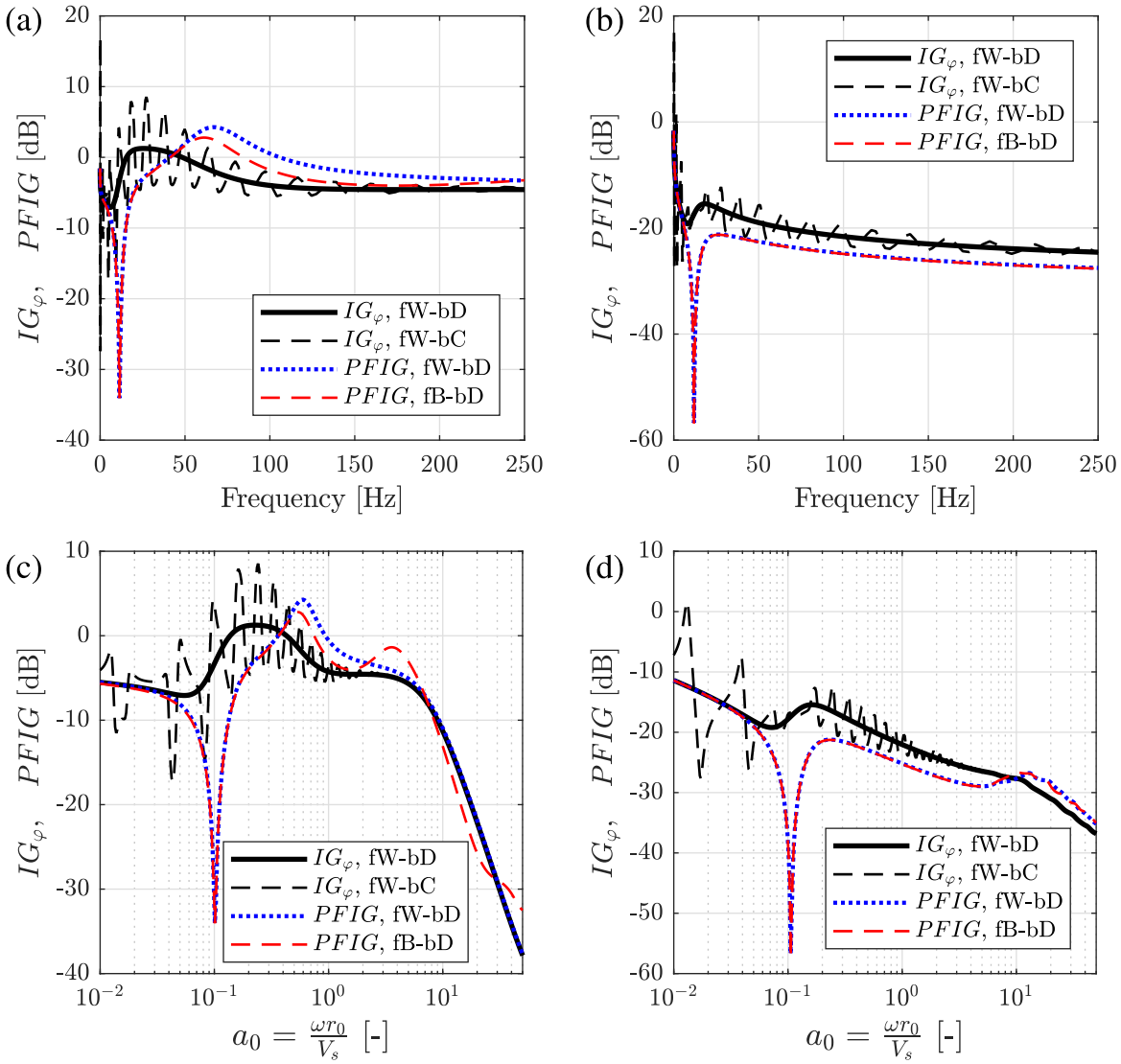

Fig. 3.30 Comparison of the Insertion Gain for the rocking DoF (IG_φ) at the base of the simplified building models and considering a rocking input φ_f. Comparison is made between the results obtained in terms of IG_φ and $PFIG$. The results in terms of the $PFIG$ for the model fB-bD (dashed red line) are also reported. Both the benchmark #1 (a) and (c), and the benchmark #2 (b) and (d) are considered with $\nu_s = 0.49$. Both the frequency range in Hz (a) and (b), and in terms of $a_0 = \omega r_0/V_s$ (c) and (d) are shown for reference. An isolation frequency of $f_S = 5$ Hz is considered with the rest of data as in Table 3.1.

frequencies that is a result of the soil-foundation-building interaction, with the modal behaviour of the building as a column that increases the level of amplification achieved. At higher frequencies, in the range of interest $20-250$ Hz, an attenuation of 3 to 27 dB and of 2 to 37 dB is achieved for benchmark #1 and #2 respectively. The results obtained with model fB-bD in terms of the $PFIG$ are in agreement with those referring to model fW-bD, indicating once more that cone models may be used as simplified models of the soil-foundation system for the evaluation of isolation performance. A final comment can be made about the metric used for the isolation performance: differences between the IG and the $PFIG$ for benchmark #1 are found only at high frequencies, while they are present in the order of 3 dB along the whole frequency-range of interest for benchmark #2.

Figure 3.30 shows the results in terms of the IG and the $PFIG$ in the same format as before, but this time for an input $\hat{\boldsymbol{u}}_{\boldsymbol{f}} = [0 \quad 0 \quad \hat{\varphi}_f]^T$. The results are shown in terms of the IG_φ referring to the rocking DoF, at the base of the building model, by means of the vector $\widehat{\boldsymbol{H}}_{\boldsymbol{nb}} = [\widehat{H}_{\varphi x}^{(bb)} \quad \widehat{H}_{\varphi z}^{(bb)} \quad \widehat{H}_{\varphi\varphi}^{(bb)}]$ as used in Equation 3.44. The isolation performance, for both benchmark #1 and #2, is characterised, approximately, by a plateau that extends up to $a_0 \approx 10$, which is the upper bound for the frequency range of interest as defined in Section 3.1.2. Moreover, a distinctive attenuation in terms of $PFIG$ is present at $a_0 \approx 0.1$ for both the benchmark problems. On the basis that the IG_φ does not show such a pronounced attenuation, this may be the result of cancelling of input and output mean vibrational power due to the horizontal-rocking coupling. The level of attenuation achieved, as for the case of vertical or horizontal input, depends strongly on the stiffness provided by the soil-foundation system; in the frequency range of interest $20-250$ Hz the IG_φ goes from 1 to -5 dB and from -15 to -25 dB for benchmark #1 and #2 respectively. A good agreement is obtained between the $PFIG$ results of model fW-bD and model fB-bD for benchmark #1 with differences of the order of 2 dB at relatively high frequencies. On the other hand, a perfect match is obtained for benchmark #2.

3.5.3 Design aspects of base-isolation

Starting from Equation 3.68 for the single-point coupling model considered in this chapter, design considerations on the influence of the isolation, the building and the soil-foundation properties on the isolation performance are discussed in the following.

Isolation and building design

It becomes evident that, although useful as a design specification, the isolation frequency f_S, as introduced in Section 2.6.3 and 3.4.1, fails to be a necessarily relevant parameter indicative of the isolation performance, as otherwise found by means of the rigid mass on a spring model (see Section 2.6.3). Equation 3.68 indicates that the isolation performance depends expressly on the isolation stiffness k_{Sz}. Although Equation 3.68 is valid for the specific case of vertical input, its conceptual significance may be well extended to the case of horizontal-rocking input. Because of the approach used in this dissertation, which is representative of the design practice, the magnitude of k_{Sz} depends on both the mass-per-column M_T, as defined in Section 3.4.1, and the target isolation frequency. It follows that an isolation system with a low f_S, say 5 Hz, does not necessarily lead to a significant isolation performance. For a given soil-foundation system (e.g. surface foundations), a specific building typology (e.g. portal-frame building), and a target isolation frequency f_S, the isolation performance ends up depending on the aspect ratio of the base-isolated building in question: squat buildings, with a low value of M_T and a large number of contact points with the foundation, will have an improved isolation performance, while tall buildings, with a generally high value of M_T and with a limited number of contact points with the foundation, will have a reduced isolation performance. In the latter case, in order to improve the isolation performance, the practising engineer may consider different options for the building design:

- a building design configuration with more closely spaced columns (i.e. contact points), than structural considerations would dictate, may be adopted for lowering the value M_T;
- lightweight structural and non-structural elements may be adopted without compromising the stiffness provided by the building, especially at the contact points with the foundation;

Whatever is the considered option, it is evident that base-isolation has profound implications on the structural building design, and that its consideration should be addressed at the early stages of the design process.

The isolation stiffness used for the results shown in Section 3.5.2 refers to the value calculated from the total mass of the column M_C, consistently with the model fW-bC. As discussed in Section 3.4.1, the total mass-per-column M_T includes the structural and non-structural mass and can be written as:

$$M_T = \frac{M_b}{n_C} = M_C(1+\sigma_M) \tag{3.72}$$

with M_b the total mass of the building (see Equation 3.35), n_C the number of columns (i.e. contact points) and σ_M the ratio between the additional mass-per-column and the mass M_C. For the reference problem $\sigma_M \approx 13$, which leads to an increase of one order of magnitude of the isolation stiffness with respect to the case examined in Section 3.5.2. The simplified expressions of the IG_z in Equations 3.69-3.71, referring to the model fW-bD, are still valid, given that the term a_{0S}^2 is substituted by $a_{0S}^2(1+\sigma_M)$. For instance, the expression for the limit value of the IG_z for benchmark #2 in Equation 3.71 can be re-written as:

$$\lim \left(IG_z\right)_{a_0 \to \infty} = -20 \log_{10} \left\{ \left| 1 + \frac{i a_{0c}}{a_{0Sc}^2 (1+\sigma_M)} \frac{\rho_c V_{Pc}}{\rho_C V_{Sc}} \frac{r_0}{L} \right| \right\} \qquad \text{for} \quad \nu_c \leq 1/3 \tag{3.73}$$

It follows that the results in Section 3.5.2 tend to overestimate the isolation performance for the benchmark problem. Figure 3.31 shows the isolation performance in terms of the PFIG for a purely horizontal input $\hat{u}_f$ (Figure 3.31(a) and (c)) and/or a purely vertical input $\hat{w}_f$ (Figure 3.31(b) and (d)) for the model fW-bD of the benchmark #2 and for different values of the isolation frequency f_S. The isolation stiffness is calculated by considering the total mass-per-column as defined in Equation 3.72. The results show a reduced isolation performance when compared with the related counterparts obtained in Section 3.5.2 (i.e. just considering the column mass M_C). In particular, for the case of an horizontal input, the amplification observed at relatively low frequencies in Figure 3.29 moves to frequencies that are relevant in ground-borne vibration. For instance, in the case of $f_S = 15$ Hz, an amplification of the mean vibrational power is expected throughout the frequency range of interest. Once more, this highlights the importance of considering both horizontal and vertical input motions in ground-borne vibration.

For the benchmark problem and for $f_S = 5$ Hz, the isolation performance, in term of the $PFIG$, may vary in the frequency range of interest in the order of -3 to -22 dB or 1 to -16 dB for vertical or horizontal input respectively. The latter represent a rather large variability of performance in the frequency range of interest; the results refer to the model fW-bD, which provides a mean value of performance. The variability of performance is expected only to increase when the modal behaviour of the building is accounted for, for instance by means of the model fW-bC, as shown in Figures 3.28 and 3.29. This aspect is addressed in Chapter 6 with the adoption of a portal-frame model for the building.

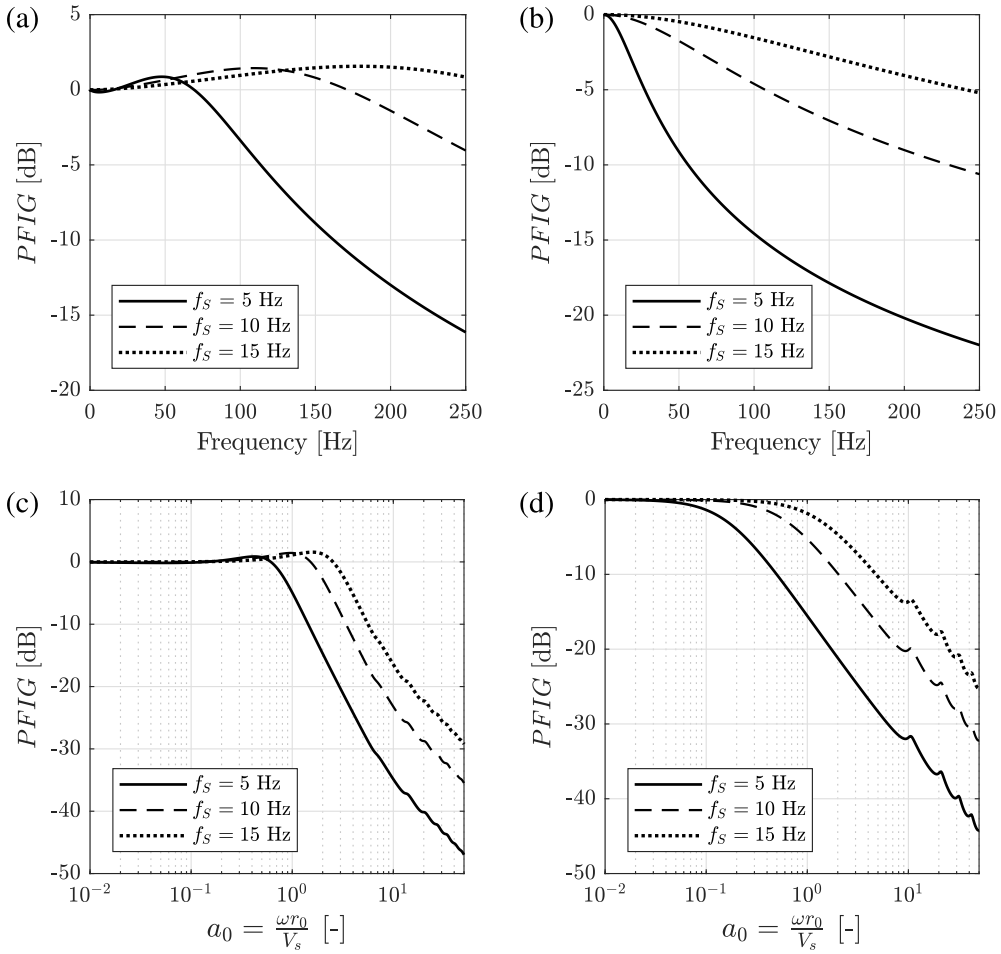

Fig. 3.31 Comparison of isolation performance, in terms of *PFIG* obtained for an horizontal (a) and (c), and vertical (b) and (d) input. The benchmark #2 model fW-bD is considered with $\nu_s = 0.49$ and for different isolation systems with $f_S = 5, 10, 15$ Hz.

Based on the assumptions for model fW-bD and for the base-isolation as defined in Section 3.4.1, an understanding of the difference in isolation performance for a vertical input referring to two different isolation systems with $f_S^{(\mathrm{A})}$ and $f_S^{(\mathrm{B})}$ may be obtained from Equation 3.68. The ratio between the IG associated with the two isolation systems can be written as:

$$\frac{\mathrm{IG}_z^{(\mathrm{B})}}{\mathrm{IG}_z^{(\mathrm{A})}} = \frac{1+\dfrac{\widehat{K}_{bz}}{k_{Sz}^{(\mathrm{A})}}\left(\dfrac{1}{1+\dfrac{\widehat{K}_{bz}}{\widehat{K}_{fz}}}\right)}{1+\dfrac{\widehat{K}_{bz}}{k_{Sz}^{(\mathrm{B})}}\left(\dfrac{1}{1+\dfrac{\widehat{K}_{bz}}{\widehat{K}_{fz}}}\right)} = \frac{1+\dfrac{\widehat{K}_{bz}}{k_{Sz}^{(\mathrm{A})}}+\dfrac{\widehat{K}_{bz}}{\widehat{K}_{fz}}}{1+\dfrac{\widehat{K}_{bz}}{k_{Sz}^{(\mathrm{B})}}+\dfrac{\widehat{K}_{bz}}{\widehat{K}_{fz}}}$$

Let us assume that $\widehat{K}_{bz}/k_{Sz}^{(\mathrm{A})} >> 1$ and $\widehat{K}_{bz}/k_{Sz}^{(\mathrm{B})} >> 1$; indeed, this is a requirement that is advised for the isolation system and that is naturally ensured at sufficiently high frequencies because of the frequency-dependency of $\widehat{K}_{bz}$ as defined in Equations 3.15 and 3.30 for the column and damper model respectively. The previous expression can be then approximated by:

$$\frac{\mathrm{IG}_z^{(\mathrm{B})}}{\mathrm{IG}_z^{(\mathrm{A})}} = \frac{\dfrac{\widehat{K}_{bz}}{k_{Sz}^{(\mathrm{A})}} + \dfrac{\widehat{K}_{bz}}{\widehat{K}_{fz}}}{\dfrac{\widehat{K}_{bz}}{k_{Sz}^{(\mathrm{B})}} + \dfrac{\widehat{K}_{bz}}{\widehat{K}_{fz}}} = \frac{\dfrac{\widehat{K}_{fz}}{k_{Sz}^{(\mathrm{A})}} + 1}{\dfrac{\widehat{K}_{fz}}{k_{Sz}^{(\mathrm{B})}} + 1}$$

Let us assume that $\widehat{K}_{fz}/k_{Sz}^{(\mathrm{A})} >> 1$ and $\widehat{K}_{fz}/k_{Sz}^{(\mathrm{B})} >> 1$, conditions that are satisfied at sufficiently high frequencies because of the frequency-dependency of $\widehat{K}_{fz}$ as defined in Appendix A. Then, an approximation of the previous expression, with consideration of Equation 3.34, is:

$$\frac{\mathrm{IG}_z^{(\mathrm{B})}}{\mathrm{IG}_z^{(\mathrm{A})}} = \frac{\dfrac{\widehat{K}_{fz}}{k_{Sz}^{(\mathrm{A})}}}{\dfrac{\widehat{K}_{fz}}{k_{Sz}^{(\mathrm{B})}}} = \frac{k_{Sz}^{(\mathrm{B})}}{k_{Sz}^{(\mathrm{A})}} = \left(\frac{f_S^{(\mathrm{B})}}{f_S^{(\mathrm{A})}}\right)^2$$

or in decibels:

$$IG_z^{(\mathrm{B})} - IG_z^{(\mathrm{A})} = 40\log_{10}\left\{\frac{f_S^{(\mathrm{B})}}{f_S^{(\mathrm{A})}}\right\} \tag{3.74}$$

The adoption of an isolation system (B) with $f_S = f_S^{(\mathrm{B})}$ will provide an improved or reduced attenuation, with respect to a firstly considered isolation system (A), in a measure defined by Equation 3.74. Based on the assumptions made to arrive at Equation 3.74, this result is only indicative along the frequency range of interest, since it represents an upper bound of the difference in isolation performance between the isolation systems (A) and (B). Nevertheless, at sufficiently high frequencies, Equation 3.74 provides a good interpretation of the results shown in Figure 3.31(d): the difference in isolation performance for isolation systems with $f_S = 10$ and 15 Hz and the reference isolation ($f_S = 5$ Hz) are in the order of 12 and 19 dB at $a_0 = 50$, as predicted by Equation 3.74. This is in agreement with the findings of Talbot [33], who concludes that differences up to 15 dB may be expected depending on the choice of the isolation frequency. It should be noted that this figure is only indicative since, as it will be seen in Chapter 6, the isolation performance for an actual building is strongly frequency-dependent and depends on the incident wave-field.

Foundation design

As for the previous discussion, the influence of the foundation design on the isolation performance may be investigated by means of Equation 3.68. A general understanding may be drawn from the latter: stiff or soft soil-foundation systems lead, respectively, to an improved or reduced isolation performance.

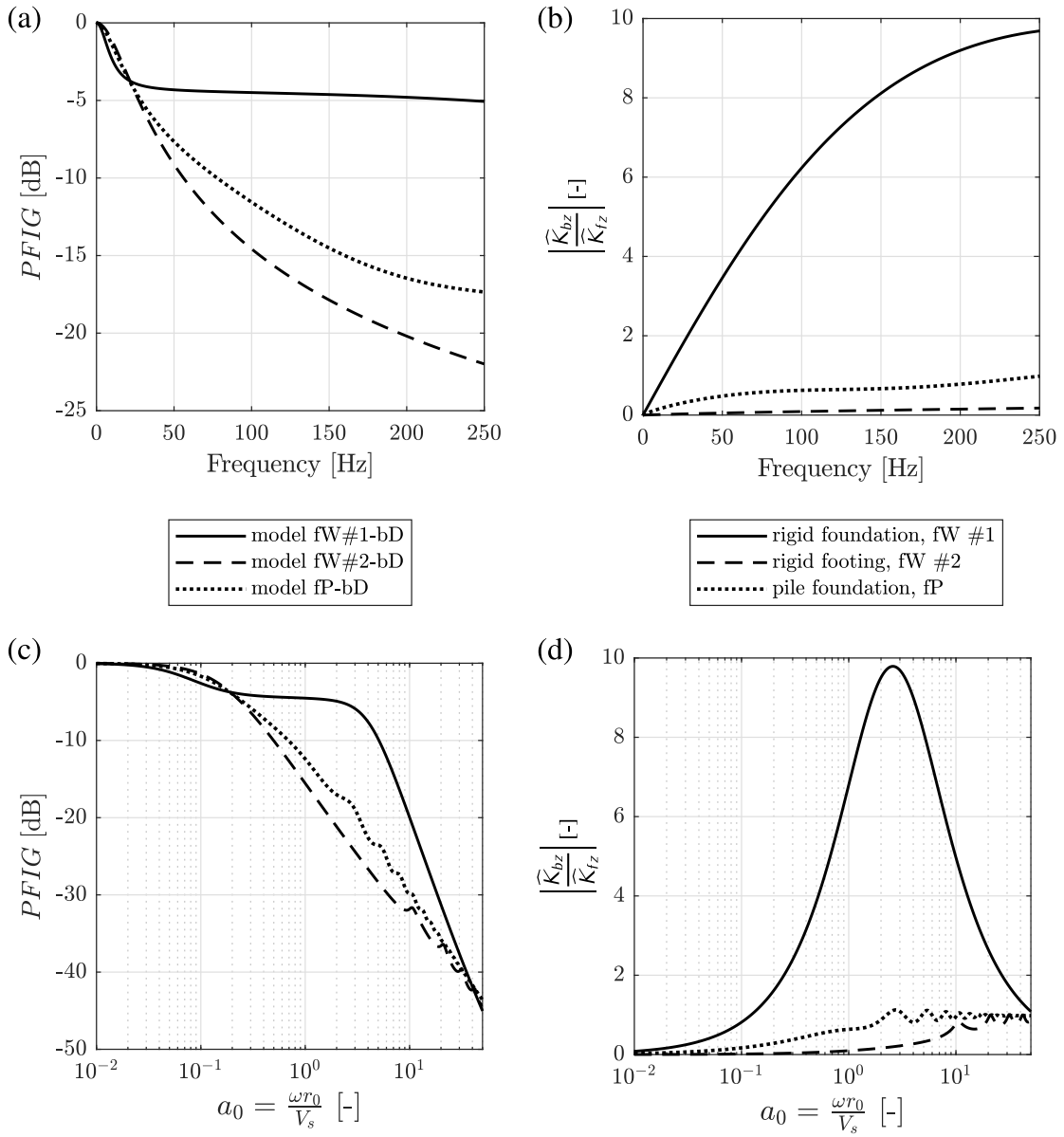

Fig. 3.32 Comparison of the isolation performance in terms of *PFIG* for a vertical input and with reference to (a) the frequency range of interest and (b) a possible frequency range for design in terms of a_0. The isolation performance refers to three different foundation typologies: a rigid foundation (solid line), a rigid footing on a 1.5 m thick slab foundation (dashed line) and a pile foundation (dotted line). The stiffness ratio $\widehat{K}_{bz}/\widehat{K}_{fz}$ is also reported in (b) and (d).

Based on the foundation typology and on the properties of the soil-foundation system, the provided building to soil-foundation stiffness ratio $\widehat{K}_{bz}/\widehat{K}_{fz}$ in Equation 3.68 indicates how efficient a given isolation system, for a given base-isolated building, will be depending on the soil-foundation system in place.

Figures 3.32(a) and (c) show the results in terms of the *PFIG* for a vertical input, for the benchmark building, and for an isolation frequency of $f_S = 5$ Hz, with different foundation typologies: a rigid foundation, a rigid footing on a 1.5 m thick slab foundation and a pile foundation with the same properties of the slab, a radius r_0 and a length $L_p = 20r_0$. The latter refers to the Novak's pile model as presented in Appendix A. Figures 3.32(b) and (d) show the magnitude of the stiffness ratio $\widehat{K}_{bz}/\widehat{K}_{fz}$ for the three foundation typologies considered. The stiffness ratio for the rigid foundation is one order of magnitude greater than the one obtained for the rigid footing and/or the pile foundation. It follows that the isolation performance expected for the rigid foundation model is smaller than the counterpart obtained for the other two foundation models. At relatively high frequencies, the stiffness ratios converge to the same value and so does the isolation performance (see Figure 3.32(c)). For the benchmark problem and for the frequency range of interest, differences up to 5 dB in isolation performance are found between the case of a pile and a footing foundation. It follows that a design consideration for improving the isolation performance would be to improve the stiffness provided by the soil-foundation system. The slab foundation is the typology that provides the best isolation

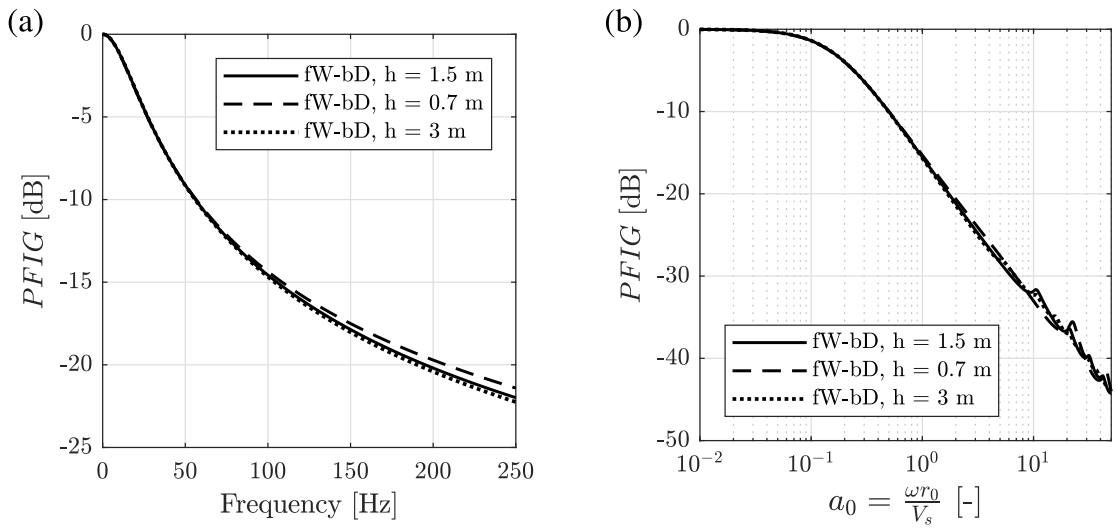

Fig. 3.33 Comparison of the isolation performance for the benchmark #2, with $\nu_s = 0.49$, in terms of the *PFIG* for a vertical input. Different values of the slab foundation thickness of $0.7, 1.5,$ and 3 m are adopted for the rigid footing model.

performance. It is instructive to investigate to what extent using a thicker slab foundation would improve the isolation performance. This is illustrated in Figure 3.33 where the results of the isolation performance for a slab foundation thickness of $0.7, 1.5,$ and 3 m are reported. The differences in isolation performance are small, at most 1 dB, indicating that, in practice, it may be challenging to stiffen the foundation system in a measure that is relevant for the isolation performance.

3.6 Overview of simplifying assumptions

Assumptions are made to redirect the general scenario described in Figure 3.1 to the simplified foundation-building model fW-bD presented in this chapter. Firstly, the general design scenario is brought back to the two-dimensional form of the reference problem (see Figure 3.2) by means of the following assumptions:

1. *two-dimensional representation* of the building with the associated horizontal, vertical and rocking DoFs. This assumption is considered on the basis that neglecting the three-dimensional arrangement of the building will not significantly change its impedance at the foundation-building interface. The latter is driving the SSI and the response of the soil-foundation-building system;

2. an *incident plane-wave* is considered as an external excitation; consistently with the previous point, the excitation is provided in the $x-z$ plane with $\theta_H = 0$;

3. an *infinitely large slab foundation* is considered on the basis that the foundation system often extends beyond the domain of the building; it is also a necessary assumption to simplify the scattering problem (i.e. added-foundation effect). The slab foundation is then of infinite extent along the x and y directions, and it can be modelled as a homogeneous and elastic layer.

The SSI can be then studied by means of the reference problem in Figure 3.2, which may still involve sophisticated modelling techniques for a rigorous approach. In this chapter, a simplified foundation-building model is suggested for solving the added-building effect, associated with the reference problem, by means of the following assumptions:

4. neglecting the *through-soil coupling* of the rigid footings. Any input $\hat{u}_f$ at the contact point l has no effect on the building response $\hat{u}_b$ at the contact point m;

5. neglecting the *through-floor coupling* within the building. Each column of the portal-frame building responds independently in both axial and bending vibration;

6. neglecting the *modal behaviour* associated with the finite dimension of the columns. Each column of the building is considered infinitely tall so that it may be represented by a damper with an associated impedance in axial and bending vibration;

7. a *cone model* is considered for obtaining the dynamic stiffness of the foundation as a rigid footing (i.e. benchmark #2) or a rigid foundation (i.e. benchmark #1). The assumptions of the latter are reported in Section 3.2 and Appendix A. The simplified foundation model has been proven to be sufficiently valid for the single-point model, as investigated in this chapter, by means of comparison of the added-building effect results obtained with a rigorous BEM model of the footing and/or the foundation.

The assumptions at the points 4, 5, 6 and 7 will be removed and investigated by means of a rigorous approach as described in Chapter 6.

3.7 Conclusions

This chapter has presented a general design scenario related to ground-borne vibration of buildings. By restricting the domain of the building and the foundation typologies, and by means of simplifying assumptions, a simplified foundation-building model, based on a single-point coupling, has been suggested. This greatly simplifies both the added-building effect and, consequently, the evaluation of the isolation performance for a base-isolated building.

The added-building effect involves the evaluation of the response at the base of the building starting from an input motion, at the same location, prior the construction of the building. By means of the suggested simplified foundation-building model, closed-form expressions are obtained for the transfer functions between the response and the input in vertical vibration and referring to both the unisolated and the isolated building for the case of a rigid foundation (i.e. benchmark #1). It is shown that closed-form expressions are hardly attainable for lateral and rocking vibration, and that the lateral-rocking coupling may play an important role especially in relation to the input motion for a given incident wave-field. Transfer functions are reported for the lateral and rocking DoFs, which

show possible amplifications in the frequency range of interest. This highlights the importance of considering both the vertical and lateral vibration; an aspect that is sometimes overlooked in practice.

The simplified foundation-building model provides a first-principles approach for evaluating the isolation performance for a base-isolated building. The equivalence between the *IG* and the *PFIG* is proven for a general single-point coupling model subjected to vertical input motion. This suggests the validity of the *PFIG* as a metric for the isolation performance, that, in general, includes the axial and the bending response of the building domain investigated. Closed-form expressions are obtained for the *IG* associated with a vertical input motion and for the case of a rigid foundation (i.e. benchmark #1), which is representative of a direct coupling of the building with the soil. It is shown that this can be extended to the case of a rigid footing (i.e. benchmark #2), which considers a possible slab foundation interposed between the soil and the building. This second case of a slab foundation is of practical significance and it is investigated further with respect to two design aspects: the isolation system and the foundation typology.

For a vertical input, it is found that the performance vary greatly depending on the adopted isolation system referring to a given isolation frequency f_S: for the benchmark 10 storeys building, *PFIG* values up to -22 dB and -5 dB are found for an isolation frequency of 5 Hz and 15 Hz respectively. It is shown that an upper bound for the difference in performance may be given by an expression involving the two values of the isolation frequency. The possibility of a horizontal input is also considered, with a resulting *PFIG* that indicates possible amplifications of the response in the frequency range of interest, if a stiff isolation system is adopted (e.g. $f_S = 15$ Hz for the benchmark #2). Once more, this suggests the importance of considering the multi-directional vibration environment. Finally, a rigid foundation (i.e. benchmark #1), a rigid footing (i.e. benchmark #2) and a pile foundation are adopted for observing the influence of the foundation typology. As expected, a stiffer foundation system provides an improved isolation performance.

In this chapter the discussion focused on the two aspects of the added-building effect and the isolation performance starting from a given input motion $\hat{\boldsymbol{u}}_{\boldsymbol{f}}$. Chapter 4 and 5 address the problem of calculating $\hat{\boldsymbol{u}}_{\boldsymbol{f}}$ starting from a given incident plane wave-field and consistently with the set up of the reference problem presented in this chapter. The following chapter addresses the added-foundation effect associated with the construction of a slab foundation on the ground subjected to an incident plane wave-field.

Chapter 4

The Added-Foundation Effect for an infinitely large slab foundation

This chapter explores the added-foundation effect provided by the slab foundation, illustrated in Section 3.1.2, and associated with different incident wave-fields representing surface (i.e. Rayleigh waves) and buried (i.e. P-, SV- body waves) vibration sources. The behaviour of a slab foundation resting on a soil subject to ground-borne vibration is a particular case of soil-structure interaction (SSI). As seen in Chapter 2, the SSI of foundation systems is extensively covered in literature, especially so for earthquake related problems. In the latter case, the problem involves long wavelengths and the foundation can be assumed to respond rigidly. On the other hand, problems related to ground-borne vibration involve relatively short wavelengths that are comparable with the dimensions of a typical foundation. In this case, the flexibility of the slab must be considered. A possible assumption is to consider the slab foundation as a homogeneous, linear-elastic and isotropic layer of infinite extent in the horizontal plane. This relates to a classical topic of continuum elasticity investigated by Rayleigh [176] and Lamb [80]. The *Rayleigh-Lamb* equation provides the dispersion relation for establishing the propagation velocity of waves in the so-called elastic layer. A comprehensive review on the topic is presented in the book of Graff [77] where reference is made to the work of Mindlin [187, 188]. Although the latter are of paramount importance for the physical interpretation of wave-propagation in an infinite layer, the focus in this chapter is more specific; the interest lies in the resulting vibration field related to a slab foundation coupled to the ground, with the latter subjected to an existing vibration field.

In this context, Auersch [1] considers the response of thin, flexural plates (representing the foundation slab) resting on an elastic half-space subjected to surface Rayleigh wave excitation. Both finite and infinitely-long plates are considered, using a combined finite-element boundary-element method, and a semi-analytical method in the frequency-wavenumber domain. Valuable results from a parametric study are presented that considers the influence of mass, stiffness and soil layering on the soil-slab interaction and the extent to which a slab attenuates ground vibration levels. In particular, Auersch concludes that the slab thickness is the dominant parameter governing the level of attenuation, since this essentially governs the frequency above which attenuation occurs.

The work presented in this chapter, which was first published by Sanitate & Talbot [157], begins by reproducing some of the results of Auersch, this time using the Stiffness Matrix Method (SMM) [189] (see Appendix C), otherwise known as the Direct Stiffness Method (DSM), implemented within the Elastodynamics Toolbox [116, 36] in MATLAB [35]. The slab foundation is modelled as an elastic layer, of infinite horizontal extent and finite thickness, overlying an elastic half-space. This allows the influence of the assumed boundary conditions at the soil-slab interface to be studied, as well as the effect of the plate-like assumption for the slab. Having considered surface Rayleigh wave excitation, the case of a buried source is investigated by considering incident P- and SV-waves, before considering the overall implications of the study for foundation design.

4.1 Overview of the problem

Our interest is the particular SSI associated with a flexible, concrete slab foundation, that is, the influence of such a slab on the free-surface vibration field, expressed in terms of the ratio of the vibration amplitudes after and before the construction of the slab. As a first approximation, the slab may be assumed to be of infinite horizontal extent. This assumption is supported by Auersch [1], who demonstrates that, for the case of Rayleigh wave excitation, the SSI associated with a finite plate may be approximated by that of an infinitely long one (see Figure 4.1). Here, the slab is treated as an elastic layer of thickness h and infinite extent in both the x and y directions, with shear modulus G_c, Poisson's ratio ν_c and mass density ρ_c (see Figure 4.2). The underlying soil is modelled as a homogeneous, isotropic, elastic half-space, with shear modulus G_s, Poisson's ratio ν_s and mass density ρ_s. As discussed in Section 3.2.3, damping in both the slab and the soil is assumed to be hysteretic, as described by a frequency-independent loss factor in shear, with no associated damping in

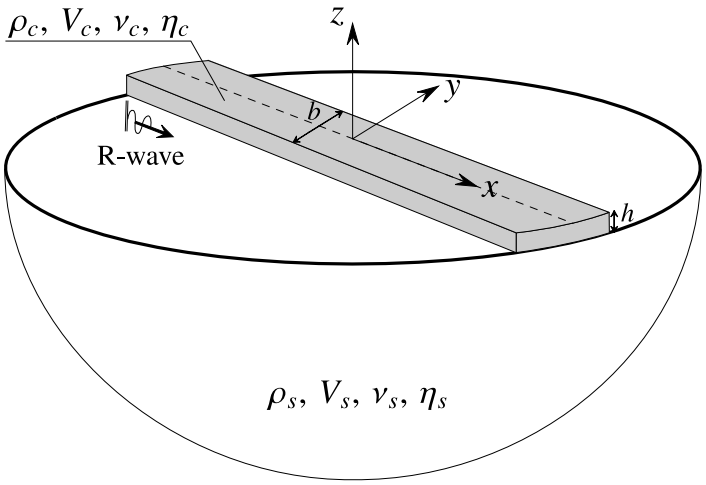

Fig. 4.1 The infinitely-long strip foundation model as considered by Auersch [1].

dilatation. Both surface and body, plane-wave excitation is considered: a Rayleigh wave travelling in the x-direction with speed V_R, and either an incident P- or SV-wave travelling respectively with speed V_P or V_S at an incidence angle θ_P or θ_S. Such excitation may be regarded as being broadly representative of that from either a surface or underground railway.

The wave excitation is assumed to be plane and therefore invariant in the y-direction. The problem can then be examined in the $x-z$ plane with reference to the vertical and horizontal displacement amplitudes. The free-field displacement $\hat{\mathbf{u}}_\mathbf{0}$ of the half-space, the interface displacement $\hat{\mathbf{u}}_\mathbf{1}$ and the free-surface displacement $\hat{\mathbf{u}}_\mathbf{2}$ of the slab in the frequency-space domain can be expressed in vector

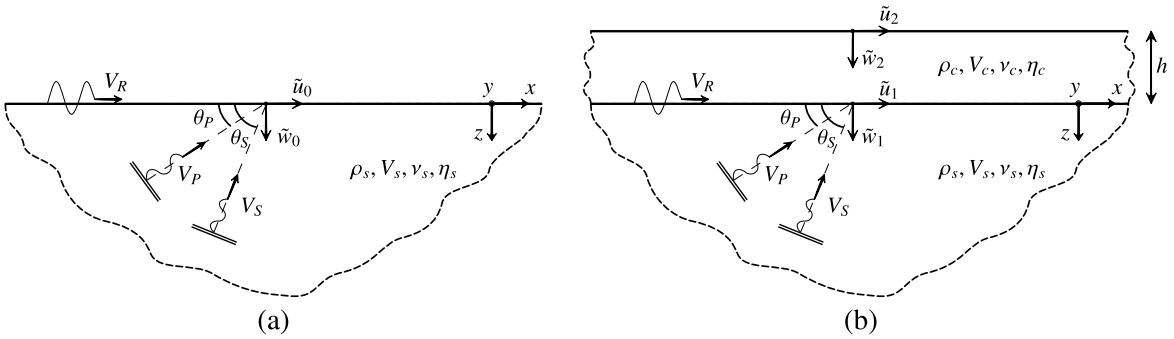

Fig. 4.2 (a) The free-field displacement amplitude $\mathbf{u_0}$ on the surface of an elastic half-space subjected to surface and body plane-wave excitation. A Rayleigh wave travelling in the x-direction with speed V_R, and a P- and SV-wave travelling with speeds V_P and V_S at incidence angles θ_P and θ_S are considered; (b) the corresponding response following the construction of a slab foundation, expressed in terms of the interface displacement $\mathbf{u_1}$ and the displacement $\mathbf{u_2}$ on the free-surface of the slab.

form as:

$$\begin{aligned}\hat{\mathbf{u}}_\mathbf{0} &= \tilde{\mathbf{u}}_\mathbf{0}\, e^{i(\omega t - k_x x)} \\ \hat{\mathbf{u}}_\mathbf{1} &= \tilde{\mathbf{u}}_\mathbf{1}\, e^{i(\omega t - k_x x)} \\ \hat{\mathbf{u}}_\mathbf{2} &= \tilde{\mathbf{u}}_\mathbf{2}\, e^{i(\omega t - k_x x)}\end{aligned} \tag{4.1}$$

where ω and k_x are the angular frequency and the horizontal wavenumber of the vibration field. The displacement vectors in the frequency-wavenumber domain $\tilde{\mathbf{u}}_\mathbf{0} = [\tilde{u}_0, \tilde{w}_0]^{\mathrm{T}}$, $\tilde{\mathbf{u}}_\mathbf{1} = [\tilde{u}_1, \tilde{w}_1]^{\mathrm{T}}$ and $\tilde{\mathbf{u}}_\mathbf{2} = [\tilde{u}_2, \tilde{w}_2]^{\mathrm{T}}$, which are independent of the x coordinate due to the infinite extent of the slab, describe the influence of the slab foundation. Depending on the type of wave excitation considered, the horizontal wavenumber k_x can be written as:

$$k_x = k_R\,; \quad k_x = k_P \cos\theta_P\,; \quad k_x = k_S \cos\theta_S \tag{4.2}$$

where k_R, k_P and k_S are the wavenumbers of the Rayleigh, P- and SV-waves respectively. More generally, introducing the ratio $\gamma = V/V_S$ with V the velocity of the incident wave, the horizontal wavenumber k_x and the horizontal wavelength can be expressed as:

$$k_x = \frac{k_S}{\gamma}\cos\theta_V; \qquad \lambda_x = \frac{2\pi}{k_x} = \frac{V_S \gamma}{f\cos\theta_V} \tag{4.3}$$

with f the frequency of the harmonic excitation considered and θ_V the angle in the $x-z$ plane of the incident wave, alternatively denoted θ_P and θ_S for P- and SV-waves respectively and being null for Rayleigh waves. The parameter γ depends only on the Poisson's ratio of the material; exact and approximate expressions of γ exist in literature for P- and Rayleigh waves respectively [77]:

$$\gamma_P = \sqrt{\frac{2-2\nu}{1-2\nu}}; \qquad \gamma_R = \frac{0.87+1.12\nu}{1+\nu}; \qquad \gamma_S = 1 \tag{4.4}$$

Because of the incident wave assumption, so-called weak coupling is assumed between source and receiver, in which only the coupling between the soil and the slab is accounted for; any coupling with the original source of the vibration is assumed to be negligible. The interest lies in the influence of the slab foundation on the free-field displacement $\hat{\mathbf{u}}_\mathbf{0}$, that is the effect of the construction of a foundation on the existing vibration levels. Having introduced the framework of the formulation, as illustrated in Figure 4.2, the coupling of the slab can be obtained by consideration of dynamic stiffness

matrices of the layer $\tilde{\mathbf{K}}_\mathbf{f}$ and the half-space $\tilde{\mathbf{K}}_\mathbf{s}$:

$$\tilde{\mathbf{K}}_\mathbf{f} = \begin{bmatrix} \tilde{\mathbf{K}}_\mathbf{f}^{11} & \tilde{\mathbf{K}}_\mathbf{f}^{12} \\ \\ \tilde{\mathbf{K}}_\mathbf{f}^{21} & \tilde{\mathbf{K}}_\mathbf{f}^{22} \end{bmatrix}; \qquad \tilde{\mathbf{K}}_\mathbf{s} = \tilde{\mathbf{K}}_\mathbf{s}^{11} \tag{4.5}$$

with the superscript 1 and 2 referring to the degrees of freedom at the interface and at the free-surface respectively. The stiffness matrices in Equation 4.5 refer to reduced stress and displacement vectors as discussed in the Appendix C. By ensuring equilibrium and compatibility at the soil-foundation interface, the displacement $\tilde{\mathbf{u}}_\mathbf{1}$ at the interface can be expressed as:

$$\tilde{\mathbf{u}}_\mathbf{1} = \left[\mathbf{I} + \tilde{\mathbf{H}}_\mathbf{s}\left[\tilde{\mathbf{H}}_\mathbf{f}^{11}\right]^{-1}\right]^{-1} \tilde{\mathbf{u}}_\mathbf{0} \tag{4.6}$$

where $\tilde{\mathbf{H}}_\mathbf{f}$ and $\tilde{\mathbf{H}}_\mathbf{s}$ are the frequency-response function (FRF) matrices of the foundation and soil respectively, which can be found by inverting the respective dynamic stiffness matrices [189]. Equation 4.6 is also found in the ground-borne vibration literature in the context of soil-building interaction [25]. After retrieving the displacement at the interface $\tilde{\mathbf{u}}_\mathbf{1}$, the displacement at the surface $\tilde{\mathbf{u}}_\mathbf{2}$ is found by imposing the free-stress condition at the top of the slab foundation, leading to the following equation:

$$\tilde{\mathbf{u}}_\mathbf{2} = \tilde{\mathbf{H}}_\mathbf{f}^{21}\left[\tilde{\mathbf{H}}_\mathbf{f}^{11}\right]^{-1} \tilde{\mathbf{u}}_\mathbf{1} \tag{4.7}$$

The displacement vectors $\tilde{\mathbf{u}}_\mathbf{0}, \tilde{\mathbf{u}}_\mathbf{1}, \tilde{\mathbf{u}}_\mathbf{2}$ in the frequency-wavenumber domain can be obtained from the reduced displacement vectors $\tilde{\mathbf{u}}_\mathbf{0}, \tilde{\mathbf{u}}_\mathbf{1}, \tilde{\mathbf{u}}_\mathbf{2}$ by means of Equation C.28. It is worth noticing that the results shown here are in terms of magnitude of displacement transfer functions, so that no difference is encountered when referring to either $\tilde{\mathbf{u}}$ or $\tilde{\mathbf{u}}$. Moreover, transfer functions referring to specific boundary conditions (e.g. relaxed boundaries) and involving FRFs only in one direction (i.e. vertical or horizontal) are independent of the transformation in Equation C.28.

In the case of finite slabs, similar expressions to Equations 4.6 and 4.7 are obtained but this time in the frequency-space domain and with reference to collocation points; in the case of infinite slabs, the solutions in Equations 4.6 and 4.7 refer to a frequency-wavenumber formulation. Auersch used the latter approach for an infinitely-long slab subjected to Rayleigh waves (see Figure 4.1), and assumed a relaxed boundary condition between the soil and the slab in which only the vertical displacements at the interface are coupled [1]. In this case, Equation 4.6 reduces to the following scalar equation for

the vertical displacement ratio at the interface:

$$\frac{\tilde{w}_1}{\tilde{w}_0} = \frac{1}{1 + \dfrac{\tilde{H}_{sz}^{11}}{\tilde{H}_{fz}^{11}}} \tag{4.8}$$

where $\tilde{H}_{fz}^{11}$ and $\tilde{H}_{sz}^{11}$ are the vertical driving-point FRFs of the slab and the soil respectively, formally in the frequency-wavenumber domain. However, since the wavenumber is a function of frequency and the Rayleigh wave speed, this ratio of the displacement amplitudes is a function of frequency alone, and independent of position due to the infinite length of the plate.

Focussing on the vertical displacements is common practice when dealing with ground-borne vibration in buildings, often based on the assumption that the flexibility of a building in the horizontal direction provides sufficient decoupling from any horizontal vibration. However, there is theoretical evidence that suggests otherwise, with all coupling degrees-of-freedom (vertical, horizontal and rotational) between a building structure and its foundation being potentially significant [147]. Furthermore, given the small strains associated with ground-borne vibration, the influence of friction at the soil-slab interface may lead to a fully-coupled boundary condition that includes coupling of the horizontal displacements. In this case, the full matrix form of Equation 4.6 must be solved, although this does reduce to a scalar equation for the vertical displacement ratio $\tilde{w}_1/\tilde{w}_0$ and for the horizontal displacement ratio $\tilde{u}_1/\tilde{u}_0$, similar to Equation 4.8, in the case of normally-incident P- and SV-waves respectively.

The fully-coupled condition calls into question the assumption of plate-like behaviour for the slab. By modelling the slab as a thin plate, the through-thickness deformation is assumed to be negligible, such that $\tilde{w}_2 = \tilde{w}_1$, and there is no consideration given to the in-plane horizontal displacement. The aim of the current study is therefore to investigate how the SSI associated with a slab foundation is influenced by the slab-soil boundary condition and the plate-like assumption, and how this varies for the different incident wave fields.

Before presenting the results, it is helpful to review the dimensionality of the problem. By dimensional analysis, the displacement ratios $\tilde{w}_2/\tilde{w}_0$, $\tilde{w}_1/\tilde{w}_0$, etc. can each be expressed as a function of the following form:

$$\frac{\tilde{w}_2}{\tilde{w}_0} = \Psi_f\left(\frac{V_s}{V_c}, \frac{\rho_s}{\rho_c}, \nu_s, \nu_c, \eta_s, \eta_c, \theta_V, \gamma, a_0\right) \tag{4.9}$$

Assuming typical values for the Poisson's ratios ν_s and ν_c (Table 3.1) and for the damping loss factor η_s and η_c, the dimensionless groups V_s/V_c and ρ_s/ρ_c enable the influence of the stiffness and density of the slab relative to the soil to be investigated for a given wave-type (expressed by γ), incidence angle θ_V and non-dimensional frequency $a_0 = \omega h/V_s$. The latter enables the thickness of the slab to be described relative to the shear wavelength in the soil. Given typical ranges for the shear wave speed in the soil $V_s = 150 - 300$ m/s, the slab thickness $h = 0.5 - 1.5$ m and the frequency range of ground-borne vibration $f = 25 - 250$ Hz, the corresponding range of interest for the dimensionless frequency a_0 lies between approximately 0.2 and 15.

4.2 A slab foundation subjected to Rayleigh wave excitation

This section explores the SSI associated with a slab foundation subjected to Rayleigh wave excitation. Before considering the slab as an elastic layer, the case of an infinitely long, strip foundation is first reviewed, following the approach of Auersch [1]. Having reproduced Auersch's results, the slab is then modelled as the elastic layer illustrated in Figure 4.2, enabling the influence of the slab-soil boundary condition and the slab's finite thickness to be investigated.

4.2.1 The slab as an infinitely long, strip foundation

The infinitely long, strip foundation is modelled as an elastic plate of width b and thickness h. The vertical dynamic stiffness of the plate in the frequency-wavenumber domain is given by [190]:

$$\tilde{K}_{fz}(\omega, k_x) = Bbk_x^4 - \rho_c bh\omega^2 \tag{4.10}$$

where $B = E_c h^3/12(1-\nu_c^2)$ is the bending stiffness. The vertical driving-point FRF is obtained as $\tilde{H}_{fz} = 1/\tilde{K}_{fz}$.

The vertical driving-point FRF of the elastic half-space $\tilde{H}_{sz}$ refers to a 2.5-D problem because of the finite width b of the plate in the y-direction. Auersch [1] solved this by assuming plane-strain conditions and using a numerical integration approach in the wavenumber k_y, regarding the plate as infinitely flexible along the y-axis by assuming a constant stress distribution across the width of the plate. According to the relaxed-boundary condition, the vertical displacement ratio $\tilde{w}_1/\tilde{w}_0$ is then obtained from Equation 4.8.

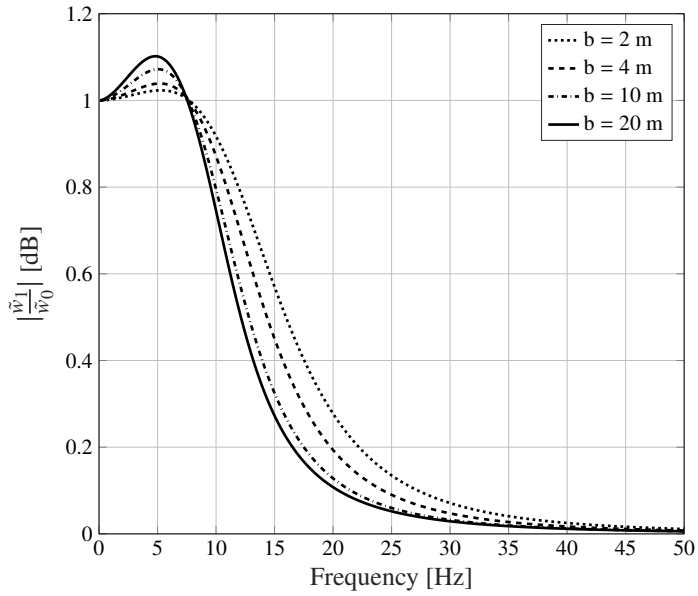

Fig. 4.3 The influence of the width of a strip foundation b on the soil-foundation interaction under Rayleigh wave excitation, as described by the ratio of the vertical displacement amplitudes at the soil-foundation interface, before ($\tilde{w}_0$) and after ($\tilde{w}_1$) the construction of the foundation. Benchmark parameter values (Table 3.1) with $\nu_s = 1/3$ and $h = 0.7$ m.

Figure 4.3 plots the magnitude of the ratio $\tilde{w}_1/\tilde{w}_0$ as a function of frequency for the parameter values of the benchmark problem considered by Auersch (see Table 3.1). Several values of the foundation width b are considered. Irrespective of the width, at a particular frequency known as the "coincidence frequency" (f_{co}), the bending stiffness and inertia of the plate are such that a unit value of $\tilde{w}_1/\tilde{w}_0$ is obtained. The coincidence point represents the scenario in which the free-flexural wavelength λ_f of the plate coincides with the horizontal wavelength λ_x of the input wave-field. The corresponding frequency can be found as [190]:

$$f_{co} = \frac{V_R^2}{2\pi}\sqrt{\frac{\rho_c h}{B}} = \frac{V_R^2}{2\pi}\sqrt{\frac{\rho_c 12(1-\nu_c^2)}{E_c h^2}} \tag{4.11}$$

The coincidence frequency is important because it governs the extent to which the plate attenuates ground vibration levels: it defines the transition from the low-frequency, mass-controlled region where amplification occurs, to the stiffness-controlled region where considerable attenuation is achieved with respect to the free-field displacement $\tilde{w}_0$. The influence of the plate mass and bending stiffness on the value of f_{co} can be determined from Equation 4.11. Increasing the plate thickness h results

in a reduction in both f_{co} and the magnitude of $\tilde{w}_1/\tilde{w}_0$ (for frequencies $f > f_{co}$). A similar effect may be obtained by decreasing the mass density ρ_c of the plate. A comprehensive discussion of the influence of the bending stiffness, mass and width of the strip foundation, and the shear wave speed V_s of the soil, can be found in Auersch [1], also with reference to a finite plate. The results of Figure 4.3 also illustrate the significance of increasing the strip width b, with the limiting case being that of a slab foundation of infinite extent along the x- and y-axis ($b \to \infty$).

4.2.2 The slab as an elastic layer

We now assume the slab foundation to be of infinite extent in both the x and y direction, modelling it as an elastic layer of finite thickness overlying the elastic half-space. The dynamic stiffness matrices $\tilde{\mathbf{K}}_\mathbf{s}$ and $\tilde{\mathbf{K}}_\mathbf{f}$ of both the half-space and the layer are calculated by means of the Dynamic Stiffness Method (DSM) [189], making use of the ElastoDynamics Toolbox (EDT) [116, 36] in MATLAB [35]. The FRF matrices appearing in Equations 4.6 and 4.7, $\tilde{\mathbf{H}}_\mathbf{s}$ and $\tilde{\mathbf{H}}_\mathbf{f}$, are obtained by inverting the respective dynamic stiffness matrices.

In the case of the relaxed boundary (RB) condition, the vertical displacement ratio $\tilde{w}_1/\tilde{w}_0$ can be retrieved from Equation 4.8, with the vertical driving-point FRFs, $\tilde{H}^{11}_{sz}$ and $\tilde{H}^{11}_{fz}$, being extracted

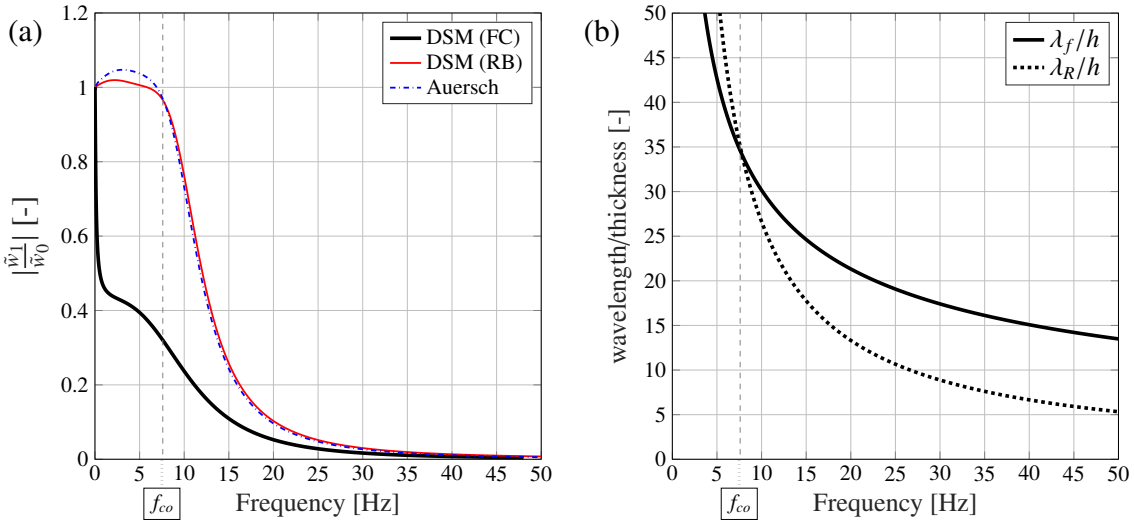

Fig. 4.4 (a) The vertical displacement ratio at the soil-foundation interface of an infinitely long (Auersch) and infinitely large (DSM) slab foundation subjected to an incident Rayleigh wave, considering the fully-coupled (FC) and relaxed (RB) boundary conditions. (b) Comparison of the Rayleigh wave-field wavelength λ_R and the free-flexural wavelength of the strip foundation λ_f. Benchmark parameter values (Table 3.1).

from the FRF matrices. Figure 4.4a plots the magnitude of the ratio $\tilde{w}_1/\tilde{w}_0$ calculated by both Auersch's strip model and the equivalent DSM (RB) model, for the same benchmark parameter values (Table 3.1). It is clear that the two different methods agree well, with the strip model achieving convergent results with the DSM (RB) model for a slab width of $b = 1000$ m. Figure 4.4b plots the wavelength-frequency curves associated with the Rayleigh wave-field and the free-flexural response of the plate model. The coincidence point again indicates the transition region from amplification to attenuation.

In the fully-coupled condition (FC), the displacement ratios $\tilde{w}_1/\tilde{w}_0$ and $\tilde{u}_1/\tilde{u}_0$ are obtained by calculating the interface displacement $\tilde{\mathbf{u}}_\mathbf{1}$ using Equations 4.6 and C.28, with reference to both the horizontal and vertical components of the Rayleigh wave [77]. The magnitude of $\tilde{w}_1/\tilde{w}_0$ obtained with this DSM (FC) model is also plotted in Figure 4.4a. In this condition, the SSI leads to significant attenuation for all frequencies, without any amplification below the coincidence frequency. The fully-coupled condition highlights the importance of considering both the horizontal and vertical components of $\tilde{\mathbf{u}}_\mathbf{0}$, and the cross-stiffness terms at the soil-foundation interface.

Figure 4.5a plots the horizontal displacement ratio $\tilde{u}_1/\tilde{u}_0$, calculated by the DSM model for both the relaxed (RB) and fully-coupled (FC) conditions. The common feature is that both conditions result in a significant attenuation of the horizontal displacement. Again, the assumption of plane-wave

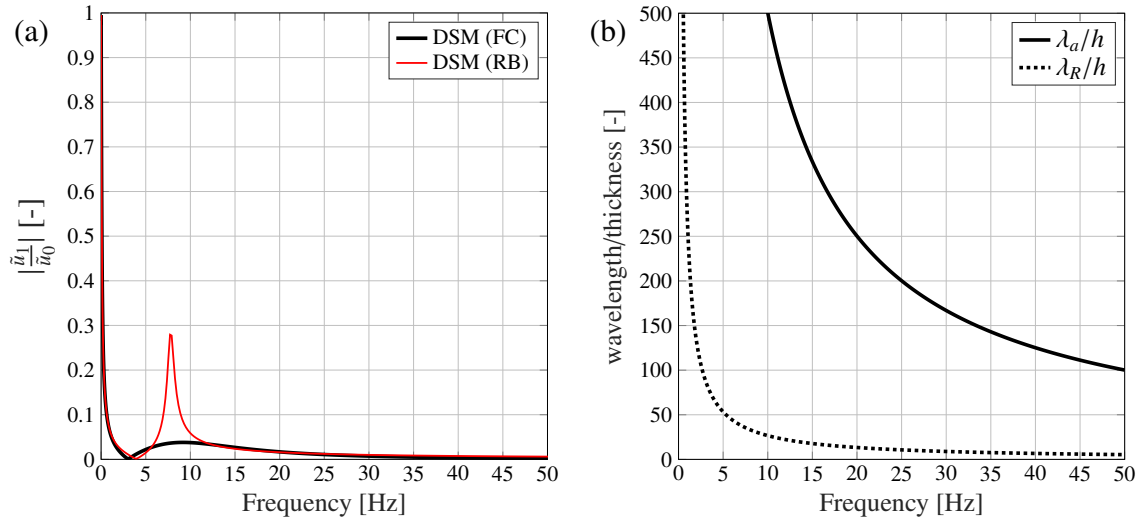

Fig. 4.5 (a) The horizontal displacement ratio at the soil-foundation interface of an infinitely large slab foundation subjected to an incident Rayleigh wave, considering the fully-coupled (FC) and relaxed (RB) boundary conditions. (b) Comparison of the Rayleigh wave-field wavelength λ_R and the free-axial wavelength of the slab λ_a. Benchmark parameter values (Table 3.1).

excitation simplifies the problem and enables a physical interpretation of the SSI. From the perspective of the (horizontal) slab, the incident wave-field is characterised by a horizontal wavelength $\lambda_x = \lambda_R$. This is true for the horizontal displacement $\tilde{u}_1$ as for the vertical displacement $\tilde{w}_1$ seen earlier. The horizontal displacement of the slab is influenced by its free-axial response along the x direction, the wavelength of which is given by:

$$\lambda_a = \frac{1}{f}\sqrt{\frac{E_c}{\rho_c\,(1-\nu_c^2)}} \tag{4.12}$$

Figure 4.5b plots this wavelength-frequency relationship together with the curve for the Rayleigh wave-field. It is clear that λ_R is always shorter than λ_a, with no coincidence possible. It follows that the axial (in-plane) behaviour of the slab always restrains the horizontal displacement at the soil-foundation interface, resulting in attenuation for all frequencies for both the fully-coupled and relaxed boundary conditions.

A better understanding of the results from the different models may be obtained by expressing the displacement ratios in decibels (dB) and referring to the non-dimensional frequency a_0 on a logarithmic scale. Figure 4.6a re-plots in this form the results of Figure 4.4a for the vertical displacement ratio at the soil-foundation interface. Also included in Figure 4.6a are the results for the magnitude of the displacement ratio $\tilde{w}_2/\tilde{w}_0$ calculated at the free-surface - the location of most interest, since this will support any future building. The plate-like behaviour of the slab at relatively low frequencies is clearly captured by the Auersch strip model, which shows a good agreement with the DSM (RB) model up to $a_0 \approx 1$. The plate-like assumption is therefore sufficient to capture the SSI, as observed at the soil-slab interface (ratio $\tilde{w}_1/\tilde{w}_0$) with the relaxed boundary condition, but only up to a restricted value of h/λ_x. For shorter wavelengths, the through-thickness effects become important, with the layer-like behaviour of the slab attenuating the wave field at the interface $\tilde{w}_1$ down to a plateau at high frequencies. This is a common feature for both the relaxed and fully-coupled boundary conditions, although the former leads to lower attenuation because it neglects the retrograde elliptical motion of particles at the soil-foundation interface, characteristic of Rayleigh waves, accounting for only the vertical component. At the free surface, the high-frequency plateau is not evident. Instead, the level of attenuation is observed to increase with frequency. In the case of the relaxed boundary condition, the vertical displacement $\tilde{w}_2$ is obtained simply as:

$$\frac{\tilde{w}_2}{\tilde{w}_1} = \frac{\tilde{H}_{fz}^{21}}{\tilde{H}_{fz}^{11}} \tag{4.13}$$

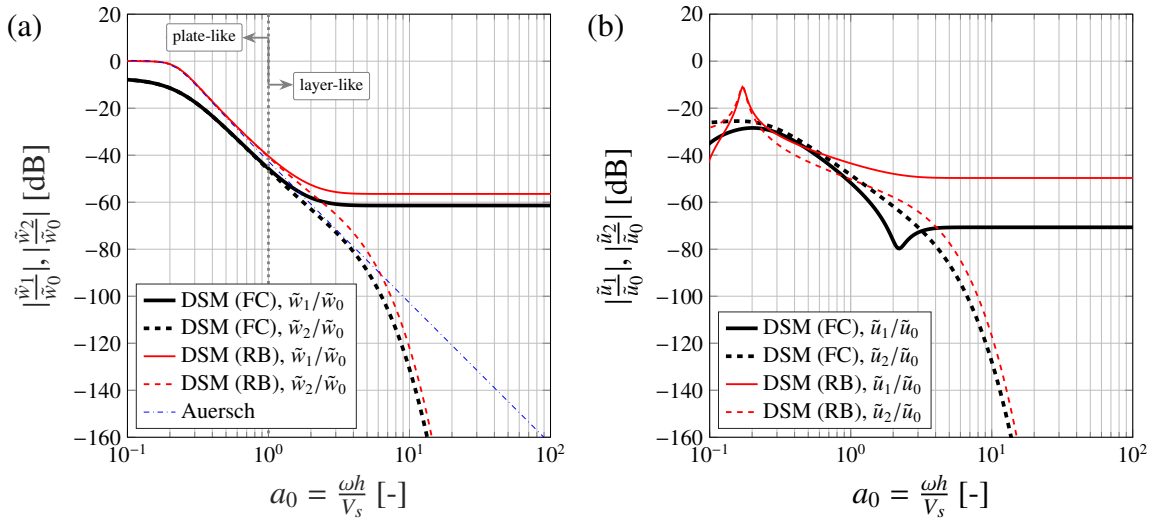

Fig. 4.6 (a) The vertical displacement ratio at the free-surface ($\tilde{w}_2/\tilde{w}_0$) and soil-foundation interface ($\tilde{w}_1/\tilde{w}_0$) of an infinitely large slab foundation subjected to an incident Rayleigh wave, considering the fully-coupled (FC) and relaxed (RB) boundary conditions. Comparison is made with Auersch's strip model. (b) The corresponding horizontal displacement ratios. Benchmark parameter values as in Table 3.1.

where $\tilde{H}_{fz}^{21}$ is the FRF for the vertical displacement at the free-surface due to a vertical traction at the interface and $\tilde{H}_{fz}^{11}$ is the vertical driving-point FRF at the interface; they can be both retrieved from the FRF matrix of the layer $\tilde{\mathbf{H}}_\mathbf{f}$. Again, it is clear from Equation 4.13 that the DSM (RB) model neglects the coupling between the horizontal and the vertical motion. The magnitude of $\tilde{w}_2/\tilde{w}_1$ approaches unity at low frequencies, when the through-thickness effects are negligible, but introduces increasing attenuation at higher frequencies.

Figure 4.6b plots the corresponding results for the horizontal displacements, this time re-plotting the results of Figure 4.5a for the displacement ratio at the interface $\tilde{u}_1/\tilde{u}_0$, together with the free-surface ratio $\tilde{u}_2/\tilde{u}_0$. A similar trend to the vertical displacements is observed but with the exception of the clearly absent amplification region at low frequencies for the DSM (RB) model, due to the lack of any coincidence phenomenon.

For both the vertical and the horizontal displacements, the results of the DSM (RB) and DSM (FC) models have common features that indicate the importance of both the finite thickness of the slab, which becomes increasingly significant with frequency, and the assumed soil-foundation boundary condition. The influence of the latter results in at least 10 dB difference in the final free-surface displacements of the slab between the two conditions, without influencing the general trend in the results.

4.3 A slab foundation subjected to incident P- and SV-waves

So far, the SSI associated with a slab foundation has only been investigated in the context of Rayleigh waves. The case of incident P- or SV-waves can be similarly investigated by using the same DSM model for the elastic layer but now with the free-field displacement components associated with these wave types [77]. Considering an incident P- or SV-wave at an incidence angle θ_P or θ_S (see Figure 4.2), the free-surface displacement field $\hat{\mathbf{u}}_\mathbf{2}$ of the coupled soil-foundation system is calculated by consideration of Equations 4.6 and 4.7 into the related expression in Equation 4.1. Only the fully-coupled slab is considered here, in the belief that this better represents the actual soil-foundation boundary condition at the low strain levels present in practice.

4.3.1 Influence on the vertical displacements ($\tilde{w}_1/\tilde{w}_0$ and $\tilde{w}_2/\tilde{w}_0$)

Figure 4.7 plots the magnitude of $\tilde{w}_1/\tilde{w}_0$, together with the wavelength-frequency curves for incident P-waves (Figure 4.7a and 4.7c) and SV-waves (Figure 4.7b and 4.7d), for the benchmark parameter values (Table 3.1) and an arbitrary incidence angle $\theta_P = \theta_S = 3\pi/8$. The results in this particular case can be qualitatively divided into the following frequency regions:

1. an initial low-frequency region of either moderate attenuation (for P-waves) or amplification (for SV-waves), up to a frequency $f_1 < f_{co}$;

2. a second region, with increased values of w_1/w_0, which are always greater than unity for SV-waves but not necessarily for P-waves. A maximum value is obtained at a frequency $f_2 > f_{co}$;

3. a third region of sharply increasing attenuation, up to a frequency f_3, beyond which w_1/w_0 tends to a limiting value.

The wavelength-frequency curves (Figure 4.7c and 4.7d) are again helpful for interpreting the SSI. The coincidence frequency f_{co} lies between f_1 and f_2, and does not correspond to a distinct feature in the $\tilde{w}_1/\tilde{w}_0$ curve. This is because the free-flexural wavelength λ_f of the slab is calculated based on the thin-plate assumption; in practice, shear deformation is likely to contribute to higher values of λ_f, resulting in lower values of f_{co}.

As seen before, a better understanding of the results is obtained by using logarithmic scales. Figure 4.8 shows such a representation for the results in Figure 4.7 (a) and (b). The trend in the

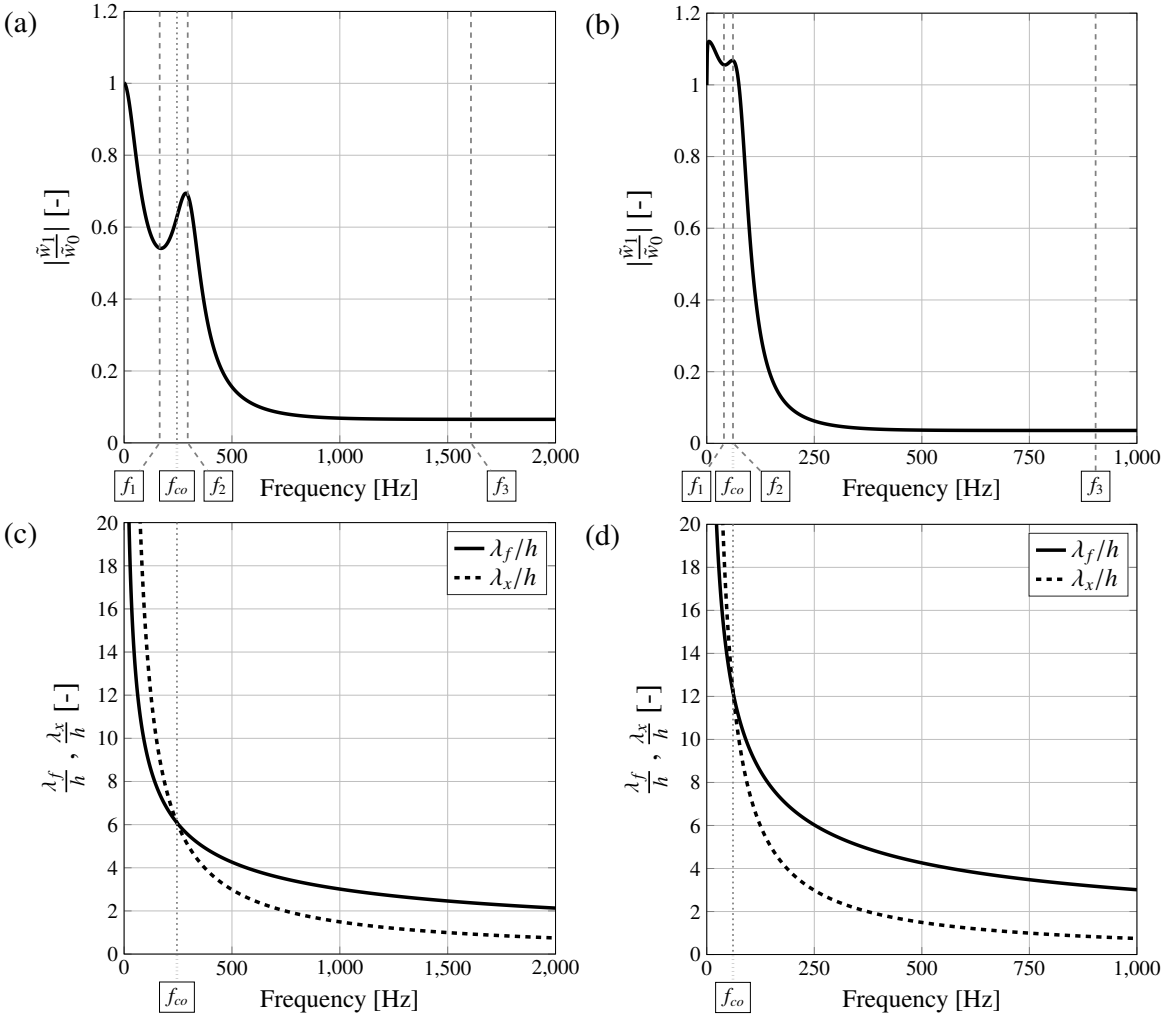

Fig. 4.7 The vertical displacement ratio $\tilde{w}_1/\tilde{w}_0$ at soil-foundation interface of an infinitely large slab foundation subjected to (a) an incident P-wave at an angle $\theta_P = 3\pi/8$ and (b) an incident SV-wave at an angle $\theta_S = 3\pi/8$. The wavelength-frequency curves are plotted below for the two cases ((c) P- and (d) SV-waves) with reference to the coincidence frequency f_{co} based on the thin-plate assumption. Benchmark parameter values as in Table 3.1.

ratio $\tilde{w}_1/\tilde{w}_0$ described before can be observed more clearly with reference to the local minimum and maximum at $a_0^{(1)}$ and $a_0^{(2)}$, and the plateau beyond $a_0^{(3)}$. Additionally, the free-surface displacement ratio $\tilde{w}_2/\tilde{w}_0$ is plotted. Analogous to what is observed for Rayleigh wave excitation, additional attenuation is obtained for the free-surface displacement $\tilde{w}_2$, compared to the interface displacement $\tilde{w}_1$, as a result of through-thickness effects at relatively short wavelengths. The results obtained using Auersch's thin-plate assumption are also included to highlight the influence of the relaxed boundary condition and the thin-plate assumptions.

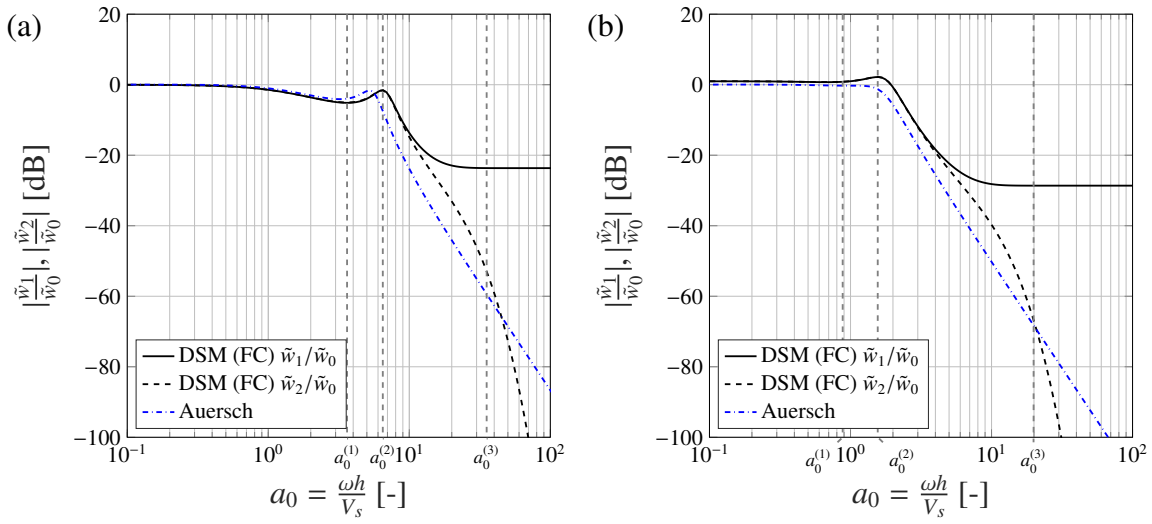

Fig. 4.8 The magnitude of the vertical displacement ratio at the free-surface ($\tilde{w}_2/\tilde{w}_0$) and soil-foundation interface ($\tilde{w}_1/\tilde{w}_0$) of an infinitely large slab foundation subjected to (a) an incident P-wave at an angle $\theta_P = 3\pi/8$ and (b) an incident SV-wave at an angle $\theta_S = 3\pi/8$. Results obtained using Auersch's thin-plate assumption are included for comparison. Benchmark parameter values as in Table 3.1.

Under Rayleigh wave excitation, investigated in Section 4.2, the attenuation provided by the fully-coupled slab is considerable for all frequencies, and significantly greater than that provided to P- and SV-waves. The horizontal wavelength λ_x associated with an incident P- or SV-wave is always longer than that of a Rayleigh wave of the same frequency (see Figure 4.7c and 4.7d). Consequently, the coincidence frequencies f_{co} associated with P- and SV-waves are always higher than that of the Rayleigh wave, and the region where strong attenuation is to be expected from the slab shifts to relatively high frequencies. The attenuation provided by the slab to Rayleigh waves therefore represents a limiting case.

Another limiting case is that of normally incident P-waves ($\theta_P = \pi/2$). In this case $\lambda_x = 0$ and the restraining effect of the slab foundation is maximum at the free-axial natural frequencies f_n of the elastic layer in the vertical direction:

$$f_n = \frac{V_{Pc}}{4h}(2n-1) \tag{4.14}$$

where V_{Pc} is the compressional wave speed in the slab. At these frequencies, the slab behaves like a dynamic vibration absorber. However, given the application, and the relatively high P-wave speed V_{Pc},

f_n lies well beyond the frequency range of interest ($f_{n=1} \approx 1270$ Hz for the parameters in Table 3.1), leading to only moderate attenuation in the frequency range of interest.

4.3.2 Influence on the horizontal displacements ($\tilde{u}_1/\tilde{u}_0$ and $\tilde{u}_2/\tilde{u}_0$)

A similar trend is observed for the horizontal displacements. This is illustrated in Figure 4.9 for incident P- and SV-waves at an arbitrary incidence angle $\theta_V = 3\pi/8$. Although, by physical interpretation, no coincidence phenomenon is expected in this case (see Section 4.2.1), local minima ($a_0^{(1)}$) and maxima ($a_0^{(2)}$) are observed for the magnitude of the ratios $\tilde{u}_1/\tilde{u}_0$ and $\tilde{u}_2/\tilde{u}_0$.

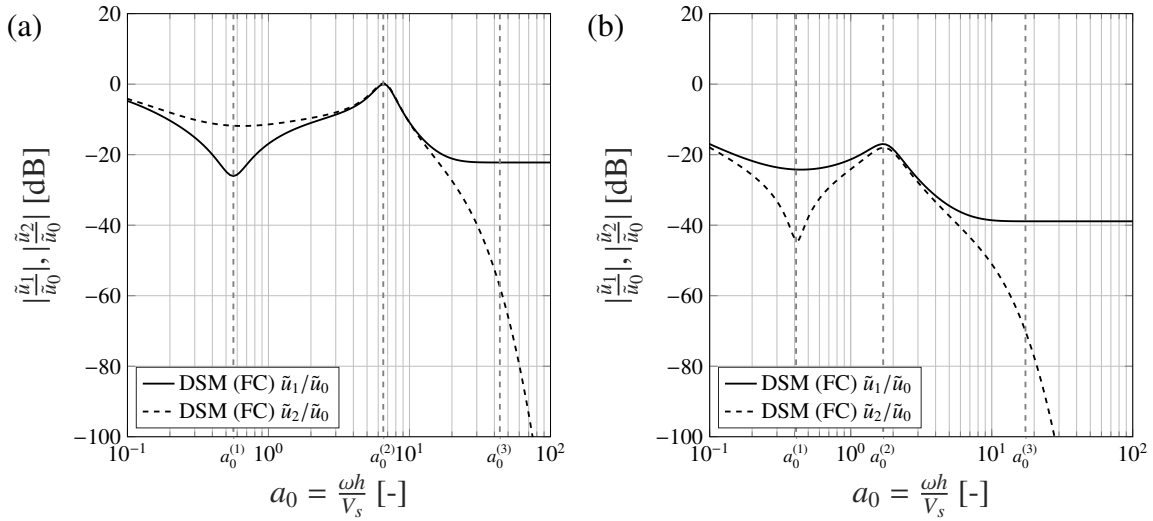

Fig. 4.9 The horizontal displacement ratio at the free-surface ($\tilde{u}_2/\tilde{u}_0$) and soil-foundation interface ($\tilde{u}_1/\tilde{u}_0$) of an infinitely large slab foundation subjected to (a) an incident P-wave at an angle $\theta_P = 3\pi/8$ and (b) an incident SV-wave at an angle $\theta_S = 3\pi/8$. Benchmark parameter values as in Table 3.1.

Moreover, the through-thickness effects at relatively short wavelengths result, once more, in additional attenuation of the free-surface displacement $\tilde{u}_2$. Following a similar argument to that used for the vertical displacements, it is clear that the Rayleigh wave and the normally incident SV-wave represent limiting cases for the horizontal displacement field $\hat{u}_2, \hat{u}_1$ and $\hat{u}_0$.

4.3.3 The case of normally incident P- and/or SV-waves

The case of normally incident waves is worth exploring further, since these may be representative of the wave field from a deep source, such as an underground railway. For normal incidence, the wave propagation problem is independent of x and effectively one-dimensional. The free-surface and

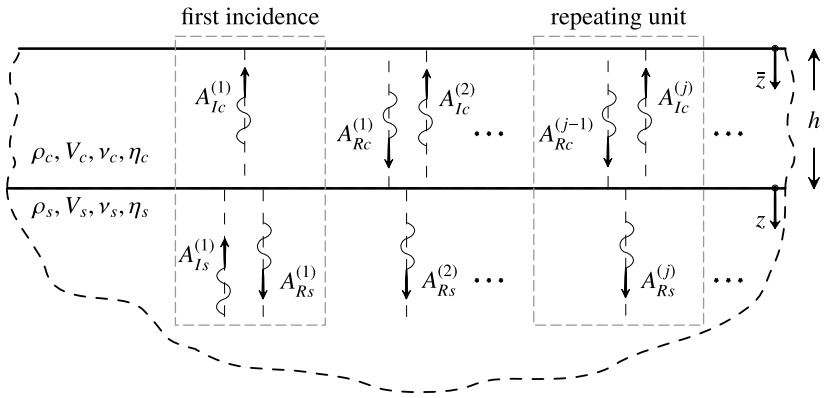

Fig. 4.10 Schematic representation of the multiple reflected-transmitted wave amplitudes in an elastic layer overlying an elastic half-space, due to a normally incident P-wave. An infinite repetition of a reflection-transmission unit follows the reflection and transmission of the incident amplitude $A_1^{(1)}$.

interface displacement amplitudes $\tilde{\mathbf{u}}_\mathbf{2}$ and $\tilde{\mathbf{u}}_\mathbf{1}$ can be found, in terms of the incident wave amplitude, by considering the superposition of multiple reflections and transmissions in the half-space-layer system, as illustrated schematically in Figure 4.10. It is clear that a normally incident P- or SV-wave will induce only vertical or horizontal displacements respectively. With a similar discussion also being valid for the case of a normally incident SV-wave, the notation adopted in the following refers to a normally incident P-wave (see Appendix C).

As shown in Figure 4.10, the multiple reflections/transmissions trace back to the incidence of the amplitude $A_{Is}^{(1)}$ at the interface, and to the repeating reflection/transmission of the amplitude $A_{Rc}^{(j-1)}$ that results from the reflection of $A_{Ic}^{(j-1)}$ at the free-surface. In general, the vertical displacement in the layer can be written as:

$$\tilde{w}_c(\bar{z}) = -ik_{Pc}\left(\sum_{j=1}^{\infty} A_{Ic}^{(j)}\, e^{(-ik_{Pc}\bar{z})} - \sum_{j=1}^{\infty} A_{Rc}^{(j)}\, e^{(ik_{Pc}\bar{z})}\right) \tag{4.15}$$

By ensuring equilibrium and compatibility at the interface for both the "first incidence" and the "repeating unit", one can find:

$$\frac{A_{Rs}^{(1)}}{A_{Is}^{(1)}} = \frac{\beta_P - 1}{\beta_P + 1}; \qquad \frac{A_{Ic}^{(1)}}{A_{Is}^{(1)}} = \frac{k_{Ps}}{k_{Pc}}\frac{2}{\beta_P + 1}\, e^{ik_{Pc}h} \tag{4.16}$$

$$\frac{A_{Ic}^{(j)}}{A_{Rc}^{(j-1)}} = \frac{1 - \beta_P}{\beta_P + 1}\, e^{i2k_{Pc}h} = \zeta; \qquad \frac{A_{Rs}^{(j)}}{A_{Rc}^{(j-1)}} = \frac{k_{Ps}}{k_{Pc}}\frac{2\beta_P}{\beta_P + 1}\, e^{ik_{Pc}h} \tag{4.17}$$

where $\beta_P = (\rho_c V_{Pc})/(\rho_s V_{Ps})$. The amplitude $A_{Rc}^{(j)} = -A_{Ic}^{(j)}$ because of the free-stress condition at $\bar{z} = 0$. It is clear that all the amplitudes involved in the repeating unit in Figure 4.10 trace back to the amplitude $A_{Ic}^{(1)}$ and that the latter refers to $A_{Is}^{(1)}$. The vertical displacement at the free-surface can then be found as:

$$\tilde{w}_2 = \tilde{w}_c(\bar{z}=0) = -ik_{Pc}\left(\sum_{j=1}^{\infty} A_{Ic}^{(j)} - \sum_{j=1}^{\infty} A_{Rc}^{(j)}\right) = -2ik_{Pc}A_{Ic}^{(1)}(1-\zeta+\zeta^2+\ldots) = -\frac{2ik_{Pc}A_{Ic}^{(1)}}{1+\zeta} \quad (4.18)$$

Substituting the value ζ and considering the free-field amplitude $\tilde{w}_0$ from Appendix C:

$$\frac{\tilde{w}_2}{\tilde{w}_0} = \frac{1}{\cos(k_{Pc}h) - i\beta_P \sin(k_{Pc}h)} \quad (4.19)$$

With a similar argument for the interface displacement $\tilde{w}_1$, we can write:

$$\frac{\tilde{w}_1}{\tilde{w}_0} = \frac{1}{1 - i\beta_P \tan(k_{Pc}h)} \quad (4.20)$$

From the latter, as anticipated from Equation 4.14, it is clear that the slab has a restraining effect on the interface displacement $\tilde{w}_1$ at the free-axial natural frequencies f_n of the elastic layer. This effect disappears at frequencies $2f_n$, when $\tilde{w}_1 = \tilde{w}_0$ if damping is neglected. The latter are frequencies for which the half-wavelength of the P-waves, or a multiple, matches the slab foundation thickness. In this case, the ratios $\tilde{w}_2/\tilde{w}_0$ and $\tilde{w}_1/\tilde{w}_0$ will converge to the same value, that is, unity in the undamped case. In general, for the case of normal incidence, the free-surface displacement $\tilde{w}_2$ is greater than, or at least equal to, the interface displacement $\tilde{w}_1$. The behaviour illustrated here depends only on the relative characteristics of the soil-slab system, that is, the impedance ratio β. This is generally greater than unity for both P-waves, $\beta_P = (\rho_c V_{Pc})/(\rho_s V_{Ps})$, and SV-waves, $\beta_S = (\rho_c V_{Sc})/(\rho_s V_{Ss})$, so that the slab has an overall attenuating effect on the displacement amplitudes. In contrast to the interface displacement, for the free-surface displacement $\tilde{w}_2$ such attenuation has a limiting value, again related to the impedance ratio β. This is shown in Figure 4.11a for normally incident P-waves and, in Figure 4.11b, for normally incident SV-waves. Figure 4.11 also shows the results for an incidence angle just off normal, that is, $\theta_V = 5\pi/12$.

It is clear that normal incidence represents a special case, when the slab behaves as a simple elastic layer, with no plate-like behaviour. For both P- and SV-waves, this ensures no amplification of the incident waves but limits the available attenuation. Once the incidence angle deviates from

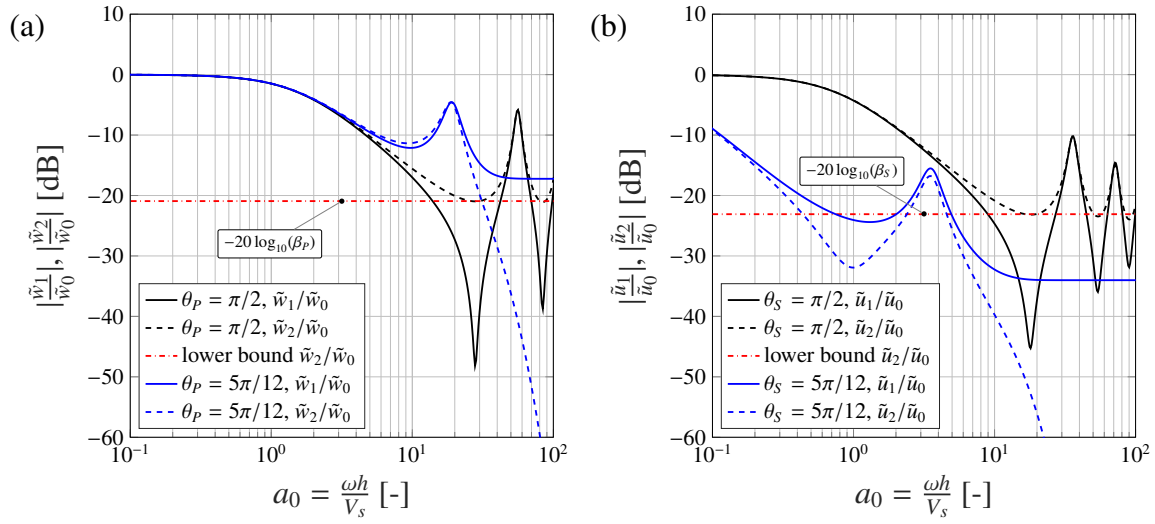

Fig. 4.11 (a) The vertical displacement ratios at the free-surface ($\tilde{w}_2/\tilde{w}_0$) and soil-foundation interface ($\tilde{w}_1/\tilde{w}_0$) of an infinitely large slab foundation subjected to an incident P-wave at angles of $\pi/2$ and $5\pi/12$. (b) The equivalent horizontal displacement ratios due to an incident SV-wave. Benchmark parameter values as in Table 3.1.

normal, even by a small amount, plate-like behaviour becomes significant, resulting in additional attenuation that increases with frequency.

4.4 Design implications of the added-foundation effect

This section considers the overall implications of this study for foundation design. In particular, it considers what guidance may be drawn regarding the design of a slab foundation to achieve a specific reduction in ground-borne vibration level. As discussed in Section 3.1.2, it is worth pointing out that the added-foundation effect represents an intermediate step, usually overlooked in practice, in the construction of a building. An attenuation obtained at this stage does not necessarily translate to the same order of attenuation of vibration levels within the completed building, which will additionally depend on the dynamic characteristics of the building (i.e. mass, stiffness, damping, etc.) and on the soil-foundation-building interaction. Nonetheless, the added-foundation effect as investigated in this chapter provides an understanding of the "*car park*" problem: given a site and an incident wave-field, to what extent the slab foundation changes the vibration levels at the free-surface.

It is clear that the SSI associated with a slab foundation is complex, even for the simplified system considered here. Nevertheless, some useful guidance may be presented in the form of Figures 4.12–4.15. These present a series of summary design plots that illustrate the influence of the

dimensionless groups V_s/V_{Sc}, ρ_s/ρ_c and θ_V, over the typical ranges associated with ground-borne vibration, for the three incident wave types (P, SV and Rayleigh). Typical values are assumed for the Poisson's ratios and damping loss factors of the slab and soil (Table 3.1). The results are given in terms of the displacement ratios at the free-surface of the slab, for the fully-coupled boundary condition at the soil-foundation interface. An alternative description of the results along the frequency spectrum can be given by the non-dimensional thickness $h_0 = 2\pi h/\lambda_x$ that compares the thickness of the layer with the apparent wavelength of the wave-field and can be obtained from the non-dimensional frequency as $h_0 = a_0 \cos\theta_V/\gamma$ (see Figure 4.13). Part (e) and (f) of Figures 4.14 and 4.15 are reproduced in Figure 4.13 with respect to h_0. It follows a better description of the influence of the directionality of the incident wave-field. A general discussion is presented in the following for surface and body waves.

4.4.1 Surface Vibration Sources

In the case of a surface source, it is reasonable to assume that the incident vibration field will be dominated by Rayleigh waves, at least for locations remote from the source. In this case, the plots in Figure 4.12 summarise concisely the behaviour of the slab. It is clear that the density ratio has a relatively weak influence, with the level of attenuation varying by no more than 6 dB over the typical range ρ_s/ρ_c = 0.6 - 1.2. A relatively dense slab is therefore desirable but probably not worth pursuing actively, given the expense of specialist high-density concrete. In contrast, the wave speed ratio has a strong influence, with the attenuation varying by up to 25 dB over the typical range V_s/V_{Sc} = 0.05 - 0.2. This sensitivity to the wave speed ratio indicates the significance of the relative stiffness of the slab, and the importance of obtaining an estimate of soil stiffness before relying on a particular slab for vibration mitigation.

For a given site, the controlling parameter is the slab thickness, which the designer is free to select in order to provide acceptable attenuation at the lowest frequency of concern, in the knowledge that any higher frequencies are attenuated further. For example, the results indicate that, for the benchmark soil properties, typical of London Clay (V_s = 200 m/s, ρ_s = 2000 kg/m^3), a concrete slab (V_{Sc} = 2284 m/s, ρ_c = 2500 kg/m^3) of thickness 0.5 m would provide 24 dB of attenuation to vertical vibration at 25 Hz, increasing to 81 dB at 250 Hz. The corresponding attenuation of horizontal vibration is slightly greater, ranging from 33 dB to 79 dB.

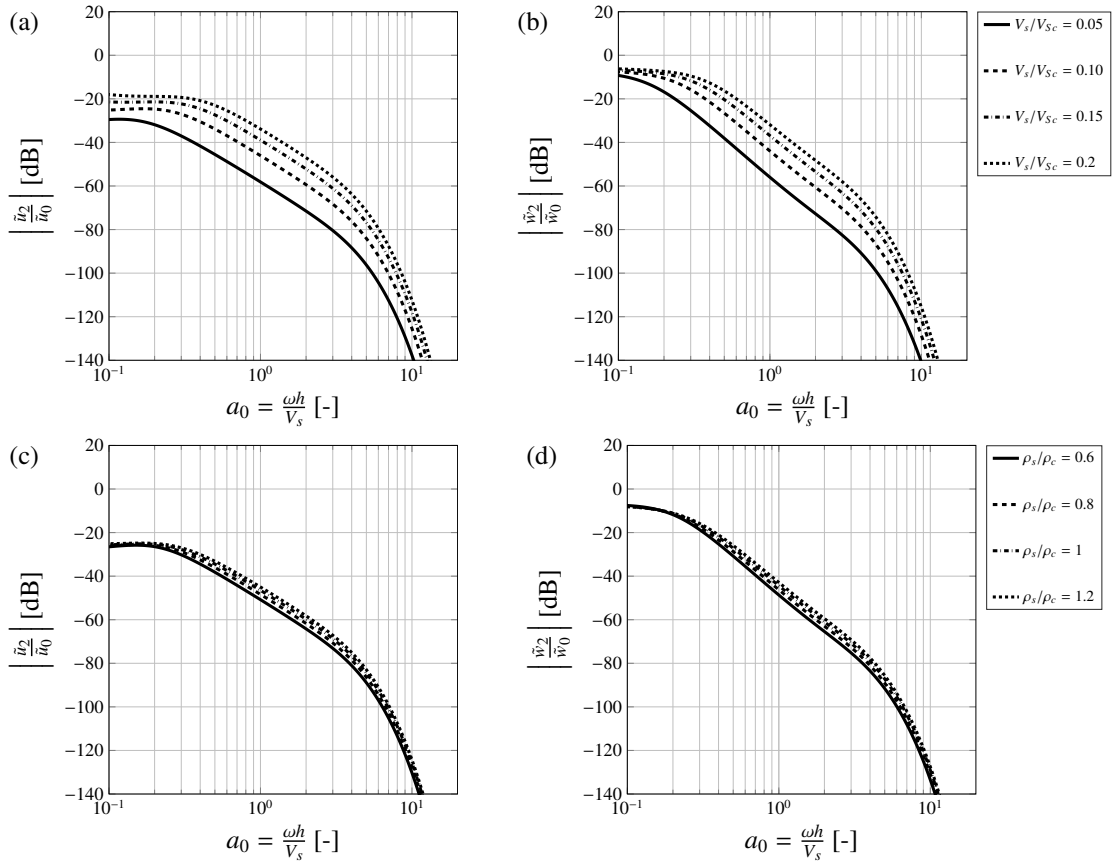

Fig. 4.12 The horizontal (left) and vertical (right) displacement ratios at the free-surface of an infinitely large slab foundation subjected to an incident Rayleigh wave, showing the influence of (a, b) the ratio V_s/V_{Sc}, for $\rho_s/\rho_c = 0.8$, and (c, d) the ratio ρ_s/ρ_c for $V_s/V_{Sc} = 0.088$.

4.4.2 Buried Sources

In the case of a buried source, when body waves are more significant, the situation is more complex. As with Rayleigh excitation, the attenuation provided by the slab is influenced only weakly by the density ratio (again, by no more than 6 dB) but strongly by the wave speed ratio, this time by up to 38 dB. For P-waves, the attenuation of vertical vibration is negligible for frequencies below approximately $a_0 = 1$ (below 64 Hz for the 0.5 m thick slab considered in Section 4.4.1) but then increases steadily with frequency. For horizontal vibration, the low-frequency attenuation may be as high as 20 dB or more, but this depends strongly on the wave speed ratio and incidence angle; the minimum attenuation may be close to zero.

For SV-waves, the most significant observation is that the slab may amplify low-frequency vibration, particularly in the vertical direction, and by up to 10 dB depending on the wave speed

ratio and incidence angle. To avoid any amplification, the slab must be sufficiently thick to ensure a minimum non-dimensional frequency of approximately $a_0 = 2$. This corresponds to a slab thickness of at least 2.5 m, assuming the benchmark properties and that the minimum frequency of concern is 25 Hz.

In general, for both P- and SV-waves, the vibration incidence angle is by far the most influential factor, causing variations in attenuation of 60 dB or more. This sensitivity presents a challenge to the designer, who may, at best, only estimate the incidence angle based on the approximate location of the source.

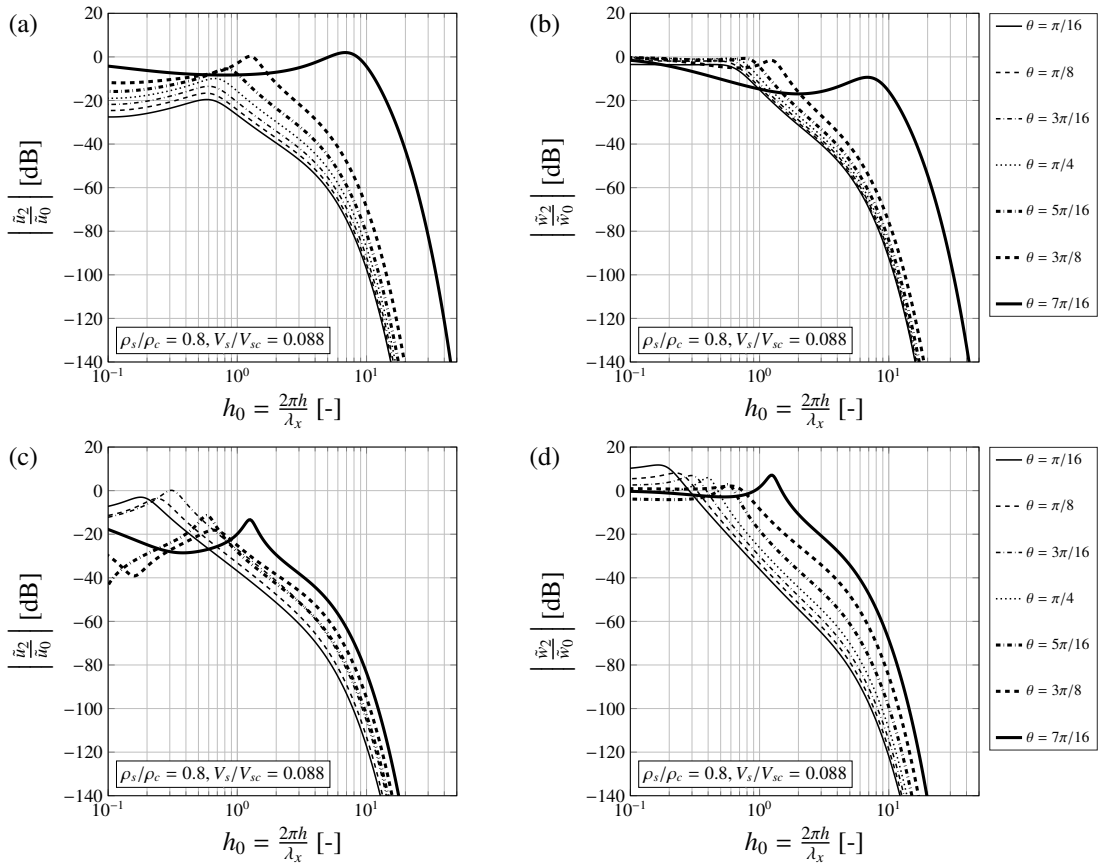

Fig. 4.13 The horizontal (left) and vertical (right) displacement ratios at the free-surface of an infinitely large slab foundation subjected to an incident P- (top) and SV-waves (bottom) at different incidence angles. The magnitude of the displacement ratios is reported against the dimensionless thickness h_0 of the slab foundation. Results refer to the ratios $\rho_s/\rho_c = 0.8$ and $V_s/V_{Sc} = 0.088$.

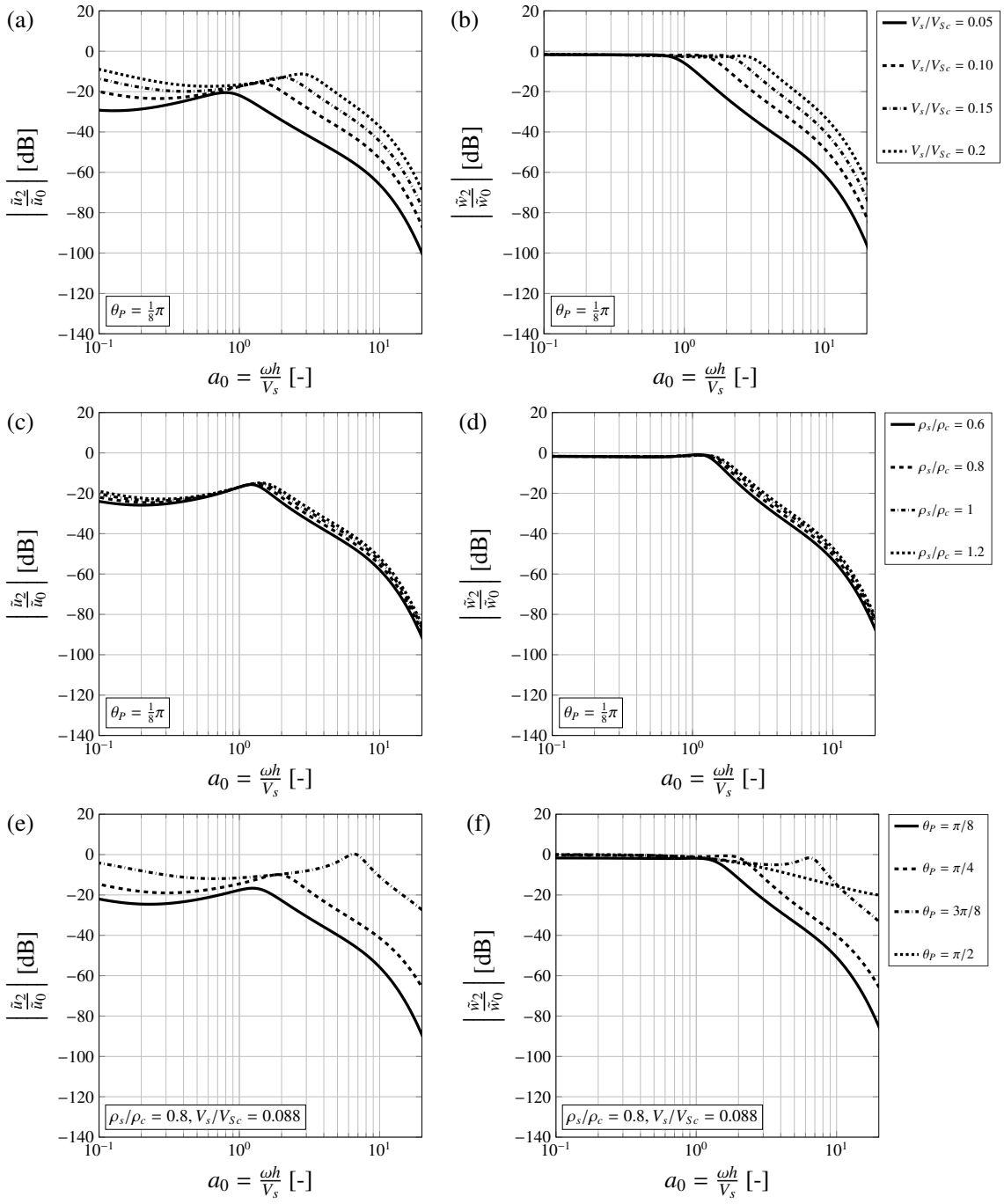

Fig. 4.14 The horizontal (left) and vertical (right) displacement ratios at the free-surface of an infinitely large slab foundation subjected to an incident P-wave at an angle $\theta_P = \pi/8$, showing the influence of (a, b) the ratio V_s/V_{Sc}, for $\rho_s/\rho_c = 0.8$, and (c, d) the ratio ρ_s/ρ_c for $V_s/V_{Sc} = 0.088$. (e, f) The influence of the incidence angle θ_P for $V_s/V_{Sc} = 0.088$ and $\rho_s/\rho_c = 0.8$.

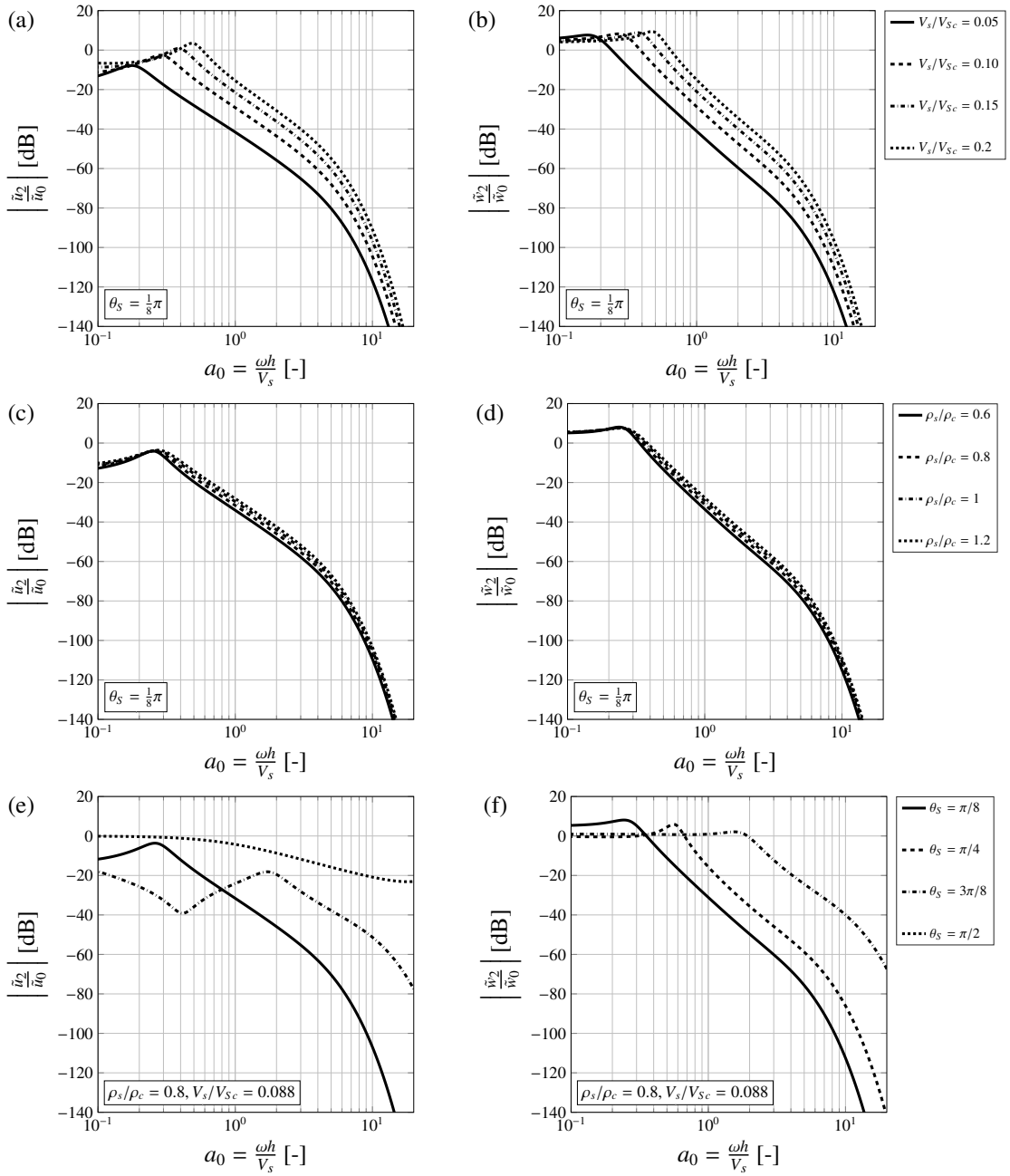

Fig. 4.15 The horizontal (left) and vertical (right) displacement ratios at the free-surface of an infinitely large slab foundation subjected to an incident SV-wave at an angle $\theta_P = \pi/8$, showing the influence of (a, b) the ratio V_s/V_{Sc}, for $\rho_s/\rho_c = 0.8$, and (c, d) the ratio ρ_s/ρ_c for $V_s/V_{Sc} = 0.088$. (e, f) The influence of the incidence angle θ_S for $V_s/V_{Sc} = 0.088$ and $\rho_s/\rho_c = 0.8$.

4.5 Horizontally layered ground

In practice, layering of the ground is commonly encountered. Experimental evidence from literature, related to sites across Europe, suggests that one or more soil layers overlying a deep soil deposit (i.e. half-space) may be present at any given site [191–193, 53, 120]. The physics related to a layered system subjected to incident plane waves becomes difficult to break down into simple concepts. The response at the free-surface of the layered system is the result of an infinite series of reflection-refraction and mode conversion of P- and SV-waves at each interface between layers. The response of the layered system can be obtained by applying the Direct Stiffness Method [189, 194]. Apart from specific cases (e.g. normally propagating waves), interpretation of the results by means of relatively simple concepts (e.g. coincidence frequency for the "slab problem") becomes simply not possible.

4.5.1 Response of layered ground to incident waves

Let us consider the case of a horizontally layered ground composed by N different soil layers (e.g. sand, clay, etc.) as represented in Figure 4.16. The underlying half-space has density ρ_1, shear wave speed V_1, Poisson's ratio ν_1 and damping loss factor η_1 with the assumption of hysteretic damping as before. The notation for the material properties of the $N-1$ superimposed layers follows as in the Figure 4.16 with the additional parameter h referring to the thickness of each layer. The horizontal $\tilde{u}_i$ and vertical $\tilde{w}_i$ displacements in the frequency-wavenumber domain refer to the i^{th} interface of the layered ground. As previously, a plane-wave excitation is considered in the form of incident P- and/or SV-waves, assuming that the geometry of the layered ground is identical along the y-axis (i.e. horizontally layered). We are interested in the free-surface response $\tilde{\mathbf{u}}_\mathbf{N} = \left[\tilde{u}_N, \tilde{w}_N\right]^T$ as this is required for the following foundation and/or building coupling. In order to calculate the response of the layered ground to an incident wave (wave-type defined by γ as in Equation 4.4) at an angle θ_V, the free-field response $\tilde{\mathbf{u}}_\mathbf{0} = \left[\tilde{u}_0, \tilde{w}_0\right]^T$ of the half-space alone is considered as input (see Figure 4.2 and Appendix C). The $N-1$ layers can then be coupled to the half-space in the same manner as for the slab in Section 4.1. The dynamic stiffness matrix $\tilde{\mathbf{K}}_\mathbf{L}$ of the $N-1$ layers can be

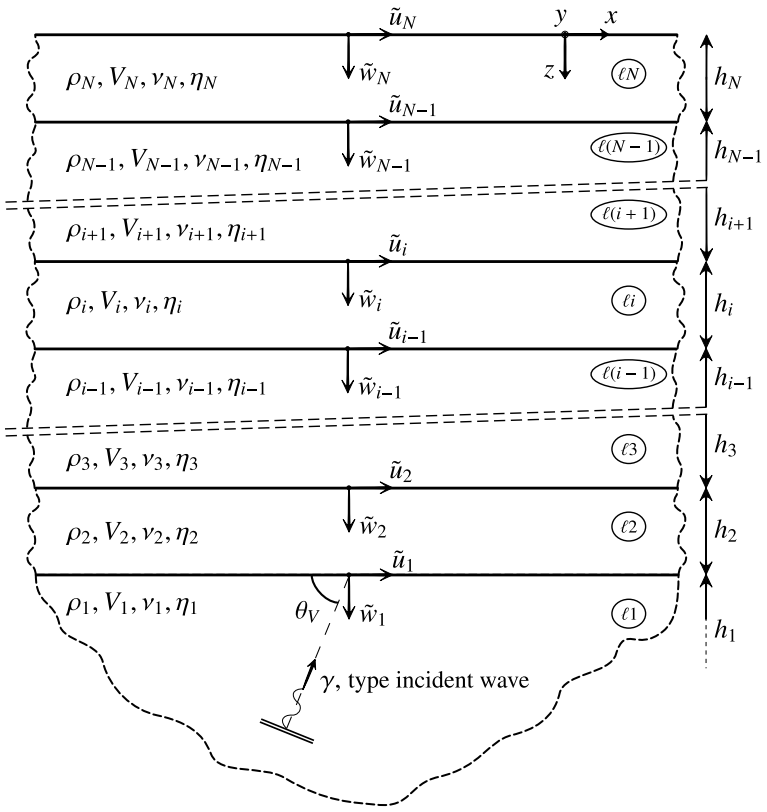

Fig. 4.16 An example of horizontally layered ground composed by N-1 layers overlying an half-space. The layers and the half-space are assumed elastic and homogeneous with density ρ_i, shear wave speed V_i and Poisson's ratio ν_i as schematically illustrated in the Figure.

obtained by assembling the stiffness matrices of each layer (with the latter as defined in Appendix C):

$$\tilde{\mathbf{K}}_{\mathbf{L}} = \begin{bmatrix} \tilde{\mathbf{K}}^{11}_{\ell 2} & \tilde{\mathbf{K}}^{12}_{\ell 2} & \mathbf{0} & \dots & \dots & \mathbf{0} \\ \tilde{\mathbf{K}}^{21}_{\ell 2} & \tilde{\mathbf{K}}^{22}_{\ell 2} + \tilde{\mathbf{K}}^{11}_{\ell 3} & \tilde{\mathbf{K}}^{12}_{\ell 3} & \mathbf{0} & \dots & \vdots \\ \mathbf{0} & \tilde{\mathbf{K}}^{21}_{\ell 3} & \tilde{\mathbf{K}}^{22}_{\ell 3} + \tilde{\mathbf{K}}^{11}_{\ell 4} & \dots & \dots & \vdots \\ \vdots & \mathbf{0} & \dots & \ddots & \dots & \vdots \\ \vdots & \dots & \dots & \dots & \tilde{\mathbf{K}}^{22}_{\ell(\mathrm{N}-1)} + \tilde{\mathbf{K}}^{11}_{\ell \mathrm{N}} & \tilde{\mathbf{K}}^{12}_{\ell \mathrm{N}} \\ \mathbf{0} & \dots & \dots & \dots & \tilde{\mathbf{K}}^{21}_{\ell \mathrm{N}} & \tilde{\mathbf{K}}^{22}_{\ell \mathrm{N}} \end{bmatrix} \tag{4.21}$$

As previously, the displacement at the first interface can be retrieved by imposing equilibrium and compatibility. The resulting matrix expression is reported in the following for convenience of notation:

$$\tilde{\mathbf{u}}_{\mathbf{1}} = \left[\mathbf{I} + \tilde{\mathbf{H}}_{\mathbf{s}} \left[\tilde{\mathbf{H}}_{\mathbf{L}}^{11}\right]^{-1}\right]^{-1} \tilde{\mathbf{u}}_{\mathbf{0}} \tag{4.22}$$

with the FRF sub-matrix $\tilde{\mathbf{H}}_{\mathbf{L}}^{11}$, which refers to the degrees-of-freedom at the first interface, being the inverse of the stiffness matrix $\tilde{\mathbf{K}}_{\mathbf{L}}$. The displacement vector at the remaining 2$^{\text{nd}}$ to N^{th} interfaces may be obtained as:

$$\tilde{\mathbf{u}}_{(\mathbf{2..N})} = \tilde{\mathbf{H}}_{\mathbf{f}}^{(2..N)1} \left[\tilde{\mathbf{H}}_{\mathbf{f}}^{11}\right]^{-1} \tilde{\mathbf{u}}_{\mathbf{1}} \tag{4.23}$$

By dimensional analysis, any of the transfer functions between displacements with and without the $N-1$ layers may be written as a function of the following non-dimensional groups:

$$\frac{\tilde{u}_i}{\tilde{u}_0} = \Psi_L \left(h_{02}, \ldots, h_{0N}, \frac{\rho_1}{\rho_2}, \ldots, \frac{\rho_1}{\rho_N}, \frac{V_1}{V_2}, \ldots, \frac{V_1}{V_N}, \nu_1, \ldots, \nu_N, \eta_1, \ldots, \eta_N, \gamma, \theta_V \right) \tag{4.24}$$

Although the latter does not provide physical insights on specific aspects of the wave-propagation in layered media, it summarises the complexity of the problem that relates to $5N-1$ non-dimensional groups. Based on Equation 4.24, it possible to suggest a minimal approach by consideration of a selection of parameters based on engineering judgement. An example is presented in the next section for a layered ground with $N = 3$ that is composed of an underlying half-space, an intermediate soil layer and a slab foundation.

4.5.2 Influence of an intermediate soil layer on the added-foundation effect

The generalised layered ground illustrated in Figure 4.16 is here contextualized to the SSI associated with the construction of a slab foundation (as in Section 4.1) with the presence of a soil layer overlying the half-space. The response of the layered ground to incident P- or SV-waves at an angle θ_V is illustrated in Figure 4.17a with displacement vectors in the frequency-wavenumber domain at the interface $\tilde{\mathbf{u}}_{\mathbf{01}} = \left[\tilde{u}_{01}, \tilde{w}_{01}\right]^T$ and at the free-surface $\tilde{\mathbf{u}}_{\mathbf{02}} = \left[\tilde{u}_{02}, \tilde{w}_{02}\right]^T$. The construction of a slab foundation may be represented by an additional layer added on top of the existing ground (Figure 4.17b) with a resulting displacement vector at the free-surface $\tilde{\mathbf{u}}_{\mathbf{3}} = \left[\tilde{u}_3, \tilde{w}_3\right]^T$.

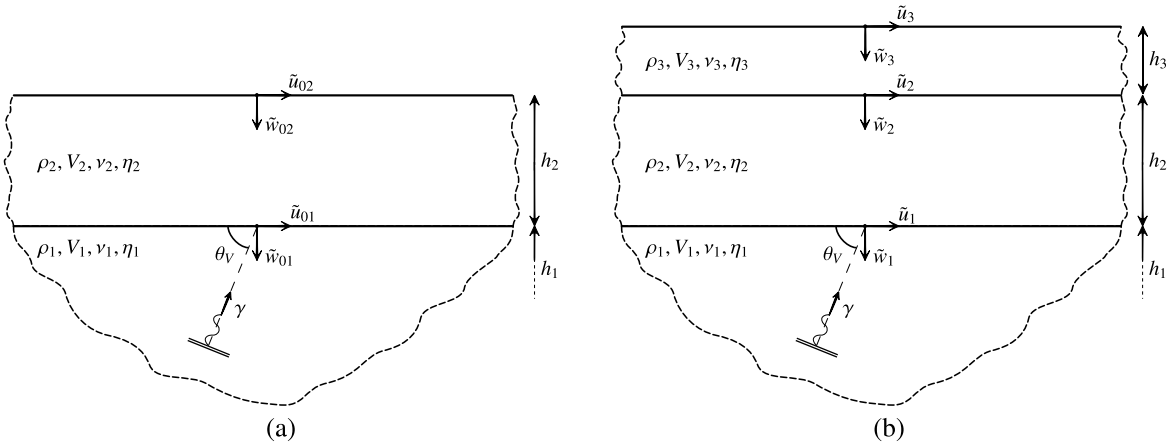

Fig. 4.17 An example of horizontally layered ground with a soil layer overlying the elastic half-space. The added-foundation effect is considered by adding an infinitely large concrete slab foundation.

Similar to the general case in Equation 4.24, transfer functions in terms of displacements between the free-field condition and the layered ground comprising the slab foundation can be written as:

$$\frac{\tilde{w}_3}{\tilde{w}_{02}} = \Psi\left(h_{02}, h_{03}, \frac{\rho_1}{\rho_2}, \frac{\rho_1}{\rho_3}, \frac{V_1}{V_2}, \frac{V_1}{V_3}, \nu_1, \nu_2, \nu_3, \eta_1, \eta_2, \eta_3, \gamma, \theta_V\right) \tag{4.25}$$

With reference to Equation 4.25, it is desired to reduce the dependency of the transfer function to a smaller number of dimensionless parameters based on engineering judgement. It is apparent, with the plane-wave assumption, that although material damping contributes to the attenuation of waves along the x axis it does not contribute to relative measures of amplitude along the z axis. It follows that the dependency on the damping loss factors can be disregarded for the amplification problem that is of interest. Considering the density of soils, it is evident from literature that differences are not greater than approximately 15% and that, in any case, the density ratio has a limited influence on the added-foundation effect as discussed in Section 4.4. Dimensionless groups related to the density of the layered system can then be neglected. Finally, considering reference values for $\nu_1, \nu_3, V_1/V_3$ as in Table 3.1 and a value of $\nu_2 = 1/3$, it is possible to study a reduced dependency of the transfer function in Equation 4.25 to:

$$\frac{\tilde{w}_3}{\tilde{w}_{02}} = \Psi\left(h_{02}, h_{03}, \frac{V_1}{V_2}, \gamma, \theta_V\right) \tag{4.26}$$

The relationship in Equation 4.26 is able to describe the influence of the relative stiffness of the intermediate soil layer, the thickness of the latter and the thickness of the slab on the added-foundation

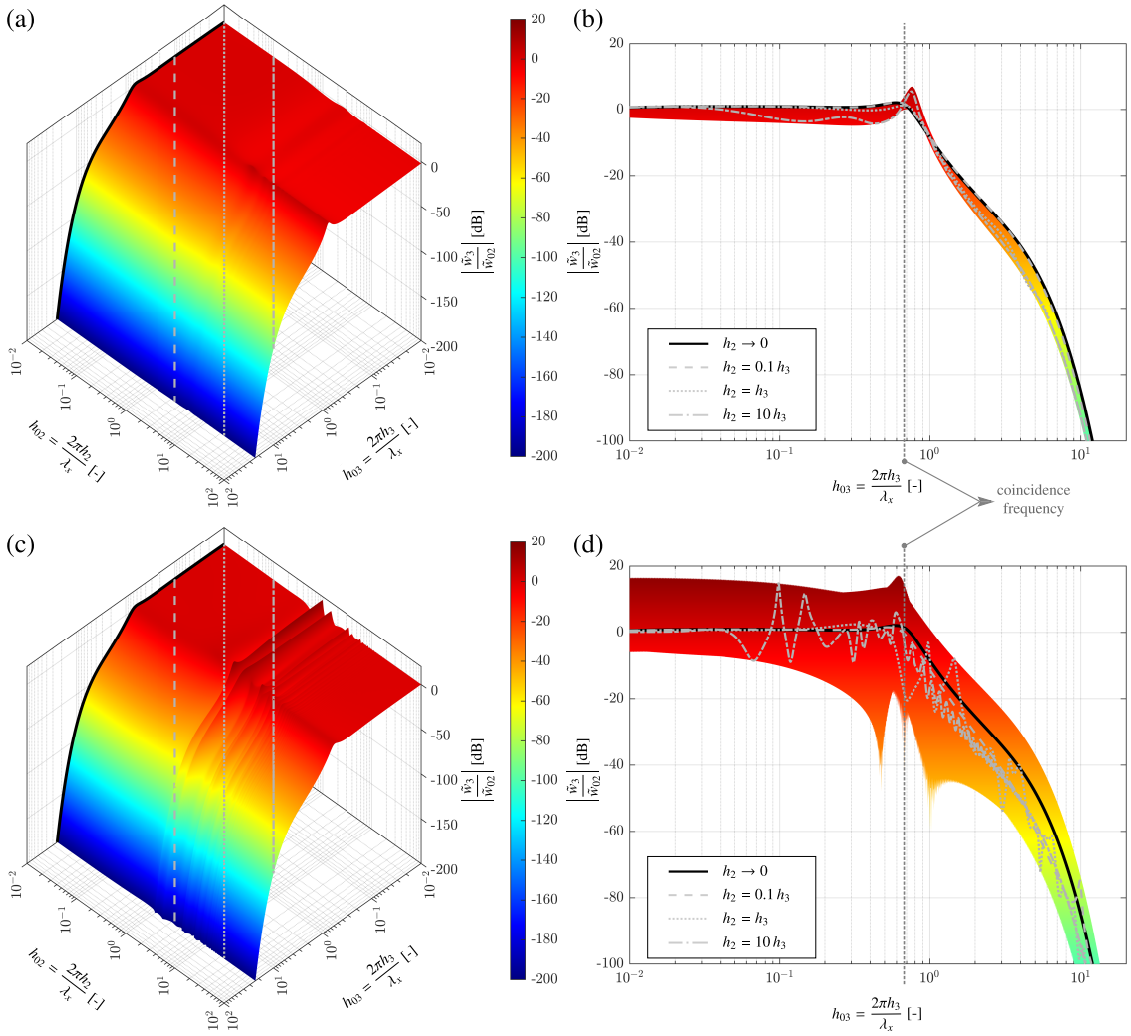

Fig. 4.18 An example of the transfer function relating to the magnitude of the vertical displacement before ($\tilde{w}_{02}$) and after ($\tilde{w}_3$) the coupling of the slab foundation to the layered ground. The dependence on the dimensionless thickness h_{02} and h_{03} is shown in a three-dimensional plot (a) and (c), and in a two-dimensional plot (b) and (d) with reference to h_{03} and the ratio h_2/h_3. The results in (a),(b) refer to a shear wave speed ratio $V_1/V_2 = 0.67$ between the half-space and the intermediate layer, and those in (c),(d) refer to $V_1/V_2 = 2$. An incident plane SV-wave at $\theta_V = 3\pi/8$ is considered.

effect related to different incident wave-fields. Figure 4.18 shows the relationship in Equation 4.26 for an incident SV-wave at $\theta_V = 3\pi/8$. Figure 4.18a and b refer to a value $V_1/V_2 = 0.67$ while Figure 4.18c and d consider a value $V_1/V_2 = 2$. Both three-dimensional plots, in terms of the dimensionless thickness h_{02} and h_{03} in logarithmic scale, and "collapsed" two-dimensional plots are shown for the two values of V_1/V_2 considered. It is evident that the ratio h_{02}/h_{03} corresponds to the ratio h_2/h_3 between the soil layer and the slab thickness. It follows that vertical plane sections, oriented at 45°in the plane $h_{03} - h_{02}$ (in logarithmic scale), of the three-dimensional plot corresponds

to different ratios h_2/h_3. This is represented in the respective two-dimensional plots where transfer functions in gray-scale are reported for different values of $h_2/h_3 = 0.1, 1$ and 10 together with the coloured scale related to the full range of h_{02} as in the three-dimensional plot. Starting from the range of a_0 (as discussed in Section 4.1) and from the considered incident wave-fields, the possible range of $h_{03} \approx 0.1 - 20$ and $h_{02} \approx 0.01 - 100$ follow. Of particular relevance is the result for $h_2 \to 0$, which relates to the added-foundation effect of the slab foundation without the presence of the intermediate soil layer (i.e. problem seen in Section 4.1). The following qualitative comments can be made on Figure 4.18 for the case of an incident SV-wave at $\theta_V = 3\pi/8$:

- the coincidence frequency related to the case $h_2 = 0$ is representative of the divide between potential amplifications and attenuations also in the case of the presence of an intermediate layer. This can be assumed as a general comment since the slab foundation mass and stiffness govern this dividing line with a small influence of the intermediate layer;
- the added-foundation effect, in the presence of an intermediate soil layer stiffer than the underlying half-space (Figure 4.18b), leads to an improved attenuation, in a measure of approximately 5 dB, with respect to the case of the slab foundation alone; an amplification of the level of vertical vibration up to 7 dB is expected around the coincidence frequency;
- the added-foundation effect, in the presence of an intermediate soil layer softer than the underlying half-space (Figure 4.18d), leads to an improved or reduced attenuation depending on the specific value of the ratio h_2/h_3 and on the range of a_0 associated with the practical case of interest. The soft intermediate layer of thickness $h_2 = 10\,h_3$ (i.e $h_2 = 7$ m for a 0.7 m thick slab foundation) may lead to differences up to 15 dB with the results obtained for the slab foundation alone.

Figure 4.19 and 4.20 show summary results for the transfer functions related to the horizontal and vertical motion before and after the construction of a slab foundation for shear wave speed ratios V_1/V_2 of 0.67 and 2 respectively. It is clear that only qualitative comments can be made and the response of the slab on the layered ground depends strongly on the specific wave-propagation problem in hand. Although it is not possible to quantify, in general terms, the influence of the presence of an intermediate soil layer on the "added-foundation effect", it is clear that the coincidence phenomenon governs the divide between potential amplification and attenuation, with the latter being of interest for design purposes.

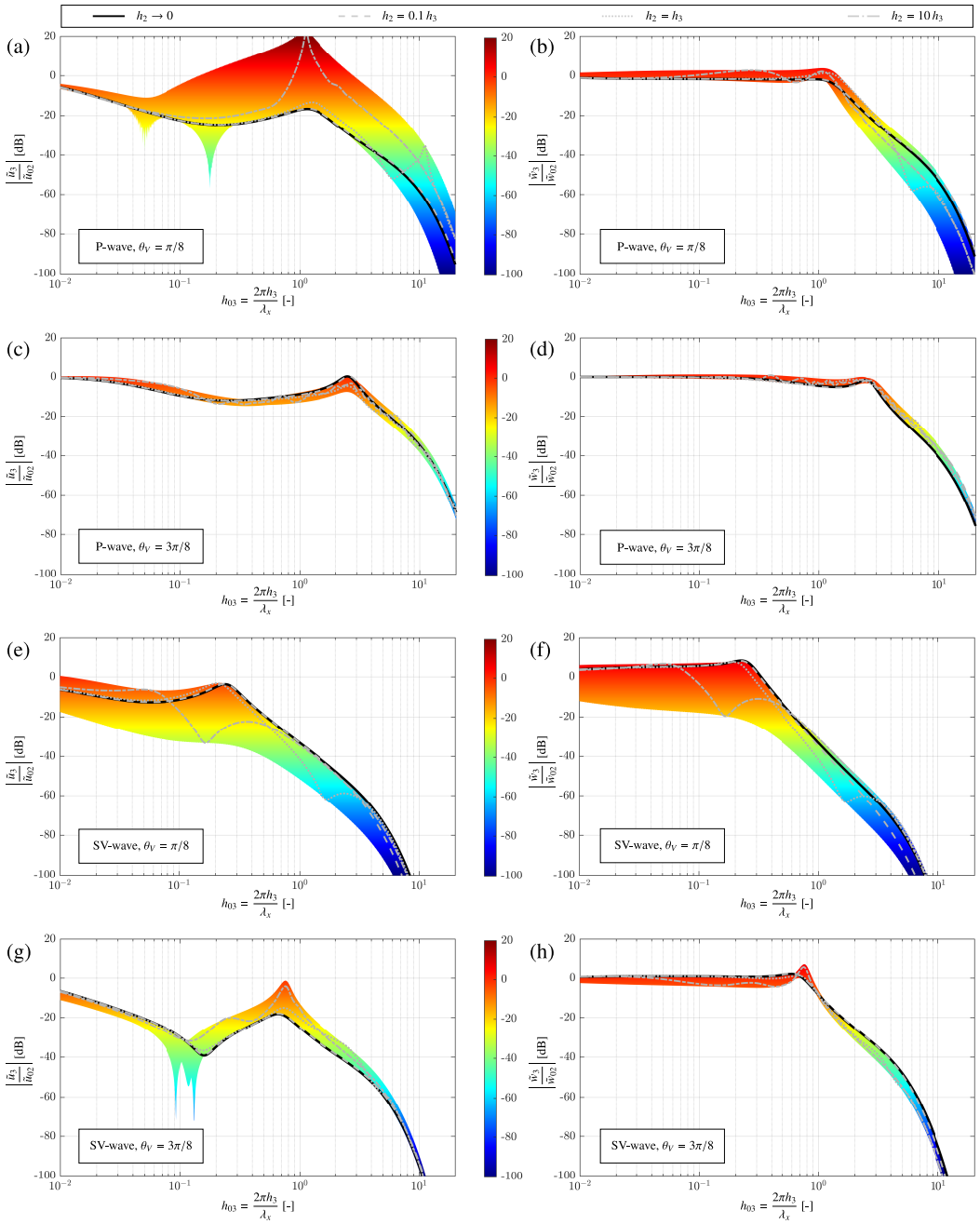

Fig. 4.19 Resulting transfer functions related to the magnitude of the horizontal (left) and vertical (right) displacement before ($\tilde{u}_{02}, \tilde{w}_{02}$) and after ($\tilde{u}_3, \tilde{w}_3$) the coupling of the slab foundation to the layered ground. Incident sub-horizontal ($\theta_V = \pi/8$) and sub-vertical ($\theta_V = 3\pi/8$) P- and SV-waves are considered. The values shown refers to h_{02} between 0.01 and 100,while the gray-scale dashed, dotted, and dashed-dotted lines refer to values of h_2/h_3 of 0.1, 1 and 10 respectively. The solid black line considers $h_2 \to 0$, which represents the case of a slab foundation on an elastic half-space as seen in Section 4.1. The plots refer to a shear wave speed ratio between the half-space and the soil layer of $V_1/V_2 = 0.67$.

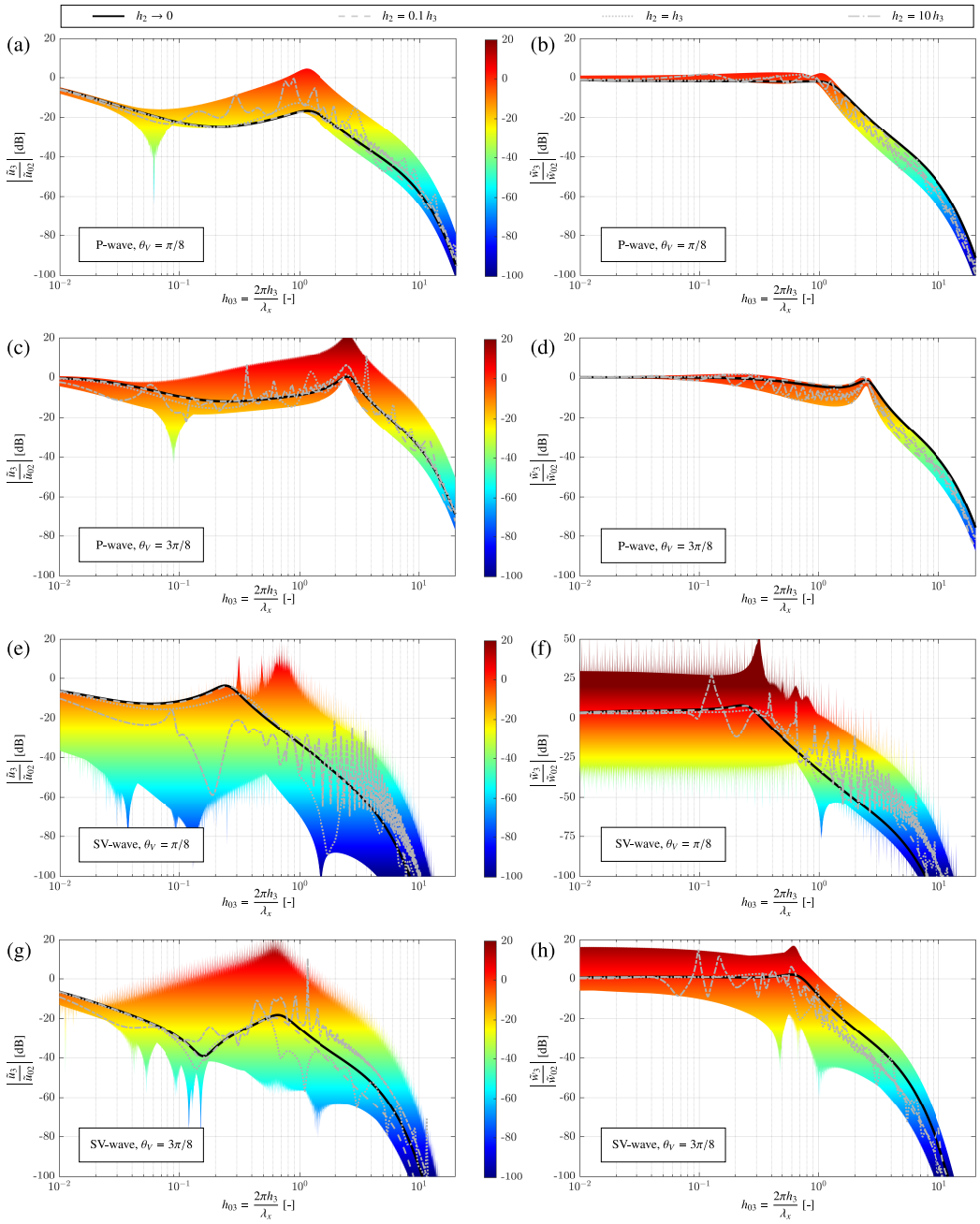

Fig. 4.20 Resulting transfer functions related to the magnitude of the horizontal (left) and vertical (right) displacement before ($\tilde{u}_{02}, \tilde{w}_{02}$) and after ($\tilde{u}_3, \tilde{w}_3$) the coupling of the slab foundation to the layered ground. Incident sub-horizontal ($\theta_V = \pi/8$) and sub-vertical ($\theta_V = 3\pi/8$) P- and SV-waves are considered. The values shown refers to h_{02} between 0.01 and 100, while the gray-scale dashed, dotted, and dashed-dotted lines refer to values of h_2/h_3 of $0.1, 1$ and 10 respectively. The solid black line considers $h_2 \to 0$, which represents the case of a slab foundation on an elastic half-space as seen in Section 4.1. The plots refer to a shear wave speed ratio between the half-space and the soil layer of $V_1/V_2 = 2$.

4.6 Conclusions

This chapter has considered the fundamental dynamic behaviour of a concrete slab foundation excited by ground-borne vibration. The interest lies in the added-foundation effect provided by the slab foundation in terms of the change in vibration levels at the free-surface before and after the construction of the foundation. By modelling the slab as an elastic layer overlying an elastic half-space, and using the corresponding dynamic stiffness matrices in a wave-based approach, the response of the slab to incident Rayleigh, P- and SV-waves has been explored. Having referred to previous work that assumes plate-like behaviour, it is clear that the use of thin-plate theory alone is insufficient for modelling the effect of a slab foundation on an existing ground vibration field over the full frequency range of interest. Furthermore, models that assume a relaxed boundary condition at the soil-slab interface have been found to underestimate the attenuation provided for the vertical vibration at the free-surface by 5 to 10 dB in the case of Rayleigh wave excitation.

The study has illustrated the importance of the coincidence phenomenon, in which the free-flexural wavelength of the slab coincides with the horizontal wavelength of the incident wave-field. For frequencies above coincidence, considerable attenuation can be achieved, but this depends on a number of dimensionless groups, as illustrated in a series of summary design plots. The least significant of these is the soil-slab density ratio, which, for all three wave types, has only a weak influence on the level of attenuation provided, with differences up to 6 dB. In contrast, the relative stiffness of the slab (expressed as a ratio of shear wave speeds) has a strong influence. Maximum differences of attenuation in the order of 25 dB and 30 dB are found for Rayleigh waves and for sub-horizontal body waves respectively. The incidence angle of the considered plane-wave excitation has the greatest influence on the added-foundation effect, indicating that the study of the source and the induced ground-borne vibration field plays an important role. For a given site and given material properties for the foundation (i.e. concrete), the controlling parameter available for the foundation design is the slab thickness. In the case of Rayleigh wave excitation, the added-foundation effect in vertical vibration leads to at least 20 dB of attenuation for the 0.7 m thick slab of benchmark #2 in the frequency range of interest. For P- and SV-waves, the situation is more complex because the coincidence frequencies associated with these wave types are always higher than that of the Rayleigh wave, which shifts the region of strong attenuation to relatively higher frequencies. It follows that the added-foundation effect, in terms of attenuation of the vibration levels, is more significant for

surface waves than for body waves. The overall attenuation depends strongly on the slab stiffness and, importantly, on the directionality of the incident wave-field.

A fundamental assumption of this study is that the ground may be represented by a homogeneous half-space, but this is often not the case due to soil layering. Layering introduces additional wave reflections and mode conversions, and this is likely to change the attenuation provided by the slab. The extent to which this occurs is qualitatively explored by accounting for the presence of an intermediate soil layer overlying the half-space. It is shown that the problem becomes rather complex and that the measure of the attenuation provided by the slab varies greatly depending on the thickness ratio between the soil layer and the slab foundation, and on the stiffness ratio between the soil layer and the half-space. A general comment can be drawn in that the coincidence phenomenon related to the stiffness and mass of the slab foundation and to the incident wave-field still marks the dividing line between potential amplifications and attenuations along the frequency spectrum.

The added-foundation effect investigated in this chapter refers to an infinitely large slab foundation and to a plane wave excitation, consistent with the reference problem considered in this dissertation. In practice, the foundation has finite dimensions as well as being embedded in the surrounding ground. Moreover, ground-borne vibration induced by surface and/or underground sources may be drastically different from the plane wave assumption. The first-principles approach adopted in this chapter forms the basis for further work that may consider cases of more practical interest, which may rely on numerical modelling techniques and that lie outside the scope of the present dissertation.

Chapter 5

The response of rigid foundations and footings to incident wave-fields

In the previous chapter it was concluded that thin-plate theory is insufficient for modelling the soil-slab interaction over the full frequency range of interest, and that the boundary conditions at the soil-slab interface have a significant effect. Thanks to the assumption of an infinitely-large slab foundation, the added-foundation effect has been investigated by means of a wave-based approach in the frequency-wavenumber domain. Although this improves our understanding of the soil-foundation interaction, it does not offer a ready-to-use foundation model for the soil-foundation-building interaction, which involves the portal-frame building model as presented in Section 3.1.2. A consistent foundation model would refer to rigid regions at the free-surface of either the ground (i.e. rigid foundations - benchmark #1) or the slab overlying the ground (i.e. rigid footings - benchmark #2).

This chapter presents an approximate strategy, based on Iguchi's method [98, 99], to obtain the response of such rigid regions to incident plane wave-fields. This may be readily incorporated as the first step of a new design framework of buildings against ground-borne vibration, as will be discussed in Chapter 6. Iguchi's method is reviewed in Section 5.1.1 starting from the Boundary-Element-Method (BEM) formulation presented in Section 5.1. The response of a single and/or multiple rigid foundations obtained by the approximate method is validated against rigorous solutions. A numerical study is also undertaken for validating Iguchi's method also for the case of a single and/or multiple rigid footings (see Section 5.2) on the free-surface of an infinitely-large slab foundation. It is worth noticing that Iguchi's method is valid for a general incident wave-field. It follows that it

may be adopted for obtaining the rigid regions response to incident wave-fields obtained by modelling of the source and the ground (e.g. PiP model [195–197], FEM-BEM approach [198, 191]). Iguchi's method can then be incorporated in a framework for the purpose of absolute predictions of vibration levels, although the latter is beyond the scope of this dissertation.

The approximate method, summarised in Section 5.3, leads to closed-form expressions for the response of the rigid regions starting from the frequency-wavenumber amplitude at the free-surface and associated with an incident plane wave-field. Additionally, the added-foundation effect, as studied in Chapter 4, may be here investigated by comparing the response of the rigid footings (benchmark #2) and the one of rigid foundations (benchmark #1). This provides an understanding of the added-foundation effect more directly related to the building design by focusing on the response at the coupling points.

For the latter purpose, additional models of the slab foundation are considered, as presented in Section 5.4, by removing the assumption of infinite in-plane extent. Two Finite Element Analysis (FEA) models, obtained with ABAQUS [114], are considered for a finite slab: a 2D thick-shell model with quadratic elements (S8R) and a 3D solid model with quadratic elements (C3D20R). Both models include the presence of rigid footings on the middle (2D model) and on the upper surface (3D model) of the slab.

Rigorous models used in this chapter refer to the application of the BEM [92, 199] models of rigid foundations and/or rigid footings that consider fundamental solutions of a homogeneous half-space or a layered half-space respectively. The BEM models used in this chapter, as for the rest of the dissertation, are obtained by means of the BEMFUN [38] toolbox, making use of the fundamental solutions from the EDT [36] toolbox in MATLAB [35].

5.1 A BEM framework for the response of rigid foundations

This section presents a general review of the formulation for the response of a number n_f of rigid, embedded foundations resting on an elastic and homogeneous half-space, with the latter being subjected to an incident plane wave-field. This is a topic of much interest in earthquake engineering that has been treated, among others [200–204], by Wong & Luco [96] and by Qian & Beskos [97]. The formulation is presented in its general form so that it can be readily used for both the implementation

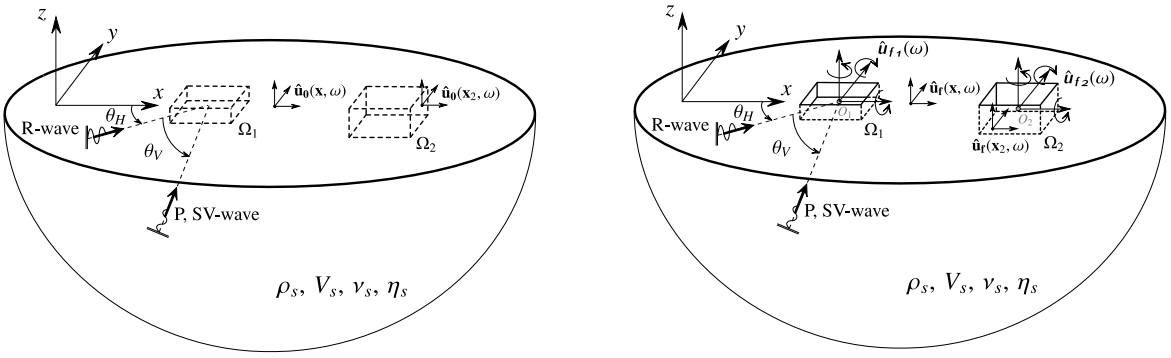

(a) (b)

Fig. 5.1 A schematic representation of multiple, embedded, rigid foundations in a homogeneous and elastic half-space: (a) the incident wave-field, in absence of foundations, is represented by $\hat{\mathbf{u}}_\mathbf{0}(\mathbf{x},\omega)$ at a generic location $\mathbf{x}$ in the half-space and by $\hat{\mathbf{u}}_\mathbf{0}(\mathbf{x}_i,\omega)$ at a location $\mathbf{x}_i$ on the domain Ω_i of the i^{th} foundation; (b) the displacement field in the presence of foundations is represented by $\hat{\mathbf{u}}_\mathbf{f}(\mathbf{x},\omega)$ at a generic location $\mathbf{x}$ in the half-space and by $\hat{\mathbf{u}}_\mathbf{f}(\mathbf{x}_i,\omega)$ at a location $\mathbf{x}_i$ on the domain Ω_i of the i^{th} foundation. The rigid response of the i^{th} foundation about its centroid O_i is denoted as $\hat{\boldsymbol{u}}_{\boldsymbol{fi}}(\omega)$.

in a Boundary-Element framework and/or for obtaining the response of the rigid foundations by means of Iguchi's method (see Section 5.1.1).

Figure 5.1 illustrates a foundation model comprising two embedded, rigid foundations with the soil-foundation interfaces Ω_1 and Ω_2. By considering incident plane wave-fields, as in Section 3.1.1, the free-field displacement $\hat{\mathbf{u}}_\mathbf{0}(\mathbf{x},\omega)$ in the half-space can be expressed as:

$$\hat{\mathbf{u}}_\mathbf{0}(\mathbf{x},\omega) = \tilde{\mathbf{u}}_\mathbf{0}(k',z,\omega)\, e^{-ik'(x\cos\theta_H + y\sin\theta_H)} = \boldsymbol{\mathcal{U}}_0(\mathbf{x},\omega)\, \tilde{\mathbf{u}}_\mathbf{0}(k',z,\omega) \tag{5.1}$$

with the exponential function $\boldsymbol{\mathcal{U}}_0$ describing the incident wave-field along x and y for the horizontal wavenumber k' in the plane of incidence, while the frequency-wavenumber amplitude $\tilde{\mathbf{u}}_\mathbf{0}$ provides the dependency along z. The latter may be obtained by means of Equation C.27 in Appendix C, after the wave amplitudes for the incident wave-field are retrieved as described in Section C.2.1. The plane-wave excitation described here belongs to a particular class of plane-strain problems for which the horizontal wavenumber, $k' = k\cos\theta_V$, depends on the angular frequency ω of the assumed harmonic excitation and on the speed and orientation of the wave-type considered. The wavenumber k is equal to $k_P = \omega/V_P$, $k_S = \omega/V_S$ and $k_R = \omega/V_R$ for P-, SV- and Rayleigh waves respectively. The vector $\tilde{\mathbf{u}}_\mathbf{0}(k',z,\omega) = [\tilde{u}_0(k',z,\omega),\ \tilde{v}_0(k',z,\omega),\ \tilde{w}_0(k',z,\omega)]^{\mathrm{T}}$ is the free-field amplitude in the

frequency-wavenumber domain, which depends on the type of the incident wave and on the properties of the half-space [78, 77].

Consider the addition of rigid, embedded foundations, of arbitrary shape, as illustrated in Figure 5.1b. In general, the presence of a foundation induces a scattered wave-field, with displacement $\hat{\mathbf{u}}_\mathbf{s}(\mathbf{x},\omega)$ and traction $\hat{\mathbf{t}}_\mathbf{s}(\mathbf{x},\omega)$, that superposes with the incident wave-field, $\hat{\mathbf{u}}_\mathbf{0}(\mathbf{x},\omega)$ and $\hat{\mathbf{t}}_\mathbf{0}(\mathbf{x},\omega)$, such that:

$$\hat{\mathbf{u}}_\mathbf{f}(\mathbf{x},\omega) = \hat{\mathbf{u}}_\mathbf{0}(\mathbf{x},\omega) + \hat{\mathbf{u}}_\mathbf{s}(\mathbf{x},\omega) \tag{5.2a}$$

$$\hat{\mathbf{t}}_\mathbf{f}(\mathbf{x},\omega) = \hat{\mathbf{t}}_\mathbf{0}(\mathbf{x},\omega) + \hat{\mathbf{t}}_\mathbf{s}(\mathbf{x},\omega) \tag{5.2b}$$

where $\hat{\mathbf{u}}_\mathbf{f}(\mathbf{x},\omega)$ and $\hat{\mathbf{t}}_\mathbf{f}(\mathbf{x},\omega)$ represent the final displacement and traction fields accounting for the kinematic interaction of the rigid foundations. This is a valid result in linear elasticity because of the validity of the superposition principle.

The n_f foundations are embedded in the half-space with their centroids O_i at $\mathbf{x_{Oi}} = (x_{Oi}, y_{Oi}, z_{Oi})$. The displacement at a location on the soil-foundation interface of the i^{th} foundation can be expressed as:

$$\hat{\mathbf{u}}_\mathbf{f}(\mathbf{x}_i,\omega) = \boldsymbol{\mathcal{S}}_i(\mathbf{x}_i)\,\hat{\boldsymbol{u}}_{\boldsymbol{fi}}(\omega) \qquad \text{with} \quad \mathbf{x}_i \in \Omega_i, \quad i = 1,\ldots,n_f \tag{5.3}$$

where $\hat{\boldsymbol{u}}_{\boldsymbol{fi}} = [\hat{u}_{fi},\ \hat{v}_{fi},\ \hat{w}_{fi},\ \hat{\varphi}_{fxi},\ \hat{\varphi}_{fyi},\ \hat{\varphi}_{fzi}]^T$ gives the rigid-body displacements of the i^{th} foundation, referring to its 6 degrees of freedom, and the 3×6 transformation matrix $\boldsymbol{\mathcal{S}}_i(\mathbf{x}_i)$ is given by:

$$\boldsymbol{\mathcal{S}}_i(\mathbf{x}_i) = \begin{bmatrix} 1 & 0 & 0 & 0 & z_i - z_{Oi} & -(y_i - y_{Oi}) \\ 0 & 1 & 0 & -(z_i - z_{Oi}) & 0 & x_i - x_{Oi} \\ 0 & 0 & 1 & y_i - y_{Oi} & -(x_i - x_{Oi}) & 0 \end{bmatrix} \qquad \text{with} \quad \mathbf{x}_i \in \Omega_i \tag{5.4}$$

The corresponding forces exerted by the i^{th} foundation on the soil can be evaluated as:

$$\hat{\boldsymbol{f}}_{\boldsymbol{fi}}(\omega) = \int_{\Omega_i} \boldsymbol{\mathcal{S}}_i^{\mathrm{T}}(\mathbf{x}_i)\,\hat{\mathbf{t}}_\mathbf{f}(\mathbf{x}_i,\omega)\,d\Omega_i \tag{5.5}$$

where $\hat{\boldsymbol{f}}_{\boldsymbol{fi}} = [\hat{s}_{fi},\ \hat{p}_{fi},\ \hat{f}_{fi},\ \hat{q}_{fxi},\ \hat{q}_{fyi},\ \hat{q}_{fzi}]^T$ again refers to the 6 degrees of freedom. The global condition for the i^{th} foundation can be obtained by pre-multiplying Equation 5.2b by $\boldsymbol{\mathcal{S}}_i^{\mathrm{T}}(\mathbf{x}_i)$ and

integrating over the domain Ω_i so that:

$$\hat{\boldsymbol{f}}_{\boldsymbol{fi}}(\omega) = \hat{\boldsymbol{f}}_{\boldsymbol{oi}}(\omega) + \hat{\boldsymbol{f}}_{\boldsymbol{si}}(\omega) = \int_{\Omega_i} \boldsymbol{\mathcal{S}}_i^{\mathrm{T}}(\mathbf{x}_i)\, \hat{\mathbf{t}}_{\mathbf{0}}(\mathbf{x}_i, \omega)\, d\Omega_i + \int_{\Omega_i} \boldsymbol{\mathcal{S}}_i^{\mathrm{T}}(\mathbf{x}_i)\, \hat{\mathbf{t}}_{\mathbf{s}}(\mathbf{x}_i, \omega)\, d\Omega_i \tag{5.6}$$

where $\hat{\boldsymbol{f}}_{\boldsymbol{oi}}$ and $\hat{\boldsymbol{f}}_{\boldsymbol{si}}$ are the forces, associated with the domain Ω_i, induced by the incident and the scattered wave-fields respectively.

Introducing the Green's function matrix for the half-space $\hat{\boldsymbol{\mathcal{G}}}(\mathbf{x}_i, \mathbf{x}'_j, \omega)$, which relates the soil displacement $\hat{\mathbf{u}}(\mathbf{x}_i, \omega)$ to the soil traction $\hat{\mathbf{t}}(\mathbf{x}'_j, \omega)$, the scattered displacement field over the domain Ω_i is given by:

$$\hat{\mathbf{u}}_{\mathbf{s}i}(\mathbf{x}_i, \omega) = \sum_{j=1}^{n_f} \int_{\Omega_j} \hat{\boldsymbol{\mathcal{G}}}_{ij}(\mathbf{x}_i, \mathbf{x}'_j, \omega)\, \hat{\mathbf{t}}_{\mathbf{s}}(\mathbf{x}'_j, \omega)\, d\Omega_j \tag{5.7}$$

Following the approach of Thau [205], the scattered traction field can be decomposed into one component related directly to the unknown, rigid-body displacements of the foundations $\hat{\boldsymbol{u}}_{\boldsymbol{fj}}(\omega)$ and a second component required to make the foundation system immobile under the incident wave-field:

$$\hat{\mathbf{t}}_{\mathbf{s}}(\mathbf{x}_i, \omega) = \sum_{j=1}^{n_f} \boldsymbol{\mathcal{T}}_{ijR}(\mathbf{x}_i, \omega)\, \hat{\boldsymbol{u}}_{\boldsymbol{fj}}(\omega) - \boldsymbol{\mathcal{T}}_{iD}(\mathbf{x}_i, \omega) \qquad \text{with} \quad \mathbf{x}_i \in \Omega_i \tag{5.8}$$

The matrix $\boldsymbol{\mathcal{T}}_{ijR}(\mathbf{x}_i, \omega)$ gives the traction field across the soil-foundation interface of the i^{th} foundation due to a rigid-body motion $\hat{\boldsymbol{u}}_{\boldsymbol{fj}}$ of the j^{th} foundation.

Let us consider Equation 5.2a as applied to the i^{th} foundation. Substituting the expression for $\hat{\mathbf{u}}_{\mathbf{f}}(\mathbf{x}_i, \omega)$ from Equation 5.3 and the expression for $\hat{\mathbf{u}}_{\mathbf{s}}(\mathbf{x}_i, \omega)$ from Equation 5.7, with the traction expressed as in Equation 5.8, the following system of integral equations is obtained, which refers to the two distinct radiation (Equation 5.9a) and diffraction (Equation 5.9b) problems:

$$\boldsymbol{\mathcal{S}}_i(\mathbf{x}_i)\, \hat{\boldsymbol{u}}_{\boldsymbol{fi}}(\omega) = \sum_{j=1}^{n_f} \int_{\Omega_j} \hat{\boldsymbol{\mathcal{G}}}_{ij}(\mathbf{x}_i, \mathbf{x}'_j, \omega) \sum_{r=1}^{n_f} \boldsymbol{\mathcal{T}}_{jrR}(\mathbf{x}'_j, \omega)\, \hat{\boldsymbol{u}}_{\boldsymbol{fr}}(\omega)\, d\Omega_j \quad \text{with} \quad i = 1, \ldots, n_f \tag{5.9a}$$

$$\hat{\mathbf{u}}_{\mathbf{0}i}(\mathbf{x}_i, \omega) = \sum_{j=1}^{n_f} \int_{\Omega_j} \hat{\boldsymbol{\mathcal{G}}}_{ij}(\mathbf{x}_i, \mathbf{x}'_j, \omega)\, \boldsymbol{\mathcal{T}}_{jD}(\mathbf{x}'_j, \omega)\, d\Omega_j \quad \text{with} \quad i = 1, \ldots, n_f \tag{5.9b}$$

By re-writing in matrix form, it is evident that Equation 5.9a may be further decomposed into the n_f integral equations that yield the unknown matrix $\boldsymbol{\mathcal{T}}_{ijR}$:

$$\boldsymbol{\mathcal{S}}_i(\mathbf{x}_i) = \sum_{j=1}^{n_f} \int_{\Omega_j} \hat{\boldsymbol{\mathcal{G}}}_{ij}(\mathbf{x}_i, \mathbf{x}'_j, \omega)\, \boldsymbol{\mathcal{T}}_{jiR}(\mathbf{x}'_j, \omega)\, d\Omega_j \quad \text{when} \quad r = i \tag{5.10a}$$

$$\mathbf{0} = \sum_{j=1}^{n_f} \int_{\Omega_j} \hat{\mathcal{G}}_{ij}(\mathbf{x}_i, \mathbf{x}'_j, \omega)\, \mathcal{T}_{jrR}(\mathbf{x}'_j, \omega)\, d\Omega_j \quad \text{with} \quad r = 1, \ldots, n_f \wedge r \neq i \tag{5.10b}$$

By definition of the matrix $\mathcal{T}_{ijR}$, the dynamic stiffness matrix relating the forces at the i^{th} foundation due to the rigid displacement at the j^{th} foundation is given by:

$$\hat{K}_{fij}(\omega) = \int_{\Omega_i} \mathcal{S}_i^{\mathrm{T}}(\mathbf{x}_i)\, \mathcal{T}_{ijR}(\mathbf{x}_i, \omega)\, d\Omega_i \tag{5.11}$$

It follows that the dynamic stiffness matrix $\hat{K}_f$ for the n_f rigid foundations can be written in the form:

$$\widehat{K}_f = \begin{bmatrix} \widehat{K}_{f11} & \cdots & \widehat{K}_{f1i} & \cdots & \widehat{K}_{f1j} & \cdots & \widehat{K}_{f1n_f} \\ & \ddots & \vdots & & \vdots & & \vdots \\ & & \widehat{K}_{fii} & \cdots & \widehat{K}_{fij} & \cdots & \widehat{K}_{fin_f} \\ & & & \ddots & \vdots & & \vdots \\ & sym & & & \widehat{K}_{fjj} & \cdots & \widehat{K}_{fjn_f} \\ & & & & & \ddots & \\ & & & & & & \widehat{K}_{fn_fn_f} \end{bmatrix} \tag{5.12}$$

Because of the validity of the reciprocity theorem in elastodynamics [206], the matrix $\widehat{K}_f$ can be proven to be symmetric.

By consideration of Equation 5.6, and substituting the expression for $\hat{\mathbf{t}}_s(\mathbf{x}_i, \omega)$ from Equation 5.8, the forces associated with the i^{th} foundation due to the scattered wave-field can be then expressed as:

$$\begin{aligned} \hat{f}_{si}(\omega) &= \int_{\Omega_i} \mathcal{S}_i^{\mathrm{T}}(\mathbf{x_i}) \left[\sum_{j=1}^{n_f} \mathcal{T}_{ijR}(\mathbf{x}_i, \omega)\, \hat{u}_{fj}(\omega) - \mathcal{T}_{iD}(\mathbf{x}_i, \omega) \right] d\Omega_i = \\ &= \sum_{j=1}^{n_f} \widehat{K}_{fij}(\omega)\, \hat{u}_{fj}(\omega) - \int_{\Omega_i} \mathcal{S}_i^{\mathrm{T}}(\mathbf{x}_i)\, \mathcal{T}_{iD}(\mathbf{x}_i, \omega) d\Omega_i \end{aligned} \tag{5.13}$$

Consider the i^{th} foundation to be massless and free of external forces so that, from Equation 5.6:

$$\hat{f}_{si}(\omega) = -\hat{f}_{oi}(\omega) \tag{5.14}$$

The rigid-body displacement $\hat{\boldsymbol{u}}_{\boldsymbol{fi}}(\omega)$ can then be expressed as:

$$\hat{\boldsymbol{u}}_{\boldsymbol{fi}}(\omega) = \sum_{j=1}^{n_f} \widehat{\boldsymbol{H}}_{\boldsymbol{fij}}(\omega) \int_{\Omega_j} \boldsymbol{\mathcal{S}}_j^{\mathrm{T}}(\mathbf{x}_j)\, \boldsymbol{\mathcal{T}}_{jD}(\mathbf{x}_j, \omega)\, d\Omega_j - \sum_{j=1}^{n_f} \widehat{\boldsymbol{H}}_{\boldsymbol{fij}}(\omega)\, \hat{\boldsymbol{f}}_{\boldsymbol{oj}}(\omega) \quad \text{with} \quad i = 1, \ldots, n_f \tag{5.15}$$

Equation 5.15 yields the displacement of multiple, rigid, massless foundations embedded in an elastic half-space subjected to an incident wave-field but free of external forces. The term $\boldsymbol{\mathcal{T}}_{jD}(\mathbf{x}_j, \omega)$ is related to the displacement wave-field $\hat{\mathbf{u}}_{\mathbf{0}}(\mathbf{x}, \omega)$ by the integral Equation 5.9b while the forces $\hat{\boldsymbol{f}}_{\boldsymbol{oj}}(\omega)$ can be retrieved from the traction field $\hat{\mathbf{t}}_{\mathbf{0}}(\mathbf{x}, \omega)$ (see Equation 5.6). The frequency-response function (FRF) matrix $\hat{\boldsymbol{H}}_{\boldsymbol{f}}(\omega)$ can be found as the inverse of the dynamic stiffness matrix $\hat{\boldsymbol{K}}_{\boldsymbol{f}}(\omega)$ in Equation 5.12.

The integral equations presented in the previous discussion can be reduced to sets of algebraic equations expressed at collocation points $\mathbf{x_c}$ of *boundary elements* that refer to a given formulation (e.g. quadratic elements). A full account of this numerical aspect is presented in the relevant literature [207, 115, 208] on the application of the Boundary-Element-Method (BEM). The numerical implementation here refers to fundamental solutions obtained by EDT [36] and a BEM model of the rigid foundations by means of BEMFUN [38] toolbox in MATLAB [35]. It follows that the integration over the domain Ω of a variable-field $\mathbf{z}(\mathbf{x})$ can be obtained as:

$$\int_{\Omega} \mathbf{z}(\mathbf{x})\, d\Omega = \sum_i \sum_j \sum_k \int_{\Gamma_k} N_i^{(k)} N_j^{(k)}\, d\Gamma_k \;\; \mathbf{z}(\mathbf{x}_{\mathbf{c}j}) \quad \text{with} \quad i, j = 1, \ldots, n_c \tag{5.16}$$

where $N_i^{(k)}$ and $N_j^{(k)}$ represent the boundary-element shape functions of the k^{th} element that includes the i^{th} and j^{th} collocation point respectively. It is clear that whenever the i^{th} and j^{th} collocation points do not share at least one element, the specific contribution to the integral is null. The integration of a variable-field $\mathbf{z}(\mathbf{x})$ expressed at the collocation points can then be obtained as:

$$\begin{aligned} &\mathbf{Z}(\mathbf{x_c}) = \mathbf{T_Q}\,(\mathbf{x_c}, \mathbf{x_c})\, \mathbf{z}(\mathbf{x_c}) \\ &\text{with} \quad \mathbf{T_Q}\,(\mathbf{x}_{\mathbf{c}i}, \mathbf{x}_{\mathbf{c}j}) = \sum_k \int_{\Gamma_k} N_i^{(k)} N_j^{(k)}\, d\Gamma_k \end{aligned} \tag{5.17}$$

with the vector $\mathbf{x_c}$ collecting the location of the collocation points for the three degrees of freedom. The integration over the k^{th} element in Equation 5.17 may be performed by a numerical integration scheme (e.g. Gaussian quadrature rule). The transformation matrix $\boldsymbol{\mathcal{S}}\,(\mathbf{x_c})$ can be evaluated at the

collocation points and assembled for the n_f foundations:

$$\mathbf{S} = \begin{bmatrix} \mathbf{S}(\mathbf{x}_{\mathbf{c}1}) & \dots & \mathbf{0} & \dots & \mathbf{0} \\ \vdots & \ddots & \vdots & \vdots & \vdots \\ \mathbf{0} & \dots & \mathbf{S}(\mathbf{x}_{\mathbf{c}i}) & \dots & \mathbf{0} \\ \vdots & \vdots & \vdots & \ddots & \vdots \\ \mathbf{0} & \dots & \mathbf{0} & \vdots & \mathbf{S}(\mathbf{x}_{\mathbf{c}n_f}) \end{bmatrix} \tag{5.18}$$

The case of surface foundations is of interest for the discussion in this dissertation. In this case the force vector $\hat{\boldsymbol{f}}_{\boldsymbol{o}}$ is null and the response vector $\hat{\boldsymbol{u}}_{\boldsymbol{f}} = [\hat{\boldsymbol{u}}_{\boldsymbol{f}\boldsymbol{1}}, \dots, \hat{\boldsymbol{u}}_{\boldsymbol{f}\boldsymbol{n_f}}]$ may be written in the form:

$$\hat{\boldsymbol{u}}_{\boldsymbol{f}}(\omega) = \mathbf{A}(\omega)\,\tilde{\mathbf{u}}_{\mathbf{0}}(k',0,\omega) = \mathbf{A}(\omega)\,\tilde{\mathbf{u}}_{\mathbf{0}}(k',\omega) \tag{5.19}$$

The terms in matrix $\mathbf{A}$ represent transfer functions, in the frequency domain, for the rigid motion of the foundations with reference to the free-surface amplitude $\tilde{\mathbf{u}}_{\mathbf{0}}$ of the incident plane wave-field. The integration matrix $\mathbf{T}_{\mathbf{Q}}$, together with the transformation matrix $\mathbf{S}$, are used to reduce Equation 5.15, for the case of surface foundations, in an algebraic equation. The generalised rigid displacement of the n_f foundations obtained with the BEM formulation can be written as:

$$\hat{\boldsymbol{u}}_{\boldsymbol{f}}(\omega) = \widehat{H}_{\boldsymbol{f}}(\omega)\,\mathbf{S}^{\mathrm{T}}\,\mathbf{T}_{\mathbf{Q}}\,[\widehat{\mathbf{G}}_{\mathbf{u}}(\omega)]^{-1}\,\mathbf{U}_{\mathbf{0}}(\omega)\,\tilde{\mathbf{u}}_{\mathbf{0}}(k',\omega) = \mathbf{A}^{(\mathrm{rig.})}(\omega)\,\tilde{\mathbf{u}}_{\mathbf{0}}(k',\omega) \tag{5.20}$$

with the boundary-element system matrix $\widehat{\mathbf{G}}_{\mathbf{u}}(\omega)$ collecting the Green's functions integrated over the domain, and the matrix $\mathbf{U}_{\mathbf{0}}(\omega)$ representing the describing function $\mathcal{U}_0$ (see Equation 5.1) of the free-field displacement evaluated at the collocation points for the three DoFs. The FRF matrix $\widehat{H}_{\boldsymbol{f}}$ is the inverse of the dynamic stiffness matrix $\widehat{K}_{\boldsymbol{f}}$, with the latter obtained by solving numerically the integral Equations 5.11 and 5.10. In the following an alternative, approximate method for obtaining the response of rigid foundations is reviewed.

5.1.1 Iguchi's method for the response of rigid foundations

Iguchi's method provides an approximate solution for the kinematic interaction of rigid foundations to incident wave-fields. It was first presented by Iguchi [98] for the case of a single rigid foundation

and extended, later on, to the case of adjacent, multiple rigid foundations [99] (paper in Japanese). In the following, Iguchi's method is reviewed starting from Equation 5.15, which for convenience can be written in the form:

$$\hat{\boldsymbol{u}}_{\boldsymbol{fi}}(\omega) = \hat{\boldsymbol{u}}^{*}_{\boldsymbol{fi}}(\omega) - \sum_{j=1}^{n_f} \widehat{\boldsymbol{H}}_{\boldsymbol{fij}}(\omega)\, \hat{\boldsymbol{f}}_{\boldsymbol{oj}}(\omega) \quad \text{with} \quad i = 1, \ldots, n_f \tag{5.21a}$$

$$\text{with} \quad \hat{\boldsymbol{u}}^{*}_{\boldsymbol{fi}}(\omega) = \sum_{j=1}^{n_f} \widehat{\boldsymbol{H}}_{\boldsymbol{fij}}(\omega) \int_{\Omega_j} \boldsymbol{\mathcal{S}}_j^{\mathrm{T}}(\mathbf{x}_j)\, \boldsymbol{\mathcal{T}}_{jD}(\mathbf{x}_j, \omega)\, d\Omega_j \tag{5.21b}$$

Let us assume that the FRF matrix $\widehat{\boldsymbol{H}}_{\boldsymbol{f}}$ and the force vector $\hat{\boldsymbol{f}}_{\boldsymbol{o}}$ related to the incident wave-field can be obtained by alternative methods (e.g. approximate impedance functions and analytical integration of tractions $\hat{\mathbf{t}}_{\mathbf{0}}$ over Ω [98]). In this case, the numerically involved part for the evaluation of the response $\hat{\boldsymbol{u}}_{\boldsymbol{f}}$ is restricted to the integral equations associated with $\hat{\boldsymbol{u}}^{*}_{\boldsymbol{f}}$ in Equation 5.21b. The objective is to find an alternative expression for $\hat{\boldsymbol{u}}^{*}_{\boldsymbol{f}}$; moreover, for the special case of surface foundations, which is of interest in this dissertation, the force vector $\hat{\boldsymbol{f}}_{\boldsymbol{o}}$ is null and the equality $\hat{\boldsymbol{u}}_{\boldsymbol{f}} = \hat{\boldsymbol{u}}^{*}_{\boldsymbol{f}}$ follows from Equation 5.21a. Thus, the alternative expression obtained by Iguchi's method gives the response of the rigid foundations that is of interest. Iguchi's method finds the rigid-body response of each foundation as a weighted average of the relevant displacement component of the incident wave-field over the footprint of the same foundation. This approximate method is obtained as follows.

Let us re-write Equation 5.21b as:

$$\sum_{i=1}^{n_f} \widehat{\boldsymbol{K}}_{\boldsymbol{fji}}(\omega)\, \hat{\boldsymbol{u}}^{*}_{\boldsymbol{fi}}(\omega) = \int_{\Omega_j} \boldsymbol{\mathcal{S}}_j^{\mathrm{T}}(\mathbf{x}_j)\, \boldsymbol{\mathcal{T}}_{jD}(\mathbf{x}_j, \omega)\, d\Omega_j \tag{5.22}$$

By substitution of the dynamic stiffness $\widehat{\boldsymbol{K}}_{\boldsymbol{fji}}$ from Equation 5.11, Equation 5.22 can be written as:

$$\begin{gathered} \sum_{i=1}^{n_f} \int_{\Omega_j} \boldsymbol{\mathcal{S}}_j^{\mathrm{T}}(\mathbf{x}_j)\, \boldsymbol{\mathcal{T}}_{jiR}(\mathbf{x}_j, \omega)\, d\Omega_j\, \hat{\boldsymbol{u}}^{*}_{\boldsymbol{fi}}(\omega) = \int_{\Omega_j} \boldsymbol{\mathcal{S}}_j^{\mathrm{T}}(\mathbf{x}_j)\, \boldsymbol{\mathcal{T}}_{jD}(\mathbf{x}_j, \omega)\, d\Omega_j \\ \therefore \int_{\Omega_j} \boldsymbol{\mathcal{S}}_j^{\mathrm{T}}(\mathbf{x}_j) \left[\sum_{i=1}^{n_f} \boldsymbol{\mathcal{T}}_{jiR}(\mathbf{x}_j, \omega)\, \hat{\boldsymbol{u}}^{*}_{\boldsymbol{fi}}(\omega) - \boldsymbol{\mathcal{T}}_{jD}(\mathbf{x}_j, \omega) \right] d\Omega_j = 0 \end{gathered} \tag{5.23}$$

A sufficient condition for Equation 5.23 is that:

$$\sum_{i=1}^{n_f} \boldsymbol{\mathcal{T}}_{jiR}(\mathbf{x}_j, \omega)\, \hat{\boldsymbol{u}}^{*}_{\boldsymbol{fi}}(\omega) = \boldsymbol{\mathcal{T}}_{jD}(\mathbf{x}_j, \omega) \tag{5.24}$$

By considering the rigid-body displacement of the r^{th} foundation and pre-multiplying both sides of Equation 5.24 by $\sum_{j=1}^{n_f} \hat{\mathcal{G}}_{rj}(\mathbf{x}_r, \mathbf{x}'_j, \omega)$, and integrating over the domain Ω_j, the following identity holds:

$$\sum_{j=1}^{n_f} \int_{\Omega_j} \hat{\mathcal{G}}_{rj}(\mathbf{x}_r, \mathbf{x}'_j, \omega) \sum_{i=1}^{n_f} \mathcal{T}_{jiR}(\mathbf{x}'_j, \omega)\, \hat{u}^*_{fi}(\omega)\, d\Omega_j = \sum_{j=1}^{n_f} \int_{\Omega_j} \hat{\mathcal{G}}_{rj}(\mathbf{x}_r, \mathbf{x}'_j, \omega)\, \mathcal{T}_{jD}(\mathbf{x}'_j, \omega)\, d\Omega_j \tag{5.25}$$

Comparing Equation 5.25 with Equations 5.9a and 5.9b, one can relate the rigid-body displacement $\hat{\boldsymbol{u}}^*_{\boldsymbol{fr}}(\omega)$ of the r^{th} foundation to the incident displacement field $\hat{\mathbf{u}}_{\mathbf{0}}(\mathbf{x}_r, \omega)$ across the footprint of the same foundation:

$$\boldsymbol{\mathcal{S}}_r(\mathbf{x}_r)\, \hat{\boldsymbol{u}}^*_{\boldsymbol{fr}}(\omega) = \hat{\mathbf{u}}_{\mathbf{0}}(\mathbf{x}_r, \omega) \qquad \text{with} \quad \mathbf{x}_r \in \Omega_r \tag{5.26}$$

Equation 5.26 represents only an approximate solution since Equation 5.24 is not a necessary condition for the identity in Equation 5.23. For instance, it is clear, by physical intuition, that Equation 5.26 completely neglects the through-soil coupling between the foundations and that the same expression is obtained for the case of a single foundation. Moreover, by inspection of the transformation (rectangular) matrix $\boldsymbol{\mathcal{S}}_r(\mathbf{x}_r)$, it is clear that the solution of Equation 5.26, in terms of the rigid response, can only be found in approximate terms, for example, by means of the least square method [98]. The latter is adopted by Iguchi [98, 99] who obtains the approximate rigid-body displacement of a foundation as a weighted average of the incident displacement field across its footprint:

$$\begin{aligned} &\hat{\boldsymbol{u}}_{\boldsymbol{fr}}(\omega) = \mathbf{P}_r^{-1} \int_{\Omega_r} \boldsymbol{\mathcal{S}}_r^{\mathrm{T}}(\mathbf{x}_r)\, \hat{\mathbf{u}}_{\mathbf{0}}(\mathbf{x}_r, \omega)\, d\Omega_r \\ &\text{with} \quad \mathbf{P}_r = \int_{\Omega_r} \boldsymbol{\mathcal{S}}_r^{\mathrm{T}}(\mathbf{x}_r)\, \boldsymbol{\mathcal{S}}_r(\mathbf{x}_r)\, d\Omega_r \end{aligned} \tag{5.27}$$

It can be shown that, with reference to the centroid O_r of the foundation, the matrix $\mathbf{P} = \mathrm{diag}[A_f, A_f, A_f, I_{fx}, I_{fy}, I_{fz}]$ is diagonal, with the components being the area A_f, the second moments of area I_{fx} and I_{fy}, and the polar moment of area I_{fz} of the rigid foundation. In principle, Equation 5.27 may be evaluated analytically for given incident wave-fields and shapes of the rigid foundation. Indeed, this is done in Section 5.3 for a rectangular foundation subjected to incident plane waves.

Alternatively, Equation 5.27 can be put in algebraic form and solved numerically according to the BEM framework presented in the previous section:

$$\hat{\boldsymbol{u}}_{\boldsymbol{f}r}(\omega) = [\mathbf{S}_r^{\mathrm{T}}\, \mathbf{T}_{\mathbf{Q}r}\, \mathbf{S}_r]^{-1}\, \mathbf{S}_r^{\mathrm{T}}\, \mathbf{T}_{\mathbf{Q}r}\, \mathbf{U}_{\mathbf{0}r}(\omega)\, \tilde{\mathbf{u}}_{\mathbf{0}}(k', \omega) = \mathbf{A}_r^{(\mathrm{app.})}(\omega)\, \tilde{\mathbf{u}}_{\mathbf{0}}(k', \omega) \tag{5.28}$$

with reference to collocation points $\mathbf{x_{cr}}$ on the domain Ω_r of the r^{th} foundation. It should be noted that Iguchi's method, as will be discussed in Section 5.3, provides closed-form expressions for the response of the r^{th} foundation that depends only on the geometry and on the incident wave-field. It is worth noticing that the comparison of the closed-form expressions in Equations 5.44 and the response obtained by Equation 5.28, with the matrix $\mathbf{T_Q}$ referring to the BEM, may provide a means to validate the adopted numerical integration scheme (see Equation 5.17).

The following sections present the validation of the matrix $\mathbf{A}$, as obtained in this dissertation, and a general discussion on the transfer functions $\hat{u}_{fi}/\tilde{u}_{0i}$ for the lateral, vertical and rocking response of a single [96] and two adjacent [97] square, surface, rigid foundations subjected to an incident, plane wave-field. Moreover, a comprehensive comparison of the rigorous and the approximate transfer functions $\hat{u}_{fi}/\tilde{u}_{0i}$, for different incident wave-fields, is also presented for validating Iguchi's method as a simplified method to approach the kinematic interaction. A validation of the method for the torsional response of a single hemispherical and/or a cylindrical foundation, and for two adjecent semi-cylindrical foundations is presented in the original papers of Iguchi [98, 99]. This refers to the application of Iguchi's method to seismic wave-fields. Additional validation is required for its application to ground-borne vibration, which involve higher frequencies and shorter wavelengths. This is done in this section with reference to a single and/or multiple rigid foundations (i.e. benchmark #1), and in Section 5.2 for the case of a single and/or multiple rigid footings (i.e. benchmark #2).

5.1.2 The case of a square, surface, rigid foundation

In the case of a surface rigid foundation, the matrix $\mathbf{A}$ in Equation 5.19 for an incident plane wave at a vertical angle θ_V and a horizontal angle $\theta_H = 0$ can be expressed as follows:

$$\mathbf{A} = \begin{bmatrix} A_{xx} & 0 & A_{zx} & 0 & A_{\varphi_y x} & 0 \\ 0 & A_{yy} & 0 & A_{\varphi_x y} & 0 & A_{\varphi_z y} \\ A_{xz} & 0 & A_{zz} & 0 & A_{\varphi_y z} & 0 \end{bmatrix}^T \tag{5.29}$$

The terms of the matrix $\mathbf{A}$ for the case of a surface and square foundation are reproduced and reported in Figure 5.2 for the cases obtained by Wong [96] (Poisson's ratio $\nu_s = 1/3$). Considering the case of incident SV-waves, one can notice that the horizontal-vertical contributions A_{xz} and A_{zx} are small compared to the direct terms A_{xx} and A_{zz} respectively. It follows that the latter terms will dominate the

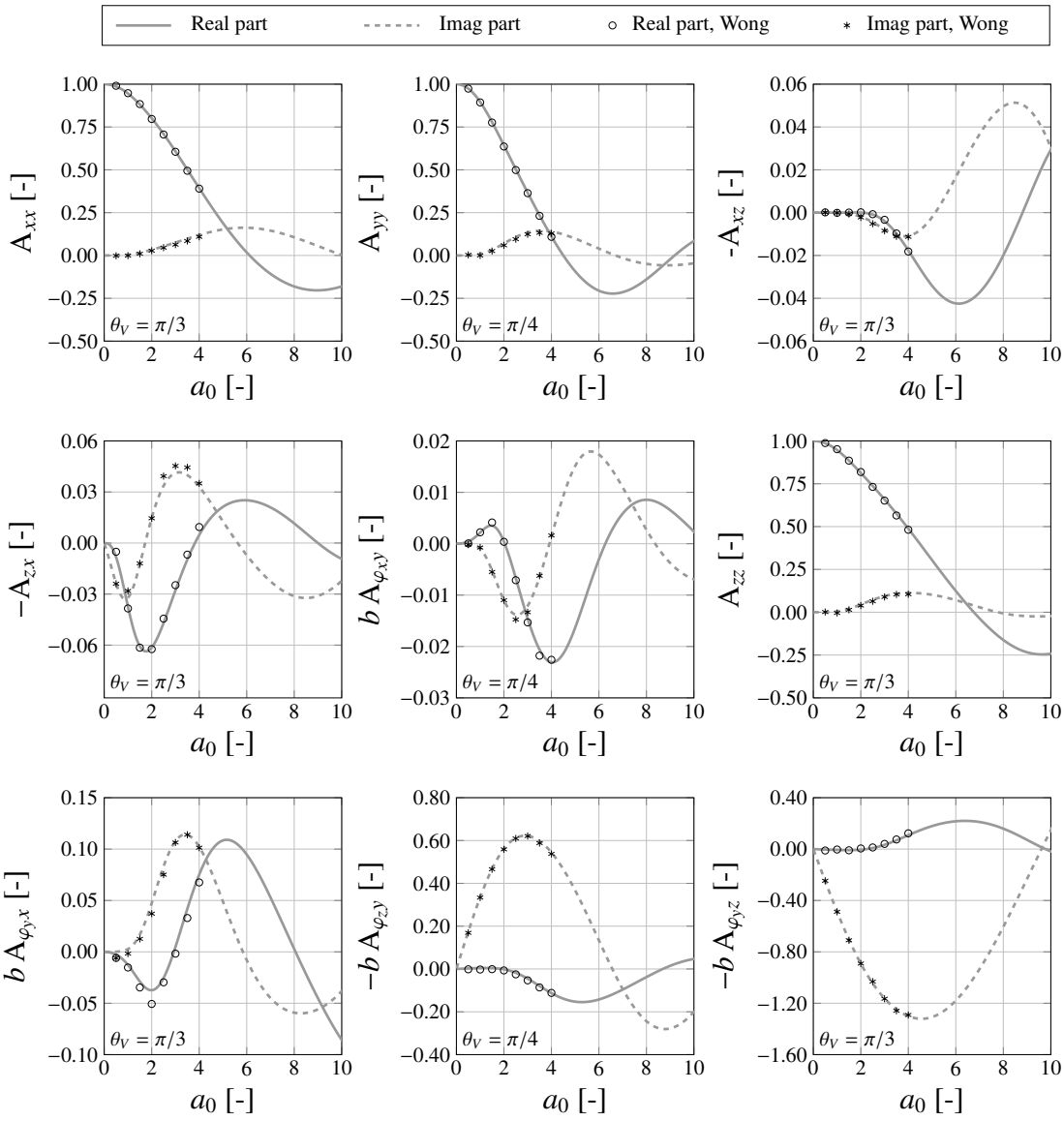

Fig. 5.2 Terms of the matrix **A** for incident SV-waves at a vertical incidence angles $\theta_V = \pi/4$ and $\pi/3$, and horizontal incidence angle $\theta_H = 0$ for a homogeneous and elastic half-space with Poisson's ratio $\nu_s = 1/3$. Comparison is made with the result of Wong [96] by using 8×8 constant elements for the rigid foundation. The plots refer to the dimensionless frequency $a_0 = \omega b/V_s$.

translational response $\hat{u}_f$ and $\hat{w}_f$ of the rigid foundation. Similarly, the rocking response $\hat{\varphi}_{fy}$ depends mostly on the component $A_{\varphi_y z}$ associated with the vertical amplitude $\tilde{w}_0$. The **A** matrix components reported in Figure 5.2 are obtained by means of Equation 5.20 by using a BEM formulation with 8×8 constant element for the rigid foundation. The results are in perfect agreement with those obtained by Wong [96], which serves as a validating check of the adopted BEM approach.

Figure 5.3 shows the application of Iguchi's method for a square, surface, rigid foundation subjected to an incident P- or SV-wave at $\theta_V = \pi/4$ and $\theta_H = 0$. The comparison is shown in terms of the transfer functions relating the lateral $\hat{u}_f$, vertical $\hat{w}_f$ and rocking $\hat{\varphi}_{fy}$ response of the foundation to the vertical amplitude $\tilde{w}_0$ in the frequency-wavenumber domain. The comparison between the approximate response by Iguchi's method and the rigorous solution, along the dimensionless frequency $a_0 = \omega b/V_s$, is favourable with the approximate magnitude that oscillates about the rigorous solution [209]. It is clear that, for an incident plane wave at $\theta_H = 0$, the single rigid foundation tends to restrain the motion at frequencies for which a multiple of the horizontal wavelength $n\lambda_x$ and a multiple of the horizontal half-wavelength $(n+1/2)\lambda_x$ match the dimension $2b$ for the translational and the rocking response respectively. The two conditions correspond to the dimensionless frequencies $a_0 = \gamma n\pi/\cos\theta_V$ and $a_0 = \gamma(n+1/2)\pi/\cos\theta_V$, with $\gamma = V/V_s$ and V corresponding to V_P, V_S or V_R for P-, SV- or Rayleigh waves respectively. This is schematically illustrated in Figure 5.4 with a physical representation of the weighted-average effect of Iguchi's method. From the results of Figure 5.3, it is clear that the restraining effect is pronounced for the results of Iguchi's method and less so for those referring to the rigorous solution. The overall effect of the rigid foundation is an increasing reduction of the amplitudes, along the frequency-spectrum, for the translational motion.

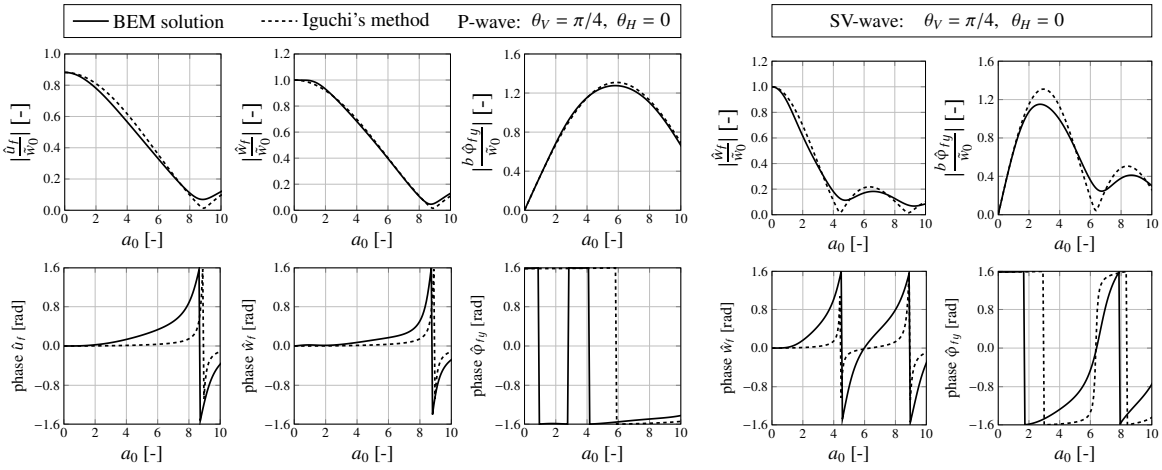

Fig. 5.3 Results for the horizontal $\hat{u}_f$, vertical $\hat{w}_f$ and rocking $\hat{\varphi}_{fy}$ response of a square, surface rigid foundation on a homogeneous and elastic half-space (Poisson's ratio $\nu_s = 1/3$) subjected to incident plane P- (left) and SV-waves (right) at an incidence angle $\theta_V = \pi/4$. Comparison is made for the magnitude (top) and phase (bottom) of the rigid-body displacement between the rigorous solution obtained with BEM (8×8 quadratic elements) and the solution obtained with Iguchi's method. The plots refer to the dimensionless frequency $a_0 = \omega b/V_s$.

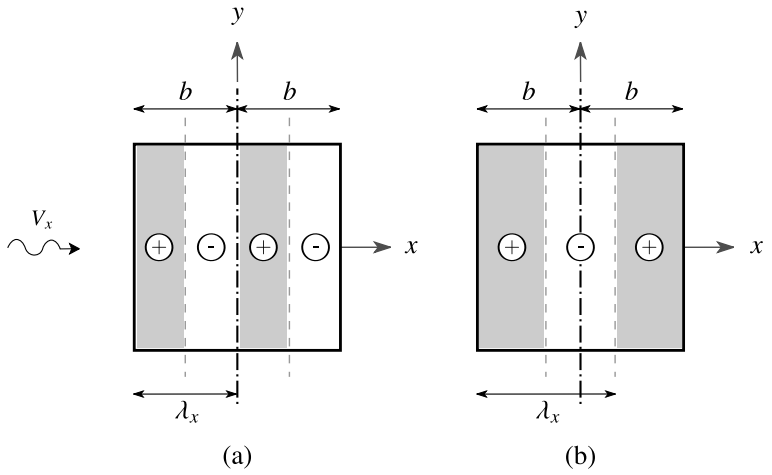

Fig. 5.4 Schematic representation of the geometric restraining effect for (a) the translational response u_f and w_f, and for (b) the rocking response φ_{fy} for an incident wave-field at $\theta_H = 0$. The restraining effect occurs at dimensionless frequencies a_0 for which (a) a multiple of the horizontal wavelength $n\lambda_x$ and (b) a multiple of the horizontal half-wavelength $(n + 1/2)\,\lambda_x$ match the dimension $2b$ of the foundation.

An additional rocking motion, considerable in magnitude, is associated with the overall response. It is convenient to introduce the dimensionless width $b_0 = 2\pi b/\lambda_x$ that appears to be driving the restraining effect of the foundation. By dimensional analysis [210], the general response of the foundation $\hat{u}_f$ can be expressed as:

$$\frac{\hat{u}_f}{\tilde{u}_0} = \Psi_{R0}\left(b_0, \gamma, \theta_V, \nu_s, \eta_s\right) \tag{5.30}$$

The dimensionless frequency a_0, which is a useful parameter in practice and commonly adopted in foundation vibration analysis [84], can be obtained from the dimensionless width as $a_0 = b_0\gamma/\cos\theta_V$.

Figure 5.5 shows a comparison between the approximate and the rigorous response of the foundation, similar to that in Figure 5.3, but this time in terms of b_0 and for different incident wave-fields: sub-horizontal ($\theta_V = \pi/8$) and sub-vertical ($\theta_V = 3\pi/8$) P- and SV-waves, and a Rayleigh wave. A good agreement, in all cases, is obtained for $b_0 \leq 2$. After this value, the approximate response shows restraining effects that may be present in the rigorous solution to a different extent depending on the type and directionality of the wave-field. The range of dimensionless width b_0 reported in Figure 5.5 is consistent with the possible range of a_0, as defined in Section 3.1.2, for the different incident waves. It follows that Iguchi's method works better for sub-vertical body waves than for surface waves. The range of b_0 for which good agreement is obtained can be re-formulated in

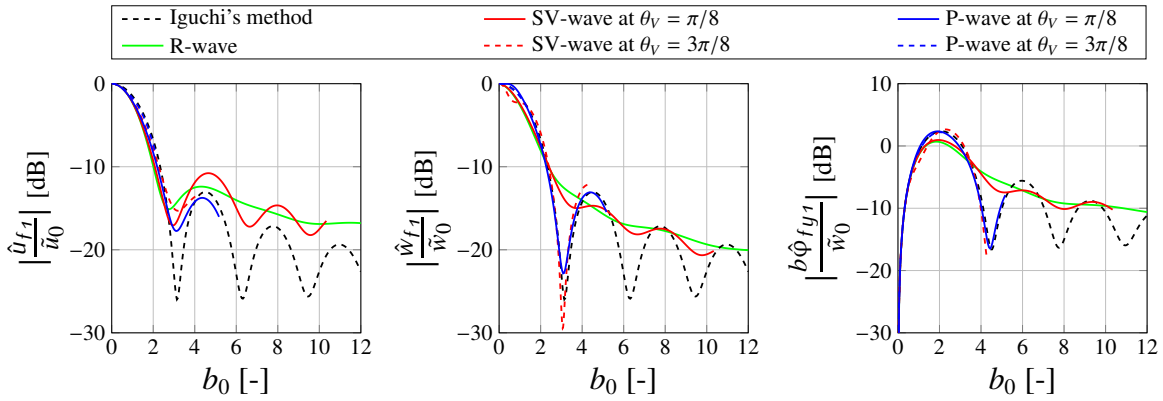

Fig. 5.5 Results for the horizontal $\hat{u}_f$, vertical $\hat{w}_f$ and rocking $\hat{\varphi}_{fy}$ response of a square, surface rigid foundation on a homogeneous and elastic half-space (Poisson's ratio $\nu_s = 1/3$) subject to a Rayleigh wave, and to incident sub-horizontal ($\theta_V = \pi/8$) and sub-vertical ($\theta_V = 3\pi/8$) P- and SV-waves at $\theta_H = 0$. Comparison is made for the magnitude of the rigid-body displacement between the rigorous solution obtained with BEM and the solution obtained with Iguchi's method. The plots refer to the dimensionless width $b_0 = 2\pi b/\lambda_x$ and to the amplitude $\tilde{\mathbf{u}}_\mathbf{0}$ at the free-field.

terms of the half-width b of the foundation as:

$$\pi b \leq \lambda_x \tag{5.31}$$

which can provide a general rule-of-thumb for the validity of the Iguchi's method in the case of a surface, square, rigid foundation on a homogeneous and elastic half-space with $\nu_s = 1/3$. For typical shear wave speeds, as discussed in Section 3.1.2, and a maximum frequency of 250 Hz, the shortest horizontal wavelength involved in the ground-borne vibration problem is in the order of $\lambda_x = 0.5 - 1.2$ m and refers to a Rayleigh wave. According to the condition in Equation 5.31, the related range of acceptable columns' dimensions for the application of Iguchi's method may be smaller than those commonly encountered in practice, as defined in Section 3.1.2. It is clear that there are limitations to the use of Iguchi's method for cases involving relatively short wavelengths (e.g. Rayleigh waves). Nonetheless, for a general problem that satisfies the condition in Equation 5.31, Iguchi's method can be deemed valid.

With the adoption of Iguchi's method for different incident wave-fields, the foundation response in Equation 5.30 effectively relates to the dimensionless width b_0, whose influence is shown in Figure 5.5 for the Poisson's ratio $\nu_s = 1/3$. There is enough evidence in literature to suggest that higher values of the Poisson's ratio are actually found in practice [191, 193, 53]. A typical value of $\nu_s = 0.49$, as

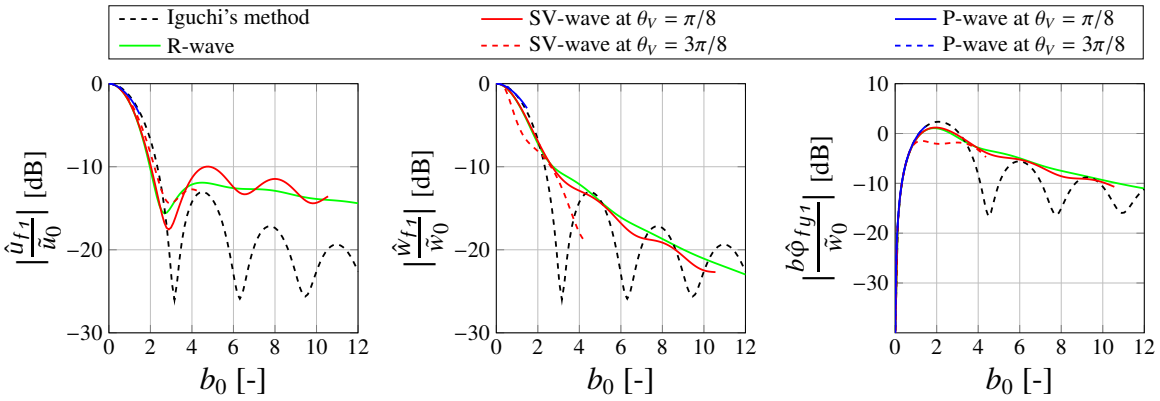

Fig. 5.6 Results for the horizontal $\hat{u}_f$, vertical $\hat{w}_f$ and rocking $\hat{\varphi}_{fy}$ response of a square, surface rigid foundation on a homogeneous and elastic half-space (Poisson's ratio $\nu_s = 0.49$) subjected to a Rayleigh wave, and to incident sub-horizontal ($\theta_V = \pi/8$) and sub-vertical ($\theta_V = 3\pi/8$) P- and SV-waves at $\theta_H = 0$. Comparison is made for the magnitude of the rigid-body displacement between the rigorous solution obtained with BEM and the approximate solution obtained with Iguchi's method. The plots refer to the dimensionless width $b_0 = 2\pi b/\lambda_x$ and to the amplitude $\tilde{\mathbf{u}}_\mathbf{0}$ at the free-field.

registered at the test site Regent's Park London [211] for London Clay [212, 213], is then considered to re-examine the validity of Iguchi's method. The comparison for such a case is reported in Figure 5.6, where good agreement is obtained for $b_0 \leq 2$ (i.e. the condition in Equation 5.31).

It is worth noticing that, since dilatational waves are associated with larger wavelengths, Figure 5.5 and 5.6 refer to relatively low values of b_0 for incident P-waves, while a larger range of b_0 is associated with incident SV-waves and Rayleigh waves. Having explored the validity of Iguchi's method for a surface, square, rigid foundation, the case of two adjacent rigid foundations is examined in the next section.

5.1.3 Two adjacent rigid foundations

The discussion in Section 5.1 illustrates the validity of Iguchi's method for the case of multiple rigid foundations on the free-surface of an elastic half-space. This can be explored with reference to two square, surface rigid foundations of width $2b$ at a centre-to-centre distance d (along x axis) and subjected to incident plane P-, SV- or Rayleigh waves at $\theta_H = 0$. An extensive study on the rigid-body response of such a foundation system has been undertaken by Qian [97] via application of the BEM. The purpose of this section is not to extend such an investigation, but rather to validate Iguchi's method for the case of multiple rigid foundations.

Figure 5.7 shows a comparison of the magnitude of the response for the upstream and downstream rigid foundations between the rigorous BEM solution and the one obtained by means of Iguchi's method for incident P- and SV-waves at $\theta_V = \pi/4$ for a centre-to-centre distance $d = 2.5b$. The restraining effect of the foundation at values of λ_x that match n and $(n+1/2)$ times the foundation dimension $2b$, for the translational and rocking motion respectively, is reduced for the rigorous solution shown in Figure 5.7. With reference to the latter, the fluctuations of the magnitude can be noted for both the translational and rotational response, with the latter being generally more accentuated, as anticipated by Qian [97]. A qualitative result from the study of Qian states that the intensity and the "period" of such fluctuations along the frequency-spectrum decrease with increasing foundation separation d. For typical building typologies (e.g. reinforced concrete and/or steel buildings), the centre-to-centre distance $d \approx 5$ m so that, in practice, the ratio d/b is most likely greater than 2.5; the case in Figure 5.7 represents then the results for two closely spaced coupling points (i.e. closely spaced columns in the building). Alternatively, a more realistic value of $d = 20\,b$ (i.e. the reference problem in Section 3.1.2) can be assumed for the columns spacing. With reference to these limits, Figure 5.8 shows the resulting wave-field $\hat{\mathbf{u}}_\mathbf{f}$ and the scattered wave-field $\hat{\mathbf{u}}_\mathbf{s}$ for the closely spaced and remote

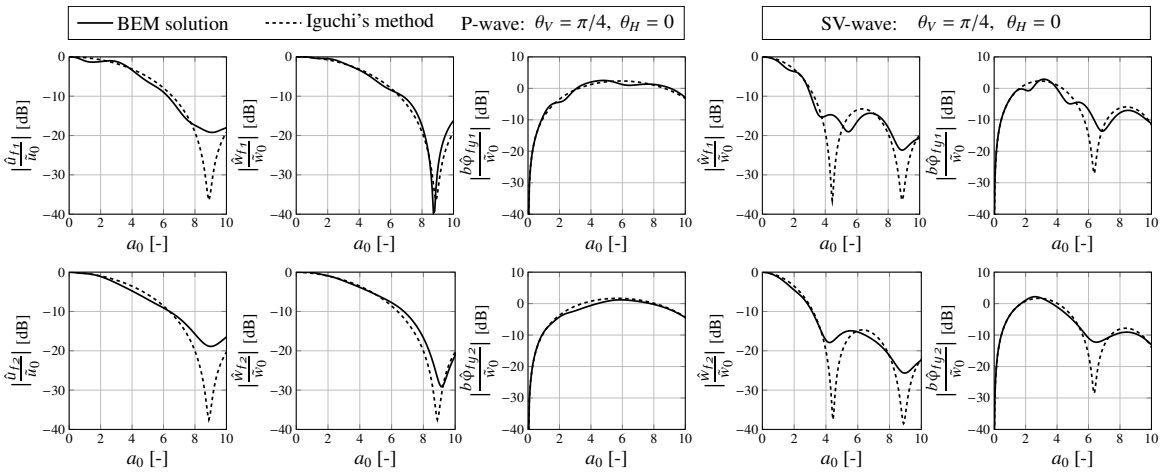

Fig. 5.7 Results for the horizontal $\hat{u}_f$, vertical $\hat{w}_f$ and rocking $\hat{\varphi}_{fy}$ response of two square, surface rigid foundations of width b on a homogeneous and elastic half-space (Poisson's ratio $\nu_s = 1/3$) at a centre-to-centre distance $d = 2.5\,b$ subjected to incident plane P- (left) and SV-waves (right) at $\theta_V = \pi/4$ and $\theta_H = 0$. Comparison is made for the magnitude of the response for the upstream (top) and downstream (bottom) foundations between the results obtained with the rigorous solution (BEM - 8×8 quadratic elements for each foundation) and that with Iguchi's method. The plots refer to the dimensionless frequency $a_0 = \omega b/V_s$.

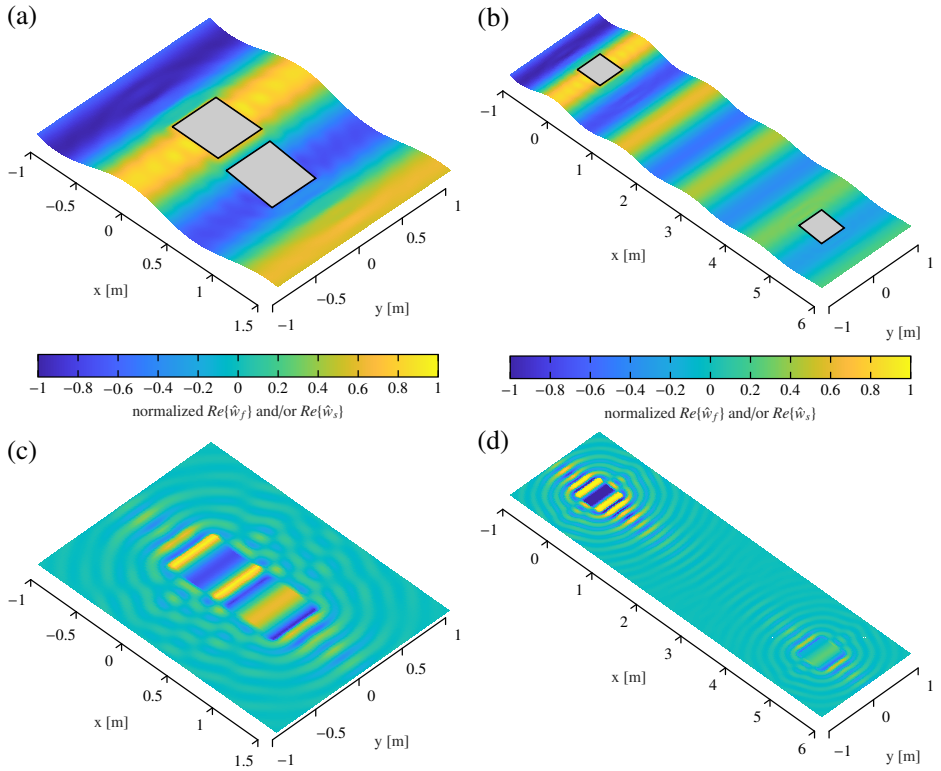

Fig. 5.8 Resulting wave-field $\hat{\mathbf{u}}_\mathbf{f}$ (a) and (b), and scattered wave-field $\hat{\mathbf{u}}_\mathbf{s}$ (c) and (d), of two, square, rigid foundations of side $2b = 0.5$ m at a centre-to-centre distance $d = 2.5b$ (a) and (c), and $d = 20b$ (b) and (d) subjected to an incident P-wave at $\theta_V = 5\pi/12$ and $\theta_H = 0$. Results are obtained with the rigorous solution (BEM - 8×8 quadratic elements for each foundation) and with reference to a dimensionless frequency $a_0 = 8$ for a Poisson's ratio $\nu_s = 1/3$.

rigid foundations subjected to an incident P-wave at $\theta_V = 5\pi/12$ and $\theta_H = 0$ for a dimensionless frequency $a_0 = 8$.

It is evident in Figure 5.8c that the scattered wave-field is significantly influenced by the through-soil coupling of the closely spaced foundations, whereas the latter has a reduced effect in the case of remote foundations as qualitatively shown in Figure 5.8d. Considering this incident wave-field, the comparison between the rigorous solution and that from Iguchi's method for the rigid-body response of the foundations, as shown in Figure 5.9, provides a similar understanding. The effect of the through-soil coupling of the foundations is confined at relatively low frequencies (long wavelengths) and it is only relevant for sufficiently close foundations, for which we have larger fluctuations about the approximate solution (see Figure 5.9a). In general, the through-soil coupling of the two, adjacent rigid foundations can be represented by an additional dimensionless group d/b and the dependency of

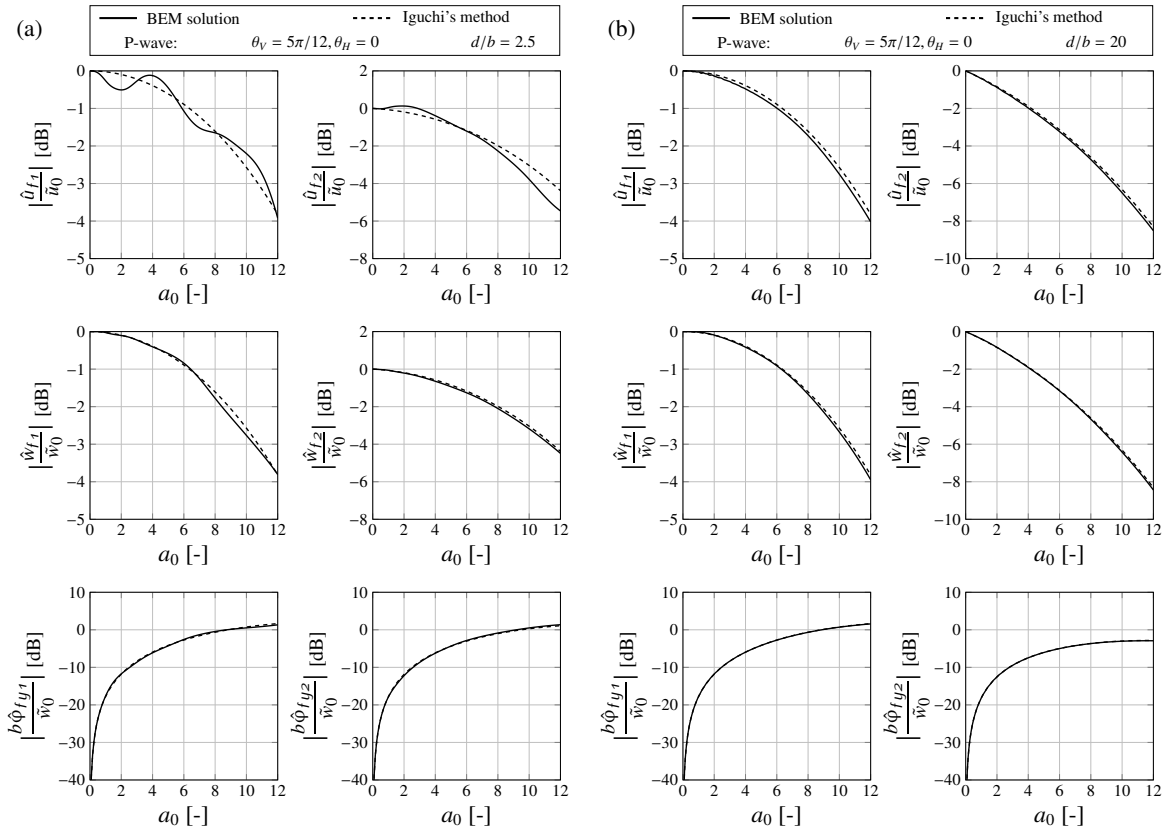

Fig. 5.9 Results for the horizontal $\hat{u}_f$, vertical $\hat{w}_f$ and rocking $\hat{\varphi}_{fy}$ response of two square, surface rigid foundations of width b on a homogeneous and elastic half-space (Poisson's ratio $\nu_s = 1/3$) at a centre-to-centre distance (a) $d = 2.5b$ and (b) $d = 20b$ subjected to an incident plane P-wave at $\theta_V = 5\pi/12$ and $\theta_H = 0$. Comparison is made for the magnitude of the response for the upstream $(i = 1)$ and downstream $(i = 2)$ foundations between the results obtained with the rigorous solution (BEM - 8×8 quadratic elements for each foundation) and that with Iguchi's method. The plots refer to the dimensionless frequency $a_0 = \omega b/V_s$.

the general foundation response can be written as:

$$\frac{\hat{u}_{fi}}{\tilde{u}_0} = \Psi^{(i)}_{R0}\left(b_0, \frac{d}{b}, \gamma, \theta_V, \nu_s, \eta_s\right) \tag{5.32}$$

Having examined the case of a quasi-normally incident P-wave, involving relatively long wavelengths, the other extreme is represented by a Rayleigh wave for which we obtain relatively short values of λ_x. This is considered in Figure 5.10 where the approximate solution is reported together with the rigorous one for two closely spaced and/or remote rigid foundations. The response of the upstream foundation $\hat{\boldsymbol{u}}_{\boldsymbol{f1}}$ is weakly affected by the presence of the downstream foundation and it follows the envelope of the approximate solution [1]. Conversely, the response of the downstream foundation

$\hat{\boldsymbol{u}}_{\boldsymbol{f2}}$ strongly depends on the dimensionless distance d/b. For closely spaced foundations, $d = 2.5b$, the agreement of the approximate and the rigorous solutions can be deemed satisfactory only up to limited values of dimensionless frequency a_0. For relatively high values of a_0, the response is greatly affected by the presence of the upstream foundation and an increased attenuation is obtained for the rigorous solution that diverges from the approximate response. For remote foundations, the increased attenuation is obtained only at relatively low values of a_0. It follows a good agreement up to $a_0 \approx 8$ and a reduced attenuation beyond this value with reference to the approximate solution. It is worth pointing out that the two extremes of quasi-normally propagating P-waves and Rayleigh waves cover the possible range of the horizontal wavelength λ_x related to an incident, plane wave-field.

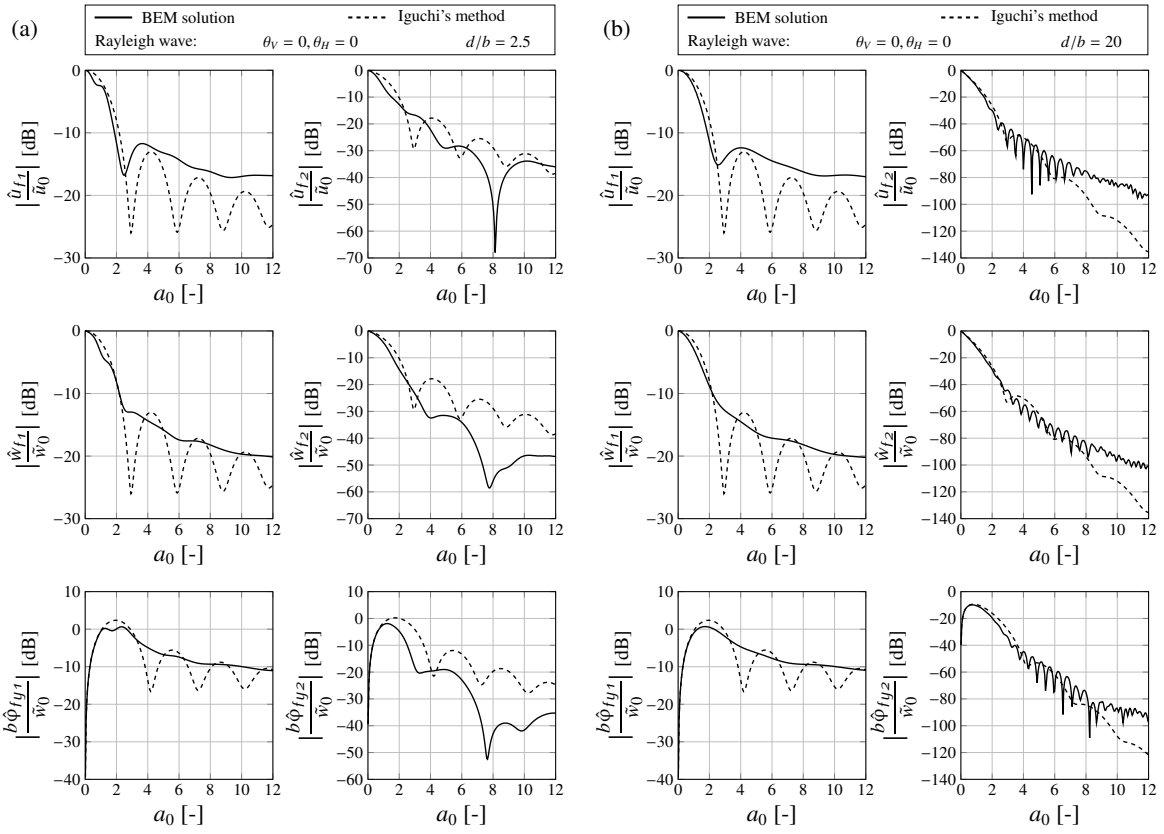

Fig. 5.10 Results for the horizontal $\hat{u}_f$, vertical $\hat{w}_f$ and rocking $\hat{\varphi}_{fy}$ response of two square, surface rigid foundations of width b on a homogeneous and elastic half-space (Poisson's ratio $\nu_s = 1/3$ at a centre-to-centre distance (a) $d = 2.5\,b$ and (b) $d = 20\,b$ subjected to a plane Rayleigh wave at $\theta_H = 0$. Comparison is made for the magnitude of the response for the upstream $(i = 1)$ and downstream $(i = 2)$ foundations between the results obtained with the rigorous solution (BEM - 8×8 quadratic elements for each foundation) and that with Iguchi's method. The plots refer to the dimensionless frequency $a_0 = \omega b/V_s$.

As for the single foundation, the physics of the problem may be better presented in terms of the dimensionless width b_0. This allows to condense the results for different wave-fields in a unified plot for each value of d/b and ν_s. This is shown in Figure 5.11 for the two values $d/b = 2.5$ and 20, and for $\nu_s = 0.49$. The condition in Equation 5.31 can still be considered valid for the range of b_0 for which good agreement of Iguchi's method with the rigorous solution is obtained. It is worth noticing that for a nearly incompressible soil (i.e. high value of Poisson's ratio), long wavelengths and low values of b_0 are associated with incident P-waves, for which a better use of Iguchi's method follows. Moreover, incident P-waves are associated with low damping because of the assumed damping model discussed in Section 3.2.3. It follows that the attenuation shown for P-waves in Figure 5.11(b)

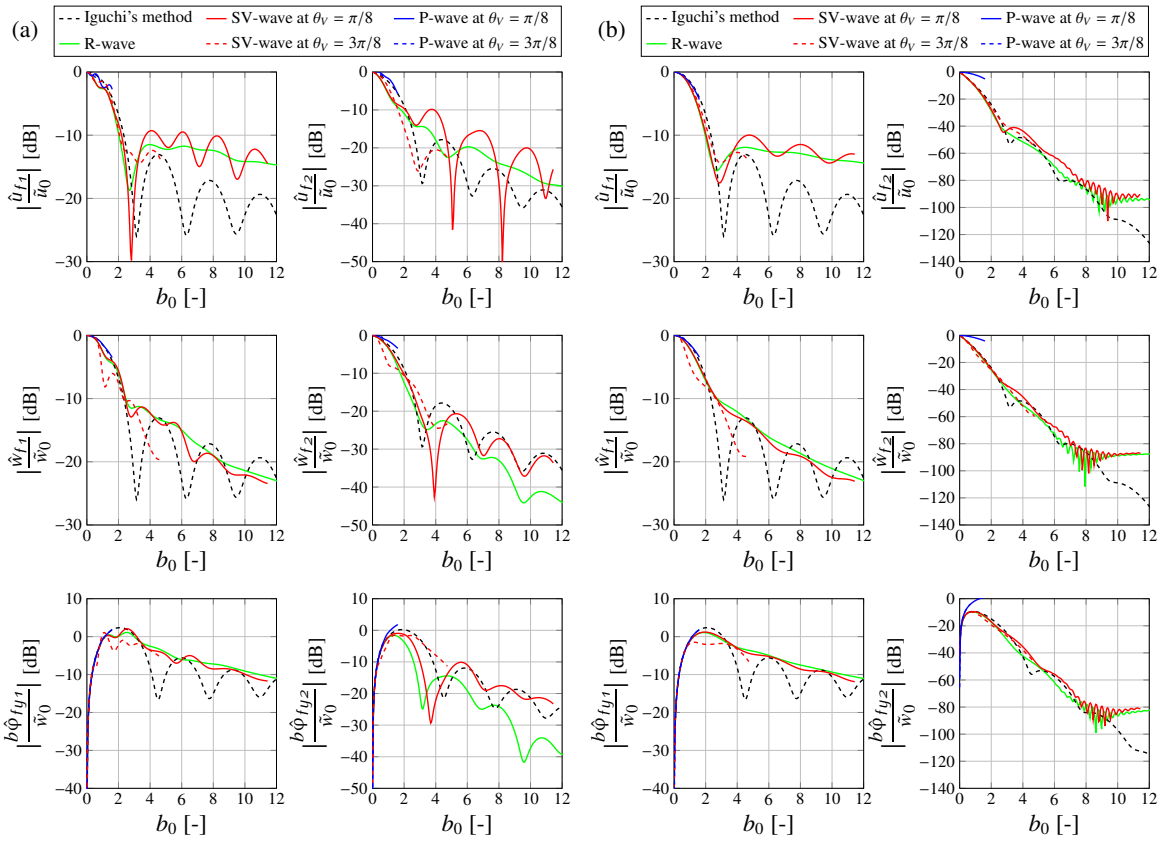

Fig. 5.11 Results for the horizontal $\hat{u}_f$, vertical $\hat{w}_f$ and rocking $\hat{\varphi}_{fy}$ response of two square, surface rigid foundations of width b on a homogeneous and elastic half-space at a centre-to-centre distance (a) $d = 2.5b$ and (b) $d = 20b$. Sub-horizontal and sub-vertical incident P- and SV-waves and Rayleigh waves are considered at $\theta_H = 0$. Comparison is made for the magnitude of the response for the upstream $(i = 1)$ and downstream $(i = 2)$ foundations between the results obtained with the rigorous solution (BEM - 8×8 quadratic elements for each foundation) and that with Iguchi's method. The plots refer to the dimensionless width $b_0 = 2\pi b/\lambda_x$ and to the Poisson's ratio $\nu_s = 0.49$.

for the downstream foundation is less accentuated when compared with the one obtained for SV- and Rayleigh waves. The results of Iguchi's method are obtained by means of Equation 5.28 with $\mathbf{U_{02}}$ calculated at the collocation points from Equation 5.1 for a Rayleigh wave. Because of the damping model adopted for the soil (see Section 3.2.3), incident P-waves are less damped than Rayleigh waves so that a different approximate response is expected. This is indeed the case and, although the results of Iguchi's method obtained by considering $\mathbf{U_{02}}$ for the incident P-wave are not shown in Figure 5.11(b), it agrees well with the respective rigorous solution.

In general, based on the previous discussion and on the results in Figure 5.11, Iguchi's method can be applied to the case of multiple, adjacent rigid foundations, with the due limitations expressed by the condition in Equation 5.31. The next section examines the more realistic case of rigid footings resting on a slab foundation (e.g. concrete slab) overlying the half-space representing the ground.

5.2 Iguchi's method for the response of rigid footings

As seen in Chapter 4, the presence of a concrete slab foundation resting on the ground can be modelled as an infinitely large elastic layer with density ρ_c, shear wave speed V_c, Poisson's ratio ν_c and damping loss factor η_c. As previously discussed, incident plane waves are considered with a resulting free-field frequency-wavenumber amplitude $\tilde{\mathbf{u}}_\mathbf{0}(k', \omega)$ at the free-surface of the half-space (see Figure 5.12(a)).

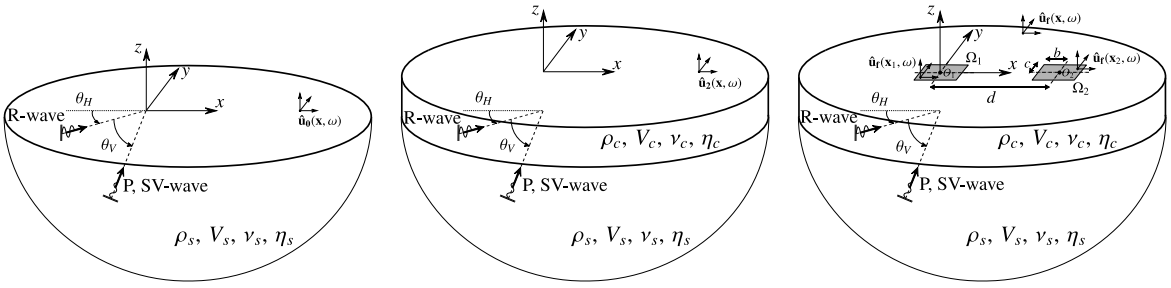

Fig. 5.12 Schematic illustration of the added-foundation effect with reference to rigid footings on a concrete slab foundation. (a) A homogeneous and elastic half-space representing the soil is subjected to an incident wave-field due to P-, SV- or Rayleigh waves with the resulting free-field displacement $\hat{\mathbf{u}}_\mathbf{0}(\mathbf{x}, \omega)$; (b) the addition of a flexible foundation as an elastic layer leads to the displacement $\hat{\mathbf{u}}_\mathbf{2}(\mathbf{x}, \omega)$ at the free-surface of the layer; (c) consideration of rigid footings at the free-surface of the layer leads to the displacement field $\hat{\mathbf{u}}_\mathbf{f}(\mathbf{x}, \omega)$ and to the related rigid-body response $\hat{u}_{f1}(\omega)$ and $\hat{u}_{f2}(\omega)$ of the upstream and downstream footing respectively.

Prior to the coupling of the elastic layer, the displacement field $\hat{\mathbf{u}}_\mathbf{0}(\mathbf{x},\omega)$ is related to the displacement amplitude $\tilde{\mathbf{u}}_\mathbf{0}$ by means of Equation 5.1. The influence of the slab foundation on the free-field displacement amplitude $\tilde{\mathbf{u}}_\mathbf{0}$ relates to a general result in the SSI literature [1, 88, 157] and can be approached as seen in Chapter 4. The dynamic stiffness matrices $\tilde{\mathbf{K}}_\mathbf{s}$ and $\tilde{\mathbf{K}}_\mathbf{f}$ of the half-space (i.e. ground) and the layer (i.e. foundation) may be obtained by the Stiffness Matrix Method [189, 36], reviewed in Appendix C, with reference to reduced displacements $\tilde{\mathbf{u}}$ and tractions $\tilde{\mathbf{t}}$. The reduced displacement amplitude $\tilde{\mathbf{u}}$ has the same magnitude of the displacement amplitude $\tilde{\mathbf{u}}$ and it is related to the latter by Equation C.28. The displacement amplitude can be then obtained by the inverse transformation $\tilde{\mathbf{u}} = \mathbf{T}_\mathbf{u}^T \tilde{\mathbf{u}}$. By ensuring equilibrium and compatibility at the soil-foundation interface, the displacement amplitude $\tilde{\mathbf{u}}_\mathbf{1}$ at the interface can be expressed as:

$$\tilde{\mathbf{u}}_\mathbf{1}(k',\omega) = \left[\mathbf{I} + \tilde{\mathbf{H}}_\mathbf{s}\tilde{\mathbf{H}}_\mathbf{f}^{-1}\right]^{-1} \tilde{\mathbf{u}}_\mathbf{0}(k',\omega) \tag{5.33}$$

where $\tilde{\mathbf{H}}_\mathbf{f}$ and $\tilde{\mathbf{H}}_\mathbf{s}$ are the frequency-response function (FRF) matrices of the elastic layer (i.e. foundation) and the half-space (i.e. ground) respectively, which can be found by inverting the respective dynamic stiffness matrices. The displacement amplitude $\tilde{\mathbf{u}}_\mathbf{2}$ at the free-surface of the slab can be obtained by considering the FRF matrix of the layer and imposing the free-stress condition and the displacement amplitude $\tilde{\mathbf{u}}_\mathbf{1}$ condition at the top and bottom of the layer respectively:

$$\tilde{\mathbf{u}}_\mathbf{2} = \tilde{\mathbf{H}}_\mathbf{f}^{21}\left[\tilde{\mathbf{H}}_\mathbf{f}^{11}\right]^{-1}\tilde{\mathbf{u}}_\mathbf{1} \tag{5.34}$$

The amplification-attenuation of the amplitude $\tilde{\mathbf{u}}_\mathbf{2}$, with respect to the amplitude $\tilde{\mathbf{u}}_\mathbf{0}$ prior to the coupling, is representative of the added-foundation effect as investigated in Chapter 4. Similarly to Equation 4.9 in Chapter 4, the general transfer function refers to the following dimensionless groups:

$$\frac{\tilde{u}_{2(i)}}{\tilde{u}_{0(i)}} = \Psi_f\left(\frac{V_s}{V_c}, \frac{\rho_s}{\rho_c}, \nu_s, \nu_c, \eta_s, \eta_c, \theta_V, \gamma, h_0\right) \tag{5.35}$$

where $h_0 = 2\pi h/\lambda_x$ is the dimensionless thickness as introduced in Section 4.4 and the subscript (i) refers to either the horizontal or vertical degree of freedom. Starting from the results of Chapter 4, the focus here is on the response of rigid footings on the free-surface of the slab foundation as illustrated in Figure 5.12.

Because of the plane-wave assumption, the displacement field at soil-foundation interface and at the free-surface can be written as:

$$\hat{\mathbf{u}}_\mathbf{1}(\mathbf{x},\omega) = \mathcal{U}_1(\mathbf{x},\omega)\,\tilde{\mathbf{u}}_\mathbf{1}(k',\omega) \tag{5.36a}$$

$$\hat{\mathbf{u}}_\mathbf{2}(\mathbf{x},\omega) = \mathcal{U}_2(\mathbf{x},\omega)\,\tilde{\mathbf{u}}_\mathbf{2}(k',\omega) \tag{5.36b}$$

where $\mathcal{U}_1$ and $\mathcal{U}_2$ are describing functions in the exponential form, as in Equation 5.1, referring to points $\mathbf{x}$ at the interface and at the free-surface respectively.

The discussion in Section 5.1 can be then reiterated with reference to Equations 5.2 – 5.19 and to the displacement field $\hat{\mathbf{u}}_\mathbf{2}$ at the free-surface of the slab. The foundation-building coupling regions on top of the flexible foundation can be then idealised as surface, rigid footings on the elastic layer as schematically illustrated in Figure 5.12c. The rigid response of such footings, similarly to the argument for rigid foundations, can be expressed as:

$$\hat{u}_f(\omega) = \mathbf{A}_\mathbf{2}(\omega)\,\tilde{\mathbf{u}}_\mathbf{2}(k',\omega) \tag{5.37}$$

The equivalence of Equation 5.25 to Equation 5.26 in Section 5.1 still holds so that Iguchi's method is applicable with the due limitations related to the conditions in Equations 5.23 and 5.24. The rigorous solution for the response of the rigid footings can be obtained, similarly to Equation 5.20, as:

$$\hat{u}_f(\omega) = \widehat{H}_f(\omega)\,\mathbf{S}^\mathrm{T}\,\mathbf{T}_\mathbf{Q}\,[\widehat{\mathbf{G}}_\mathbf{u}(\omega)]^{-1}\,\mathbf{U}_\mathbf{2}(\omega)\,\tilde{\mathbf{u}}_\mathbf{2}(k',\omega) = \mathbf{A}_\mathbf{2}{}^{(\mathrm{rig.})}(\omega)\,\tilde{\mathbf{u}}_\mathbf{2}(k',\omega) \tag{5.38}$$

with $\mathbf{U}_\mathbf{2} = \mathbf{U}_\mathbf{0}$, but this time the boundary element matrix $\widehat{\mathbf{G}}_\mathbf{u}$ refers to a layered half-space (i.e. slab foundation + soil). The approximate response of the r^{th} rigid footing may be obtained by application of Iguchi's method as:

$$\hat{u}_{fr}(\omega) = [\mathbf{S}_r^\mathrm{T}\,\mathbf{T}_{\mathbf{Q}r}\,\mathbf{S}_r]^{-1}\,\mathbf{S}_r^\mathrm{T}\,\mathbf{T}_{\mathbf{Q}r}\,\mathbf{U}_{\mathbf{2}r}(\omega)\,\tilde{\mathbf{u}}_\mathbf{2}(k',\omega) = \mathbf{A}_{\mathbf{2}r}^{(\mathrm{app.})}(\omega)\,\tilde{\mathbf{u}}_\mathbf{2}(k',\omega) \tag{5.39}$$

with $\mathbf{U}_{\mathbf{2}r} = \mathbf{U}_{\mathbf{0}r}$, from which follows that $\mathbf{A}_{\mathbf{2}r}^{(\mathrm{app.})} = \mathbf{A}_r^{(\mathrm{app.})}$.

It is clear that, according to Iguchi's method, the transfer function relating, for instance, the rigid footing horizontal motion $\hat{u}_{fr}^{(F)}$ to the free-surface horizontal amplitude $\tilde{u}_2$ is equal to the transfer function relating the rigid foundation horizontal motion $\hat{u}_{fr}^{(R)}$ to the free-surface horizontal

amplitude $\tilde{u}_0$ as found by Equation 5.28. Such transfer function $\Psi_{Ig\,(i)}$, referring to the i^{th} degree of freedom of the rigid response, is reported in Section 5.3 as a closed-form expression by solving Equation 5.27 for rectangular rigid regions and for incident plane wave-fields. In general, the same it is not true for the rigorous counterparts of the rigid foundation and the rigid footing transfer functions $\Psi_{R0\,(i)} = \hat{u}^{(R)}_{fr(i)}/\tilde{u}_{0(i)}$ and $\Psi_{F2\,(i)} = \hat{u}^{(F)}_{fr(i)}/\tilde{u}_{2(i)}$ respectively. In the following the cases of a single and two adjacent rigid footings are investigated with the focus on the comparison between the rigorous and the approximate solutions.

5.2.1 The case of a single rigid footing

Similarly to the argument used for the single rigid foundation, the validity of Iguchi's method for a rigid footing is investigated in terms of its rigid-body displacement $\hat{\boldsymbol{u}}_{\boldsymbol{f}}$ in relation to the involved dimensionless groups:

$$\frac{\hat{u}_f}{\tilde{u}_0} = \Psi_{F0}\left(\frac{V_s}{V_c}, \frac{\rho_s}{\rho_c}, \nu_s, \nu_c, \eta_s, \eta_c, \theta_V, \gamma, b_0, \frac{h}{b}\right) = \frac{\hat{u}_f}{\tilde{u}_2}\cdot\frac{\tilde{u}_2}{\tilde{u}_0} = \Psi_{F2}\cdot\Psi_f \tag{5.40}$$

which is valid, in general, for each of the 6 DoF of the response so that the subscript i for the i^{th} DoF is omitted in the following. It is worth noticing that the transfer function $\hat{u}_f/\tilde{u}_0$ may be expressed as the product of the transfer functions Ψ_{F2} and Ψ_f, with the latter referring to the amplitudes of the displacement in the frequency-wavenumber domain before ($\tilde{\mathbf{u}}_0$) and after ($\tilde{\mathbf{u}}_2$) the addition of the slab, as found in Chapter 4 and reported in Equation 5.35.

The transfer function Ψ_{F2} is reported for two different values of the Poisson's ratio and for a value of $h_0/b_0 = h/b = 2.8$ (i.e. $h = 0.7$ m for the benchmark #2) in Figure 5.13. It is possible to acknowledge a limited variation of the response, of the order of 0.5 dB at most, with reference to the two values of ν_s. Differences of about 4 dB are found for the response to different incident waves (i.e. influence of the parameters θ_V and γ). The latter are restricted around the frequencies where the restraining effect occurs, while no differences are registered in the rest of the frequency spectrum. A value of $h_0/b_0 = h/b = 6$ (i.e $h = 1.5$ m for benchmark #2) is assumed for the results shown in Figure 5.14 with the other parameters referring to Table 3.1 and $\nu_s = 0.49$. It is apparent that the dimensionless thickness h_0 has a limited effect on the transfer function $\hat{u}_f/\tilde{u}_2 = \Psi_{F2}$ and that differences of, at most, 2 dB are obtained for comparison with the case of $h/b = 2.8$ in Figure 5.13. The agreement is even more favourable for values of $b_0 \leq 2$ that satisfy the condition in Equation 5.31.

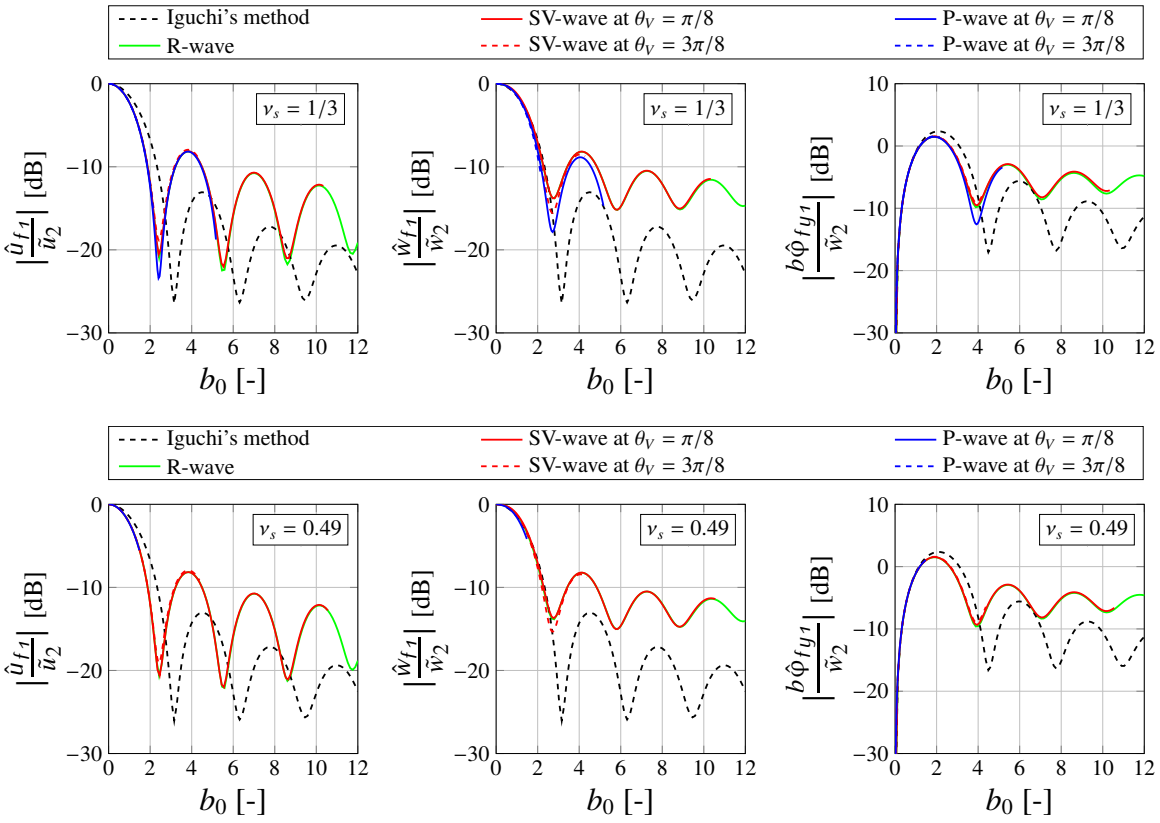

Fig. 5.13 Results for the horizontal $\hat{u}_f$, vertical $\hat{w}_f$ and rocking $\hat{\varphi}_{fy}$ response of a square, surface rigid footing on the free-surface of a slab foundation overlying the ground. Plane-wave excitation is considered in the form of a Rayleigh wave, and to incident sub-horizontal ($\theta_V = \pi/8$) and sub-vertical ($\theta_V = 3\pi/8$) P- and SV-waves at $\theta_H = 0$. Comparison is made for the magnitude of the rigid-body displacement between the rigorous solution obtained with BEM and the approximate solution obtained with Iguchi's method. The plots refer to the dimensionless width $b_0 = 2\pi b/\lambda_x$ and to two values of Poisson's ratio: $\nu_s = 1/3$ (top) and $\nu_s = 0.49$ (bottom).

Although, in general, the transfer function Ψ_{F2} depends on all the dimensionless groups reported in Equation 5.40, the argument here is that the kinematic interaction of the rigid footing is governed by the parameter b_0 and that Iguchi's method may be a suitable approximation regardless of the values assumed by the rest of the dimensionless groups in Equation 5.40, which are accounted for in the transfer function Ψ_f. In other words, it is envisaged to divide the transfer function Ψ_{F0} into two parts: one related to the addition of the slab as a layer (i.e. Ψ_f as found in Chapter 4) with a dependency shown in Equation 5.35, and one related (mostly) to the kinematic interaction of the rigid footing (i.e. Ψ_{F2}):

$$\frac{\hat{u}_f}{\tilde{u}_0} = \Psi_{F2}(b_0) \cdot \Psi_f \left(\frac{V_s}{V_c}, \frac{\rho_s}{\rho_c}, \nu_s, \nu_c, \eta_s, \eta_c, \theta_V, \gamma, h_0 \right) \tag{5.41}$$

Iguchi's method provides a transfer function Ψ_{Ig}, which is an approximation of Ψ_{F2}. This approximation may be deemed satisfactory in a limited range of $b_0 \leq 2$ (see Figures 5.13 and 5.14), as for the case of a rigid foundations. In this range of b_0, differences up to 5 dB, 2 dB and 1 dB are found for the horizontal, vertical and rocking response respectively. Hence, the general rule-of-thumb in Equation 5.31 for the validity of Iguchi's method for rigid foundations can be extended to the case of rigid footings on a slab foundation.

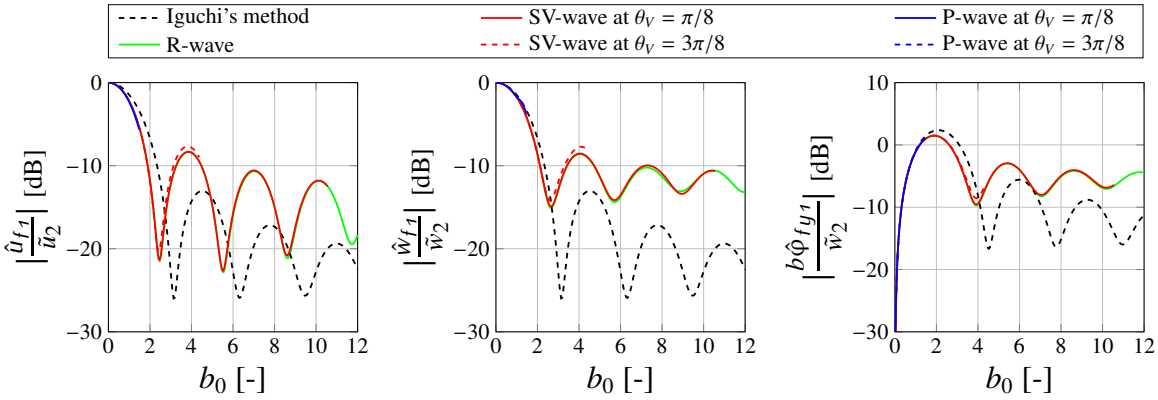

Fig. 5.14 Results for the horizontal $\hat{u}_f$, vertical $\hat{w}_f$ and rocking $\hat{\varphi}_{fy}$ response of a square, surface rigid footing as in Figure 5.13 for $\nu_s = 0.49$. Here a thicker slab foundation is considered with $h = 1.5$ m and an associated value of $h_0/b_0 = h/b = 6$.

5.2.2 Two adjacent rigid footings

It is desired to extend the validity of Iguchi's method to the case of multiple rigid footings by considering the slab foundation with two adjacent surface, square, rigid footings as represented in Figure 5.12c. The response of the footings depends on the dimensionless groups as in Equation 5.40 and, additionally, on the dimensionless distance d/b:

$$\frac{\hat{u}_{fr}}{\tilde{u}_0} = \Psi_{F0}^{(r)}\left(\frac{V_s}{V_c}, \frac{\rho_s}{\rho_c}, \nu_s, \nu_c, \eta_s, \eta_c, \theta_V, \gamma, b_0, \frac{h}{b}, \frac{d}{b}\right) \tag{5.42}$$

Figure 5.15 shows the results of the upstream ($r = 1$) and downstream ($r = 2$) rigid footings response for sub-horizontal ($\theta_V = \pi/8$) and sub-vertical ($\theta_V = 3\pi/8$) incident P- and SV-waves and Rayleigh waves for the values of the dimensionless distance $d/b = 2.5$ and 20. The comparison between the rigorous solution and Iguchi's method yields differences in the order of 0-20 dB, along the frequency spectrum, for the response of the upstream footing for both cases of closely-spaced (i.e. $d = 2.5b$) and remote (i.e. $d = 20b$) rigid footings. For the latter, results are a perfect match to those observed in

Figure 5.14; this suggests that, as far as the kinematic interaction of the upstream footing is concerned, the through-soil coupling may be neglected for remote footings with $d \geq 20b$. The same cannot be said with reference to the kinematic interaction of the downstream footing. For both closely-spaced and remote footings, the rigorous response of the downstream footing, at relatively high values of b_0, diverges from the approximate response obtained by Iguchi's method; this indicates that the through-soil coupling has an important role for the kinematic interaction of the downstream footing regardless of the dimensionless distance d/b. For instance, the response of the downstream footing for the case $d = 20b$ agrees well with Iguchi's approximation up to a dimensionless width $b_0 \approx \pi$, which corresponds approximately to a ratio $d/\lambda_x \approx 10$. For greater values of the latter, that is for higher frequencies, the rigorous solution diverges from that obtained by Iguchi's method. This may be

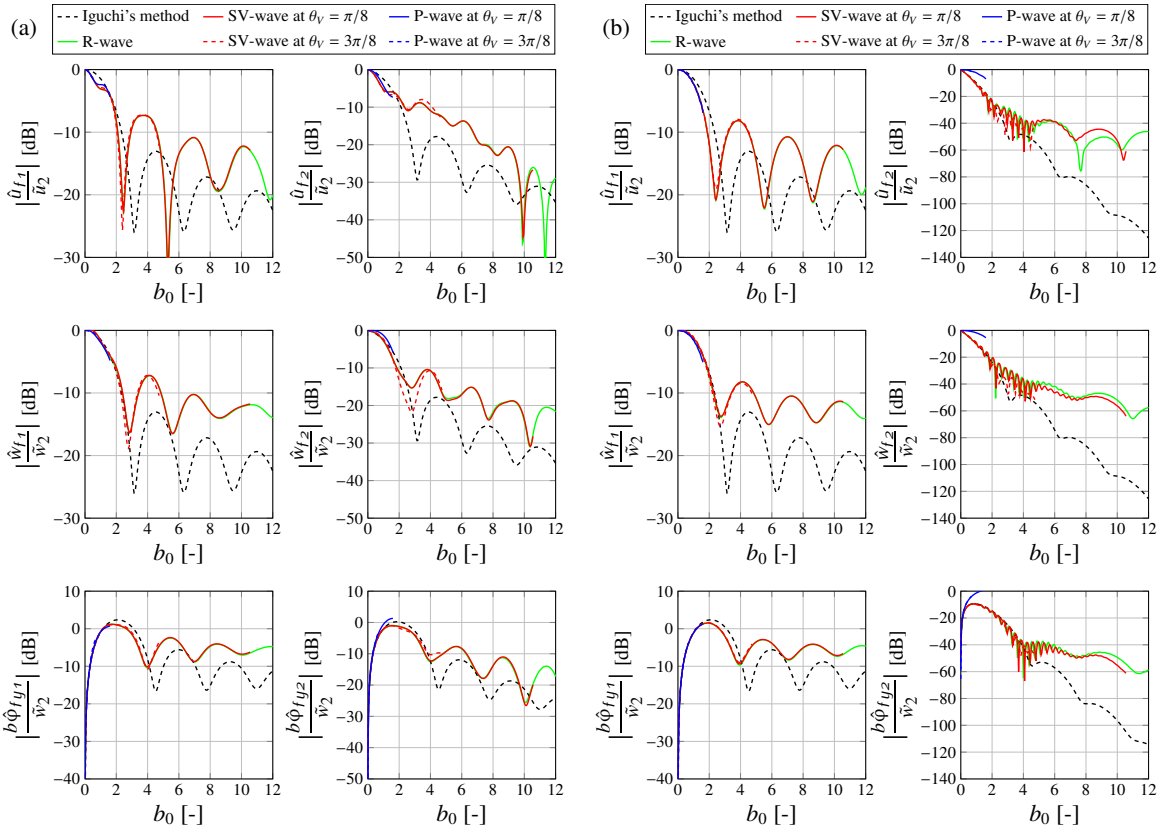

Fig. 5.15 Results for the horizontal $\hat{u}_f$, vertical $\hat{w}_f$ and rocking $\hat{\varphi}_{fy}$ response of two square, surface rigid footings of width b on the free-surface of the slab foundation at a centre-to-centre distance (a) $d = 2.5b$ and (b) $d = 20b$. Sub-horizontal and sub-vertical incident P- and SV-waves and Rayleigh waves are considered at $\theta_H = 0$. Comparison is made for the magnitude of the response for the upstream $(r = 1)$ and downstream $(r = 2)$ footings between the results obtained with the rigorous solution (BEM - 8×8 quadratic elements for each foundation) and with Iguchi's method. The plots refer to the dimensionless width $b_0 = 2\pi b/\lambda_x$ and to the Poisson's ratio $\nu_s = 0.49$.

qualitatively explained by examining the scattered wave-field generated by the presence of the two rigid footings as illustrated in Figure 5.16. The scattered wave-field $\hat{w}_s$ associated with a relatively low frequency excitation has a limited magnitude relative to that of the free-field $\hat{w}_2$ around the downstream footing. Conversely, at relatively high frequencies, the scattered $\hat{w}_s$ and the free-field $\hat{w}_2$ vertical displacement have comparable magnitudes around the downstream footing so that the effect of the through-soil coupling becomes important and relevant for the response of the downstream footing. This effect is relevant for the assumed (damped) plane-wave excitation originated in the soil; for a given frequency, the horizontal wavelength λ_x is always smaller than the horizontal wavelength $\lambda_x^{(\text{scat.})}$ of the scattered wave-field associated with the tractions exerted at the free-surface of the upstream foundation, because of the associated driving point response of the footing on a concrete layer overlying the soil (i.e higher wave speed and higher wavelengths). It follows that at relatively

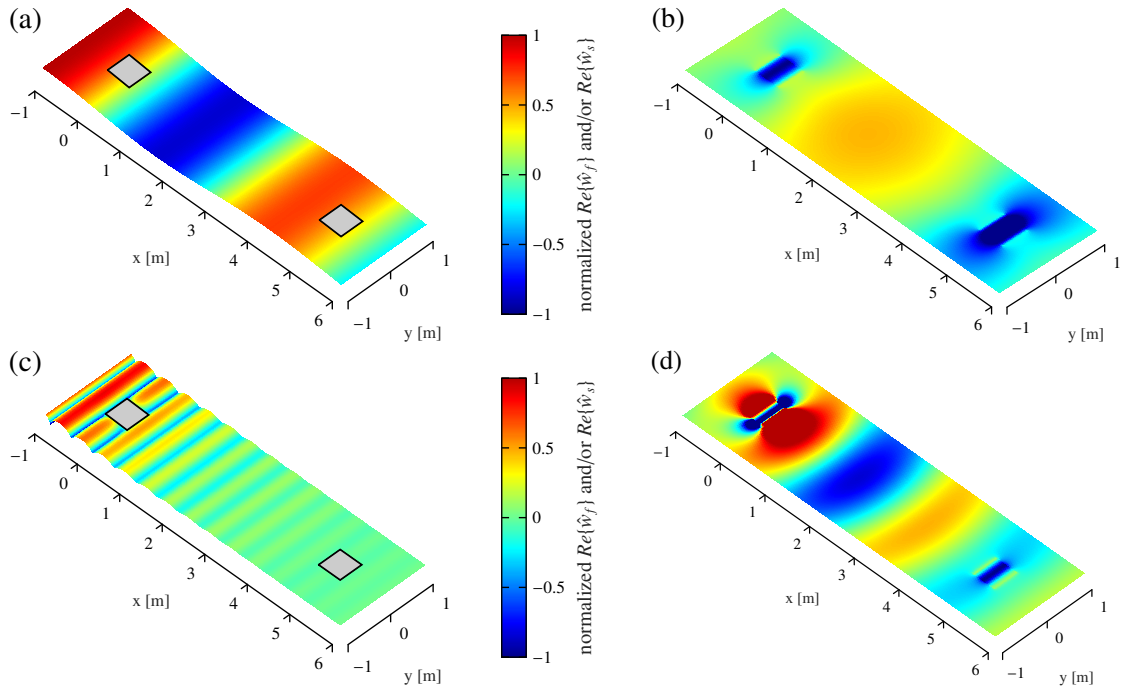

Fig. 5.16 Resulting wave-field $\hat{\mathbf{u}}_\mathbf{f}$ (a) and (c), and the related scattered wave-field $\hat{\mathbf{u}}_\mathbf{s}$ (b) and (d), of two, square, rigid footings of side $2b = 0.5$ m at a centre-to-centre distance $d = 20b$ subjected to a sub-horizontal incident SV-wave at $\theta_V = \pi/8$ and $\theta_H = 0$. Results are obtained with the rigorous solution (BEM - 8×8 quadratic elements for each footing) and with reference to a dimensionless width $b_0 = 0.1\pi$ (a) and (b), and $b_0 = \pi$ (c) and (d) related to a dimensionless distance $d/\lambda_x = 1$ and $d/\lambda_x = 10$ respectively. The coloured scale refers to either: (a) and (c) the normalised vertical displacement $\hat{w}_f(x,y,h,\omega)$ of the resulting wave-field $\hat{\mathbf{u}}_\mathbf{f}$, (b) and (d) the normalised vertical displacement $\hat{w}_s(x,y,h,\omega)$ of the scattered wave-field $\hat{\mathbf{u}}_\mathbf{s}$.

high frequencies the incident wave-field is sufficiently damped at the location of the downstream footing that the scattered wave-field becomes relevant instead.

Comparison of the rigorous and the approximate response in Figure 5.15 validates the use of Iguchi's method also for the case of multiple rigid footings, with both $d/b = 2.5$ and 20, for values of $b_0 \leq 2$, with differences up to 5 dB. The agreement is as good as that obtained for a single rigid footing. It can be concluded that, for both the case of rigid foundations on the ground (i.e. direct coupling of the portal-frame building with the ground - benchmark #1) and the case of rigid footings on a concrete slab foundation overlying the ground (i.e. coupling of the portal-frame building with a foundation system - benchmark #2), Iguchi's method provides a valuable means of estimating the kinematic interaction of the rigid regions. The resulting input motion $\hat{\boldsymbol{u}}_{\boldsymbol{f}}$ can then be used for the subsequent soil-foundation-building interaction analysis.

5.3 An approximate strategy for the response of rigid footings

Following the discussion in Section 5.1 and 5.2, Iguchi's method may be adopted as a valid approximate approach for the kinematic interaction of rigid foundations and/or footings. This is a necessary step to obtain the input motion $\hat{\boldsymbol{u}}_{\boldsymbol{f}}$ needed for the purpose of coupling a portal-frame building model to the soil-foundation system. The results shown so far demonstrate that Iguchi's method may be considered valid for multiple rigid foundations and/or rigid footings with reference to the rule-of-thumb dictated by Equation 5.31. Although the latter may seem restrictive, for commonly encountered soil properties (e.g. see Table 3.1) with an associated Rayleigh wave speed of about $V_R \approx 190$ m/s and for a column's cross-section of $2b = 0.5$ m, the maximum frequency that can be considered according to Equation 5.31 is $f_{\max} \approx 242$ Hz, which corresponds to the upper bound of the frequency range of interest for problems related to ground-borne vibration.

Here, Equation 5.27 is evaluated analytically for a surface, rectangular, rigid footing on a layered ground subjected to a plane-wave excitation with a free-surface amplitude $\hat{\mathbf{u}}_r = [\hat{u}_r, \hat{v}_r, \hat{w}_r]^T$ at the centroid of the r^{th} footing. The free-surface amplitude for plane-wave excitation may be found by application of the Stiffness-Matrix-Method [189] as seen in Chapter 4. The result can be expressed as transfer functions $\Psi_{Ig\,(i)}$ for the response of the rigid footing referring to the i^{th} degree of freedom. According to the results in Equation 5.27, the response of a surface, rectangular rigid footing, as

illustrated in Figure 5.12(c), may be obtained as:

$$[\hat{u}_{fr}(\omega),\hat{v}_{fr}(\omega),\hat{w}_{fr}(\omega)]^{\mathrm{T}}=\frac{1}{A_f}\int_{-b}^{b}\int_{-c}^{c}[\hat{u}_r(\mathbf{x},\omega),\hat{v}_r(\mathbf{x},\omega),\hat{w}_r(\mathbf{x},\omega)]^{\mathrm{T}}dy\,dx \tag{5.43a}$$

$$\hat{\varphi}_{fxr}(\omega)=\frac{1}{I_{fx}}\int_{-b}^{b}\int_{-c}^{c}\hat{w}_r(\mathbf{x},\omega)\cdot y\,dy\,dx \tag{5.43b}$$

$$\hat{\varphi}_{fyr}(\omega)=\frac{1}{I_{fy}}\int_{-b}^{b}\int_{-c}^{c}-\hat{w}_r(\mathbf{x},\omega)\cdot x\,dy\,dx \tag{5.43c}$$

$$\hat{\varphi}_{fzr}(\omega)=\frac{1}{I_{fz}}\int_{-b}^{b}\int_{-c}^{c}\{\hat{v}_r(\mathbf{x},\omega)\cdot x-\hat{u}_r(\mathbf{x},\omega)\cdot y\}\,dy\,dx \tag{5.43d}$$

The rigid-body response $\hat{\boldsymbol{u}}_{\boldsymbol{fr}}$ in Equations 5.43 is a weighted average of the free-surface displacement $\hat{\mathbf{u}}_{\mathbf{r}}$ on the domain Ω_r of the footing. By solving the integrals in Equation 5.43, the following closed-form solutions for the transfer functions $\Psi_{Ig\,(i)}$ can be obtained:

for $\quad \theta_H \neq (n-1)\pi \wedge \theta_H \neq (2n-1)\dfrac{\pi}{2} \qquad n=1,2,\ldots$

$$\begin{aligned}
&\frac{\hat{u}_{fr}}{\hat{u}_r}=\frac{\sin\alpha\sin\beta}{\alpha\beta}\\
&\frac{c\,\hat{\varphi}_{fxr}}{\hat{w}_r}=-\frac{3i\sin\alpha\left[\sin\beta-\beta\cos\beta\right]}{\alpha\beta^2}\\
&\frac{b\,\hat{\varphi}_{fyr}}{\hat{w}_r}=\frac{3i\sin\beta\left[\sin\alpha-\alpha\cos\alpha\right]}{\alpha^2\beta}\\
&\frac{b\,\hat{\varphi}_{fzr}}{\hat{u}_r}=\frac{3i}{\alpha\beta\,(1+\chi^2)}\left\{\frac{\chi\sin\alpha\left[\sin\beta-\beta\cos\beta\right]}{\beta}-\frac{\hat{v}_i}{\hat{u}_i}\frac{\sin\beta\left[\sin\alpha-\alpha\cos\alpha\right]}{\alpha}\right\}
\end{aligned} \tag{5.44a}$$

for $\quad \theta_H = (n-1)\pi \qquad n=1,2,\ldots$

$$\begin{aligned}
&\frac{\hat{u}_{fr}}{\hat{u}_r}=\frac{\sin\alpha}{\alpha}\\
&\frac{c\,\hat{\varphi}_{fxr}}{\hat{w}_r}=0\\
&\frac{b\,\hat{\varphi}_{fyr}}{\hat{w}_r}=\frac{3i\left[\sin\alpha-\alpha\cos\alpha\right]}{\alpha^2}\\
&\frac{b\,\hat{\varphi}_{fzr}}{\hat{v}_r}=-\frac{3i\left[\sin\alpha-\alpha\cos\alpha\right]}{\alpha^2(1+\chi^2)}
\end{aligned} \tag{5.44b}$$

$$
\begin{aligned}
&\text{for} \quad \theta_H = (2n-1)\frac{\pi}{2} \qquad n = 1,2,\dots \\
&\frac{\hat{u}_{fr}}{\hat{u}_r} = \frac{\sin\beta}{\beta} \\
&\frac{c\,\hat{\varphi}_{fxr}}{\hat{w}_r} = -\frac{3i\left[\sin\beta - \beta\cos\beta\right]}{\beta^2} \\
&\frac{b\,\hat{\varphi}_{fyr}}{\hat{w}_r} = 0 \\
&\frac{b\,\hat{\varphi}_{fzr}}{\hat{u}_r} = \frac{3i\chi\left[\sin\beta - \beta\cos\beta\right]}{\beta^2(1+\chi^2)}
\end{aligned}
\tag{5.44c}
$$

where $\chi = c/b$ is the aspect ratio of the rectangular footprint Ω, $\alpha = b_0\cos\theta_H$, $\beta = \chi b_0 \sin\theta_H$ and $b_0 = 2b/\lambda_x$.

The resulting rigid-body response $\hat{\boldsymbol{u}}_{\boldsymbol{f}r}$ of the r^{th} footing is of interest for main design aspects. It provides the necessary input for the following soil-foundation-building interaction analysis with reference to a portal-frame building [214]. For instance, a useful parameter that can be obtained from Equation 5.44 is the transfer function Θ_f, already adopted in Section 3.5.1 for the investigation of the added-building effect and here defined for the r^{th} footing as:

$$
\Theta_{fr} = \frac{\hat{\varphi}_{fyr}}{\hat{u}_{fr}} = \frac{\tilde{w}_r}{\tilde{u}_r}\frac{3i}{b}\frac{(\sin\alpha - \alpha\cos\alpha)}{\alpha\sin\alpha}
\tag{5.45}
$$

for incident wave-fields at $\theta_H = 0$.

Moreover, the comparison between the response $\hat{\boldsymbol{u}}_{\boldsymbol{f}r}^{(\mathrm{F})}$ and $\hat{\boldsymbol{u}}_{\boldsymbol{f}r}^{(\mathrm{R})}$ for the r^{th} footing and foundation respectively, at the same location in plan and with the same geometry, provides an understanding of the added-foundation effect, as already investigated in Chapter 4, but this time with reference to the particular coupling points of interest for the soil-foundation-building interaction analysis. Such transfer functions, with reference to a given DoF, can be expressed as:

$$
\frac{\hat{u}_{fr}^{(\mathrm{F})}}{\hat{u}_{fr}^{(\mathrm{R})}} = \frac{\hat{u}_{fr}^{(\mathrm{F})}}{\tilde{u}_0}\cdot\frac{\tilde{u}_0}{\hat{u}_{fr}^{(\mathrm{R})}} = \frac{\hat{u}_{fr}^{(\mathrm{F})}}{\tilde{u}_2}\cdot\frac{\tilde{u}_2}{\tilde{u}_0}\cdot\frac{\tilde{u}_0}{\hat{u}_{fr}^{(\mathrm{R})}} = \Psi_{F2}\cdot\Psi_f\cdot\frac{1}{\Psi_{R0}}
\tag{5.46}
$$

Based on the discussion in Sections 5.1 and 5.2, we understand that the transfer functions Ψ_{R0} and Ψ_{F2} are both driven by the kinematic interaction and the geometric restraining effect illustrated in Figure 5.4 and are dependent on b_0. We have seen that, in both cases, a good approximation for the these is given by the transfer function Ψ_{Ig} as defined in Equation 5.44. It follows that Equation 5.46

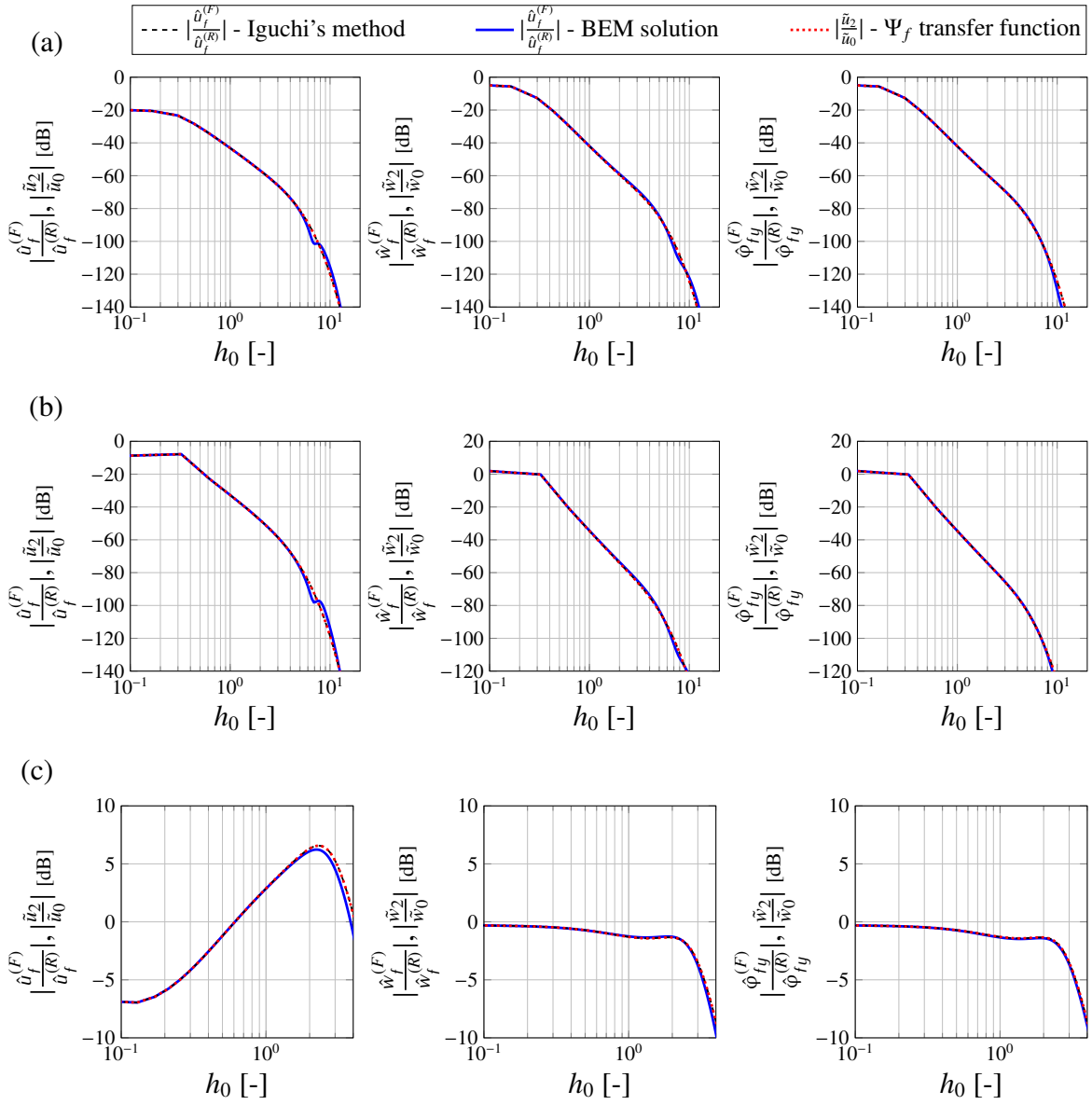

Fig. 5.17 Comparison between the transfer functions related to the rigid-body displacement $\hat{u}_f^{(\mathrm{F})}/\hat{u}_f^{(\mathrm{R})}$ of a single footing and foundation, as obtained by Iguchi's method and BEM approach, and the ones related to the displacement amplitudes $\tilde{u}_2/\tilde{u}_0$ in the frequency-wavenumber domain. The results refer to a Rayleigh wave (a), and sub-horizontal incident SV- (b), and P-waves (c) at $\theta_V = \pi/8$. Poisson's ratio $\nu_s = 0.49$ and $h = 0.7$ m are assumed with the rest of the parameters as in Table 3.1.

may be simplified further:

$$\frac{\hat{u}_{fr}^{(\mathrm{F})}}{\hat{u}_{fr}^{(\mathrm{R})}} = \Psi_{F2} \cdot \Psi_f \cdot \frac{1}{\Psi_{R0}} = \Psi_{Ig} \cdot \Psi_f \cdot \frac{1}{\Psi_{Ig}} = \Psi_f \tag{5.47}$$

and the added-foundation effect, with reference to the coupling points, is described by the one transfer function Ψ_f referring to the frequency-wavenumber amplitudes, as explored in Chapter 4.

The comparison of the transfer functions representative of the added-foundation effect are reported in Figure 5.17 for a Rayleigh wave and for sub-horizontal P- and SV-waves. A very good agreement is obtained between the rigorous and approximate transfer functions with differences of, at most, 10 dB that appear at relatively high frequencies. It is possible to conclude that the approximate strategy leads back to the results obtained in Chapter 4 for the added-foundation effect, and that the latter remains unaltered with reference to the rigorous response of the rigid footings as the subsequent coupling points for the soil-foundation-building interaction.

The added-foundation effect is often of interest as a salient "relative" measure for the design of buildings when the effect of adopting different configurations of foundation needs to be studied. We can conclude that Iguchi's method for analysing the soil-foundation interaction, with reference to rigid footings on the free-surface, may be adopted with the final focus on both "absolute" measures of the vibration field (as seen in Section 5.1 and 5.2) and to relative measures (i.e. the added-foundation effect); it must be noted that in both cases the limitation expressed by Equation 5.31 applies and must be considered for the particular problem in hand.

5.4 The response of rigid footings on a finite slab foundation

The assumption of infinite horizontal extent for the slab foundation is tested in this section by considering a finite slab foundation. Two Finite Element Method (FEM [106]) models are considered by means of the Finite Element Analysis software ABAQUS [114]: a three-dimensional model (*3D model*) that fully accounts for continuum deformations based on the C3D20R element; and a two-dimensional model, related to the mid-surface of the slab, that considers only through-thickness first-order shear deformations based on the S8R element (see Figure 5.18). A coarse (*2D model A*) and a refined (*2D model B*) mesh configurations are adopted for its validation against the incident wave-field.

Rigid footings on the upper surface of the foundation are considered as the subsequent coupling points with a building. These are reference points for which the response may be compared with the one obtained by the previously discussed approximate (i.e. Iguchi's method) or rigorous (i.e. BEM solution) strategies that refer to an infinitely large slab foundation. Wave-fronts perpendicular

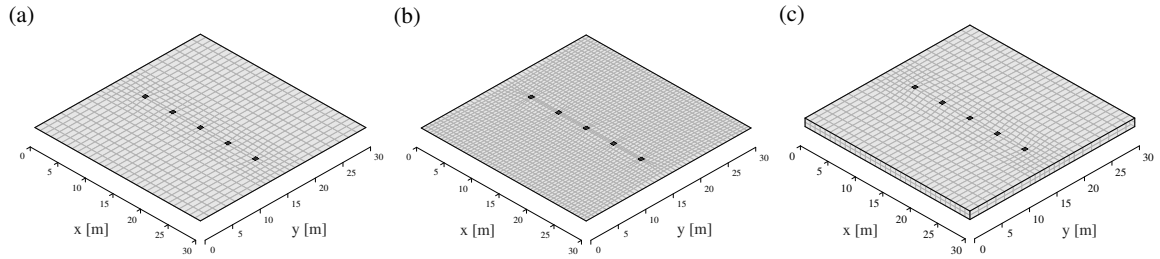

Fig. 5.18 Mesh configurations for FEM models of the finite slab foundation: (a) a coarse *2D model A*, (b) a refined *2D model B*, both with shell elements S8R, and (a) a *3D model* with solid elements C3D20R.

to an alignment of five rigid footings (i.e. $\theta_H = 0$) are considered so as to compare the results of benchmark #2 for the reference problem introduced in Section 3.1.2. The rigid footings have a geometry consistent with the cross-section of the columns (i.e. $b = 0.25$ m), they have a centre-to-centre distance $d/b = 20$ and they are centred in the $x-y$ plane of a 30 m by 30 m slab foundation. For the purpose of simplified notation, the subscript 'p' and the noun 'plate' is adopted in the following for describing each of the finite slab foundation models. This is not intended to hold a specific meaning for the assumptions of each model, which are intrinsic of the FEM models, but rather to ease the discussion and the comparison with previously discussed results.

5.4.1 A combined finite-element boundary-element method

A combined finite-element boundary-element method is used to calculate the soil-foundation interaction. A conforming coupling is considered with the involved collocation points as on the lower surface Ω_ℓ of the examined plate model.

The boundary element method (BEM) is used to calculate the dynamic stiffness matrix $\hat{\mathbf{K}}_\mathbf{s}$ of the soil starting from the displacements $\hat{\mathbf{G}}_\mathbf{u}$ and tractions $\hat{\mathbf{G}}_\mathbf{t}$ boundary-element system matrices referring to the collocation points on a domain corresponding to Ω_ℓ on the free-surface of an elastic half-space. These are obtained by means of the BEMFUN toolbox [38] by making use of the Green's functions as calculated by the ElastoDynamics toolbox [36, 37], both implemented in MATLAB [35]. For the unbounded domain represented by the elastic half-space (i.e. ground), the traction-displacement relationship at the collocation points may be written as [115, 207, 208, 38]:

$$\hat{\mathbf{t}}(\mathbf{x_s},\omega) = \left[\hat{\mathbf{G}}_\mathbf{u}(\mathbf{x_s},\mathbf{x_s},\omega)\right]^{-1}\left[\mathbf{I}+\hat{\mathbf{G}}_\mathbf{t}(\mathbf{x_s},\mathbf{x_s},\omega)\right]\hat{\mathbf{u}}(\mathbf{x_s},\omega) = \hat{\mathbf{G}}_\mathbf{tu}(\mathbf{x_s},\mathbf{x_s},\omega)\,\hat{\mathbf{u}}(\mathbf{x_s},\omega) \tag{5.48}$$

with the vector $\mathbf{x_s}$ indexing the degrees-of-freedom for the collocation points on the domain Ω_ℓ at the free-surface of the ground. The conforming soil-foundation coupling is ensured by the adoption of quadratic elements for both the BEM and the FEM models of the soil and the plate respectively. These refer to 8 collocation points per element on the domain Ω_ℓ, with the mesh defined by the FEM models as in Figure 5.18. The forces at the soil-plate interface for the i^{th} collocation point on Ω_ℓ due to the displacement at the j^{th} collocation point may be obtained by integration of the tractions as:

$$\begin{aligned}\hat{\mathbf{f}}_{\mathbf{s}}(\mathbf{x}_{\mathbf{s}i},\omega) = \int_{\Omega_\ell} \hat{\mathbf{t}}(\mathbf{x}_{\mathbf{s}i},\omega)\, d\Omega_\ell = \sum_k \int_{\Omega_{\ell k}} \mathcal{N}_i^{(k)} \mathcal{N}_j^{(k)}\, \hat{\mathbf{G}}_{\mathbf{tu}}(\mathbf{x}_{\mathbf{s}i},\mathbf{x}_{\mathbf{s}j},\omega)\, \hat{\mathbf{u}}(\mathbf{x}_{\mathbf{s}j},\omega)\, d\Omega_{\ell k} = \\ = \mathbf{T_Q}(\mathbf{x}_{\mathbf{s}i},\mathbf{x}_{\mathbf{s}j})\, \hat{\mathbf{G}}_{\mathbf{tu}}(\mathbf{x}_{\mathbf{s}i},\mathbf{x}_{\mathbf{s}j},\omega)\, \hat{\mathbf{u}}(\mathbf{x}_{\mathbf{s}j},\omega) = \hat{\mathbf{K}}_{\mathbf{s}}(\mathbf{x}_{\mathbf{s}i},\mathbf{x}_{\mathbf{s}j},\omega)\, \hat{\mathbf{u}}(\mathbf{x}_{\mathbf{s}j},\omega)\end{aligned} \tag{5.49}$$

with the integration scheme on the boundary element mesh and the matrix $\mathbf{T_Q}$ as defined in Equations 5.16 and 5.16 respectively. The dynamic stiffness matrix of the soil $\hat{\mathbf{K}}_{\mathbf{s}}(\mathbf{x}_{\mathbf{s}i},\mathbf{x}_{\mathbf{s}j},\omega)$ is obtained by integration of the traction-displacement BEM system matrix $\hat{\mathbf{G}}_{\mathbf{tu}}(\mathbf{x}_{\mathbf{s}i},\mathbf{x}_{\mathbf{s}j},\omega)$ over the domain Ω_ℓ.

The finite-element analysis is adopted to calculate the dynamic stiffness matrices of the FEM models by means of ABAQUS. The static stiffness $\mathbf{K_p}$ and the mass $\mathbf{M_p}$ matrices of the plate models are retrieved with reference to the degrees-of-freedom and to the collocation points of the considered element formulation and the mesh configuration as shown in Figure 5.18. The global dynamic stiffness matrix can then be obtained as:

$$\hat{\mathbf{K}}_{\mathbf{pd}}(\mathbf{x_p},\mathbf{x_p},\omega) = \mathbf{K_p}(\mathbf{x_p},\mathbf{x_p})(1+i\eta) - \omega^2 \mathbf{M_p}(\mathbf{x_p},\mathbf{x_p}) \tag{5.50}$$

with the vector $\mathbf{x_p}$ indexing the degrees-of-freedom for the collocation points that compose the plate model. A hysteretic damping model is adopted by applying the correspondence principle to the static stiffness matrix $\mathbf{K_p}$ as shown in Equation 5.50. This is equivalent to consider a complex Young's modulus $E' = E(1+i\eta)$, with η the damping loss factor that here has the value 0.1 (as in Table 3.1). This damping model has the conceptual significance of considering equal damping for both P- and S-waves within the plate. Although this differs from the previously adopted damping model, as presented in Section 3.2.3, no substantial differences are to be expected given that the plane-wave excitation is defined in the soil, whose damping model is defined as in Section 3.2.3.

In general, for the FEM models used here, the degrees-of-freedom (DoFs) of a given model may be collected in the following vector:

$$\mathbf{x_p} = \mathbf{x_s} \cup \mathbf{x_{p\varphi}} \cup \mathbf{x_{p}}_F \cup \mathbf{x_{p}}_f \tag{5.51}$$

where $\mathbf{x_s}$, $\mathbf{x_{p\varphi}}$, $\mathbf{x_{p}}_F$ and $\mathbf{x_{p}}_f$ collect the DoFs of the BEM model of the soil, the DoFs related to the rotations at each collocation point on Ω_ℓ (i.e. 3 rotations for the shell element S8R and none for the solid element C3D20R), the DoFs of the rigid footings and the remainder of the DoFs of the plate model, respectively. For an incident wave-field applied on the domain Ω_ℓ, the degrees-of freedom directly related to the coupling may be indexed as $\mathbf{x_E} = \mathbf{x_s}$, while those related to the free-part of the plate model are $\mathbf{x_N} = \mathbf{x_{p\varphi}} \cup \mathbf{x_{p}}_F \cup \mathbf{x_{p}}_f$. It follows that the condensed dynamic stiffness matrix of the plate that contributes to the soil-plate interaction may be written as [168]:

$$\hat{\mathbf{K}}^{(c)}_{\mathbf{pd}}(\mathbf{x_E}, \mathbf{x_E}, \omega) = \hat{\mathbf{K}}_{\mathbf{pd}}(\mathbf{x_E}, \mathbf{x_E}, \omega) - \hat{\mathbf{K}}_{\mathbf{pd}}(\mathbf{x_E}, \mathbf{x_N}, \omega) \left[\hat{\mathbf{K}}_{\mathbf{pd}}(\mathbf{x_N}, \mathbf{x_N}, \omega)\right]^{-1} \hat{\mathbf{K}}_{\mathbf{pd}}(\mathbf{x_N}, \mathbf{x_E}, \omega) \tag{5.52}$$

Let us consider the incident wave-field $\hat{\mathbf{u}}_\mathbf{0}(\mathbf{x_s}, \omega)$ defined by Equation 5.1 on the domain Ω_ℓ on the free-surface of the ground. After the coupling of the plate, the response on the same domain may be written as:

$$\hat{\mathbf{u}}_\mathbf{f}(\mathbf{x_s}, \omega) = \hat{\mathbf{u}}_\mathbf{0}(\mathbf{x_s}, \omega) + \hat{\mathbf{H}}_\mathbf{s}(\mathbf{x_s}, \omega)\hat{\mathbf{f}}_\mathbf{s}(\mathbf{x_s}, \omega) \tag{5.53}$$

with $\hat{\mathbf{H}}_\mathbf{s}$ the FRF matrix of the soil obtained by inversion of the dynamic stiffness matrix $\hat{\mathbf{K}}_\mathbf{s}$. The forces exerted by the plate on the soil may be obtained as:

$$\hat{\mathbf{f}}_\mathbf{s}(\mathbf{x_s}, \omega) = -\hat{\mathbf{f}}_\mathbf{p}(\mathbf{x_E}, \omega) = -\hat{\mathbf{K}}^{(c)}_{\mathbf{pd}}(\mathbf{x_E}, \mathbf{x_E}, \omega)\, \hat{\mathbf{u}}_\mathbf{f}(\mathbf{x_s}, \omega) \tag{5.54}$$

By substitution of the latter into Equation 5.53, the response at the soil-foundation interface is given by:

$$\hat{\mathbf{u}}_\mathbf{f}(\mathbf{x_s}, \omega) = \left[\mathbf{I} + \hat{\mathbf{H}}_\mathbf{s}(\mathbf{x_s}, \mathbf{x_s}, \omega)\, \hat{\mathbf{K}}^{(c)}_{\mathbf{pd}}(\mathbf{x_E}, \mathbf{x_E}, \omega)\right]^{-1} \hat{\mathbf{u}}_\mathbf{0}(\mathbf{x_s}, \omega) \tag{5.55}$$

The response of the plate can be obtained by partitioning $\hat{\mathbf{K}}_\mathbf{pd}$ and applying the *Dirichlet boundary condition* $\hat{\mathbf{u}}_\mathbf{f}(\mathbf{x_E}, \omega) = \hat{\mathbf{u}}_\mathbf{f}(\mathbf{x_s}, \omega)$ on the DoFs $\mathbf{x_E}$ and the force-free *Neumann boundary condition* on

the DoFs $\mathbf{x_N}$. This gives:

$$\hat{\mathbf{u}}_\mathbf{f}(\mathbf{x_N},\omega) = -\left[\hat{\mathbf{K}}_\mathbf{pd}(\mathbf{x_N},\mathbf{x_N},\omega)\right]^{-1}\hat{\mathbf{K}}_\mathbf{pd}(\mathbf{x_N},\mathbf{x_E},\omega)\,\hat{\mathbf{u}}_\mathbf{f}(\mathbf{x_E},\omega) \tag{5.56}$$

The response $\hat{\mathbf{u}}_\mathbf{f}(\mathbf{x_p},\omega) = \hat{\mathbf{u}}_\mathbf{f}(\mathbf{x_E},\omega) \cup \hat{\mathbf{u}}_\mathbf{f}(\mathbf{x_N},\omega)$ of the foundation system to an incident wave-field is then obtained. This includes the response of the rigid footings $\hat{\mathbf{u}}_\mathbf{f}(\mathbf{x}_{\mathbf{p}F},\omega) = \boldsymbol{u}_f^{(p)}(\omega)$ that is of interest for the comparison with the results obtained by modelling the slab foundation as an elastic layer.

5.4.2 Results for different models of the finite plate

The use of different FEM models for the plate can be investigated with reference to the response of the footings. Figure 5.19 shows the horizontal and vertical response of the first footing (i.e. upstream footing) to a Rayleigh wave. From a numerical perspective, this is the most restrictive case of plane-wave excitation since it involves the shortest horizontal wavelength (i.e. λ_R).

A first comment about the accuracy of the numerical approach can be made by comparison of the 2D models *A* and *B*. The maximum dimension of the quadratic element, along the direction of propagation x, is $\delta = 1.12\,\mathrm{m}$ and $\delta = 0.56\,\mathrm{m}$ for the coarse and refined mesh respectively. By comparison of the first footing response to a Rayleigh wave, as illustrated in Figure 5.19, it is possible to acknowledge a good agreement between the two models up to a frequency of 80 Hz. The latter corresponds to a ratio δ/λ_R of approximately $1/2$ and $1/4$ for the 2D models *A* and *B* respectively. The condition $\delta/\lambda_x < 1/2$, with λ_x the shortest apparent wavelength in the wave propagation problem, may represent a general requirement for the mesh size of FEM models based on a quadratic element formulation. A rule-of-thumb of $1/8 < \delta/\lambda_x < 1/5$ may be found in literature [108, 107, 57] for soil-structure interaction problems analysed by a FEM approach with a linear element formulation.

Figure 5.19 shows also the result of the first footing translational response obtained with the 3D model. While differences, with the 2D model, of at most 3 dB are registered for the vertical response, important discrepancies of up to 18 dB are found for the horizontal response. Although it is not shown here, a similar trend is registered for the response of the other footings. Based on the discussion in Section 3.5.2, both horizontal and vertical vibration should be correctly accounted for; it follows that the three-dimensional modelling of the foundation is a necessary requirement in the context of ground-borne vibration. It may be more so when the focus is on absolute predictions of vibration levels.

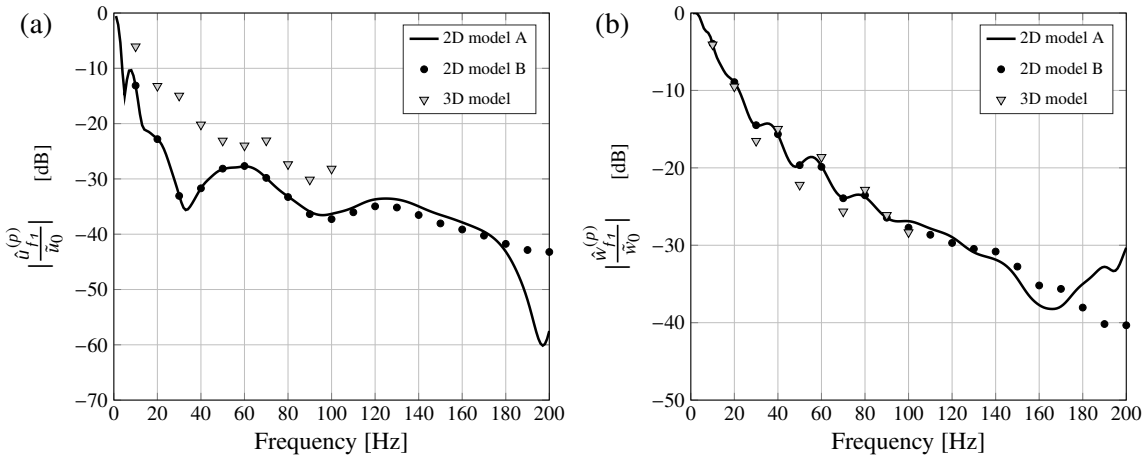

Fig. 5.19 Comparison of the (a) horizontal and (b) vertical response of the first footing for the examined FEA models of the finite plate subject to an incident Rayleigh wave. The response is normalised against the amplitude of the incident wave-field in the frequency-wavenumber domain. Data from Table 3.1 are assumed with $h = 1.5$ m.

The SSI associated with a finite plate, as studied here, is inevitably complex and difficult to decipher. Some features may be qualitatively explained by looking at the modal response of the finite plate (see Figure 5.20(a)). A restraining effect at about 33.7 Hz is evident in Figure 5.19(a) for the horizontal response of the footing. One may be inclined to explain this by looking at the modal response of the plate. The examined frequency is indeed a natural frequency for the plate with the mode shape, as reported in Figure 5.20(a), showing a nodal line along the $x-$direction at the location of the footings. However, the restraining effect is less evident for the vertical response of the footing because of the plane-wave excitation (see Figure 5.20(b) and (c)). It appears that the results of the SSI analysis of the finite, flexible plate may be difficult to interpret; the extent to which the modal

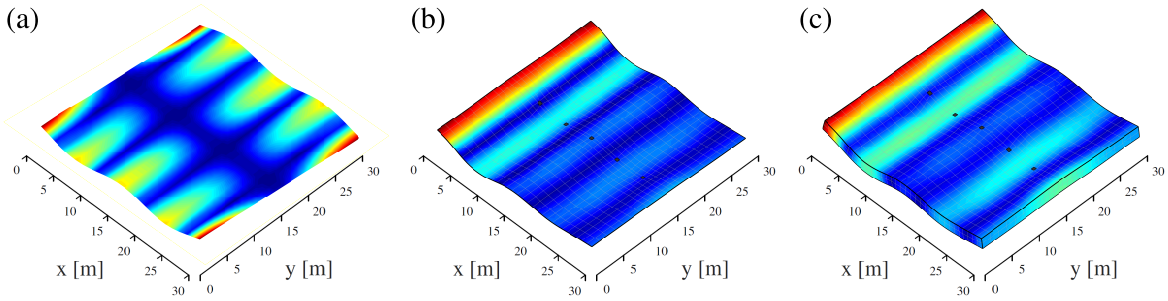

Fig. 5.20 Magnitude of the displacement field $\mathbf{u}(\mathbf{x})$ for the (a) mode shape of the 2D finite plate at $f_n = 33.7$ Hz, and for the displacement $\hat{\mathbf{u}}_\mathbf{f}(\mathbf{x})$ at the same frequency for both (b) the response of the 2D model and (c) the 3D model to a Rayleigh wave.

response of the plate influences the overall response depends on the wave-excitation considered and may only be determined properly by using validated numerical approaches.

5.4.3 The added-foundation effect of a finite slab foundation

As discussed in Section 5.3, the added-foundation effect referring to coupling points and to the infinitely large slab foundation has been found to be well approximated by the results of the frequency-wavenumber approach as discussed in Chapter 4 (see Figure 5.17). Here, the added-foundation effect is investigated with reference to the response of the rigid footings on the slab foundation as a finite plate.

Figure 5.21 shows the horizontal, vertical and rocking response of the first footing to a Rayleigh wave and to sub-horizontal P- and SV-waves. The results refer to the magnitude of the response ratio of the rigid regions after (i.e. footings) and before (i.e. foundations) the coupling of the finite plate. This is defined as the added-foundation effect referring to the coupling points of interest, as examined in Figure 5.17 for the infinitely large slab foundation. The results of the latter case are reported alongside those of the finite plate; they both refer to benchmark #2 of the reference problem (see Section 3.1.2) with the soil's Poisson ratio $\nu_s = 0.49$ and the slab thickness $h = 1.5$ m (see Table 3.1).

In general, as observed before, a good agreement between the 3D and the 2D models of the plate is obtained for the vertical and rocking response of the rigid footing, with maximum differences up to 3 dB or less depending on the incident wave-field. On the other hand, the discrepancies observed in the previous section for the horizontal response to a Rayleigh wave are found in the order of, at most, 20 dB also in the case of sub-horizontal P- and SV-waves. A common feature for the added-foundation effect is to result in no attenuation at zero-frequency; this is because of the associated wave-field that has, virtually, an infinite wavelength, which result in a rigid motion. As this is an excitation imposed by the incident wave-field, no differences are to be expected for the case of rigid foundation and/or rigid footings, hence an added-foundation effect that approaches unity is obtained.

The agreement between the results for the infinite and the finite slabs is poor, especially for wave-fields with relatively short wavelengths (i.e. R- and SV-waves); this suggests that the SSI associated with a finite slab foundation cannot be properly studied with the assumption of in-plane infinite extent. It is worth noticing that the attenuation of the response is more significant for incident wave-fields with relatively short wavelength. A maximum attenuation of 20 and 30 dB is obtained for the horizontal

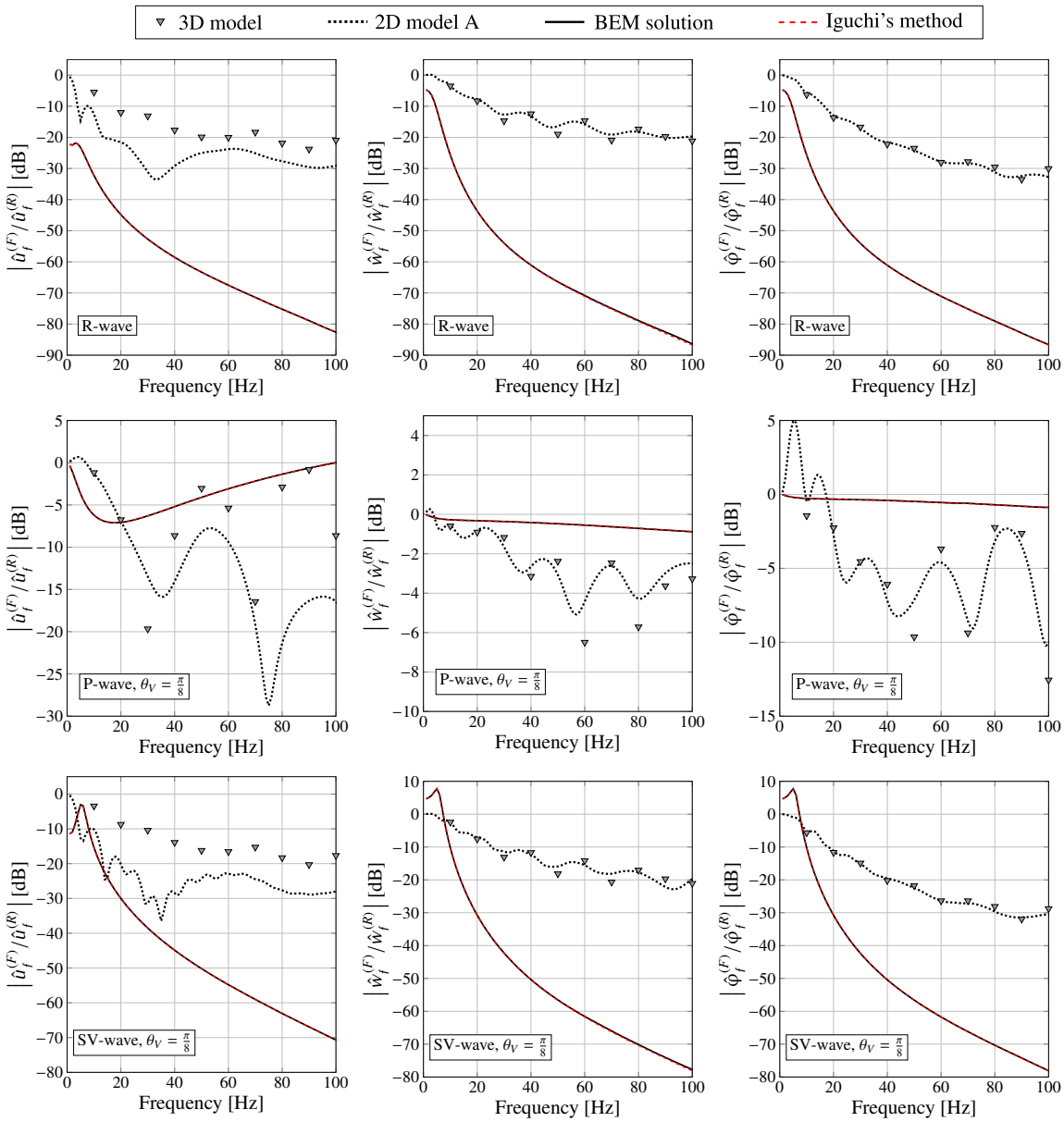

Fig. 5.21 Comparison of the added-foundation effect for the horizontal, vertical and rocking response of the first footing $(r = 1)$ for the benchmark #2 with Poisson's ratio $\nu_s = 0.49$ and the slab foundation thickness $h = 1.5$ m. A Rayleigh wave and sub-horizontal P- and SV- waves are considered as plane-wave excitation. The results referring to the 3D and 2D models of the finite slab are reported together with those obtained with the assumption of the slab as an elastic layer (see Section 5.3).

and vertical, and for the rocking response respectively. This result refers to the 3D model and to both Rayleigh waves and sub-horizontal SV-waves. As seen in Section 5.3, the results shown here

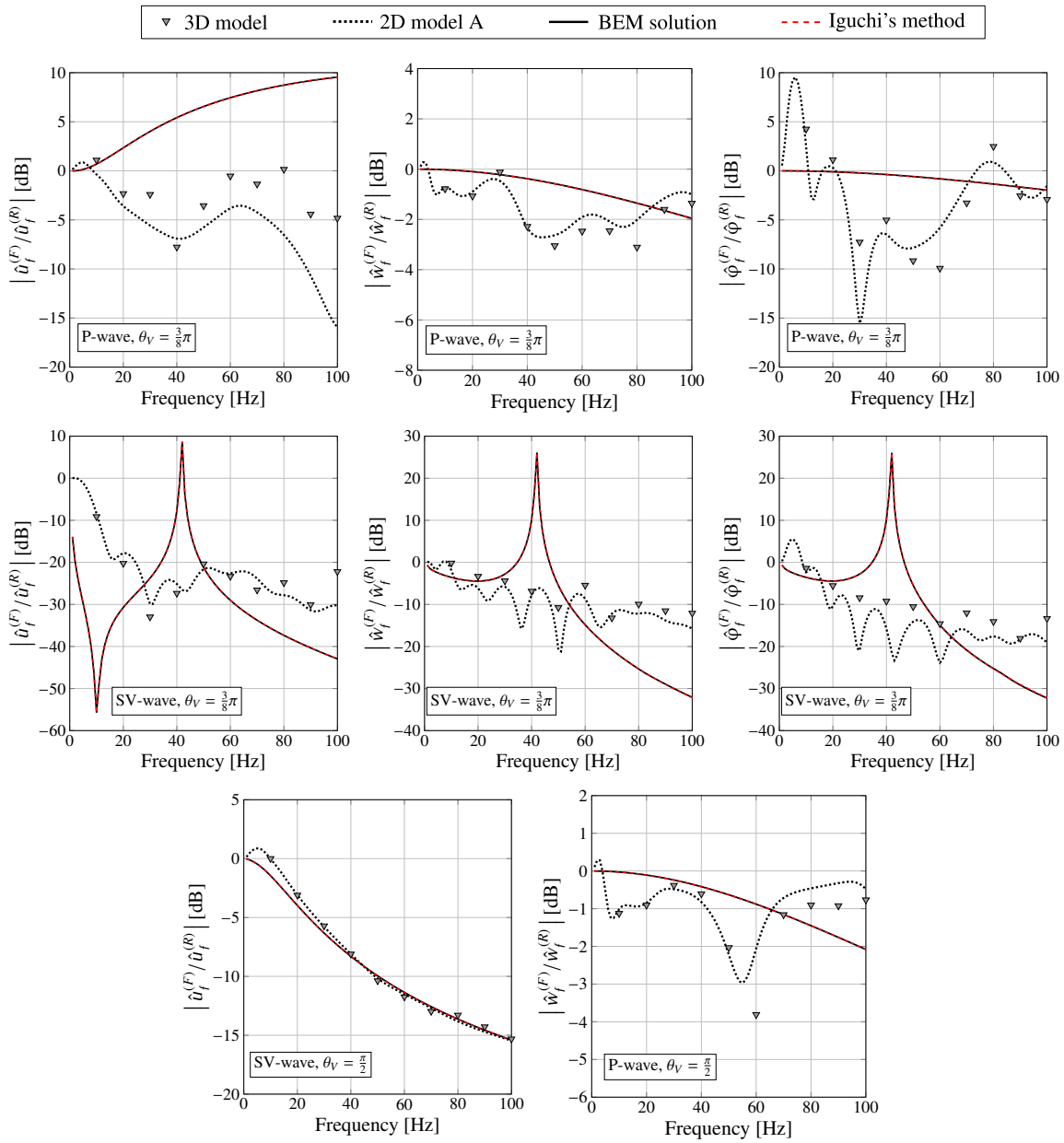

Fig. 5.22 Comparison of the added-foundation effect for the horizontal, vertical and rocking response of the first footing ($r = 1$) for the benchmark #2 with Poisson's ratio $\nu_s = 0.49$ and the slab foundation thickness $h = 1.5$ m. Sub-vertical and normally incident P- and SV- waves are considered as plane-wave excitation. The results referring to the 3D and 2D models of the finite slab are reported together with those obtained with the assumption of the slab as an elastic layer (see Section 5.3).

are comparable, at least in principle, with those obtained by the frequency-wavenumber approach in Chapter 4.

While poor agreement is obtained for the general case with $\theta_V \neq \pi/2$, the case of normal incidence provides an interesting upper bound for the attenuation achieved with the finite plate. As seen in Figure 4.11, the upper bound for the attenuation with reference to the horizontal displacemet and to a normally incident SV-wave may be found as:

$$\left(\frac{\tilde{w}_2}{\tilde{w}_0}\right)^{(\min)} = -20\log_{10}(\beta_S) = -20\log_{10}\left(\frac{\rho_c V_{Sc}}{\rho_s V_S}\right) \approx -23\,\mathrm{dB} \tag{5.57}$$

Interestingly, the value in Equation 5.57 provides an approximate upper bound for the attenuation expected by the addition of a finite slab. Although the latter argument may be useful during foundation design, it is clear that it may serve only as an approximate reference since it is based on the highly idealised case of an infinite slab foundation subject to a normally incident SV-wave.

Figure 5.22 shows the results of the added-foundation effect with reference to sub-vertical and normally incident P- and SV-waves. The horizontal wavelengths involved are larger than those in the previous case and the agreement between the results of the finite and infinite slab foundation models is generally better. It is worth noticing that the results for the finite and infinite slab foundation are in reasonable agreement for the case of normally incident P- and SV-waves, a scenario that is hardly representative of ground-borne vibration.

5.5 Conclusions

This chapter has summarised the soil-foundation interaction associated with a plane-wave excitation and to rigid regions at the free-surface of the homogeneous and/or the layered half-space representing the soil and/or the soil-foundation system respectively. This is consistent with the assumption of the soil-foundation system represented by a slab foundation, modelled as an infinitely large elastic layer, overlying the ground, which is modelled as an homogeneous and elastic half-space. The soil-foundation interaction, as studied in this chapter, is a necessary step that provides the input motion at the coupling points for the subsequent soil-foundation-building interaction.

The response of rigid foundations and/or footings is analysed in its general form with the aim of introducing the dynamic stiffness matrix associated with multiple rigid foundations and/or footings and to obtain their response to incident wave-fields. The integral equations involved in the formulation are then reformulated in algebraic form by means of the Boundary-Element-Method (BEM). An account on the relevant numerical aspects is given, although a full review is beyond the scope of

this dissertation and can be found in literature. The results obtained here refer to the use of the EDT [36, 37] and the BEMFUN [38] toolboxes for obtaining the Green's function of a layered half-space and for the application of the BEM.

The adopted formalism leads naturally to Iguchi's method as an approximate strategy for obtaining the response of rigid foundations to incident wave-fields. The application of Iguchi's method is investigated and compared with rigorous solutions obtained by the BEM for both rigid foundations and footings. The influence of dimensionless parameters such as the Poisson's ratio ν_s, the slab-thickness to footing-dimension ratio h/b and the distance to footing-dimension ratio d/b is investigated with the conclusion that the kinematic interaction of each rigid foundation and/or footing is driven by the horizontal-wavelength to footing-dimension ratio λ_x/b. It is illustrated that the approximate response obtained by Iguchi's method agrees well with the rigorous solution for values of λ_x/b greater than π, with differences of up to 5 dB. This condition serves as a rule-of-thumb for the application of Iguchi's method to ground borne vibration problems.

Closed-form expressions are obtained for the rigid foundation/footing response with reference to the amplitude of the incident wave-field at the centroid of the rigid foundation and/or footing. This allows the definition of an approximate input motion for the subsequent soil-foundation-building interaction analysis for a given plane-wave excitation. Moreover, it is possible to find a relationship between the horizontal and the rocking response of the rigid foundation and/or footing such that transfer functions for the horizontal and rocking added-building effect may be found in the form already investigated in Chapter 3. It is pointed out that similar results for the added-foundation effect, as examined in Chapter 4, may be found with reference to the coupling points represented by the rigid footings.

Finally, the assumption of in-plane infinite extent for the slab foundation is removed and the soil-foundation interaction is studied by means of a combined FEM-BEM approach. Both two-dimensional and three-dimensional FEM models of the slab foundation as a plate are considered. It is found that small differences in the order of 3 dB are found for the vertical response of the rigid footings when 2D and 3D models of the plate are explored; nonetheless, important differences up to 20 dB are found for the horizontal response of the rigid footings, indicating that accurate modelling of soil-foundation systems may be a necessary requirement in ground-borne vibration problems. The added-foundation effect associated with different incident wave-fields and related to the coupling points is investigated by means of the finite plate models. It is found that the assumption of the infinitely large foundation

greatly overestimates the attenuation provided by the addition of the foundation. The SSI associated with the finite plate is generally complex with the rigid footings response that depends on both the plane-wave excitation and the modal response of the plate. A general comment can be made in that an indicative upper bound for the attenuation provided by the plate can be obtained from the case examined in Chapter 4 for normally incident SV-waves and with the slab foundation as an elastic layer. The level of attenuation seems to be governed by the impedance mismatch between the concrete slab and the soil.

Chapter 6

A design analysis framework for base-isolated buildings

The previous discussion has presented and validated simplified models and methods that may be used to account for the soil-foundation-building interaction during the analysis of buildings against ground-borne vibration. This is reviewed in current section with the definition of a *design analysis framework*, which is then contextualized to the design of base-isolated buildings and to the evaluation of the isolation performance. A *rigorous analysis framework* is then presented with the purpose of validating the results in terms of isolation performance.

6.1 A design analysis framework

As seen in Section 2.4.3, empirical [134, 16] and semi-empirical [135] methods are commonly used in practice to carry out ground-borne vibration assessments. These are based on the definition of curves for the green-field vibration level, associated with a specific database of experimental evidence, and on the subsequent use of transfer functions for considering the nature of the source, the propagation path characteristics, the coupling of a foundation-building system and the vibration transmission to a receiver in the building interior (e.g. floor). As set out in Chapter 3.1.2, the part concerning the coupling of a foundation-building system is of interest in this dissertation. For instance, the Federal Transit Administration (FTA) [16] suggests the use of a *coupling loss factor*, associated with different foundation-building typologies, for obtaining the vibration levels at the foundation level of a building starting from the ground vibration levels as obtained by the assessment procedure.

The values of the suggested coupling loss factors range from -5 dB for wood frame houses to -13 dB for large masonry buildings on footings. The general rule, suggested by the FTA, is the heavier the building construction, the greater the coupling loss. The definition of a coupling loss factor, as described by the FTA, is based on measured data that refer to a design scenario with the building present. It is clear that, at the design stage, the interest of the practising engineer lies on the variation of the ground vibration levels before and after the construction of the building. The latter corresponds to the added-foundation effect and the added-building effect as investigated in Chapters 3, 4 and 5. It has been demonstrated that such effects are complex in nature and lead to an attenuation that, in general, is frequency-dependent and, of course, involves both the vertical and the horizontal vibration, which may both be important for the overall response of the building. On this basis it is clear that, while the empirical methods may provide a general assessment of vibration levels for a building on a specific site, they should not be used beyond their intended scope, for instance, for a detailed prediction of vibration levels. A more complete understanding of the coupling loss,

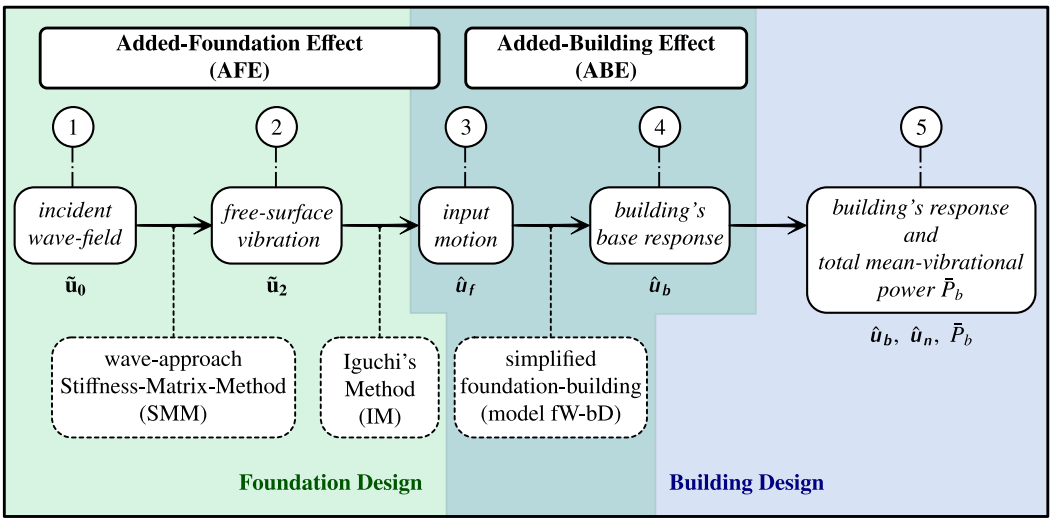

Fig. 6.1 The design framework as suggested and used in this dissertation. (1) An incident plane wave-field is considered with a resulting free-field vibration $\tilde{\mathbf{u}}_0$. (2) A wave-based approach (SMM) allows to add a slab foundation as an elastic layer and to retrieve the modified free-surface vibration $\tilde{\mathbf{u}}_2$.(3) The input motion $\hat{u}_f$ of a rigid footing at the free-surface is then obtained by means of Iguchi's method (IM) from $\tilde{\mathbf{u}}_2$. (4) The added-building effect (ABE) can be evaluated by coupling the cone model of the soil-foundation system and the building as a damper (i.e. model fW-bD). (5) With reference to the general single-point coupling model, the response at the base $\hat{u}_b$ and in the interior $\hat{u}_n$ of the building can be evaluated. The total mean-vibrational power entering the building $\bar{P}_b$ serves as a general measure of the vibration levels associated with the building's response. This depends on both the foundation and the building design alike.

yet referring to reasonable simple models and methods, may be obtained by the analysis of the added-foundation effect and the added-building effect as discussed in Chapters 3, 4 and 5.

The simplified models and methods discussed in this dissertation provide the basis for a design analysis framework that starts with an assumed green-field, which may be represented by an incident wave-field $\tilde{\mathbf{u}}_\mathbf{0}$, and gives the response at the base $\hat{\boldsymbol{u}}_\boldsymbol{b}$ and in the interior $\hat{\boldsymbol{u}}_\boldsymbol{n}$ of a portal-frame building. This design framework is adopted in this dissertation for the evaluation of the isolation performance, which is a relative measure of vibration levels between two different design configurations of the building. However, it is instructive to contextualize the design analysis framework to the absolute prediction of vibration levels. The diagram shown in Figure 6.1 summarises the several steps involved:

1. consider the green-field as the result of an incident plane wave-field $\tilde{\mathbf{u}}_\mathbf{0}$ in an elastic and homogeneous half-space representing the ground;

2. consider the addition of a slab foundation as an elastic layer and retrieve the free-surface vibration field $\tilde{\mathbf{u}}_\mathbf{2}$ by means of the Stiffness-Matrix-Method (SMM). Alternatively, a different incident wave-field may be assumed for the layered half-space (i.e. ground + slab) with a resulting free-surface vibration field $\hat{\mathbf{u}}_\mathbf{2}$ associated with a describing function $\boldsymbol{\mathcal{U}}_\mathbf{2}$ and an amplitude $\tilde{\mathbf{u}}_\mathbf{2}$ at the origin (see Equation 5.36); the assumed wave-field may refer to available vibration measurements or may be obtained by some source-propagation modelling (e.g. PiP model [197]);

3. consider rigid regions at the free-surface representative of the subsequent coupling points with a portal-frame building; their rigid response $\hat{\boldsymbol{u}}_\boldsymbol{f}$ to the incident wave-field may be obtained by application of Iguchi's Method (IM);

4. consider the coupling of a portal-frame building; the response $\hat{\boldsymbol{u}}_{\boldsymbol{b}r}$ at the base of the building for the r^{th} coupling point may be obtained by means of the simplified foundation-building model fW-bD as described in Chapter 3;

5. depending on the purpose, either a global metric (i.e. mean vibrational-power entering the building) or a local metric (i.e. vibration in one direction at one location in the building) may be of interest; in the former case, the simplified foundation-building model fW-bD may be used; in the latter case, the response at the base of the building $\hat{\boldsymbol{u}}_\boldsymbol{b}$ may be applied at the base of a

detailed structural model (e.g. FEM model of a building), already available to the structural engineer, to obtained the response $\hat{\boldsymbol{u}}_{\boldsymbol{n}}$ in the interior of the building.

Figure 6.1 illustrates the added-foundation effect (AFE), which may be influenced by the design of the foundation, and the added-building effect (ABE), which relates to both the design of the foundation and the building. In general, the response of the building is then the result of both the AFE and the ABE, and of the assumed incident wave-field. It is clear that the effectiveness of, for instance, a foundation design change (e.g. slab thickness) in reducing the vibration levels, should not be evaluated by looking at the added-foundation effect alone, but at the resulting response of the building. Especially in these cases, when a relative measure of performance between design configurations is of interest, the mean-vibrational power-flow in the building is a useful metric for the design. An example is the evaluation of the isolation performance for a base-isolated building in terms of the PFIG. The adoption of the design analysis framework for such a purpose is illustrated in Figure 6.2. In this case the interest lies in the comparison between the unisolated and the isolated building configurations. It

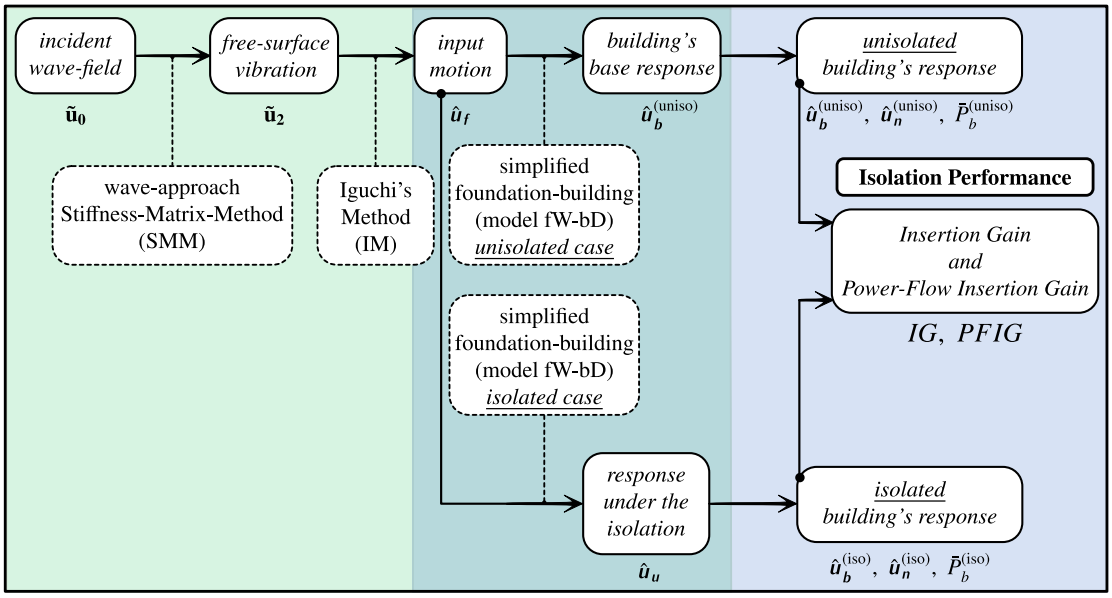

Fig. 6.2 The design framework as used for the evaluation of the *isolation performance* in terms of the Insertion Gain (*IG*) and/or the Power-Flow Insertion Gain (*PFIG*). As the insertion of an isolation system involves a change in the building configuration only, the soil-foundation-building interaction analysis refers to the same input motion $\hat{\boldsymbol{u}}_{\boldsymbol{f}}$ for both the isolated and unisolated case. The added-building effect and the building's response is then obtained for the isolated and unisolated configurations. A comparison of the total mean-vibrational power entering the building in the two configurations ($\bar{P}_b^{(\text{iso})}$ and $\bar{P}_b^{(\text{uniso})}$) provides the *PFIG* referring to the whole building and accounting for both the axial and the bending response.

is worth noticing that, once the soil-foundation-building interaction is approached in separate steps, as illustrated in Figure 6.2, the consideration of different building designs may be addressed starting from the input motion obtained by the soil-foundation interaction analysis. The same does not happen in a fully-coupled analysis (i.e. direct method) where the soil-foundation-building interaction is solved at once. The disadvantage of using such a strategy is twofold: there are no intermediate steps that may provide a conceptual understanding of the correctness of results, for instance the coincidence phenomenon observed for the AFE of a slab foundation; and the increase in computational cost for a parametric design of the building. The steps of the analysis framework in Figure 6.1 and 6.2 refer to a sub-modelling technique, such as used by Hussein et al. [166], that follows naturally by looking at the construction stages of the building, as discussed in Section 3.1, but is often, crucially, overlooked in practice. This strategy may be also adopted with more rigorous methods and models. This is illustrated in the next section where the rigorous analysis framework is presented.

6.2 A rigorous analysis framework

A rigorous model of a portal-frame building (model bF) and of a series of rigid footings (model fB) are illustrated in Figure 6.3. These are the rigorous counterparts of the building and the foundation

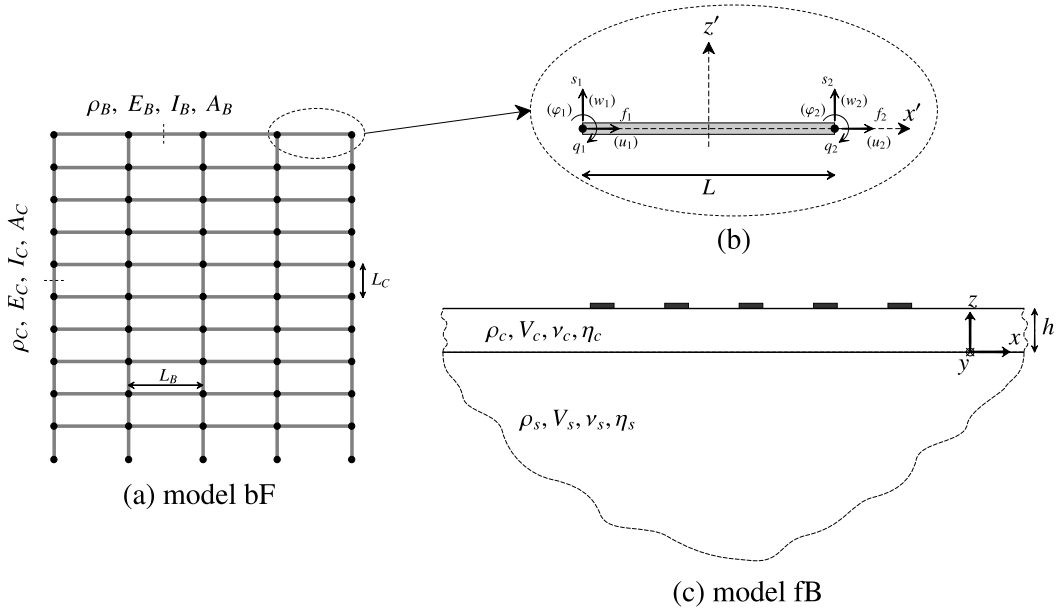

Fig. 6.3 A rigorous model of a portal-frame building (a) based on the Dynamic Stiffness Method of a beam-bar element (b), and of a rigorous Boundary Element Method model of a series of rigid footings on the free-surface of a slab foundation overlying the ground (c).

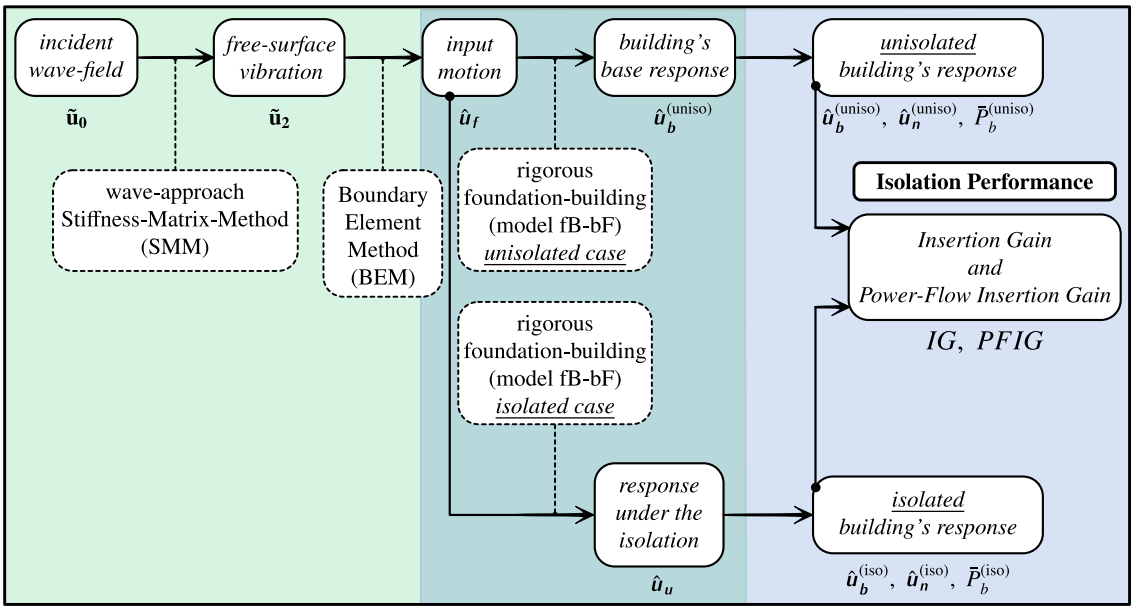

Fig. 6.4 The rigorous analysis framework as used for the evaluation of the *isolation performance* in terms of the Insertion Gain (*IG*) and/or the Power-Flow Insertion Gain (*PFIG*). As the insertion of an isolation system involves a change in the building configuration only, the soil-foundation-building interaction analysis refers to the same input motion $\hat{\boldsymbol{u}}_f$ for both the isolated and unisolated case. The latter is obtained by solving the kinematic interaction of the rigid footings by means of the Boundary Element Method. The added-building effect and the building's response is then obtained for the isolated and unisolated configurations with reference to a Dynamic Stiffness Method of the portal-frame building. A comparison of the total mean-vibrational power entering the building in the two configurations ($\bar{P}_b^{(\mathrm{iso})}$ and $\bar{P}_b^{(\mathrm{uniso})}$) provides the *PFIG* referring to the whole building and accounting for both the axial and the bending response.

models used in Chapter 3 for the evaluation of the added-building effect and the isolation performance. This section introduces these models as a means of validating those of the proposed design analysis framework. It is worth noticing that the sub-modelling technique (or substructure method), as previously adopted, applies also in the case of a rigorous analysis framework. Figure 6.4 shows a diagram for the evaluation of the isolation performance by means of model fB and model bF for the foundation and the building. The kinematic interaction of the rigid footings at the free-surface subjected to an incident wave-field is solved rigorously by means of a Boundary Element approach as seen in Chapter 5. The added-building effect is then evaluated by means of Equations 3.48, with the adoption of the dynamic stiffness matrix at the base of the unisolated and isolated portal-frame building $\widehat{\boldsymbol{K}}_{bF}$ and $\widehat{\boldsymbol{K}}_{bF}^{(\mathrm{iso})}$, and the FRFs matrix $\widehat{\boldsymbol{H}}_{fB}$ obtained by a BEM model of the rigid footings. It is worth noticing that the notation adopted for the SSI and for the isolation performance in Chapter 3 is still valid for the rigorous analysis framework. However, in this case, there are multiple contact

points at the foundation-building interface so that the generalised force and displacement vectors at the base of the building are defined as:

$$\hat{\boldsymbol{u}}_{\boldsymbol{b}} = \left[\hat{u}_{b1}, \hat{w}_{b1}, \hat{\varphi}_{b1}, \ldots, \hat{u}_{br}, \hat{w}_{br}, \hat{\varphi}_{br}, \ldots, \hat{u}_{bn_f}, \hat{w}_{bn_f}, \hat{\varphi}_{bn_f},\right]^T$$

$$\hat{\boldsymbol{f}}_{\boldsymbol{b}} = \left[\hat{s}_{b1}, \hat{f}_{b1}, \hat{q}_{b1}, \ldots, \hat{s}_{br}, \hat{f}_{br}, \hat{q}_{br}, \ldots, \hat{s}_{bn_f}, \hat{f}_{bn_f}, \hat{q}_{bn_f},\right]^T$$

with n_f the number of coupling points at the foundation-building interface. By assuming rigorous foundation and building models, the through-soil and the through-floor coupling in the soil and the building are considered in the analysis. This leads to the matrices $\widehat{\boldsymbol{K}}_{\boldsymbol{bF}}$ and $\widehat{\boldsymbol{H}}_{\boldsymbol{fB}}$ being fully populated.

As a general reference, it is worth to discuss briefly the computational cost associated with the rigorous analysis framework. For the benchmark problem in Figure 6.3 and by considering a 8×8 quadratic elements BEM mesh for each footing, the execution time for the rigorous framework, as in Figure 6.4, for 250 frequencies is approximately 30 minutes on a workstation with a 6-core CPU with 3.50 GHz. This figure may drastically increase when a three-dimensional model of the building and/or a high-fidelity model of the foundation are considered. For the same benchmark problem and with reference to the mean-vibrational power entering at the base of the building, the design analysis framework, as in Figure 6.2, runs in seconds, thus being more suitable for design purposes. In the following a summary of the rigorous foundation and building models is given.

6.2.1 Modelling the foundation

The foundation models used within the rigorous analysis framework may refer to either rigid foundations or rigid footings, as described in Chapter 5. Figure 6.3(c) shows the case of the benchmark #2 of the reference problem, as introduced in Section 3.1.2. By considering an incident wave-field, the soil-foundation interaction analysis may be approached rigorously by means of a BEM approach, as described in Chapter 5. It has been seen that the formulation yields the dynamic stiffness matrix related to the rigid footings, as presented in Equation 5.12. For further reference, this is labelled as $\widehat{\boldsymbol{K}}_{\boldsymbol{fB}}$, with the letter B indicating the BEM approach. The FRF matrix $\widehat{\boldsymbol{H}}_{\boldsymbol{fB}}$ of the rigid foundations and/or footings may be obtained by inversion of $\widehat{\boldsymbol{K}}_{\boldsymbol{fB}}$. Because of the through-soil coupling of the foundations and/or footings, the matrix $\widehat{\boldsymbol{H}}_{\boldsymbol{fB}}$ of model fB is fully-populated. This is used for the added-building effect in the rigorous analysis framework (see Figure 6.4). The vertical, horizontal and rocking compliance terms, obtained by the BEM approach for a single rigid foundation on an

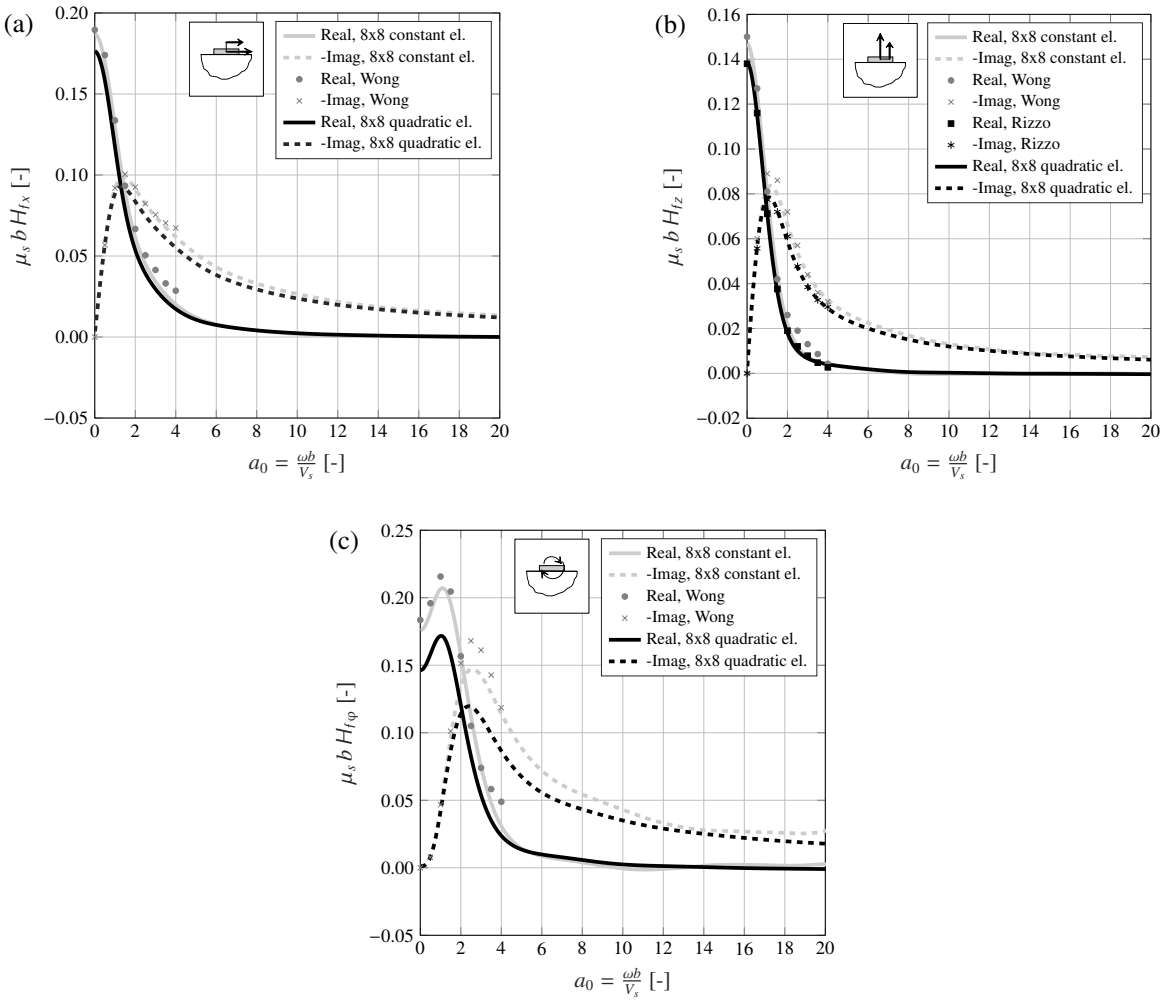

Fig. 6.5 Results for the horizontal (a), vertical (b) and rocking (c) compliance terms of a single rigid foundation on an elastic half-space with $\nu_s = 1/3$ (benchmark #1). Both a constant (8×8 elements) and a quadratic (8×8 elements) formulation are used by means of the BEMFUN and the EDT toolboxes in MATLAB. Comparison is made with the results of Wong & Luco [92] and by Rizzo et al. [215].

elastic half-space with $\nu_s = 1/3$, are reported in Figure 6.5. Comparison is made with the solutions obtained by Wong & Luco [92] and by Rizzo et al. [215] referring to a constant (8×8 elements) and a quadratic (4×4 elements) formulation respectively. Both the results for the constant and the quadratic formulation are reproduced by means of the BEM approach and by using the BEMFUN and the EDT toolboxes in MATLAB. Figure 6.5 shows a good agreement of the resulting compliances with the results reported by the reference studies. Moreover, other results of the BEM approach referring to the case of a rigid footing and to the kinematic interaction have been validated in Chapter 3 and 5 respectively. The resulting rigorous foundation model is three-dimensional: both the radiation of

energy away from the foundation and the scattering of the incident wave-field are properly accounted for. An hysteretic damping model is assumed for both the soil and the slab foundation, as seen in Section 3.2.3. This results in compressional waves being less damped then shear waves, in a a measure defined by Equation 3.9.

6.2.2 Modelling the building

In general, as illustrated for the general scenario in Figure 3.1, a building is a three-dimensional structure that comprises different structural elements such as columns, beams, walls, floors and partitions. As seen in Section 3.1.2, the discussion in this dissertation is restricted to the case of portal-frame buildings that feature an assembly of columns and beams as representative of the main structure. Although the presence of other structural elements (e.g. structural core), may change considerably the distribution of mass, stiffness and damping within the building, this assumption is a necessary sacrifice to simplify the investigation, with the reservation that the presence of a structural core and/or partitions may be the subject of further work.

Modelling a three-dimensional portal-frame building would require, given that a beam-bar formulation is used for each element, the consideration of 6 degrees of freedom at any point of the discretised domain. While this may be a requirement in practice, for instance, for accurate absolute predictions of vibration levels, a two-dimensional representation of a portal-frame building subject to in-plane excitation greatly simplifies the analysis and it is often used by many researchers (see Section 2.4.2). The consideration of the third-dimension extends the coupled axial-bending response of the 2D portal-frame in three dimensions and enables the modelling of torsion in the structural elements. The result is an increased modal density and an additional mechanism of vibration transmission [33] (i.e. torsional motion). The extent to which the latter may be relevant depends greatly on the incident wave-field considered. For instance, it is clear from Section 5.3 that the torsional motion associated with an incident wave-field at $\theta_H = 0$ (i.e. wave-front perpendicular the footings' alignment) is null so that the use of a 2D-portal-frame model should be restricted to this case. On the other hand, in general, torsional motion may arise also from diffracted wave-fields and/or from the coupling of the three-dimensional building to the ground.

It is worth mentioning that the two-dimensional portal-frame model accounts for the conversion of axial and flexural vibration from the column into flexural and axial vibration of the beam, and vice versa. This is an important effect that the 2D portal-frame model is able to capture, unlike, for

instance, the simplified column model bC presented in Chapter 3. Based on this general discussion, the two-dimensional portal-frame model is considered to be a meaningful representation of a portal-frame building, with the understanding that a more detailed study of the influence of considering the third dimension may be relevant for further investigations.

A comment can be made on the use of the beam-bar formulation for each structural element of the portal-frame. As discussed in Section 3.1.2, a rigid-like contact is intrinsically assumed at the foundation-building interface when a beam-bar formulation is considered for the portal-frame. Based on the ability of the rigid contact to follow the incident wave-field, an upper-bound of $60-120$ Hz for the range of frequency has been defined in Section 3.1.2. It is worth stressing that this limitation may be conservative and that higher frequency may be investigated still referring to the beam-bar formulation. The extent to which this may be possible is case-sensitive and depends on the actual contact that materialises at the foundation-building interface. Despite the implications of using a two-dimensional portal-frame building over the three-dimensional counterpart, a model of the former is adopted in this dissertation, believing that the related assumptions are necessary for addressing the problem in its simplest form, and that their influence in assessing isolation performance is likely to be limited.

Application of the Dynamic Stiffness Method

The Dynamic Stiffness Method (DSM) [49] is chosen for modelling the two-dimensional portal-frame building. Compared to the FEM, the DSM has the advantage of referring to exact solutions of the governing equations for the beam-bar element (see Appendix B), hence, it represents a high-accuracy method that does not require a significant discretisation of the model at high frequencies (conversely to the FEM). The application of the DSM to building structures is supported by the work of Cryer [47], Hunt [125] and Talbot [33]. A summary of the method for a 2D portal-frame building is presented in the following, with reference to the Dynamic-Stiffness formulation presented in Appendix B.

A typical element of the two-dimensional portal-frame is illustrated in Figure 6.3(b) and it is defined by its length L, cross-sectional area A, second moment of area I, Young's modulus E and density ρ. Each element of the portal-frame may be assigned with different values of these properties. The beam-bar DSM formulation used in this dissertation is presented in Appendix B and refers to the dynamic longitudinal and transverse response of each element by the analytical solutions for an elastic bar and Euler beam. The latter is a beam model for which shear deformation and the influence of

rotational inertia are assumed negligible. The adoption of the beam-bar element leads to the additional assumption that the longitudinal and the transverse response of the element are uncoupled, which may be a reasonable hypothesis given the low amplitudes involved in ground-borne vibration. For the assumed harmonic motion, the generalised forces at the nodes of the j^{th} element are related to the respective displacements, in the global reference system (x,z), by Equation B.13. The individual dynamic-stiffness matrices $\mathbf{K_g^{(j)}}$ corresponding to each element j of the portal-frame are assembled to yield the global dynamic stiffness matrix $\widehat{K}_g$ by adding the dynamic-stiffness contributions to each degree of freedom of each node shared by the relevant elements, a technique used in the FEM [106] and commonly adopted in structural analysis [168]. In agreement with the notation adopted in Chapter 3 (see Equation 3.11), the letter F is used to denote the use of a portal-frame building model. The relationship between the forces and displacements at the nodes of the DSM model can be then written in an expanded form as follows:

$$\hat{f}_{gF} = \begin{bmatrix} \hat{f}_{bF} \\ \hat{f}_{nF} \end{bmatrix} = \begin{bmatrix} \widehat{K}_{bbF} & \widehat{K}_{bnF} \\ \widehat{K}_{nbF} & \widehat{K}_{nnF} \end{bmatrix} \begin{bmatrix} \hat{u}_{bF} \\ \hat{u}_{nF} \end{bmatrix} = \widehat{K}_{gF}\, \hat{u}_{gF} \tag{6.1}$$

with the subscripts b and n referring to the base and to the internal nodes of the portal-frame model respectively. Imposing the free condition $\hat{f}_{nF} = \mathbf{0}$ in the building's interior, the force-response relation at its base may be written:

$$\hat{f}_{bF} = \widehat{K}_{bF}\, \hat{u}_{bF} = \left[\widehat{H}_{bF}\right]^{-1} \hat{u}_{bF} \quad \text{with} \quad \widehat{K}_{bF} = \widehat{K}_{bbF} - \widehat{K}_{bnF}\left[\widehat{K}_{nnF}\right]^{-1} \widehat{K}_{nbF} \tag{6.2}$$

with $\widehat{K}_{bF}$ the condensed dynamic stiffness matrix at the base of the portal-frame, as used in Equation 3.48a for the added-building effect. A similar formulation, not reproduced here for brevity of discussion, to that seen in Sections 3.1.3 and 3.4.2 may be written also for the SSI associated with the rigorous analysis framework. The **B** matrix for the unisolated and the isolated case are obtained via Equations 3.48 and are reported in the next section. The response at the nodes of the portal-frame may be obtained as:

$$\hat{u}_g = \begin{bmatrix} \hat{u}_{bF} \\ \hat{u}_{nF} \end{bmatrix} = \begin{bmatrix} \widehat{H}_{bbF} & \widehat{H}_{bnF} \\ \widehat{H}_{nbF} & \widehat{H}_{nnF} \end{bmatrix} \begin{bmatrix} \hat{f}_{bF} \\ \hat{f}_{nF} \end{bmatrix} = \widehat{H}_{gF}\, \hat{f}_{gF} \tag{6.3}$$

with the $\widehat{H}_{gF}$ the global FRFs matrix of the portal-frame building obtained by inversion of $\widehat{K}_{gF}$. Given an input motion at the base of the building, the response at the n internal nodes of the portal-frame may be obtained as seen in Equations 3.5 and 3.42 for the unisolated and isolated configurations respectively. Once the response at the nodes of each element is obtained, the response along the element j can be calculated by combining Equation B.9 and B.7, prior transformation of the displacement vector $\hat{\mathbf{u}}_g^{(j)}$ in the local coordinate system as $\mathbf{u_j}$ (see Equation B.12). Besides the displacement field along the element, the corresponding force distribution, in the local coordinate system, can be obtained by using Equation B.6. Once the internal forces are retrieved, the calculation of the mean-vibration power is straightforward, as demonstrated by Langley [162]. As discussed in Section 2.6.4, the mean-vibrational power associated with a structural domain is an important metric that may be adopted for design purposes. By considering a cross-section at x' of the j^{th} element, the mean-vibrational power flow through that section is given by the mean rate at which the forces $f(x'), s(x')$ and $q(x')$ do work against the generalised displacements $u(x'), w(x')$ and $\varphi(x')$. Hence, for a time-harmonic motion at angular frequency ω, the mean-vibrational power through the section at x' of the element j can be found as:

$$\bar{P}_j(\mathbf{x}) = -\frac{1}{2} Re\left\{ i\omega \left[u_j(x') f_j^{\star}(x') + w_j(x') s_j^{\star}(x') + \varphi_j(x') q_j^{\star}(x') \right] \right\} \tag{6.4}$$

with '$\star$' the complex conjugate symbol. The vector symbol $\mathbf{x}$ indicates the location of the cross-section (i.e. x' in the local coordinates) in the global reference system. The power flow analysis of portal-frame buildings is discussed in Section 6.4.1 with the goal of defining the Power-Flow-Insertion-Gain for different incident wave-fields for the reference problem in Section 3.1.2.

Additional comments on the beam-bar formulation

A discussion on two aspects of the beam-bar formulation is needed. The first relates to the damping model assumed for each element. A summary of damping models that may be assigned in a beam-bar formulation has been presented in Section 3.3.2. The same discussion applies for the definition of damping for the j^{th} element of the portal frame. It should be noted that, in general, different damping models may be used for the elements comprising the portal-frame, should any indications of different damping mechanisms arise. Here, the hysteretic damping model as assumed in Chapter 3.3.2 is assigned to all the elements of the portal-frame building.

Another aspect regards the Euler beam formulation adopted in the definition of the DSM used in this dissertation. This model ignores the shear deformation and the rotatory inertia that, in general, should be included in the formulation for more accurate results. It has been demonstrated by Talbot [33] that for problems related to ground-borne vibration, with typical dimensions of the beam element, the maximum error for the natural frequencies ω_n^E is in the order of 8 % for the frequency-range of interest. This value refers to the improved Timoshenko beam model, which considers both the shear deformation and the rotatory inertia and for which an expression for the modified natural frequencies of a simply-supported beam can be found in Timoshenko et al. [216], as reported by Talbot. An additional concern may be the influence of any static axial loading in the beam. This has also been considered by Timoshenko et al. [216], who give an expression of the modified natural frequencies of a simply-supported beam subject to a constant axial force. By considering the latter as large as 10 % of the Euler buckling load for the beam, Talbot [33] finds that the first natural frequency is reduced by 5 %, with the higher modes being affected less. Although the use of the Euler beam model is indeed a simplification, the previous discussion supports this assumption for the investigation of portal-frame buildings in ground-borne vibration. After reviewing the rigorous foundation and building models used in this dissertation, the added-building effect, resulting form their application, is investigated in the next section.

6.3 The Added-Building Effect

It is has been seen in Section 6.2 that the adoption of a rigorous analysis framework leads to the consideration of the multiple coupling points at the foundation-building interface. When the added-building effect is considered, as described in Section 3.5.1, the matrix **B** refers to the motion of the n_f coupling regions before and after the addition of the building. In general, the matrix **B** is a fully-populated, non-symmetric matrix and it is representative of the added-building effect on the displacement amplitude at the foundation level. The i^{th} displacement component of the r^{th} rigid footing (or rigid foundation) after the addition of the building can then be related to the j^{th} displacement component of the m^{th} rigid footing (or rigid foundation) prior the coupling:

$$\hat{u}_{b\,r}^{(i)} = \sum_{m=1}^{n_f} \sum_{j=1}^{3} B_{(r,m)}^{(i,j)}\, \hat{u}_{f\,m}^{(j)} \tag{6.5}$$

The following investigation of the components of the **B** matrix, for both the unisolated and the isolated case, is not intended to be exhaustive for the general added-building effect but rather to be representative of the results for the reference problem presented in Section 3.1.2, which corresponds to common features found in practice for reinforced-concrete buildings. Results are shown for the different simplified and rigorous models of both the foundation and the building, which refer to the assumptions at the points 4 to 7 listed in Section 3.6. Table 6.1 illustrates schematically each tested assumption for the comparison of the results for two different combinations of foundation-building models, as labelled throughout the dissertation. The capital letters refer to the theoretical model (F - DSM portal-frame, C - independent columns, D - independent dampers, B - BEM model, W - Wolf's model), while lower-case letters, associated with the previous one, specify the case of a foundation model with 'f' or a building model with 'b'. Table 6.1 reports also the properties of the FRFs matrix $\widehat{\boldsymbol{H}}_f$ of the foundation, the dynamic stiffness matrix at the base of the building $\widehat{\boldsymbol{K}}_f$ and of the resulting **B** matrix for different foundation-building models. The following discussion investigates the implications of using different foundation-building models on the results for the matrix **B** with

Models	*fB - bF*	*fB - bC*	*fB - bD*	*fW - bF*	*fW - bC*	*fW - bD*
fB - bF	full $\widehat{H}_f$ full $\widehat{K}_b$ full **B**	through-floor	through-floor modal behaviour	through-soil	through-floor through-soil	through-floor through-soil modal behaviour
fB - bC		full $\widehat{H}_f$ sparse $\widehat{K}_b$ full **B**	modal behaviour	through-soil through-floor	through-soil	through-soil modal behaviour
fB - bD			full $\widehat{H}_f$ sparse $\widehat{K}_b$ full **B**	through-soil through-floor modal behaviour	through-soil modal behaviour	through-soil
fW - bF				diag $\widehat{H}_f$ full $\widehat{K}_b$ full **B**	through-floor	through-floor modal behaviour
fW - bC					diag $\widehat{H}_f$ sparse $\widehat{K}_b$ sparse **B**, $\mathbf{B}_{(r,m)} = 0$	modal behaviour
fW - bD						diag $\widehat{H}_f$ sparse $\widehat{K}_b$ sparse **B**, $\mathbf{B}_{(r,m)} = 0$

Table 6.1 Overview of the adopted foundation-building models. The diagonal entries summarise the key features of each model; the off-diagonal entries summarise the physical phenomena that may be investigated by comparing any two foundation-building models: through-floor coupling, through-soil coupling and/or modal response of the building.

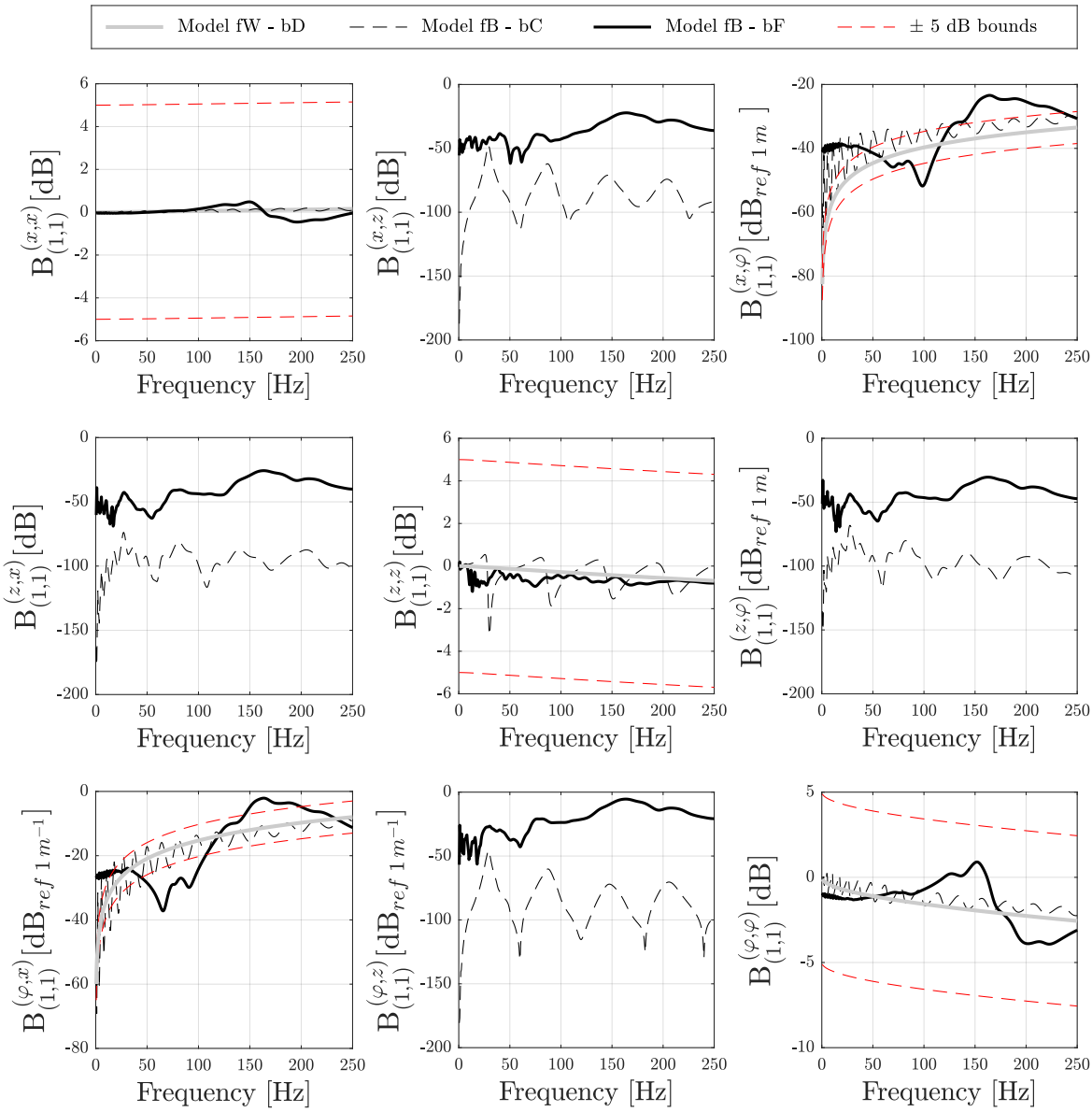

Fig. 6.6 Absolute values in dB of the components of the direct $\mathbf{B}_{(1,1)}$ matrix considering the foundation-building models fW-bD, fB-bC and fB-bF for benchmark #2 with $h = 1.5$ m and $\nu_s = 0.49$. An upper bound and a lower bound of ± 5 dB are shown starting from the values obtained with the simplified model fW-bD.

reference to the diagonal $\mathbf{B}_{(1,1)}$ of the first rigid footing (or foundation) and the off-diagonal $\mathbf{B}_{(1,m)}$ sub-matrices. The purpose is to suggest the design analysis framework, based on the *model fW-bD*, for the evaluation of the added-building effect; this approach is limited by the basic assumptions of neglecting the influence of the through-soil coupling, the through-floor coupling and the modal behaviour of the building.

Figure 6.6 shows the results, for the first rigid footing ($r = m = 1$), for the components of the **B** matrix related to the unisolated case and for the benchmarck #2 (i.e. rigid footings on a slab foundation). For brevity, the results for the isolated case are not reported here, since conceptually they are no different from those seen in Chapter 3, and this investigation is not aimed at commenting on quantitative results. The results obtained with the model fW-bD, which are the same as those obtained in Chapter 3, are in favourable agreement with those obtained with the rigorous model fB-bF. The agreement for the horizontal-rocking terms $B^{(x,\varphi)}$ and $B^{(\varphi,x)}$ is good, although maximum differences up to, approximately, 15 dB are registered. Because of the uncoupled axial and bending behaviour of model bD, and the neglected through-soil coupling for model fW, the terms related to the vertical-horizontal and the vertical-rocking are null for the model fW-bD. The comparison between the results of model fB-bC and model fB-bF gives an idea of the influence of the through-floor coupling within the portal-frame building. For the direct terms $B^{(x,x)}$, $B^{(z,z)}$ and $B^{(\varphi,\varphi)}$, the results for the independent column model are, overall, a good fit to the results of the portal-frame model. The resulting higher modal density associated with the latter, compared to the former, has the effect of 'smoothing' the response at the natural frequencies of the column, although additional amplification and/or attenuation effects are present, inherently due to the coupling of the several columns by floors.

Figure 6.7 shows the results obtained with the rigorous foundation-building model fB-bF for both the direct $\mathbf{B}_{(\mathbf{1},\mathbf{1})}$ and the off-diagonal $\mathbf{B}_{(\mathbf{1},\mathbf{m})}$ matrices. Two general comments follow. First, the terms $B^{(x,x)}$, $B^{(z,z)}$ and $B^{(\varphi,\varphi)}$ referring to the off-diagonal matrix $\mathbf{B}_{(\mathbf{1},\mathbf{m})}$ are, at least, 20 dB smaller than those related to the matrix $\mathbf{B}_{(\mathbf{1},\mathbf{1})}$. This suggests that the contribution of the m^{th} coupling point, with the input motion $\hat{u}_{fm}^{(i)}$, to the response $\hat{u}_{br}^{(i)}$ of the r^{th} footing may be negligible. Second, the matrix components referring to $\mathbf{B}_{(\mathbf{1},\mathbf{m})}$ have, in general, the same order of magnitude when two remote footings are considered, say, the 3$^{\text{rd}}$ and the 5$^{\text{th}}$ footing. This suggests that the through-soil and the through-floor coupling in the soil-foundation and building systems for two remote coupling points are efficient: an input motion $\hat{u}_{fm}^{(i)}$ imposed at the m^{th} footing leads to a response of the coupled system at the r^{th} footing $\hat{u}_{br}^{(j)}$ of similar order of magnitude, regardless of the distance between the m^{th} and the r^{th} footings. Although the rigorous and the design analysis framework may be used, in principle, for evaluating the added-building effect for absolute predictions, as summarised in Section 6.1, the interest in this dissertation is related to the isolation performance as investigated in the next section.

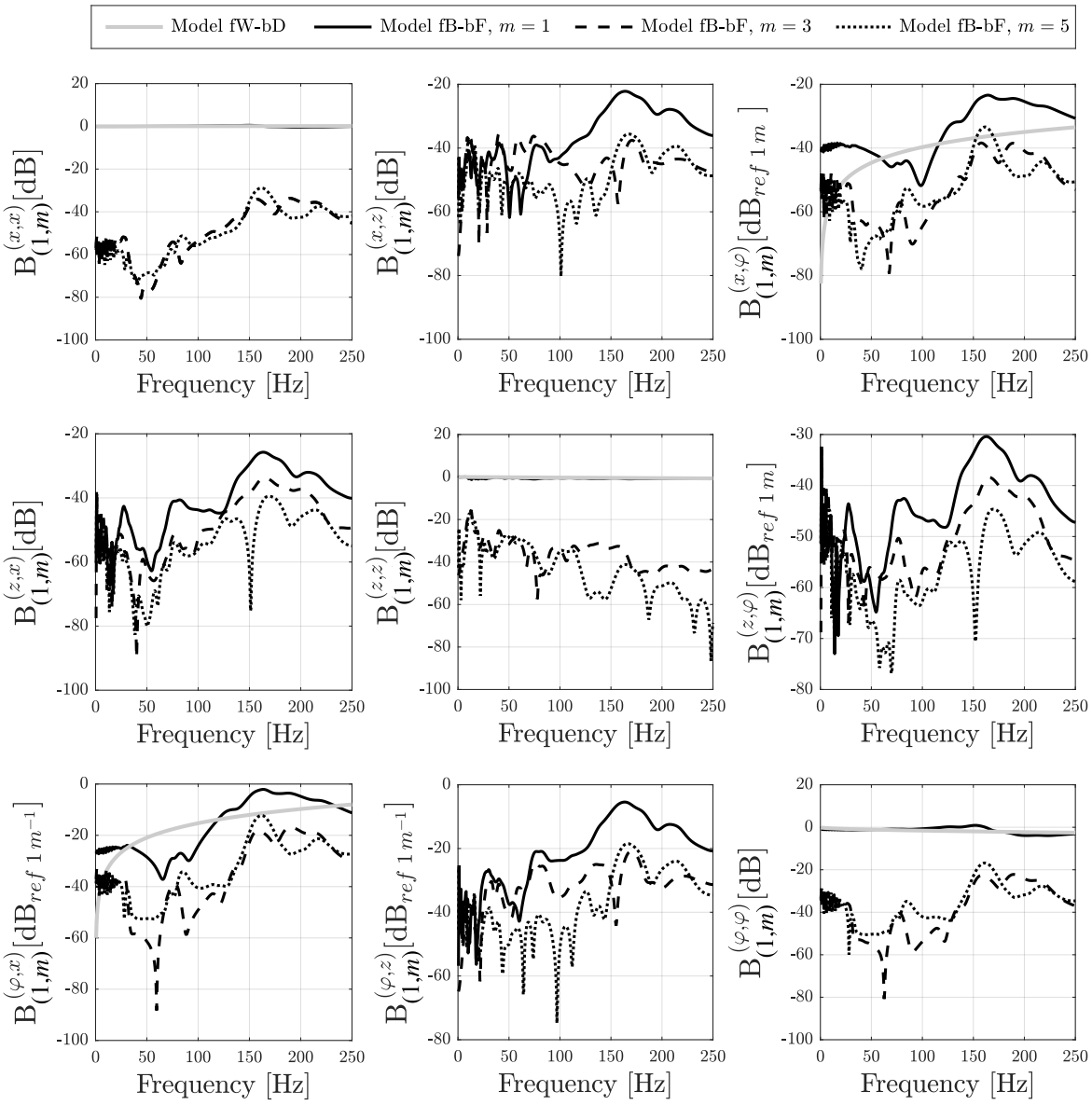

Fig. 6.7 Absolute values in dB of the components of the direct $\mathbf{B}_{(\mathbf{1},\mathbf{1})}$ and off-diagonal $\mathbf{B}_{(\mathbf{1},\mathbf{m})}$ matrices considering the rigorous foundation-building models fB-bF for benchmark #2 with $h = 1.5$ m and $\nu_s = 0.49$. The results of $\mathbf{B}_{(\mathbf{1},\mathbf{1})}$ for the simplified foundation-building model are also reported for reference.

6.4 Base-Isolation performance for different incident wave-fields

In this section, the isolation performance is investigated with reference to the design and the rigorous analysis frameworks introduced in Sections 6.1 and 6.2 respectively. First, the case of normally incident P- and SV-waves are considered. Although they hardly represent an appropriate incident wave-field in ground-borne vibration, they may offer insights into the limit design scenarios of in-

phase, predominantly vertical and/or horizontal input motion $\hat{\boldsymbol{u}}_f$ respectively, at the coupling points. The more realistic scenarios of incident sub-horizontal and sub-vertical P- and SV-waves, and Rayleigh waves, are also explored to observe the difference in isolation performance with reference to the case of normal incidence. The main metric used for the isolation performance is the Power Flow Insertion Gain, but the commonly used Insertion Gain is adopted for comparison of results. A brief summary of the power-flow analysis of portal-frame buildings is presented for introducing the main parameters of reference for the following discussion.

6.4.1 Power Flow analysis of portal-frame structures

The application of the Dynamic Stiffness Method to portal-frame buildings has been discussed in Section 6.2. Equation 6.4 provides the mean-vibrational power at a location **x** of the building referring to a local coordinate x' of the j^{th} element. This represents the time average, over one cycle, of the rate at which the internal forces at x' do work. Let us consider a sub-domain $\mathcal{b}$ of the portal-frame building $\mathcal{B}$ in Figure 6.3(a). The mean-vibrational power associated with the sub-domain $\mathcal{b}$ can be found as:

$$\bar{P}_{\mathcal{b}} = \bar{P}_{\mathcal{b}}^{(\text{out})} - \bar{P}_{\mathcal{b}}^{(\text{in})} = \bar{P}_{\mathcal{b}}^{(\text{diss.})} \tag{6.6}$$

The power $\bar{P}_{\mathcal{b}}$ is the dissipated power within the sub-domain $\mathcal{b}$ in one cycle of vibration and can be found as the difference between the output and input mean-vibrational power at the boundary of the sub-domain. As discussed in Section 2.6.4, this may represent a measure of the vibration associated with the sub-system and can be adopted for the definition of the $PFIG$ as a metric for the isolation performance. It may be argued that both the dissipated power and, consequently, the $PFIG$ depend on the damping model assumed for the building. In lightly damped structures, the values of the dissipated power are small even though the vibration amplitude may be high enough to induce annoyance for the building occupants. However, it has been demonstrated in Section 3.5.2 that, for the single-point coupling model subject to vertical input, the consideration of the dissipated power for the definition of the $PFIG$ is indeed representative of the change in vibration levels when an isolation system is inserted. This gives us confidence that, as long as the building has some form of damping, which is always the case in practice, the $PFIG$ is a meaningful metric for the isolation performance. Figure 6.8 illustrates the result of a power-flow analysis for the reference building (benchmark #2) subject to an normally incident P-wave at $\theta_V = \pi/2$. The mean-vibrational power at the location

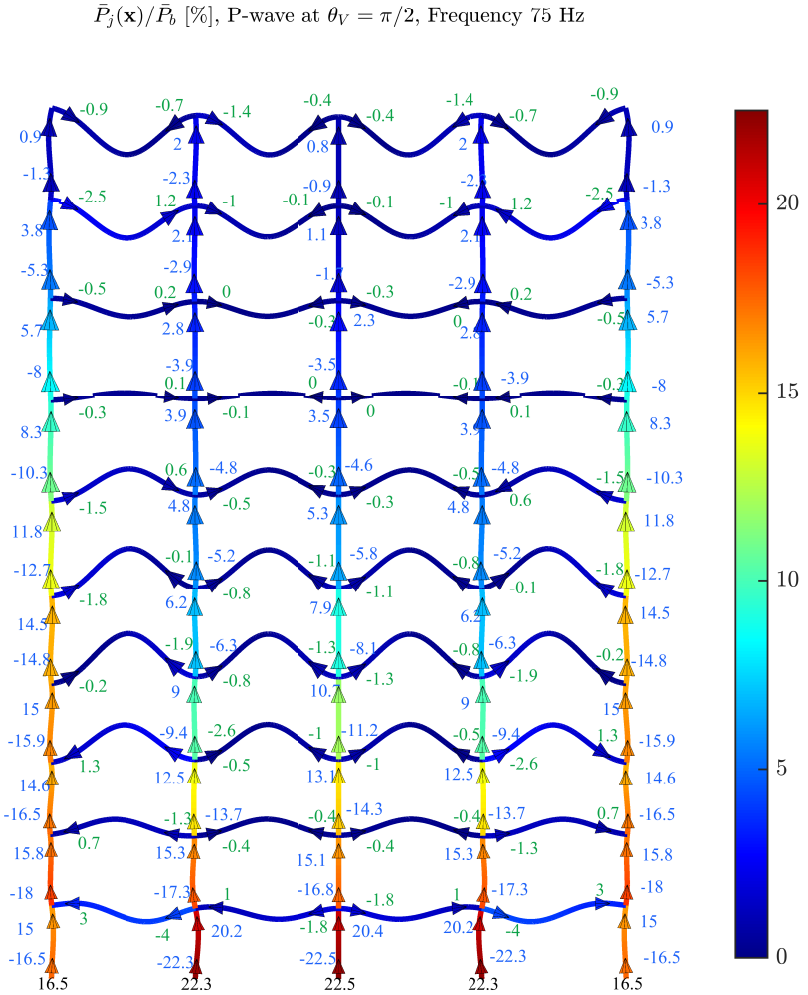

Fig. 6.8 The mean-vibrational power-flow within the unisolated building. The results refer to the benchmark #2 and to a normally incident P-wave at 75 Hz. The mean-vibrational power at a location $\mathbf{x}$ of the j^{th} element $\bar{P}_j(\mathbf{x})$ is shown as percentage of the total mean-vibrational power $\bar{P}_b$ entering the building at its base.

$\mathbf{x}$ associated with the element j is shown as a percentage over the total mean-vibrational power entering the building at its base $\bar{P}_b$. The numbers in blue are associated with the column elements while those in green relate to the floor elements. As a consequence of Equation 6.6, at each node of the portal-frame, continuity must be ensured in that the output power is equal to the input power. An additional comment can be made on the subdivision of the dissipated power between axial and bending motion. A general understanding is that people are more susceptible to vibration normal to the structural member, and also because this is responsible for the radiation of sound [190]. It may be then instructive to consider the dissipated power associated with the bending of the elements

comprising the portal-frame. Equation 6.4 can be then divided into two parts for the axial and bending power associated with the axial and the bending motion of the j element:

$$\begin{aligned} \bar{P}_j(\mathbf{x})^{(ax)} &= -\frac{1}{2} Re\{ i\omega\, u_j(x')\, f_j^{\star}(x') \} \\ \bar{P}_j(\mathbf{x})^{(bend)} &= -\frac{1}{2} Re\{ i\omega \left[w_j(x')\, s_j^{\star}(x') + \varphi_j(x')\, q_j^{\star}(x') \right] \} \end{aligned} \tag{6.7}$$

The latter may be used in the analysis also to investigate the mechanism of vibration transmission associated with an incident wave-field. Different cases of normally and obliquely incident P- and SV-waves, and of Rayleigh waves, are considered in the follwing with the goal of defining the isolation performance in each case. This may help with the definition of guidelines, based on the results of the design framework for the design of base-isolated buildings.

6.4.2 The case of normally incident P- and SV-waves

Normally incident P- and SV-waves are first considered as limit scenarios. Although these particular incident wave-fields are hardly experienced in ground-borne vibration, they may provide useful insights for comparison with the results of the single-point coupling model investigated in Chapter 3.

Vertical input motion

A normally incident P-wave has a resulting in-phase vertical input motion $\hat{\boldsymbol{u}}_f$ at the coupling points of the building. This scenario is consistent with the case of a purely vertical input motion for the single-point coupling model examined in Section 3.5.2. The added-building effect and the response of the isolated and unisolated building may be obtained with reference to the notation already presented in Section 3.1.3 and 3.4.2 respectively. A power-flow analysis of the isolated and unisolated building follows from Section 6.4.1. The isolation performance may be then obtained in terms of *IG* and/or *PFIG* as discussed in Section 2.6.4. The difference between the two metrics is evident in that the *PFIG* refers to a sub-domain of the building and considers all the DoFs associated with the motion, while the *IG* refers to specific locations within the building and to a single direction of vibration. The *IG* related to the vertical DoF, and to locations at the base (green lines) and at the top (red lines) of the building, is shown in Figure 6.9. Although both the building and the input motion $\hat{\boldsymbol{u}}_f$ are symmetrical, important differences are found for the vertical *IG*. This is the result of two effects: first, the added-building effect changes the input motion so that, in general, horizontal and rocking

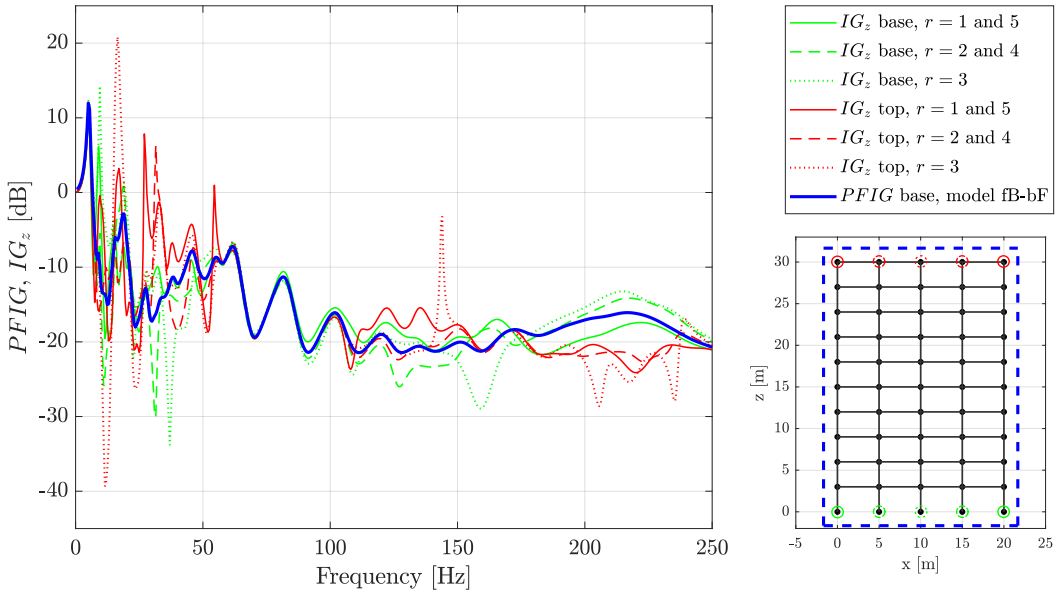

Fig. 6.9 Isolation performance referring to the benchmark #2 and reported in terms of both the $PFIG$ for the whole building (blue line) and the IG_z in the vertical direction for points at the bottom (green lines) and at the top (red lines) of the building. A normally incident P-wave is considered and the results refer to the rigorous SMM-BEM-model fB-bF. An isolation frequency f_S = 5 Hz and a slab foundation thickness of h = 1.5 m are considered.

motion may be associated with the purely vertical response of the building at its base; second, the building remains a complex multi-modal structure for which the response at any location cannot be representative of the whole building. It is possible to notice a frequency-band around $70 - 100$ Hz for which no differences are found. Because of the considered wave-field, this region of the frequency spectrum is mostly associated with axial vibration of the columns. This is clearly shown in Figure 6.8 where the power-flow analysis for the unisolated building at 75 Hz indicates the majority of power "flowing" through the columns. It follows that the through-floor coupling is negligible and that the system converges to a model of independent columns, responding in axial vibration, with additional mass and stiffness contributions provided by the floors and concentrated at the floor-level. The two-dimensional portal-frame may be then described by a single-point coupling model excited by a vertical input. Hence, the results of Section 3.5.2 apply in this frequency-range and the vertical IG has the same value for multiple locations within the "equivalent column". Moreover, as seen in Section 3.5.2, the vertical IG is equivalent to the $PFIG$. The latter can be calculated for the whole building by considering the $\bar{P}_b$ entering the building, at its base, in the isolated and unisolated configuration. This value is also plotted in Figure 6.9 (blue line); as expected, between 70 and 100 Hz

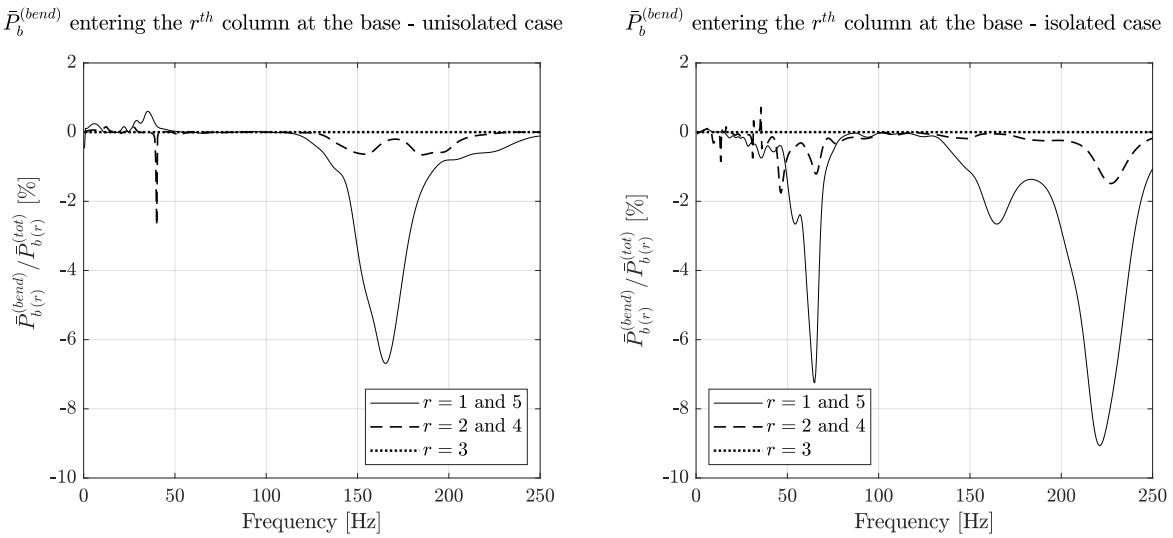

Fig. 6.10 Percentage of mean-vibrational power associated with bending motion at the base of the r^{th} column over the total mean-vibrational power $\bar{P}_{b(r)}$ entering the same column. Values for the unisolated (left) and isolated case (right) are shown.

the *PFIG* and the *IG* converge to the same value. This feature serves as a conceptual example for the application of the power-flow for the analysis of the mechanism of vibration transmission within the building. The predominant axial vibration can also be visualised by considering the division between the bending and the axial mean-vibrational power entering the building. Figure 6.10 shows the mean-vibrational power associated with bending motion at the base of each column as a percentage of the total mean-vibrational power entering the same column. The previous argument of the axial motion being dominant over the frequency range $70-100$ Hz is confirmed by the low quota of the bending mean vibrational power, in the same frequency range, at all the coupling points at the base of the building. As expected, along the frequency spectrum, a higher influence of the bending motion is shown for the peripheral columns, while no bending motion is associated with the 3$^{\text{rd}}$ column in accordance with the symmetry condition of no rocking and no horizontal motion possible for a vertical input.

An additional consideration regards the spatial variability of the *IG* and the *PFIG* for different locations and different sub-domains of the building. With the idea that the motion perpendicular to the member is responsible for radiating sound in the room, the *IG* for horizontal motion (dashed gray lines) at the mid-height of the column elements and the *IG* for the vertical motion (solid gray lines) at the mid-span of the beam elements are plotted in Figure 6.11. As mentioned earlier a large variability is expected, in both cases, due to the multi-directional motion and to the multi-modal

response of the building. The $PFIG$ for the whole building (blue line) is also shown together with the $PFIG$ calculated with reference to the mean power dissipated in two different rooms at the top (red line) and bottom (green line) of the building. Although differences of up to 10 dB are found, the same trend of the $PFIG$ is valid for different parts of the building, indicating that the isolation is beneficial for both higher and lower floors. If the $PFIG$ is regarded as a representative metric for the isolation performance, different values can be obtained for different sub-domains of the building. This is plotted in Figure 6.12(b) for each room comprising the building (gray lines) and compared with the $PFIG$ for the whole building (blue line), and with the limit value of Equation 3.73, which refers to the design analysis framework with a vertical input. Maximum differences of up to 18 dB are found for the isolation performance referring to different rooms, indicating a large variability of the expected reduction in vibration levels within the building. This is an intrinsic characteristic of the problem that depends on the complex dynamic response of the unisolated and isolated building. It demonstrates that,

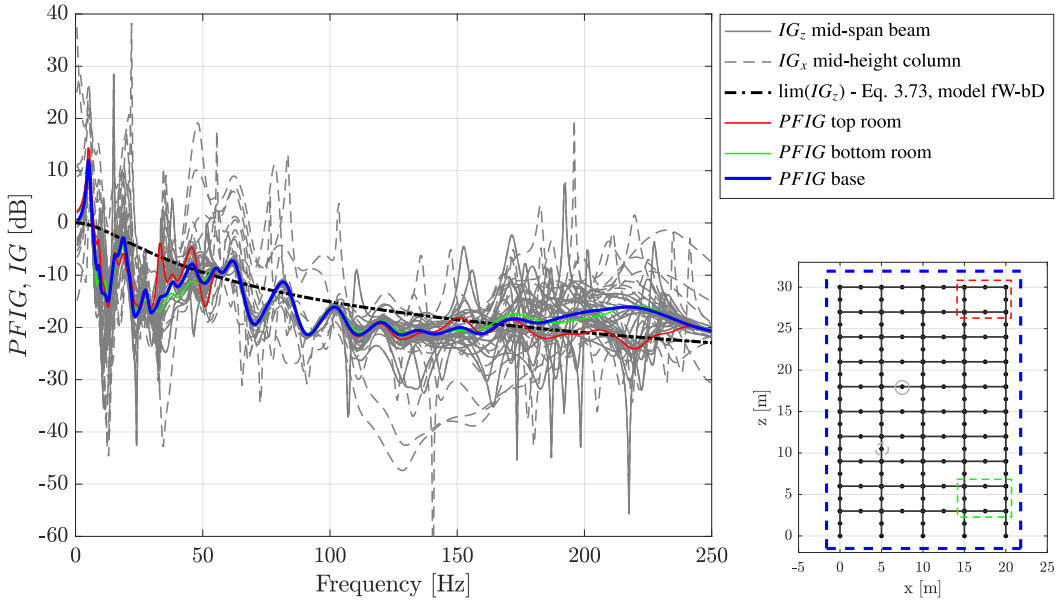

Fig. 6.11 Results of the $PFIG$ and the IG for the soil-foundation-building system (benchmark #2) subjected to a normally incident P-wave. The results refer to the rigorous framework SMM-BEM-model fB-bF and to the design framework SMM-IM-model fW-bD. An approximation of the latter, for a purely vertical input, is given by the limit value in Equation 3.73 and reported here (chained black line). (a) Comparison between the $PFIG$ for the whole building (blue line), the IG_z in the vertical direction for points at the mid-span of the beam elements (solid gray lines), the IG_x in the horizontal direction for points at the mid-height of the column elements (dashed gray lines), and the $PFIG$ referring to two rooms at the top (red line) and bottom (green line) of the building. An isolation frequency $f_S = 5$ Hz and a slab foundation thickness of $h = 1.5$ m are considered.

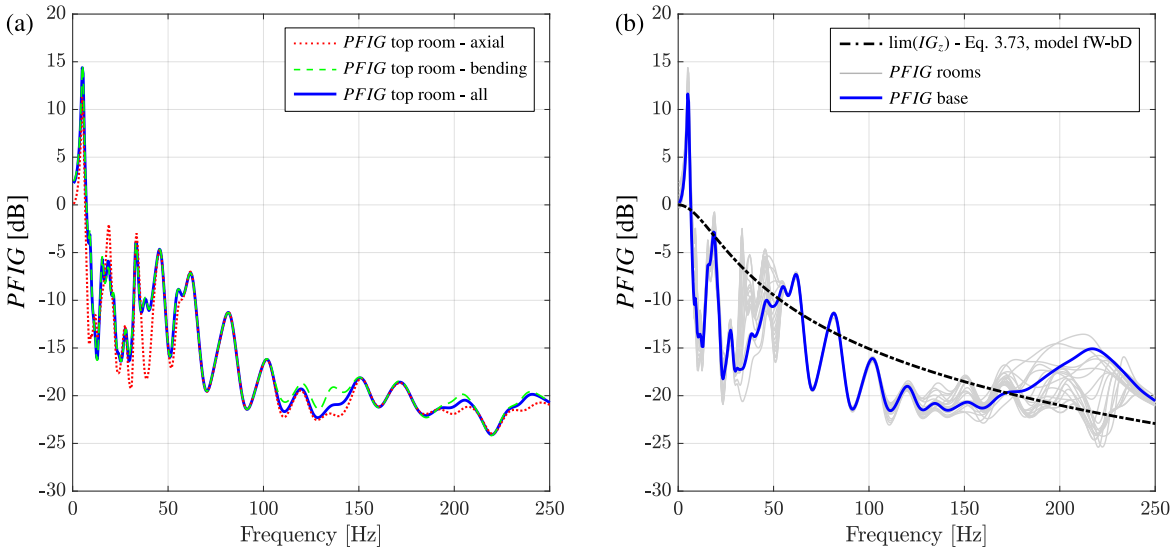

Fig. 6.12 Comparison between the *PFIG* for the whole building (blue line), (a) the *PFIG* for a room at the top (red line) and/or botton (green line) of the building, and (b) for each individual room in the building (gray lines). (b) The limit value of Equation 3.73 is also reported. An isolation frequency $f_S = 5$ Hz and a slab foundation thickness of $h = 1.5$ m are considered.

even by considering deterministic mechanical and geometrical properties for the soil-foundation-building system (as done in this dissertation), care should be taken to define the isolation performance with a unique, frequency-dependent value. Even for a symmetric building and a symmetric input motion, such the case discussed here, large spatial variability of the isolation performance should be expected. An additional comment may regard the use of the mean-vibration power associated with only bending motion or the complete structural response of the considered building's sub-domain. Figure 6.12(a) plots the results of the *PFIG* for the three alternatives of considering axial, bending or the complete response of the room at the top of the building. Maximum differences up to 2 dB are found between the results obtained with the total or the bending mean-vibrational power. The *PFIG* referring to the total mean-vibrational power will be used in the following with the understanding that the character of the general discussion presented here does not rely on this detail.

Horizontal input motion

A similar analysis may be carried out for the case of normally incident SV-waves. An in-phase horizontal input motion $\hat{\boldsymbol{u}}_f$ at the coupling points is obtained by means of Iguchi's Method (IM). At this point, the design analysis framework may be adopted by considering a horizontal input for the simplified model fW-bD. The comparison of the isolated and unisolated building response provides

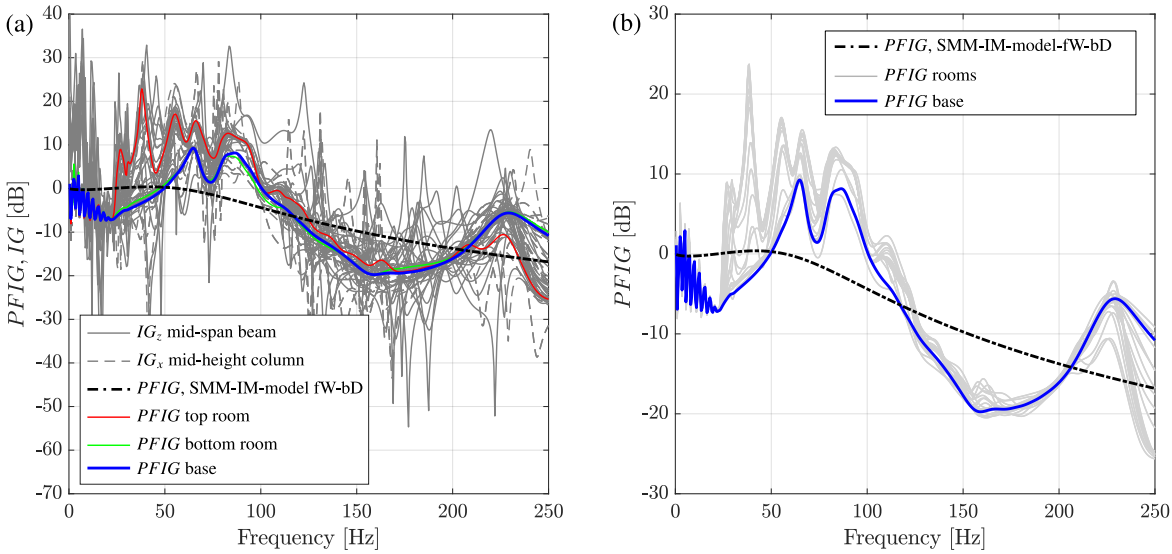

Fig. 6.13 Results of the $PFIG$ and the IG for the soil-foundation-building system (benchmark #2) subjected to a normally incident SV-wave. The results refer to the rigorous framework SMM-BEM-model fB-bF and to the design framework SMM-IM-model fW-bD (chained black line). (a) Comparison between the $PFIG$ for the whole building (blue line), the IG_z in the vertical direction for points at the mid-span of the beam elements (solid gray lines), the IG_x in the horizontal direction for points at the mid-height of the column elements (dashed gray lines), and the $PFIG$ referring to two rooms at the top (red line) and bottom (green line) of the building. (b) Comparison of the $PFIG$ for the whole building (blue line) and the $PFIG$ referring to each room (light gray lines). An isolation frequency $f_S = 5$ Hz and a slab foundation thickness of $h = 1.5$ m are considered.

a frequency-dependent value of the $PFIG$, as plotted in Figure 6.13 (chained black line), which is the result of the design staged approach as schematically illustrated in Figure 6.2.

The rigorous analysis framework is adopted to obtain results for the $PFIG$ for the whole building (blue line), the IG in the lateral and vertical directions at the mid-height of columns (dashed gray lines) and at the mid-span of beams (solid gray lines), and the $PFIG$ referring to two rooms at the top (red line) and bottom (green line) of the building. These results, as shown in Figure 6.13(a), confirm the large spatial variability of the isolation performance. Similarly to that shown for the case of incident P-waves, the PFIG referring to each room of the building is plotted in Figure 6.13(b). While there is a strong influence of the resonances and the anti-resonances in the isolated and unisolated building for the results in terms of the IG, the $PFIG$ results provide a smoother trend that may be easier to decipher, although not being necessarily more representative of the IG in terms of the "correct" value of isolation performance. Also in this case, differences of up to 26 dB may be found for the isolation performance as "observed" in different rooms of the building. It should be stressed that such spatial

variability could be partly due to the adoption of a two-dimensional portal-frame building model, which exhibits a strong modal behaviour. This represents a limitation since real buildings, which are three-dimensional and composed of two-dimensional floors, walls and partitions, are likely to have increased modal density and, as a result, a reduced spatial variability of the isolation performance. This is a matter open to questions that may well benefit from further investigations.

Overall, as can be seen from Figure 6.13(a), the *PFIG*, referring to the mean vibrational power entering the whole building, provides some form of "average" performance, when compared with the values of the *IG* at different locations. Figure 6.13 shows that the design analysis framework, as described in Section 6.1, provides a value of the *PFIG* that matches the trend observed for the results of the rigorous analysis framework. Although an in-phase horizontal input motion is hardly representative of ground-borne vibration, it is worth noticing that, in this case, potential amplifications are expected in the range of $20 - 120$ Hz, which is of interest for induced vibration and re-radiated noise within the building. We find then an incident wave-field for which mounting a building on springs may be actually detrimental for vibration and re-radiated noise: a scenario that is not foreseen by means of typical simplified models used for base-isolated buildings (i.e. mass on a spring model). The extent to which this may actually occur is investigated next by considering the case of an incident Rayleigh wave, which is more representative of the ground-borne vibration induced by surface railways.

6.4.3 The case of incident Rayleigh waves

As mentioned in Appendix C, a Rayleigh wave is confined to the surface of the elastic and homogeneous half-space (i.e. the ground), and involves a retrograde elliptical motion at the free-surface, thus both horizontal and vertical particle motion. The latter and the reduced horizontal wavelength associated with Rayleigh waves represent the major differences with the normally incident wave-fields considered in previous sections. Hence, the input motion $\hat{\boldsymbol{u}}_f$ associated with the coupling points comprises the horizontal, vertical and rocking motion of the rigid regions and includes, generally, a phase difference at each coupling point. Analogous to the cases examined in Section 6.4.2, Figure 6.14 shows the results for the *PFIG* and *IG* obtained with the rigorous framework as well as those referring to the design analysis framework (chained black line). The latter provides a good fit to the isolation performance obtained with the rigorous framework, which inherently accounts for the spatial variability of the response within the building. A plot of the *PFIG* associated with each

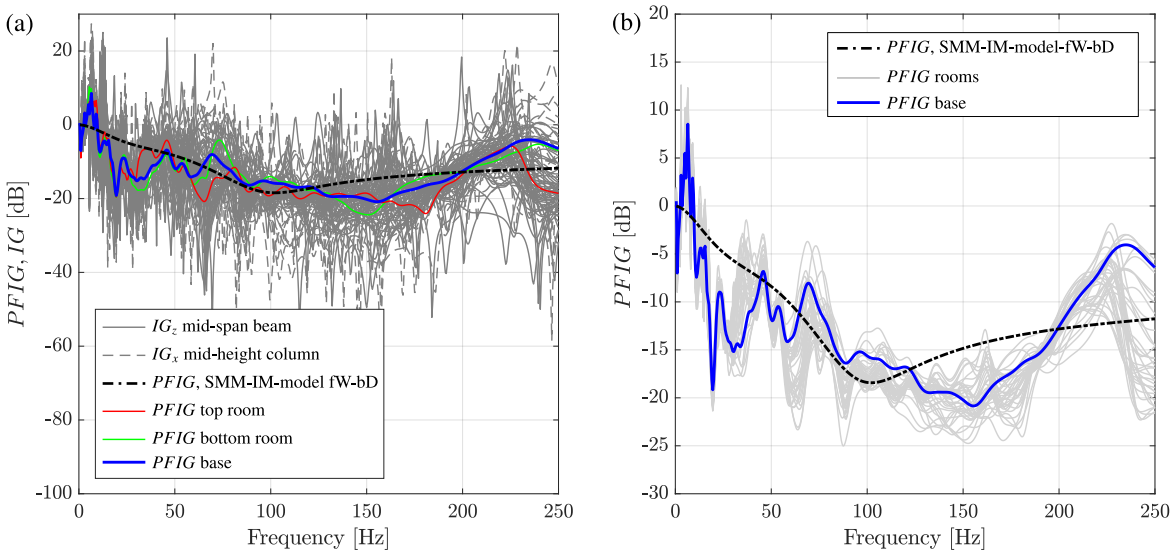

Fig. 6.14 Results of the $PFIG$ and the IG for the soil-foundation-building system (benchmark #2) subjected to a Rayleigh wave. The results refer to the rigorous framework SMM-BEM-model fB-bF and to the design framework SMM-IM-model fW-bD (chained black line). (a) Comparison between the $PFIG$ for the whole building (blue line), the IG_z in the vertical direction for points at the mid-span of the beam elements (solid gray lines), the IG_x in the horizontal direction for points at the mid-height of the column elements (dashed gray lines), and the $PFIG$ referring to two rooms at the top (red line) and bottom (green line) of the building. (b) Comparison of the $PFIG$ for the whole building (blue line) and the $PFIG$ referring to each room (light gray lines). An isolation frequency $f_S = 5$ Hz and a slab foundation thickness of $h = 1.5$ m are considered.

room of the building (see Figure 6.14(b)) shows a spatial variability of the isolation performance up to 27 dB at relatively high frequencies, somewhat of the same order as the value obtained for the case of a normally incident SV-wave. The isolation performance,with reference to the design framework and in terms of attenuation of vibration levels expressed as the $PFIG$, goes from a value of 4 dB at 20 Hz, reaches a maximum of 18.5 dB at around 100 Hz and a reduced value of about 12 dB at 250 dB. A reduced attenuation is then obtained in this case when compared to the results for a normally incident P-wave (see Figure 6.12). However, Figure 6.14 illustrates that the potential amplification of vibration levels seen for the case of normally incident SV-wave is hardly obtainable with an incident wave-field more representative of ground-borne vibration (i.e. a Rayleigh wave).

Figure 6.15 shows a power-flow analysis of the unisolated (left) and the isolated (right) portal-frame building subjected to an input motion $\hat{\boldsymbol{u}}_f$ associated with a Rayleigh wave. By comparison with the power-flow analysis of Figure 6.8 for a normally incident P-wave, it is possible to notice that, in this case, the majority of the total mean-vibration power is entering the first column. This is because

of the assumed wave-field: an incident Rayleigh wave that meets the first column and then decays at a rate that depends on the material damping in the soil η_s. Because of the plane-wave excitation, no radiation damping is associated with the incident wave-field, and the effect of the material damping on the free-surface motion, hence on the input motion $\hat{u}_f$, can be calculated by using Equation 4.1. For the reference values in Table 3.1, as used for the results in Figure 6.14, the frequency-space wave amplitude ratio at different coupling points may be obtained as:

$$\left|\frac{\hat{u}_{2\,(r)}}{\hat{u}_{2\,(1)}}\right| = \left|\frac{e^{-ik_x x_r}}{e^{-ik_x x_1}}\right| = \left|e^{-ik_x x_r}\right| \tag{6.8}$$

with $k_x = \omega/V_R'$ the complex horizontal wavenumber for Rayleigh waves, the first footing is taken at the origin of the coordinate system (i.e. $x_1 = 0$) and x_r indicates the x coordinate of the r^{th} footing's centroid. It follows that the free-surface motion associated with the following coupling points, with $r = 2\ldots5$, has a magnitude attenuated by about 3.3 dB, 6.9 dB, 10.2 dB and 13.5 dB with respect to

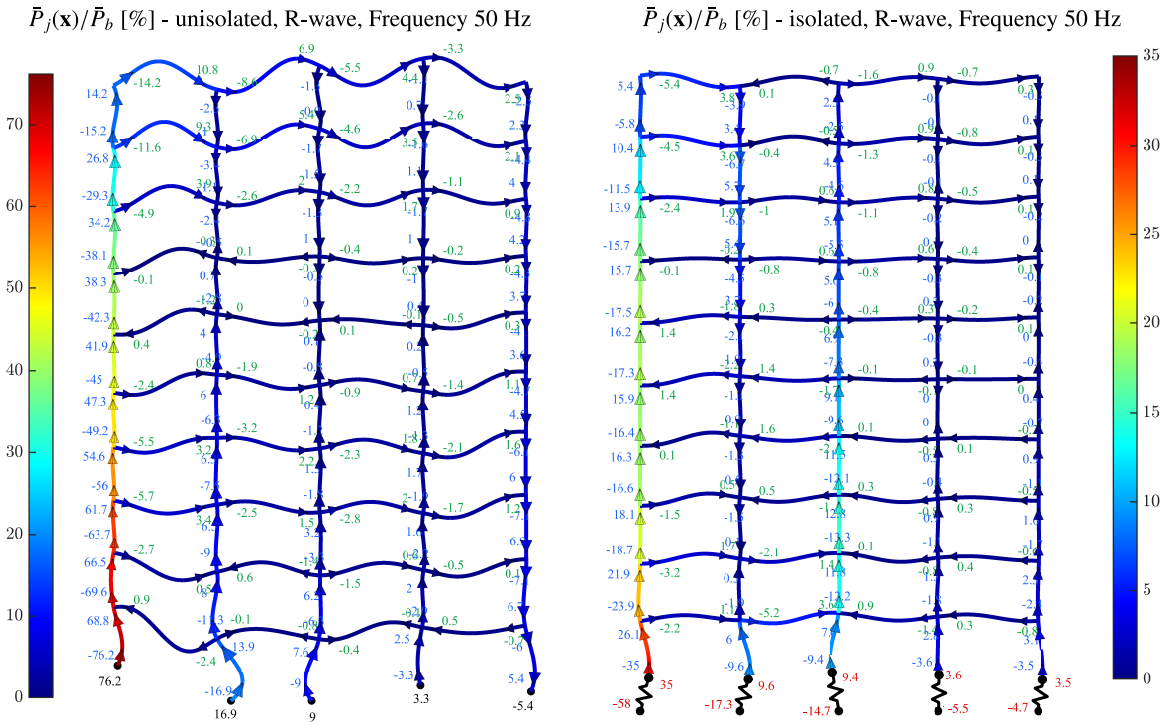

Fig. 6.15 Power-flow analysis of the portal-frame building (benchmark #2) subjected to an input motion $\hat{\mathbf{u}}_f$ associated with a Rayleigh wave. The unisolated (left) and isolated (right) configurations of the building are examined with the coloured scale referring to the total mean-vibrational power $\bar{P}_j(\mathbf{x})$, at the location $(\mathbf{x})$ of the j^{th} element, as a percentage of the total mean-vibrational power $\bar{P}_b$ entering the unisolated or the isolated building, respectively, at its base. An isolation frequency $f_S = 5$ Hz and a slab foundation thickness of $h = 1.5$ m are considered.

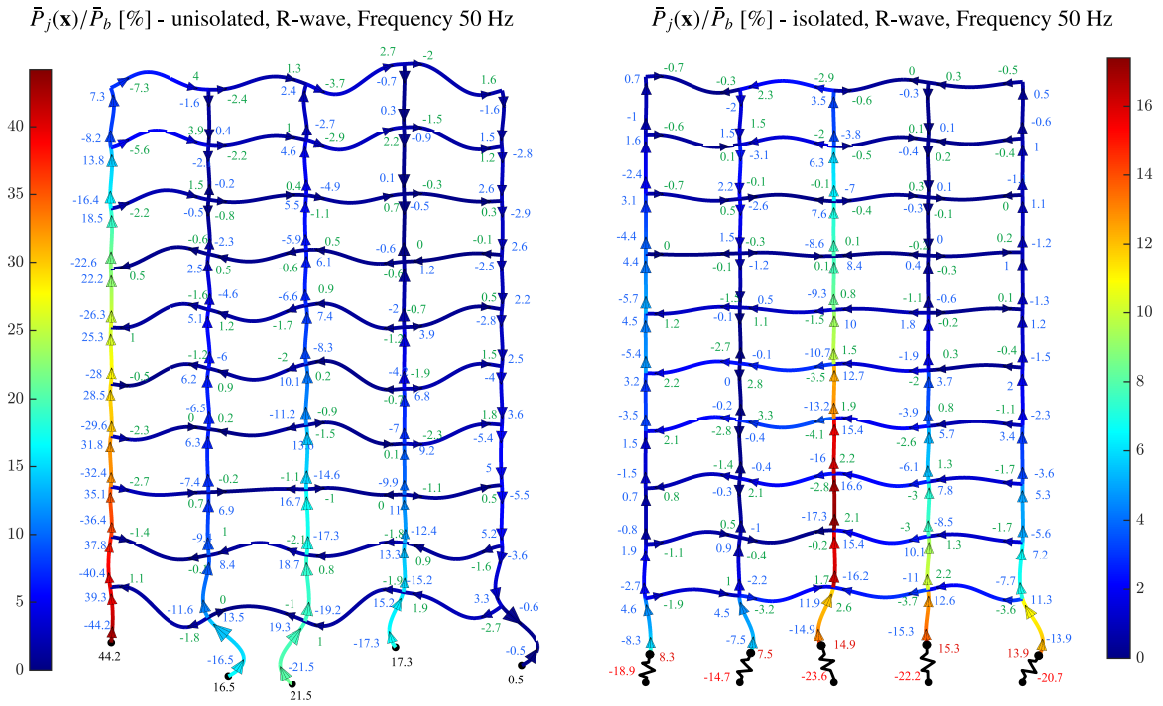

Fig. 6.16 Power-flow analysis of the portal-frame building (benchmark #2) subjected to an input motion $\hat{\boldsymbol{u}}_f$ associated with a Rayleigh wave. The unisolated (left) and isolated (right) configurations of the building are examined with the coloured scale referring to the total mean-vibrational power $\bar{P}_j(\mathbf{x})$, at the location $(\mathbf{x})$ of the j^{th} element, as a percentage of the total mean-vibrational power $\bar{P}_b$ entering the unisolated or the isolated building, respectively, at its base. Lightly damped soil and concrete are considered, with $\eta_s = \eta_c = 0.01$, resulting in a small variation on the magnitude of the input motion across the footprint of the building. An isolation frequency $f_S = 5$ Hz and a slab foundation thickness of $h = 1.5$ m are considered.

the free-surface motion at the first footing's centroid. By virtue of Equations 5.44, we understand that, at least, the same order of attenuation is expected for the vertical and horizontal input motion $\hat{u}_{fr}$ at the r^{th} footing. This may explain, in qualitative terms, the power-flow analysis in Figure 6.15, with an important share of power dissipated in the upstream part of the building. A comparative analysis may be undertaken by considering a lower value of material damping in the soil $\eta_s = 0.01$ and in the slab $\eta_c = 0.01$. Figure 6.16 shows the power-flow related to this case for the unisolated (left) and isolated (right) building. In this case, the free-surface motion associated with the following coupling points, with $r = 2 \ldots 5$, has a magnitude attenuated by, at most, 1.3 dB with respect to the free-surface motion at the first footing's centroid. As a result, the power-flow analysis shows a more uniform distribution of the total mean-vibrational power at the coupling points, especially in the isolated case, compared with the previous case in Figure 6.15. However, it should be stressed that the power-flow

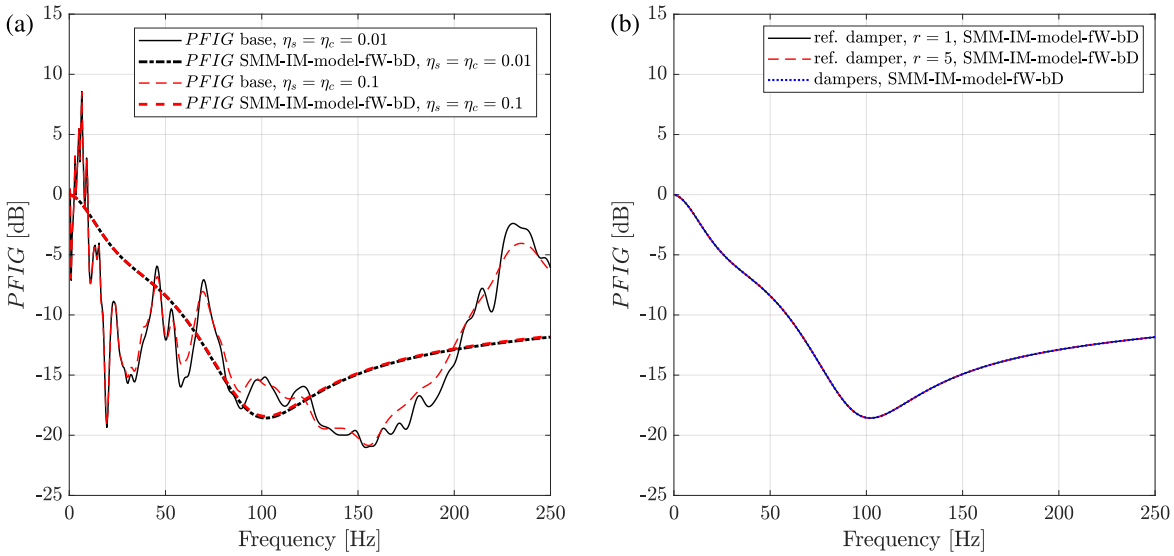

Fig. 6.17 (a) Comparison of the *PFIG* related to the mean-vibrational power entering the base of the building, obtained for a damped (red lines) and a lightly damped (black lines) soil-foundation system. The results for $\eta_s = \eta_c = 0.1$ are the same as those reported in Figure 6.14. (b) Comparison of the *PFIG* as obtained by the design analysis framework with reference to a single-point coupling model fW-bD for the r^{th} coupling point and the result obtained with reference to the total mean-vibrational power entering the series of dampers representing the building as a whole. An isolation frequency $f_S = 5$ Hz and a slab foundation thickness of $h = 1.5$ m are considered.

depends not only on the motion at the section considered, but also on the internal dynamic forces at that point of the complex portal-frame structure (see Equation 6.4). Hence, the argument that, for a sufficiently damped incident Rayleigh wave, the majority of the mean-vibrational power is dissipated in the upstream part of the building can be only supported qualitatively on the basis that the input motion across the footprint of the building varies significantly in magnitude.

It is instructive to compare the isolation performance obtained for the case of a lightly damped soil-foundation system and the one investigated in Figure 6.14. Figure 6.17(a) shows such a comparison in order to acknowledge the influence of the material and, potentially, of the radiation damping, on the isolation performance. These, in general, deliver different magnitude levels of the input motion at the coupling points for a given incident wave-field (i.e. for a given source of vibration). While the latter may play an important role for the power-flow within the portal-frame building (as seen in Figures 6.15 and 6.16), it does not seem to bear significance for the isolation performance. Figure 6.17(a) shows maximum differences of the *PFIG*, between the two cases, in the order of 2 dB, at most. This indicates that, as long as the horizontal, vertical and rocking motion at a given coupling point are in the same proportions and have the same phase difference, which depend on

the particular source of vibration, no significant differences of the *PFIG* are found with regard to having an input motion with a substantially different magnitude.

This last argument also indicates the validity of the design analysis framework as used to obtain the *PFIG* in Figure 6.17(a) (thick lines). Even though the design framework refers to a single-point coupling model as presented in Chapter 3, the staged approach presented schematically in Figure 6.2 is able to properly capture the added-foundation effect of the rigid footings (see Chapter 4 and 5) and obtain the input motion for each footing with comparable proportions and phase differences between the horizontal, vertical and rocking motion as the rigorous counterpart. Then, the use of the simplified foundation-building model fW-bD, referring to any of the coupling points, provides, approximately, the same value of the isolation performance (see Figure 6.17(b)). This is possible because of the regularity of the portal-frame building considered in the reference problem, which basically ensures the same added-building effect with respect to each footing. It should be noted that, for a general building with different columns' size and, perhaps, a different subdivision of the total mass amongst the columns (i.e. different isolation stiffness for each bearing), the isolation performance with the design analysis framework should be calculated with reference to the total mean-vibrational power entering the series of dampers representing the building as a whole. This value is reported with the label *dampers* in Figure 6.17(b) for the reference problem (benchmark #2 with the soil and the slab lightly damped). As anticipated, the isolation performance calculated as such is equal to the isolation performance referring to the single-point coupling model referring to any of the coupling points. In the following the case of an obliquely incident P- or SV-wave is investigated in order to assess how the isolation performance changes depending on the free-surface particle motion related to different incident wave-fields.

6.4.4 The case of incident P- and SV-waves at an angle θ_V

Different incident P- and SV-waves are considered in the following: sub-horizontal ($\theta_V = \pi/8$), diagonal ($\theta_V = \pi/4$) and sub-vertical ($\theta_V = 3\pi/8$). They all involve a free-surface particle motion that, in general, includes both horizontal and vertical motion. These in turn lead to a general input motion $\hat{\boldsymbol{u}}_f$ that includes horizontal, vertical and rocking motion of each rigid footing. Figure 6.18 shows the results for the *PFIG*, referring to the total mean-virbational power entering the building, for (a) P-waves and (b) SV-waves with different values of the incidence angle θ_V. These are compared with the results of the closed-form expression in Equation 3.73, which refers to a vertical input,

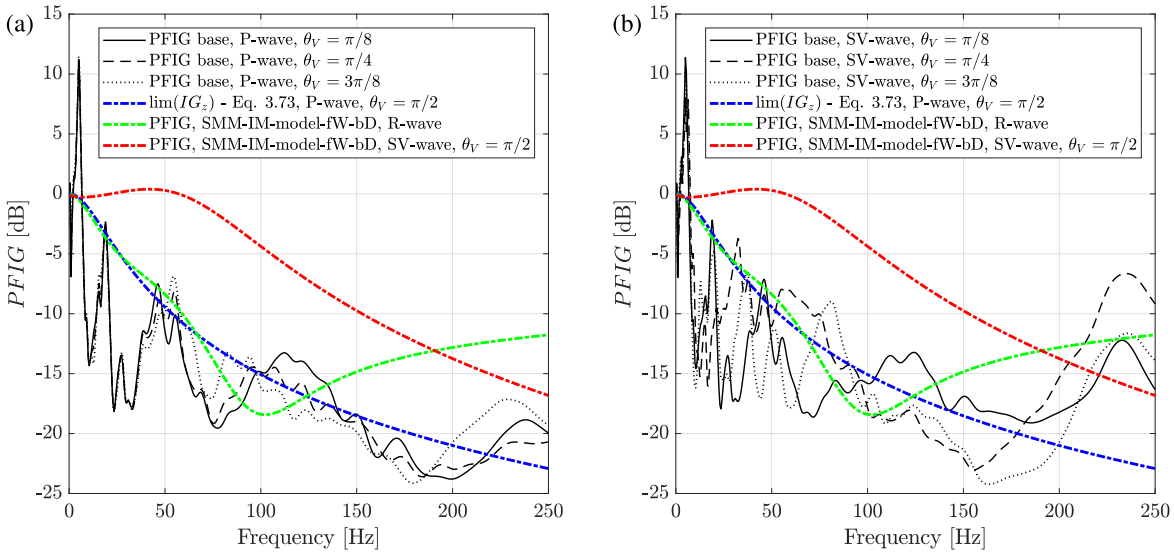

Fig. 6.18 Comparison of the PFIG, related to the mean-vibrational power entering the base of the building, obtained for incident (a) P- and (b) SV-waves at different angles θ_V. Reference values of the $PFIG$ for the case of normally incident P- (blue line) and SV-waves (red line), and for an incident Rayleigh wave (green line) are also reported. An isolation frequency $f_S = 5$ Hz and a slab foundation thickness of $h = 1.5$ m are considered.

thus to the case of a P-wave at $\theta_V = \pi/2$, and those obtained with the design analysis framework for an incident Rayleigh wave (green line) and a normally incident SV-wave (red line). The $PFIG$ expressed by Equation 3.73 provides a reasonable lower bound for the isolation performance, as obtained by the rigorous framework for both incident P-and SV-waves, up to about 150 Hz, with an over-estimated performance of 4 dB, at most, for the considered wave-fields. At relatively high frequencies, a reduced isolation performance is observed, especially for the case of incident SV-waves. In the frequency range $150 - 250$ Hz, a lower bound of the isolation performance may be given by the results of the design framework for an incident Rayleigh wave (green line), with an over-estimated performance of 6 dB, at most, for the considered wave-fields. It is interesting to notice that the reduced attenuation and/or amplification at relatively low frequencies (around 50 Hz), obtained for the case of SV-waves at $\theta_V = \pi/2$, seems to be not relevant for incident P- and SV-waves at an angle θ_V. The analysis of P- and SV-waves at different incidence angles shows that the results of the isolation performance for the limit cases of a normally incident P-wave and an incident Rayleigh wave, obtained via the design analysis framework, may be adopted as reference values for the design of base-isolated buildings. This idea is tested in the following section with regard to an incident

wave-field that is more representative of the induced ground-borne vibration from a localised source on the free-surface.

6.4.5 The case of a localised source

Let us consider the case of a localised source represented by a forced-excitation at a distance d_P from the first footing of the building and applied on a surface rigid footing resting on the free-surface of the concrete slab foundation overlying the ground. We assume that the forced-excitation is unaffected by the coupling with the building, so that an external source is providing a given force $\hat{\boldsymbol{P}}$ on the footing. The response of the six rigid footings may be written as follows:

$$\begin{bmatrix} \hat{\boldsymbol{u}}_{\boldsymbol{P}} \\ \hat{\boldsymbol{u}}_{\boldsymbol{b}} \end{bmatrix} = \begin{bmatrix} \widehat{\boldsymbol{H}}_{\boldsymbol{f}}^{(\boldsymbol{PP})} & \widehat{\boldsymbol{H}}_{\boldsymbol{f}}^{(\boldsymbol{Pb})} \\ \widehat{\boldsymbol{H}}_{\boldsymbol{f}}^{(\boldsymbol{bP})} & \widehat{\boldsymbol{H}}_{\boldsymbol{f}}^{(\boldsymbol{bb})} \end{bmatrix} \begin{bmatrix} \hat{\boldsymbol{P}} \\ \hat{\boldsymbol{f}}_{\boldsymbol{b}}' \end{bmatrix} \tag{6.9}$$

Because of the presence of the building, we can write:

$$\hat{\boldsymbol{f}}_{\boldsymbol{b}}' = -\hat{\boldsymbol{f}}_{\boldsymbol{b}} = -\widehat{\boldsymbol{K}}_b \, \hat{\boldsymbol{u}}_{\boldsymbol{b}} \tag{6.10}$$

with $\widehat{\boldsymbol{K}}_b$ the dynamic stiffness matrix of the building condensed at its base, as already seen in Chapter 3 and in Section 6.2.2. By substitution of Equation 6.10 into Equation 6.9, after some algebraic manipulation, it is possible to relate the response at the base of the building $\hat{\boldsymbol{u}}_{\boldsymbol{b}}$ and the response of the loaded footing $\hat{\boldsymbol{u}}_{\boldsymbol{P}}$ to the forced-excitation $\hat{\boldsymbol{P}}$:

$$\hat{\boldsymbol{u}}_{\boldsymbol{b}} = \left[\mathbf{I} + \widehat{\boldsymbol{H}}_{\boldsymbol{f}}^{(\boldsymbol{bb})} \widehat{\boldsymbol{K}}_b\right] \widehat{\boldsymbol{H}}_{\boldsymbol{f}}^{(\boldsymbol{bP})} \hat{\boldsymbol{P}} \tag{6.11a}$$

$$\hat{\boldsymbol{u}}_{\boldsymbol{P}} = \left[\widehat{\boldsymbol{H}}_{\boldsymbol{f}}^{(\boldsymbol{PP})} - \widehat{\boldsymbol{H}}_{\boldsymbol{f}}^{(\boldsymbol{Pb})} \widehat{\boldsymbol{K}}_b \left[\mathbf{I} + \widehat{\boldsymbol{H}}_{\boldsymbol{f}}^{(\boldsymbol{bb})} \widehat{\boldsymbol{K}}_b\right]^{-1} \widehat{\boldsymbol{H}}_{\boldsymbol{f}}^{(\boldsymbol{bP})}\right] \hat{\boldsymbol{P}} \tag{6.11b}$$

The first term in the squared brackets in Equation 6.11b provides the driving point response of the loaded footing, whereas the second term is the contribution provided by the presence of the building, thus representative of the source-receiver interaction. The response of the portal-frame building may be calculated as described in Section 6.2.2 and in Chapter 3 starting from the response at its base $\hat{\boldsymbol{u}}_{\boldsymbol{b}}$ induced by a force $\hat{\boldsymbol{P}}$ at the first footing. The latter is assumed in the form of a vertical load $\hat{\boldsymbol{P}} = [0 \quad \hat{P}_z \quad 0]^T$. The resulting power-flow analysis for the unisolated and isolated portal-frame building is reported in Figure 6.19 for an excitation frequency of 50 Hz. A qualitative comment can

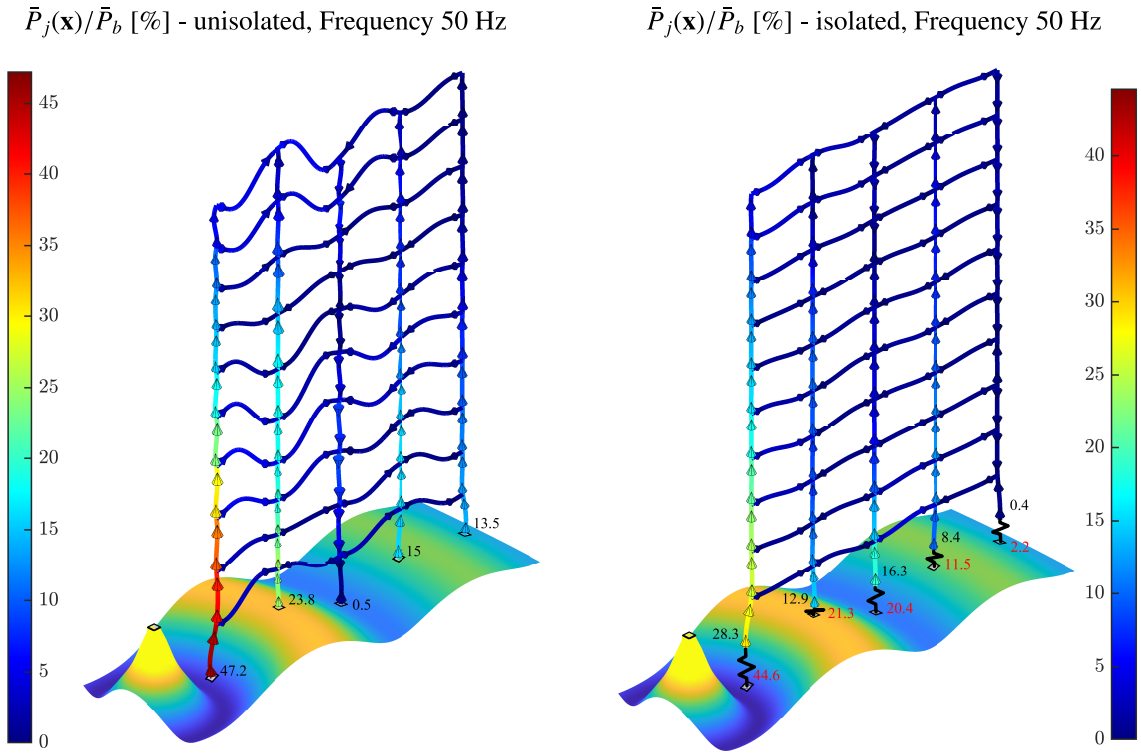

Fig. 6.19 Power-flow analysis of the reference portal-frame building (benchmark #2) with an incident wave-field induced by a vertical load $\hat{P}_z$ on a rigid footing at a distance d_P = 5 m from the upstream footing of the building. The power-flow analysis refers to a frequency of 50 Hz and to the unisolated (left) and isolated (right) configuration of the portal-frame building. An isolation frequency $f_S = 5$ Hz and a slab foundation thickness of $h = 1.5$ m are considered.

be made in that the power-flow analysis is similar to the one obtained for the case of an incident Rayleigh wave examined in Figure 6.15. This is because the localised forced-excitation induces, in the far field, a Rayleigh wave with circular wave-front. The wave speed of the latter is generally greater than the Rayleigh wave speed of the ground alone, as used for the incident wave-field in the previous sections, and depends on the properties of the layered system composed of the concrete slab overlying the ground.

Figure 6.20(a) shows the isolation performance of the reference portal-frame building (benchmark #2) for an isolation frequency $f_S = 5$ Hz. The *PFIG* referring to the total mean-vibrational power entering the base of the building (black line) and the PFIG referring to the power dissipated in each room (gray lines) are calculated by means of the rigorous analysis framework. As seen for the case of generally incident P- and SV-waves in Figure 6.18, the reference values referring to the design Equation 3.73 for a vertical input and to the *PFIG* for a Rayleigh wave obtained with the

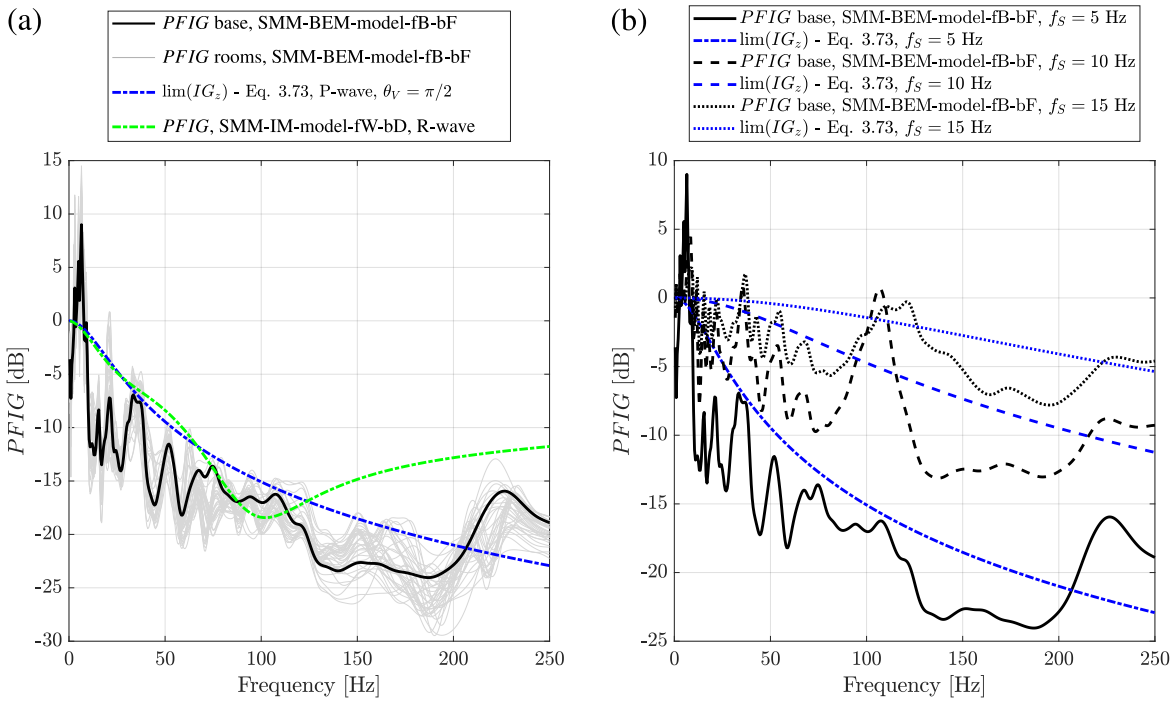

Fig. 6.20 Isolation performance obtained for the reference problem (benchmark #2) subjected to a vertical load applied on a surface, rigid footing at a distance d_P = 5 m from the upstream footing of the building. (a) Comparison of the PFIG entering the whole building (black line) and the PFIG for each room of the portal-frame building (gray lines), as obtained by the rigorous framework SMM-BEM-model-fB-bF. The value the limit IG_z (blue line) for a vertical input, from Equation 3.73, and the result of the $PFIG$ for an incident Rayleigh wave obtained with the design framework SMM-IM-model-fW-bD are shown for reference. An isolation frequency $f_S = 5$ Hz and a slab foundation thickness of h = 1.5 m are considered. (b) Comparison of the $PFIG$ obtained by means of the rigorous framework and the design Equation 3.73 for different values of the isolation frequency f_S = 5, 10 and 15 Hz.

design framework provide a good lower bound for the isolation performance to be expected for the case of a localised, vertical source of vibration. Moreover, Figure 6.20(b) shows the results obtained, with reference to the rigorous analysis framework (black lines) and to the design Equation 3.73 (blue lines), for the $PFIG$ referring to different values of the isolation frequency $f_S = 5, 10$ and 15 Hz as investigated in Section 3.5.3. It is clear that, in all cases, the design Equation 3.73 captures well the trend of the isolation performance obtained with the rigorous framework, although the latter is strongly dependent on frequency.

This section has provided some indication that the design analysis framework, as presented in Section 6.1, may be a valid, simplified, staged approach for the design of base-isolated buildings with reference to more realistic sources of vibration than the plane-wave excitation assumed in previous

sections. Another important assumption regarding the slab foundation is tested in the following section with the purpose of validating the design analysis framework for a surface foundation with finite in-plane dimensions.

6.4.6 On the validity of the infinitely-large slab foundation model

In this section, the assumption of an infinitely-large slab foundation is tested by comparing the results of the isolation performance for an incident Rayleigh wave, as obtained in the previous Section 6.4.3, to those calculated by considering the 2D Model A of the finite plate as introduced in Section 5.4. It has been acknowledged that the assumption of in-plane infinite extent for the slab leads to an over-estimated added-foundation effect (see Section 5.4.3). Here, the interest lies in the relative measure of the isolation performance, which, as seen in Chapter 3, strongly depends on the impedance mismatch between the building and the soil-foundation system, and the isolation and the building. It should be noted that, as it is clear from the diagrams in Figure 6.2 and 6.4, the response of the unisolated and the isolated buildings is obtained starting from the same input motion $\hat{\boldsymbol{u}}_f$, which is the result of the soil-foundation interaction under a given incident wave-field. Thus, the comparison of results of the isolation performance with a finite or infinite slab foundation is aimed at investigating how sensitive the isolation performance is to a change of the input motion due to the modal response of the finite slab foundation. The response of the rigid footings $\hat{\boldsymbol{u}}_f$ to incident wave-fields can be calculated as in Section 5.4, where the added-foundation effect of the finite slab is examined. The added-building effect can be then approached by considering the dynamic stiffness $\widehat{\boldsymbol{K}}_{fP}$ of the soil-foundation composed of the finite plate on the elastic and homogeneous half-space. This can be obtained by:

- coupling the dynamic stiffness matrix of the plate model $\widehat{\mathbf{K}}_{\mathbf{pd}}$ (see Equation 5.50) to dynamic stiffness matrix of the soil $\widehat{\mathbf{K}}_{\mathbf{s}}$ (see Equation 5.49) at the relevant degrees of freedom $\mathbf{x}_{\mathbf{E}}$;
- condense the resulting stiffness matrix of the soil-foundation system to the degrees of freedom of the footings $\mathbf{x}_{\mathbf{p}F}$.

Once the the dynamic stiffness $\widehat{\boldsymbol{K}}_{fP}$ of the soil-foundation system is retrieved, the FRF matrix $\widehat{\boldsymbol{H}}_{fP} = \left[\widehat{\boldsymbol{K}}_{fP}\right]^{-1}$ can be calculated, and the added-building effect and the response within the unisolated and the isolated building may be approached, formally, as in Chapter 3 in Equations 3.4 and 3.5, and Equations 3.41 and 3.42 respectively. Once the response of the building is retrieved, a power-flow

analysis can be carried out, for both the unisolated and the isolated configurations, as described in Section 6.4.1. The response referring to the rigorous approach with the finite plate is referenced in the following as SMM-FEM-BEM-model-fP-bF.

Figure 6.21 shows the results of the $PFIG$ for the whole building referring to the rigorous analysis framework (blue line) and to the same rigorous approach with the exception of considering the finite slab foundation (black line). Although differences of up to 10 dB are found for the two rigorous solutions along the frequency spectrum, it appears that the overall trend, captured by the result of the design analysis framework (green line), has not substantially changed. This supports, as long as the relative measure of the isolation performance is concerned, the use of the infinitely-large slab foundation model as adopted in both the design and the rigorous analysis framework. Moreover, the results of Figure 6.21 show that not only the isolation performance is only marginally influenced by

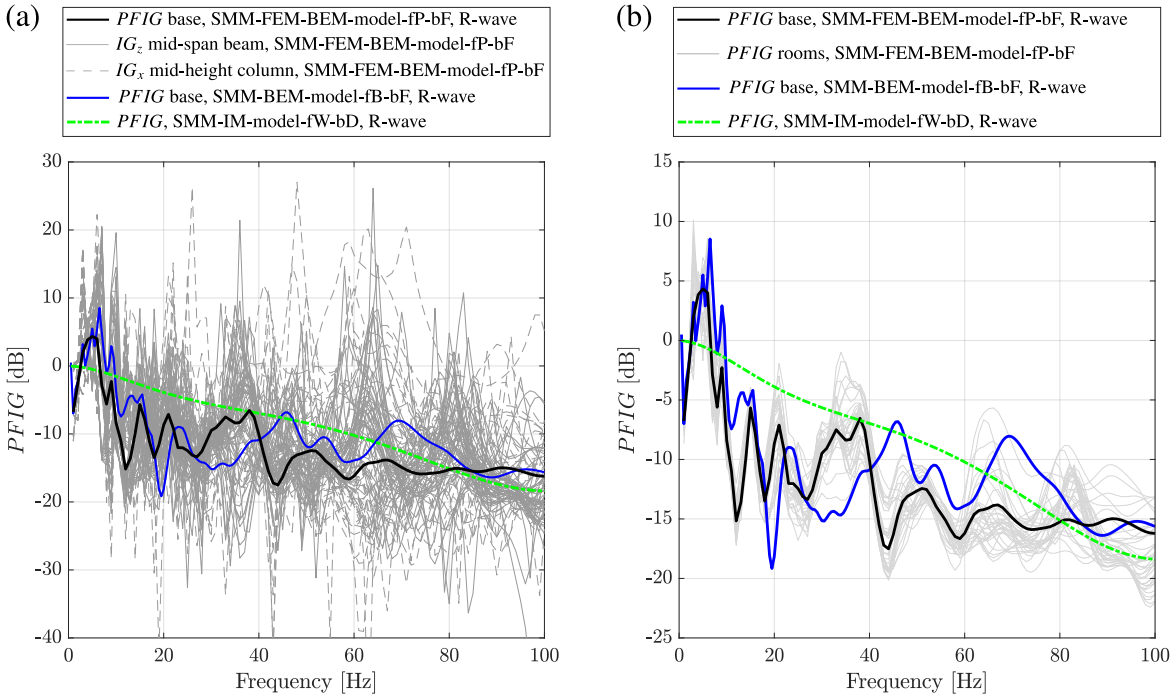

Fig. 6.21 Comparison of the isolation performance, for the case of an incident Rayleigh wave, in terms of the $PFIG$ for the whole building referring to the rigorous analysis framework (blue line) and to the same rigorous approach with the exception of considering the finite slab foundation (black line). The results of the design analysis framework are also shown alongside with a green line. Additionally (a) the IG_x and the IG_z referring to the mid-height of the columns and to the mid-span of beams are shown together with (b) the $PFIG$ referring to the power dissipated in each room of the portal-frame building. An isolation frequency f_S = 5 Hz and a slab foundation thickness of h = 1.5 m are considered.

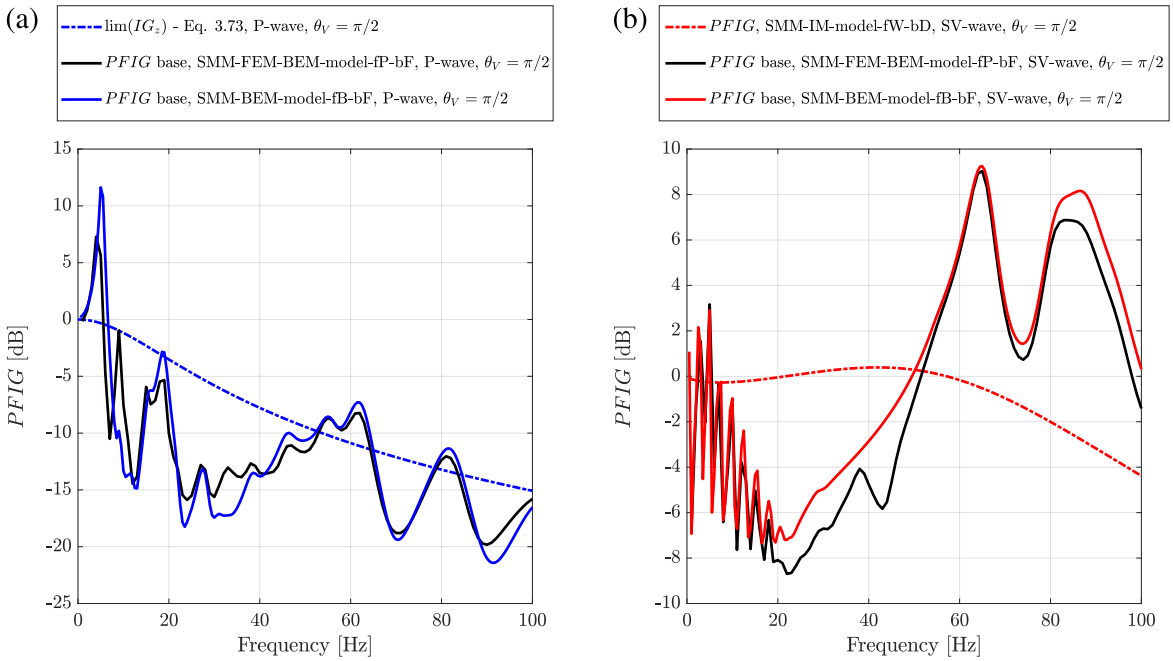

Fig. 6.22 Comparison of the isolation performance, for normally incident (a) P- and (b) SV-waves, in terms of the *PFIG* for the whole building referring to the rigorous analysis framework SMM-BEM-model-fB-bF and to the same rigorous approach with the exception of considering the finite slab foundation (SMM-FEM-BEM-model-fP-bF). The limit value of the IG_z for a vertical input (chained blue line), from Equation 3.73, is shown alongside the results for the incident P-wave, while the result of the design analysis framework SMM-IM-model-fW-bD (chained red line) is shown alongside the rigorous results for the incident SV-wave. An isolation frequency f_S = 5 Hz and a slab foundation thickness of h = 1.5 m are considered.

a change of the input motion $\hat{\boldsymbol{u}}_f$ due to the modal response of the finite slab foundation, but also that the latter provides the same order of magnitude for the soil-foundation impedance obtained with the infinitely-large slab foundation model.

The values of the *IG*, along the horizontal and vertical directions, and the *PFIG* referring to the power dissipated in each room of the portal-frame building are also shown in Figure 6.21. They do not seem to add any additional understanding compared to the results shown in previous sections, if not reiterating the significant spatial variability of the isolation performance with reference to a specific location and/or room within the building.

Additional results are shown in Figure 6.22 for normally incident P- and SV-waves. The comparison of the results of the rigorous solutions obtained with a finite plate or with an infinite slab foundation gives differences of, at most, 9 dB and 4 dB for the case of a normally incident P- and SV-wave respectively. This supports the argument that a surface foundation, representative of a concrete slab

foundation beneath a building, can be treated as infinitely large for the purpose of the evaluation of the isolation performance. The resulting comments on this and other aspects investigated in this chapter are summarised in the following.

6.5 Conclusions

This chapter has presented a design analysis framework that adopts simplified models and methods thoroughly investigated in Chapter 3, 4 and 5. The design framework has been used for the evaluation of the isolation performance for a base-isolated building against ground-borne vibration, and it has been tested against a rigorous analysis framework. The latter follows the same staged approach, for the soil-foundation-building interaction, but this time adopting a rigorous Stiffness Matrix Method and a Boundary Element Method (BEM) approach, presented in Chapter 4 and 5, to solve the added-foundation effect and considers a Dynamic Stiffness Method (DSM) model of the portal-frame building coupled to a BEM model of the soil-foundation system for solving the added-building effect.

A first consideration relates to the latter. The design framework may, in principles, be used in the context of absolute predictions of vibration levels, in conjunction with an accurate building model. For this purpose, it has been shown that, although the overall trend of the added-building effect, referring to different degrees of freedom, is clearly captured by the results of the design framework, differences up to 15 dB with the rigorous counterpart may be found in certain frequency bands for the portal-frame building referring to the reference problem introduced in Chapter 3. Thus, the use of the design framework for capturing the soil-foundation-building interaction, with reference to the response at the base of the building, is open to questions and it may represent an interesting topic for further investigations.

Both the design and the rigorous frameworks have been then adopted for the evaluation of the isolation performance. Unlike any absolute measure of vibration levels, this is a relative measure of performance that it may be correctly captured by properly accounting for the foundation-building impedance mismatch. This has been investigated with reference to the case of the portal-frame building of benchmark #2, as presented in Chapter 3, for different incident wave-fields, in an effort to validate the design framework. Preference has been given to the Power Flow Insertion Gain ($PFIG$) as a scalar metric that is able to describe the isolation performance, which accounts for the general

bending and axial motion associated with the complex response of a building. The Insertion Gain (IG), describing the isolation performance in terms of attenuation of vibration levels at one location in the building along one direction, has been also considered as a more traditional metric. It has been demonstrated that the three limit scenarios of normally incident P- and SV-waves, and an incident Rayleigh wave completely define the possible isolation performance that may be obtained with a more general incident wave-field is considered. For the latter purpose, incident P- and SV-waves, at different angles θ_V, have been considered as well as a localised vertical source in the vicinity of the building. In all cases, a good match of the $PFIG$ of the design framework has been observed when compared to the results of the rigorous analysis framework. Moreover, the examined case of a normally incident SV-wave has indicated a frequency-range for which amplifications of vibration levels may be obtained with base-isolation. This trend has been shown to be hardly obtainable for incident wave-fields more representative of ground-borne vibration. By comparison of the results of the design and the rigorous analysis framework, it has been shown that the results of the isolation performance, obtained by the design framework, for the case of an incident Rayleigh wave and a normally incident P-wave have the potential to drive the design of base-isolated building for a large variety of incident wave-fields. In particular, the closed-form expression, related to the design framework and obtained for the single point-coupling model subject to a vertical input, of the Insertion Gain has been shown to provide a valid approximation to the isolation performance for different incident wave-fields. This may have profound implications on how base-isolated buildings are designed in practice, which nowadays relies on the fallacious mass-on-a-spring model without accounting for the soil-foundation-building interaction.

Finally, another important assumption of the design framework is tested in order to validate its results in terms of isolation performance. The assumption of an infinitely-large slab foundation is removed by solving the soil-foundation-building interaction via a FEM-BEM approach that considers a finite 2D plate representative of the slab foundation. Although the infinite in-plane extent of the slab foundation leads to a considerable over-estimation of the added-foundation effect (see Chapter 5), the results in terms of the $PFIG$ have demonstrated that this assumption does not greatly affect the isolation performance. Possible differences with the results of the rigorous analysis framework have been found in the order of 10 dB, or less, in certain bands along the frequency spectrum. However, the isolation performance obtained with the design analysis framework has been shown to provide a

valuable trend of the frequency-dependent isolation performance obtained by the rigorous solution with the finite slab foundation.

Chapter 7

A measurement campaign at South Bank, London

This chapter describes a measurement campaign conducted at the Shell Centre redevelopment site at South Bank, London. The discussion of the measurement results is general and aims at validating the concepts of the added-foundation and the added-building effect as investigated in the previous part of the thesis. A brief introduction of the construction site is given in the following before commenting on the vibration levels registered during the several construction stages.

7.1 The construction site

The measurement campaign focuses on monitoring the vibration levels during the construction of a building, which is part of the Shell Centre redevelopment site. The latter is composed of a mixture of commercial and residential buildings together with a two-storey and a three-storey basement at the north and south of the site respectively. The master-plan of the redevelopment involves the area of the pre-existing "upstream" Shell Centre, completed in 1962 [217], and retains the 107 m high Shell Tower while demolishing the original wing buildings to make space for the new ones. The site is situated on the south bank of the Thames in the London Borough of Lambeth, and it is bounded by York Road to the east, Chichely Street to the south, Jubilee Gardens to the west and the Waterloo-Charing Cross viaduct to the north. Major transport hubs are present in the vicinity of the construction site, including Waterloo Station. The Waterloo-Charing Cross viaduct, and the Bakerloo and the Northern line tunnels, which run beneath the site, are the main sources of ground-borne vibration for the new,

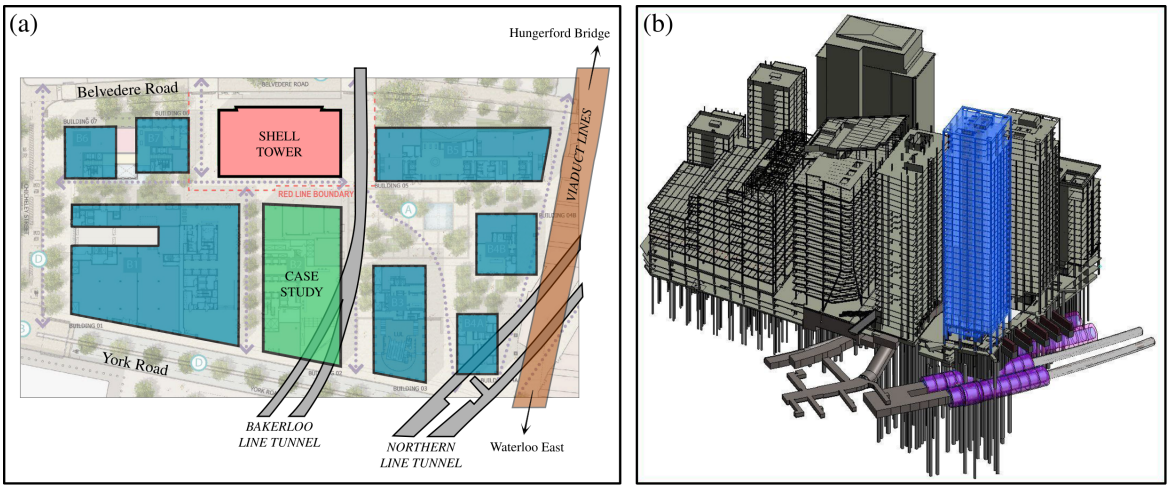

Fig. 7.1 (a) A plan view (derived from [218]) and (b) a 3D view of the underground railway infrastructure at the Shell Centre redevelopment site.

and the existing, buildings on site. An illustrative plan view of the transportation infrastructure that intersects the site is shown in Figure 7.1. The building highlighted in green is the *case study* building for the measurement campaign. The complexity of both the redevelopment, its foundation system and the Bakerloo and the Northern line tunnels are shown in a three-dimensional view as taken from a report of the Structural Engineer, WSP Ltd [218].

The geotechnical aspects of the design are given by the Geotechnical Engineer, ARUP Ltd [4]. These are based on the results of the project-specific site investigation and on the geological survey undertaken for the construction of the original Shell Centre. This, as described by Measor & Williams [217], consisted of 51 cased borings on land to various depths up to 40 m and an additional 70 m deep boring beneath the Shell Tower to ascertain the presence of a chalk bedrock. The resulting layered ground at the construction site is reported in Table 7.1. After an overall 7 m thick layer of soft silty clay and sandy gravel, the London clay is the predominant layer under the site. A detailed discussion on the design features of the original Shell Centre project was carried out by Measor & Williams [217]. This gives a detailed insight into the operational difficulties of the project, given the vicinity of the site to the river and to the underground tunnels. With regard to the latter, the Bakerloo line tunnels run beneath the case study building as they did originally for the York wing building of the Shell Centre. The tunnels are situated in the London clay layer, and the crown of the upper tunnel is only just more than 2 m from the basement floor of the original Shell Centre (see Figure 7.2). At the time, the foundation design philosophy focused on the protection of the tunnels

Stratum		Thickness [m]
Made ground	Predominately granular	2.5
	Predominately cohesive	1.4
Alluvium		3.3
Terrace gravel		3.8
London clay		31.5
Lambeth group		17
Thanet sand		8.5
Chalk		Not proven

Table 7.1 Layering of the ground at the construction site as reported by the geotechnical engineer [4]

from both construction operations (e.g. tunnel heave resulting from the ground excavation) and, in the long term, from the additional loads from the buildings [217]. As seen in Figure 7.2, this was achieved by the design of a complex basement infrastructure composed of peripheral retaining walls, a 1 m thick slab foundation, deep concrete piles with enlarged bases that are able to bring the concentrated loads into the London clay layer and away from the tunnel, and of pre-stressed concrete beams that are able to transfer the loads across and away from the tunnels. The foundation design for the new complex of buildings retains most of the basement infrastructure of the original Shell Centre, and extends and/or modifies some parts for increasing the bearing capacity.

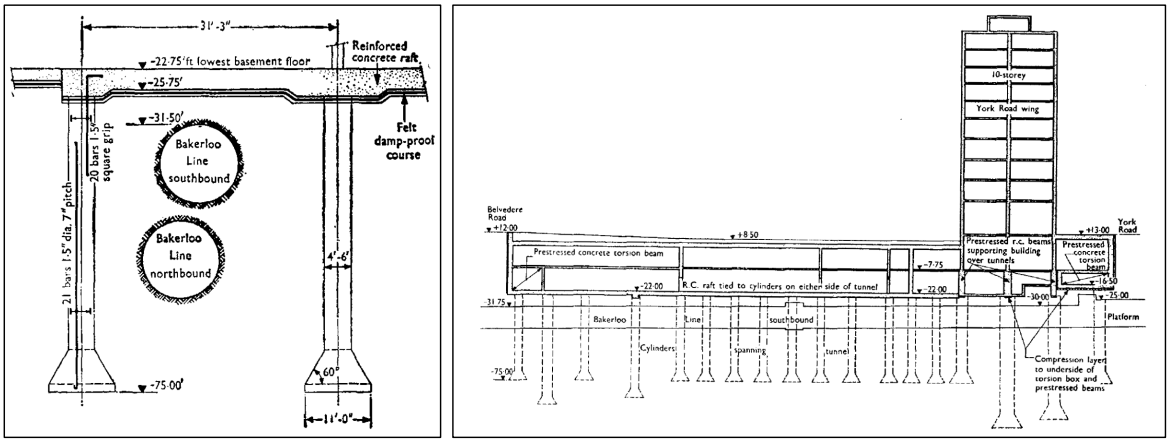

(a) (b)

Fig. 7.2 Basement infrastructure of the original Shell Centre from Measor & Williams [217]: (a) the original slab-piled foundation in the vicinity of the Bakerloo line tunnels; (b) the basement infrastructure composed of the slab-piles foundation across the site and the pre-stressed concrete beams transferring the loads away from the tunnels.

The case study building is a 17-storey, steel-framed building with steel-concrete floors and a glazed façade. The structural plan consists of a core of structural walls situated at the south, which is able to bear horizontal loads, and perimetral columns on the west, north and east sides. There is a two-storey basement beneath the ground floor, before reaching the foundation level (i.e. basement floor). The foundation design for this building involves the construction of an additional slab foundation, of about 1.3 m thickness, over the original 1 m thick slab, and additional bearing piles to support the concentrated loadings from the new building. An important aspect of the building design relates to its isolation against ground-borne vibration. This is achieved by isolating the structural core, which is designed to rest on a floating-slab overlying an elastomeric layer at the foundation level, and by isolating each individual column at the ground-floor level by means of rubber bearings. After reviewing the main features of the construction site and the case-study building, the vibration measurement objectives and planning are described in the following sections.

7.2 Objectives of the measurement campaign

The main objective of the measurement campaign is to corroborate the added-foundation and the added-building effect, as observed in theory in this dissertation, by means of experimental evidence. This is possible when the vibration levels, for the case-study as investigated here, are monitored during the construction of the building. The measurement sessions, planned for the case-study, follow the construction stages schematically shown in Figure 7.3: (a) the brown-field vibration levels are registered after the in-situ construction of the new bearing piles through the existing slab-piled foundation of the original Shell Centre; (b) part of the new slab foundation is cast over the existing one; (c) the floating-slab is added over the area that is subsequently occupied by the structural core; (d) the new slab foundation is completed over the remainder of the building's footprint together with the 2-storey basement and the concrete structural core; (e) the steelwork is erected; (f) the glass façade is installed. It is clear that because of both the complexity of the construction process and the peculiarity of the base-isolated building under investigation, the added-foundation and the added-building effect do not correspond to the idealised scenario, as introduced in Section 3.1.2, of a portal-frame building on a slab foundation of thickness h overlying an homogeneous half-space. Nevertheless, an added-foundation effect, similar to that studied in Chapter 4 and 5, may be expected for the construction stages referring to Figure 7.3(a) and (b), with the influence of the existing slab-

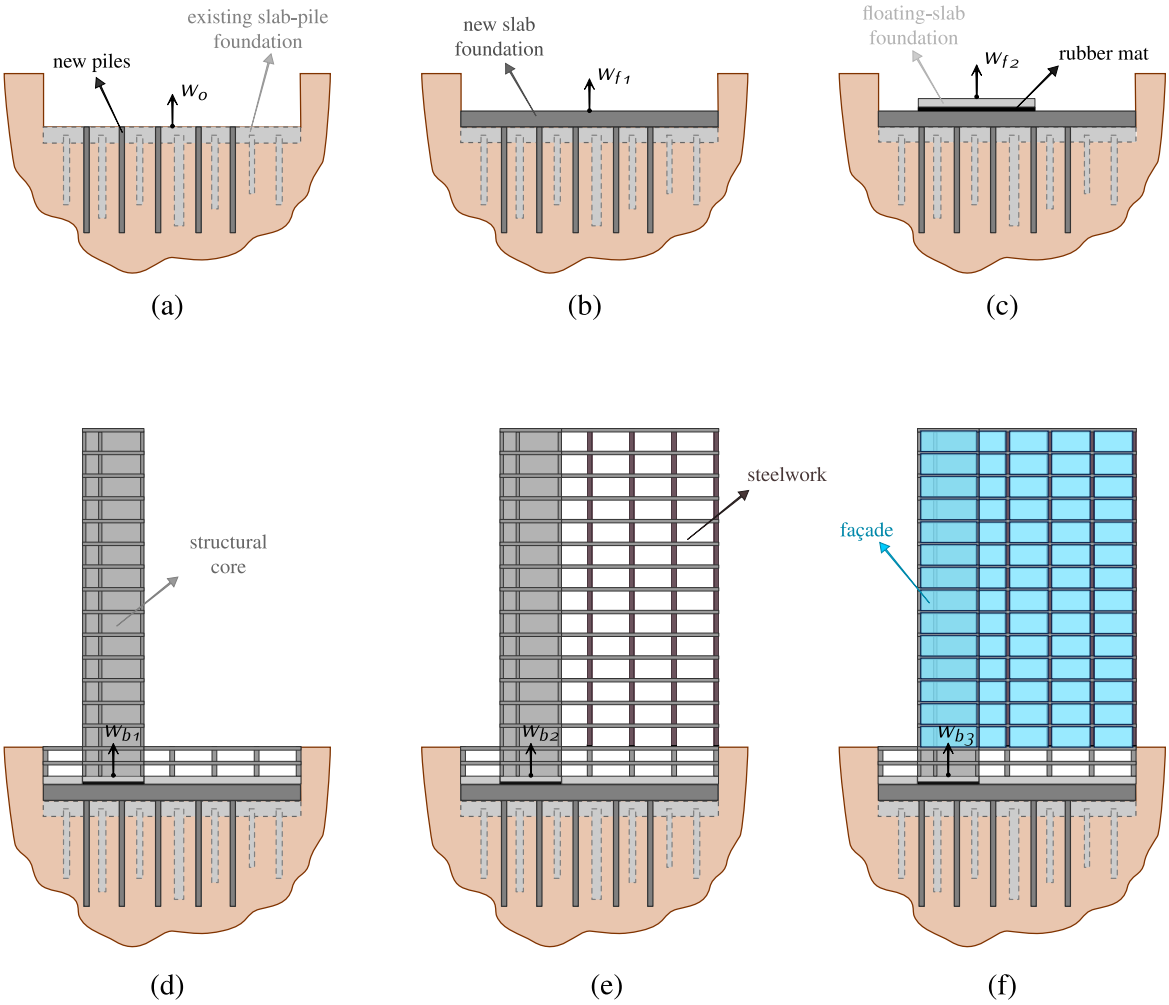

Fig. 7.3 A schematic illustration of the construction stages and the associated measurement sessions for the case study: (a) new piles are cast in-situ on the existing slab-pile foundation with the resulting vibration levels w_o; (b) part of the new concrete slab foundation is cast in-situ with the resulting free-surface vibration levels w_{f_1}; (c) a floating-slab on a layer of elastomeric material is built, for isolating the structural core, with the resulting free-surface vibration levels w_{f_2}; (d) after the construction of the structural core, the vibration levels w_{b_1} at the foundation-building interface; (e) the structural steelwork is completed and the vibration levels are labelled w_{b_2}; (f) finally, the façade is completed and the vibration levels w_{b_3} are registered at the foundation-building interface.

piled foundation and of the new piles. The added-building effect, referring to the several construction stages in Figure 7.3(d), (e) and (f), is that related to a base-isolated building, with the isolation of the structural core at the basement level and the isolation of the individual columns at the ground level. It is worth pointing out that the discussion assumes constant underground conditions with reference to both the underground railways (e.g. no change in rail roughness) and the soil properties, which may be altered by seasonal changes (e.g. saturation level dependent on the water table level).

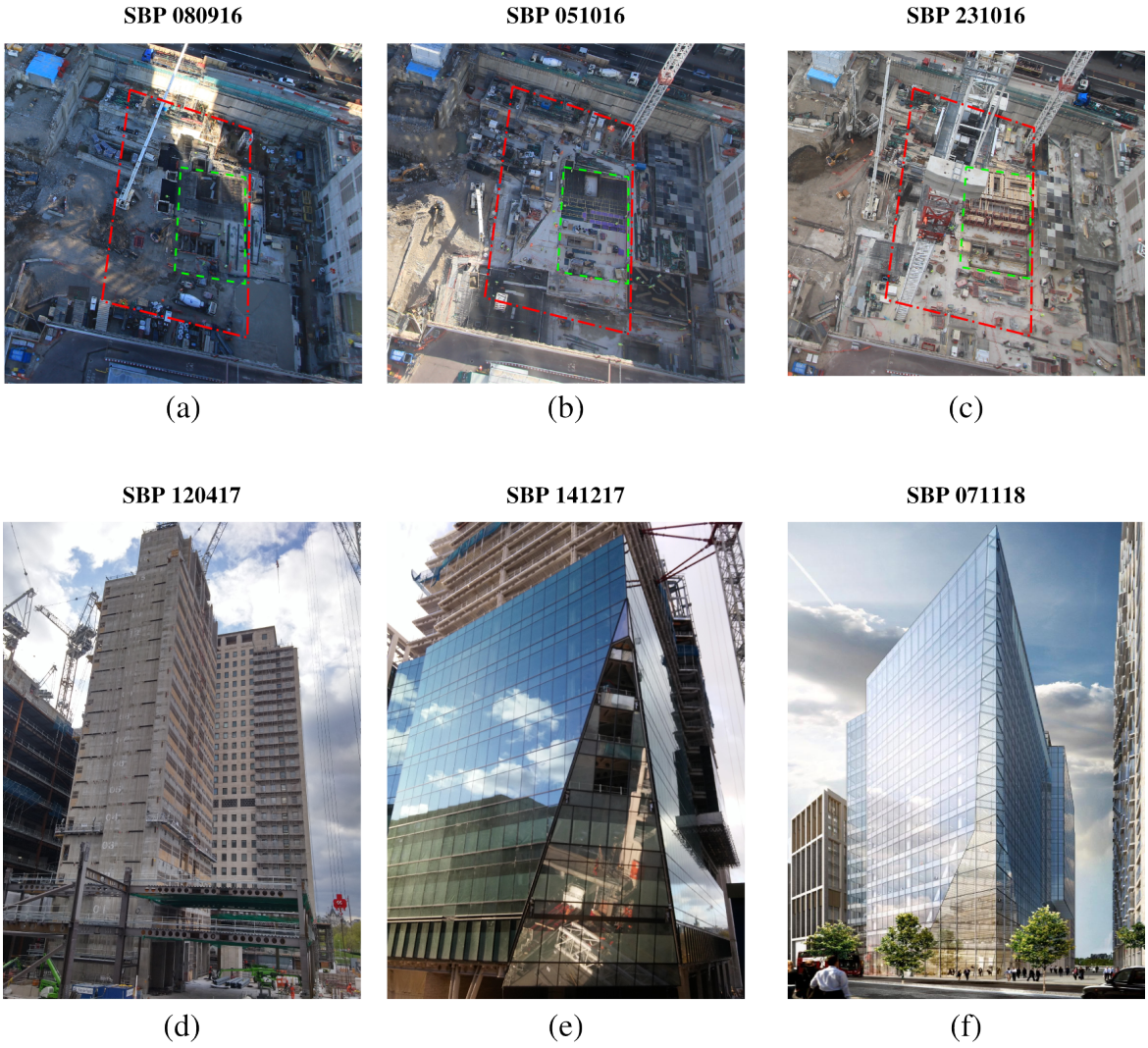

Fig. 7.4 Site configuration, for the case study building, for each measurement session at different construction stages: (a) the stage preceding the addition of a concrete slab foundation over the footprint of the structural core (dashed green line) and that of the entire building (chained red line); (b) after the slab foundation has been cast in-situ and in preparation of the isolation of the structural core by means of a elastomeric mat; (c) after the construction of a floating, concrete slab over the footprint of the structural core; (d) after the construction of the 17-storey high structural core; (e) after the completion of the concrete-steel work of the structural columns and floors, and partial installation of the façade; (f) at the completion of the main structural work, including the installation of the façade, but still with flooring work ongoing in the unfurnished building.

Figure 7.4 shows the same construction stages reported in Figure 7.3, but this time as pictures taken on site from a camera installed on the Shell Tower (kindly provided by Canary Wharf Contractors Ltd) for (a), (b) and (c), as pictures of the building taken from York road for (d) and (e), and as an image for the completed building taken from a WSP report [219]. The approximate footprint for the structural

core and for the case-study building are highlighted with a green and red line, respectively, in the aerial pictures in Figure 7.4(a), (b) and (c). A brief description of the site configuration for each measurement session is given, in chronological order, as follows:

- **SBP 08/09/2016** - Measurement session on the 8th September 2016. The excavation activities are finished next to the case-study building, but are still ongoing for the adjacent building. The piling activities are finished for what concerns the area of the structural core footprint, but they have not started yet for the rest of the case-study building's footprint. This is because the construction process will start with the structural core and will continue with the framed part only when the core is completed. A drainage layer has been installed over the existing slab with a covering layer of screed. The south part of the core footprint is already covered by the reinforcing steel-bars of the new slab foundation;

- **SBP 05/10/2016** - Measurement session on the 5th October 2016. The new slab foundation has been cast over the structural core footprint and, partly, on the footprint of the case-study building. The south-east part of the structural core footprint is covered with the elastomeric layer used for the floating-slab beneath the core. Construction activities on site include the installation of reinforcing steel-bars for the new slab foundation over the basement floor and excavation activities in the adjacent area;

- **SBP 23/10/2016** - Measurement session on the 23th October 2016. The floating-slab has been cast over the footprint of the structural core. The south area of the latter is occupied by the scaffolding for the two-storey basement. The new slab foundation has been cast over the basement floor adjacent to the case-study building up to the Shell Tower, but an area on the east side of the case-study building is still on the existing slab foundation, close to ongoing piling operations for the adjacent building;

- **SBP 12/04/2017** - Measurement session on the 12th April 2017. The structural core has been completed, having reached the 17th storey. The two-storey basement levels have been completed and the construction of the steelwork for the first and second storey is taking place;

- **SBP 14/12/2017** - Measurement session on the 14th December 2017. The steelwork and the concrete-steel floors have been completed for the 17-storey building. The installation of the glazed façade is ongoing on the east side of the building.

- **SBP 07/11/2018** - Measurement session on the 7th November 2018. The installation of the façade is completed and the flooring and the furnishing operations are taking place at the ground-floor.

Although the description of the site during construction operations is far from being exhaustive, it gives a glimpse of how complicated the construction site is and how vibration measurement sessions may have several constraints because of the construction activities. Moreover, the several construction stages do not take place in a orderly fashion, as idealised in Figure 7.3, but rather in an order that optimises the construction site efficiency. The next section discusses the methodology adopted for the vibration measurement sessions.

7.3 Methodology

An overview of the measurement plan is given in the following together with the methodology adopted for the selection of train pass-by signals and their processing.

7.3.1 Measurement plan

The vibration measurements are taken across the south-north alignment of the case-study building, following an imaginary line across the footprint of the building that meets, in plan, the Bakerloo line tunnels running at the border of the building. Figure 7.5 illustrates the measurement plan with the location of the Bakerloo line tunnels. Generally, at least four measurement locations are considered across the structural core and one location at what will be the mid-span of the floor. Due to occasional constraints at the construction site (e.g. inaccessible location and/or location occupied by stocked material), the measurement locations may have been changed slightly from session to session. Whenever possible, more than five measurement locations are adopted in order to have redundancy of measurements, should any malfunctioning take place. For the sake of summarising the results, this chapter refers to the measurement locations from channel 1 (Ch.1) to channel 5 (Ch.5), as reported in Figure 7.5. Ideally, preference would be given to the locations closer to the tunnels, which are in the north-east corner of the building. However, as can be seen from the pictures in Figure 7.4, this area was hardly accessible during several sessions, thus preference was given to keeping a consistent measurement alignment throughout the campaign, although further away from the tunnels.

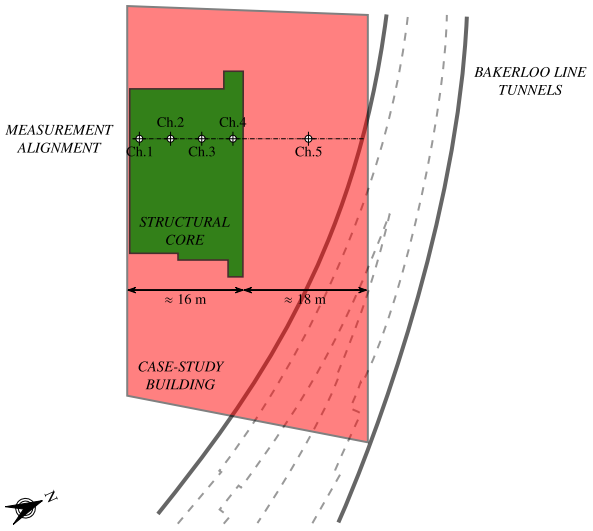

Fig. 7.5 Plan view of the alignment of the measurement locations within the case-study building. Measurements are taken at a number of locations (usually 4 - channel #1 to #4) within the structural core footprint and, where possible, at a location of what will be the mid-span floor (channel #5). An approximate length-scale of the structural core width and the floor span is shown. The area, beneath the building, occupied by the Bakerloo line tunnels is also reported, showing that the tunnels run just along the border of the building for the chosen measurement alignment.

7.3.2 Data acquisition

Up to 8 high-sensitivity, 'seismic', accelerometers with a sensitivity of 10 V/g and a measuring range of ± 0.49 g (± 5 V) have been used for the measurements. These have mounted on levelling, steel plates on a three points support system, as shown in Figure 7.6. The data have been acquired by a National Instruments acquisition system with a connected laptop. As it will be seen later in Section 7.3.4, a sampling frequency of 2048 Hz has been assumed for properly investigating the frequency range of interest up to 250 Hz. A last comment can be made on the logistics of the measurement campaign: because of the weight and volume of the measuring instrumentation (cables included), a minimum of two people were required. Moreover, the construction site is an ever-evolving environment, which can change drastically in time, with possible presence of stocked tools and materials at the locations of interest, and, in unfortunate situations, the presence of water due to construction activities and/or weather conditions. Figure 7.6 shows two pictures taken during the measurement session SBP 14/12/2017 at both the south side of the structural core at the ground level (Figure 7.6(a)), and at the middle-span location of the +2 level (Figure 7.6(b)). In both cases, the pictures show the set up of the alignment with 4 accelerometers along the structural core and one at the mid-span of the steelwork.

(a) (b)

Fig. 7.6 An overview of the measurement alignment for the measurement session SBP 14/12/2017 and the associated accelerometer set up: (a) a view from the location of channel 1 at the ground level and (b) a view from the location of channel 5 at +2 level.

7.3.3 The measurement campaign in numbers

The measurement campaign has a total of 10 measurement sessions. Six of them are discussed in this chapter, while the remaining 4 relate to either an intermediate construction stage or to unsuccessful attempts because of present construction activity on site. The measurements were taken at the end of the working day so as to minimise the influence of any activities on site. Each measurement session, as described in Section 7.2, has a number of measurement events. Each one of them refers to an acceleration time-history with a maximum duration of 1 to 2 minutes . This is a requirement introduced for keeping the size of the data files manageable and to ease the data processing. Typically, it is possible to identify a number of passing trains (one to three train pass-bys) for each measurement event. The first four measurement sessions (i.e. SBP 08/09/2016, SBP 05/10/2016, SBP 23/10/2016 and SBP 12/04/2017) refer to vibration levels taken at the level -2, which means two storeys below ground level. The remaining two sessions, SBP 14/12/2017 and SBP 07/11/2018, have considered measurements at levels -2, 0, +2 and +6 in order to observe the variation in vibration levels up the height of the building. A first analysis of the measurement campaign can be carried out by looking at the number of train pass-bys for each measurement session. The number N of the train pass-bys for the first 4 measurement sessions is reported in Figure 7.7. These are shown on a histogram

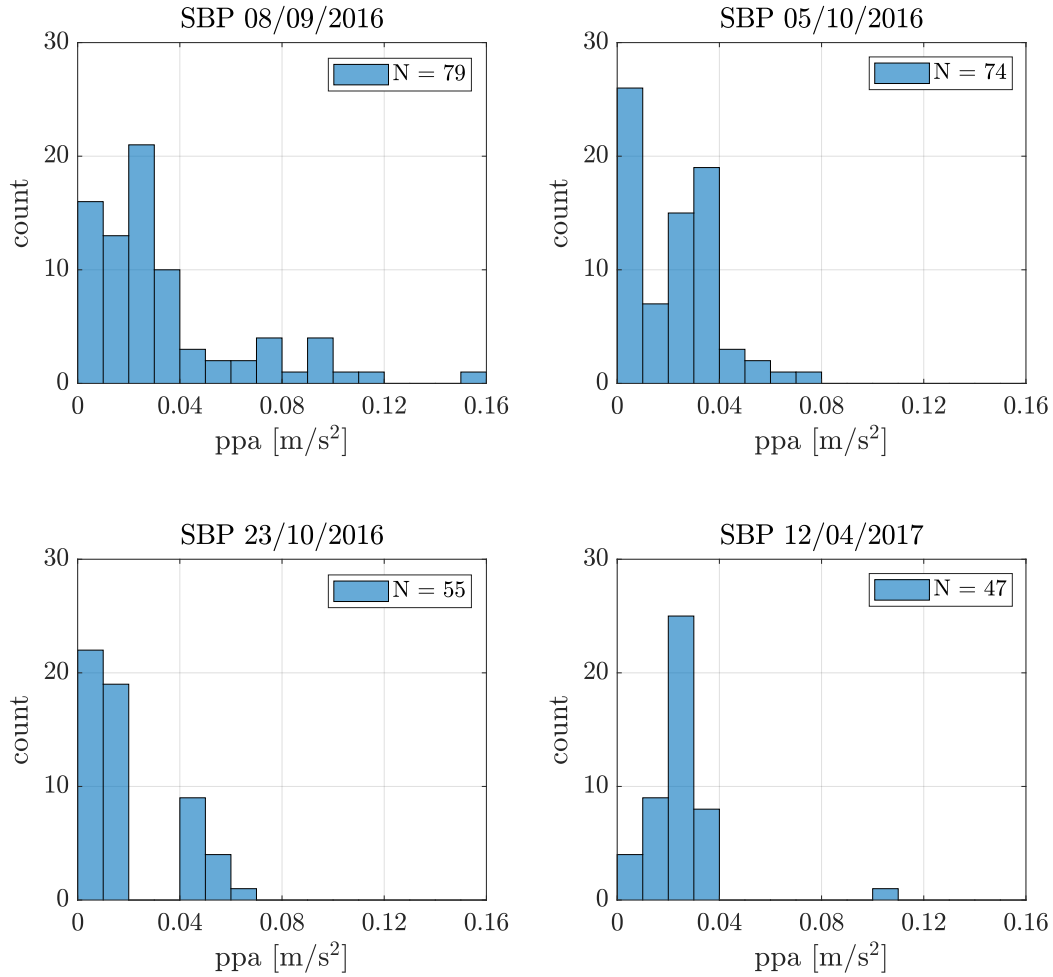

Fig. 7.7 Histogram of the peak-particle-acceleration (ppa) values of the first 4 measurement sessions at -2 level.

according to the value of the peak-particle-acceleration (ppa), as a describing parameter for each acceleration time-history. The first session, before the construction of the new slab foundation, shows the majority of the pass-bys having ppa < 0.04 m/s^2, but almost 25% of the recorded time-histories have a larger value up to 0.16 m/s^2. With the construction of the new slab foundation (SBP 05/10/2016), only about 10% of the pass-bys have a value of ppa greater than 0.04 m/s^2, up to a maximum value of 0.08 m/s^2. After the construction of the floating slab (SBP 23/10/2016), 25 % of the pass-bys have ppa values grater than 0.04 m/s^2 up to a maximum of 0.07 m/s^2. With the construction of the structural core (SBP 12/04/2017), most of the recorded pass-bys have ppa values smaller than 0.04 m/s^2, with the exception of one acceleration time-history having ppa = 0.105 m/s^2. Although the ppa is a somewhat simple parameter, which conveys limited information of the vibration

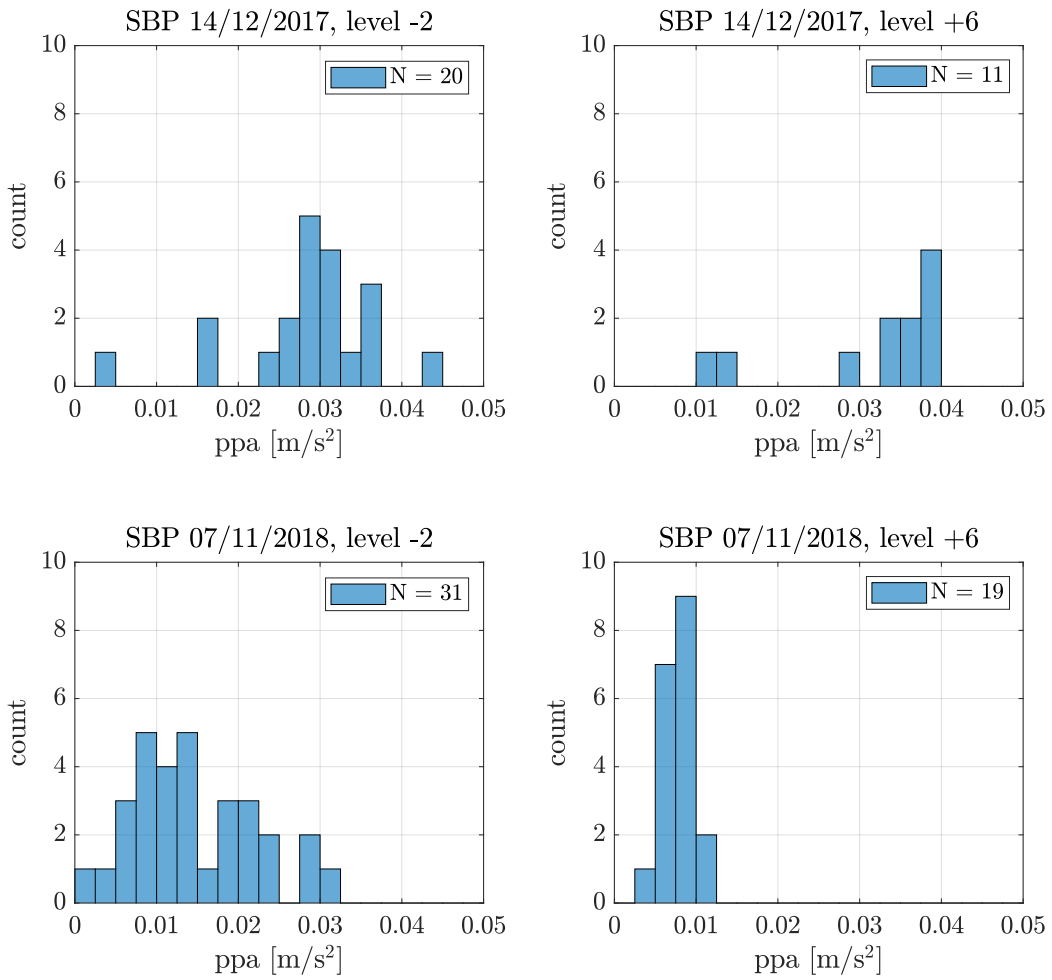

Fig. 7.8 Histogram representation of the distribution of the acceleration time-history for the measurement sessions SBP 14/12/2017 and SBP 07/11/2018 according to the peak-particle-acceleration values.

levels, it is possible to notice a reduction of the maximum peak-particle-acceleration values, for sets of 50 to 80 recorded time-histories, during the construction of the foundation and the structural core of the building. The time-histories considered here refer to the position of channel 3 (Ch.3) in the measurement plan in Figure 7.5. A similar understanding follows from the data presented for the measurement sessions SBP 14/12/2017 and SBP 07/11/2018 (see Figure 7.8), associated with the construction of the steelwork and the façade respectively. The maximum value of ppa, at the level -2, decreases, as the steelwork and the façade are installed, to a value 0.043 m/s^2 and 0.031 m/s^2 respectively. In general, a reduction of the ppa values is also observed for measurement locations at the level +6, although this seems to be more significant for the completed building. After introducing

the measurement campaign, the next section gives details on the more representative characteristics of the train pass-bys in the frequency domain.

7.3.4 Summary of the data processing

This section provides a general overview of the processing tools adopted for analysing the acceleration time-histories. First, the methodology adopted for the calculation of the Power Spectral Density (PSD) and the third-octave band Root Mean Square (RMS) values, starting from an acceleration time-history, is presented. Two measurement events are then discussed, each one taken as a whole. This gives insights into how the train pass-bys have been selected from the raw data and into their features. Finally, the vibration levels of the first measurement session are discussed before moving on to the experimental added-foundation and added-building effects investigated in the following sections.

Calculation of the Power Spectral Density and RMS values

Let us start by considering a single acceleration time-history $x(t)$, representative of a train pass-by. This is available in the form of a finite sample data x_r that is truncated from the raw data of a measurement event. We want to discuss here the implications of deducing information about the frequency content of the acceleration time-history, which is idealised as a random process, by analysing the sample data. As stated by Newland [220], even assuming the random process to

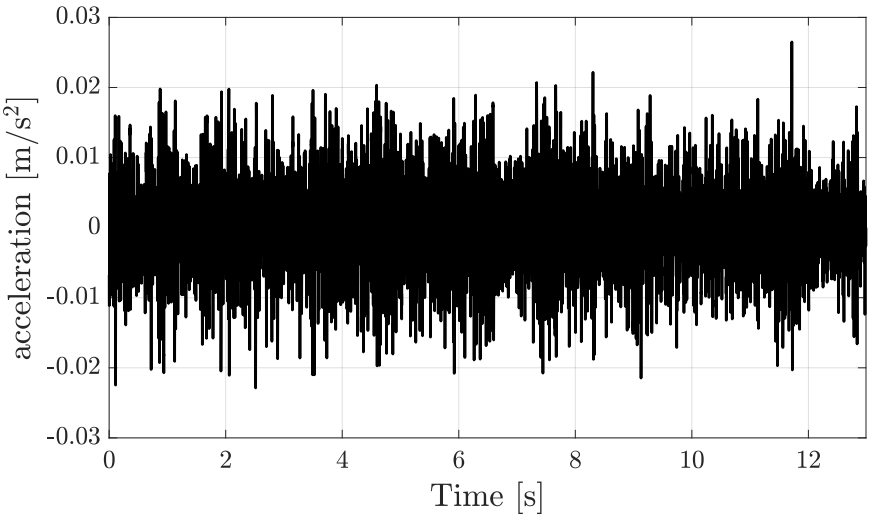

Fig. 7.9 Acceleration time-history of a typical train pass-by of the measurement session SBP 07/11/2018. A section of approximately constant level of acceleration is selected.

be ergodic, which indicates any time-history to be representative of the infinite ensemble of the random process (i.e. time averages equal to ensemble averages), there are errors related to having a discrete time-history of finite length (i.e. sample data). Here, we shall not discuss the statistics of the random process associated with the acceleration time-history of a train pass-by, but we will consider the procedure defined by Newland [220] to calculate the Power Spectral Density (PSD) associated with a sample data x_r obtained from the measurements. The procedure considers the accuracy of measurements by providing estimates of the PSD with a given accuracy at the cost of frequency resolution. The details of the theoretical background will be not discussed here as they are available in the relevant literature [220]. Figure 7.9 shows a typical acceleration time-history associated with a possible train pass-by at the site during the measurement session SBP 07/11/2018 taken at level -2. This is a discrete time series x_r of N sample data with a duration T. Typically, for the train pass-by recorded on site, the duration of the time series ranges from 10 to 16 seconds. This is a limitation for the calculation of the PSD, since one would ideally increase the recorded time to increase the frequency resolution and the accuracy of the measurements. Starting from this "fixed" parameter, the procedure for the calculation of the PSD is given, as used in this dissertation and as reported by Newland [220], in the following:

1. Estimate the frequency range of interest and the maximum frequency that can be obtained from x_r (i.e. Nyquist frequency). The maximum frequency of interest is $f_{max} = 250$ Hz, the sampling frequency $f_s = 2048$ Hz so that the Nyquist frequency $f_{Nyq} = 1024\,\text{Hz} > 4f_{max}$. The time sampling is $\Delta = 1/f_s \approx 4.9 \cdot 10^{-4}$ s;

2. Decide the required accuracy for the measurement, defined by the ratio between the standard deviation σ and the mean m of a measurement of spectral density. If σ/m is small there is a high confidence that a sample measurement lies close to the mean value; Newland [220] provides an approximate level of confidence associated with a spectral density estimate when σ/m is known. This is based on the assumption that the spectral estimates can be expressed in terms of k statistically independent Gaussian random variables. A Chi-square (χ^2_k) probability distribution with k statistical degree-of-freedom may be then associated with the true mean m. For $k = 20$, 95% of all values of possible spectral estimate S_0 will lie in the band:

$$\frac{10.851}{20} < \frac{S_0}{m} < \frac{31.41}{20}$$

and, consequently, the 95% confidence levels for the mean are given by:

$$0.637\,S_0 < m < 1.843\,S_0 \tag{7.1}$$

which means that, given a measured spectral estimate S_0, the true mean lies, with the 95% of probability, in the range defined by Equation 7.1. For the processing of the data we choose $k = 20$ and a related accuracy of $\sigma/m = 0.3162$ (see Newland [220]);

3. Estimate the required effective bandwidth, for the averaging scheme of the spectral estimates, based on the duration T of the time-history:

$$\begin{gathered}\frac{\sigma}{m} = \frac{1}{\sqrt{B_e T}} \quad \Rightarrow \quad B_e = \frac{1}{T}\left(\frac{m}{\sigma}\right)^2 \\ \therefore\ B_e^{(\min)} = \frac{(3.162)^2}{16} = 0.625\,\text{Hz} \qquad B_e^{(\max)} = \frac{(3.162)^2}{10} = 1\,\text{Hz}\end{gathered} \tag{7.2}$$

with $B_e^{(\max)}$ and $B_e^{(\min)}$ defining the possible range of the frequency resolution of the calculated PSDs depending on the duration of the analysed time-series x_r;

4. Determine the number of data points $N = T/\Delta$ in x_r;

5. Find the number of added zeros L to increase the number of data points to $N_{FFT} = N + L$ to the nearest power of 2;

6. Determine the number of $2n+1$ of adjacent spectral estimates which must be averaged to give the required bandwidth:

$$(2n+1)\left(\frac{N}{N+L}\right) = B_e T$$

7. Execute the calculation procedure that can be found in the book of Newland [220] and that gives S_x the discrete series of spectral coefficients of the discrete time series x_r;

8. Calculate estimates of the continuous spectrum from the formula:

$$\tilde{S}_x'' = \frac{T}{2\pi}\left(\frac{N+L}{N}\right) S_x \tag{7.3}$$

9. Modify the estimates to correct for the zero-padding:

$$\tilde{S}'_x = \left(\frac{N+L}{N}\right)\tilde{S}''_k \tag{7.4}$$

10. Carry out the smoothing of the spectrum by averaging $(2n+1)$ adjacent estimates as described by Newland:

$$\tilde{S}'_{n(j)} = \frac{1}{2n+1}\sum_{m=-n}^{n}\tilde{S}'_x(\omega_{(j+m)}) \tag{7.5}$$

11. Adjust the two-sided Power Spectral Density in the angular frequency ω_j to the one-sided PSD in cycles per second f_j:

$$\tilde{S}_n = (4\pi)\tilde{S}'_n \quad , \qquad \tilde{S}_x = (4\pi)\tilde{S}'_x \tag{7.6}$$

The results in terms of the Power Spectal Density and the related third-octave band RMS values, obtained with the above procedure, and referring to the time-history in Figure 7.9, are shown in Figure 7.10. The PSDs $\tilde{S}_x$ and $\tilde{S}_n$ are shown together with the PSD $\tilde{S}_p$ calculated by means of the *pwelch function* in MATLAB [35]. This implements Welch's algorithm to calculate the PSD by

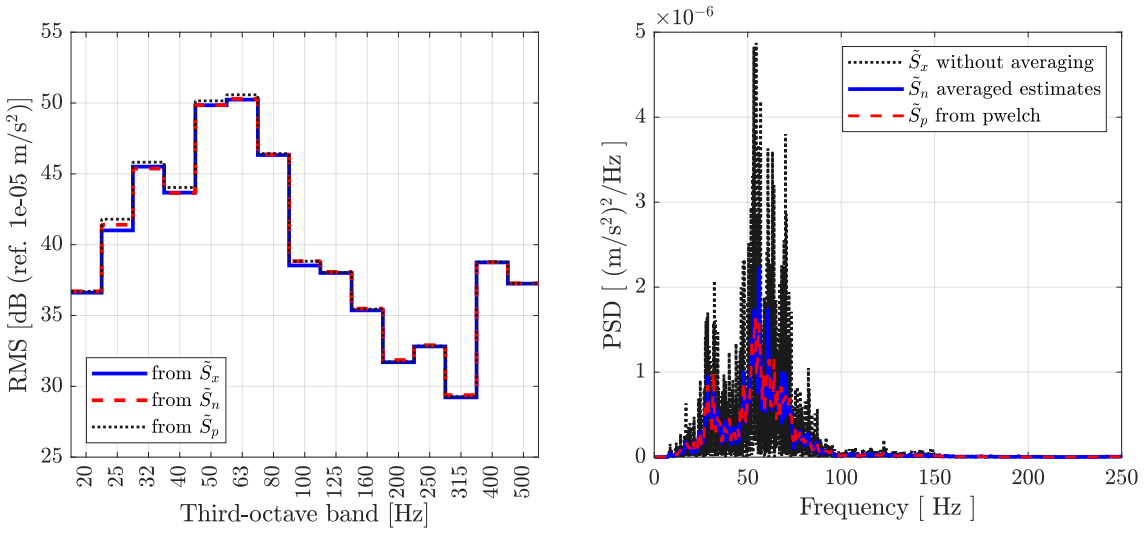

Fig. 7.10 Third-octave band Root Mean Square (RMS) values (left) and the related Power Spectral Density PSD (right) of an acceleration time-history representing a train pass-by. Two procedures are tested for the calculation of the PSD: an average of adjacent spectral coefficients (see Newland [220]) or Welch's algorithm [221] as implemented in MATLAB [35].

breaking the original time series in N_W time windows. With no overlapping of the windows, the statistical degrees of freedom of the chi-square distribution associated with the spectral estimates are given by $k = 2N_W$ [221]. We can then obtain the same accuracy σ/m, of that used for $\tilde{S}_n$, by considering $N_W = 10$ windows for the calculation of S_p. Moreover, in order to have comparable results, no filtering window is applied to the time windows of sample data. It can be seen in Figure 7.10 that the agreement between the two procedures is excellent, with maximum differences in the RMS values of up to 0.4 dB. This suggests that the use of one or the other procedure should not lead to significant differences in ground-borne vibration problems, particularly when the aim is to monitor for differences. The time-history obtained from several measurement events, and their frequency content, are discussed in the following.

Train signatures

Different measurement events referring to the first and to the last measurement sessions, namely SBP 08/09/2016 and SBP 07/11/2018, are considered here as examples of the different recorded time-histories registered at the site. They refer to the basement floor level on the footprint of the

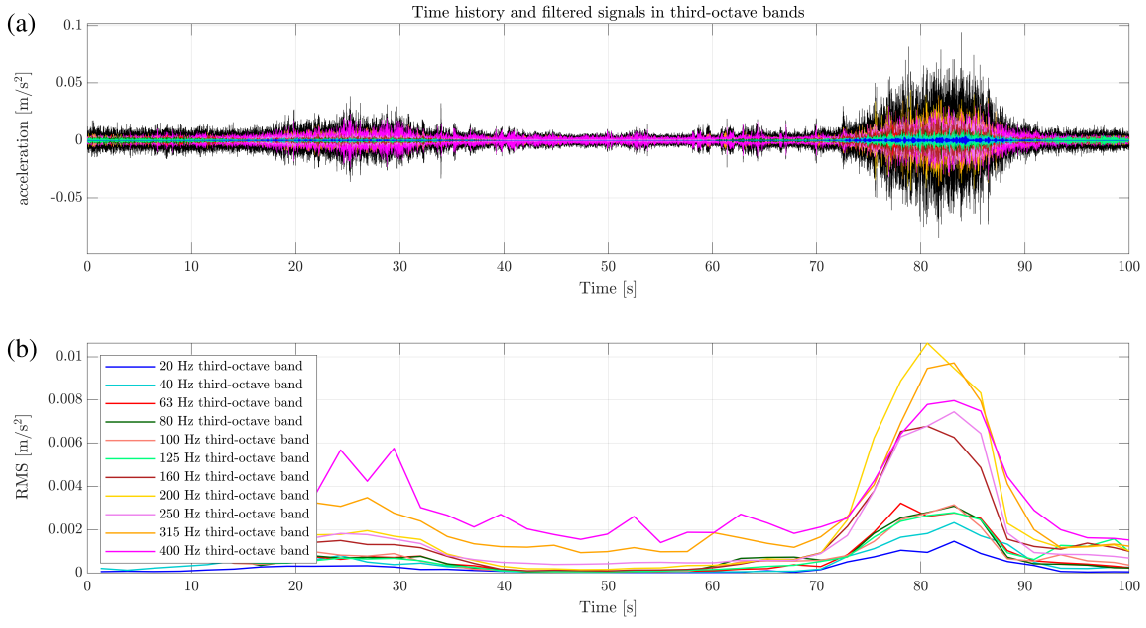

Fig. 7.11 Acceleration time-history and running third-octave band RMS values for a measurement event of the SBP 08/09/2018 session: (a) comparison of the acceleration time-history and the associated filtered time-histories in third-octave bands; (b) time-history of the third-octave band RMS values calculated by truncating the original time-history in 50 time-windows.

structural core, although the first is taken at the level of the existing slab foundation and the last at the level of the floating-slab of the structural core (see Figure 7.3(a) and (f)).

Figure 7.11(a) shows the acceleration time-history (black line) of a measurement event of the first session. A time-history of the third-octave band RMS values, obtained by sampling and processing 50 adjacent time-windows of the original signal, is shown alongside for observing changes in the RMS values next to the signal of a possible passing train. Two train pass-bys are visible, both with a rather high-frequency content. The first one has relatively low levels of associated RMS values with predominant 315-400 Hz third-octave bands. The second has a significant frequency content for the same bands, but a predominant content of the 200 Hz third-octave band together with important levels in the 160 Hz and 250 Hz third-octave band. This is a frequency content that is more likely, compared with the high frequency content in the 315 Hz and 400 Hz bands, to be representative of trains passing underground. A similar range of frequency in the 63-250 Hz bands has been observed by Brookes et al. [12] in measurements taken at the basement level of the Grand Central Recording Studios, in London, and related to multiple underground train lines. Whether or not the high-frequency content (315-400 Hz bands) may be actually representative of a passing train is open to questions, with

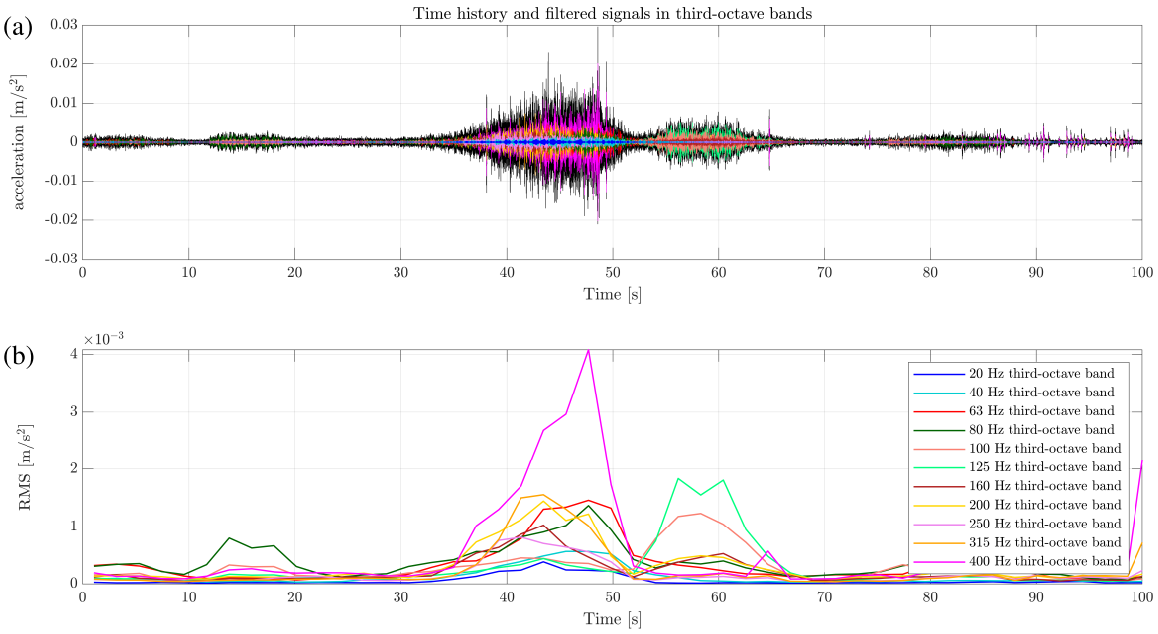

Fig. 7.12 Acceleration time history and running third-octave bands RMS values for a measurement event of the SBP 07/11/2018 session: (a) comparison of the acceleration time-history and the associated filtered time-histories in third-octave bands; (b) time-history of the third-octave band RMS values calculated by truncating the original time-history in 50 time-windows.

the possibility that it may be due to filtering/amplification effects, due to the complex underground structure, and/or to operating machinery at the site, although it was registered none in the close proximity to the measurement locations.

Figure 7.12 shows a similar plot, this time for a measurement event of the session SBP 07/11/18. It is clear that the vibration levels are decreased from both the values of the ppa of the train pass-bys and on the related third-octave band RMS values. A first train pass-by is registered with a high frequency content in the 400 Hz band. RMS values in the 63 Hz, 80 Hz, 200 Hz and 315 Hz bands are comparable at a level of 0.001-0.0015 m/s^2. The second train pass-by is characterised by a clear frequency content in the 100-125 Hz third-octave bands.

More examples of train pass-by measurements are shown in Figure 7.13 and 7.14 for measurement events of the first and the last session respectively. The first one features two train pass-bys with predominant third-octave bands of 63, 80 and 100 Hz, and 40, 63 and 80 Hz respectively. Both train pass-bys have an absent or limited high-frequency content, conversely to what seen previously.

Three train pass-bys are visible in the measurement event of the last session. The first one has a frequency content in the 63, 80, 100 and 125 Hz third-octave bands, with very low RMS values at

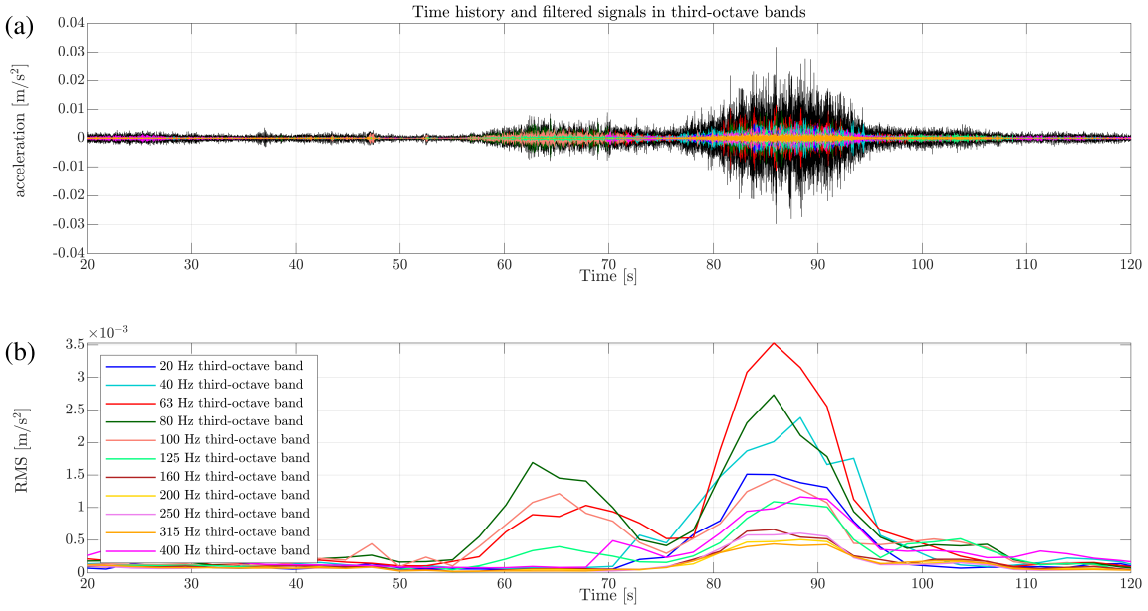

Fig. 7.13 Acceleration time history and running third-octave bands RMS values for a measurement event of the SBP 08/09/2016 session: (a) comparison of the acceleration time-history and the associated filtered time-histories in third-octave bands; (b) time-history of the third-octave band RMS values calculated by truncating the original time-history in 50 time-windows.

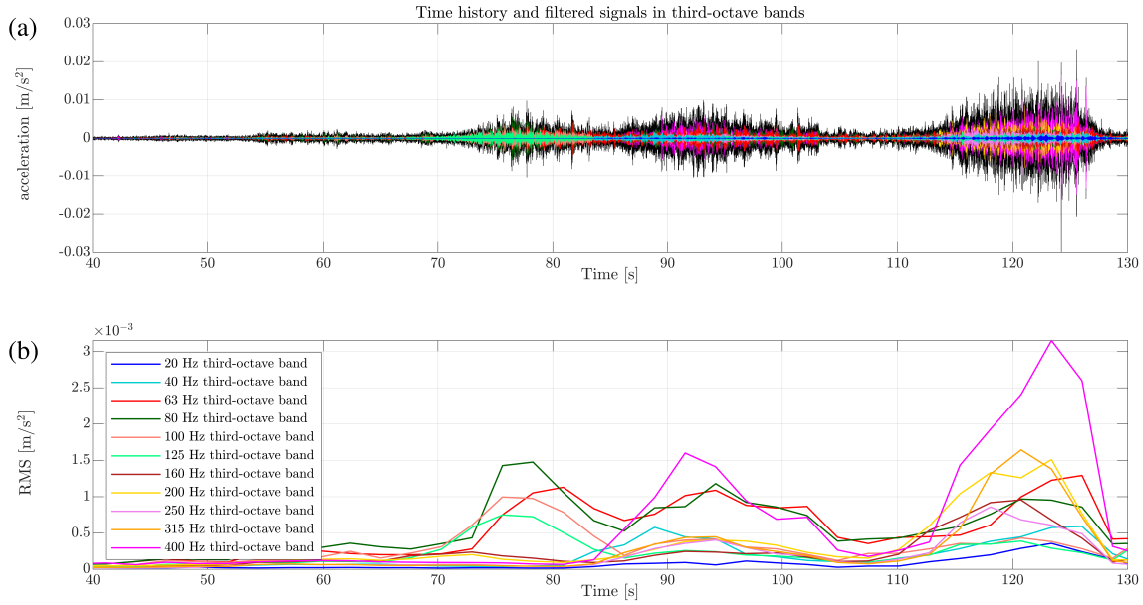

Fig. 7.14 Acceleration time history and running third-octave bands RMS values for a measurement event of the SBP 07/11/2018 session: (a) comparison of the acceleration time-history and the associated filtered time-histories in third-octave bands; (b) time-history of the third-octave band RMS values calculated by truncating the original time-history in 50 time-windows.

higher frequencies. The second train pass-by has the same order of magnitude of the RMS values of the first one in the 63-80 Hz, but it also has a significant RMS value in the 400 Hz third-octave band. The third train pass-by has a quite broad band frequency content with a predominant RMS value in the 400 Hz band.

From this qualitative analysis of the train pass-bys registered at the site, one can realise that it is challenging to categorise them in different, distinctive train signatures. Indeed, this is something that it is not attempted here. The interest lies on the variation of the vibration levels as the construction of the building progresses. For this purpose, the train pass-bys that result in the highest levels of the RMS values, in the third-octave bands from 40 Hz to 125 Hz, will be grouped together, as Group 1, to represent the higher vibration levels to be expected on site. As discussed later, the high frequency content beyond 125-150 Hz might be related to a local condition, rather then to an actual feature of the underground trains. The remaining pass-bys belong to the Group 2 representing lower vibration levels. The following section explains how this subdivision of the train pass-bys is carried out and presents results for the first measurement session SBP 08/09/16.

Brown-field measurements

A summary of the vibration levels, in terms of the RMS values in third-octave bands, for the first session SBP 08/09/16 is presented here. This corresponds to the *brown-field* stage in which the foundation and the building are yet to be constructed. The terminology brown-field indicates that measurements are taken at a site strongly influenced by man-made structures. In practice, measurements are taken at the free-surface of the existing slab foundation, of the original Shell Centre, surrounded by the excavating ground, some basement structures and adjacent buildings (e.g. the Shell Tower). The condition of an ideal construction site, without any surrounding structure, that is known as *green-field* does not really apply here.

Based on the previous discussion about the different train signatures, the train pass-bys are categorised, qualitatively, in two groups. We want to separate the main group of pass-bys (Group 1) that have a significant frequency content in the range 40–125 Hz. This is done by considering the RMS values in the pertinent third-octave bands (i.e. 40–125 Hz centre frequency), taking their mean value $RMS^{(mean)}_{(i)\,40\text{–}125}$ for each i^{th} train pass-by and dividing the train pass-bys in two groups:

- Group 1, in which each train pass-by satisfies the condition:

$$RMS^{(mean)}_{(i)\,40\text{–}125} > RMS^{(mean)}_{(max)\,40\text{–}125} - \text{dB}_{range}$$

- Group 2, the remaining train pass-bys that satisfy the condition:

$$RMS^{(mean)}_{(i)\,40\text{–}125} \leq RMS^{(mean)}_{(max)\,40\text{–}125} - \text{dB}_{range}$$

with $RMS^{(mean)}_{(max)\,40\text{–}125}$ the maximum among the $RMS^{(mean)}_{(i)\,40\text{–}125}$ for all the train pass-bys of the session, and dB_{range} a range arbitrarily chosen to obtain the two groups. Although this procedure is purely arbitrary and based only on practical judgement, it provides a means of selecting the pass-bys that have higher vibration levels in the frequency range of interest.

Figure 7.15 shows the third-octave bands RMS acceleration values and the PSDs estimates for each group identified for channel 3 of the measurement session (see Figure 7.5). In agreement with what seen before, a high-frequency content is present, which actually shows a large variability in the PSDs estimates and the related third-octave bands RMS values. The value dB_{range} is taken as 6 dB. The RMS values are shown in a *boxplot*, which provides, visually, statistics related to the finite set of

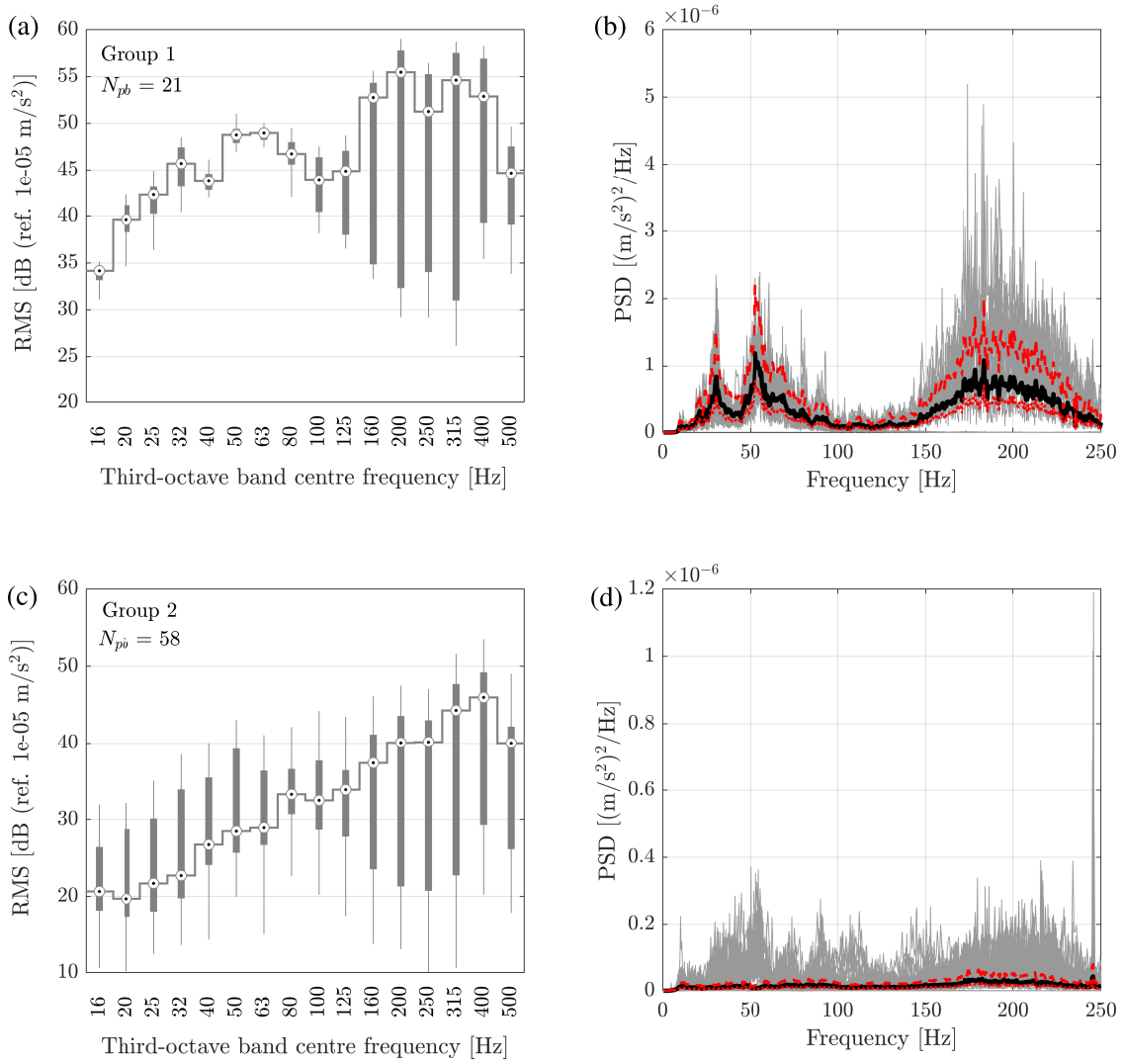

Fig. 7.15 Third-octave band acceleration RMS (left) and PSD (right) values for train pass-bys of (a) and (b) Group 1, and (c) and (d) Group 2 of the measurement session SBP 08/09/2016 obtained at the location of channel 3 (see Figure 7.5). The average value of the estimated PSDs of the N_{pb} train pass-bys is shown in a black thick line with the upper and lower 95 % confidence levels, referring to $k = 20$ statistical degrees of freedom, shown with a dashed and a dotted red line respectively.

N_{pb} pass-bys for each third-octave band: the black-white circular marker and the stair-line provide the median value, the bar provides the interquartile range (IQR) from the 25$^{\text{th}}$ to the 75$^{\text{th}}$ percentile, the whiskers show any maximum and minimum value beyond the IQR, and circular markers beyond the whiskers (if any) represent outliers. It should be noted that these statistics are inferred from the value of each PSD estimate referring to a given pass-by of the analysed set (Group 1 and/or Group 2). Any PSD estimate suffers not only from the measurement accuracy, as seen before, but also from

the statistics of the random process itself (i.e. acceleration time-history), which are not discussed here. However, just for reference, the confidence levels as obtained in Equation 7.1, referring to the accuracy of the adopted procedure, are reported with a dashed and a dotted red lines starting from the mean value (black line) obtained by averaging the PSDs estimate of the train pass-bys (gray lines). A comment that can be made on Figure 7.15, confirmed by the results shown in those that follow (Figure 7.16 and 7.17), is that Group 1 collects pass-bys with high-level acceleration and

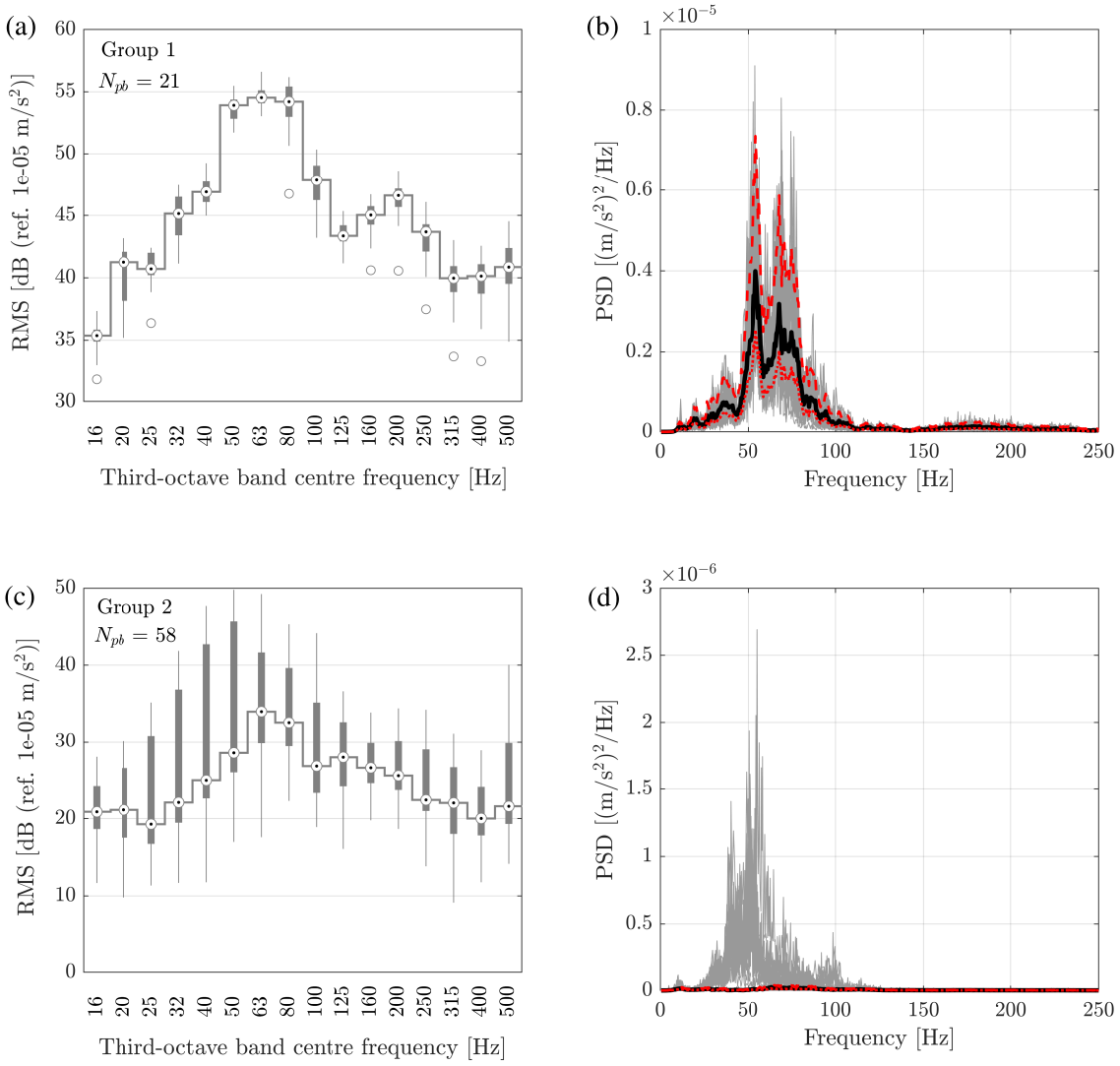

Fig. 7.16 Third-octave band acceleration RMS (left) and PSD (right) values for train pass-bys of (a) and (b) Group 1, and (c) and (d) Group 2 of the measurement session SBP 08/09/2016 obtained at the location of channel 4 (see Figure 7.5). The average value of the estimated PSDs of the N_{pb} train pass-bys is shown in a black thick line with the upper and lower 95 % confidence levels, referring to $k = 20$ statistical degrees of freedom, shown with a dashed and a dotted red line respectively.

excellent repeatability of ±3 dB in the frequency range of interest, while Group 2 collects pass-bys with low-level acceleration and high variability. This gives us an indication that the method adopted for the subdivision can be qualitatively assumed appropriate.

It is instructive to investigate to what extent the vibration levels change along the measurement alignment in Figure 7.5. Figure 7.16 and 7.17 show similar plots for the RMS and PSD values as before, but this time for the locations at channel 4 and channel 1 respectively. The former is closer

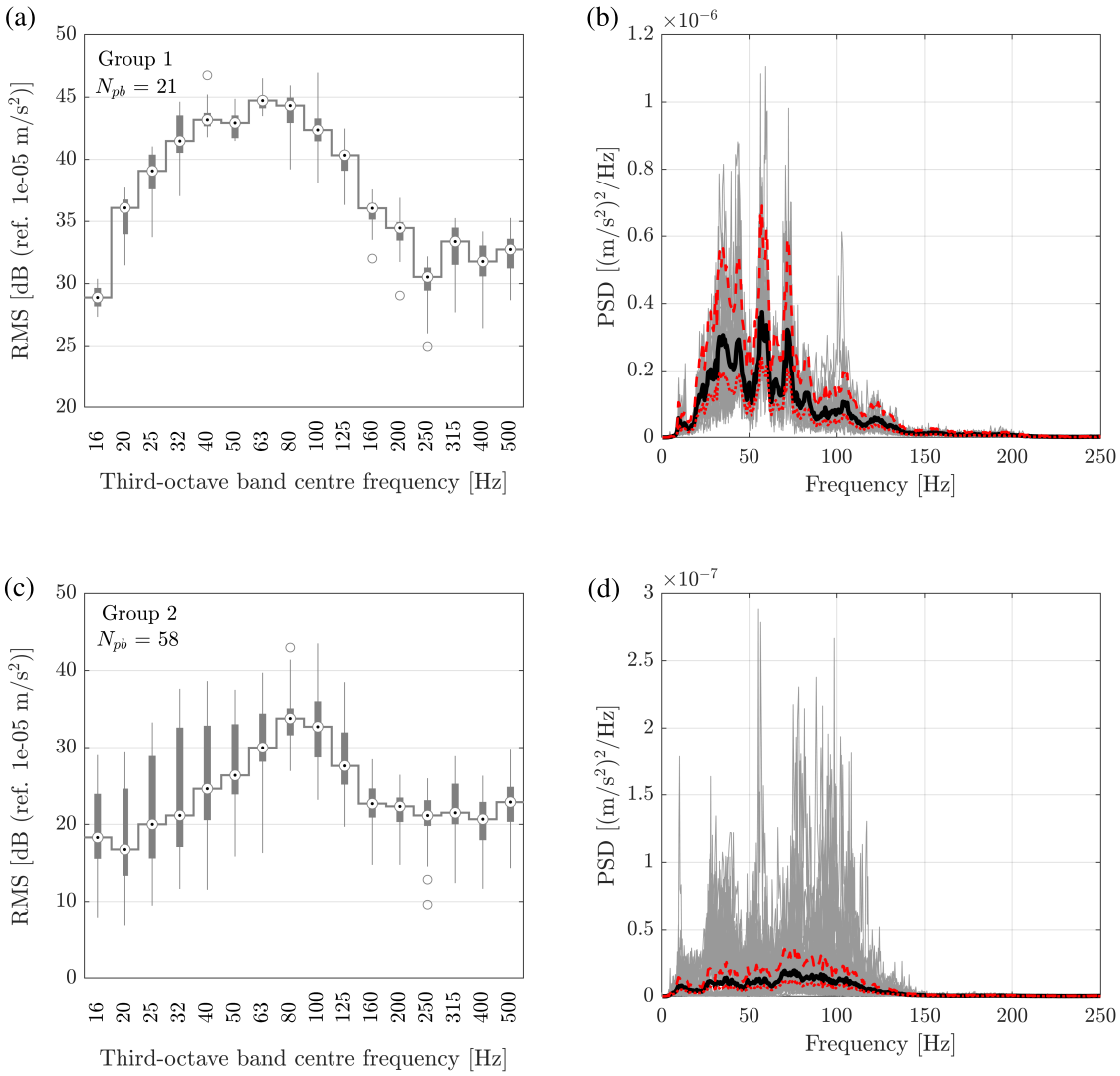

Fig. 7.17 Third-octave band acceleration RMS (left) and PSD (right) values for train pass-bys of (a) and (b) Group 1, and (c) and (d) Group 2 of the measurement session SBP 08/09/2016 obtained at the location of channel 1 (see Figure 7.5). The average value of the estimated PSDs of the N_{pb} train pass-bys is shown in a black thick line with the upper and lower 95 % confidence levels, referring to $k = 20$ statistical degrees of freedom, shown with a dashed and a dotted red line respectively.

to the Bakerloo line while the latter is further away. Few comments can be made. First, in both cases, the high-frequency content beyond 125 Hz has considerably reduced, if not disappeared. This suggests that the high-frequency content, beyond 125–150 Hz, observed for channel 3 may be due to an unknown phenomenon at that location rather than a feature of the running trains underground. In both locations, channel 1 and channel 4, the frequency content, for the Group 1 of the train pass-bys, is confined in the 40–125 third-octave bands, a feature common for underground trains [12]. Second, there is a clear attenuation of the vibration levels from the north to the south side of the footprint of the structural core. For instance, the RMS values in the 63 Hz third-octave band go from 54.5 dB, 49 dB to 44.7 dB for channel 4, 3 and 1 respectively, with an overall attenuation of about 10 dB across the measurement alignment on the footprint of the structural core, which is roughly 15 m long. The next sections are dedicated to the investigation of the added-foundation and the added-building effect by looking at the different measurement sessions, listed in Section 7.2, by adopting the procedure summarised in this section.

7.4 Post-slab measurements: The Added-Foundation Effect

This section presents the measurement results of sessions SBP 05/10/2016 and SBP 23/10/2016, after the construction of the new slab foundation and the floating-slab beneath the structural core, respectively. The same procedure and methodology, summarised in the previous section, is followed for obtaining the third-octave bands RMS acceleration values of the train pass-bys categorised in the Group 1. This induces the highest level of vibration, and the interest lies in investigating how this may vary during the construction of the foundation.

Figure 7.18 shows the results for the session SBP 05/10/2016 at the locations of channel 1 and channel 4. A difference of about 5 dB is found for the RMS values in the 63 Hz third-octave band between the two locations, which indicates a limited attenuation across the measurement alignment compared to that obtained for the brown-field case examined earlier. Similar to that seen before, the train pass-bys are characterised by a frequency content in the 40–160 Hz range. From the spectrum of the third-octave band RMS values, a distinctive frequency content in the 500 Hz third-octave band is present, probably due, as commented before, to a local feature rather than to characteristics of the underground trains. The 63 Hz third-octave band is, also in this session, pre-dominant with levels of about 44 dB and 48.5 dB at channel 1 and 4, respectively. Compared with that obtained in the last

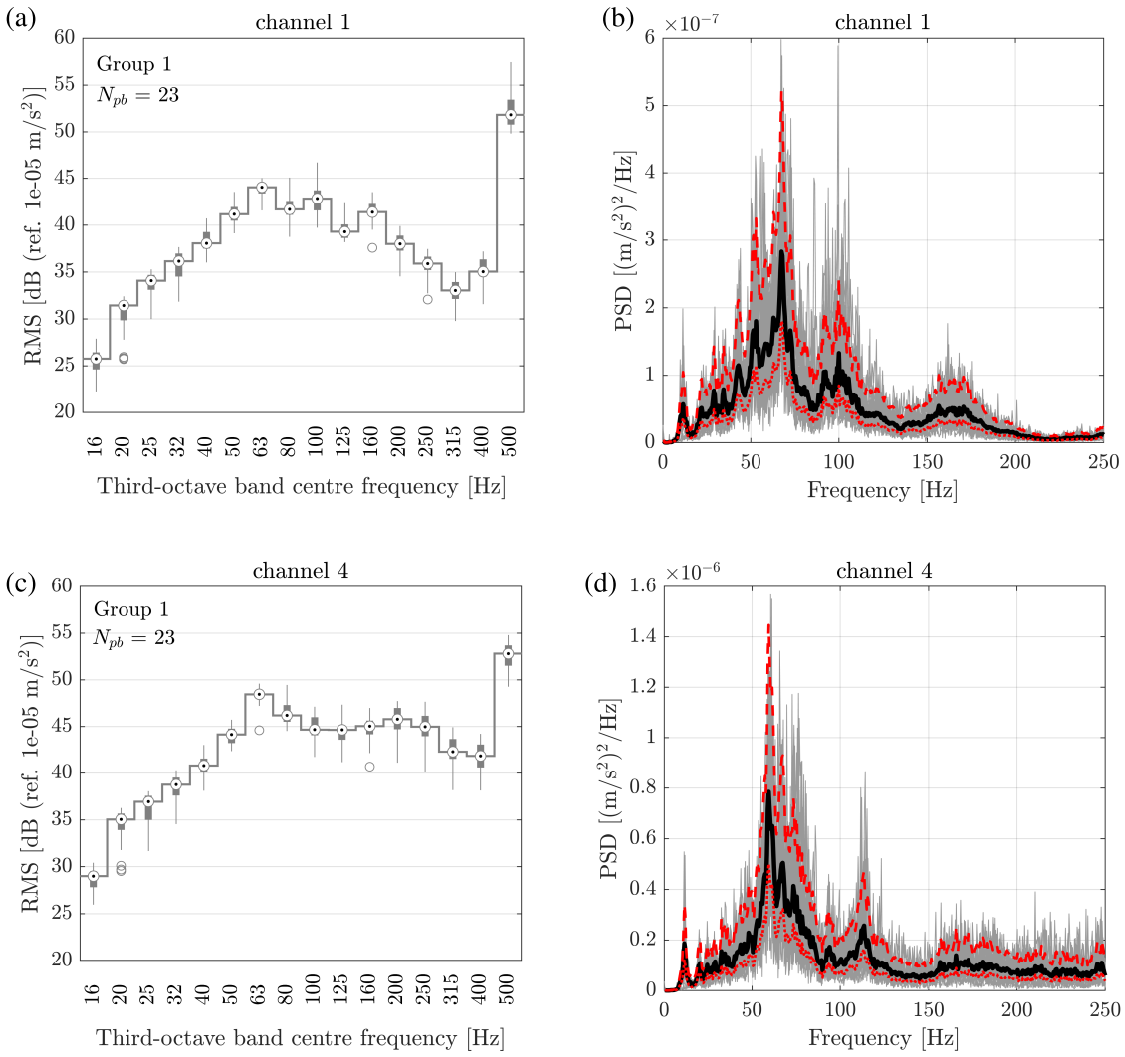

Fig. 7.18 Third-octave bands acceleration RMS (left) and PSD (right) values for train pass-bys of Group 1 referring to (a) and (b) channel 1, and (c) and (d) channel 4 (see Figure 7.5) of the measurement session SBP 05/10/2016. The average value of the estimated PSDs of the N_{pb} train pass-bys is shown in a black thick line with the upper and lower 95 % confidence levels, referring to $k = 20$ statistical degrees of freedom, shown with a dashed and a dotted red line respectively.

section, this represents an attenuation of about 6 dB and less than 1 dB for locations closer and further away from the Bakerloo line. This is a somewhat limited value of attenuation when compared with the 10–20 dB attenuation obtained for the added-foundation effect examined in Section 5.4.3, with reference to a numerical model of a finite slab foundation. This may be because of the increased impedance provided by the existing, underlying 1 m thick, slab foundation and/or because of the

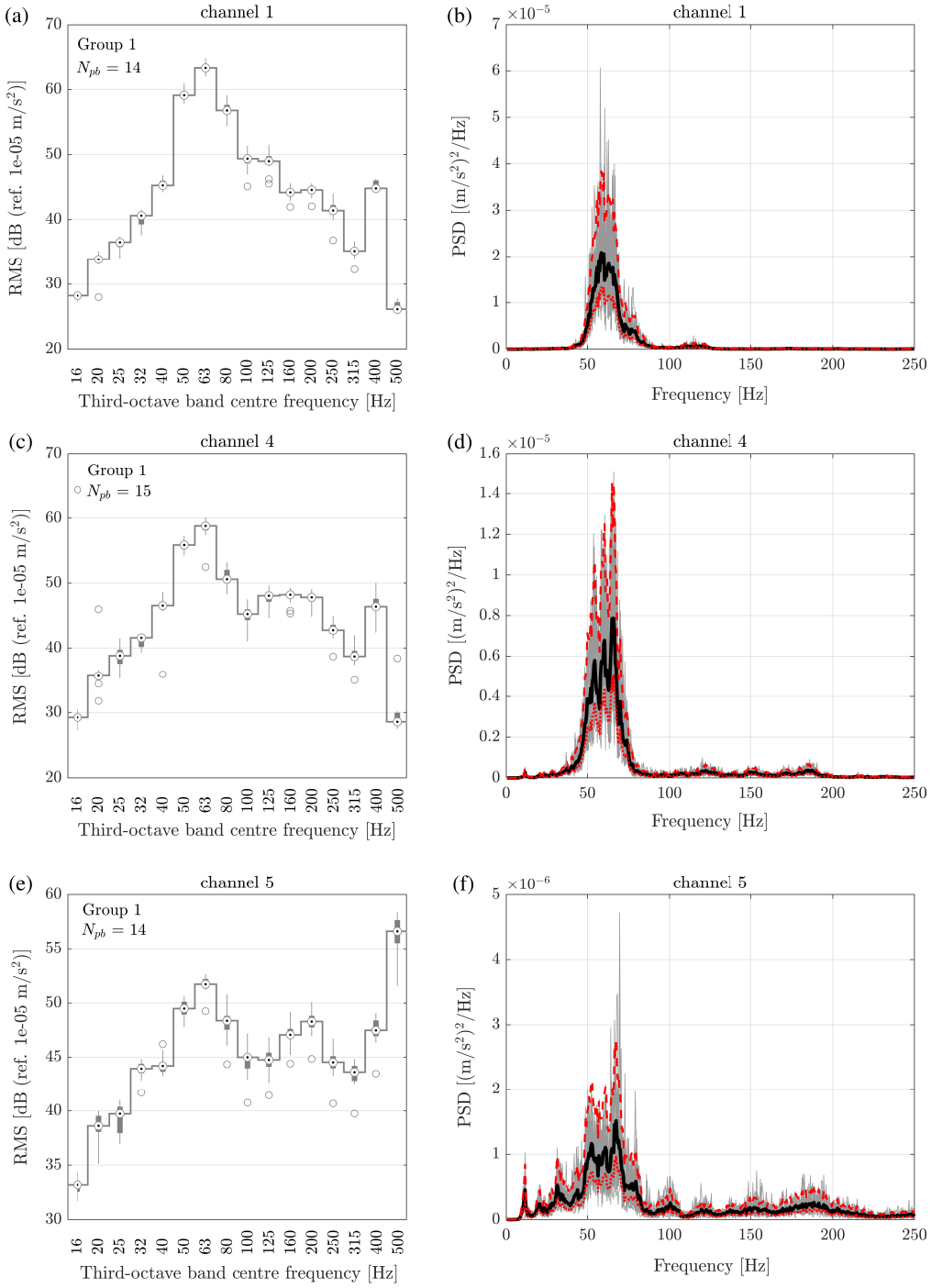

Fig. 7.19 Third-octave bands acceleration RMS (left) and PSD (right) values for train pass-bys of Group 1 referring to (a) and (b) channel 1, (c) and (d) channel 4, and (e) and (f) channel 5 (see Figure 7.5) of the measurement session SBP 23/10/2016. The average value of the estimated PSDs of the N_{pb} train pass-bys is shown in a black thick line with the upper and lower 95 % confidence level ($k = 20$) shown with a dashed and a dotted red line respectively.

incident wave-field from the underground trains, which hardly may be represented by a plane-wave excitation.

Figure 7.19 shows the measurements results for the session SBP 23/10/2016 at the locations of channel 1, 4 and 5 as in Figure 7.5. Channel 1 and 4 are situated on the floating-slab overlying an elastomeric layer, which was installed on the new slab foundation (see Figure 7.4(b)), to isolate the structural core. Channel 5 is installed as in Figure 7.5 on the area beyond the footprint of the structural core and directly on the new slab foundation, which, at this point of the construction, has been cast in-situ on this area. As before, we comment on the median RMS values in the 63 Hz third-octave band by observing a value of 63.3 dB, 58.8 dB and 51.7 dB for channel 1, 4 and 5 respectively. Hence, for the two locations on the floating-slab an amplification of about 20 dB and 10 dB is observed at the locations of channel 1 and 4 respectively. This is because of the relatively soft elastomeric material, which provides, effectively, a spring beneath the floating-slab that tends to amplify the vibration levels in the frequency range of interest. However, the extent to which this occurs is challenging to predict because of the particular incident wave-field from the underground trains, the complexity of

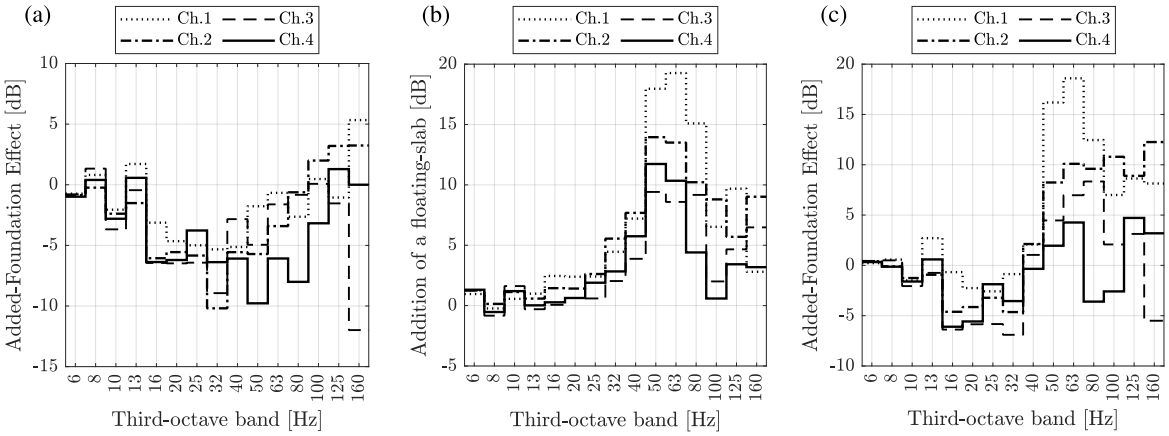

Fig. 7.20 Experimental Added-Foundation Effect for the case-study building during the construction of the foundation beneath the footprint of the structural core. A comparison of the third-octave band RMS acceleration values, in dB, is obtained between different sessions: (a) after and before the construction of the new slab foundation (SBP 05/10/2016 vs. SBP 08/09/2016), (b) after and before the construction of the floating-slab (SBP 23/10/2016 vs. SBP 05/10/2016) and (c) after and before the construction the foundation system for the structural core (SBP 23/10/2016 vs. SBP 08/09/2016). The results with reference to different locations, at the footprint of the structural core (-2 level), are shown with a solid line (Ch.4), dashed line (Ch.3), chained line (Ch.2) and dotted line (Ch.1) (see Figure 7.5).

the foundation structure (mass, stiffness and damping) and the different elastomeric materials, used on the footprint (see Figure 7.4), with variable properties.

An overview of the added-foundation effect is given in Figure 7.20, with reference to the different construction stages of the foundation system of the structural core. The comparison is shown in terms of the reduction and/or amplification of the third-octave band median RMS acceleration values with respect to different measurement sessions. Figure 7.20(a) shows the difference obtained with the construction of the new slab foundation. An attenuation of up to 10 dB is obtained for all the four locations investigated across the footprint up to the 32 Hz third-octave band. At higher frequencies the attenuation reduces until amplification occurs, especially at the locations Ch.1 and Ch.2 on the south side of the footprint of the structural core (i.e. further away from the Bakerloo line).
Figure 7.20(b) shows the comparison of vibration levels after and before the construction of the floating-slab, while Figure 7.20(c) provides the overall added-foundation effect provided by the combination of the floating-slab overlying the new slab foundation. The results obtained for the added-foundation effect of the floating-slab are of conceptual interest. It is clear that, although to a different extent for the several locations, an amplification of the vibration levels up to about 20 dB is observed, particularly in the 50, 63 and 80 Hz third-octave bands. This is a significant experimental evidence, which suggests that the construction of a floating-slab, without any consecutively supported structure, may be the cause of potential amplifications, which should be checked against in the frequency range of interest. However, in our case, these are interim data that describe only the added-foundation effect. The following step is the construction of the structural core with an associated added-building effect, as explored in the next section.

7.5 Post-building measurements: The Added-Building Effect

A similar investigation to that of the last section can be carried out for sessions related to the construction of the building. We want to acknowledge the added-building effect, as investigated in Chapter 3 and 6, with reference to experimental measurements of vibration levels. These refer to locations on the footprint of the structural core, at the basement level (i.e. -2 level). The reference vibration levels are those of the measurement session SBP 23/10/2016, in which the construction of the foundation system has been completed, but any parts of the building (e.g. core, steelwork, etc.) are yet to be constructed. As the construction of the latter progresses, a change in vibration levels is to

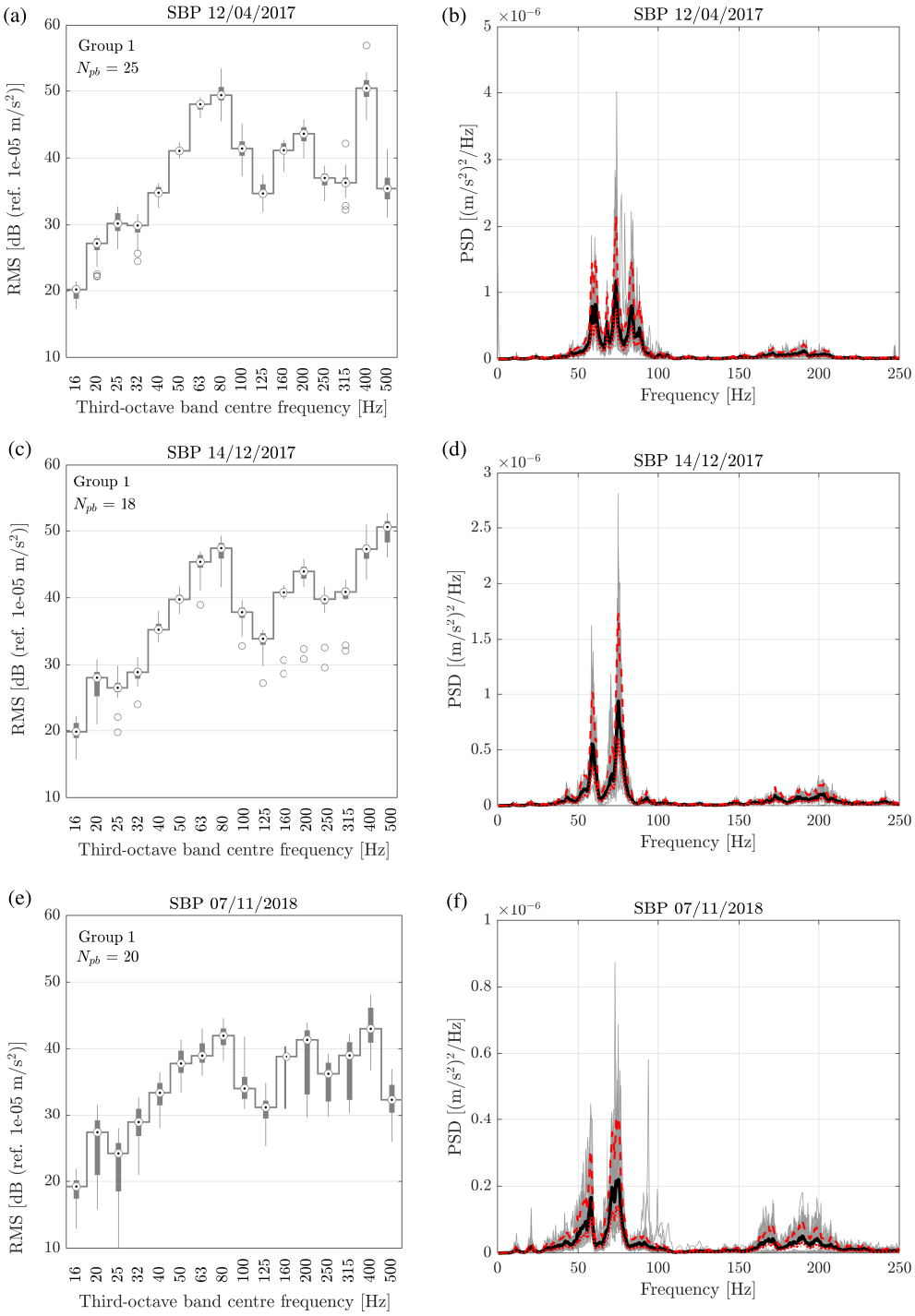

Fig. 7.21 Third-octave bands acceleration RMS (left) and PSD (right) values for train pass-bys of Group 1 referring to (a) and (b) SBP 12/04/2017, (c) and (d) SBP 14/12/2017, and (e) and (f) SBP 07/11/2018 (see Figure 7.3), all referring to the location of channel 1. The average value of the estimated PSDs of the N_{pb} train pass-bys is shown in a black thick line with the upper and lower 95 % confidence level ($k = 20$) shown with a dashed and a dotted red line respectively.

be expected, generally an attenuation of vibration levels, as seen in Section 3.5.1 for the single-point coupling model and in Section 6.3 for the portal-frame building.

Figure 7.21 shows the the resulting vibration levels in terms of the third-octave band RMS acceleration values and the related PSDs for the measurement sessions: (a) and (b) after the construction of the structural core (SBP 12/04/2017), (c) and (d) after the construction of the steelwork (SBP 14/12/2017), and (e) and (f) after the installation of the façade (SBP 07/11/2018). For the latter, there are no data available at the location of channel 4 due to a malfunctioning of the accelerometer. From Figure 7.21, a qualitative comment can be made in that the frequency content is still visible within the 63–80 Hz third-octave bands, although with sharpened peaks rather than the broader frequency content previously observed in Figure 7.19(b). Starting from the 63 Hz median RMS value, observed in the session SBP 23/10/2016, of 63.3 dB, the vibration levels in this band are reduced to 48 dB, 45.4 dB and 39 dB in the consecutive construction stages of the building. The added-building effect can be then obtained, for the three measurement sessions involving the construction of the different parts of the building, as the difference, in dB, of the median RMS vibration levels after construction of the structural core, the steelwork and the façade, and the median RMS vibration levels of session SBP 23/10/2016. This is shown in Figure 7.22, for the four locations under investigation. For the

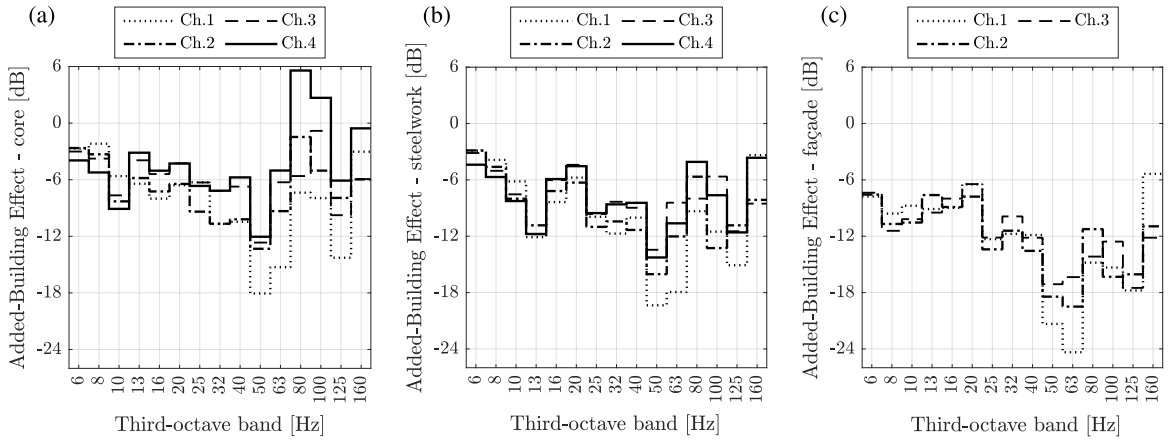

Fig. 7.22 Experimental Added-Building Effect for the case-study building during the construction of the structural core, the steelwork and the façade of the building. A comparison of the third-octave band RMS acceleration values, in dB, is obtained between the relevant sessions and the vibration levels of reference of session SBP 23/10/2016: (a) after the construction of the structural core (SBP 12/04/2017), (b) after the construction of the steelwork (SBP 14/12/2017) and (c) after the installation of the façade (SBP 07/11/2018). The results with reference to different locations, at the footprint of the structural core (-2 level), are shown with a solid line (Ch.4), dashed line (Ch.3), chained line (Ch.2) and dotted line (Ch.1) (see Figure 7.5).

three construction stages, an incremental attenuation of the vibration levels is expected, although the reduction is, in general, frequency-dependent. The construction of the structural core reduces the vibration levels from 6 dB to 18 dB, with a better attenuation for locations further away from the Bakerloo line (e.g. channel 1). An amplification and a limited attenuation are observed at the 80–100 Hz third-octave bands for channel 4 and channels 1–3 respectively. As the construction progresses with the steelwork, the added-building effect provides an attenuation of levels for all the third-octave bands of interest up to 160 Hz, although differences as large as 10 dB may be found between the levels of different frequency-bands and/or the different locations examined. A similar trend is observed for the completed building, with an increased attenuation of up to 24 dB for the location further away from the Bakerloo line (channel 1). Figure 7.23 shows the added-building effect referring to the completed building, as in Figure 7.22(c), but this time up to higher frequencies and by reporting the spatial average of the median RMS acceleration values referring to the three considered

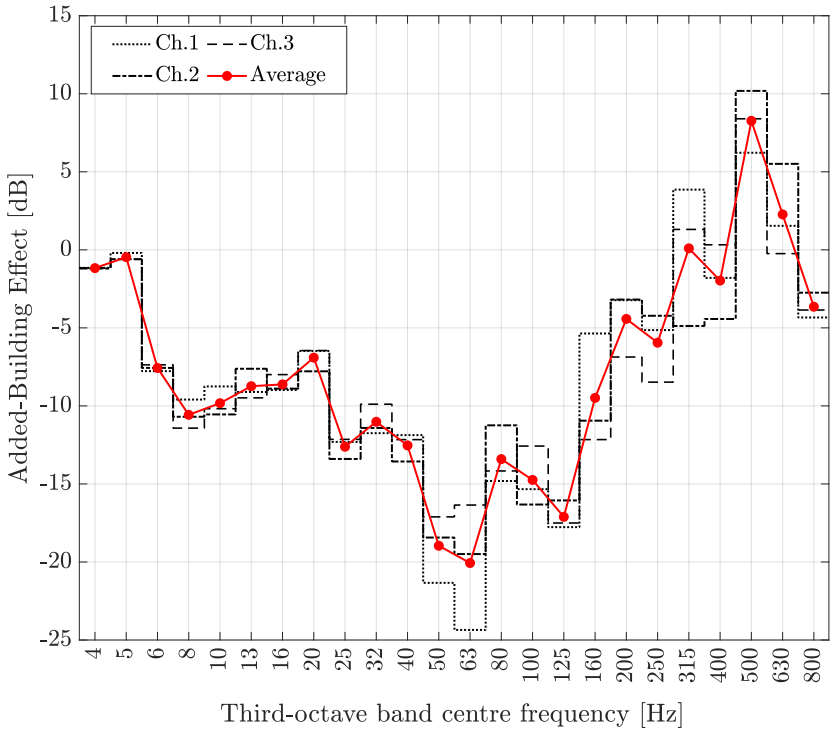

Fig. 7.23 Experimental Added-Building Effect for the case-study building. A comparison of the third-octave band RMS acceleration values, in dB, is obtained between the measurement session SBP 23/10/2016, before the construction of any part of the building, and the session SBP 07/11/2018 with the completed building. The results with reference to different locations, at the footprint of the structural core (-2 level), are shown with a dashed line (Ch.3), chained line (Ch.2) and dotted line (Ch.1) (see Figure 7.5) and their average is reported with a red line.

locations (channel 4 not shown because of a malfunctioning). From the results, with an attenuation of up to 20 dB in the 63 Hz third octave band, we understand that the experimental added-building effect, obtained for the case-study, provides a significantly greater attenuation of vibration levels compared to that seen for a portal-frame building in Section 3.5.1 and 6.3. Let us consider the basic expression of the added-building effect in Equation 3.51. This is governed by the impedance mismatch at the foundation-building interface between the building and the foundation (i.e. $\widehat{K}_b/\widehat{K}_f$). The reason for a greater attenuation than expected may be then found by realising that, for this case study, we may have a softer foundation system (because of the presence of the elastomeric layer) and a stiffer building system, since we are considering structural walls instead of slender columns. The actual configurations of the foundation and building systems leads then to an increased impedance mismatch $\widehat{K}_b/\widehat{K}_f$ and, consequently, to an increased added-building effect. An approximate idea of the actual (vertical) impedance mismatch that may materialise in practice, with reference to the configuration of the case-study, may be then obtained from Equation 3.51 as:

$$\frac{\widehat{K}_b}{\widehat{K}_f} = 10^{\alpha/20} - 1 \tag{7.7}$$

with α the amount of attenuation observed (in dB). From Figure 7.23, we observed that attenuation values of 6, 12, 18, and 24 dB are possible within the frequency-range of interest, corresponding approximately to a ratio $\widehat{K}_b/\widehat{K}_f$ of 1, 3, 7 and 15 respectively. This suggests that, in practice, the impedance mismatch, with reference to the structural core of the building, may vary considerably, perhaps by one order of magnitude, within the frequency range of interest.

7.6 Conclusions

This chapter has reported the results of a measurement campaign undertaken at the Shell Centre re-development site at South Bank, London. By describing the construction site and giving a summary of the measurement plan, it has been shown that experimental measurements are considerably challenging to obtain, and to interpret, especially during the construction process of a building. Nonetheless, by making any effort possible in keeping reference locations for the vibration measurements at all the construction stages, it has been possible to report two main aspects of practical interest.

First, the added-foundation effect, as explored, in theory, in Chapter 4 and 5, has been observed with reference to the construction of the new slab foundation over the existing slab foundation of the

original Shell Centre. Although differences between locations and along the frequency spectrum are important, a reduction of vibration levels of the order of 6 dB is observed for the lower part of the frequency range of interest.

Second, the added-building effect, as observed, in theory, in Chapter 3 and 6, has been reported with reference to locations at the footprint of the structural core of the building. A considerable attenuation of vibration levels, in the range of approximately 6–24 dB, has been registered, indicating that a significant impedance mismatch between the building and the foundation system may be present, in practice, at the foundation-building interface on the basement level of the structural core.

Chapter 8

Conclusions and future work

This dissertation has explored the use of simplified methods and models for the definition of design guidelines for base-isolated buildings against ground-borne vibration. A design analysis framework has been suggested, which is intended to bring the practising engineer one step closer towards a performance-based design of base-isolated buildings. This has the two-fold consequence of easing the design and of interpreting results obtained by a more involved numerical model. Here, a summary of the main concluding remarks is presented. For specific aspects the reader is redirected to the conclusions of the relevant chapters. Comments on possible future research directions are also summarised.

8.1 Conclusions

An important aspect presented throughout this dissertation is the role played by the soil-foundation-building interaction in problems related to ground-borne vibration of buildings. This has been broken down into several parts for the pursuit of a design analysis framework for base-isolated buildings against ground-borne vibration. This has been possible by referring to a general design scenario with a surface foundation and a portal-frame building. In the following, general conclusions are presented for the isolation performance of a base-isolated building (Chapter 3 and 6), and for the added-foundation (Chapter 4 and 5) and the added-building effects (Chapter 3 and 6).

Isolation performance: a conclusion

A first-principles approach has been adopted for evaluating the isolation performance associated with a portal-frame building. Thanks to the introduction of a general single-point coupling model, useful insights have been deduced for the response of base-isolated buildings. First, as an extension of the work of Talbot [33], the equivalence of the Insertion Gain (IG) to the Power Flow Insertion Gain ($PFIG$) has been proved for the case of a purely vertical input. Although the result refers to the single-point coupling model, the equivalence has been observed also for the examined portal-frame building, subject to in-phase vertical input, in a frequency-range where the axial response of columns dominates. This supports the use of the $PFIG$ as a valid alternative to the IG as a metric of isolation performance.

An important design consideration has been made on the basis of the tractable results referring to the single-point coupling model subject to vertical input: the isolation performance does not depend strictly on the isolation frequency, as deduced by the mass-on-a-spring model, but rather on the impedance mismatch between the building and the foundation, and between the building and the isolation system at the foundation-building interface.

In addition, a simplified foundation-building model has been adopted in the form of a cone model for the foundation, and a damper for the building at each coupling point of the foundation-building system. By considering the cone-damper model subject to a vertical input, a closed-form expression has been obtained for the isolation performance in terms of the $PFIG$. This has been tested against the results of a rigorous base-isolated building subjected to different incident wave-fields including the case of a vertical, localised source at the free-surface. The results suggest that the closed-form expression captures the trend of the isolation performance along the frequency spectrum. Thus, the closed-form expression may serve as a guideline for hand-calculations of the isolation performance during preliminary design considerations.

On the other hand, the design analysis framework, based on the cone-damper model, may be used in a more advanced stage of the design. By comparison with a rigorous foundation-building model, it has been shown that the design framework is able to properly capture the frequency-dependency of the isolation performance, in terms of the $PFIG$, for several incident wave-fields in the form of P-, SV- and Rayleigh waves.

Valuable design considerations have been presented involving the design of the isolation system, the building and the foundation of base-isolated buildings. In particular, the choice of a relatively soft or stiff isolation system (equivalent to $f_S = 5$ Hz or $f_S = 15$ Hz), may lead to differences in the

isolation performance up to 17 dB in the frequency-range of interest. This conclusion is in agreement with what found by Talbot [33]. Although this result refers to the single-point coupling model for a purely vertical input, it has been shown that it is indicative also for the case of a localised source, as suggested by the results of the rigorous framework.

A final conclusion refers to the results of the rigorous analysis framework. It has been shown that relevant variability of the isolation performance is obtained when considering the mean vibrational power dissipated in different sub-domains of the building (i.e. different rooms). This is something to consider: even by using deterministic values for the different parameters involved in the problem, the performance of a given isolation-system should be associated with a frequency-dependent range of values rather than a single frequency-dependent value.

The added-foundation and the added-building effects

An important part of the thesis has been dedicated to the added-foundation effect of surface foundations subjected to incident, plane wave-fields. The extent to which the incident wave-field is influenced by the addition of a concrete slab foundation has been examined by a wave-based approach. It has been shown that the thickness of the slab and the coincidence phenomenon are the main aspects that drive the attenuation of the vibration levels. It has been also demonstrated that the through-thickness effects may be relevant in the frequency-range of interest. This clearly shows that the thin-plate theory alone is insufficient for modelling the effect of a slab foundation. Furthermore, models that assume a relaxed boundary condition at the soil-slab interface have been found to underestimate the attenuation provided for the vertical vibration at the free-surface by 5 to 10 dB in the case of Rayleigh wave excitation. In addition, results of the added-foundation effect are presented for different incident wave-fields showing that the attenuation of vibration levels is more significant for surface waves than for body waves.

With reference to the response at subsequent coupling points (with the building) at the free-surface of the infinitely-large slab foundation, it has been shown that Iguchi's method is an excellent alternative to the rigorous BEM approach. The limitations of the adoption of this approximate method for obtaining input motions in ground-borne vibration of buildings have been explored for different incident wave-fields. It can be concluded that the kinematic interaction is governed by the horizontal-wavelength (λ_x) to the footing-dimension ($2b$) ratio. By comparison with rigorous results, a rule-of-thumb of $\lambda_x/b > \pi$ has been defined for the use of Iguchi's method. As a result, this strategy

is more suited for incident body-waves and care must be taken when adopting it with an incident Rayleigh wave at relatively high frequencies.

Further investigation on the added-foundation effect of a slab foundation of finite dimensions has shown that the infinitely-large assumption for the foundation leads to overestimating the provided attenuation. This suggests that, as far as the soil-foundation interaction is concerned, the foundation system, with all its features, has to be appropriately described by three-dimensional models. On the other hand, the isolation performance obtained via the design framework has been proven to be in good agreement with the rigorous counterpart referring to the finite slab foundation model. This suggests that the in-plane infinite extent assumption for the slab foundation may be deemed valid for the evaluation of relative measures of performance (e.g. $PFIG$ associated with a base-isolated building).

An additional aspect investigated in this dissertation is the influence of adding a building to pre-existing vibration levels at the foundation level. It has been shown that, although there are numerous simplifying assumptions associated with the cone-damper model of the design framework, the overall added-building effect is well-captured for the horizontal, vertical and rocking degrees of freedom. The extent to which this may be satisfactory for absolute predictions of vibration levels depends greatly on the modal behaviour exhibited by the building. Discrepancies in the added-building effect in certain frequency bands may be found in the order of 15 dB, and this may change considerably on a case-to-case bases.

A final comment relates to the experimental work undertaken at South Bank, London. The added-foundation effect and the added-building effect have been captured experimentally with reference to the level at the basement. It has been shown that the insertion of an elastomeric material, beneath the floating-slab, introduces potential amplifications that may fall in the frequency-range of interest. In the examined practical case, the addition of a floating slab has been followed by the construction of the building. This has reduced the vibration levels as a result of the added-building effect.

8.2 Future work

Following the concluding remarks, some recommendations for further work can be given. The design and the rigorous analysis framework have been set up in the form of a general staged-approach. This allows a more representative incident wave-field of train-induced vibration to be readily considered.

This can be part of further investigation with the use, for instance, of the PiP model for obtaining an incident wave-field from an underground train and for evaluating the isolation performance by following the analysis framework presented in this dissertation.

So far, the design analysis framework has been set up for surface foundations and for portal-frame buildings. An important extension would be to consider the influence of different foundation typologies (e.g. pile foundations) and different structural components such as a structural core and/or partitions within the building, both features that are typically found in practice.

A feature observed by means of the rigorous analysis framework is the spatial variability of the isolation performance, both in terms of the IG and, to a lesser extent, the $PFIG$. A further development in this direction would require the consideration of a three-dimensional building model to study the effect of the increased modal density on the spatial variability of these two metrics. Further investigations are required to ascertain the range in which these metrics can vary within the building domain.

A disadvantage of considering a high-fidelity model for the foundation is an involved numerical approach that has a high computational cost and can hardly be used for design purposes. In this context, further work is required to seek alternative, efficient routes to solve the added-foundation effect, still considering the three-dimensional features of the foundation.

A different, but related, topic of interest is the consideration of the added-foundation effect for additional types of foundations, for instance, embedded foundations (i.e. basements) and/or piled foundations. The latter are the subject of current research in Cambridge with the development of an efficient, numerical approach to tackle the source-soil-foundation interaction in ground-borne vibration problems.

It has been seen that, in principle, the added-foundation effect and the added-building effect may be evaluated by rather simplified methods and models. This could be the focus of further research in order to adopt the design analysis framework for the prediction of absolute vibration levels. For this purpose, the cone-damper model remains to be tested for the added-building effect, while an alternative method for addressing the added-foundation effect needs to be identified.

References

[1] L. Auersch, "Response to harmonic wave excitation of finite or infinite elastic plates on a homogeneous or layered half-space," *Comput. Geotech.*, vol. 51, pp. 50–59, jun 2013.

[2] R. Sen, T. G. Davies, and P. K. Banerjee, "Dynamic analysis of piles and pile groups embedded in homogeneous soils," *Earthq. Eng. Struct. Dyn.*, vol. 13, pp. 53–65, jan 1985.

[3] BS 6472:2008, "Guide to evaluation of human exposure to vibration in buildings (1 to 80 Hz) - Part1: Vibration sources other than blasting," British Standard Institution, 2008.

[4] K. Kolodiy and S. Hardy, "Southbank Place - Geotechnical input to the sub-structure design report submission," tech. rep., ARUP Ltd, 2014.

[5] United Nations, *World Urbanization Prospects 2018: Highlights*. New York: Department of Economic and Social Affairs, 2019.

[6] Office for National Statistics, "Indication of the future size and age structure of the population in the regions, local authorities, clinical commissioning groups and NHS regions of England.," *Subnational Popul. Proj. Engl. 2016- based.*, pp. 1–12, 2018.

[7] Crossrail project, "www.crossrail.co.uk," 2008.

[8] Crossrail 2 project, "www.crossrail2.co.uk," 2016.

[9] S. Bennett, "Crossrail project to deliver London's Elizabeth line: From options to parliamentary bill," *Proc. Inst. Civ. Eng. Civ. Eng.*, vol. 170, no. 6, pp. 3–9, 2017.

[10] D. Lazarus and H. I. Jung, "Damage assessment and monitoring for buildings on the Elizabeth line," *Struct. Eng.*, vol. 96, no. 7, pp. 14–24, 2018.

[11] G. Giardina, P. Milillo, M. J. DeJong, D. Perissin, and G. Milillo, "Evaluation of InSAR monitoring data for post-tunnelling settlement damage assessment," *Struct. Control Heal. Monit.*, vol. 26, no. 2, pp. 1–19, 2019.

[12] D. Brookes, W. I. Hamad, J. P. Talbot, H. E. Hunt, and M. F. Hussein, "The dynamic interaction effects of railway tunnels: Crossrail and the Grand Central Recording Studios," *Proc. Inst. Mech. Eng. Part F J. Rail Rapid Transit*, vol. 232, pp. 542–559, feb 2018.

[13] S. Baldwin, E. Holroyd, and R. Burrows, "Mapping the Subterranean Geographies of Plutocratic London: Luxified Troglodytism?," no. May, 2018.

[14] D. Batty, C. Barr, and P. Duncan, "What lies beneath : the subterranean secrets of London's super rich," The Guardian, 2018.

[15] K. Wiggins, "Squire's Shell Centre revamp called in," *Archit. J.*, 2013.

[16] C. Hanson, D. Towers, and L. Meister, "Transit Noise and Vibration Impact Assessment, Report FTA-VA-90-1003-06," Tech. Rep. May, U.S. Department of Transportation, Federal Transit Administration, Office of Planning and Environment, 2006.

[17] M. O'Connor, K. Jefferson, and J. D'Avillez, "An investigation of numerical procedures to assess the rail - induced noise and vibration response of tall buildings," *Proc. 23rd Int. Congr. Sound Vib. Florence, Italy*, 2016.

[18] ISO 2631-2:2003, "Mechanical vibration and shock - Evaluation of human exposure to whole-body vibration - Part 2: Vibration in buildings (1 Hz to 80 Hz)," 2003.

[19] E. Peris, J. Woodcock, G. Sica, C. Sharp, A. T. Moorhouse, and D. C. Waddington, "Guidance for new policy developments on railway noise and vibration," *Transp. Res. Part A Policy Pract.*, vol. 85, pp. 76–88, mar 2016.

[20] M. G. Smith, M. Ögren, J. Ageborg Morsing, and K. Persson Waye, "Effects of ground-borne noise from railway tunnels on sleep: A polysomnographic study," *Build. Environ.*, vol. 149, no. July 2018, pp. 288–296, 2019.

[21] C. G. Gordon, "Generic Criteria For Vibration-Sensitive Equipment," *Proc. Int. Soc. Opt. Eng.*, vol. 1619, no. Vc, pp. 22–33, 1999.

[22] D. P. Connolly, G. P. Marecki, G. Kouroussis, I. Thalassinakis, and P. K. Woodward, "The growth of railway ground vibration problems - A review," *Sci. Total Environ.*, oct 2015.

[23] D. Stiebel, R. Müller, E. Bongini, and A. Ekblad, "Definition of reference cases typical for hot-spots in Europe with existing vibration problems," tech. rep., 2012.

[24] R. A. Waller, "Buildings on springs," *Nature*, vol. 2011, no. 5051, pp. 794–796, 1966.

[25] J. P. Talbot, "Base-isolated buildings: towards performance-based design," *Proc. Inst. Civ. Eng. - Struct. Build.*, vol. 169, pp. 574–582, aug 2016.

[26] T. Boxoen, D. Risbey, and C. Weber, "Train Induced Vibration Isolation of theskyvue , Sydney Australia," in *Proc. 20th Int. Congr. Acoust.*, (Sydney, Australia), pp. 2204–2212, 2010.

[27] A. K. Sharif, *Dynamic performance investigation of base-isolated structures*. Ph.d. dissertation, Imperial College of Science Technology and Medicine, 1999.

[28] Anderson D., "Isolation of Buildings from railway vibration: a case study," in *Proc. Inst. Acoust.*, pp. 17–25, 1999.

[29] D. Commins, "Vibration isolation of trains under a French art complex," in *Proc. Insitute Acoust.*, no. 12(7), pp. 31–38, 1990.

[30] P. Henson and J. G. Charles, "Vibration isolation of the IMAX Cinema, Waterloo, London," in *Proc. Insitute Acoust.*, no. 22, pp. 255–262, 2000.

[31] P. Henson, "The isolation from railway vibration of the BBC Egton Wing, Portland Place, London," in *Proc. Euronoise*, (Edinburgh), 2009.

[32] P. Grootenhuis, "Structural elastomeric bearings and resilient seatings," in *Polym. Polym. Compos. Constr.* (L. e. Hollaway, ed.), 1990.

[33] J. P. Talbot, *On the performance of base-isolated buildings: A generic model*. PhD thesis, University of Cambridge, 2001.

[34] J. P. Talbot and H. E. M. Hunt, "A Generic Model for Evaluating the Performance of Base-Isolated Buildings," *Low Freq. Noise Vib. Act. Control*, vol. 22, no. 3, pp. 149–160, 2003.

[35] The Mathworks Inc., *MATLAB 2018b*. Natick, Massachusetts, United States, 2018.

[36] M. Schevenels, S. François, and G. Degrande, "EDT: An ElastoDynamics Toolbox for MATLAB," *Comput. Geosci.*, vol. 35, no. 8, pp. 1752–1754, 2009.

[37] M. Schevenels, S. François, and G. Degrande, "EDT: elastodynamics toolbox for matlab," Tech. Rep. July, Katholieke Universiteit Leuven, Leuven, 2010.

[38] S. François, M. Schevenels, and G. Degrande, "Bemfun: Matlab toolbox for boundary elements in elastodynamics," Tech. Rep. May, Katholieke Universiteit Leuven, Leuven, 2009.

[39] H. E. M. Hunt, *Measurement and modelling of traffic-induced ground vibration*. PhD thesis, University of Cambridge, 1988.

[40] S. Ng, *Transmission of ground-borne vibration from surface railway trains*. PhD thesis, University of Cambridge, 1995.

[41] J. A. Forrest, *Modelling of ground vibration from underground railways*. PhD thesis, University of Cambridge, 1999.

[42] M. F. M. Hussein, *Vibration from underground railways*. PhD thesis, University of Cambridge, 2005.

[43] M. F. M. Hussein and H. E. M. Hunt, "The PiP model, a software apllication for calculating vibration from underground railways," in *14th Int. Congr. Sound Vib.*, no. July 2007, 2007.

[44] K. T. Lo, *Measurement and modelling of vibration transmission through piled foundations*. PhD thesis, University of Cambridge, 1994.

[45] K. A. Kuo, *Vibration from underground railways: considering piled foundations and twin tunnels, Tese de doutoramento*. PhD thesis, University of Cambridge, 2010.

[46] S. Jones, *Ground vibration from underground railways: how simplifying assumptions limit prediction accuracy*. PhD thesis, University of Cambridge, 2010.

[47] D. P. Cryer, *Modelling of vibration in buildings with application to base isolation.* PhD thesis, University of Cambridge, 1994.

[48] D. Mead, "Wave propagation in continuous periodic structures: research contributions from southampton, 19641995," *J. Sound Vib.*, vol. 190, pp. 495–524, feb 1996.

[49] A. Y. T. Leung, *Dynamic Stiffness and Substructures*. London: Springer London, 1993.

[50] M. J. Griffin, "Perception of Whole-body Vibration and the Assessment of Vibration in Buildings," in *Handb. Hum. Vib.*, pp. 221–269, Accademic Press, 1990.

[51] P. Alves Costa, R. Calçada, and A. Silva Cardoso, "Ballast mats for the reduction of railway traffic vibrations. Numerical study," *Soil Dyn. Earthq. Eng.*, vol. 42, pp. 137–150, 2012.

[52] J. P. Talbot, "Lift-over crossings as a solution to tram-generated ground-borne vibration and re-radiated noise," *Proc. Inst. Mech. Eng. Part F J. Rail Rapid Transit*, vol. 228, pp. 878–886, nov 2014.

[53] P. Coulier, V. Cuéllar, G. Degrande, and G. Lombaert, "Experimental and numerical evaluation of the effectiveness of a stiff wave barrier in the soil," *Soil Dyn. Earthq. Eng.*, vol. 77, pp. 238–253, 2015.

[54] J. P. Talbot and H. E. M. Hunt, *On the Performance of Base-isolated Buildings and Isolation of Buildings from Rail-tunnel Vibration: a Review*. Multi-science, 2009.

[55] R. A. Waller, *Building on Springs*. Oxford, UK: Pergamon Press, 1969.

[56] J. P. Talbot, "Base isolation of buildings for control of ground-borne vibration," *Handb. Noise Vib. Control*, pp. 1464 – 1472, 2007.

[57] S. L. Kramer, *Geotechnical Earthquake Engineering*. Prentice Hall, 1996.

[58] H. Sucuolu and S. Akkar, *Basic Earthquake Engineering*. Cham: Springer International Publishing, 2014.

[59] D. M. Wood, *Soil Behaviour and Critical State Soil Mechanics*. Cambridge: Cambridge University Press, 1991.

[60] G. Gazetas, "Soil dynamics: an overview," in *Dyn. Behav. Found. Buried Struct.* (P. K. Banerjee and R. Butterfield, eds.), London: Elsevier Applied Science, volume 3 ed., 1987.

[61] D. Connolly, G. Kouroussis, P. Woodward, P. Alves Costa, O. Verlinden, and M. Forde, "Field testing and analysis of high speed rail vibrations," *Soil Dyn. Earthq. Eng.*, vol. 67, pp. 102–118, dec 2014.

[62] D. M. Hiller and V. S. Hope, "Groundborne vibration generated by mechanized construction activities," *Proceeding Inst. Civ. Eng. Geotech. Eng.*, vol. 131, pp. 223–232, 1998.

[63] BS 6472:1992, "Evaluation Of Human Exposure To Vibration In Buildings (1 Hz to 80 Hz) - Guide For The Evaluation Of Human Exposure To Whole-Body Vibration," British Standard Institution, 1992.

[64] BS 7385-2:1993, "Evaluation and measurement for vibration in buildings - Part 2: Guide to damage levels from groundborne vibration," British Standard Institution, 1993.

[65] D. J. Rockhill, M. D. Bolton, and D. J. White, "Ground-borne vibrations due to press-in piling operations," *BGA Int. Conf. Found. Innov. Obs. Des. Pract.*, no. Figure 1, pp. 743–755, 2003.

[66] F. Deckner, K. Viking, and S. Hintze, "Ground vibrations due to pile and sheet pile driving - prediction models of today," in *Proc. 22nd Eur. Young Geotech. Eng. Conf.*, (Gothenburg), 2012.

[67] H. Hao, T. C. Ang, and J. Shen, "Building vibration to traffic-induced ground motion," *Build. Environ.*, vol. 36, no. 3, pp. 321–336, 2001.

[68] G. R. Watts, "Vehicle generated ground-borne vibration alongside speed control cushions and road humps," in *Gr. Dyn. Man-made Process. Predict. Des. Manag.* (B. O. Skipp, ed.), Thomas Telford Ltd, 1997.

[69] G. Lombaert, G. Degrande, S. François, and D. J. Thompson, "Ground-borne vibration due to railway traffic: A review of excitation mechanisms, prediction methods and mitigation measures," *Notes Numer. Fluid Mech. Multidiscip. Des.*, vol. 126, pp. 253–287, 2015.

[70] D. J. Thompson, G. Kouroussis, and E. Ntotsios, "Modelling, simulation and evaluation of ground vibration caused by rail vehicles," *Veh. Syst. Dyn.*, vol. 57, pp. 1–48, apr 2019.

[71] M. Heckl, G. Hauck, and R. Wettschureck, "Structure-Borne Sound and Vibration From Rail Traffic," *J. Sound Vib.*, vol. 193, no. 1, pp. 175–184, 1996.

[72] D. J. Thompson and C. J. Jones, "Review of the modelling of wheel/rail noise generation," *J. Sound Vib.*, vol. 231, no. 3, pp. 519–536, 2000.

[73] S. L. Grassie, "Rail corrugation: Characteristics, causes, and treatments," *Proc. Inst. Mech. Eng. Part F J. Rail Rapid Transit*, vol. 223, no. 6, pp. 581–596, 2009.

[74] P. J. Remington, "Wheel/rail noise- Part I: Characterization of the wheel/rail dynamic system," *J. Sound Vib.*, vol. 46, no. 3, pp. 359–379, 1976.

[75] P. J. Remington, "Wheel/rail noise-Part IV: Rolling noise," *J. Sound Vib.*, vol. 46, no. 3, pp. 419–436, 1976.

[76] D. J. Thompson, B. Hemsworth, and N. Vincent, "Experimental validation of the twins prediction program for rolling noise, part 1: Description of the model and method," *J. Sound Vib.*, vol. 193, no. 1, pp. 123–135, 1996.

[77] K. Graff, *Wave motion in elastic solids*. Oxford: Clarendon, 1975.

[78] W. Ewing, W. Jardetzky, and F. Press, *Elastic waves in layered media*. McGraw-Hill, 1957.

[79] Lord Rayleigh, "On Waves Propagated along the Plane Surface of an Elastic Solid," *Proc. London Math. Soc.*, vol. s1-17, pp. 4–11, nov 1885.

[80] H. Lamb, "On Waves in an Elastic Plate," *Proc. R. Soc. A Math. Phys. Eng. Sci.*, vol. 93, pp. 114–128, mar 1917.

[81] G. F. Miller and H. Pursey, "The Field and Radiation Impedance of Mechanical Radiators on the Free Surface of a Semi-Infinite Isotropic Solid," *Proc. R. Soc. A Math. Phys. Eng. Sci.*, vol. 223, no. 1155, pp. 521–541, 1954.

[82] G. F. Miller and H. Pursey, "On the partition of energy between elastic waves in a semi-infinite solid," *Proc. R. Soc. London. Ser. A. Math. Phys. Sci.*, vol. 233, pp. 55–69, dec 1955.

[83] J. W. Meek and J. P. Wolf, "Cone models for nearly incompressible soil," *Earthq. Eng. Struct. Dyn.*, vol. 22, no. 8, pp. 649–663, 1993.

[84] J. P. Wolf, *Foundation vibration analysis using simple physical models*. Pearson Education, 1994.

[85] R. D. Woods, "Screening of surface waves in soils," *J. Soil Mech. Found. Div.*, vol. 94, no. 4, pp. 951–980, 1968.

[86] G. Gazetas, "Simple physical methods for foundation impedances," in *Dev. Soil Mech. Found. Eng. Vol.3* (P. K. Banerjee and R. Butterfield, eds.), pp. 45–93, London: Elsevier Applied Science, 1987.

[87] J. W. Meek and J. P. Wolf, "Cone Models for Homogeneous Soil. I," *J. Geotech. Eng.*, vol. 118, pp. 667–685, may 1992.

[88] E. Kausel, "Early history of soil-structure interaction," *Soil Dyn. Earthq. Eng.*, vol. 30, no. 9, pp. 822–832, 2010.

[89] E. Reissner, "Stationäre, axialsymmetrische, durch eine schüttelnde Masse erregte Schwingungen eines homogenen elastischen Halbraumes," *Ingenieur-Archiv*, vol. 7, no. 6, pp. 381–396, 1936.

[90] A. S. Veletsos and Y. T. Wei, "Lateral and rocking vibration of footings," tech. rep., Rice University, Dept. of Civil Engineering, 1971.

[91] J. E. Luco and R. a. Westmann, "Dynamic Response of a Rigid Footing Bonded to an Elastic Half Space," *J. Appl. Mech.*, vol. 39, no. 2, p. 527, 1972.

[92] H. L. Wong and J. E. Luco, "Dynamic response of rigid foundations of arbitrary shape," *Earthq. Eng. Struct. Dyn.*, vol. 4, no. 6, pp. 579–587, 1976.

[93] D. L. Karabalis and D. E. Beskos, "Dynamic-Response of 3-D Rigid Surface Foundations By Time Domain Boundary Element Method," *Earthq. Eng. Struct. Dyn.*, vol. 12, no. 1, pp. 73–93, 1984.

[94] J. W. Meek and A. S. Veletsos, "Simple models for foundations in lateral and rocking motion," in *Proc. fifth world Conf. Earthq. Eng.*, (Rome), pp. 2610–2613, 1974.

[95] J. W. Meek and J. P. Wolf, "Cone Models for Soil Layer on Rigid Rock. II," *J. Geotech. Eng.*, vol. 118, pp. 686–703, may 1992.

[96] H. L. Wong and J. E. Luco, "Dynamic response of rectangular foundations to obliquely incident seismic waves," *Earthq. Eng. Struct. Dyn.*, vol. 6, no. 1, pp. 3–16, 1978.

[97] J. Qian and D. E. Beskos, "Harmonic wave response of two 3-D rigid surface foundations," *Soil Dyn. Earthq. Eng.*, vol. 15, no. 2, pp. 95–110, 1996.

[98] M. Iguchi, "An approximate analysis of input motions for rigid embedded foundations," *Trans. Archit. Inst. Japan*, vol. 315, pp. 61–75, 1982.

[99] M. Iguchi, "An approximate evaluation method of foundation input motions for adjacent embedded foundations," *J. Struct. Constr. Eng. (Transactions AIJ)*, vol. 81, no. 721, pp. 515–523, 2016.

[100] M. Iguchi and J. E. Luco, "Dynamic response of flexible rectangular foundations on an elastic halfspace," *Earthq. Eng. Struct. Dyn.*, vol. 9, no. 3, pp. 239–249, 1981.

[101] L. Tham, J. Qian, and Y. Cheung, "Dynamic response of a group of flexible foundations to incident seismic waves," *Soil Dyn. Earthq. Eng.*, vol. 17, pp. 127–137, feb 1998.

[102] L. Auersch and G. Schmid, "A simple boundary element formulation and its application to wavefield excited soil-structure interaction," *Earthq. Eng. Struct. Dyn.*, vol. 19, pp. 931–947, oct 1990.

[103] J. O. Blanch, J. O. Robertsson, and W. W. Symes, "Viscoelastic Finite Difference Modeling," tech. rep., Rice University, Houston, Texas, 1993.

[104] R. M. Thornely-Taylor, "FINDWAVE ®, finite-difference-time-domain modelling software,"

[105] R. M. Thornely-Taylor, "Modelling of vibration and ground-borne noise from underground railway tunnels by a finite difference method," in *Proc. 6th Int. Congr. Sound Vib.*, (Copenhagen, Denmark), International Institute of Acoustics and Vibration, IIAV, 1999.

[106] O. Zienkiewicz, R. Taylor, and D. Fox, "The Finite Element Method for Solid and Structural Mechanics," in *Finite Elem. Method Solid Struct. Mech.*, p. i, Elsevier, 2014.

[107] J. Lysmer, T. Udaka, C.-F. Tsai, and H. B. Seed, "FLUSH - a computer program for approximate 3D analysis of soil-structure interaction problems," tech. rep., Earthquake Engineering Research Center, 1975.

[108] R. L. Kuhlemeyer and J. Lysmer, "Finite element method accuracy for wave propagation problems," *J. Soil Mech. Found. Div.*, vol. 99, no. SM5, pp. 421–427, 1973.

[109] J. Lysmer and R. L. Kuhlemeyer, "Finite dynamic model for infinite media," *J. Eng. Mech. Div.*, vol. 95, no. 4, pp. 859–878, 1969.

[110] E. Kausel, "Local Transmitting Boundaries," *J. Eng. Mech.*, vol. 114, pp. 1011–1027, jun 1988.

[111] P. Bettess, "Infinite elements," *Int. J. Numer. Methods Eng.*, vol. 11, no. 1, pp. 53–64, 1977.

[112] P. Bettess and O. C. Zienkiewicz, "Diffraction and refraction of surface waves using finite and infinite elements," *Int. J. Numer. Methods Eng.*, vol. 11, no. 8, pp. 1271–1290, 1977.

[113] U. Basu and A. K. Chopra, "Perfectly matched layers for time-harmonic elastodynamics of unbounded domains: theory and finite-element implementation," *Comput. Methods Appl. Mech. Eng.*, vol. 192, pp. 1337–1375, mar 2003.

[114] Dassault Systemes, "Simulia - ABAQUS," 2014.

[115] M. Bonnet, *Boundary integral equation methods for solids and fluids*. J. Wiley, 1995.

[116] M. Schevenels, G. Degrande, and S. François, "EDT: An ElastoDynamics Toolbox for MATLAB," in *Proc. Inaug. Int. Conf. Eng. Mech. Inst.*, (Minneapolis, U.S.A), pp. 82–82, 2008.

[117] S. Jones and H. E. M. Hunt, "Voids at the tunnelsoil interface for calculation of ground vibration from underground railways," *J. Sound Vib.*, vol. 330, no. 2, pp. 245–270, 2011.

[118] S. Jones and H. E. M. Hunt, "Predicting surface vibration from underground railways through inhomogeneous soil," *J. Sound Vib.*, vol. 331, no. 9, pp. 2055–2069, 2012.

[119] S. Jones, K. Kuo, M. Hussein, and H. E. M. Hunt, "Prediction uncertainties and inaccuracies resulting from common assumptions in modelling vibration from underground railways," *Proc. Inst. Mech. Eng. Part F J. Rail Rapid Transit*, vol. 226, no. 5, pp. 501–512, 2012.

[120] K. Kuo, H. Verbraken, G. Degrande, and G. Lombaert, "Hybrid predictions of railway induced ground vibration using a combination of experimental measurements and numerical modelling," *J. Sound Vib.*, vol. 373, pp. 1–22, 2016.

[121] D. E. Newland, *Mechanical vibration analysis and computation*. Longman, 1989.

[122] J. P. Talbot, W. I. Hamad, and H. E. M. Hunt, "The significance of soil-structure interaction for the base-isolation of ground-borne vibration.," *SECED2015 Earthq. risk Eng. Towar. a resilient world*, 2015.

[123] D. E. Newland and H. E. M. Hunt, "Isolation of buildings from ground vibration: a review of recent progress," *Proc. Inst. Mech. Eng. Part C J. Mech. Eng. Sci.*, vol. 205, no. 1, pp. 39–52, 1991.

[124] J. C. Swallow, "Modelling of isolation of buildings from ground-borne vibration," in *Proc. 12th Int. Conf. Acoust.*, (Canada), 1986.

[125] H. E. M. Hunt, "Prediction of Vibration Transmission from Railways into Buildings using Models of Infinite Length," *Veh. Syst. Dyn.*, vol. 24, no. sup1, pp. 234–247, 1995.

[126] K. Chua, K. Lo, and T. Balendra, "Building response due to subway train traffic," *J. Geotech. Eng.*, vol. 121, no. November, pp. 747–754, 1995.

[127] P. Fiala, G. Degrande, and F. Augusztinovicz, "Numerical modelling of ground-borne noise and vibration in buildings due to surface rail traffic," *J. Sound Vib.*, vol. 301, no. 3-5, pp. 718–738, 2007.

[128] P. Fiala, S. Gupta, G. Degrande, and F. Augusztinovicz, "A numerical model for re-radiated noise in buildings from underground railways," *Notes Numer. Fluid Mech. Multidiscip. Des.*, vol. 99, pp. 115–121, 2008.

[129] A. Clot, R. Arcos, and J. Romeu, "Efficient three-dimensional building-soil model for the prediction of ground-borne vibrations in buildings," *J. Struct. Eng. (United States)*, vol. 143, no. 9, pp. 1–13, 2017.

[130] M. Papadopoulos, S. François, G. Degrande, and G. Lombaert, "The influence of uncertain local subsoil conditions on the response of buildings to ground vibration," *J. Sound Vib.*, vol. 418, pp. 200–220, 2018.

[131] J. Woodhouse, "An introduction to statistical energy analysis of structural vibration," *Appl. Acoust.*, vol. 14, no. 6, pp. 455–469, 1981.

[132] R. J. M. Craik, "The prediction of sound transmission through buildings using statistical energy analysis," *J. Sound Vib.*, vol. 82, no. 4, pp. 505–516, 1982.

[133] A. Trochides, "Ground-borne vibrations in buildings near subways," *Appl. Acoust.*, vol. 32, no. 4, pp. 289–296, 1991.

[134] R. A. Hood, R. J. Greer, M. Breslin, and P. R. Williams, "The calculation and assessment of ground-borne noise and perceptible vibration from trains in tunnels," *J. Sound Vib.*, vol. 193, no. 1, pp. 215–225, 1996.

[135] H. Kuppelwieser and A. Ziegler, "A Tool for Predicting Vibration and Structure-Borne Noise Immissions Caused By Railways," *J. Sound Vib.*, vol. 193, no. 1, pp. 261–267, 1996.

[136] J. Melke, "Noise and vibration from underground railway lines: Proposals for a prediction procedure," *J. Sound Vib.*, vol. 120, no. 2, pp. 391–406, 1988.

[137] C. Madshus, B. Bessason, and L. Hårvik, "Prediction model for low frequency vibration from high speed railways on soft ground," *J. Sound Vib.*, vol. 193, pp. 195–203, may 1996.

[138] DIN 4150-2:1999, "Structural Vibration - Part 2: Human exposure to vibration in buildings," Deutsches Institut für Normung, 1999.

[139] TfL (Transport for London), "Noise and Vibration Asset Design Guidance," (London), Reference:G1323, LUL Document, 2012.

[140] J. A. Zapfe, H. Saurenman, and S. Fidell, *Ground-borne noise and vibration in buildings caused by rail transit*. Transportation Research Board of National Academies, transit co ed., 2009.

[141] FICON, *Federal Agency Review of Selected Airport Noise Analysis Issues*. Federal Interagency Committee On Noise, 1992.

[142] H. V. Howarth and M. J. Griffin, "The annoyance caused by simultaneous noise and vibration from railways," *J. Acoust. Soc. Am.*, vol. 89, no. 5, pp. 2317–2323, 1991.

[143] E. Peris, J. Woodcock, G. Sica, C. Sharp, A. Moorhouse, and D. Waddington, "Guidance for new policy developments on railway vibration," in *Proc. Meet. Acoust.*, vol. 19, 2013.

[144] G. Wilson, H. Saurenman, and J. Nelson, "Control of ground-borne noise and vibration," *J. Sound Vib.*, vol. 87, pp. 339–350, mar 1983.

[145] H. H. Hung, Y. B. Yang, and D. W. Chang, "Wave Barriers for Reduction of Train-Induced Vibrations in Soils," *J. Geotech. Geoenvironmental Eng.*, vol. 130, pp. 1283–1291, dec 2004.

[146] D. J. Thompson, J. Jiang, M. G. R. Toward, M. F. M. Hussein, A. Dijckmans, P. Coulier, G. Degrande, and G. Lombaert, "Mitigation of railway-induced vibration by using subgrade stiffening," *Soil Dyn. Earthq. Eng.*, vol. 79, pp. 89–103, 2015.

[147] J. P. Talbot and H. E. M. Hunt, "Isolation of Buildings from Rail-Tunnel Vibration: a Review," *Build. Acoust.*, vol. 10, no. 3, pp. 177–192, 2003.

[148] G. K. Hueffman, "Comparison of vibration and structure-borne noise control efficiency of different elastic mounts," in *Proceeding of Internoise*, 1991.

[149] A. H. Muhr, "A comparison of rubber and metal springs for vibration isolation," *Plast. Rubber Compos. Process. Appl.*, vol. 18, pp. 3–7, 1992.

[150] H. G. Wagner, "Application of steel springs in the support of buildings," *Proc. Insitute Acoust.*, vol. 22, no. 2, pp. 221–230, 2000.

[151] P. B. Lindley, *Engineering design with natural rubber*. The Malausian Rubber Producer's Research Association, 1984.

[152] F. Naeim and J. M. Kelly, *Design of Seismic Isolated Structures: From Theory to Practice*. John Wiley & Sons, 1999.

[153] J. M. Kelly and D. A. Konstantinidis, *Mechanics of Rubber Bearings for Seismic and Vibration Isolation*. 2011.

[154] A. M. Wahl, *Mechanical Springs*. McGraw-Hill, 1963.

[155] BS 6177:1982, "Guide to selection and use of elastomeric bearings for vibration isolation of buildings," British Standard Institution, 1982.

[156] B. R. Barben and L. M. Hanagan, "Investigation of a slab on grade supporting sensitive equipment," in *Mech. Biol. Syst. Mater. - Proc. 2013 Annu. Conf. Exp. Appl. Mech.* (F. N. Catbas, ed.), Conference Proceedings of the Society for Experimental Mechanics Series, (Orlando), pp. 53–60, Springer New York LLC, 2014.

[157] G. Sanitate and J. Talbot, "On the plate-like and layer-like response of slab foundations to ground-borne vibration," *Comput. Geotech.*, vol. 114, p. 103141, oct 2019.

[158] C. Hepburn and R. J. W. Reynolds, *Elastomers: Criteria for Engineering Design*. Applied Science Publishers, 1979.

[159] M. Villot and P. Jean, "Railway vibration : Predicting the field performances of mitigation measures in buildings," in *Proc. 9th Int. Conf. Struct. Dyn. EURODYN*, no. July, (Porto, Portugal), pp. 835–840, 2014.

[160] B. Trévisan, L. Grau, D. B. Bozzetto, M. Villot, and P. Jean, "In-situ performance prediction of base-isolated buildings," in *Proc. - Eur. Conf. Noise Control*, (Crete), pp. 1653–1658, 2018.

[161] M. O'Connor and K. Jefferson, "Southbank Place, Building 2 - Vibration Isolation Assessment," tech. rep., 2014.

[162] R. Langley, "Analysis of power flow in beams and frameworks using the direct-dynamic stiffness method," *J. Sound Vib.*, vol. 136, no. 3, pp. 439–452, 1990.

[163] M. F. M. Hussein and H. E. M. Hunt, "A power flow method for evaluating vibration from underground railways," *J. Sound Vib.*, vol. 293, no. 3-5, pp. 667–679, 2006.

[164] P. Coulier, G. Lombaert, and G. Degrande, "The influence of source-receiver interaction on the numerical prediction of railway induced vibrations," *J. Sound Vib.*, vol. 333, no. 12, pp. 2520–2538, 2014.

[165] J. P. Talbot and H. E. M. Hunt, "The effect of side-restraint bearings on the performance of base-isolated buildings," *Proc. Inst. Mech. Eng. Part C J. Mech. Eng. Sci.*, vol. 217, no. 8, pp. 849–859, 2003.

[166] M. Hussein, H. E. M. Hunt, K. Kuo, P. Alves Costa, and J. Barbosa, "The use of sub-modelling technique to calculate vibration in buildings from underground railways," *Proc. Inst. Mech. Eng. Part F J. Rail Rapid Transit*, vol. 229, no. 3, pp. 303–314, 2013.

[167] European Standard, "Eurocode 2: Design of concrete structures - Part 1: General rules and rules for buildings," vol. 1, CEN (European Commitee for Standardization), 2005.

[168] J. S. Przemieniecki, *Theory of Matrix Structural Analysis*. Dover, 1985.

[169] G. Ehlers, "The effect of soil flexibility on vibrating systems," *Bet. und Eisen*, vol. 41, pp. 197–203 (in German), 1942.

[170] J. W. Meek and J. P. Wolf, "Why cone models can represent the elastic halfspace," *Earthq. Eng. Struct. Dyn.*, vol. 22, no. 9, pp. 759–771, 1993.

[171] W. Rücker, "Dynamic behaviour of rigid foundations of arbitrary shape on a halfspace," *Earthq. Eng. Struct. Dyn.*, vol. 10, pp. 675–690, sep 1982.

[172] J. E. Luco and A. Mita, "Response of a circular foundation on a uniform half-space to elastic waves," *Earthq. Eng. Struct. Dyn.*, vol. 15, pp. 105–118, jan 1987.

[173] B. Prange, "Parameters affecting damping properties," in *Dyn. methods soil rock Mech. 1 Dyn. response wave Propag. soils* (B. Prange, ed.), Karlsruhe: Proceedings of DSMR 77, 1977.

[174] B. O. Hardin and V. P. Drnevich, "Shear modulus and damping in soils: measurement and parameter effects," *J. Soil Mech. Found. Div.*, vol. 98, no. SM6, pp. 603–624, 1972.

[175] H. B. Seed and I. M. Idriss, "Soil Moduli and Damping Factors for Dynamic Response Analyses [Report No. EERC 70-10]," Tech. Rep. December, Earthquake Engineering Research Centre, University of California, Berkeley, 1970.

[176] Lord Rayleigh, *The Theory of Sound*. New York: Dover Publications, vol. i and ii ed., 1894.

[177] D. R. Bland, *Theory Of Linear Viscoelasticity*. Pergamon Press, 1960.

[178] S. H. Crandall, "The role of damping in vibration theory," *J. Sound Vib.*, vol. 11, no. 1, pp. 3–18, 1970.

[179] D. E. Newland and H. E. M. Hunt, "Isolation of buildings from ground vibration: a review of recent progress," *Proc. Inst. Mech. Eng. Part C J. Mech. Eng. Sci.*, vol. 205, no. 1, pp. 39–52, 1991.

[180] T. Guo, Z. Cao, Z. Zhang, and A. Li, "Frequency domain-based analysis of floor vibrations using the dynamic stiffness matrix method," *J. Vib. Control*, vol. 25, pp. 763–776, feb 2019.

[181] M. Sanayei, A. A. Kayiparambil, J. A. Moore, and C. R. Brett, "Measurement and prediction of train-induced vibrations in a full-scale building," *Eng. Struct.*, vol. 77, pp. 119–128, 2014.

[182] L. Auersch, "Building response due to ground vibration - Simple prediction model based on experience with detailed models and measurements," *Int. J. Acoust. Vib.*, vol. 15, no. 3, pp. 101–112, 2010.

[183] R. H. Lyon and R. G. DeJong, *Theory and application of Statistical Energy Analysis*. Butterworth-Heinemann, 2nd ed., 1995.

[184] R. Kelly, "The importance of including bearing stiffness in structural analysis," in *24th Int. Congr. Sound Vib.*, (London), 2017.

[185] European Standard, "Eurocode 1: Actions on structures - Part 1-1: General actions - Densities, self-weight,imposed loads for buildings," CEN (European Commitee for Standardization), 2002.

[186] European Standard, "Eurocode - Basis of structural design," CEN (European Commitee for Standardization), 2001.

[187] R. D. Mindlin, "Waves and vibrations in isotropic, elastic plates," in *Proc. 1st Symp. Nav. Struct. Mech.* (J. Goodies and N. Hoff, eds.), (Oxford, UK), pp. 199–232, Pergamon Press, 1960.

[188] R. D. Mindlin and J. Yang, *An Introduction to the Mathematical Theory of Vibrations of Elastic Plates*. World scientific, dec 2006.

[189] E. Kausel and J. M. Roesset, "Stiffness matrices for layered soils," *Bull. Seismol. Soc. Am.*, vol. 71, no. 6, pp. 1743–1761, 1981.

[190] F. Fahy and P. Gardonio, *Sound and Structural Vibration*. Elsevier, 2006.

[191] G. Degrande, D. Clouteau, R. Othman, M. Arnst, H. Chebli, R. Klein, P. Chatterjee, and B. Janssens, "A numerical model for ground-borne vibrations from underground railway traffic based on a periodic finite element-boundary element formulation," *J. Sound Vib.*, vol. 293, no. 3-5, pp. 645–666, 2006.

[192] P. Hölscher, V. Hopman, G. Degrande, and D. Clouteau, "The influence of dynamic soil characteristics on vibration predictions," in *Proc. Eighth Int. Work. Railw. Noise*, (Buxton), 2004.

[193] S. Gupta, G. Degrande, and G. Lombaert, "Experimental validation of a numerical model for subway induced vibrations," *J. Sound Vib.*, vol. 321, no. 3-5, pp. 786–812, 2009.

[194] E. Kausel, *Fundamental Solutions in Elastodynamics A Compendium*. Massachusetts Institute of Technology: Cambridge University Press, 2006.

[195] J. A. Forrest and H. E. M. Hunt, "A three-dimensional tunnel model for calculation of train-induced ground vibration," *J. Sound Vib.*, vol. 294, no. 4, pp. 678–705, 2006.

[196] M. F. M. Hussein and H. E. M. Hunt, "A numerical model for calculating vibration from a railway tunnel embedded in a full-space," *J. Sound Vib.*, vol. 305, no. 3, pp. 401–431, 2007.

[197] H. E. M. Hunt, M. Hussein, and W. Hamad, "The PiP model and progress in ground vibration from railways," *Proc. Acoust. 2017*, no. 1, pp. 1–9, 2017.

[198] S. François, M. Schevenels, P. Galvín, G. Lombaert, and G. Degrande, "A 2.5D coupled FE-BE methodology for the dynamic interaction between longitudinally invariant structures and a layered halfspace," *Comput. Methods Appl. Mech. Eng.*, vol. 199, no. 23-24, pp. 1536–1548, 2010.

[199] J. Qian, L. Tham, and Y. Cheung, "Dynamic analysis of rigid surface footings by boundary element method," *J. Sound Vib.*, vol. 214, no. 4, pp. 747–759, 1998.

[200] R. Conti, M. Morigi, and G. M. Viggiani, "Filtering effect induced by rigid massless embedded foundations," *Bull. Earthq. Eng.*, vol. 15, no. 3, pp. 1019–1035, 2017.

[201] S. Kim and J. P. Stewart, "Kinematic Soil-Structure Interaction from Strong Motion Recordings," *J. Geotech. Geoenvironmental Eng.*, vol. 129, no. 4, pp. 323–335, 2003.

[202] J. E. Luco, "Torsional response of structures to obliquely incident seismic sh waves," *Earthq. Eng. Struct. Dyn.*, vol. 4, pp. 207–219, jan 1976.

[203] R. H. Scanlan, "Seismic wave effects on soil-structure interaction," *Earthq. Eng.*, vol. 4, no. 4, pp. 207–388, 1976.

[204] H. Yamahara, "Ground motions during earthquakes and the input loss of earthquake power to an excitation of buildings," *Soils Found.*, vol. 10, no. 2, pp. 145–161, 1970.

[205] S. A. Thau, "Radiation and Scattering From a Rigid Inclusion in an Elastic Medium," *J. Appl. Mech.*, vol. 34, no. 2, p. 509, 1967.

[206] L. T. Wheeler and E. Sternberg, "Some Theorems in Classical Elastodynamics," *Arch. Ration. Mech. Anal.*, vol. 31, pp. 402–402, dec 1968.

[207] D. E. Beskos, C. A. Brebbia, J. T. Katsikadelis, and G. D. Manolis, *Boundary Elements XXIII*. WIT Press / Computational Mechanics, advances 1 ed., 2001.

[208] J. Domínguez, *Boundary elements in dynamics*. Southampton Boston: WIT Press / Computational Mechanics, internatio ed., 1993.

[209] A. L. Pais and E. Kausel, "On rigid foundations subjected to seismic waves," *Earthq. Eng. Struct. Dyn.*, vol. 18, no. 4, pp. 475–489, 1989.

[210] E. S. Taylor, *Dimensional analysis for engineers*. Oxford: Clarendon, 1974.

[211] P. Holscher and V. Hopman, "Test site Regent's Park London, Soil Description, Report 381540-104," *CONVURT EC-Growth Proj. G3RD-CT-2000-00381*, 2003.

[212] D. W. Hight, "Some characteristics of London Clay," in *Characterisation Eng. Prop. Nat. Soils*, Lisse: Swets & Zeitlinger, 2003.

[213] D. W. Hight, A. Gasparre, S. Nishimura, R. J. Jardine, M. R. Coop, and N. A. Minh, "Characteristics of the London Clay from the Terminal 5 site at Heathrow Airport," in *Stiff Sediment. Clays*, pp. 167–182, London: Thomas Telford Ltd, jan 2011.

[214] G. Sanitate and J. P. Talbot, "Soil-Structure Interaction and the added-building effect: simplified models for assisting with the prediction of ground-borne vibration in buildings," *25th Int. Congr. Sound Vib.*, pp. 1–8, 2018.

[215] F. J. Rizzo, D. J. Shippy, and M. Rezayat, "Boundary Integral Equation Analysis for a Class of Earth-Structure Interaction Problems," tech. rep., Department of Engineering Mechanics, Univeristy of Kentucky, Lexington, Kentucky, 1985.

[216] S. P. Timoshenko, D. H. Young, and W. Weaver, *Vibration Problems in Engineering*. New York: Wiley, 4th editio ed., 1974.

[217] E. O. Measor and G. J. M. Williams, "Features in the design and construction of the Shell Centre, London.," *Proc. Inst. Civ. Eng.*, vol. 21, pp. 475–502, mar 1962.

[218] A. Mciver and J. Golding, "Southbank place basement and infrastructure: Structural Design Philosophy," tech. rep., WSP Ltd, 2016.

[219] B. Scott, S. Miller, S. Wong, D. Orczyk, and A. Mciver, "Southbank Place - Building 2: Structural design philosophy," tech. rep., WSP Ltd, 2016.

[220] D. E. Newland, *An introduction to random vibrations, spectral and wavelet analysis*. Mineola, New York: Dover Publications, third edit ed., 2005.

[221] P. Welch, "The use of fast Fourier transform for the estimation of power spectra: A method based on time averaging over short, modified periodograms," *IEEE Trans. Audio Electroacoust.*, vol. 15, pp. 70–73, jun 1967.

[222] A. L. Pais and E. Kausel, "Approximate formulas for dynamic stiffnesses of rigid foundations," *Soil Dyn. Earthq. Eng.*, vol. 7, no. 4, pp. 213–227, 1988.

[223] M. Novak, "Dynamic Stiffness and Damping of Piles," *Can. Geotech. J.*, vol. 11, pp. 574 – 598, 1974.

[224] M. Novak, "Vertical vibration of floating piles," *J. Eng. Mech. Div.*, pp. 153 – 167, 1977.

[225] G. N. Bycroft, "Forced Vibrations of a Rigid Circular Plate on a Semi-Infinite Elastic Space and on an Elastic Stratum," *Philos. Trans. R. Soc. A Math. Phys. Eng. Sci.*, vol. 248, pp. 327–368, jan 1956.

[226] M. Novak and F. Aboul-Ella, "Impedance functions of piles in layered media," *J. Eng. Mech. Div.*, vol. 104, no. 3, pp. 643–661, 1978.

[227] W. T. Thomson, "Transmission of elastic waves through a stratified solid medium," *J. Appl. Phys.*, vol. 21, no. 2, pp. 89–93, 1950.

[228] N. A. Haskell, "The dispersion of surface waves on multilayered media," *Bull. Seismol. Soc. Am.*, vol. 43, pp. 17–34, jan 1953.

Appendix A

Simplified foundation models

In the following, a summary of two examples of well-established simplified foundation models is presented: the cone model for a rigid, surface foundation and/or footing and the Novak's pile model as an example of a deep foundation. The former are used extensively throughout the dissertation while the latter is adopted comparatively in Chapter 3.

A.1 Cone foundation models

The necessity of dynamic modelling of foundations is often encountered in the context of earthquake-related problems in which the dimension of the entire surface foundation (i.e. slab foundation) is relatively small compared to the wavelength of the excitation. As a result, research efforts have considered the assumption of a rigid response for the foundation. A simplified approach for obtaining the dynamic stiffness of such foundation system is based on a strength-of-material approach and dates back to Ehlers [169] for the case of vertical motion. Substantial contributions to the so-called *cone model* [87] of a rigid foundation have been made by several researchers over the years. A thorough review of the *cone model* is reported by Wolf [84] with application to foundation vibration analysis. The *cone model* of a rigid foundation is based on the following assumptions:

- the soil-foundation interface is regarded as a massless base-mat to which a rigid motion is imposed;
- the soil is idealised, for each degree of freedom, as a truncated semi-infinite, homogeneous, linear-elastic cone with its apex at z_0 from the rigid foundation as illustrated in Figure 3.4;

- the cone is regarded as a tapered rod with the displacement in a cross-section at z defined by the corresponding value at its axis (i.e. plane sections remain plane).

A.1.1 Dynamic stiffness of a rigid foundation in vertical direction

With the assumptions as above, let us consider the dynamic force-response relationship in vertical direction for a *cone model* of a circular disk of radius r_0 as represented in Figure. This is done by examining the equilibrium of the truncated cone in the static and dynamic case.

Static case

Being free from external forces, the static equilibrium of an infinitesimal element at depth z gives:

$$\frac{dN(z)}{dz} = \frac{d}{dz}\left(EA(z)\frac{dw(z)}{dz}\right) = E\frac{dA(z)}{dz}\frac{dw(z)}{dz} + EA(z)\frac{d^2w(z)}{dz^2} = 0 \tag{A.1}$$

with E the Young's modulus, $N(z)$ and $A(z)$ the compressive internal force and the cross-section area respectively at depth z. From geometrical considerations:

$$\frac{A(z)}{A_0} = \frac{r^2(z)}{r_0^2} = \frac{z^2}{z_0^2} \tag{A.2}$$

By substituting Equation A.2 into A.1 the resulting governing equation for the static case is obtained:

$$\frac{d^2w(z)}{dz^2} + \frac{2}{z}\frac{dw(z)}{dz} = \frac{d^2\left(z\,w(z)\right)}{dz^2} = 0 \tag{A.3}$$

The solution of the latter is in the form:

$$w(z) = \frac{C_1}{z} + C_2 \tag{A.4}$$

For a rigid motion of the foundation w_0 at z_0, the radiation condition at $z \to \infty$ of null displacement $w(\infty) = 0$ provides the constant $C_2 = 0$ so that $C_1 = z_0 w_0$. The decrement of the displacement along the depth z follows the equation:

$$w(z) = \frac{z_0}{z} w_0 \tag{A.5}$$

The external force exerted at the soil-foundation interface $(z = z_0)$ may be obtained as:

$$f_0 = -N(z_0) = -EA_0 \frac{dw(z)}{dz}\bigg|_{z=z_0} = \frac{EA_0}{z_0} w_0 = K_{fz}^{(\mathrm{st})} w_0 \tag{A.6}$$

with $K_{fz}^{(\mathrm{st})}$ the vertical static stiffness of the rigid foundation on the soil idealised as a truncated cone. The *apex distance* z_0 is found by imposing the equality of $K_{fz}^{(\mathrm{st})}$ in Equation A.6 with the closed-form elastic solution:

$$K_{(\mathrm{st})z} = \frac{4G_s r_0}{1-\nu_s} \tag{A.7}$$

The geometry of the *cone model* is then defined for convergence to the exact solution as the frequency tends to zero. The dynamic equilibrium can be then investigated to establish the frequency dependency of the vertical stiffness of the foundation.

Dynamic case

The dynamic equilibrium of an infinitesimal element at depth z may be written as:

$$\frac{dN(z,t)}{dz} - \rho_s A(z) \frac{d^2 w(z,t)}{dt^2} = 0 \tag{A.8}$$

with t the time variable and ρ_s the soil density. For the assumption of the *cone model* as a tapered bar, the compressional wave speed can be found as $V_P = \sqrt{E/\rho_s}$. By consideration of the latter and by following the same algebra in Equations A.1-A.3, one can arrive at the wave equation:

$$\frac{d^2\big(z\,w(z,t)\big)}{dz^2} - \frac{1}{V_P^2} \frac{d^2\big(z\,w(z,t)\big)}{dt^2} = 0 \tag{A.9}$$

The solution of Equation A.9 may be expressed in the d'Alambert form:

$$z w(z,t) = z_0\, f\left(t - \frac{z-z_0}{V_P}\right) + z_0\, g\left(t + \frac{z-z_0}{V_P}\right) \tag{A.10}$$

where f and g are waves that propagate in the positive and negative direction respectively. Focussing on the response due to a displacement $w(z_0,t) = w_0(t)$ and considering the unbound domain of the *cone model*, there is no incoming wave g and the outgoing wave f defines the response. For $z = z_0$

Equation A.10 reduces the the following identity:

$$w_0(t) = f(t)$$

which provides the unknown function f representing the propagating wave. Substituting the latter back into Equation A.10, one can write:

$$w(z,t) = \frac{z_0}{z}\, w_0\left(t - \frac{(z-z_0)}{V_P}\right) \tag{A.11}$$

The external force $f_0(t)$ may be found as in Equation A.6, this time with reference to the motion in Equation A.11. The derivative in z of the latter may be obtained as:

$$\frac{dw(z,t)}{dz} = -\frac{z_0}{z^2}\, w_0\left(t - \frac{(z-z_0)}{V_P}\right) - \frac{1}{V_P}\frac{z_0}{z}\, w_0'\left(t - \frac{(z-z_0)}{V_P}\right) \tag{A.12}$$

where the differentiation denoted with $'$ is in the variable $\big(t-(z-z_0)/V_P\big)$. At $z=z_0$ the velocity $w_0'(t) = dw_0(t)/dt$ and the force exerted on the foundation (i.e. $z=z_0$) can be written as:

$$\begin{aligned} f_0(t) = -EA_0 \frac{dw(z,t)}{dz}\bigg|_{z=z_0} &= -EA_0\left[-\frac{w_0(t)}{z_0} - \frac{1}{V_P}\frac{dw_0(t)}{dt}\right] = \\ &= \frac{EA_0}{z_0} w_0(t) + \rho_s V_P A_0 \frac{dw_0(t)}{dt} = K\, w_0(t) + C\, \frac{dw_0(t)}{dt} \end{aligned} \tag{A.13}$$

The force-response relationship in Equation A.13 is indicative of the *spring* K and *damper* C constants associated with the displacement w_0 and the velocity dw_0/dt respectively. By considering a time-harmonic excitation of the kind $w_0(t) = \hat{w}_0(\omega)\, e^{i\omega t}$, with ω the angular frequency, Equation A.13 may be reformulated as:

$$\hat{f}_0(\omega) = K_{fz}^{(\mathrm{st})}\Big[k_{fz}(\omega) + i\omega\, c_{fz}(\omega)\Big]\hat{w}_0(\omega) = \hat{K}_{fz}(\omega)\, \hat{w}_0(\omega) \tag{A.14}$$

Equation A.14 shows the general form of the time-harmonic force-response relationship with reference to frequency-dependent *spring* k_{fz} and the *damping* c_{fz} coefficients that are conveniently scaled by the static stiffness $K_{fz}^{(\mathrm{st})}$. By comparison of the latter with Equation A.13, it is evident that the *cone model* provides frequency-independent spring and damping coefficients. The vertical dynamic stiffness at

high-frequencies may be obtained as:

$$\lim_{\omega\to\infty} \hat{K}_{fz}(\omega) = i\omega K_{fz}^{(\mathrm{st})} c_{fz} = i\omega\rho_s V_P A_0 \tag{A.15}$$

This is indicative of the high-frequency behaviour of the *cone model* as an elastic bar, which acts as a damper that dissipates the energy associated with the excitation at $z = z_0$.

Equations A.7 and A.15 are representative of the limiting values of the vertical dynamic stiffness of a rigid foundation at low and high frequencies respectively. The *cone model* is then based on this *doubly-asymptotic* assumption that is reasonably valid by comparison of a more rigorous solution (see Section 3.2). In general, the *spring* k_{fz} and the *damping* c_{fz} coefficients, associated with a rigorous solution of a rigid foundation, are not constants along the frequency spectrum. In particular, the cone models represent a better approximation in case of *compressible* soils ($\nu_s \leq 3$). For *nearly incompressible* soils the cone model approximation works well only at low relatively low frequencies; moreover, a trapped mass effect and a different wave propagation speed must be accounted for in this case (see Section 3.2).

A.1.2 Dynamic stiffness matrix for a rigid foundation

Similarly to the previous discussion for the vertical motion, cone models can be obtained for the horizontal and rocking motion of the rigid foundation. The reader is redirected to the book of Wolf [84] for a review of the complete formulation. Here the properties of the cone models for the horizontal, vertical and rocking motion of a rigid foundation are reported in Table A.1 as they are implemented and used in this dissertation. Formulae for the approximate static stiffness, the spring and the damping coefficients are also reported in Table A.2 with reference to a rectangular rigid foundation of half-width b (along x) and c (along y), and to the customary dimensionless frequency $a_0 = \omega r_0/V_s$. Summarising, the force-response relationship for a rigid foundation by means of the cone model can be written as:

$$\hat{\mathrm{s}}_o(a_0) = \hat{K}_{fx}(a_0)\,\hat{u}_o(a_0) = K_{fx}^{(\mathrm{st})}\left[k_{fx}(a_0) + ia_0 c_{fx}(a_0)\right]\hat{u}_o(a_0) \tag{A.16a}$$

$$\hat{f}_o(a_0) = \hat{K}_{fz}(a_0)\,\hat{w}_o(a_0) = K_{fz}^{(\mathrm{st})}\left[k_{fz}(a_0) + ia_0 c_{fz}(a_0)\right]\hat{w}_o(a_0) \tag{A.16b}$$

$$\hat{q}_o(a_0) = \hat{K}_{f\varphi}(a_0)\,\hat{\varphi}_o(a_0) = K_{f\varphi}^{(\mathrm{st})}\left[k_{f\varphi}(a_0) + ia_0 c_{f\varphi}(a_0)\right]\hat{\varphi}_o(a_0) \tag{A.16c}$$

Motion	Equivalent radius r_0	Aspect ratio $\frac{z_0}{r_0}$	Poisson's ratio ν_s	Wave speed V	Trapped mass δ_m
Horizontal	$\sqrt{\frac{A_0}{\pi}}$	$\frac{\pi}{8}(2-\nu_s)$	all ν_s	V_S	0
Vertical	$\sqrt{\frac{A_0}{\pi}}$	$\frac{\pi}{4}(1-\nu_s)\left(\frac{V}{V_S}\right)^2$	$\leq \frac{1}{3}$	V_P	0
			$\frac{1}{3} < \nu_s \leq \frac{1}{2}$	$2V_S$	$2.4\left(\nu_s - \frac{1}{3}\right)$
Rocking	$\sqrt[4]{\frac{I_0}{\pi}}$	$\frac{9\pi}{32}(1-\nu_s)\left(\frac{V}{V_S}\right)^2$	$\leq \frac{1}{3}$	V_P	0
			$\frac{1}{3} < \nu_s \leq \frac{1}{2}$	$2V_S$	$1.2\left(\nu_s - \frac{1}{3}\right)$

Table A.1 Cone models properties for the horizontal, vertical and rocking motion of a rigid foundation with area A_0, polar moment of inertia I_0 resting on a soil with Poisson's ratio ν_s and shear wave speed V_S.

Motion	Static Stiffness (*from Pais* [222])	spring coeff. $k_f(a_0)$	damping coeff. $c_f(a_0)$
u_o	$\frac{\mu\, c\left[6.8(b/c)^{0.65}+2.4\right]}{(2-\nu_s)}$	$1-\frac{\delta_m}{\pi}\frac{z_0}{r_0}\left(\frac{V_S}{V}a_0\right)^2$	$\frac{z_0}{r_0}\frac{V_S}{V}$
w_o	$\frac{\mu\, c\left[3.1(b/c)^{0.75}+1.6\right]}{(1-\nu_s)}$		
φ_o	$\frac{\mu\, c^3\left[3.73(b/c)^{2.4}+0.27\right]}{(1-\nu_s)}$	$1-\frac{4\delta_m z_0}{3\pi r_0}\frac{(V_S a_0)^2}{V^2}-\frac{a_0^2}{3\frac{(r_0V)^2}{(z_0V_S)^2}+a_0^2}$	$\frac{z_0V_S}{3r_0V}\frac{a_0^2}{\frac{(r_0V)^2}{(z_0V_S)^2}+a_0^2}$

Table A.2 Expressions for the static stiffness $K_f^{(\mathrm{st.})}$, the spring k_f and the damping c_f coefficients for a rectangular rigid foundation.

A.1.3 Dynamic stiffness of a rigid footing in vertical direction

Based on previous results, a simplified force-response relationship can be established for the case of a rigid footing. The wave pattern is simplified by means of an unfolded cone model. Firstly, the underlying half-space is assumed to be rigid (i.e. bedrock, see Figure 3.7a) so that wave reflections are expected at the interface. This assumption is then removed (see Figure 3.7b) for obtaining an expression of a refraction coefficient for the wave propagating into the half-space.

Case of elastic layer on rigid bedrock

Additionally to what seen for the cone model in Section A.1.1, the unfolded cone model in Figure 3.7a accounts for:

- decay of waves as they propagate away from the footing within the layer;
- reflections at both the interface and the free-surface.

Moving the z reference as in Figure 3.7a, the displacement expression in Equation A.11 may be re-written:

$$w_1(z,t) = \frac{z_0}{z+z_0}\,\bar{w}_0\left(t-\frac{z}{V}\right) = \frac{z_0}{z+z_0} f_1\left(t-\frac{z}{V}\right) \tag{A.17}$$

with $\bar{w}_0$ referring to the displacement of the equivalent cone model (i.e. thickness h of the layer assumed infinite), and V the wave speed according to Table A.1. In general for superposition of multiple reflections at both the fixed and free boundary, we can write:

$$w(z,t) = \sum_{i=1}^{\infty} w_i(z,t) \tag{A.18}$$

with w_i the displacement referring to the equivalent semi-infinite cone models with apex i, as illustrated by the unfolded cone models in Figure 3.7a. Figure A.1 shows a more convenient representation with the cones referring to the different boundary conditions unfolded in a single layered cone. Equation A.18 may be written in terms of wave amplitudes f and g that are both propagating downwardly in the layered model:

$$w(z,t) = \sum_{j=1}^{\infty}\left[\frac{z_0}{z_0+z_{2j-1}} f_{(2j-1)}\left(t-\frac{z_{(2j-1)}}{V}\right) + \frac{z_0}{z_0+z_{(2j)}} g_{(2j)}\left(t-\frac{z_{(2j)}}{V}\right)\right] \tag{A.19}$$

The actual propagation of waves within the layer is restored by the change of variables into the global

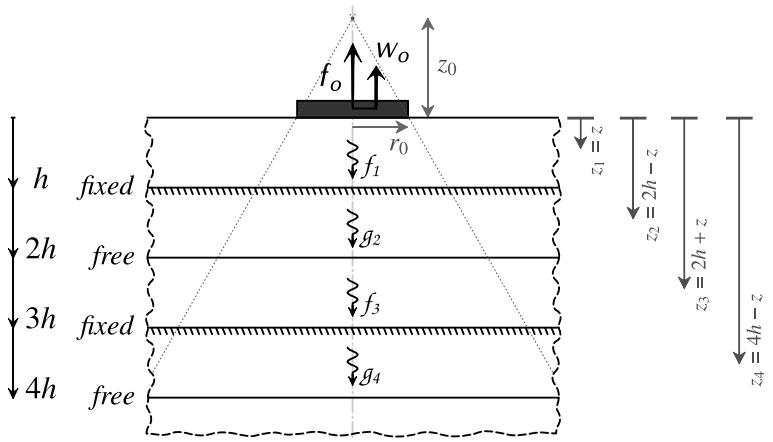

Fig. A.1 Unfolded layered cone model for a rigid footing on an elastic layer of thickness h resting on a rigid bedrock.

coordinate z as schematically reported in Figure A.1. Moreover, substituting Equation A.17 into Equation A.19:

$$w(z,t) = \frac{z_0}{z_0+z}\,\bar{w}_0\left(t-\frac{z}{V}\right) + \\ + \sum_{j=1}^{\infty}\left[\frac{z_0}{z_0+2jh-z}g_{(2j)}\left(t-\frac{2jh}{V}+\frac{z}{V}\right) + \frac{z_0}{z_0+2jh+z}f_{(2j+1)}\left(t-\frac{2jh}{V}-\frac{z}{V}\right)\right] \tag{A.20}$$

By ensuring compatibility of displacements at the free-surface and null displacement at fixed boundary for each wave reflection, one can write:

$$g_{(2j)} = (-1)f_{(2j-1)} \quad \text{at the fixed boundary} \tag{A.21}$$

$$f_{(2j+1)} = g_{(2j)} \quad \text{at the free boundary} \tag{A.22}$$

By consideration of the latter into Equation A.20, the wave amplitudes can be traced back to $f_1(t)$ that is equal to $\bar{w}_0(t)$. The following general expression is obtained for the displacement within the layer:

$$w(z,t) = \frac{z_0}{z_0+z}\bar{w}_0\left(t-\frac{z}{V}\right) + \\ + \sum_{j=1}^{\infty}(-1)^j\left[\frac{z_0}{z_0+2jh-z}\bar{w}_0\left(t-\frac{2jh}{V}+\frac{z}{V}\right) + \frac{z_0}{z_0+2jh+z}\bar{w}_0\left(t-\frac{2jh}{V}-\frac{z}{V}\right)\right] \tag{A.23}$$

The process of generating waves due to reflections is infinite. However, the unfolded layered cone model in Figure A.1 demonstrates that late reflections may contribute marginally to the total displacement by virtue of the general solution in Equation A.11: an increase of the z coordinate will result in a decrease in displacement amplitude and radiation in the horizontal direction of the layer.

Limiting the calculation to N reflection cycles, the resulting displacement at $z = 0$ may be written:

$$w_0(t) = \bar{w}_0(t) + 2\sum_{j=1}^{N}(-1)^j \frac{\bar{w}_0(t-jT)}{1+j\kappa} \tag{A.24}$$

with the time constant $T = 2h/V$ and the space constant $\kappa = 2h/z_0$. Introducing *echo constants* ε_j, a compact relation may be written between the response of the rigid footing and that of the equivalent rigid foundation:

$$\begin{aligned} w_0(t) = \sum_{j=0}^{N} \varepsilon_j \, \bar{w}_0(t-jT) \qquad \text{with} \quad \varepsilon_0 = 1 \qquad \text{for } j = 0 \\ \varepsilon_j = \frac{2(-1)^j}{1+j\kappa} \quad \text{for } j \geq 1 \end{aligned} \tag{A.25}$$

A Fourier transformation of Equation A.25 by virtue of the time-shift theorem provides a relationship in the frequency domain:

$$\hat{w}_0(\omega) = \sum_{j=0}^{N} \varepsilon_j \, e^{-ij\omega T} \hat{\bar{w}}_0(\omega) \tag{A.26}$$

From Equation A.13, the force-response relationship in the frequency domain may be written:

$$\hat{f}_0(\omega) = K\left[1 + i\omega\frac{C}{K}\right]\hat{\bar{w}}_0(\omega) = K\left[1 + i\omega\frac{T}{\kappa}\right]\hat{\bar{w}}_0(\omega) \tag{A.27}$$

and by substitution of $\hat{\bar{w}}_0(\omega)$ from Equation A.26:

$$\begin{aligned} \hat{f}_0(\omega) = K\frac{1+i\omega\dfrac{T}{\kappa}}{\displaystyle\sum_{j=0}^{N}\varepsilon_j e^{-ij\omega T}}\,\hat{w}_0(\omega) = K\frac{1+i\omega\dfrac{T}{\kappa}}{1+2\displaystyle\sum_{j=1}^{N}(-1)^j\frac{e^{-ij\omega T}}{1+j\kappa}}\,\hat{w}_0(\omega) = \\ = K_{fz}^{(\mathrm{st})}\, S(\omega)\,\hat{w}_0(\omega) = \hat{K}_{fz}(\omega)\,\hat{w}_0(\omega) \end{aligned} \tag{A.28}$$

The dynamic stiffness $\hat{K}_{fz}(\omega)$ for the rigid footing on a layer resting on a bedrock is obtained from the static stiffness $K_{fz}^{(\mathrm{st})}$ of an equivalent rigid foundation (see A.2) and from a dynamic factor $S(\omega)$

that accounts for the multiple reflections and radiation of energy within the layer in agreement with the model assumptions discussed in this section.

Case of elastic layer on elastic half-space

The fixed-boundary adopted at the rigid bedrock may be relaxed in order to account for the presence of an elastic half-space with different properties from the layer. The boundary condition in Equation A.21 may be revisited and written in the form:

$$\frac{g_{(2j)}(\omega)}{f_{(2j-1)}(\omega)} = \frac{g_2(\omega)}{f_1(\omega)} = (-\alpha(\omega)) \tag{A.29}$$

The reflection coefficient for the j reflection can be obtained by ensuring equilibrium and compatibility for the first reflection. Wolf argues that the more rigorous procedure of a reflection coefficient dependent on j is not necessary [84].

The presence of the elastic half-space may be then accounted for by substitution of the factor $(-1)^j$ in Equation A.28 with the factor $(-\alpha(\omega))^j$.

A.1.4 Dynamic stiffness matrix for a rigid footing

The horizontal, vertical and rocking dynamic stiffness terms for a rigid footing on an elastic layer of thickness h resting on an elastic half-space (see Figure 3.7b) are reported in the following. Formally, the expressions are the same for the horizontal and vertical motion, given that the appropriate static stiffness and wave speed are adopted from Table A.1 and A.2. Different formulas for $S(\omega)$ and $\alpha(\omega)$ are obtained for the rocking case [84].

Translational motion

$$S(\omega) = \frac{1 + i\omega\dfrac{T}{\kappa}}{1 + 2\displaystyle\sum_{j=1}^{N}(-\alpha(\omega))^j \frac{e^{-ij\omega T}}{1 + j\kappa}} \tag{A.30}$$

$$-\alpha(\omega) = \frac{i\omega(\rho_c V_c - \rho_s V_s) + \dfrac{\rho_c V_c^2}{z_{0c} + h} - \dfrac{\rho_s V_s^2}{z_{0s}}}{i\omega(\rho_c V_c + \rho_s V_s) + \dfrac{\rho_c V_c^2}{z_{0c} + h} + \dfrac{\rho_s V_s^2}{z_{0s}}} \tag{A.31}$$

The dynamic stiffness, in terms of the dimensionless frequency a_0, for the horizontal and vertical motion may be written:

$$\hat{s}_o(a_0) = K_{fx}^{(\mathrm{st})} S_x(a_0)\, \hat{u}_o(a_0) = \hat{K}_{fx}(a_0)\, \hat{u}_o(a_0) \tag{A.32}$$

$$\hat{f}_o(a_0) = K_{fz}^{(\mathrm{st})} S_z(a_0)\, \hat{w}_o(a_0) = \hat{K}_{fz}(a_0)\, \hat{w}_o(a_0) \tag{A.33}$$

Rocking motion

$$S_\varphi(\omega) = \frac{1 - \dfrac{1}{3}\dfrac{(\omega T)^2}{\kappa^2 + (\omega T)^2} + i\dfrac{\omega T}{3\kappa}\dfrac{(\omega T)^2}{\kappa^2 + (\omega T)^2}}{1 + \dfrac{2}{1 + \dfrac{i\omega T}{\kappa}} \left\{ \displaystyle\sum_{j=1}^{N} (-\alpha(\omega))^j \frac{e^{-ij\omega T}}{(1+j\kappa)^3} + \frac{i\omega T}{\kappa} \sum_{j=1}^{N} (-\alpha(\omega))^j \frac{e^{-ij\omega T}}{(1+j\kappa)^2} \right\}} \tag{A.34}$$

$$-\alpha(\omega) = \frac{-\dfrac{1 + i\dfrac{\omega}{V_c}(z_{0c}+h)}{1 + i\dfrac{\omega}{V_s} z_{0s}} + \dfrac{3 + 3i\dfrac{\omega}{V_c}(z_{0c}+h) + \left(\dfrac{i\omega}{V_c}\right)^2 (z_{0c}+h)^2}{3 + 3i\dfrac{\omega}{V_s} z_{0s} + \left(\dfrac{i\omega}{V_s}\right)^2 z_{0s}^2} \cdot \dfrac{\rho_c V_c^2 z_{0s}}{\rho_s V_s^2 (z_{0c}+h)}}{\dfrac{1 + i\dfrac{\omega}{V_c}(z_{0c}+h)}{1 + i\dfrac{\omega}{V_s} z_{0s}} + \dfrac{3 + 3i\dfrac{\omega}{V_c}(z_{0c}+h) + \left(\dfrac{i\omega}{V_c}\right)^2 (z_{0c}+h)^2}{3 + 3i\dfrac{\omega}{V_s} z_{0s} + \left(\dfrac{i\omega}{V_s}\right)^2 z_{0s}^2} \cdot \dfrac{\rho_c V_c^2 z_{0s}}{\rho_s V_s^2 (z_{0c}+h)}} \tag{A.35}$$

The dynamic stiffness for the rocking case may be written as:

$$\hat{q}_o(a_0) = K_{f\varphi}^{(\mathrm{st})} S_\varphi(a_0)\, \hat{\varphi}_o(a_0) = \hat{K}_{f\varphi}(a_0)\, \hat{\varphi}_o(a_0) \tag{A.36}$$

A.2 Novak's pile

In Chapter 3, a simplified model for the vertical vibration of a single pile foundation is adopted for sake of comparison with the rigid footing and rigid foundation models. The pile model used is also known in literature as the Novak's pile [223, 224] from the author who first introduced it. The model assumes that the reactions provided by the surrounding soil, during the vertical vibration of the pile, may be obtained by assuming each infinitesimal portion of the pile to behave rigidly and independently. It follows that the reaction provided by the soil per unit length of the pile may be

obtained by the analytical solution of anti-plane motion of an infinitely-long, rigid, cylindrical cavity in a full-space. The force per unit length of the rigid cavity required to sustain a unit amplitude motion at a frequency a_0 can be found as [33]:

$$S_w = 2\pi a_0 \frac{H_1^{(2)}(a_0)}{H_0^{(2)}(a_0)} \tag{A.37}$$

with $H_n^{(2)}$ the Hankel functions of the second kind of order n. By modelling a finite pile as a bar, the governing equation for the axial vibration in Appendix B.1a, with the element aligned along the z axis and with consideration of the soil reacting force, may be written as:

$$E_p A_p \frac{\partial^2 w(z,t)}{\partial z^2} - \rho_p A_p \frac{\partial^2 w(z,t)}{\partial t^2} - G_s S_w w = 0 \tag{A.38}$$

with E_p, A_p, ρ_p the Young's modulus, the cross-sectional area and the density of the pile, ans G_s the shear modulus of the surrounding soil. Assuming a time-harmonic response of the type $w(z,t) = \hat{w}(z,\omega)\, e^{i\omega t}$, the solution of Equation A.38 may be found as:

$$\hat{w}(z,\omega) = c_1\, e^{ik_p z} + c_2\, e^{-ik_p z} \tag{A.39}$$

with:

$$k_p = \sqrt{\frac{\omega^2 \rho_p A_p - G_s S_w}{E_p A_p}} \tag{A.40}$$

and $i = \sqrt{-1}$, with the dependence of frequency ω omitted in the following and expressed by the symbol '$\hat{}$' in the following. The interest lies on the dynamic stiffness at the pile-head for coupling the foundation model to a building, as seen in Chapter 3. Assuming the origin of the local reference system at the lower-end of the pile, the following boundary conditions apply:

$$\begin{cases} \hat{w}(L_p) = 1 \\ \hat{f}_p(0) = -\hat{f}_d \end{cases} \tag{A.41}$$

with $\hat{f}_d$ the force transmitted at the lower end of the pile to the underlying soil and L_p the pile's length. Consistently with the assumption of the surrounding soil responding as a series of independent, infinitely-thin horizontal layers, the reaction at the lower-tip of the pile may be retrieved from the

impedance of a rigid disk of area A_p on an elastic half-space of properties $\rho_{br}, V_{br}, \nu_{br}$. The force on the disk required for the motion at the lower-end of the pile may be expressed as:

$$\hat{f}_d = \widehat{K}_d \hat{w}(0) \tag{A.42}$$

By consideration of the derivative of Equation A.39 as:

$$\frac{\partial w}{\partial z} = ik_p(c_1\, e^{ik_p z} - c_2\, e^{-ik_p z}) \tag{A.43}$$

the force at the lower-end of the pile may be written as:

$$\hat{f}_p(0) = -E_p A_p \frac{\partial w}{\partial z}\bigg|_{z=0} = -E_p A_p ik_p(c_1 - c_2) \tag{A.44}$$

and, by substitution, the boundary conditions give the system of equations for the two unknown constant:

$$\begin{cases} c_1\, e^{ik_p L_p} + c_2\, e^{-ik_p L_p} = 1 \\ E_p A_p ik_p(c_1 - c_2) = \widehat{K}_d(c_1 + c_2) \end{cases} \tag{A.45}$$

After some algebra, the system of equations can be solved to give the force at the pile-head required for a unit motion, which is the dynamic stiffness of interest:

$$\widehat{K}_{fPz} = -E_p A_p k_p \left(\frac{E_p A_p k_p \sin(k_p L_p) - \widehat{K}_d \cos(k_p L_p)}{E_p A_p k_p \cos(k_p L_p) + \widehat{K}_d \sin(k_p L_p)} \right) \tag{A.46}$$

The dynamic stiffness for a *floating pile*, which considers a free lower-end, can be obtained from Equation A.46 by setting $\widehat{K}_d = 0$:

$$\widehat{K}_{fPz}^{(\text{free-end})} = -E_p A_p k_p \tan(k_p L_p) \tag{A.47}$$

which is formally in agreement with the dynamic stiffness at the base of a free-end column, as reported in Equation 3.15, but this time with the wavenumber obtained by consideration of the soil reactions as in Equation A.40.

The dynamic stiffness of the rigid disk, used for the pile model in this dissertation, is that of the cone model for a rigid foundation $\widehat{K}_{fWz}$ as presented in this appendix. The original Novak's model [224]

makes use of the approximate expression by Bycroft [225] that are consistent with the cone model but limited to two values of Poisson's ratio. Here, the "*bedrock*" representing the half-space at the bottom of the pile has the same properties of the surrounding soil, which is consistent with the pile being embedded in a homogeneous soil. It is customary in foundation analysis to define the flexibility coefficients associated with the dynamic stiffness as:

$$F_{zz} = \frac{K_{fPz}^{(\mathrm{st.})}}{\widehat{K}_{fPz}} = I_{zz} + iJ_{zz} \tag{A.48}$$

These are compared in Figure A.2 with those obtained by a rigorous boundary element of a single pile in a homogeneous and elastic half-space [2]. Although the comparison of the Novak's pile results are favourable in terms of the general frequency-dependence of the flexibility coefficients, important differences up to 40 % may be found with the rigorous counterparts. Nevertheless, there is experimental evidence [47, 226] suggesting that the pile-head driving-point response is adequately captured up to approximately 100 Hz, which corresponds, for experiments carried out by Cryer [47],

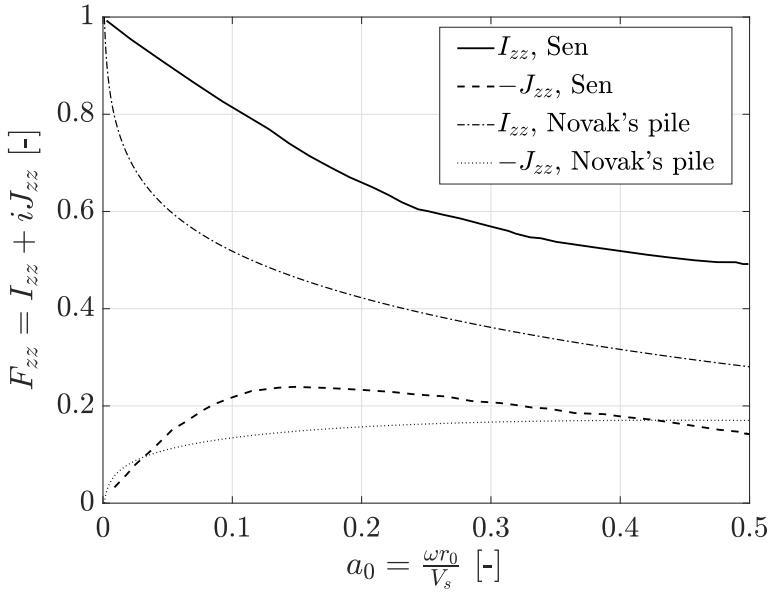

Fig. A.2 Comparison of the vertical pile-head flexibility coefficients obtained by the Novak's pile model presented here and the rigorous model of Sen *et al.*[2]. The coefficients refer to a single pile with $L_p/r_0 = 20$, a ratio $E_p/E_s = 100$, aratio $\rho_p/\rho_s = 0.75$ and a Poisson's ratio $\nu_s = 0.4$ for the surrounding soil. The lower end of the pile is coupled to cone model of a rigid circular disk of radius r_0.

to $a_0 \approx 1$. Differences at higher frequencies are observed and expected due to the shorter wavelengths involved that make the assumption of the soil responding as independent, infinitely-thin layers invalid.

Appendix B

The Dynamic-Stiffness Method for portal-frame structures

A rigorous building model in the form of a 2D portal-frame structure is discussed and adopted in this dissertation. Here, the dynamic-stiffness method (DSM) is reviewed with reference to analytical solutions [121] of an elastic bar and an Euler beam for the axial and bending response of a single element as represented in Figure B.1.

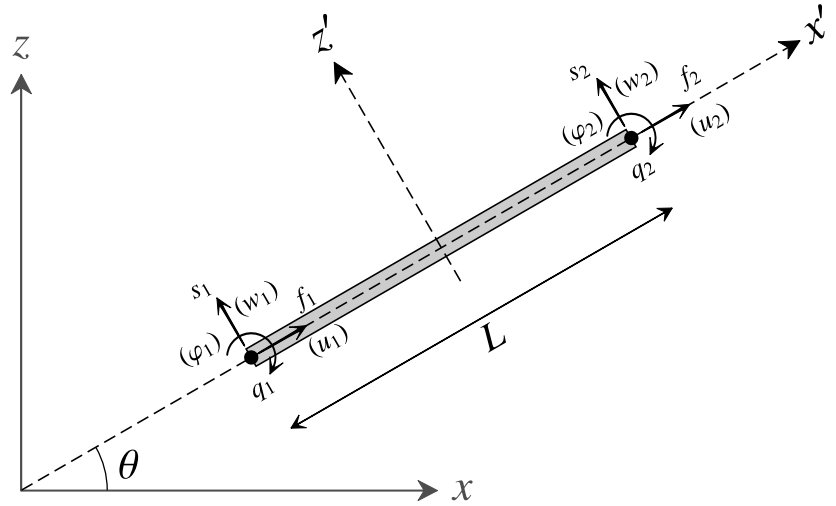

Fig. B.1 Representation of a beam-bar element of length L in the global reference system $x-z$. An element dynamic-stiffness matrix $\mathbf{K_e}$ relates the generalised forces f, s, q to the respective displacements u, w, φ at the ends of the element in the local reference system $x'-z'$.

A typical element of a 2D portal frame building is defined by its length L, cross-sectional area A, second moment of area I, density ρ and Young's modulus E.

The governing equations for the dynamic equilibrium of an undamped bar and an undamped Euler beam are given respectively by:

$$E\,\frac{\partial^2 u(x,t)}{\partial x^2} - \rho\,\ddot{u}(x,t) = 0 \tag{B.1a}$$

$$EI\,\frac{\partial^4 w(x,t)}{\partial x^4} + \rho A\,\ddot{w}(x,t) = 0 \tag{B.1b}$$

For time-harmonic motion at frequency ω, the general solutions for the axial and bending motion may be written respectively as:

$$u(x,t) = Re\{u(x,\omega)\,e^{i\omega t}\} \tag{B.2a}$$

$$w(x,t) = Re\{w(x,\omega)\,e^{i\omega t}\} \tag{B.2b}$$

By substitution of the latter in the respective Equations B.1a and b, the following ordinary differential equations are obtained:

$$\frac{\partial^2 u(x,\omega)}{\partial x^2} + k_A^2\,u(x,\omega) = 0 \tag{B.3a}$$

$$\frac{\partial^4 w(x,\omega)}{\partial x^4} - k_B^4\,w(x,\omega) = 0 \tag{B.3b}$$

with k_A and k_B the axial and bending wavenumbers respectively given by:

$$k_A = \frac{\omega}{V_A} = \omega\sqrt{\frac{\rho}{E}}; \qquad k_B = \frac{\omega}{V_B} = \sqrt{\omega}\sqrt[4]{\frac{\rho A}{EI}} \tag{B.4}$$

V_A and V_B are the wave speeds of the axial and bending waves respectively. The solutions of Equations B.3 may be written in the form [121]:

$$u(x,\omega) = c_1\,e^{ik_A x} + c_2\,e^{-ik_A x} \tag{B.5a}$$

$$w(x,\omega) = c_3\,e^{k_B x} + c_4\,e^{ik_B x} + c_5\,e^{-k_B x} + c_6\,e^{-ik_B x} \tag{B.5b}$$

with $i = \sqrt{-1}$ and the constants c_1 to c_6 to be determined. For the sign convention as in Figure B.1, the rotation, the bending moment, the shear force and the axial force at a point x may be found as:

$$\varphi = -\frac{\partial w}{\partial x}; \quad q = -EI\,\frac{\partial^2 w}{\partial x^2}; \quad s = -EI\,\frac{\partial^3 w}{\partial x^3}; \quad f = EA\,\frac{\partial u}{\partial x} \tag{B.6}$$

The generalised forces and displacements at the ends of the element may be written:

$$u_1 = u; \quad w_1 = w; \quad \varphi_1 = \varphi; \quad f_1 = -f; \quad s_1 = -s; \quad q_1 = -q; \qquad \text{at } x = -L/2 \tag{B.7}$$

$$u_2 = u; \quad w_2 = w; \quad \varphi_2 = \varphi; \quad f_2 = f; \quad s_2 = s; \quad q_2 = q; \qquad \text{at } x = L/2 \tag{B.8}$$

The generalised displacements may be written in terms of the unknown constants by means of Equations B.5 with the resulting matrix equation:

$$\begin{bmatrix} u_1 \\ w_1 \\ \varphi_1 \\ u_2 \\ w_2 \\ \varphi_2 \end{bmatrix} = \begin{bmatrix} e^{-ik_A\frac{L}{2}} & e^{ik_A\frac{L}{2}} & 0 & 0 & 0 & 0 \\ 0 & 0 & e^{-k_B\frac{L}{2}} & e^{-ik_B\frac{L}{2}} & e^{k_B\frac{L}{2}} & e^{ik_B\frac{L}{2}} \\ 0 & 0 & -k_B e^{-k_B\frac{L}{2}} & -ik_B e^{-ik_B\frac{L}{2}} & k_B e^{k_B\frac{L}{2}} & ik_B e^{ik_B\frac{L}{2}} \\ e^{ik_A\frac{L}{2}} & e^{-ik_A\frac{L}{2}} & 0 & 0 & 0 & 0 \\ 0 & 0 & e^{k_B\frac{L}{2}} & e^{ik_B\frac{L}{2}} & e^{-k_B\frac{L}{2}} & e^{-ik_B\frac{L}{2}} \\ 0 & 0 & -k_B e^{k_B\frac{L}{2}} & -ik_B e^{ik_B\frac{L}{2}} & k_B e^{-k_B\frac{L}{2}} & ik_B e^{-ik_B\frac{L}{2}} \end{bmatrix} \begin{bmatrix} c_1 \\ c_2 \\ c_3 \\ c_4 \\ c_5 \\ c_6 \end{bmatrix} \tag{B.9}$$

$$\therefore \mathbf{u_e} = \mathbf{M}\,\mathbf{c}$$

Similarly, for the generalised forces at the ends of the element one can write:

$$\begin{bmatrix} f_1 \\ s_1 \\ q_1 \\ f_2 \\ s_2 \\ q_2 \end{bmatrix} = EA \begin{bmatrix} -ik_A e^{-ik_A\frac{L}{2}} & ik_A e^{ik_A\frac{L}{2}} & 0 & 0 & 0 & 0 \\ 0 & 0 & r^2k_B^3 e^{-k_B\frac{L}{2}} & -r^2ik_B^3 e^{-ik_B\frac{L}{2}} & -r^2k_B^3 e^{k_B\frac{L}{2}} & r^2ik_B^3 e^{ik_B\frac{L}{2}} \\ 0 & 0 & r^2k_B^2 e^{-k_B\frac{L}{2}} & -r^2k_B^2 e^{-ik_B\frac{L}{2}} & r^2k_B^2 e^{k_B\frac{L}{2}} & -r^2k_B^2 e^{ik_B\frac{L}{2}} \\ ik_A e^{ik_A\frac{L}{2}} & -ik_A e^{-ik_A\frac{L}{2}} & 0 & 0 & 0 & 0 \\ 0 & 0 & -r^2k_B^3 e^{k_B\frac{L}{2}} & r^2ik_B^3 e^{ik_B\frac{L}{2}} & r^2k_B^3 e^{-k_B\frac{L}{2}} & -r^2ik_B^3 e^{-ik_B\frac{L}{2}} \\ 0 & 0 & -r^2k_B^2 e^{k_B\frac{L}{2}} & r^2k_B^2 e^{ik_B\frac{L}{2}} & -r^2k_B^2 e^{-k_B\frac{L}{2}} & r^2k_B^2 e^{-ik_B\frac{L}{2}} \end{bmatrix} \begin{bmatrix} c_1 \\ c_2 \\ c_3 \\ c_4 \\ c_5 \\ c_6 \end{bmatrix} \tag{B.10}$$

$$\therefore \mathbf{f_e} = \mathbf{N}\,\mathbf{c}$$

with r the radius of gyration of the cross section. The vector $\mathbf{c}$ collecting the unknown constants in Equation B.10 may be eliminated by use of Equation B.9. A force-response relationship can then be established at the ends of the element:

$$\mathbf{f_e} = \mathbf{N}\left[\mathbf{M}\right]^{-1}\mathbf{u_e} = \mathbf{K_e}\,\mathbf{u_e} \tag{B.11}$$

with $\mathbf{K_e}$ the dynamic-stiffness matrix of the beam-bar element in the local reference system $x-z$. In general, the element is part of a larger assembly that refers to a global coordinate system as in Figure B.1. A coordinate transformation allows to refer to forces and displacements vectors in the global reference system given the angle of orientation θ:

$$\mathbf{f_g^{(e)}} = \mathbf{R}\,\mathbf{f_e}; \quad \mathbf{u_g^{(e)}} = \mathbf{R}\,\mathbf{u_e}; \quad \text{with} \quad \mathbf{R} = \begin{bmatrix} \cos\theta & -\sin\theta & 0 & 0 & 0 & 0 \\ \sin\theta & \cos\theta & 0 & 0 & 0 & 0 \\ 0 & 0 & 1 & 0 & 0 & 0 \\ 0 & 0 & 0 & \cos\theta & -\sin\theta & 0 \\ 0 & 0 & 0 & \sin\theta & \cos\theta & 0 \\ 0 & 0 & 0 & 0 & 0 & 1 \end{bmatrix} \tag{B.12}$$

with the transformation matrix $\mathbf{R}$ being orthogonal. The element dynamic stiffness matrix in the global reference system follows by substitution of Equation B.11 into Equation B.12:

$$\mathbf{f_g^{(e)}} = \mathbf{R}\,\mathbf{f_e} = \mathbf{R}\,\mathbf{K_e}\,\mathbf{u_e} = \mathbf{R}\,\mathbf{K_e}\left[\mathbf{R}\right]^{-1}\mathbf{u_g^{(e)}} = \mathbf{R}\,\mathbf{K_e}\,\mathbf{R}^T\,\mathbf{u_g^{(e)}} = \mathbf{K_g^{(e)}}\,\mathbf{u_g^{(e)}} \tag{B.13}$$

Appendix C

The Stiffness-Matrix Method for horizontally layered media

A rather common representation of a layered ground is composed by a number of horizontal layers overlying an half-space, as illustrated schematically in Figure 4.16, which are all assumed to be homogeneous, linear-elastic and isotropic. In reality the ground is a complex structure intrinsically heterogeneous and anisotropic. Moreover, the assumption that layering of the ground carries a specific directionality (i.e. vertical) may be misleading and dependent strongly on the geological structure of the site that is under investigation. Despite the actual complexity of the ground, a great deal of existing literature on wave propagation in soils refers to the assumption of horizontally layered media. Considering the purpose of this dissertation in the context of ground-borne vibration, this model of the ground may be sufficient to capture the essential features of wave propagation in the underground of a building's site. Early developments for the response of such stratified media to plane-wave excitation refer to the *transfer matrix* method of Thomson [227] and Haskell [228]. A superior *stiffness or impedance matrix method* has been developed by Kausel and Röesset [189]. The latter is, in principle, an exact method that provides mathematical expressions for the general response of the layered system (i.e. displacement and/or stresses) that is free from errors [194]. However, such expressions are intractable by analytical means and must be implemented numerically. In the following, the method is reviewed, as it is used in this dissertation, starting from the equilibrium of a homogeneous, linear-elastic and isotropic solid.

C.1 The governing equations

Consider a Cartesian coordinate system, denoted by the axes $x, y,$ and z, in which we define a homogeneous, linear-elastic and isotropic solid $\mathcal{B}$ of density ρ and Lamé constants λ, μ with associated displacement and force fields $\mathbf{u}(\mathbf{x},t)$ and $\mathbf{f}(\mathbf{x})$ respectively. The equilibrium, constitutive and compatibility equations of motion can be written in the following indexed form:

$$\sigma_{ij,j} + \rho f_i = \rho \ddot{u}_i \tag{C.1}$$

$$\sigma_{ij} = \lambda \varepsilon_{kk} \delta_{ij} + 2\mu \varepsilon_{ij} \tag{C.2}$$

$$\varepsilon_{ij} = \frac{1}{2}\left(u_{i,j} + u_{j,i}\right); \qquad \omega_{ij} = \frac{1}{2}\left(u_{i,j} - u_{j,i}\right) \tag{C.3}$$

with the infinitesimal strain tensor $\boldsymbol{\varepsilon}$, the infinitesimal rotation tensor $\boldsymbol{\omega}$, the stress tensor $\boldsymbol{\sigma}$ and the Kronecker symbol δ_{ij} . The index notation refers to the i^{th}, j^{th} axes in the coordinate system with a comma- and dot-notation denoting a space and time partial-derivative respectively. By substitution into the constitutive Equation C.2, the equations of motion can be written in terms of the displacement field $\mathbf{u}(\mathbf{x},t)$ in vectorial form as:

$$(\lambda + \mu)\nabla(\nabla \cdot \mathbf{u}) + \mu \nabla^2 \mathbf{u} + \rho \mathbf{f} = \rho \ddot{\mathbf{u}} \tag{C.4}$$

which is known as the Navier's equation. Introducing the scalar $\Phi(\mathbf{x},t)$, $F(\mathbf{x})$ and the vector $\mathbf{H}(\mathbf{x},t)$, $\mathbf{B}(\mathbf{x})$ potentials and following a Helmholtz decomposition, the displacement and force fields can be written:

$$\mathbf{u} = \nabla\Phi + \nabla \times \mathbf{H} \qquad \text{with} \quad \nabla \cdot \mathbf{H} = 0 \tag{C.5}$$

$$\mathbf{f} = \nabla F + \nabla \times \mathbf{B} \qquad \text{with} \quad \nabla \cdot \mathbf{B} = 0 \tag{C.6}$$

Substituting the latter expressions into Equation C.4 and neglecting any force field $\mathbf{f}(\mathbf{x})$ present in the medium, after some algebra manipulation [77] we arrive at the two equations:

$$\nabla^2 \Phi = \frac{1}{V_P^2}\ddot{\Phi} \qquad \text{with} \quad V_P = \sqrt{\frac{\lambda + 2\mu}{\rho}} \tag{C.7}$$

$$\nabla^2 \mathbf{H} = \frac{1}{V_S^2}\ddot{\mathbf{H}} \qquad \text{with} \quad V_S = \sqrt{\frac{\mu}{\rho}} \tag{C.8}$$

that represent the propagation of dilatational (Equation C.7) and rotational (Equation C.8) disturbances with speed V_P and V_S respectively, otherwise known as compressional P-waves and shear S-waves. For a plane-wave excitation in the $x-z$ plane the any of the variables in the problem is independent of the coordinate y. Moreover, for such excitation, the displacement field is uniquely defined by the propagation of dilatational waves (P-waves), and rotational waves polarized in the vertical (SV-waves) and horizontal (SH-waves) planes. Based on the plane-wave assumption, the following partial differential equations hold the solution of the problem:

$$\Phi_{,xx}+\Phi_{,zz}=\frac{1}{V_P^2}\ddot{\Phi} \qquad \text{P-waves} \tag{C.9}$$

$$\mathrm{H}_{y,xx}+\mathrm{H}_{y,zz}=\frac{1}{V_S^2}\ddot{\mathrm{H}}_y \qquad \text{SV-waves} \tag{C.10}$$

$$\mathrm{H}_{p,xx}+\mathrm{H}_{p,zz}=\frac{1}{V_S^2}\ddot{\mathrm{H}}_p \quad \text{with } p=x,z \quad \text{and} \quad \mathrm{H}_{x,x}+\mathrm{H}_{z,z}=0 \qquad \text{SH-waves} \tag{C.11}$$

Equations C.9 and C.10 are related to the 2D in-plane wave propagation that is uncoupled from the 2D out-of-plane wave propagation related to Equation C.11. For problems related to ground-borne vibration, the in-plane wave propagation represents better the vibration field generated at the source (i.e. train-line along y axis). For a time-harmonic plane-wave excitation, the relation between the potentials in the time-space and frequency-wavenumber domain can be written as:

$$\begin{aligned}\Phi(x,z,t)&=\tilde{\Phi}(k_x,z,\omega)\,e^{i(\omega t-k_x x)}\\ \mathrm{H}_y(x,z,t)&=\tilde{\mathrm{H}}_y(k_x,z,\omega)\,e^{i(\omega t-k_x x)}\end{aligned} \tag{C.12}$$

with ω the angular frequency of the time-harmonic excitation, k_x the wavenumber along the x axis, and $i=\sqrt{-1}$. By substitution of the latter expressions into the respective Equations C.9 and C.10, the following ordinary differential equations are obtained:

$$(ik_x)^2\,\tilde{\Phi}+\frac{d^2\tilde{\Phi}}{dz^2}+k_P^2\,\tilde{\Phi}=0 \qquad \text{with} \quad k_P=\frac{\omega}{V_P} \tag{C.13}$$

$$(ik_x)^2\,\tilde{\mathrm{H}}_y+\frac{d^2\tilde{\mathrm{H}}_y}{dz^2}+k_S^2\,\tilde{\mathrm{H}}_y=0 \qquad \text{with} \quad k_S=\frac{\omega}{V_S} \tag{C.14}$$

with k_P and k_S the wavenumbers related to the compressional and shear waves respectively. The solution of the latter equations is in the form of incoming and outgoing waves:

$$\tilde{\Phi}(k_x, z, \omega) = A_I\, e^{-ik_{zP}z} + A_R\, e^{ik_{zP}z} \tag{C.15}$$

$$\tilde{\mathrm{H}}_y(k_x, z, \omega) = B_I\, e^{-ik_{zS}z} + B_R\, e^{ik_{zS}z} \tag{C.16}$$

with k_{zP} and k_{zS} the wavenumbers along the z axis for compressional and shear waves respectively. Equations C.15 and C.16 are harmonic solutions in the variable z of the potentials, which refer impicitly to the case $k_x \leq k_P$ and $k_x \leq k_S$ respectively. Substitution of these solutions into the respective C.13 and C.14, excluding the trivial solution related to zero-amplitude waves, gives the dispersion relation for P- and SV-waves as:

$$k_x^2 + k_{zP}^2 = k_P^2 \tag{C.17}$$

$$k_x^2 + k_{zS}^2 = k_S^2 \tag{C.18}$$

The plane-wave propagation problem is then defined for a given horizontal wavenumber k_x in that the vertical wavenumbers can be retrieved from the dispersion relations in Equations C.17 and C.18. Propagation of P- or S-waves in a full-space occupied by a homogeneous, isotropic and elastic material remains undisturbed with an elastic state that relates to the propagating wave. Introducing boundary conditions related to stress and/or displacement fields on a sub-domain of the body results in scattering with the origination of different wave types.

C.2 2D in-plane wave Propagation in a Half-space

An example of boundary condition relates to a plane $z = 0$ being stress-free for the plane-wave excitation previously examined. This is illustrated in Figure 4.2 where P- or SV-waves are impinging the free-surface of a half-space. An incident P-wave, of amplitude A_I, at an angle θ_P is reflected at the free-surface with an outgoing P-wave of amplitude A_R. Moreover, mode conversion occurs in that an outgoing SV-wave at an angle θ_S and an amplitude B_R is originated. Because of the plane-wave assumption, the following relationship between the horizontal wavenumber and the directionality of

the associated P- and SV-wave holds:

$$k_x = k_P \cos\theta_P = k_S \cos\theta_S \tag{C.19}$$

The same argument applies to the alternative case of an incident SV-wave. It is apparent that, in general, for values of $k_x > k_P$ and/or $k_x > k_S$ the associated angle θ_P and/or θ_S are not real-valued. In this case the potentials $\tilde{\Phi}$ and/or $\tilde{\mathrm{H}}_y$ are evanescent functions along the z axis. For instance, an evanescent potential $\tilde{\Phi}$ along the z axis is obtained when considering an incident SV-wave at $\theta_S < \theta_S^{(c)}$. The latter is called *critical angle* and satisfies the condition $\gamma_P \cos\theta_S^{(c)} = 1$ with $\gamma_P = V_P/V_S$. The critical angle assumes the value of $\pi/3$ for the soil properties in Table 3.1. In general, the values to be assigned to k_{zP} and k_{zS} and used in Equations C.15 and C.16 may be summarised as in Table C.1.

P-wave		SV-wave	
$k_x \leq k_P$	$k_x > k_P$	$k_x \leq k_S$	$k_x > k_S$
$k_{zP} = \sqrt{k_P^2 - k_x^2}$	$k_{zP} = -i\sqrt{k_x^2 - k_P^2}$	$k_{zS} = \sqrt{k_S^2 - k_x^2}$	$k_{zS} = -i\sqrt{k_x^2 - k_S^2}$
or $k_{zP} = k_P \sin\bar{\theta}_P$		or $k_{zS} = k_S \sin\bar{\theta}_S$	
$\bar{\theta}_P = \theta_P$	$\bar{\theta}_P = -\theta_P$	$\bar{\theta}_S = \theta_S$	$\bar{\theta}_S = \theta_S$

Table C.1 Values of the vertical wavenumbers k_{zP} and k_{zS} to be used in Equations C.15 and C.16 depending on the value of the horizontal wavenumber k_x with respect to k_P and k_S. The angle of P- and SV-waves θ_P and θ_S are obtained from Equation C.19 for a given value of k_x.

C.2.1 The case of incident P- or SV-waves

For the case of incident plane P- or SV-waves at an angle θ_P or θ_S, the horizontal wavenumber k_x is uniquely defined by Equation C.19. Consequently, the vertical wavenumbers can be found from Table C.1 and the solution can be obtained, in terms of potentials, from Equations C.15 and C.16 for the incident wave-amplitude A_I or B_I, the reflected wave-amplitude A_R or B_R and the originated amplitude B_R or A_R. By imposing the free-stress condition at the free-surface of the half-space ($z = 0$), one can obtain the reflected and originated amplitudes in terms of the incident P- or SV- incident wave:

- Case of incident P-wave

$$\frac{A_R}{A_I} = \frac{\sin 2\bar{\theta}_P \sin 2\bar{\theta}_S - \gamma_P^2 \cos^2 2\bar{\theta} a_S}{\sin 2\bar{\theta}_P \sin 2\bar{\theta}_S + \gamma_P^2 \cos^2 2\bar{\theta}_S} \tag{C.20a}$$

$$\frac{B_R}{A_I} = \frac{2 \sin 2\bar{\theta}_P \cos 2\bar{\theta}_S}{\sin 2\bar{\theta}_P \sin 2\bar{\theta}_S + \gamma_P^2 \cos^2 2\bar{\theta}_S} \tag{C.20b}$$

- Case of incident SV-wave

$$\frac{B_R}{B_I} = \frac{\sin 2\bar{\theta}_P \sin 2\bar{\theta}_S - \gamma_P^2 \cos^2 2\bar{\theta}_S}{\sin 2\bar{\theta}_P \sin 2\bar{\theta}_S + \gamma_P^2 \cos^2 2\bar{\theta}_S} \tag{C.21a}$$

$$\frac{A_R}{B_I} = -\frac{\gamma_P^2 \sin 4\bar{\theta}_S}{\sin 2\bar{\theta}_P \sin 2\bar{\theta}_S + \gamma_P^2 \cos^2 2\bar{\theta}_S} \tag{C.21b}$$

Our interest remains the vibration field generated by such wave propagation at the free-surface. This can be obtained in terms of displacements $\tilde{\mathbf{u}}_\mathbf{0} = [\tilde{u}_0 \; \tilde{w}_0]$ in the frequency-wavenumber domain by consideration of Equation C.5:

- Case of incident P-wave

$$\frac{\tilde{u}_0}{-ik_P A_I} = \cos\bar{\theta}_P \left(1 + \frac{A_R}{A_I}\right) - \gamma_P \sin\bar{\theta}_S \frac{B_R}{A_I} \tag{C.22a}$$

$$\frac{\tilde{w}_0}{-ik_P A_I} = \sin\bar{\theta}_P \left(\frac{A_R}{A_I} - 1\right) + \cos\bar{\theta}_P \frac{B_R}{A_I} \tag{C.22b}$$

- Case of incident SV-wave

$$\frac{\tilde{u}_0}{-ik_P B_I} = \cos\bar{\theta}_P \frac{A_R}{B_I} + \gamma_P \sin\bar{\theta}_S \left(1 - \frac{B_R}{B_I}\right) \tag{C.23a}$$

$$\frac{\tilde{w}_0}{-ik_P B_I} = \sin\bar{\theta}_P \frac{A_R}{B_I} + \cos\bar{\theta}_P \left(1 + \frac{B_R}{B_I}\right) \tag{C.23b}$$

C.2.2 The case of Rayleigh waves

For a homogeneous, linear-elastic, isotropic half-space an additional type of wave exists, which is confined closely to the free-surface. This was first investigated by Rayleigh [79], who obtained a characteristic equation and the travelling wave speed for such waves. The effects of Rayleigh waves decrease rapidly with depth and their velocity of propagation is smaller than that of body waves,

which depends only on Poisson's ratio. This type of wave relates to the free-boundary condition of the half-space, thus they arise further away from the source (i.e. far-field). Because of their evanescent nature along the z axis, both the dilatational $\tilde{\Phi}$ and rotational $\tilde{\mathrm{H}}_y$ potential are evanescent and the conditions $k_x > k_P$ and $k_x > k_S$ apply with the outgoing waves of amplitude A_R and B_R. The free-stress condition can be written as:

$$\begin{cases} k_P^2 \sin 2\bar{\theta}_P A_R + k_S^2 \cos 2\bar{\theta}_S B_R = 0 \\ \cos 2\bar{\theta}_S A_R - \sin 2\bar{\theta}_S B_R = 0 \end{cases} \tag{C.24}$$

Solving the system in Equation C.24, the following non-trivial solution is obtained:

$$\sin 2\bar{\theta}_P \sin 2\bar{\theta}_S + \gamma_P^2 \cos^2 2\bar{\theta}_S = 0 \tag{C.25}$$

The latter is the denominator of Equations C.20 and C.21, which indicates Rayleigh waves may be thought as the "*natural mode*" of the homogeneous and elastic half-space. The displacement vector in the frequency-wavenumber domain associated to a Rayleigh wave can be found as:

$$\frac{\tilde{u}_0}{-ik_S A_R} = \frac{1}{2\cos\bar{\theta}_S} \tag{C.26a}$$

$$\frac{\tilde{w}_0}{-ik_S A_R} = \frac{\sin\bar{\theta}_P}{\gamma_P} + \frac{\cos 2\bar{\theta}_S}{2\sin\bar{\theta}_S} \tag{C.26b}$$

Retrieving the Rayleigh wave velocity V_R for the homogeneous half-space from the characteristic equation of Rayleigh [79] or from simplified expressions suggested by different authors [77, 78], the horizontal wavenumber associated with a travelling Rayleigh wave is $k_x = k_R = \omega/V_R$. From Equation C.19, θ_P and θ_S can be obtained as the complex angles associated with the evanescent potentials $\tilde{\Phi}$ and $\tilde{\mathrm{H}}_y$ respectively. The displacement-field with the amplitude as in Equation C.26 is characterised by a retrograde elliptical particle motion at the free-surface with out-of-phase horizontal and vertical motion. A value of $\tilde{w}_0 \approx 1.5\,\tilde{u}_0$ is obtained for $\nu = 1/3$.

C.3 Stiffness matrix formulation

Horizontal layering may be reduced to stress and/or displacement boundary conditions at $z = \bar{z}$ in the full-space for which the governing equations in Section C.1 hold. This is done in the *stiffness*

matrix method [189, 194] where a relation between tractions and displacement at one (i.e. halfspace) or two (i.e. layer) horizontal planes is obtained by cancellation of the unknown wave-amplitudes. The formulation is in the frequency-wavenumber domain and, because of the plane-wave assumption, variables in the time-space domain may be obtained by similar expressions to Equation C.12. From the governing equations the displacement vector can be written as:

$$\begin{aligned}\tilde{\mathbf{u}}(k_x,z,\omega) = \begin{bmatrix}\tilde{u}\\ \tilde{w}\end{bmatrix} &= \begin{bmatrix}\cos\bar{\theta}_P & \sin\bar{\theta}_S\\ -\sin\bar{\theta}_P & \cos\bar{\theta}_S\end{bmatrix}\begin{bmatrix}e^{ik_P\sin\bar{\theta}_P z} & 0\\ 0 & e^{ik_S\sin\bar{\theta}_S z}\end{bmatrix}\begin{bmatrix}-ik_P A_I\\ -ik_S B_I\end{bmatrix} +\\ &+\begin{bmatrix}\cos\bar{\theta}_P & -\sin\bar{\theta}_S\\ \sin\bar{\theta}_P & \cos\bar{\theta}_S\end{bmatrix}\begin{bmatrix}e^{-ik_P\sin\bar{\theta}_P z} & 0\\ 0 & e^{-ik_S\sin\bar{\theta}_S z}\end{bmatrix}\begin{bmatrix}-ik_P A_R\\ -ik_S B_R\end{bmatrix} =\\ &= \mathbf{R_I}\,\mathbf{E_z^I}\,\mathbf{a_I} + \mathbf{R_R}\,\mathbf{E_z^R}\,\mathbf{a_R} =\\ &= \begin{bmatrix}\mathbf{R_I} & \mathbf{R_R}\end{bmatrix}\begin{bmatrix}\mathbf{E_z^I} & \mathbf{0}\\ \mathbf{0} & \mathbf{E_z^R}\end{bmatrix}\begin{bmatrix}\mathbf{a_I}\\ \mathbf{a_R}\end{bmatrix} = \mathbf{R}\,\mathbf{E_z}\,\mathbf{a}\end{aligned} \tag{C.27}$$

In order to obtain symmetric matrices a change of variable is performed [194] obtaining a reduced displacement vector:

$$\tilde{\mathbf{u}} = \begin{bmatrix}\tilde{\mathrm{u}}_x\\ \tilde{\mathrm{u}}_z\end{bmatrix} = \begin{bmatrix}\tilde{u}\\ i\,\tilde{w}\end{bmatrix} = \begin{bmatrix}1 & 0\\ 0 & i\end{bmatrix}\tilde{\mathbf{u}} = \mathbf{T_u}\,\tilde{\mathbf{u}} \tag{C.28}$$

The strain vector related to the plane-wave assumption can be retrieved from Equation C.3:

$$\begin{aligned}\tilde{\boldsymbol{\epsilon}} = \begin{bmatrix}\tilde{\varepsilon}_{xx}\\ \tilde{\varepsilon}_{zz}\\ \tilde{\gamma}_{xz}\end{bmatrix} &= \begin{bmatrix}-ik_P\cos^2\bar{\theta}_P & -ik_S\cos\bar{\theta}_S\sin\bar{\theta}_S\\ -ik_P\sin^2\bar{\theta}_P & ik_S\cos\bar{\theta}_S\sin\bar{\theta}_S\\ ik_P\sin 2\bar{\theta}_P & -ik_S\cos 2\bar{\theta}_S\end{bmatrix}\mathbf{E_z^I}\,\mathbf{a_I} +\\ &+\begin{bmatrix}-ik_P\cos^2\bar{\theta}_P & ik_S\cos\bar{\theta}_S\sin\bar{\theta}_S\\ -ik_P\sin^2\bar{\theta}_P & -ik_S\cos\bar{\theta}_S\sin\bar{\theta}_S\\ -ik_P\sin 2\bar{\theta}_P & -ik_S\cos 2\bar{\theta}_S\end{bmatrix}\mathbf{E_z^R}\,\mathbf{a_R} = \mathbf{S_I}\,\mathbf{E_z^I}\,\mathbf{a_I} + \mathbf{S_R}\,\mathbf{E_z^R}\,\mathbf{a_R} = \mathbf{S}\,\mathbf{E_z}\,\mathbf{a}\end{aligned} \tag{C.29}$$

The stress vector related to the plane-wave assumption can be retrieved from Equation C.2:

$$\tilde{\boldsymbol{\sigma}} = \begin{bmatrix} \tilde{\sigma}_{xx} \\ \tilde{\sigma}_{zz} \\ \tilde{\sigma}_{xz} \end{bmatrix} = \begin{bmatrix} \lambda + 2\mu & \lambda & 0 \\ \lambda & \lambda + 2\mu & 0 \\ 0 & 0 & \mu \end{bmatrix} \tilde{\boldsymbol{\epsilon}} = \mathbf{Q}\,\tilde{\boldsymbol{\epsilon}} \tag{C.30}$$

As for the displacement, we refer to a reduced stress vector:

$$\tilde{\boldsymbol{\sigma}} = \begin{bmatrix} \tilde{\sigma}_{xx} \\ \tilde{\sigma}_{zz} \end{bmatrix} = \begin{bmatrix} \tilde{\sigma}_{xz} \\ i\,\tilde{\sigma}_{zz} \end{bmatrix} = \begin{bmatrix} 0 & 0 & 1 \\ 0 & i & 0 \end{bmatrix} \tilde{\boldsymbol{\sigma}} = \mathbf{T}_{\boldsymbol{\sigma}}\,\mathbf{Q}\,\tilde{\boldsymbol{\epsilon}} \tag{C.31}$$

C.3.1 Half-space

Let us re-consider the case of incident waves of amplitude $\mathbf{a_I}$ as in Section C.2.1. The problem can be equivalently approached by imposing the free-stress condition on the plane $z = 0$ making reference to Equation C.31:

$$\begin{aligned} -\tilde{\boldsymbol{\sigma}}|_{z=0} = \mathbf{0} \quad &\Leftrightarrow \quad -\mathbf{T}_{\boldsymbol{\sigma}}\,\mathbf{Q}\,\tilde{\boldsymbol{\epsilon}}|_{z=0} = -\mathbf{T}_{\boldsymbol{\sigma}}\,\mathbf{Q}\left[\mathbf{S_I}\,\mathbf{E}^{\mathbf{I}}_{\mathbf{z}}|_{z=0}\,\mathbf{a_I} + \mathbf{S_R}\,\mathbf{E}^{\mathbf{R}}_{\mathbf{z}}|_{z=0}\,\mathbf{a_R}\right] = \mathbf{0} \\ &\therefore \quad -\mathbf{T}_{\boldsymbol{\sigma}}\,\mathbf{Q}\,\mathbf{S_I}\,\mathbf{a_I} = \mathbf{T}_{\boldsymbol{\sigma}}\,\mathbf{Q}\,\mathbf{S_R}\,\mathbf{a_R} \\ &\therefore \quad \mathbf{a_R} = -\left[\mathbf{T}_{\boldsymbol{\sigma}}\,\mathbf{Q}\,\mathbf{S_R}\right]^{-1}\left[\mathbf{T}_{\boldsymbol{\sigma}}\,\mathbf{Q}\,\mathbf{S_I}\right]\mathbf{a_I} \end{aligned} \tag{C.32}$$

Although the result is conceptually equivalent to what obtained in Equations C.20 and C.21, it refers to the reduced stress and displacement vectors $\tilde{\boldsymbol{\sigma}}, \tilde{\mathbf{u}}$. The free-surface wave-field in terms of displacement, equivalently to Equation , can be obtained as:

$$\tilde{\mathbf{u}}_{\mathbf{0}} = \mathbf{T_u}\,\tilde{\mathbf{u}}|_{z=0} = \mathbf{R}\,\mathbf{a} \quad \Longrightarrow \quad \tilde{\mathbf{u}}_{\mathbf{0}} = [\mathbf{T_u}]^T\,\mathbf{R}\,\mathbf{a} \tag{C.33}$$

with $\tilde{\mathbf{u}}_{\mathbf{0}}$ equivalent to the one obtained in Equations C.22 and C.23.

The dynamic stiffness matrix for the half-space element refers tractions and displacement vectors at the free-surface in the reduced form as in Equations C.31 and C.28. The half-space responds to a disturbance at the free-surface with outgoing waves of amplitudes $\mathbf{a_R}$. The displacement and traction

vectors related to the outgoing wave-amplitude vector can be written as:

$$\tilde{\mathbf{u}}^e = \mathbf{T_u}\tilde{\mathbf{u}}|_{z=0} = \mathbf{T_u}\,\mathbf{R_R}\,\mathbf{a_R} \tag{C.34}$$

$$\tilde{\mathbf{t}}^e = -\tilde{\boldsymbol{\sigma}}|_{z=0} = -\mathbf{T_\sigma}\,\mathbf{Q}\,\tilde{\boldsymbol{\epsilon}}|_{z=0} = -\mathbf{T_\sigma}\,\mathbf{Q}\,\mathbf{S_R}\,\mathbf{a_R} \tag{C.35}$$

Eliminating the unknown wave-amplitude $\mathbf{a_R}$, the following dynamic stiffness matrix $\tilde{\mathbf{K}}^e$ of the half-space is obtained:

$$\tilde{\mathbf{t}}^e = -\mathbf{T_\sigma}\,\mathbf{Q}\,\mathbf{S_R}\left[\mathbf{T_u}\,\mathbf{R_R}\right]^{-1}\tilde{\mathbf{u}}^e = \tilde{\mathbf{K}}^e\,\tilde{\mathbf{u}}^e \tag{C.36}$$

C.3.2 Layer

Similarly to what seen for the half-space, the dynamic stiffness matrix of a layer with thickness h can be obtained by seeking a relationship between traction and displacement vectors. The layer displacement vector $\tilde{\mathbf{t}}^e = \begin{bmatrix}\tilde{\mathbf{u}}|_{z=h} & \tilde{\mathbf{u}}|_{z=0}\end{bmatrix}^T$ collects the displacements at $z=h$ and $z=0$, and it is equal to:

$$\begin{aligned}\tilde{\mathbf{u}}^e = \begin{bmatrix}\tilde{\mathbf{u}}_1^e\\ \tilde{\mathbf{u}}_2^e\end{bmatrix} &= \begin{bmatrix}\mathbf{T_u}\,\mathbf{R_I}\,\mathbf{E_z^I}|_{z=h} & \mathbf{T_u}\,\mathbf{R_R}\,\mathbf{E_z^R}|_{z=h}\\ \mathbf{T_u}\,\mathbf{R_I}\,\mathbf{E_z^I}|_{z=0} & \mathbf{T_u}\,\mathbf{R_R}\,\mathbf{E_z^R}|_{z=0}\end{bmatrix}\begin{bmatrix}\mathbf{a_I}\\ \mathbf{a_R}\end{bmatrix} =\\ &= \begin{bmatrix}\mathbf{T_u} & \mathbf{0}\\ \mathbf{0} & \mathbf{T_u}\end{bmatrix}\begin{bmatrix}\mathbf{R_I}\,\mathbf{E_h^I} & \mathbf{R_R}\,\mathbf{E_h^R}\\ \mathbf{R_I} & \mathbf{R_R}\end{bmatrix}\begin{bmatrix}\mathbf{a_I}\\ \mathbf{a_R}\end{bmatrix}\end{aligned} \tag{C.37}$$

Similarly, the layer traction vector $\tilde{\mathbf{t}}^e = \begin{bmatrix}\tilde{\boldsymbol{\sigma}}|_{z=0} & -\tilde{\boldsymbol{\sigma}}|_{z=0}\end{bmatrix}^T$ collects the traction vector at $z=h$ and $z=0$ and can be written as:

$$\begin{aligned}\tilde{\mathbf{t}}^e = \begin{bmatrix}\tilde{\mathbf{t}}_1^e\\ \tilde{\mathbf{t}}_2^e\end{bmatrix} &= \begin{bmatrix}\mathbf{T_\sigma}\,\mathbf{Q} & \mathbf{0}\\ \mathbf{0} & -\mathbf{T_\sigma}\,\mathbf{Q}\end{bmatrix}\begin{bmatrix}\mathbf{S_I}\,\mathbf{E_z^I}|_{z=h} & \mathbf{S_R}\,\mathbf{E_z^R}|_{z=h}\\ \mathbf{S_I}\,\mathbf{E_z^I}|_{z=0} & \mathbf{S_R}\,\mathbf{E_z^R}|_{z=0}\end{bmatrix}\begin{bmatrix}\mathbf{a_I}\\ \mathbf{a_R}\end{bmatrix} =\\ &= \begin{bmatrix}\mathbf{T_\sigma}\,\mathbf{Q} & \mathbf{0}\\ \mathbf{0} & -\mathbf{T_\sigma}\,\mathbf{Q}\end{bmatrix}\begin{bmatrix}\mathbf{S_I}\,\mathbf{E_h^I} & \mathbf{S_R}\,\mathbf{E_h^R}\\ \mathbf{S_I} & \mathbf{S_R}\end{bmatrix}\begin{bmatrix}\mathbf{a_I}\\ \mathbf{a_R}\end{bmatrix}\end{aligned} \tag{C.38}$$

By elimination of the unknown wave-amplitude vector $\mathbf{a}$, the following dynamic stiffness matrix $\tilde{\mathbf{K}}^e$ of the layer is obtained:

$$\tilde{\mathbf{t}}^e = \begin{bmatrix} \mathbf{T_\sigma Q} & \mathbf{0} \\ \mathbf{0} & -\mathbf{T_\sigma Q} \end{bmatrix} \begin{bmatrix} \mathbf{S_I E_h^I} & \mathbf{S_R E_h^R} \\ \mathbf{S_I} & \mathbf{S_R} \end{bmatrix} \left\{ \begin{bmatrix} \mathbf{T_u} & \mathbf{0} \\ \mathbf{0} & \mathbf{T_u} \end{bmatrix} \begin{bmatrix} \mathbf{R_I E_h^I} & \mathbf{R_R E_h^R} \\ \mathbf{R_I} & \mathbf{R_R} \end{bmatrix} \right\}^{-1} \tilde{\mathbf{u}}^e \tag{C.39}$$

$$\therefore \quad \tilde{\mathbf{t}}^e = \tilde{\mathbf{K}}^e \tilde{\mathbf{u}}^e$$